AN INVESTIGATION OF HEAT TRANSFER ENHANCEMENT DUE TO PULSED FLOW IN MINICHANNELS

PARTH S. KUMAVAT

Department of Mechanical, Manufacturing and Biomedical Engineering

Parsons Building

University of Dublin, Trinity College

Dublin 2

Ireland

January 2023

A thesis submitted to the University of Dublin in partial fulfilment of the requirements for the degree of Ph. D.

Declaration

I declare that this thesis has not been submitted as an exercise for a degree at this or any other university and it is entirely my own work.

I agree to deposit this thesis in the University's open access institutional repository or allow the library to do so on my behalf, subject to Irish Copyright Legislation and Trinity College Library conditions of use and acknowledgement. I consent to the examiner retaining a copy of the thesis beyond the examining period, should they so wish (EU GDPR May 2018).

Parth S. Kumavat, January 2023

Abstract

The development of current and next generation high performance electronic devices has led to smaller components in more densely packed spaces. The increasing power levels has resulted in ever-increasing heat flux densities which necessitates the evolution of new liquid-based heat exchange technologies. Pulsating flow in single-phase cooling systems is viewed as a potential solution to the problems involving high heat flux densities. A comprehensive review of literature indicates a lack of time-resolved and space-resolved investigations of unsteady flows on heat transfer resulting from the disruption of hydrodynamic and thermal boundary layers associated with pulsating flows. This study aims to bridge the knowledge gap by using experimental and computational methods to investigate the complex flow characteristics of laminar pulsating flows in a heated rectangular minichannel, and couple that analysis with an investigation of the heat transfer performance. Local time and space dependent distributions and spatial distributions of hydrodynamic and thermal characteristics are discussed by focussing on the hydrodynamically and thermally fully developed region of the minichannel. A wide parameter space is investigated with variations of pulsation waveforms, associated frequency and flow rate amplitudes. Experimental analysis involves a uniformly heated thin foil approximating a constant heat flux bottom wall. Local, non-intrusive and high spatial resolution spatial measurements of the heated surface are recorded using an infrared thermography system. Analogous to the experimental conditions, a three-dimensional conjugate heat transfer computational model is developed. A volumetric heat generation source is imposed on the solid domain. Results for the axial velocity profile in response to a symmetric sinusoidal flowrate waveform showed that a parabolic shape was attained, typical of laminar flow. At low, frequency the oscillating velocity profiles was in phase with the axial pressure gradient and bottom wall shear stress. However, as frequency increases, the peaks in the velocity profiles are shifted to the near wall vicinity and there is clear evidence of phase lag between the flowrate and axial pressure gradients as the bulk inertial forces are strengthened. Certain cases of asymmetric sinusoidal and half rectified flowrate waveforms presents evidence of the flow reversal phenomenon in the near wall regions. Consequently, the flow reversal effect promotes the heat transfer as stronger diffusion of heat from wall to bulk region takes place. A greater rise in the

friction factor is determined for the non-conventional waveforms Oscillating wall temperature profiles present peak magnitudes in the near wall vicinity for moderate to high frequency range and similar behaviour exists for the oscillating velocities. The space averaged Nusselt number increased with the corresponding rise in the flowrate amplitudes which correlates to stronger, enhanced convection effects. There exists an optimum band of frequencies which reflect enhancements in the time-space averaged heat transfer, whereas the other frequencies show a deterioration. Thus, the moderate-high frequency pulsating flows of all waveforms studied, present an appreciable heat transfer enhancement over the steady flows with a satisfactory thermal performance factor.

Acknowledgements

This work would not have been possible without the immense support and guidance of the following essential people. I would at first like to thank my supervisor Dr. Séamus O'Shaughnessy for his attention to detail and offering crucial contributions throughout till the last minute. I would like to thank Dr. Sajad Alimohammadi for his guidance and extensive support with the computational analysis. Special mention to Emer Prof. Darina Murray for sharing her exceptional knowledge on the subject of heat transfer and her enthusiasm towards challenges that I initially faced. I would like to further extend thanks to Dr. Tim Persoons and Dr. Tony Robinson for their support and direction in the initial stages.

My deepest gratitude goes to Gerry Byrne for his experience and assistance with tackling experimental hurdles. I would like to thank Michael Reilly, Gordon O'Brien for their support with the challenges faced in the designing phase and for accommodating my machining requests timely. Thanks to the workshop team of Rob, Alex, Brendan for providing essential tips and precisely fabricating the components. I'm grateful to Paul Normoyle for his extensive assistance throughout the setup of control systems. Further I would like to thank our head of department, Prof. Ciaran Simms for extending his support during the hard pandemic stage. I immensely appreciate the financial support grant from the School of Engineering and HEA towards the execution of this research. I'm grateful to the Trinity College Center for High Performance Computing and the Irish Center for High End Computing for their support and facilities to aid the computations.

To my colleagues and friends in the department, thank you for their advice and enriching my time at Trinity. Thanks to Dr. Richard, Dr. Jaakko, Dr. Michael and Dr. Nico for their crucial tips with the project. Thanks to Kevin, Dominik, Bobby, Pengfei, Shi, Robi, Clara, Daniel, Morgane, Karina, Aggie, Eoghan and Fazeel. Special thanks to Niall and Paula for equal amounts of entertainment and consultations. Note of mention to Yiming for lending his share of those essential high performance computing hours. Further thanks to my desi friends around for putting up with me and offering their unwavering support: Soumya, Sushant, Mitya, Omzy, Pradnya, Oshin, Anush, Abhinav and Shivani. Special thanks to Sally for offering all sorts of technical support. Last but certainly not least, I would like to thank my family: Mummy, Papa. I would not have made this far without your support and for encouraging me throughout my life. Special thanks to my grandparents (miss you dada), cousins and close relatives for offering their constant love and blessings. It will never be possible for me to express my gratitude for all that you have done for me.

Table of Contents

List of Figures

List of Tables

Nomenclature

Symbol	Description	Unit
$a,2b$	Channel height, width	*[m]*
c_p	Specific heat capacity	*[J/kg.K]*
D_h	Hydraulic diameter	*[m]*
f	Pulsation frequency	*[Hz]*
g	Gravitational acceleration	*[m/s^2]*
h	Heat transfer coefficient	*[W/m^2.K]*
I	Current	*[A]*
k	Thermal conductivity	*[W/m.K]*
L	Channel length	*[m]*
L_e	Hydrodynamic entry length	*[m]*
L_{th}	Thermal entry length	*[m]*
$\dot{m}$	Mass flow rate	*[kg/s]*
P	Pressure	*[Pa]*
∇P	Pressure gradient	*[Pa/m]*
Q	Flow rate	*[m^3/s]*
q	Heat flux	*[W/m^2]*
q_{cap}	Capacitive heat flux component	*[W/m^2]*
q_{cond}	Air gap conductive heat flux component	*[W/m^2]*

q_{conv}	Convective heat flux component	*[W/m²]*
q_{gen}	Generated heat flux component	*[W/m²]*
q_{lc}	Lateral conduction heat flux component	*[W/m²]*
q_{rad}	Radiation heat flux component	*[W/m²]*
$\dot{q_{gen}}$	Heat generated	*[W/m³]*
R	Resistance	*[Ω]*
t	Time	*[s]*
T	Temperature	*[K]*
u	Axial velocity component	*[m/s]*
V	Voltage	*[V]*
w	Foil thickness	*[m]*
x	Transverse coordinate direction	*[m]*
y	Vertical coordinate direction	*[m]*
z	Axial coordinate direction	*[m]*

Dimensionless Numbers	**Description**	**Unit**
Ar	Archimedes number	*[-]*
A_0	Flow rate amplitude	*[-]*
F_n	Dimensionless pulsation frequency	*[-]*
F_0	Dimensionless fluid displacement amplitude	*[-]*
Gr	Grashof number	*[-]*
Nu	Nusselt number	*[-]*
Pr	Prandtl number	*[-]*
P_o	Pressure gradient amplitude	*[-]*
Ra	Rayleigh number	*[-]*

Re	Reynolds number	*[-]*
Re_{tot}	Total Reynolds number	*[-]*
Re_{max}	Maximum Reynolds number	*[-]*
Re_{osc}	Oscillating Reynolds number	*[-]*
Re_p	Pulsating Reynolds number	*[-]*
St	Strouhal number	*[-]*
Wo	Womersley number	*[-]*

Greek Symbols	**Description**	**Unit**
α	Thermal diffusivity	$[m^2/s]$
ω	Angular oscillation frequency	$[rad/s]$
μ	Dynamic viscosity	$[kg/ms]$
ν	Kinematic viscosity	$[m^2/s]$
ρ	Density	$[kg/m^3]$
θ	Oscillatory phase	*[rad]*
χ	Axial displacement	*[-]*
σ	Darcy friction factor	*[-]*
τ	Bottom wall shear stress	*[Pa]*
λ	Pulsating time period	*[s]*
δ_v	Stokes layer thickness	*[m]*
η	Heat transfer performance	*[-]*

Subscripts	**Description**	**Unit**
b	Bulk fluid property	*[-]*
In	Channel inlet	*[-]*

Out	Channel out	*[-]*
max	Maximum component	*[-]*
min	Minimum component	*[-]*
m	Mean component	*[-]*
N	Normalized value	*[-]*
osc	Oscillating component	*[-]*
P	Pulsating component	*[-]*
S	Steady component	*[-]*
w	Wall property	*[-]*

Other symbols	**Description**	**Unit**
$\|A\|$	Space averaged component	*[-]*
$\bar{A}$	Time averaged component	*[-]*
A_{osc}	Oscillating component	*[-]*
A_p	Pulsating component	*[-]*
A_s	Steady component	*[-]*
A_N	Normalized component	*[-]*

Publications

- **Conferences:**
  - P. S. Kumavat, S. Alimohammadi, and S. M. O'Shaughnessy, "Heat Transfer Enhancement In A Minichannel Due To Asymmetric Sinusoidal Pulsating Flows," in *2022 28th International Workshop on Thermal Investigations of ICs and Systems (THERMINIC)*, 2022, pp. 1–6.
  - P. Kumavat and S. M. O'Shaughnessy, "Experimental Investigation of Heat Transfer Enhancement by Pulsating Flow in a Minichannel," *J. Phys. Conf. Ser.*, vol. 2116, no. 1, p. 012031, Nov. 2021.
  - P. Kumavat, R. Blythman, D. B. Murray, and S. M. O'Shaughnessy, "Experimental Study Of Heat Transfer Enhancement By Pulsating Flow In A Rectangular Minichannel," *Proceedings of the 14th International Conference on Heat Transfer, Fluid Mechanics and Thermodynamics*, Dublin, 2019, pp. 663-68.
- **Journals:**
  - P. S. Kumavat, S. Alimohammadi, and S. M. O'Shaughnessy, "An experimental-numerical study of heat transfer enhancement in a minichannel using asymmetric pulsating flows," *IEEE Trans. Components, Packag. Manuf. Technol.*, p. 1, 2023, doi: 10.1109/TCPMT.2023.3299085.
  - P. S. Kumavat, S. Alimohammadi, and S. M. O'Shaughnessy, "A computational conjugate heat transfer study of a rectangular minichannel undergoing sinusoidal flow pulsations," *Int. J. Therm. Sci.*, vol. 182, p. 107790, 2022.
- **Book Chapter:**
  - P. S. Kumavat, R. Blythman, D. B. Murray, and S. M. O'Shaughnessy, "Study of Heat Transfer Enhancement by Pulsating Flow in a Rectangular Mini Channel," in *Advances in Heat Transfer and Thermal Engineering*, 2021, pp. 253–257.

1) Introduction

1.1 Overview of liquid cooling systems

Moore's law projects the integration density of integrated photonic circuits and microprocessor units to double every 18-24 months [1], which since the early 60s, has resulted in a near constant evolution in the information-technology sector with regard to electronics cooling solutions. Although significant progress has been made it is now well known that Moore's law is approaching the upper limits of suitable technology and economy [2]. One of the main challenges predicted in power electronics and microchip industries is the effective removal of high heat fluxes of up to 300 W/cm^2 while retaining the component temperatures below 85$^{\circ}C$. This challenge is complicated by increasingly constricted component spaces and an ever-increasing demand for heat dissipation [3].

Conventional air-cooled systems are no longer seen as effective. With the increase of heat flux beyond 100 W/cm^2, air cooling methods were determined to be inefficient for most cooling applications [4]. Therefore, liquid cooled systems are viewed as being suitable for handling high-power heat dissipation applications. Water is typically used as a coolant for convection cooling since it exhibits greater cooling capacity than that of air. For example, liquid cooling systems have been employed to control battery temperatures during periods of fast charging or for use in extreme climate conditions [5]. Another implementation of liquid cooling in data centres uses naturally cooled water from lakes or the sea, which reduces the need for water chillers in data centres and reduces overall energy consumption. Presently, several types of rack-level liquid-cooling solutions are employed in order to retain liquid refrigerants closer to servers [6], an example shown in Figure 1-1.

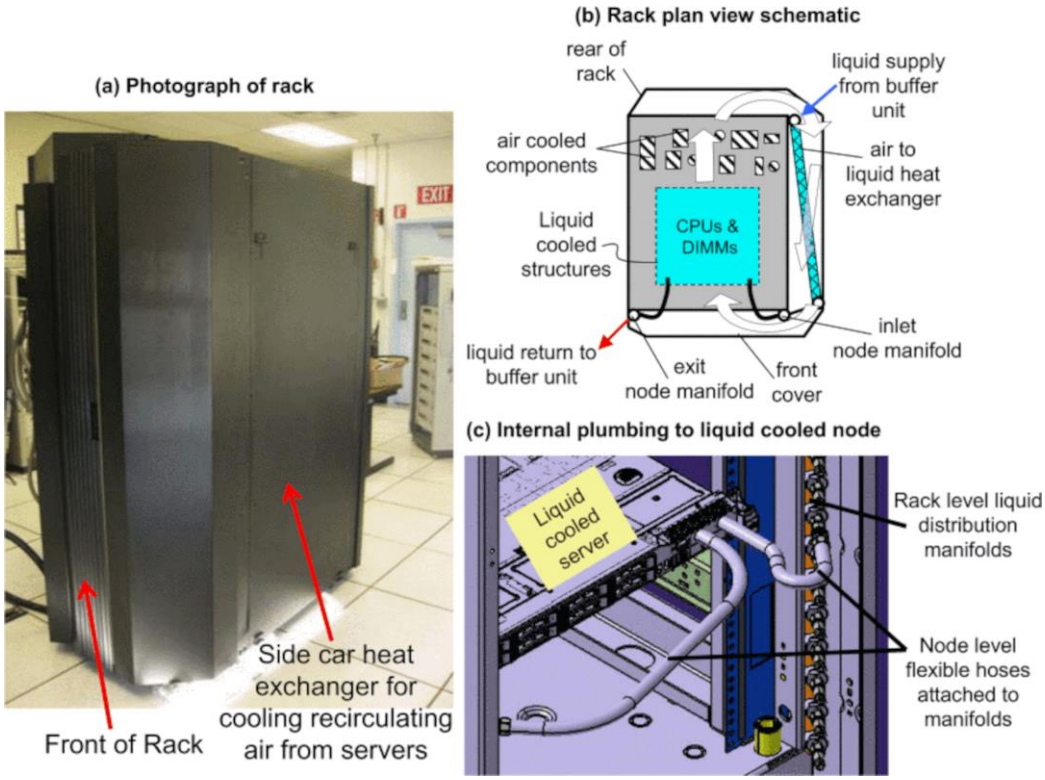

Figure 1-1: Server rack liquid cooling design [7]

The miniaturization of electronics packages and their associated high-power density circuits requires ever more innovative cooling solutions. Two viable options exist for liquid cooling technology: single-phase cooling and two-phase cooling. Two-phase systems exploit the latent energy of phase-change to dissipate heat, such as studies of boiling in mini-channels [3]. However, owing to the high pressure drop and complexity involved with two-phase cooling, single phase liquid cooling technology using micro-pumping mechanisms is considered the preferred option for many applications [5, 8–10]. Indeed, microfluidic liquid cooling, which typically consists of a liquid pumped through several small channels positioned near the heat source, is now viewed as a plausible solution. As an example, in a study by Tang *et al.* [9], shown in Figure 1-2, microelectronic devices designed for high power chips to be operated in high performance servers and amplifiers have demonstrated high operating efficiency and enhanced performance. A heat dissipation capability of 350 W/cm^2 on a chip size of 7 *mm* x 7 *mm* under 0.1 *W* pumping power was attained using a single-phase liquid cooling system consisting of a silicon-based hybrid micro-cooler embedded with multiple drainage micro-trenches (MDMT) and a liquid-liquid heat exchanger.

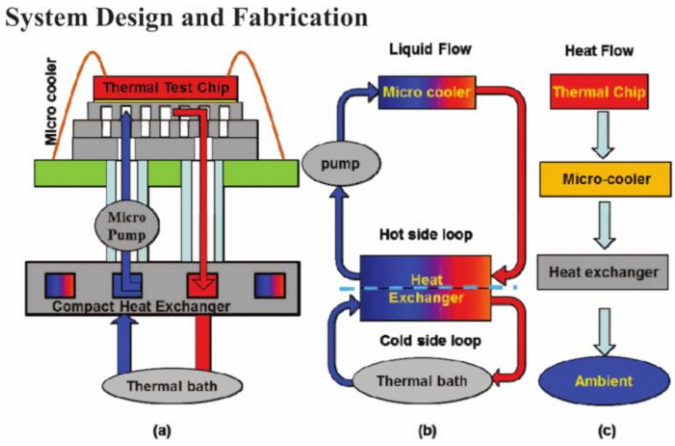

Figure 1-2: Schematic of compact liquid cooling system as used by Tang *et al.* (a) concept design of system, (b) liquid flow paths, (c) heat flow path [9]

The suitability of microchannel heat sinks to electronics cooling is their compact size, as is illustrated in Figure 1-3. Minimizing the pumping requirements is also essential to optimize the performance of microchannel heat sinks. Micropumps can be integrated with optoelectronics packages with considerations of compactness, reliability and energy efficiency. Pumping mechanisms still remain an active area of research due to increasing space constraints and pumping requirements to produce the desired cooling rates [11].

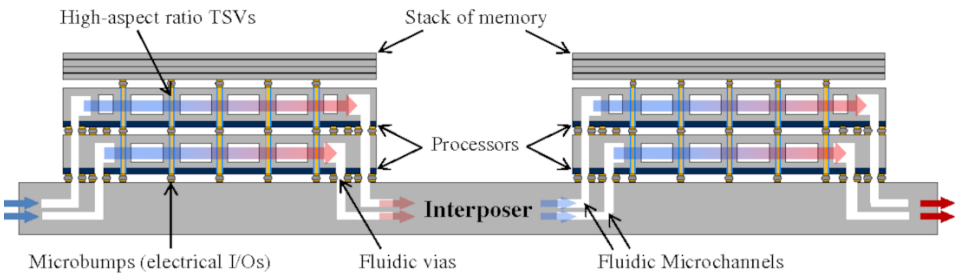

Figure 1-3: Microfluidic cooling delivery channels embedded within electric interface package chip [11]

In a range of micropumps presented by Singhal *et al.* [11] and Garimella and Singhal [11,12] so far, vibrating diaphragm with check valves, electroosmotic, valve-less using nozzle-diffuser elements achieved highest pressure heads and have emerging applications in the technologies for integrated circuit thermal management as at smaller dimensions, surface forces dominate the volume forces. Electrowetting mechanism is viewed to be effective for unidirectionally moving flows. However, the highest flow rate per unit area was projected to be achieved using vibrating diaphragm pumps such as injection-type EHD, flexural plate, piezo-electric, rotary, and valve-less since these operate at resonant frequency but their operation is at a cost of large surface area (surface effects) and thus are inapplicable in most electronic cooling applications. Thereby, with electro-static actuation,

vibrating diaphragm micropumps performed satisfactorily under lower power requirements with a potential for very high flow rates [13]. Reciprocating displacement micropumps as also shown in Figure 1-4 were reported to be widely used micropumps owing to a wide variety of chamber configurations, valve types, drivers and construction mechanisms. Thus, for current demands as per the mini/micro channel dimensions, the micropumps relying on body forces over surface forces are said to be best suited for heat sink applications.

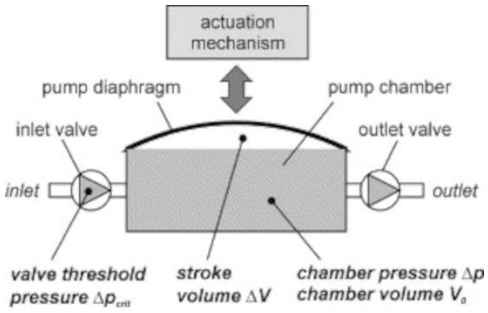

Figure 1-4: Piston type micropump set, reported by Woias [14]

1.2 Pulsating Flow

The work carried out by the author and detailed in this study relates to hydrodynamically and thermally developed single-phase pulsating liquid flows in rectangular minichannels. It is important to first distinguish between a pulsating flow and an oscillating flow, as sometimes these terms are (incorrectly) used interchangeably. Pulsating flow is a transient flow that exhibits a non-zero mean flow, while oscillating flow has a zero-mean flow. Both types of flow are described in Figure 1-5. A pulsating flow can be considered as the sum of a steady flow plus an oscillating flow.

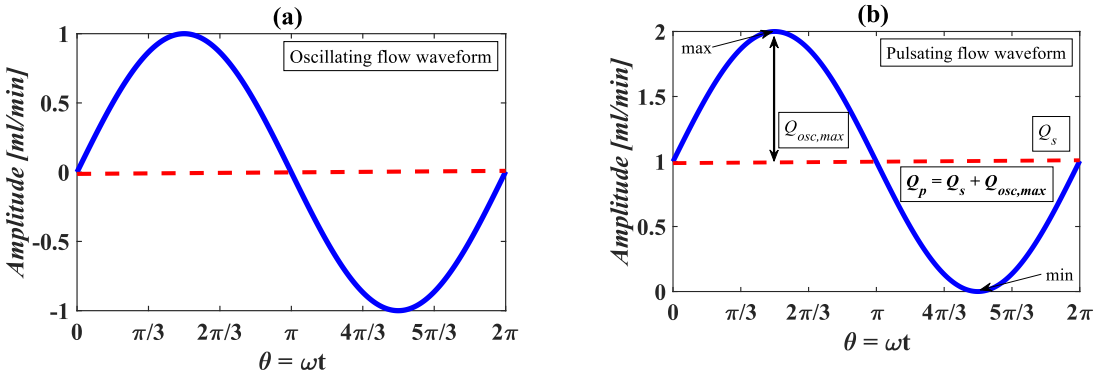

Figure 1-5: Example waveforms showing oscillating (left) and pulsating (right) flows.

Equation (1-1) defines a general parameter in relation to pulsating flow, which can be separated into steady (ξ_s) and oscillating (ξ_{osc}) components. The magnitude of the parameter varies during

the pulsation in accordance with the oscillatory component. The maximum magnitude is given by Equation (1-2).

$$\xi_p = \xi_s + \xi_{osc} \tag{1-1}$$

$$\xi_{p,max} = \xi_s + \xi_{osc,max} \tag{1-2}$$

The characteristics of a pulsating flow waveform depend on the (flow rate) amplitude and frequency. Phase angles in oscillatory and pulsating flows are defined by a periodic progression of the excitation waveform, and they are represented by $\theta = \omega t$ where ω is the angular (oscillatory) frequency. A full cycle of a characteristic waveform profile is the path from phase angles of (initial) 0 to (final) 2 π in correspondence to the time period. A form of the Reynolds number, which represents the ratio of inertial to viscous forces, can be used to distinguish between the steady and pulsating components of flow through pipes or ducts. In Equation (1-3)

u_s refers to the average steady flow velocity, $u_{osc.\ max.}$ is the maximum velocity of the oscillating flow, υ_f is the kinematic viscosity of the fluid, and D_h is the hydraulic diameter of the duct or pipe. In more general terms, the Reynolds number is a ratio of convective and diffusive time scales. The critical Reynolds number for a duct flow (which represents the current study) is taken to be 2300 [15].

$$Re_s = \frac{u_s D_h}{\upsilon_f}\,(\text{steady flow});\ Re_{osc.\ max.} = \frac{u_{osc.\ max.} D_h}{\upsilon_f}\,(\text{oscillating flow}) \tag{1-3}$$

In the present study, the steady and pulsating flows are maintained within the laminar range to avoid turbulent effects. For the experimental study, a low Reynolds number of $Re_S = 40$ is considered for steady flows, maintained at a constant flow rate 21 *ml/min*. The Reynolds decomposition technique is adopted wherein the peak of the fluctuating component in pulsating flows determines the maximum flow rate amplitude attainable. For this study, the maximum oscillating Reynolds number range of $60 \leq Re_{osc.max.} \leq 250$. The kinetic Reynolds number (Re_ω) is an oscillatory non-dimensional parameter dependent on the pulsation frequency, given by $Re_\omega = \omega\ {D_h}^2 / \upsilon_f$. The expected Re_ω range in the current study is between 1-200.

Pulsating flows are regularly described by the Womersley number (Wo), given by Equation (1-4)

and representing the ratio of oscillatory and diffusive time scales. The Womersley number governs the formation of the Stokes layer thickness, which is explained in further detail in Section 3.1. For pipe or channel flows, a variation in Wo or a variation in pulsating frequency, results in distinct flow profiles. For low Womersley numbers ($Wo < 1$), viscous forces dominate the flow regime and a parabolic profile of velocity is predicted for rectangular channels. With increase in Womersley

number to an intermediate range ($Wo = 1$), plug-like profiles are formed in the channel core as shown in the Figure 1-6. At very high Womersley numbers ($Wo > 1$), the effect of inertial forces is higher in the central channel regions whereas viscous forces are evident near the boundaries.

$$Wo = \frac{D_h}{2}\sqrt{\frac{\omega}{\upsilon_f}} \tag{1-4}$$

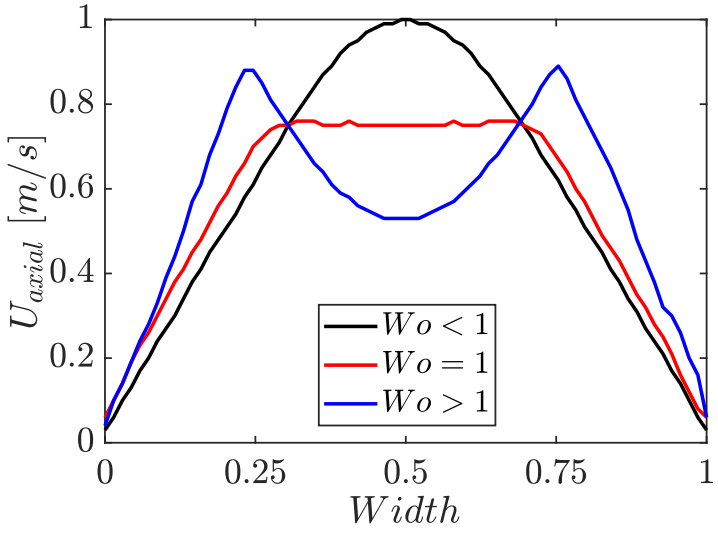

Figure 1-6: Typical Womersley number profiles in a rectangular duct.

For a pulsating flow, as per Figure 1-5, Q_{osc} and $Q_{osc,max}$ are measured relative to the mean or steady flow value. A dimensionless volumetric flow rate amplitude is introduced in pulsating flows which is a ratio of the maximum oscillating $(Q_{osc,max})$ volumetric flow rate to the cycle averaged or equivalent steady flow (Q_s) volumetric flow rate. This factor governs the nature of the flow regime, analogous to the Reynolds number. Variations of flow rate amplitude are shown in Figure 1-7. For $A_0 < 1$, in a laminar regime, there are no significant flow reversal effects. For $A_0 > 1$, flow reversal effects can be significant which can lead to intermittent turbulence in the flow, even at Reynolds numbers typical of laminar flow. For clarity, the steady flow rate is determined by time-averaging the flow rate measurement in the absence of any oscillating component of the flow.

$$A_0 = \frac{Q_{osc,max}}{Q_s} \tag{1-5}$$

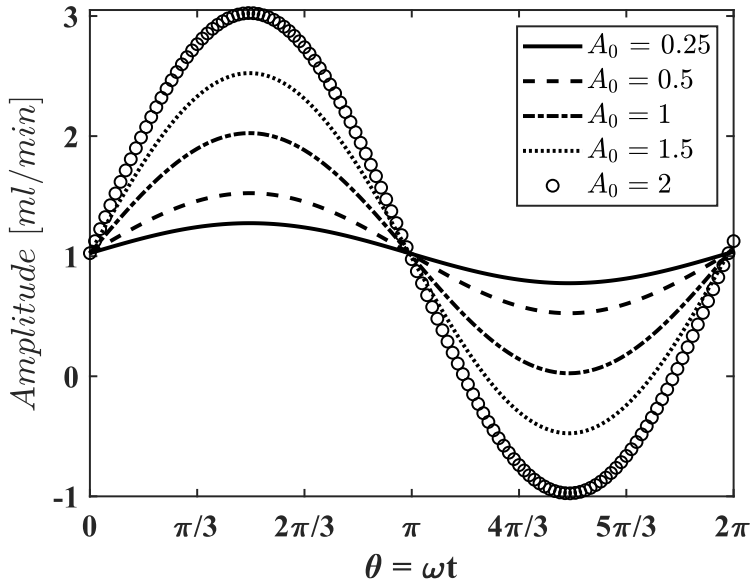

Figure 1-7: Examples of flow rate amplitudes in a sinusoidal pulsating flow with steady underflow at $Q_s = 1\ (ml/min)$.

The fluid displacement χ_m is defined wherein the fluid moves as a plug flow with a mean velocity u_m. Thus, the maximum fluid displacement is χ_{max} which accounts for the maximum distance traversed by the piston pump (details in section 5.1.7.).

$$\chi_m = \frac{\chi_{max}}{2}(1 - cos\omega t) \tag{1-6}$$

Differentiating the above equation with respect to time, results in cross-sectional mean velocity u_m:

$$u_m = u_{max}\, sin\, \emptyset \tag{1-7}$$

where ∅ is the phase angle (0 to 2π) of the cross-sectional mean velocity. The maximum amplitude attainable of the cross-sectional mean velocity u_{max} of Equation (1-7)

relates to the amplitude of fluid displacement χ_{max} given by:

$$u_{\max} = \frac{\chi_{\max}\omega}{2} \tag{1-8}$$

The dimensionless fluid displacement (also termed as tidal displacement in a few cases) amplitude (F_0) can be defined as:

$$F_0 = \frac{\chi_{max}}{D_h} \tag{1-9}$$

The unsteady flow pulsations uniquely exhibit rapid fluctuations of near-wall velocities compared to the conventional unidirectional flows. The unsteady characteristics of constantly developing flow results in disruption of thermal and hydrodynamic boundary layers. Flow rate pulsation encounters the near-wall high viscous forces offered by high velocity magnitudes, thus promoting effective withdrawal/supply of heat from/to the (heated) high temperature wall to low temperature fluid core regions.

1.2.1 Thermal characteristics of pulsating flow

Since fluid and flow parameters dictate pulsating flow behaviour, hydrodynamic dimensionless numbers are considered as a measure to elucidate the heat transfer properties. The Prandtl number is defined as the ratio of rate of viscous diffusion to thermal diffusion:

$$Pr = \frac{\upsilon_f}{\alpha_f} \tag{1-10}$$

The thermal diffusivity is determined by $\alpha_f = k_f/(\rho_f c_{p,f})$ where k_f, ρ_f and $c_{p,f}$ represent the fluid density, thermal conductivity, and specific heat respectively. The heat transfer coefficient (h_s) for a unidirectional flow as defined from Newton's law of cooling is a proportionality relation between the generated heat flux q'' and the difference between the wall $(T_{w,s})$ and fluid temperatures $(T_{f,s})$ under steady forced convection. The equation is given as

$$h_s = \frac{q''}{T_{w,s} - T_{f,s}} \tag{1-11}$$

At the wall, from Fourier's law, the heat is diffused by conduction and the heat flux is defined as being proportional to the normal (y-direction here) temperature gradient:

$$q'' = k_f \frac{\partial T}{\partial y} \tag{1-12}$$

The steady flow Nusselt number, a heat transfer enhancement parameter, is expressed as the ratio of convective to conductive heat transfer of a steady flow:

$$Nu_s = \frac{h_s D_h}{k_f} \tag{1-13}$$

Explicit definitions for the heat transfer parameters with their subsequent analytical expressions based on the methodology adopted is extensively described under Sections 5) and 6).

1.3 Research Objectives

To better understand pulsating flows a comprehensive literature review has been conducted and is detailed in chapters 3 and 4. With regards to potential heat transfer improvements linked to flow pulsation, many previous studies have explored the heat transfer performance in minichannels and pipes. Many of the approaches involved inspecting the underlying mechanics of pulsating and oscillating flows *either* in hydrodynamically *or* thermally developed fields.

This research aims to bridge the knowledge gap by using experimental and computational methods to investigate the complex flow characteristics of pulsating flows and couple that analysis with an investigation of the heat transfer performance. The overarching goal of this study is to investigate if hydrodynamically and thermally developed pulsating flow can enhance heat transfer in a rectangular minichannel. The specific objectives are as follows:

i. To develop an experimental apparatus capable of generating repeatable results for pulsating laminar flow through a heated rectangular minichannel in response to various waveform functions, frequencies, and flow rate amplitudes.
ii. To develop computational models capable of accurately representing the experimental conditions, and to validate those models against published data on pulsating flows as well as experimental data from the current study.
iii. To characterise the flow dynamics of pulsating flows using the combined experimental and computational approach.
iv. To determine the effect of flow modulation in terms of characteristic waveform functions, frequencies, and flow rate amplitudes.
v. To quantify the heat transfer enhancement, if any, from the various experimental conditions, using time and space resolved heat transfer measurements.

2) Steady Laminar Flow Through Ducts

A steady flow is defined as the flow wherein all hydrodynamic and thermal conditions at any point in the flow field remain constant with respect to time. A true steady flow case can only exist in laminar flow, whereas in turbulent flow there exists continual fluctuations in the streamwise velocity and pressure. Steady flow can be categorised as uniform and non-uniform flow. In an ideal scenario, the velocity of a uniform flow is constant in both magnitudes and direction at all points in the fluid. Although for real fluid cases, the velocity varies across a cross-section and is termed as non-uniform flow.

Real fluids exhibit viscous effects which are caused by the interaction of cohesive forces present between the liquid molecules. Flows that are laminar in nature typically demonstrate significant frictional effects and thus are also termed as viscous flows.

2.1 Hydrodynamics of Steady Laminar Flow Through Ducts

For internal flow through a duct a velocity gradient develops resulting in zero relative velocity (relative to the duct wall velocity) at the walls due to the no-slip condition. To conserve the mass flow, the velocity at the duct centre is increased, as illustrated in Figure 2-1. The region of flow under the influence of the viscous shearing forces caused due to the fluid viscosity is known as the velocity boundary layer. The thickness of the boundary layer increases axially until it merges with the central core region. Thus, the region from the duct inlet to the merge point of the boundary layer at the duct centreline is known as hydrodynamic entrance region [16]. The length of this region measured from the duct inlet is the hydrodynamic entry length and the flow in the entrance region is distinguished as hydrodynamically developing flow, as the velocity profile develops.

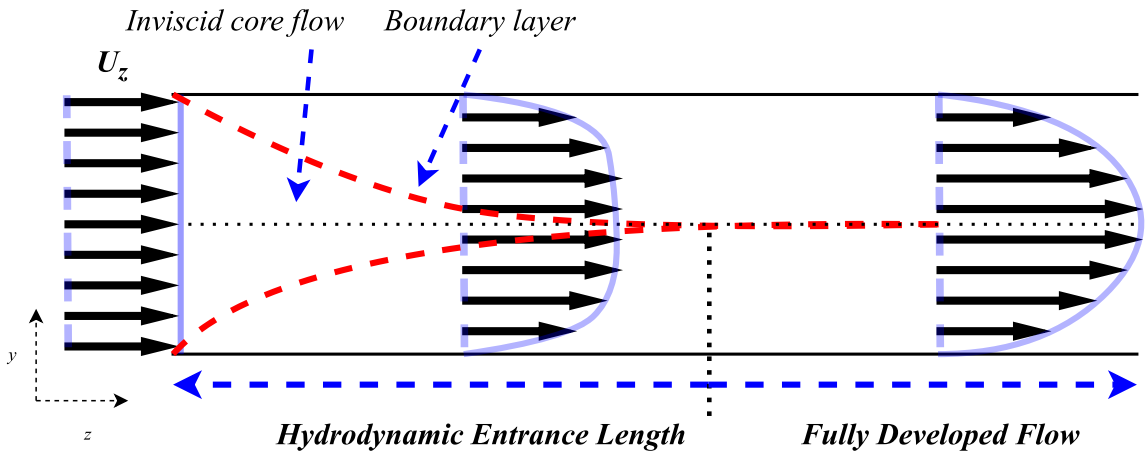

Figure 2-1: Development of velocity profile through a duct.

The hydrodynamic entry length is defined as the distance from the duct entrance to the region wherein the wall shear stress reaches within 2% of the fully developed value. To simplify in terms of velocity, it is defined as the distance from the duct entrance to the axial location where the flow reaches the parabolic velocity profile typical of "Hagen-Poiseuille flow" [16, 17]. This classification of flow through a duct relates to an incompressible Newtonian fluid driven by a pressure difference along the symmetry plane. The region further downstream where the velocity profile is fully established and no longer shows axial variation is termed as the hydrodynamically fully developed region. As a result of the unchanging velocity profile in the hydrodynamically fully developed region, as expressed by Equation (2-1), the wall shear stress remains constant. The wall shear stress is highest at the duct inlet as the thickness of the boundary layer is the smallest, and it further decreases gradually as the flow gets axially progressed. As a result of this, the pressure drop is higher in the entry regions of duct.

$$\text{Hydrodynamically fully developed:} \frac{\partial u(y,z)}{\partial z} = 0, u = u(y) \tag{2-1}$$

The hydrodynamic entry length (L_e) for channel flows generally presented in the literature includes the correlation $L_e/D_h = CRe_s$, where D_h is the hydraulic diameter and C is the relation constant. However, this correlation does not account for the diffusion transport in the axial direction. A more precise correlation was computed numerically over a wide range of laminar flow Reynolds numbers by Durst *et al.* [18] , leading to a generalised expression in the form of $L_e/D_h = C_0 + C_1 Re_s$. The expanded form by substituting for the constants ($C_0$and C_1) is given as:

$$\frac{L_e}{D_h} = [(0.631)^{1.6} + (0.0442 Re_s)^{1.6}]^{1/1.6} \tag{2-2}$$

The thermal entrance length of the duct is the region in which the temperature boundary layer is developing. In this region, the temperature profile presents a significant variation from the initial profile at the duct inlet where the heating is introduced until a pseudo stable state is achieved in the downstream locations, as illustrated in the Figure 2-2. The flow in the thermal entrance length is termed thermally developing flow. For a region in which the cross-section temperature distribution as expressed by Equation (2-3) [19] is invariant and independent of axial locations, the flow is distinguished as thermally fully developed. Here, $T_{w,m}$ and $T_{f,m}$ refer to the mean wall and fluid temperature in the duct respectively. The fluid temperature is a function of spatial locations (x, y, z). A hydrodynamically and thermally developed flow is termed simply as fully developed flow.

$$\frac{\partial}{\partial z}\left[\frac{T_{w,m} - T}{T_{w,m} - T_{f,m}}\right] = 0 \tag{2-3}$$

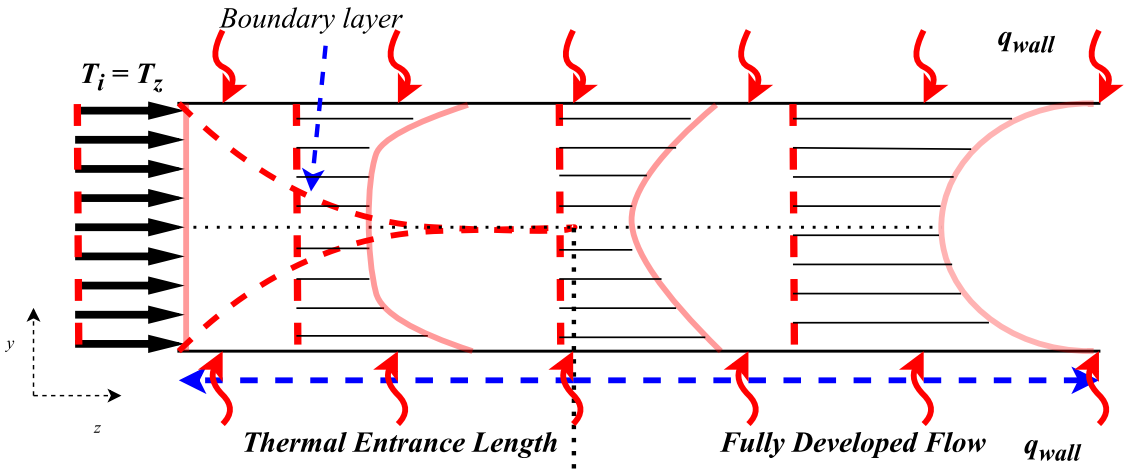

Figure 2-2: Thermal boundary layer development in a duct.

Laminar duct flow Reynolds numbers up to 2300 are dominated by viscous forces, thus the flow fluctuations which are prominent in the turbulent regime are suppressed, The Reynolds number at which the flow transitions from laminar to turbulent is defined as the critical Reynolds number which is a dependent factor on the duct's geometry and flow conditions. Reynolds number for flow through noncircular ducts is typically described in terms of the hydraulic diameter (D_h) given as:

$$D_h = \frac{4A_c}{P_p} = \frac{4A_c}{2 \times (a + b)} \tag{2-4}$$

where A_c is the cross-sectional area of the duct and P_p is the wetted perimeter with side lengths a and b. For most practical conditions, laminar flow through a duct exists within $Re_s \leq 2300$.

The wall shear stress for axisymmetric flow in a rectangular duct [19] is defined as the average wall shear (τ) stress with respect to the duct perimeter, at any axial location *z* is expressed as:

$$\tau_z = -\frac{\mu}{2g(a+b)}\left[\int_{-a}^{a}\left(\frac{\partial u}{\partial x}\right)_{x=b} dz + \int_{-b}^{b}\left(\frac{\partial u}{\partial y}\right)_{y=a} dy\right] \tag{2-5}$$

The pressure drop (ΔP) represents the pressure drop referring to the pressure at duct inlet (1) and outlet (2). For a steady internal flow this is expressed as:

$$\Delta P = P_1 - P_2 = \frac{32\mu L U_{avg}}{D_h^2} \tag{2-6}$$

The pressure drop is proportional to the fluid viscosity μ. The pressure drop from P_1 to P_2 is purely due to viscous effects, regarded as irreversible and termed as the friction pressure loss, ΔP_L.The generalized expression for friction pressure loss in fully developed flows through ducts is:

$$\Delta P_L = \sigma \frac{L}{D_h}\frac{\rho U_{avg}^2}{2} \tag{2-7}$$

Where $\rho U_{avg}^2/2$ is the dynamic pressure and σ is the Darcy friction factor. The mean friction factor [19] in the hydrodynamic entrance region is given as:

$$\sigma_m = \frac{1}{z}\int_0^x f_x dx = \frac{8\tau_{w,m}}{\rho U_{avg}^2} \tag{2-8}$$

σ is also termed as Darcy-Weisbach friction factor. For fully developed laminar flows, friction factor is generally expressed as ($\sigma \times Re_s = constant$) and is a function of Reynolds number and the duct's cross-section. The Fanning friction factor (also denoted as the friction coefficient σ_f) is defined as $\sigma_f = 2\tau_w/\rho U_{avg}^2 = \sigma/4$. Typically, in the case of a fully developed flow, the uniform velocity profile is invariant across the cross-section and the wall shear stress shows no axial variation, thus the peripheral average friction factor is the same as the local friction factor in the region beyond the hydrodynamic entry length. Based on the current study, for rectangular ducts with aspect ratio $a/2b = 0.07$, the equivalent Darcy friction factor is found to be $\sigma \times Re_s = 87.5$ [19–21].

2.2 Heat Transfer to Steady Laminar Flow Through Ducts

To solve for heat transfer to a flow through duct requires determination of the heat flux distribution as well as the bulk fluid and duct wall temperatures. If the fluid inlet boundary conditions are known, the outlet boundary conditions can be estimated only in the case where the duct wall heat

flux distribution is known for a given geometry. The heat transfer coefficient, *h* links the wall heat flux to the associated wall and bulk fluid mean temperatures.

The duct peripheral mean wall temperature $T_{w,m}$ and bulk fluid mean temperature $T_{f,m}$ for a duct cross section along *z* is given by:

$$T_{w,m} = \frac{1}{P_p}\int T_w ds \tag{2-9}$$

$$T_{f,m} = \frac{1}{AU_m}\int U\,T dA \tag{2-10}$$

The peripheral average local heat transfer coefficient (h_z) [19,22] for a unidirectional flow as defined from Newton's law of cooling is a proportionality relation between the generated heat flux *q″* and the difference between the wall $(T_{w,m})$ and bulk fluid temperatures $(T_{f,m})$ under steady forced convection. The equation is given as:

$$h_z = \frac{q^{"}}{(T_{w,m} - T_{f,m})} \tag{2-11}$$

The convection heat transfer, h_z exhibits a dependency on the fluid motion. At the wall, from Fourier's law, the heat is diffused by conduction and the heat flux is defined as being proportional to the normal (y-direction here) peripheral average temperature gradient at the wall:

$$q'' = k_f \left(\frac{\partial T}{\partial y}\right)_{w,m} \tag{2-12}$$

The ratio of convective heat transfer to pure molecular thermal conduction is quantified by the Nusselt number. The peripheral average local Nusselt number for a rectangular duct is expressed as:

$$Nu_z = \frac{h_z D_h}{k} = \frac{q_z^{"} D_h}{k(T_{w,m-}T_{f,m})} \tag{2-13}$$

The local Nusselt number Nu_z [19,22] can be estimated as positive, infinite, or negative and is dependent on the magnitude of local heat transfer coefficient (h_z). For a hydrodynamically and thermally fully developed flow, the analytically derived laminar Nusselt number shows a functional dependence on the associated thermal boundary condition, $Nu_{bc} = Nu$ (bc: duct geometry) [19].

2.2.1 Duct Thermal Boundary Conditions

Thermal boundary conditions such as a uniform temperature, uniform heat flux, or combinations of both have been used to describe the heat transfer behaviour in ducts under forced convection. A pioneering study in this regard was carried out by Shah and London, who analytically determined time averaged Nusselt numbers imposed with thermal boundary conditions T, H1 and H2 for rectangular ducts of various aspect ratios, as shown in Table 2-1. The analytical calculations omitted the effects of axial heat conduction, viscous diffusion, and mass diffusion. The flow was laminar and fully developed. The authors used the notation in

Table 2-2 to describe the thermal boundary conditions. The H2 boundary condition of interest was analysed with all four heated walls (version 4) based on the analytical variational approach adopted by Siegel [23], Sparrow and De Farias [24] and a discrete least squares technique by Shah [20], a good agreement was obtained.

Table 2-1: Nusselt numbers for varying aspect ratio and thermal boundary conditions (4-T, 4-H1, 4-H2) for the case of fully developed laminar flow through rectangular ducts, as given by Shah & London [25].

$\propto^*$	fRe	Nu_T	Nu_{H1}	Nu_{H2}
1	14.22708	2.976	3.60795	3.091
0.9	14.26098	-	3.62045	-
1/1.2	14.32808	-	3.64531	-
0.8	14.3778	-	3.66382	-
0.75	14.4757	-	3.70052	-
1/1.4	14.56482	3.077	3.73419	-
0.7	14.60538	-	3.74961	-
2/3	14.71184	3.117	3.79033	-
0.6	14.97996	-	3.89456	-
0.5	15.54806	3.391	4.1233	3.02
0.4	16.3681	-	4.47185	-
1/3	17.08967	3.956	4.7948	2.97
0.3	17.51209	-	4.98989	-
0.25	18.23278	4.439	5.33106	2.94
0.2	19.0705	-	5.73769	2.93
1/6	19.7022	5.137	6.04946	2.93
1/7	20.1931	-	6.29404	2.94
0.125	20.58464	5.597	6.49033	2.94
1/9	20.90385	-	6.65106	2.94
1/10	21.16888	-	6.78495	2.95
1/12	21.58327	-	6.99507	-
1/15	22.01891	-	7.21683	-
1/20	22.47701	-	7.45083	-
1/50	23.36253	-	7.90589	-
0	24	7.541	8.23529	8.235

Table 2-2: Nomenclature of thermal boundary conditions as followed by Shah and London [25].

T	Temperature is constant both peripherally and axially
H1	Temperature is constant peripherally and heat flux is constant axially
H2	Heat flux is constant both peripherally and axially

Siegel [23] performed analytical studies to decipher the heat transfer behaviour in a forced convection flow with imposed arbitrary and time-varying wall temperature. Analysis was carried out on two-dimensional geometries; a parallel-plate channel and a circular tube. The system initially was in an isothermal state, with no difference in temperatures between the fluid and the wall. The analytical approach differed for the geometric profiles; for the circular tube, numerical integration of the ordinary differential equations (ODE) was employed, and for the parallel plate channels, a series expansion technique was used to include the variations of velocity and temperature over the channel cross section. A step change in wall temperature as a result of pure conduction and transient heat flux cases were examined, and a comparison was drawn from a finite thickness rectangular slab undergoing pure conduction with sharp changing temperatures. A good agreement was noted for the results of transient heat flux and the steady state heat flux as a function of location along the parallel plates channel.

A study by Morini [26] examined the two-dimensional temperature distributions in the thermally developed region of channels of varying aspect ratio ($2b/a < 1$). Based on the boundary conditions outlined above by Shah and London (see

Table 2-2), three boundary condition configurations were considered, which produced eight different thermal boundary condition combinations, as shown in Table 2-3 and previously introduced by Gao and Hartnett [27]. Analytical solutions were obtained using a finite-integral transform technique and eigenvalues and eigenfunctions were solved with the method of separation of variables.

The effect of duct aspect ratio on temperature distribution was evident. Dimensionless temperature distributions for a rectangular duct with $2b/a = 0.25$ for the 4-H2 case (fixed wall heat flux on all 4 sides) was analysed. It was seen that minimum wall temperature approached the minimum fluid temperature at the central core of the duct. High corner temperatures also dominated the peripheral (transverse) average wall temperature leading to a reduced heat transfer in comparison with the 4-H1 and 4-T conditions.

By examining the role of velocity distribution on the channel thermal behaviour, the Nu obtained were twice the value for the H2 case with slug flow in comparison to the fully developed velocity profile. With small aspect ratio channels, higher heat transfer enhancement was achieved due to the influence of stronger corner temperature distributions.

Table 2-3: Nomenclature for thermal versions of heated and adiabatic walls as described by Gao and Hartnett [27].

4	four heated sides
3L	three heated sides and one adiabatic short side
3S	three heated sides and one adiabatic long side
2L	two heated long sides and two adiabatic short sides
2S	two heated short sides and two adiabatic long sides
2C	one heated short and long side, two adiabatic sides
1L	one heated long side and three adiabatic sides
1S	one heated short side and three adiabatic sides
2S	two heated short sides and two adiabatic long sides

In a subsequent study by Spiga and Morini [28], a forced convection laminar flow of a Newtonian fluid through a rectangular duct was considered. Analytical solutions for the eight thermal combinations as described in Table 2-3 were produced for the H2 thermal boundary condition. It was concluded that the solutions of slug flow modelled by Morini [26] for Newtonian fluids couldn't be extended for this study as the spatial effects of velocity distribution had greater impact near the corner regions and along the narrow wall aspect ratio ducts. Using the modified H2 condition which involved heating of one or more wall while maintaining the remaining walls adiabatic, the fluid temperature exhibited linear axial variation.

The variation of temperature distribution was discussed for different channel aspect ratios and similar results were obtained for the case of four heated walls (4-H2). It was found that with an increase in aspect ratio in the range $0.1 \leq 2b/a \leq 1$, wall temperature distributions along the long sides were flatter and along the short sides the temperature gradient was considerable, as shown for one of the cases in Figure 2-3. The minimum fluid temperature was at the central region (opposite to the adiabatic side) and the maximum fluid temperature was found near the corner regions (representing the heated sides), which was in agreement with the velocity distribution. The variation of Nu predicted for different aspect ratios lies between $2.686 \leq Nu \leq 4.558$ for $0.1 \leq 2b/a \leq 1$.

Morini [26] extended the analysis of two-dimensional duct temperature distributions as a function of aspect ratio for the T, H1, and H2 thermal boundary conditions involving combinations of heated and adiabatic duct walls. A particular case of small duct $2b/a = 0.25$, with four heated walls (version 4) is shown in Figure 2-3. For the H2 thermal boundary condition the minimum wall temperatures were reached at minimum fluid temperatures in the central duct region, illustrated in Figure 2-4. For T and H1 cases, the temperature distribution decreased strongly near the heated walls with an extended central core region showed low temperatures.

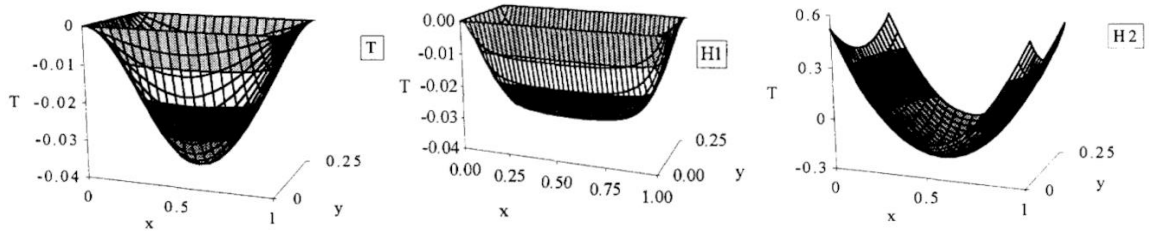

Figure 2-3: Dimensionless temperature distributions in a rectangular duct ($2b/a = 0.25$) with four sides heated for the T, H1 and H2 cases, as shown by Morini [26].

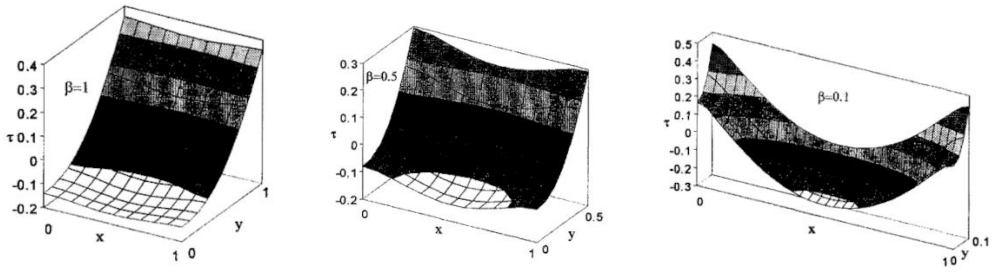

Figure 2-4: Dimensionless temperature distributions in a rectangular duct for varying aspect ratios (β) imposed with H2-1L boundary condition, from Spiga and Morini [28].

The effect of peripheral heat conduction within the heated long walls and non-conducting short side walls was analysed via the wall temperature distributions in an analytical study by Siegel and Savino [29]. The wall heat conduction was coupled with the convective energy equation, described for the fluid by an integral equation and modelled under the assumption of uniform temperature across the thin broad walls with insulated short side walls. The dimensionless wall temperature was deemed to be governed by the variation in wall to fluid conductivity, channel aspect ratio, and width of the imposed heat flux relative to the channel width.

With an increase in thermal conduction along the heated long walls, wall temperatures reached thermal uniformity with a substantial decrease in peak fluid temperatures, as the convection to the fluid increased. For larger aspect ratio channels of $2b/a = 10$ and $2b/a = 20$, removal of the localised heat source at a short distance away from the duct corner, resulted in large reductions in peak temperatures since the heat concentrations were found to occur at these locations. It was pointed out for best heat transfer performance, the optimum aspect ratio for ducts with any wall conductivity is in the range of $10 \leq 2b/a \leq 20$.

In an extension to their earlier study based on uniform heating of all four channel walls, wherein the fluid conductivity and total heat flux per unit channel was considered fixed, Savino and Siegel [30], [31] discussed their analytical solutions in terms of wall heat flux ratios and the variation of channel aspect ratio. The peak temperature for all aspect ratios remained constant which was seen to occur in the corners in accordance with the previously mentioned effect of velocity distribution

along the transverse section of the channel, as seen by Morini [26]. For a square duct ($2b/a = 1$) imposed with two uniformly heated walls, the heat flow paths from the two heated walls moving towards regions of high fluid velocity exhibited nearly similar magnitudes for all positions on the heated side, thus maintaining a uniform temperature pattern along the walls. As the aspect ratio further increased, as shown in Figure 2-5 (solid curves), due to the narrower ducts, the heat flow paths moving to the region of high velocities were shortened. For these configurations, energy conducted from the corner regions must travel a longer path to reach higher velocity regions within the fluid. Also, since the region of low fluid velocity occupies less cross-sectional area for higher aspect ratios, the width of heat conduction path parallel to the heated side is decreased since the duct becomes narrower. It is conceptually understood that there always should exist a (spanwise) transverse temperature gradient to transport the heating away from the low velocity regions from the corners and side walls to evenly distribute it to the more rapidly moving fluid. For the cases of uniform heating of all peripheral walls, Figure 2-5 (dotted curves) presents that the peak wall temperature remains the same across increasing channel aspect ratio, since the corner regions were heated from all the sides. The relation between peak wall temperatures as a function of aspect ratio for varying wall heat flux ratios was investigated. There existed a large reduction in corner temperatures for the case of heated broad walls for ducts with $2b/a \approx 10$. Whereas beyond $2b/a = 10$, only a small reduction in corner temperatures was noted. Thus, the optimum range $10 \leq 2b/a \leq 20$ was determined. As more thermal energy is concentrated in the corner regions affected by poor convection, high temperature gradients near the corner regions are observed for all the aspect ratios. A similar conclusion was drawn by Sparrow and Siegel [32].

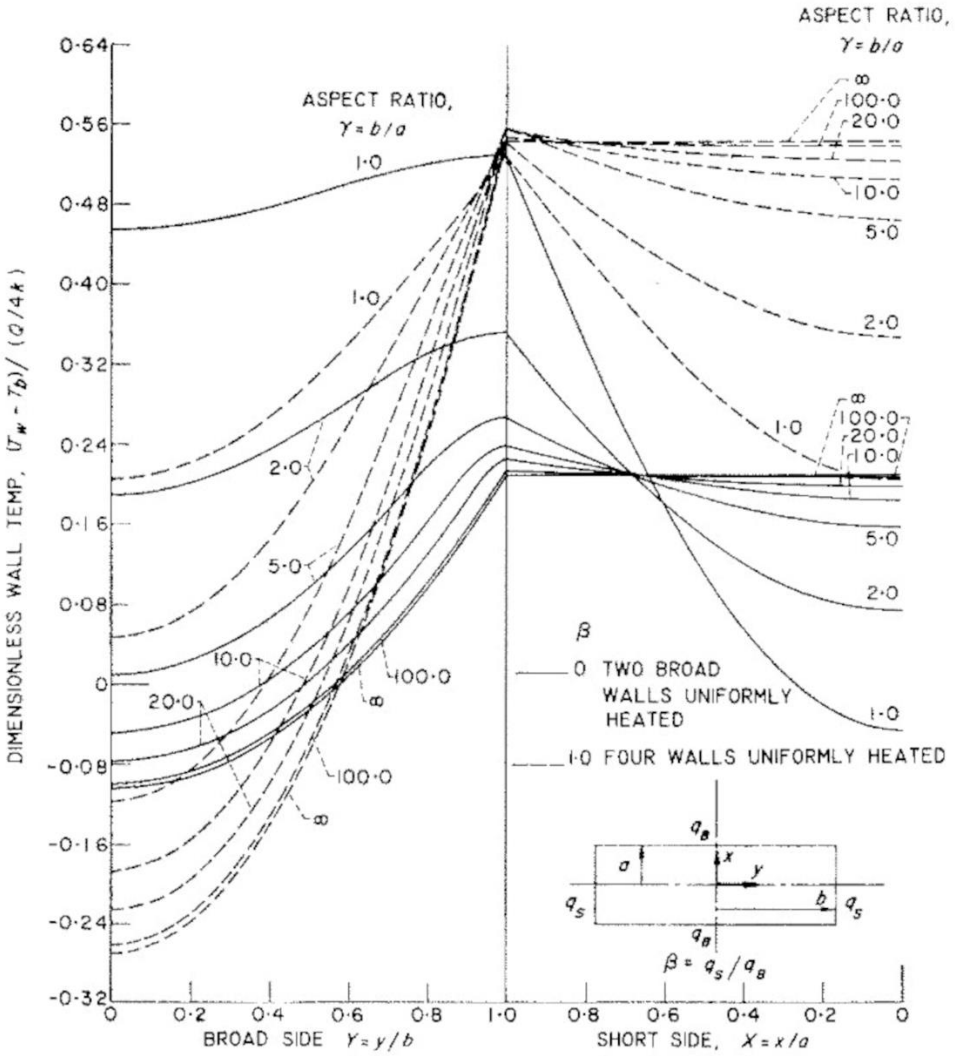

Figure 2-5: Dimensionless wall temperatures for rectangular ducts for the cases of uniform heat flux on two walls (2L-H2) and four walls (4-H2), by Savino and Siegel [31].

3) Literature Review Part 1: Hydrodynamics of Internal Oscillating and Pulsating Flows

Internal pulsating flow remains an active research topic although it was first introduced in the mid-1800s. Early researchers focussed on the mathematical understanding of single-phase pulsating flows to predict the coupled pressure-velocity profiles. Analytical techniques such as Fourier series expansions by Uchida [33], Laplace transforms by Ito [34] and Green's function methods by Fan and Chao [35] were derived and modelled to analyse the wall shear stress profiles and dependence of frequency and amplitudes on pressure and velocity. With the eventual development of experimental techniques, transient velocity profiles were the first to be verified in simple geometries using hot-wire anemometry, laser Doppler velocimetry and flow visualisation. Experimentally obtained profiles were compared with mathematical predictions.

By comparison, our understanding of the heat transfer associated with single-phase pulsating flows is still developing. To date, the focus of many researchers has been application-based analyses rather than a broader perspective. The focus of current study, *i.e.*, A combined analysis highlighting the interdependency of hydrodynamic and heat transfer parameters is currently lacking in the literature. Of the studies that do investigate pulsating flow heat transfer, the interdependence of flow variables and their effect on heat transfer is detailed in Chapter 4).

3.1 Early years

A mathematical description of laminar single-phase oscillating flow in a rectangular channel was established by Stokes in early 1851 and is often known as Stokes second problem. He considered the cases of oscillating wall and oscillating fluid (stream). The spanwise propagation of flow was a

result of a combined effect of fluid diffusion and molecular momentum. The amplitude of the velocity oscillations decayed exponentially in the spanwise fluid distribution as the distance was increased from the wall. The dominance of viscous effects near the boundary led to a phenomenon known as Stokes boundary layer. The thickness of this boundary layer was dependent on the frequency of the oscillations, although much thinner than the distance between the channel walls (2h*). The Stokes layer shows time-space dependent modulation along the streamwise direction. The spatial development of this layer is a dependent factor on the near-wall and freestream amplitudes of velocity. Viscous stresses reduced the fluid layer momentum near the wall, which was directionally dependent on the pressure gradients. The streamwise flow, as illustrated in Figure 3-1 is described by the steady parabolic velocity profile of plane Poiseuille flow reported by Stokes [36] in an analytical study.

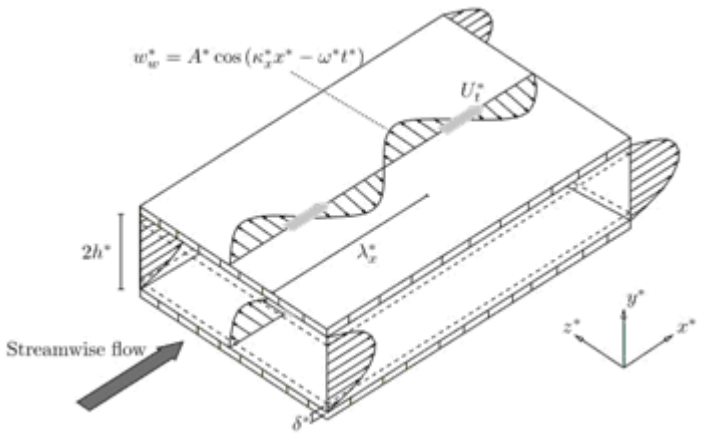

Figure 3-1: Schematic of physical domain for laminar channel flow with forward-travelling wall waves.δ^* represents the Stokes layer thickness, λ_x^* is the streamwise wavelength and Ut* is the phase speed, by Quadrio and Ricco [37].

3.2 Velocity distribution, Pressure Gradients, and Influence of Fluid Parameters

The flow regimes of oscillating flow were first observed in Helmholtz resonator tubes with orifices of circular cross section in a study by Richardson [38]. The oscillations were generated using an adjusting stroke reciprocating cylinder with a long crank. The velocity amplitude variations were recorded using a hot-wire anemometer. The results highlighted the near-wall maximum velocity in an oscillating flow. This experimental study was further extended by Richardson and Tyler [39], who used other orifice profiles such as square and oval and resulted in the identification of what is now

known as the annular effect. In the case of a laminar oscillating flow, a local peak in the velocity profile was developed near the walls of the duct, with a more uniform distribution along the core region, as shown Figure 3-2 below.

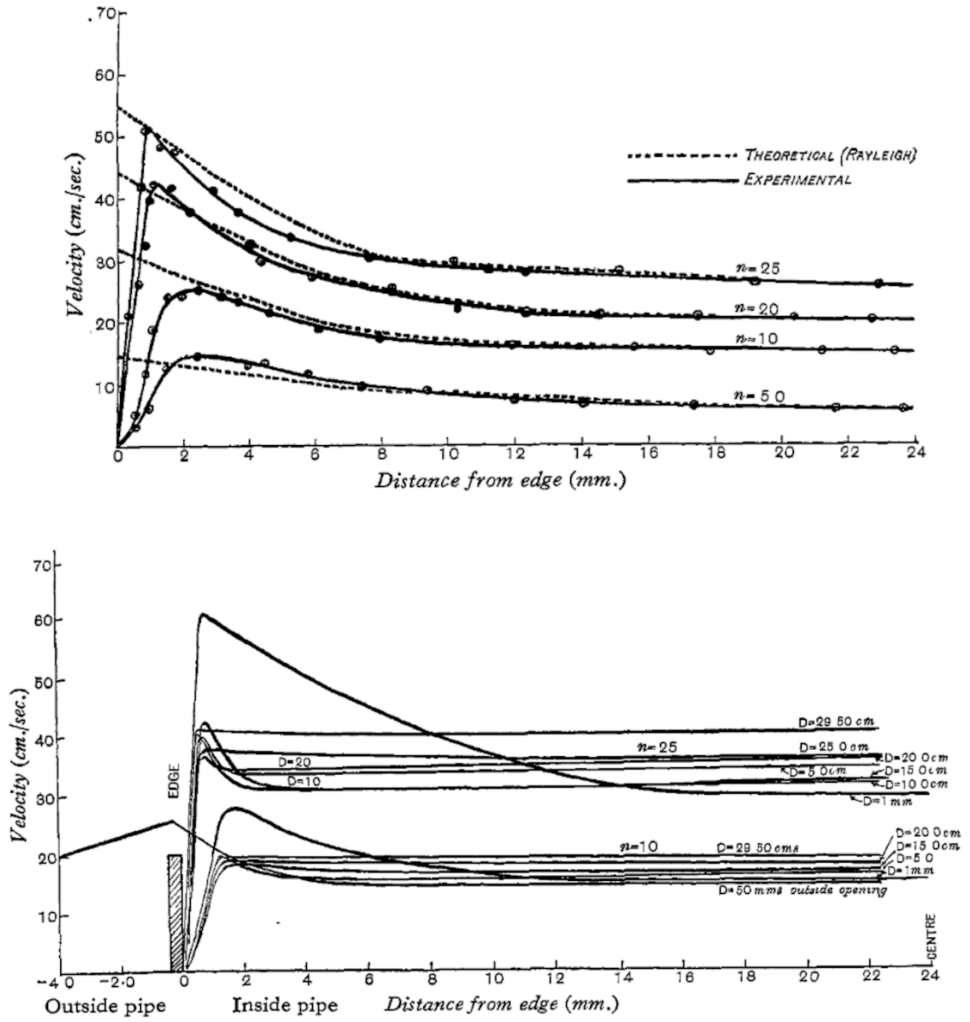

Figure 3-2: Transverse velocity profiles for different oscillating frequencies at different axial locations, for a round cross-section pipe (top figure) and a square cross-section pipe (bottom figure), by Richardson and Tyler [39].

In a work carried out by Holmes and Vermeulen [40], a flow visualization technique using phosphorescent powder was employed to measure local velocity gradients at the wall for the case of oscillating Newtonian fluid flow through a rectangular duct with varying aspect ratios ($2b/a$) of 0.10, 0.15, 0.25 and 1. Close agreement was found between the experimental and theoretical results. In a subsequent flow visualization study by Harris *et al.* [41], a similar observation of the annular effect established previously by Richardson [38] and Richardson and Tyler [39] was obtained using a circular tube fed with micro polystyrene spheres. For low oscillation frequencies,

the transverse velocity profiles were observed to be parabolic in nature while at high frequencies the local peak in velocity was found to be close to the wall.

Womersley [42] developed a relationship between the flow rate of fluid in motion inside a cylinder and the pressure gradient, accounting for a phase-lag due to viscous drag effects. The amplitude of the flow rate was maximum at lower pulsation frequencies and the pressure gradient was in phase with the flow rate amplitude. For an increase in frequency, the flow rate decayed to a minimum and the pressure gradient lagged the flow rate amplitude by an asymptotic value of 90°, shown in the Figure 3-3 below.

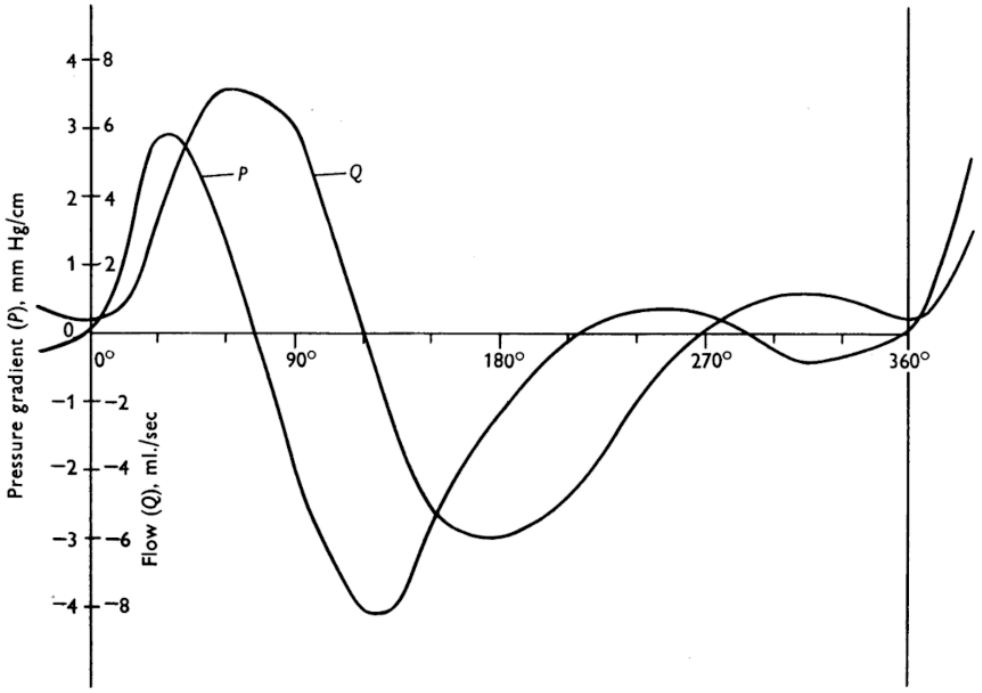

Figure 3-3: Oscillating flow relation of flow (Q) to the pressure gradient (P) in the femoral artery of a dog, as obtained by Womersley [42].

Analytical solutions to the experimental investigations of Richardson & Tyler were determined by Sexl [43]. The Navier-Stokes equations were solved to obtain the characteristic velocity distributions of oscillating laminar flow inside a circular tube. Uchida [33] extended the analysis for a laminar oscillating flow superposed with a mean steady flow in a circular pipe. The influence of mass flow, pressure gradient, and wall shear were examined. Uchida modelled the phase-lag between the flow rate and the (velocity) pressure gradient, which increased to up to $\pi/2$ for higher frequencies, as shown in Figure 3-4.

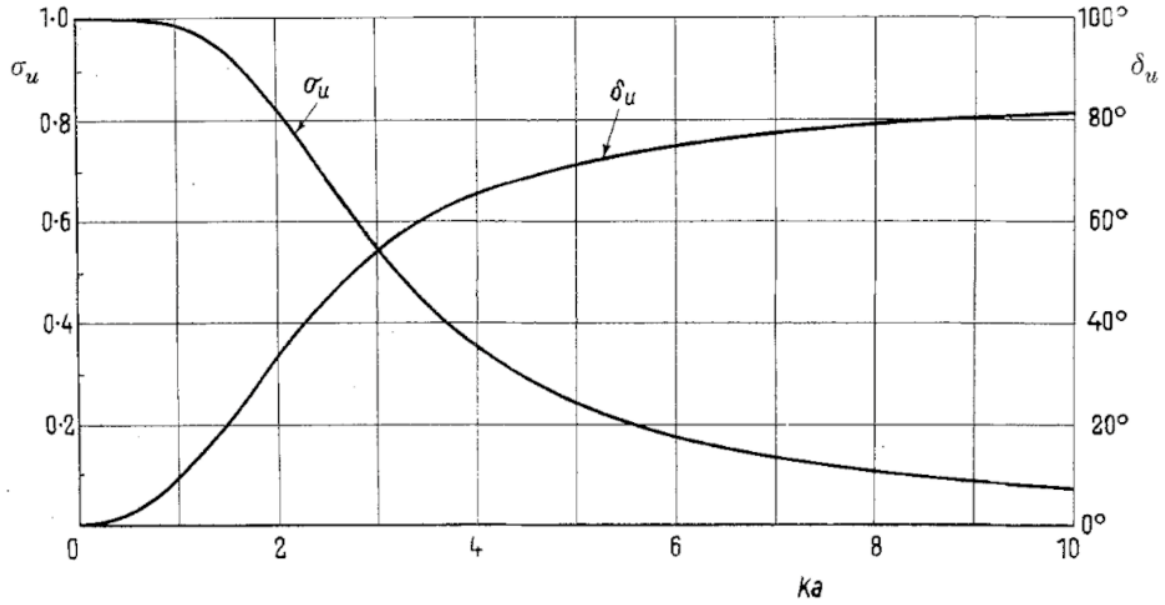

Figure 3-4: Variation of the amplitude of the flow rate (σ_u) and pressure gradient (δ_u) and the corresponding phase evolution with dimensionless frequency in a pipe, in a study by Uchida [33].

Similar behaviour was observed by Fan and Chao [35] who used long rectangular ducts to quantify the transient characteristics involved in low and high frequency flow oscillations, using analytical solutions as is presented in Figure 3-5. It was shown that for low frequencies, parabolic velocity profiles were determined with the flow rate and pressure gradient in phase. At higher frequencies, the flow rate and pressure gradient were out of phase by $\pi/2$. Additionally, their predictions resembled the experimental results of Richardson and Tyler [39] for higher frequencies: flatter velocity profiles existed at central regions of the duct with maximum velocity observed near the wall.

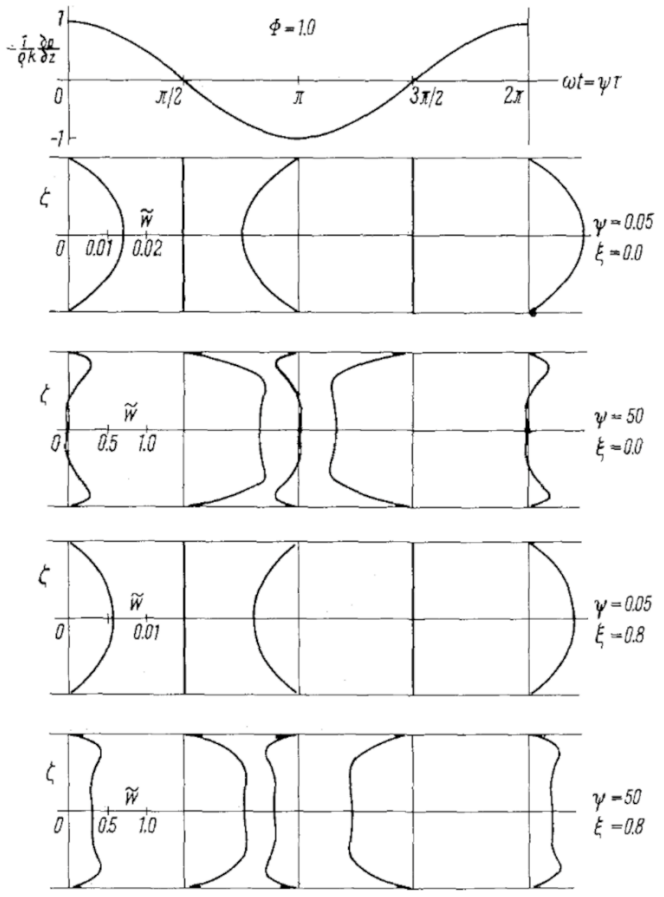

Figure 3-5: Oscillating velocity profiles for a rectangular duct with an aspect ratio of 10 at low frequency ($\psi = 0.5$) and high frequency ($\psi = 500$) along the duct centre ($\zeta = 0$) and near the wall ($\zeta = 0.8$), by Fan and Chao [35].

Experimental visualisation techniques have helped better understand the influence of pulsating parameters. A testing apparatus used by Lingford and Ryan [44] introduced a thin filament of black ink into the pulsing fluid and a frame by frame analysis was performed to obtain local velocity measurements along the tube radius. Pulsations were driven in a piston-cylinder arrangement paired with a variable speed cam. The maximum error between the parameters was limited to less than 5% of the peak magnitude of velocity. Agreeable validation of the experimental results was supported by the numerical solutions from Womersley [42]. Near-wall velocity peaks were observed on a time-dependent case for Womersley numbers in the range $1.83 \leq Wo \leq 21.0$. Although an occurrence of turbulence at high frequencies was detected in experiments, the agreement between the experimental velocity profiles and numerical predictions remained unaffected.

Laser doppler velocimetry was preferred by Denison and Stevenson [45] to decipher the nature of pulsating flow profiles in a rigid tube. Their setup involved a directionally sensitive beam using an

offset frequency shift which aided in attaining laser beam excitation frequencies of up to 1 *MHz*. The axial velocity and pressure gradients were measured along the central regions of tube for a pure oscillating flow. The theoretical velocity profiles were generated by using a Fourier analysis on the experimental pressure gradient measurements. Satisfactory agreement with theory was attained with the measured normalized velocities within 1.4% of the pressure gradient trends for a range of $1.71 \leq Wo \leq 14.1$. The RMS error was also within 2% of the theory, considering minor noise.

A time-dependent velocity distribution flow visualisation study was carried out by Muto and Nakane [46] for steady, oscillating, and pulsating flow profiles for a cylindrical geometry using a dual slit deflector mechanism. This technique was the first time-synchronous acquisition of the fully developed laminar regime. A flow rate amplitude range of $1.3 \leq A_0 \leq 23$ and Womersley number range of $0.5 \leq Wo \leq 2$ were investigated. The theoretical predictions obtained using Laplace transform methods assuming a sinusoidal pulsating velocity at the inlet showed good agreement with the experimental results.

Inspecting the characteristics of the transition-turbulent regime for oscillating flows, a study by Clamen and Minton [47] used a circular pipe and a then-novel hydrogen-bubble technique. The authors claimed that the technique showed an advantage of being sensitive to disturbances in the flow during transition, shown by the transients in Figure 3-6. A mean Reynolds number range of $1275 \leq Re_s \leq 2900$ was studied with a Womersley number range of $11.2 \leq \mathrm{Wo} \leq 26.7$. A non-dimensional parameter introduced by the authors, which modelled the ratio of harmonic flow Reynolds number (oscillating) with Womersley number to aid in predicting time-dependent oscillatory flow, was maintained at 294 to ensure laminar flow. Turbulence intermittency showed a direct proportionality with the mean flow Reynolds number, frequency, and amplitude of harmonic motion. The authors therefore inferred a greater than previously thought dependency on the harmonic flow Reynolds number.

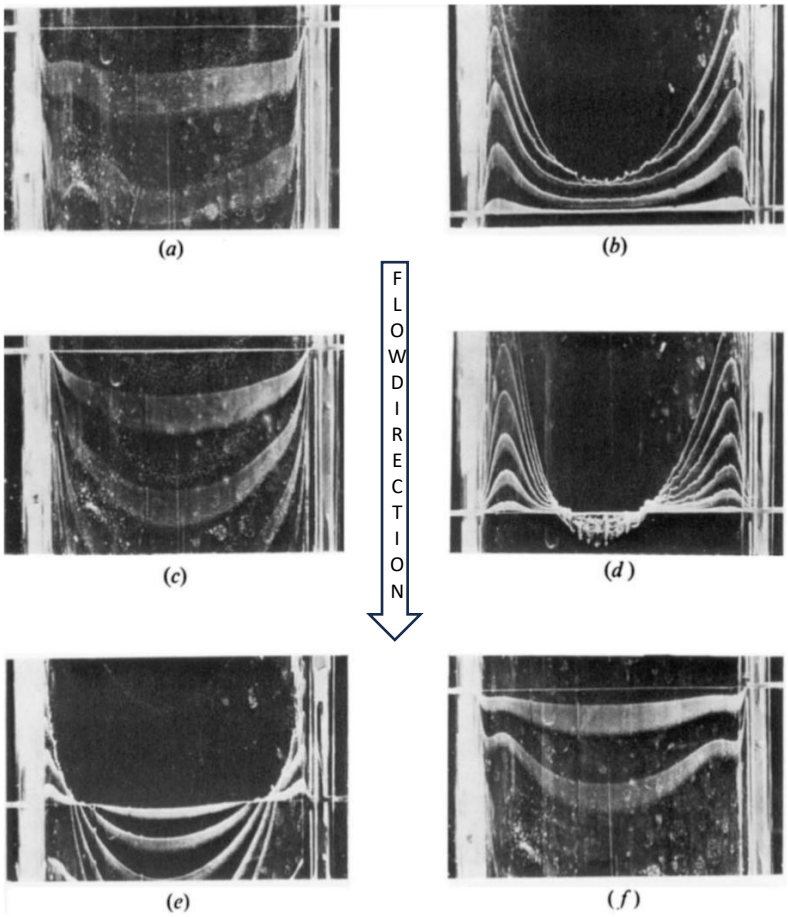

Figure 3-6: Hydrogen bubble images of pulsating flow obtained by Clamen and Minton [47] for a mean flow $Re_S = 1535$, oscillation amplitude $X/R = 5.8$, $Wo = 18.7$ (a) $\omega t = 0$, (b) $\omega t = 180$, (c) $\omega t = 60$, (d) $\omega t = 240$, (e) $\omega t = 120$, (f) $\omega t = 300$.

With the goal of improved spatial resolution, a photochromatic dye measurement system was devised by Ojha *et al.* [48] to study the instantaneous velocity profiles in a pulsating flow. A split-beam measurement technique aided in simultaneous tracking of multiple axial velocity profiles. The photochromatic properties of a usually colourless test fluid were used in this method, in which a pulsed UV laser was incident on the solution. This led to a change of colour of the fluid which produced a coloured illumination in the beam direction. Tracking this trace, the velocity and displacement profiles were determined. This method was postulated to be of greater advantage over LDA for its non-invasiveness and instantaneous tracing of high spatial resolutions near the wall of the circular pipe.

A single Womersley number of $Wo = 7.52$ at a flow rate amplitude of $A_0 = 1.21$ was generated using a cam-driven piston pump. Velocity gradients at the wall during the accelerating phase were observed to be higher. This occurred since pressure gradient time scales are longer and inertial effects are dominant in the central lamina. The measured and predicted centreline velocity profiles

showed close agreement. The measured phase lag between the flow rate and pressure gradient was about 16° ± 2° in comparison to the predicted value of 14°.

A comprehensive study of laminar, fully developed, sinusoidally pulsating mass flow was presented by Ünsal *et al.* [49] using the hot-wire anemometer technique in a circular tube for a Womersley number range of $0.8 \leq Wo \leq 6.6$. The flow was generated by an electronic control circuit in sync with an electrodynamic coil, as outlined by Durst *et al.* [50]. The relationship between the pulsating mass flow rate and the axial pressure gradient was investigated at different frequencies. At low frequencies the phase lag wasn't evident as the flow was in a quasi-steady state maintaining a unity ratio of mass flow rate to axial pressure gradient, and parabolic velocity profiles were evident. In the moderate frequency range, a phase lag between the pulsating mass flow rate and the pressure gradient appeared due to a consistent increase of the pressure gradient. For inertial dominant high frequency regimes, the phase lag approached a maximum at $\pi/2$ with a substantial increase in the pressure gradient. High frequency flows exhibited quasi-steady state with minimal variation of velocity near the channel centre, while more prominent effects were seen near the walls. Furthermore, with the mass flow variation a flow reversal trend was also predicted theoretically. The analytical model outlined by Uchida [33] was used for comparison and a reasonable agreement was achieved.

An extended study by Haddad *et al.* [51] developed an analytical solution for pulsating velocity profiles in channels and pipes to determine the interdependence of parameters. A wide range of Womersley numbers $0.01 \leq Wo \leq 10$ indicated interesting effects where the phase shift between the pressure gradient and mass flow rate was more pronounced as the frequencies were increased for both geometries. Additionally, weak flow reversal effects were observed at low frequencies, while for higher frequencies the reversal region appeared to be shifted away from the wall. The effect of increasing the frequency resulted in an increasing velocity amplitude in the radial direction. This was due to a redistribution of the momentum in the radial/transverse direction which was induced by pulsations.

3.3 Flow reversal effects

A broad attempt at quantifying the flow reversal effect in pulsating flow for channel and pipe geometries was established by the authors Haddad *et al.* [51]. The occurrence of flow reversal is dependent upon the pulsation frequency, dimensionless flowrate amplitude or pressure gradient amplitude, and phase angles. The flow reversal effect is viewed to be initiated from the wall regions. With a change of flow direction, the shear stress vanishes and thus this effect occurs when the

velocity gradient becomes less than 0 ($\partial u/\partial r \leq 0$ for a pipe). Based on theoretical predictions for pipe and channel flows, the mass flow and frequency relationships were established regarding flow reversal effects. For high mass-flow rates, the reversal occurred at low pulsation frequency, while for flow reversal to occur at low mass flow rates, extreme high frequency is essential, as viewed from Figure 3-7 for pipe and channel flows. Comparing the two cross-sections, for the same mass flow rate the applied pulsation frequency for a pipe should be higher than that of the channel.

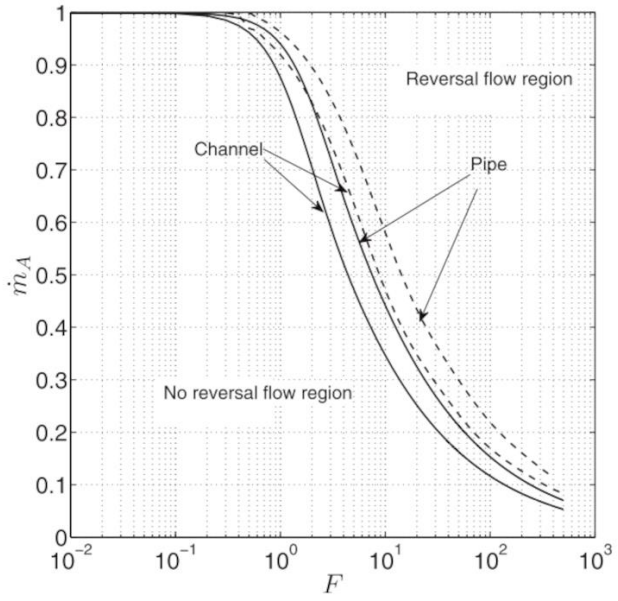

Figure 3-7: Regions of flow reversal for pipe and channel flows. Solid lines and dotted lines depict the wall-attached and off-wall reversal, as shown by Haddad *et al.* [51].

The effect of radial location on reversal velocity amplitude shows a relation where it increases up to a certain radial location, attaining a maximum value close to the wall, before decreasing to 0 at the wall. This behaviour is shown to be similar for all pulsation frequencies and mass flow rates. With increasing pulsation frequency, the corresponding decrease of mass flow rate predicts the location of maximum reversal velocity amplitude to move away from the wall. It is also shown that the duration of reversal is longer for higher pulsation frequencies.

The reversed mass flow rate was shown to vary with phase angle. Here, the reversible mass flow rate increased with phase angle until a maximum was attained. Further increases in phase angle led to a reduction in reversible mass flow rate. The reversal location traversed towards the central lamina and then shifted back to the wall. The percentage of reversed mass to total mass in one pulsation cycle showed a continual rise with pulsation frequency, as shown in Figure 3-8.

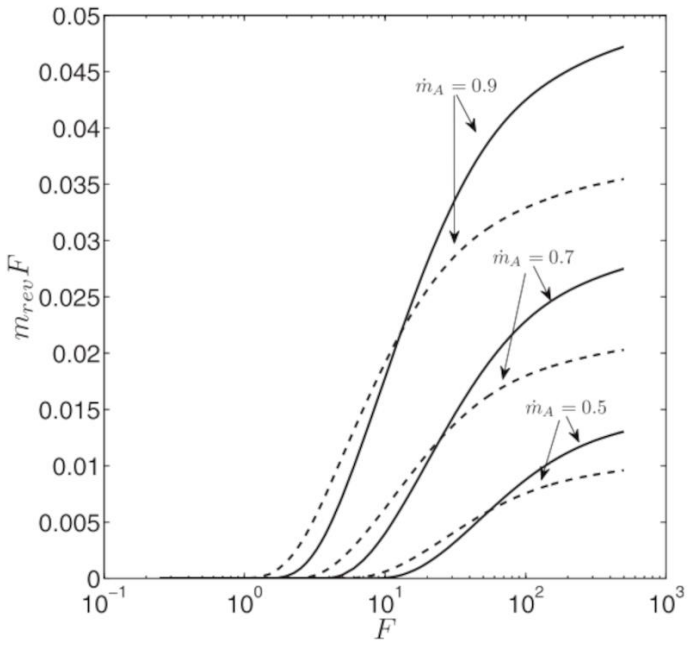

Figure 3-8: Comparative chart between the percentage variation of reversed mass to total mass with F for one cycle. Solid, Dashed lines show pipe and channel flow respectively [51].

In a study by Aygun and Aydin [52], the effect of pulsation frequencies in a pipe flow with flow reversal was analysed and interesting profiles were observed. The piston-driven, laminar, fully developed flow was generated by varying the angular velocity of a DC motor and piston rod positions. Flow patterns for the Womersley number range $1.07 \leq \mathrm{Wo} \leq 402$ were investigated at constant $Re = 1000$ and fixed flow rate amplitude $A_0 = 0.48$. Radial velocity distributions were obtained via by hot wire anemometry, and pressure drop by pressure transmitter. A good agreement was achieved between numerical, analytical, and experimental results for a fully developed, phase dependent axial velocity profile. It was seen that with an increase in frequency, the velocity also increased. Phase dependent behaviour also showed the effect of acceleration and deceleration of the flow. Low values of frequency and phase angle had negligible effect while a more pronounced effect was observed with increasing frequencies. Particularly for high frequencies of $Wo = 105$, 226, and 402, greater effects of flow reversal were visible at near-wall and off-wall locations, as shown in Figure 3-9.

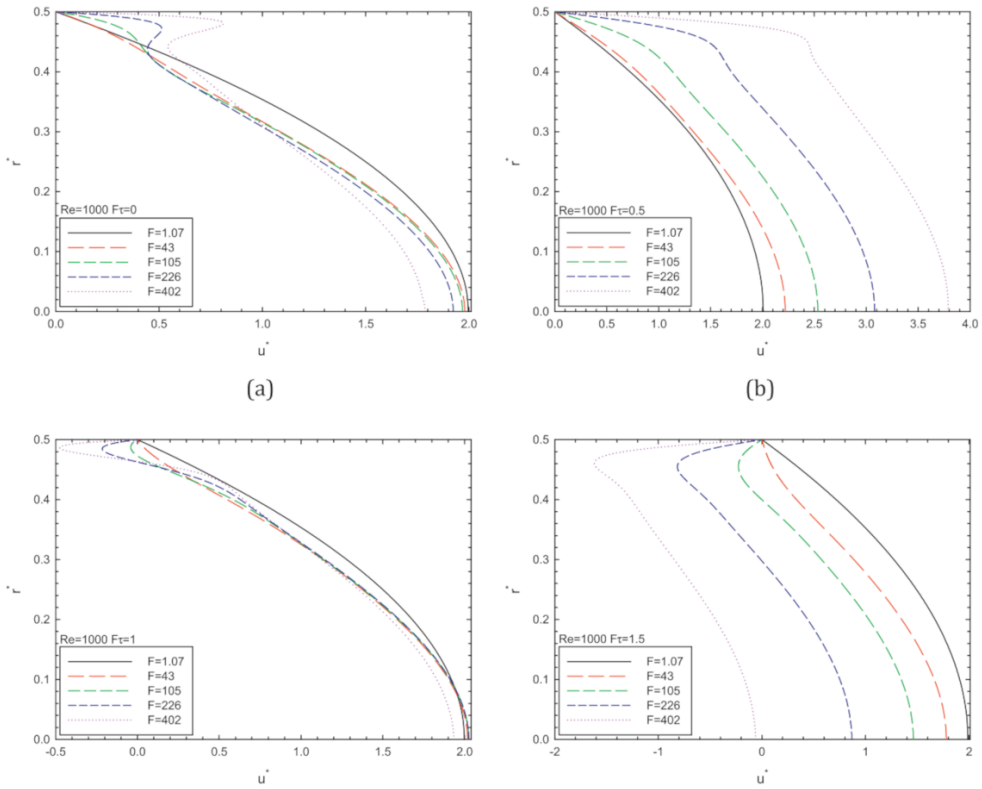

Figure 3-9: Effect of frequency (F) on radial (r*) velocity profile (u*) for a pipe at different phase intervals , as reported by Aygun and Aydin [52].

Lower frequencies of $Wo = 1.07$ and $Wo = 43$ showed no flow reversal in the velocity distributions near the wall [53]. For example, at $Wo = 105, 226, 403$, during the second part of the acceleration phase ($\theta = \pi/2 - 2\pi$) where the flow re-enters the pipe, near and off-wall flow reversal was distinguishable as shown in Figure 3-9. However, for $Wo = 226$, at the phase angle of 0, flow reversal shifted away from wall. This phenomenon was predicted previously by Haddad *et al.* [51]. For very high frequencies of $Wo = 402$, flow reversal occurred near the wall for the phase angles of 0 and $\pi/2$ and off-wall for the phase angle of $3\pi/2$.

Qi *et al.* [54] experimentally investigated the flow field distribution and turbulence structures exhibited by pulsating flows in a 5×5 rod bundle arrangement at a constant $\overline{Re} = 7940$ using deionized water with 1% sodium chloride solution. Analysis involved phase-locked PIV measurements across the second row, labelled as PA2, with matching refractive index for variations in the flow rate amplitude ($0.31 \leq A_0 \leq 0.65$) and Womersley number ($0.000371 \leq \mathrm{Wo} \leq 0.000865$) representing pulsating time periods of $3 \leq \lambda(\mathrm{s}) \leq 7$. The presence of annular effects, previously studied by Richardson and Tyler [39] existed. Higher velocity gradient near the wall led to increased instantaneous friction factors for the pulsating flows compared to steady flow. As the pulsating frequency was increased, high local peaks of velocities existed in near the wall regions,

whereas a corresponding reduction in local velocity amplitudes was evident in the core bulk regions, as seen in Figure 3-10. A development of phase lag between the bulk core and near-wall regions for high pulsation frequencies occurred since the core region velocities respond with a delay to the imposed pulsations than the wall regions. For a fixed pulsation frequency and varying pulsation flow rate amplitude indicated insignificant effect on the modulation of velocity amplitudes between the core and near-wall regions of the rod bundles as shown in Figure 3-10 with a narrow variation.

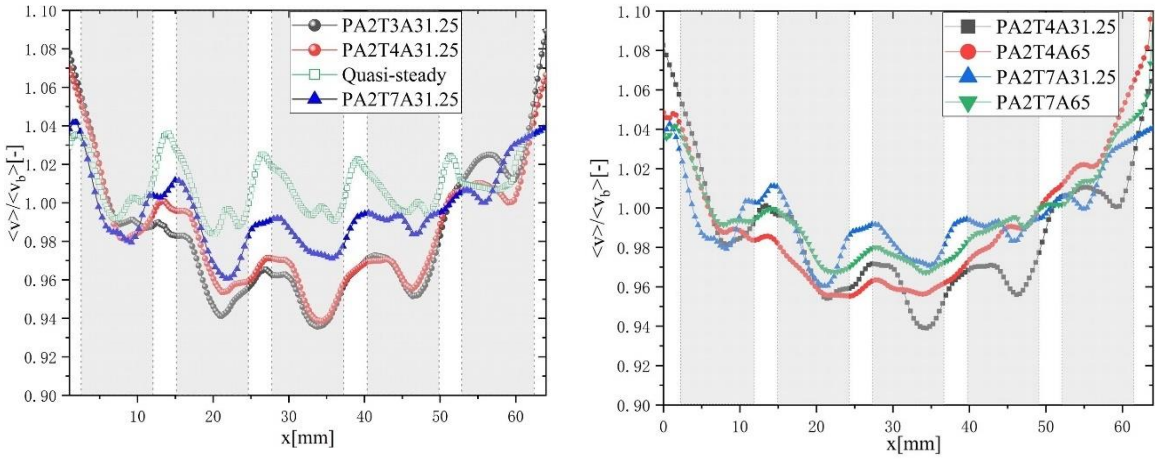

Figure 3-10: Effect of pulsation flow parameters along the second row tube (legend describes a function of time period *t (s)* and pulsation amplitude in %) on local amplitude of velocity modulation (v/v_b) ($= U_{osc}/U_s$) by varying frequency (Wo) (LEFT) and velocity flow rate amplitudes (A_0) (RIGHT) by Qi *et al.* [54].

3.4 Wall Shear Stress and Shear Rate

The wall shear stress of oscillating internal flows was first theoretically predicted by Uchida [33], involving the characteristic parameters of influence which are the flow rate amplitude and pulsation frequency. It was observed, for constant pressure gradient pulsations, that the magnitude of the wall shear stress decreased with increasing pulsation frequency and correspondingly decreasing flow-rate amplitude, as indicated from Figure 3-11. However, the evolution of phase delay was lesser, attaining up to $\pi/4$ in comparison to a peak phase delay of $\pi/2$ as is noted for the flowrate amplitude and pressure gradient from Figure 3-4.

Generalized analytical solutions for the mean friction factor (as introduced in the Section 2.1) were developed for fully developed steady laminar flows through rectangular ducts by Shah and London [19]. Since the velocity profile is fully developed, the wall shear stress is invariant axially. Thus, the local and average friction factor are effectively the same quantities. Solutions were developed to

determine the friction factor and its dependency on the laminar flow Reynolds number, duct geometry, and aspect ratio.

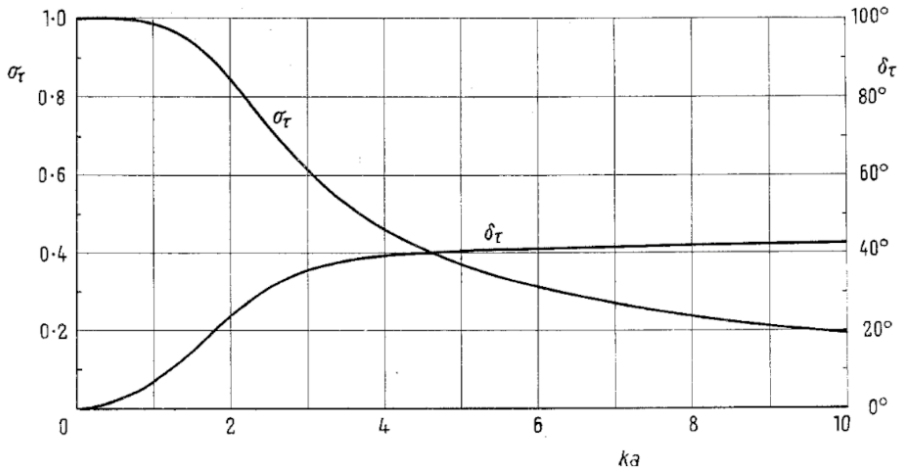

Figure 3-11: Comparison of pressure gradient amplitude (σ_τ) and phase evolution (δ_τ) of wall shear stress with frequency (ka) for sinusoidal flowrate oscillations, in a study by Uchida [33].

By analysing the wall shear stress profiles, a prospective solution was identified for the problem of the removal and prevention of fouling deposits on the walls of industrial piping. Thus, a threshold wall shear and the thermal state of deposit can be identified with which the pulsation frequency and amplitude can be predicted to solve this problem. In a study performed by Haddad *et al.* [51] for channel and pipe geometries, the results predicted that the wall shear stress increased with frequency and higher magnitudes were recorded for the channel geometry. For the range of frequencies evaluated, the phase shift for the channel flow was higher than that for the pipe flow, with both the cases showing a phase lag of $\pi/4$ relative to the pressure gradient.

Accurate experimental measurements of wall shear rate are challenging due to the large uncertainties associated with the small pressure gradient values. This has been addressed by several previous studies. For example, the work by Hughes and How [55] highlights the use of an improvised pulsed Doppler ultrasound system to effectively reduce the measurement errors to determine the wall shear profiles. The spatial resolution was enhanced using a deconvolution mechanism in the frequency-domain. The instantaneous velocity profiles were determined for $9.6 \leq \mathrm{Wo} \leq 14.1$ using trigger control from a piston pump and subsequently phase-averaged along the radial locations. Using Fast Fourier Transform and noise reduction techniques, a corrected velocity profile was obtained. The accuracy of the centreline profile was within 4.5%, and the average error over the full velocity profile relative to the mean velocity was 0.9%, thus showing close agreement with analytical predictions of Womersley [42], and with experimental results of Denison and Stevenson [45] and Ojha *et al.* [48].

However, large discrepancies were observed in the case of flow reversal effects. The average value for shear stress profiles, expressed as the difference between experimental values and theoretical values as a percentage of theoretical values, presented an accuracy of 3% with deconvolution techniques while with the unconvoluted data it was 5%. The accuracy of the analytical solution was expressed as a percentage difference between the experimental and analytical results. Deconvolution of data in the form of signal filtering improved the accuracy of determining the peak-peak wall shear rate. Wall shear rate ($1/s$) was estimated from the gradient of the measured velocity profile. A much higher frequency response was suggested to measure the wall shear rate in comparison to the velocity. Across the radial locations extending away from the wall, the amplitudes and mean values of wall shear rates decreased, and the phase lag subsequently increased, as shown in Figure 3-12. It was seen that as the fit was extended to points away from the wall, the amplitude and mean value of shear rate decreased along the curve while the phase lag increased.

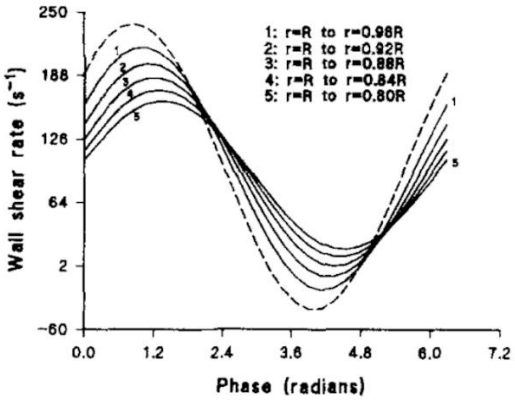

Figure 3-12: Indicators of fit with varying radial locations to determine pulsatile wall shear rate. Solid, dotted lines show the theoretical near-wall velocity profile and theoretical value at the wall, respectively in a study by Hughes and How [55].

The wall shear stress profiles reported by Ojha *et al.* [48] were obtained using the photochromatic dye technique as described previously. The profiles were estimated by evaluating the velocity gradients using a polynomial fitted curve. The results show good agreement with theory in the central tube region. Near wall profiles were compromised as the peak flow amplitudes were lower than that of the predicted values, which the authors suspected to be due to the non-circular tube geometry. The phase difference between the measured wall shear stress and volumetric flow rate was about $31° \pm 4°$ in comparison to the theoretical value of $36°$.

In another study by Zhao and Cheng [56], a time-resolved and cycle-averaged friction coefficient relationship was developed for a sinusoidal laminar oscillating flow in a circular pipe. Based on the

analytical solutions of Uchida [33], a modified expression for predicting the friction coefficient for purely oscillating flow was defined based on a kinetic Reynolds number and oscillating flow rate amplitude. Oscillations were generated using a double acting pump attached to a sinusoidal crank and yoke mechanism. The temporal variations of mean axial velocity gradients were recorded using hot-wire anemometry. The estimated uncertainty in the velocity was reported to be $\pm 2.5\%$ while for the cycle-averaged friction coefficient it was $\pm 10.5\%$. Air flows with laminar kinetic Reynolds number of $23.1 \leq Re_\omega \leq 395$ and fluid displacement amplitude $F_0 \leq 26.42$ were investigated. It was observed that with an increase in Re_ω from 144.1 to 324.3 the pressure drop increased due to a more pronounced annular effect. Radial velocity gradients were found to be steeper adjacent to the pipe wall, and so the friction force also increased with an increase in Re_ω. Additionally, the inertial component in the momentum balance also showed an increasing trend. By analysing the instantaneous friction coefficient during one cycle, a sinusoidal temporal variation was reported. The instantaneous friction coefficient decreased for both the cases shown in Figure 3-13; (1) with an increase of Re_ω at a set value of the dimensionless fluid oscillation amplitude and (2) an increase of the dimensionless fluid oscillation amplitude for a fixed Re_ω.

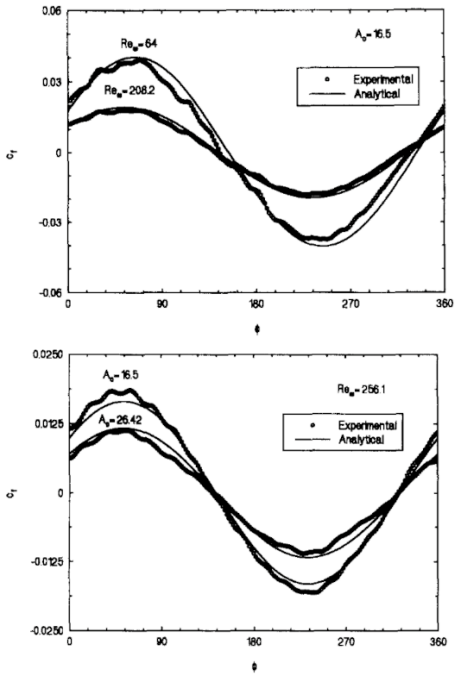

Figure 3-13: Comparison of instantaneous friction coefficient for analytical and experimental cases, from Zhao and Cheng [56] (a) $Re_\omega = 64$ and 208.2 at $F_0 = 10$, (b) $F_0 = 16.5$ and 26.42 at $Re_\omega = 256.1$.

In their analytical investigation of a sinusoidal turbulent pulsating flow, flow pattern diagrams were evaluated by Omhi *et al.* [57]. The authors classified 3 regimes: quasi-steady, intermediate and inertia dominant. The low-frequency regime was dominated by the viscous forces with minimal

phase lag between the mean velocity and the axial pressure gradient, whereas the phase lag is increased to $\pi/2$ for the inertial dominant high frequency flows. Analytical expressions were derived based on the variation of the pulsation frequency. It was proposed that under low inertia at low frequencies, the quasi-steady and equivalent viscosity (which the authors described as a relation between local coefficient of friction, fluid viscosity and radial dimension), agreed with the analytical results in the range of $Wo \leq 1.41$. While for higher frequencies $Wo \geq 14.1$ a significant deviation was observed in the results which is understood to be due to an overestimation of inertial terms. The modified equivalent viscosity and analytical predictions agreed well for the region of $1.41 \leq Wo \leq 14.1$. A phase lag between the mean velocity and shear stress was observed, approaching $90°$ ($= \pi/2$) as the pulsation frequency was increased, which was in accordance with previous studies.

While most of the studies presented above are focussed on *laminar* flow through pipes, an interesting experimental and numerical investigation of large amplitude sinusoidal oscillating flows was performed by Mao and Hanratty [58]. Wall shear rate profiles were investigated for turbulent flows through a pipe with $Re_s = 10{,}610$ at a fixed pulsation frequency $Wo = 0.0514$ for flow rate amplitudes of $A_0 = 0.1888$ and $A_0 = 0.375$. A reciprocating plunger controlled with a variable stroke and frequency introduced the flow oscillations to the pipe. A then novel method of measuring the instantaneous mass transfer rates was employed which made use of two probes within a very thin insulation sheet. Data was evaluated using the inverse mass transfer method. This technique demonstrated the ability to measure the instantaneous flow reversals at the wall. The instantaneous results of shear rate fluctuations over three periodic cycles are identified from Figure 3-14 (a) which depicts the occurrence of peaks at the location of flow reversal at the wall. The time-averaged wall shear rate, normalized with corresponding steady shear rate of Figure 3-14 (b) was noted to be significantly lower to the steady flow, suggesting a reduction in drag due to the occurrence of large flow reversal. The peaks in Figure 3-14 (c) which plots the phase-averaged intensities of wall shear rate fluctuations, normalized with mean shear rate of corresponding steady flow were noted to occur at the locations along the wall where the flow reverses its direction. This occurrence was said to be caused because of drifting of flow reversal separation and reattachment times. The observed intensity of wall shear fluctuations is analogous to the case of separating flows. However, the numerical simulations could only predict the time-mean shear rate, phase-averaged shear rate and the intensities away from the shear reversal points.

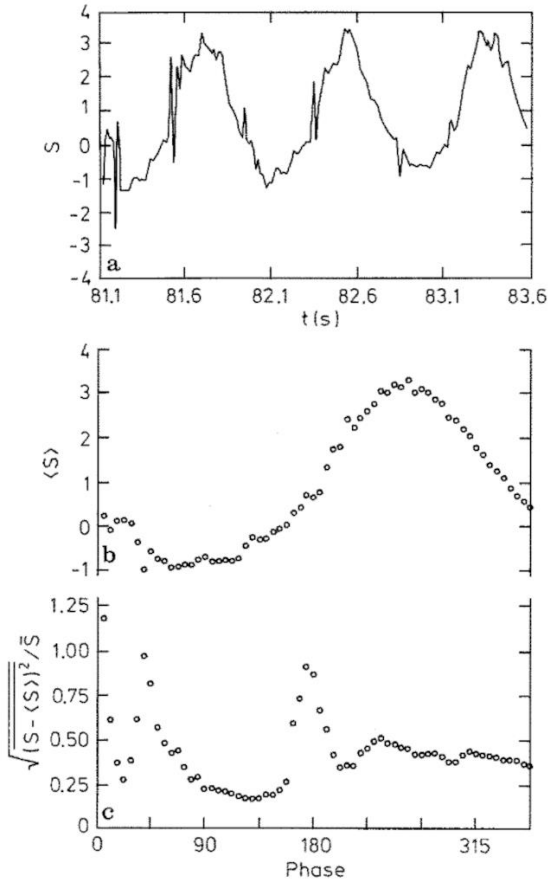

Figure 3-14: Measured wall shear rate (S) for $Re_s = 10{,}610$, Wo $= 0.0514$, $A_0 = 0.375$, as shown by Mao and Hanratty [58] (a) Instantaneous wall shear rate signals, (b) Phase-averaged wall shear variations, (c) Phase-averaged intensity of wall shear fluctuations.

The technique of measuring friction coefficient inside a pipe using the root mean square value (RMS) as described above by Ohmi *et al.* [57] was also preferred in an experimental study by Aygun and Aydin [53] using distinctive piston-driven pulsating flows. This form of pulsation does not follow the classical pressure driven flow and hence the velocity of piston needs to be accounted in addition to the pressure distribution. A direct relationship was observed between the magnitude of the friction coefficient and the frequency. For low frequency flows ($Wo < 50$) and steady flows, the RMS friction coefficient was almost constant, as is seen from Figure 3-15. Whereas, due to the flow reversal effects as outlined previously, for high frequency flows ($Wo \geq 50$) the friction factor magnitudes are increased substantially, since for such flow formats the axially driven fluid necessitates higher power as frequency and the magnitudes of friction factor are interrelated. These high frequency pulsations led to higher shear factors and corresponding increased friction values.

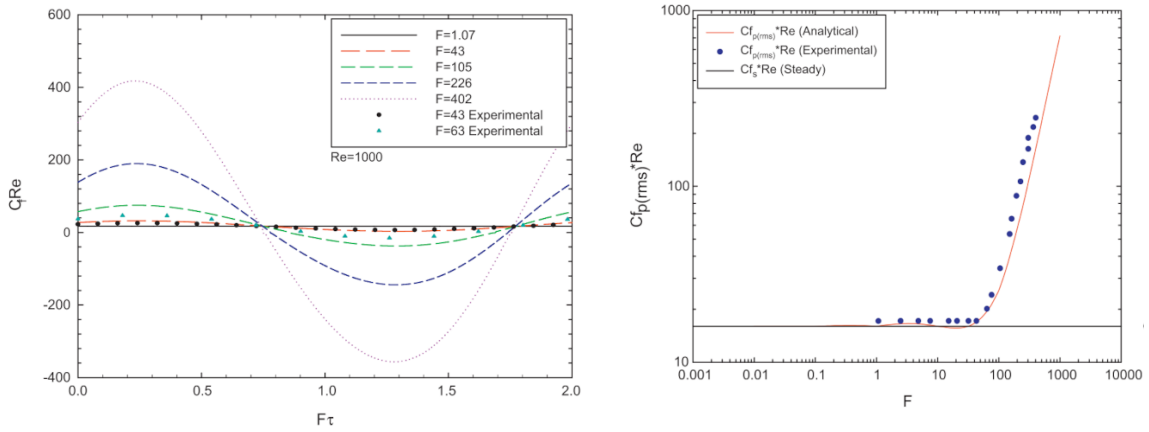

Figure 3-15: Parameter based variation with RMS friction coefficient (c_f), as obtained by Aygun and Aydin [53]. Variation of phase angle with friction coefficient (left), and variation of pulsation frequency (right).

An experimental and theoretical analysis of flow resistance characteristics at ambient temperature with rectangular channels of varying aspect ratio ($3.72 \leq D_h \leq 5.87$) under pulsating laminar flow was performed by Zhuang *et al.* [15]. The pulsating frequency was varied as $0.2 \leq Wo \leq 2$ and the velocity amplitude ratio varied between $0.05 \leq A \leq 0.92$. The coefficient of friction (C_f) was defined as the ratio of the time-average pulsating flow friction coefficient to the steady flow friction coefficient. It was found that the aspect ratio showed no significant effect on the coefficient of friction. As the oscillating Reynolds number was increased, the flow appeared to be in a laminar-turbulent transition state with turbulent bursts, despite the time-average Reynolds number (Re_s) being less than the critical Reynolds number for transition. Since pulsatile flow consists of acceleration and deceleration phases, in particular with the increase in time-average Reynolds number closer to the critical value, the instantaneous pulsating velocity distribution couldn't always be in a laminar state.

As seen from Figure 3-16, the pulsation frequency exerts a significant influence on the pulsating friction coefficient. It is observed that the friction coefficient is inversely proportional to the pulsating period. Thus, at larger periods the friction coefficient approaches the steady flow value due to smaller acceleration time at a time average Reynolds number of $Re_s = 1000$. Increasing the pulsating frequency and the oscillating Reynolds number led to an increase in the friction coefficient. The instantaneous value of the maximum pressure drop for pulsating flow was observed to increase with a relative increase in velocity amplitude and pulsation frequency.

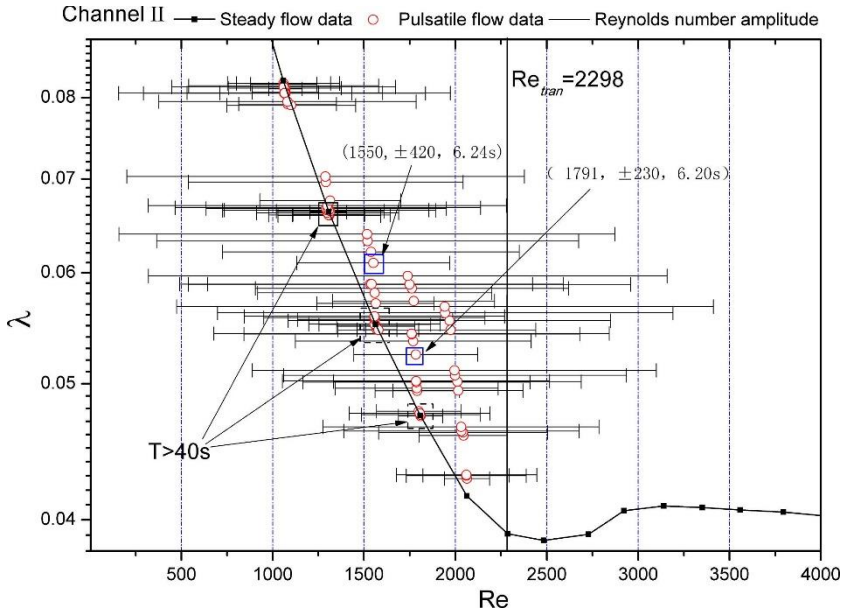

Figure 3-16: Comparison of flow characteristics (λ: frictional factor) of pulsatile flow and steady flow for a rectangular minichannel configuration of (AR = 0.075 and $Re_s = 230 - 11{,}025$), by Zhuang *et al.* [21].

Blythman *et al.* [59] analytically and experimentally using PIV studied the nature of the wall shear stress and pressure gradient profiles in rectangular minichannels in response to varying pulsation frequencies. The study investigated the various flow regimes inside the channel such as quasi-steady, transitional, and inertia dominated. A micro gear pump was used to generate the steady and pulsating flows, with Womersley number range $1.49 \leq Wo \leq 10.54$ used in the experiments which was extended to 33.33 for the analytical solutions. The shear stress near the wall regions was seen to increase with pulsation frequency, which was due to the simultaneous increase of the near-wall velocity gradient. The pressure gradient to drive such flows was observed to be significantly higher than that for steady flows. For low frequencies, since the axial motion of fluid is insignificant, the flow was observed to be in a quasi-steady state with the pressure gradient in phase with the viscous forces near the wall. With an increase in pulsation frequency, the inertial forces were prominent and a phase difference up to $\pi/2$ between the pressure gradient and volumetric or mass flow rate was observed.

3.5 Summary of hydrodynamic studies of pulsating flows

A summary table is provided in Table 3-1. The major findings from the literature review of the hydrodynamics of internal pulsating flows are:

- 'annular effects' wherein the local peaks of velocities appeared in near-wall regions and not in the central bulk core were first demonstrated experimentally for a velocity distribution in sinusoidal oscillating flows and later established by several authors.
- A relationship was drawn between the volumetric or mass flow rate of the fluid and pressure gradient. At low pulsation frequencies, both entities were in phase. At high pulsation frequencies the amplitude of the volumetric or mass flow rate decayed, and pressure gradient lagged the volumetric or mass flow rate, reaching a phase delay of up to $90°$ (= $\pi/2$).
- The occurrence of flow reversal effects was determined to be dependent on the pulsation frequency, amplitude of the flow rate, and phase angle. For low frequencies, it was observed to be near the wall regions. It was shifted away from the wall for high frequency flows.
- An inverse proportionality was seen between the variations of frequency and volumetric or mass flow rates for the occurrence of flow reversal.
- Based on the phase angle during a pulsation, a shift of the location of flow reversal from central lamina to channel/pipe wall was observed.
- The wall shear stress was inversely proportional to flow rate amplitude and pulsation frequency. With a variation of transverse locations from wall to central regions of the flow, the amplitude of shear rate decreased.
- In general, since low frequency flows were dominated by viscous forces, minimal phase delay was found between velocity and shear stress profiles. While for the inertia dominated, high frequency flows, a considerable phase lag of up to $\pi/4$ between velocity and shear stress profiles was observed.
- Studies involving estimation of the friction coefficient were based on the relationship between the kinetic Reynolds number and amplitude of the flow rate. A direct proportionality was shown between the friction force and the two, due to steeper velocity gradients adjacent to the wall regions.
    - A relation between friction coefficient and frequency showed that at low pulsation frequencies the friction coefficient matched the value of steady flow.
    - In effect with the flow reversal effects, higher friction values were measured at high frequency flows.
    - No significant effect of aspect ratio was found with coefficient of friction.

Table 3-1:Summary of selected studies of pulsating or oscillating flows that focus on improved understanding of the hydrodynamics.

Reference	Year	Flow/Type	Geometry	Analysis Technique	Fluid	Variables	*Wo or f (Hz)*	*Re*	*A_0 or F_0*
Richardson [38]	1927	Oscillating/Mass	Circular	Hot-wire anemometer	Air	Amplitude	5-25	-	0.035-0.20
Fan & Chao [35]	1965	Pulsating/Mass	Parallel plates	Analytical	Incompressible fluid	Radial distance	0.05-500	-	-
Lingford & Ryan [44]	1965	Pulsating/Mass	Circular	Pressure transducers	Water-glycol mixture	Radial distance, Instantaneous	1.83-21.0	-	-
Holmes & Vermeulen [40]	1967	Oscillating/Mass	Square, Rectangular	Flow visualization	High μ transparent fluid		-	-	-
Harris *et al.* [41]	1969	Oscillating/Mass	Circular	Flow visualization	High μ fluid	Radial Distance	1-7	-	-
Denison & Stevenson [45]	1970	Oscillating/Mass	Circular	Laser doppler velocimetry	Incompressible	Radial distance, normalized	1.71-14.1	-	-
Clamen & Minton [47]	1976	Oscillating/Mass	Circular	Hydrogen-bubble technique	Water	Radial distance	11.2-26.7	1275-2900	1.45-5.8
Muto & Nakane [46]	1980	Pulsating/Mass	Circular	Flow visualization	High μ fluid	Radial distance	0.5-2	-	1.3-23
Ohmi *et al*. [57]	1981	Pulsating/Mass/Wall Shear	Circular	Analytical	-	Instantaneous	1.4-14.1	>2300	
Ojha *et al.* [48]	1988	Pulsating/Mass	Circular	Photochromatic dye	Transparent fluid	Radial distance	7.52	-	1.21
Mao & Hanratty [58]	1992	Oscillating/Wall shear rate	Circular	Analytical + Dual probe	Potassium iodide	Radial distance/ Instantaneous	0.0514	10,610	0.18-0.37
Hughes & How [55]	1994	Pulsating/Mass/Wall Shear	Circular	Pulsed Doppler Ultrasound	High μ fluid	Radial distance/Instantaneous	9.6-14.1	408-1151	-
Zhao & Cheng [56]	1996	Oscillating/Wall Shear	Circular	Hot-wire anemometer + Analytical	Air	Radial distance/ Instantaneous	-	23.1-395	10-26.42
Ünsal *et al.* [49]	2005	Pulsating/Mass	Circular	Hot-wire anemometer + Analytical	Air	Radial distance/ Instantaneous	0.8-6.6	-	-
Haddad *et al.* [51]	2010	Pulsating/Mass/Wall shear	Rectangular, Circular Pipe	Analytical	Incompressible fluid	Time and space dependent	0.01-10	-	0.6-1
Aygun & Aydin [53]	2014	Pulsating/Mass/Wall Shear	Circular	Analytical + Numerical + Hot wire anemometer	Air	Radial distance/ Instantaneous	1.07-402	1000	0.48
Zhaung *et al.* [21]	2014	Pulsating/Wall shear	Channel	Analytical + Differential Pressure	Purified water	Instantaneous	0.2-2	142-11025	0.05-0.9
Blythman *et al.* [60]	2017	Pulsating/Mass/Wall Shear	Rectangular	Analytical + PIV	Deionised water	Transverse distance/ Instantaneous	1.4-10.5	-	0.9
Qi *et al.* [54]	2020	Pulsating/Mass	Rod bundle	PIV	Deionised water	Instantaneous	0.0003-0.0008	2870-13525	0.31-0.65

4) Literature Review Part 2: Heat Transfer Studies of Internal Oscillating and Pulsating Flows

Heat transfer studies associated with internal oscillating and pulsating flows were in the early years formulated analytically in a similar manner to the hydrodynamics studies described in the previous chapter. An analytical study of laminar pulsating flow in a pipe carried out by Faghri *et al.* [61] showed the interaction of velocity and temperature oscillations. There existed a relationship with the diffusivity term in the energy equation that contributed to higher heat transfer rates based on the interaction of pulsating velocity and temperature profiles. The pipe was modelled with a constant wall heat flux boundary condition and axial heat convection was considered in the energy equation. Eliminating the axial conduction as it was accounted for by the Peclet number, the resulting equation with pulsating velocity components is a non-homogeneous Bessel equation and was solved using the method of undetermined coefficients. As a result, axial convective diffusion flux resulting from the pulsation motion was evaluated on the basis of flow rate amplitude and fluid Prandtl number. High flow rate amplitudes contributed to a stronger convection, thereby increasing the heat transfer rate. Whereas a high Prandtl number of fluid was expected to reduce the heat transfer due to weak thermal diffusivity. Extending the correlations to determine the Nusselt number (Nu) showed that the existence of the pulsating motion of fluid increased Nu in the fully developed region and the *Nu* was proportional to the flow rate amplitude and Prandtl number. For higher harmonics at low frequency pulsations Nu did not depend on the frequency. The effect of flow reversal showed the time averaged Nu to be greater than the steady flow Nu due to the flow mixing.

4.1 Axial (Streamwise) Diffusion Transport: An Introduction to Axial Thermal Diffusivity

Large axial oscillating temperature gradients can exist when the fluid oscillates under a thermal gradient. During the acceleration stage of the oscillation, hotter fluid from core regions moves to colder regions of fluid due to heat flow within the boundary layers and colder solid walls. The rate of heat transfer is increased with a thinner boundary layer and a corresponding increase in flow frequency. During the deceleration portion of the oscillation, the hotter fluid from the boundary and walls diffuses into the cold fluid core. The possibility of the onset of turbulence needs to be considered for high frequency and tidal displacement flows due to greater inertial forces. Narrower channels and related viscous effects can be large enough to prevent turbulence.

Dispersion of a soluble matter into a slow steady flow has shown the combined action of molecular diffusion and velocity variation over the cross-section of a tube. This has been determined analytically and verified experimentally in one of the fundamental studies by Taylor [62]. Interesting features describing the motion of a coloured streaks showed a symmetric spread which travelled with the fluid velocity despite the velocity distribution over the section being asymmetric. Since this dispersion in steady flow is the result of combined action of axial convection and radial molecular diffusion, a case-by-case method was adopted to evaluate this effect using equations for mean and time-varying solute concentrations. Due to the greater influence of molecular diffusion, the dissolved substance was prevented from being dispersed. This was evident when comparing the maximum value of concentration obtained versus the uniformly distributed concentration, with a significant difference observed. The asymmetries in the experimental curves were investigated by Chatwin [63], who deduced that either the injected contaminant could be initially asymmetric, or the cloud of contaminant had a long tail upstream or downstream. Theoretical relations were applied for a Poiseuille flow in a pipe using asymptotic series for the distribution of solute concentration based on the assumption that solute diffusion obeyed Fick's law. Using cross-sectional analyses, it was shown from Figure 4-1 that at the AA region, due to the walls' influence, the diffusion transport of the fluid was directing inwards where velocity was greater than that of the wall. A similar trend was found for the CC region but with an expected decrease in concentration. Since the velocity gradient at the pipe axis is zero, concentration was almost uniform near the pipe core and around CC.

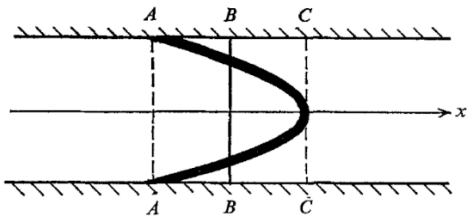

Figure 4-1: Initial dispersion of cloud containment in Poiseuille flow, by Chatwin [63].

In a subsequent study by Chatwin [64] who adopted an axial pressure gradient varying harmonically with time, the axial dispersion of the containment was predicted. The transient features of an axially dispersed containment cloud demonstrated interesting features of transverse dispersion. Further, the amplitudes of extent to which the cloud appeared to be periodically expanding and contracting was extensively analysed. Based on the effect of the oscillatory frequencies, low frequency flow demonstrates characteristic features, wherein the time period of fluid viscous effects to readily adjust with the transverse variations in vorticity was considerably lower than the time period of imposed oscillation. Additionally, the time period of dispersion of concentrations in the transverse direction to adjust with the molecular diffusion is lower too. Thus, the time scales of velocity and concentrations were unaffected by the instantaneous pressure gradient. At high frequencies the time scales of velocity and concentrations in transverse direction was greater than the molecular diffusion and thus the velocity and concentrations varied less in the transverse direction except near the tube boundary, whereas more significantly axially.

The context of the results presented by Chatwin [64] were formulated using analytical expressions by Watson [65], who showed that the rate of mass transfer (axial diffusion) of a substance is augmented by an oscillatory motion of ambient fluid. Asymptotic relations were developed for concentration distributions across the boundary layer for the cases of two-dimensional channels and circular cross-section geometries. The effective diffusivity of the contaminant, based on the average linear concentration gradient, governed the dispersion of the substance when a small quantity of diffusing material was introduced in the pipe. The flux energy of the contaminant increased significantly at high frequencies along with the pressure gradient. However, this energy (or increase of flux) was retained within the boundary layer for high frequencies, while for low frequencies it was dissipated throughout the pipe.

Determination of the early stages of dispersion of a contaminant was analysed further by Smith [66] using a delay-diffusion process. In accordance with the work of Chatwin [64], there exists a limitation of the diffusion equation for very long intervals after discharge, since the rate of dispersion depends on the manner in which the contaminant has mixed across the flow upstream.

For wider channels (described as 'estuary – a geographic water connection between the tide and stream' by the authors), small scale cross-sectional mixing is achieved over a period of one tidal oscillation (periodic oscillation). At every flow reversal regime, a longer time span is said to exist wherein the contaminant cloud undergoes a contraction. This leads to an undesirable negative axial-diffusion coefficient which was modified in terms of periodic contraction and expansion of contaminant in their study. For a water depth variation, the study was extended for shallow and deep estuaries using two-layer approximation theory, results showed diffusivity to be proportional to the tidal current (oscillatory velocity) and time-dependent dispersion coefficient showed agreeable value at maximum depth of 10 *m*. While at a deeper regime of up to 100 *m*, less cross-sectional mixing was achieved based on the timescale of one tidal oscillation. Hence the effect of transverse oscillatory shear had little effect on longitudinal dispersion.

Based on the previous analytical predictions by Watson [65], an experimental investigation was performed by Joshi *et al.* [67] to determine the effective diffusivity for the axial transport of gas under oscillatory flow through a circular tube. Comparison of the results of the two studies showed satisfactory agreement. The axial spread of the concentration was found to depend on both the axial convection and the radial molecular diffusion. This combination of transport mechanisms was termed as 'augmented diffusion'. Time-progression studies have shown radial molecular diffusion tends to reduce the rate of dispersion from the fluid mixture having zero molecular diffusivity, thus leading to migration of dispersion species at locations of rapid fluid motion near the tube centreline and the slow-motion regions near the wall. This dispersion is widely described as 'diffusion-limited convective transport'. For the estimation of steady flow, a modified approach from the one used by Watson was followed with a split expression for velocity and concentration with an area-averaged mean value over one cycle and other with the time-dependent perturbations. An effective axial diffusion coefficient was defined based on the area-averaged and time-averaged concentration quantities. A non-invasive infrared absorption technique was used for measurements. Methane gas, driven in an oscillatory motion by a motor-crank assembly, was smoothly introduced into the tube. Tests were performed at a single frequency $Wo = 7.33$ for different flow rate amplitudes. On comparing analytical results with subsequent studies, for increase in the oscillation frequency at a fixed velocity amplitude, a rapid fall in the rate of axial dispersion was observed for oscillation frequencies values up to $Wo = 20$. Experiments were also carried out with a steady flow component which showed minimal effect on the process of augmented diffusion.

Evaluating the previously established problem of contaminant diffusion with oscillatory conditions by Chatwin [64], Kurzweg [68] proposed a theoretical solution for time-dependent radial

temperature variation within conducting channel walls. A pressure-gradient induced periodic viscous flow was considered in a long parallel plate channel maintained with different temperature reservoirs. An equation for the effective averaged thermal diffusivity was developed, wherein the time-averaged convective thermal flux was a non-zero parameter, thus showing heat flow in the system. The time-averaged velocity was zero which meant no net mass transport accompanied the heat flow. By relating the thermal diffusivity to the pulsation frequency and tidal displacement (equivalent to Equation (1-9)), it was inferred that at very high frequencies, the enhanced thermal diffusivity increased with the square root of the frequency. Such behaviour was also noted in a contaminant dispersion study by Watson [65]. For low frequencies, there was a direct proportionality to the square of oscillation frequency. Thus, for a fixed frequency there existed an optimum channel width to maximise the relationship to obtain maximum axial heat transport.

Zhang and Kurzweg [69] extended the numerical study to a more complex two-dimensional geometry. The primary consideration was of axially dependent heat exchange between an oscillating fluid (water) and the bounding walls of a steel/glass pipe. A time-dependent study of velocity and temperature profiles in the range $0.1 \leq Wo \leq 100$ was examined. The velocity profiles at low oscillation frequencies exhibited the typical behaviour: quasi-parabolic shape and in phase with the pressure gradient. For high frequencies, typical boundary layer thickness was observed near the wall with a slug-like flow in core regions, with a phase shift of $\pi/2$ between the velocity and pressure gradient.

The results for time-averaged heat flux versus Wo showed the increase in heat storage capacity with subsequent enhancement of radial and axial heat transfer due to the existence of conducting walls. This increase of axial heat flux was seen with higher pulsation frequencies and similarly with higher power demands to drive the fast-oscillating fluid. Although, for a fixed $Wo = 3$, parameters such as the pure molecular conductive axial heat flux in the wall (ϕ_w) and fluid $\left(\phi_f\right)$ were shown to decrease, along with the enhanced axial heat flux (noted to be magnitudes higher than pure molecular conduction). With an increase in tidal displacement, the enhanced axial heat flux increased rapidly, whereas ϕ_w and ϕ_f decreased slightly due to a weakening axial temperature gradient in central pipe sections for large fluid displacements. Higher magnitudes of enhanced axial heat flux were seen over the respective pure axial conductive heat flux cases of wall and fluid at higher Wo at a fixed axial displacement of fluid as shown in Figure 4-2. This was seen as an effect of magnification of axial temperature gradient to a higher radial temperature gradient as a result of periodic oscillations. The enhanced axial heat flux was noted to be higher than the pure axial conductive heat flux for both fluid cases. It was observed that the existence of conducting walls

make the enhanced axial heat transfer process more efficient due to additional heat storage capacity near the fluid-solid interfaces.

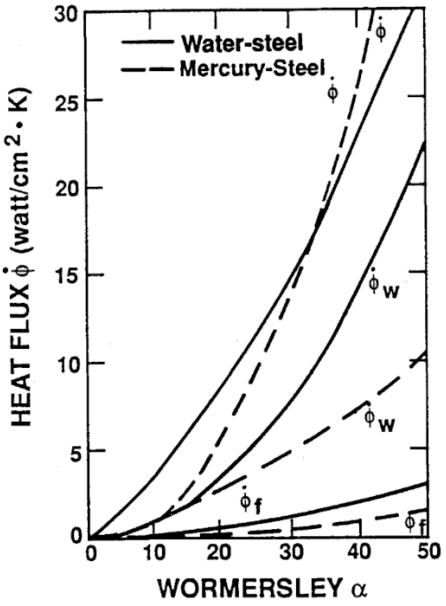

Figure 4-2: Variation of axial heat flux ($\dot{\phi}$) vs. Womersley number (α) for a fixed tidal displacement $x = 10\ cm$, as obtained by Zhang and Kurzweg [69].

The transverse diffusion of heat and heat accumulation near the wall leading to an axial heat transfer enhancement under sinusoidal oscillatory fluid motion was examined by Ozawa and Kawamoto [70], who developed a time-dependent, two-dimensional channel numerical model to analyse the flow and temperature fields for the range $7.1 \leq Wo \leq 23$. The numerical model was validated with measurements obtained using a thermos-sensitive liquid-crystal tracer visualization technique for a corresponding pipe and channel flow. A vertical channel maintained at different top and bottom boundary temperatures was used. The temperature history at each (axial) position along the channel height indicated a gradual increase in fluid temperature with a corresponding decrease in the amplitude of temperature fluctuations over the computational flow time along the vertical regions of channel. However, the temperature oscillations increased over the flow time at lower locations of the channel. For the state of fully developed heat transfer, the mean (steady) temperature during the oscillation exhibited a linear distribution along the channel. From the experimental verification of the numerical results, it was inferred from the Figure 4-3 that typical transverse velocity profile exhibited a phase difference with temperature profile due to the imposed fluid oscillations, as seen from Figure 4-3. This phase delay was primarily due to the fluid motion in the region near the wall and across the channel width, leading to a formation of transverse temperature gradients. It explains that the thermal boundary layer is formed as a result

of velocity profiles and hence the thickness of the thermal boundary layer coincides with the velocity boundary layer with sinusoidal fluid motion as shown using isotherms for every 0.43 ℃ in the Figure 4-3. The heat transfer was deemed to be dominated by transverse heat diffusion as a result of a phase delay in the transverse temperature gradient, heat storage accumulation in the vicinity of velocity boundary layer thickness and axial convection as an effect of bulk sinusoidal oscillating flow. One-dimensional lumped heat transfer analysis was carried out to determine the effective thermal diffusivity as a function of axial heat transfer enhancement. It was found to increase with a corresponding increase in oscillation frequency and oscillation amplitude of the fluid. Novel Nusselt number correlations were established using this mechanism with a dependence on fluid Prandtl number similar to two-dimensional flow and applicable for a range of $Pr = 2 - 40$ and $Re_P = 0.1 - 50$, shown in Figure 4-4.

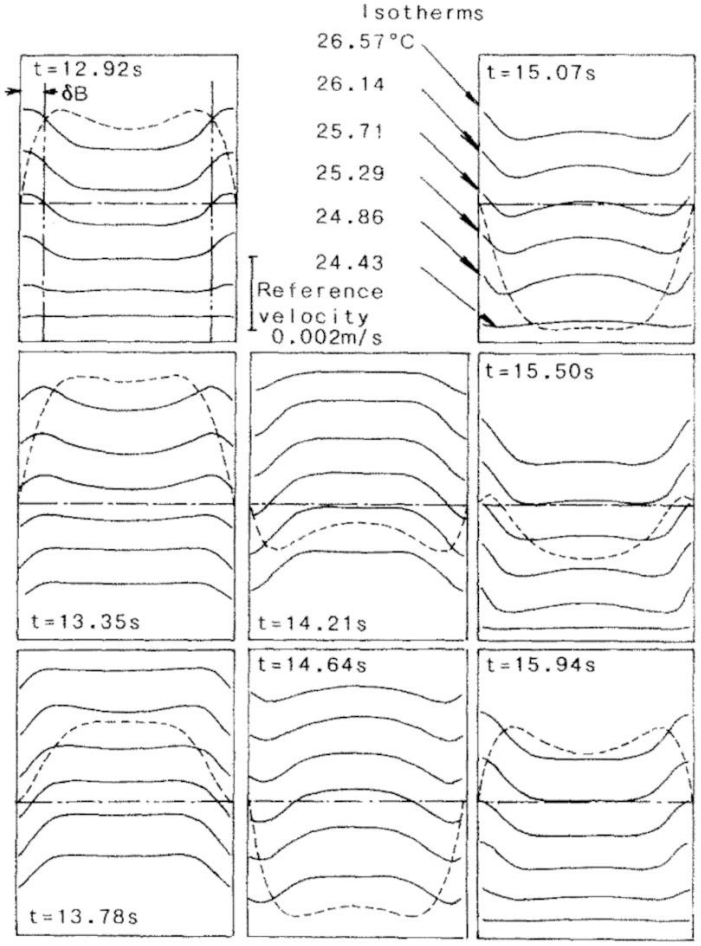

Figure 4-3: Velocity (dashed lines) and temperature (solid lines) contours for an oscillation frequency $f = 0.32\ Hz$ and amplitude $L = 3.0\ mm$, reported by Ozawa and Kawamoto [70].

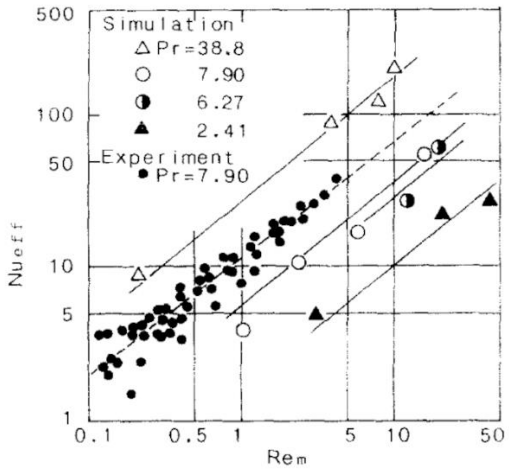

Figure 4-4: Variation of effective heat transfer coefficient with Re_p, as shown by Ozawa and Kawamoto [70].

4.2 Axial (Streamwise) Temperature Profiles

For heat exchanger applications in Stirling engines and regenerative-type refrigerators, the working fluid is theoretically confined to a thermally developing region. This is primarily due to the abrupt variation of wall temperatures in the axial direction, and due to an equal or longer swept length (defined as the function of average velocity over a full periodic cycle; $0 - 2\,\pi$) of working fluid than the characteristic length of the heat exchanger. A theoretical study characterising this problem was conducted by Lee *et al.* [71], who studied heater and cooler heat exchangers of circular pipe profile with fixed isothermal walls and fixed wall heat flux. A square-wave thermal waveform was used to represent the alternating states of heater and cooler. Owing to the thermal discontinuity in the system, in the isothermal case, the thermal developing length increases with an increase in oscillation frequency for a Womersley number range of $1 \leq Wo \leq 16$, but converges to the swept length of the fluid if $Wo > 2$ since in downstream locations, the oscillating fluid particles do not experience thermal discontinuity. Thus, at high oscillation frequencies the hydrodynamic entry length for oscillating velocity to attain a fully developed state is also predicted to be equal to the swept length. For the uniform heat flux case it was seen that the thermal developing length increased with the square of the oscillation frequency at low Womersley numbers. Additionally, the local Nu was seen to be inversely proportional to the square root of the distance from the thermal discontinuity. It was concluded that for the fully developed region the heat transfer followed the sinusoidal temperature distribution.

Sparrow and De Farias [24] numerically modelled the performance of a heat exchanger simplified as a rectangular duct. Assessment was made in terms of the energy flux carried across the exit cross-section relative to the entrance. Transient laminar heat transfer in the duct was modelled, in

which the fluid inlet temperature varied periodically using a sinusoidal profile at arbitrary frequency. From this, the thermal conditions at the wall were determined, meaning the wall temperature was a function of axial location and time. A non-dimensional parameter ($b^* = f(a/2(\rho c)_w w/2)/k$) and associated range ($1 \leq b^* \leq 100$) was defined as a combination of wall and fluid properties, geometric dimensions, oscillating frequency, and temperature variation. The amplitude of wall temperature variation during an oscillating cycle reduced with distance from the duct inlet. A corresponding increase in phase lag existed between the variation of wall temperature and b^*. This effect was related to the wall heat capacity, where the wall dampens the amplitude of wall temperature oscillations as the flow progresses axially downstream, as shown in Figure 4-5. Bulk fluid temperatures showed identical phase shift to the wall temperatures at low values of $b^* = 1$. At higher values of b^*, bulk fluid temperatures showed insignificant axial variation in comparison to the near wall temperatures. The heat transfer was positive in most of the cycle indicating that the heat flow was from wall to fluid for $T_w > T_b$, however for a short period Nu was negative, signifying that heat flowed from fluid to wall for $T_w < T_b$. Thus, it was inferred that the smaller the energy flux at the exit, the more effective the duct acts as a heat exchanger.

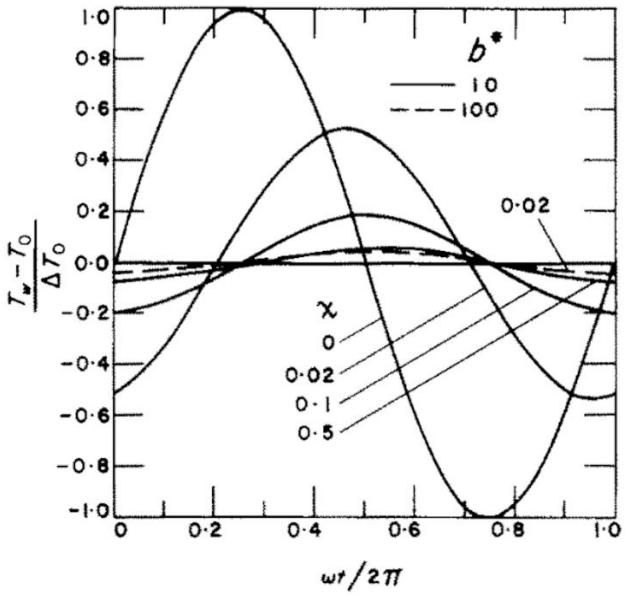

Figure 4-5: Time-dependent dimensionless wall temperature variation along the axial locations [x] for $b^* = 10$ and 100, by Sparrow and De Farias [24].

For low frequency flows it is generally observed that forced convection dominates the heat transfer process in a channel with uniform heat addition, however it has been shown that the effect of oscillation-induced diffusion can play a quite significant role. This was studied analytically for a parallel plate channel flow with uniformly heated axial walls by Siegel [72], who showed the

interaction of flow oscillations with the wall temperature gradient in terms of an axial (streamwise) transport of energy due to the presence of a mean steady flow. Axial transport was a result of transverse diffusion during the flow oscillations. Since the oscillations account for periodic variations in the transverse temperature gradient, this leads to a non-zero transverse energy diffusion progressing in the axial direction.

A numerical analysis of local heat transfer behaviour in response to pulsating flows in a uniformly heated parallel plate channel by Seo *et al.* [73] for $1 \leq Wo \leq 10$ and $0 \leq \mathrm{A}_0 \leq 0.75$ showed axial Nu enhancements near the channel entrance. This was an extended study of the flow configurations of the analytical work by Siegel and Perlmutter [74]. Low Reynolds number flows ($Re_P = 50$) were considered since pulsation effects could be distinctly predicted. For large flow rate amplitudes, the effect of pulsation on the oscillating Nu was more pronounced primarily in the channel entrance regions as is evident from Figure 4-6(b). Additionally, non-symmetric characteristics were noted due to the presence of higher harmonics with shorter time periods. It was seen for low to moderate frequencies that the heat transfer due to pulsation was pronounced in downstream locations of the channel, while in the upstream regions (i.e., close to the channel entrance) a reduction in heat transfer was noted. For high frequencies, small changes were visible near the entrance of channel, but downstream regions remained unchanged. Thus, the axial advective term of the energy equation is viewed to have a greater significance in the determination of overall heat transport in a pulsating flow, which is in agreement with the findings of Faghri *et al.* [61]. The physical significance for heat transfer behaviour between the uniformly axially heated walls and the fluid was drawn; in entrance regions the fluid temperatures are raised since the axial bulk temperature gradient is steep for pulsating flows, thereby reducing the heat transfer from channel wall to fluid in comparison to steady flows, as indicated by zone (I) in Figure 4-7. As the fluid progresses further downstream ($X^* > 1$ in Figure 4-7), a less steep axial bulk temperature gradient is observed in comparison with steady flows and oscillation-induced heat conduction is less effective in this region. Thus, the heat transfer from wall to fluid is increased for a pulsating flow, represented by zone (II) of Figure 4-7. Far downstream ($X^* > 3.5$) such changes are insignificant and hence no change in heat transfer is observed as bulk temperatures tend to the wall temperatures.

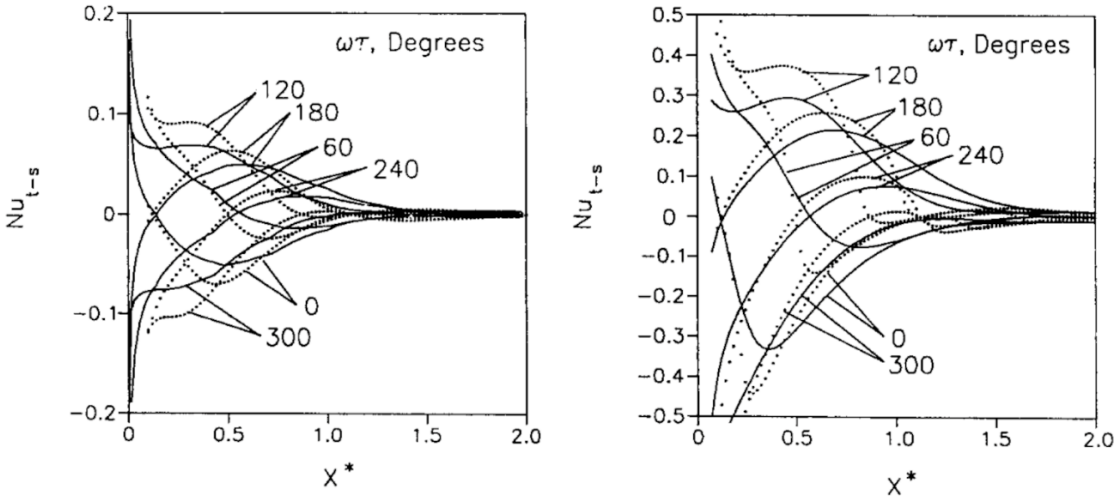

Figure 4-6: Axial variation (X^*) for oscillating Nusselt number between pulsating and steady flows (Nu_{t-s}) $(= Nu - Nu_s)$ for different phase angles at $Wo = 2$ (a)$A_0 = 0.15$, (b)$A_0 = 0.75$. From Seo *et al.* [73].

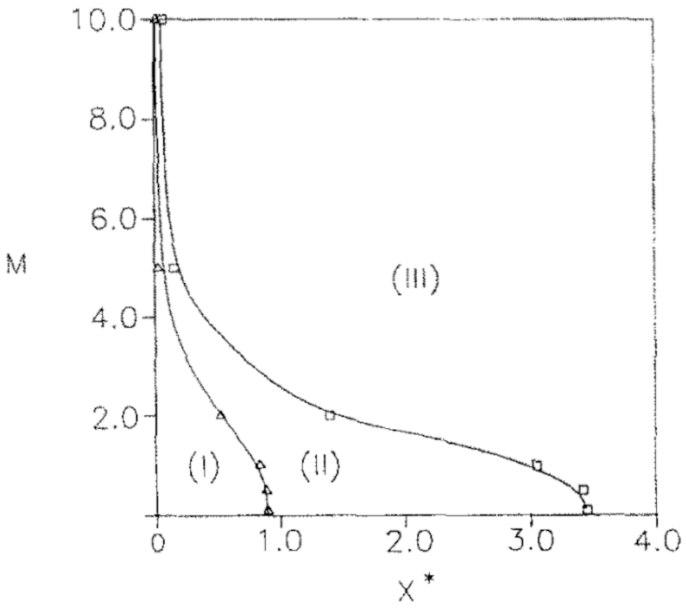

Figure 4-7: Plots of oscillating Nusselt number for a custom plane over varying axial locations (X^*) and Wo (M); zones (I), (II), (III) denote reductions, enhancements, no change in local heat transfer over steady flow values, respectively. Plot taken from Seo *et al.* [73].

A comprehensive numerical analysis of pulsating flow in a pipe imposed with isothermal conditions was performed by Cho and Hyun [75] for time-dependent boundary layer equations at different axial locations for a wide range of pulsating frequencies of $0 \leq Wo \leq 15$ and flow rate amplitudes of $0.01 \leq A_0 \leq 0.20$. Along the pipe radius, the fluctuating temperature component was zero near the entrance and mid-section, while near the wall it reached a maximum before returning to zero at the wall. At downstream axial locations, the parabolic nature was more prominent. The peak

fluctuating temperature amplitudes decreased with pulsation frequency, which showed a contrast with the fluctuating wall friction component. The time averaged Nu was observed to increase above the steady value for an increasing flow rate amplitude. For low frequencies, a maximum heat transfer enhancement was noticed for $Wo = 2$ with enhancement occurring for the narrow range of $0 \leq Wo \leq 3.3$, as seen from Figure 4-8. Along the streamwise axial locations of the pipe it was seen that the time averaged Nu decreased rapidly from a high value near the pipe entrance to smaller values in the bulk regions away from the pipe entrance. Thus, for extreme low and high frequency flows the heat transfer reduced below the steady flow value. Fluids having $Pr < 1$ presented prominent effects of heat transfer induced due to pulsations, with the occurrence of significant enhancement and reduction compared to the steady flows.

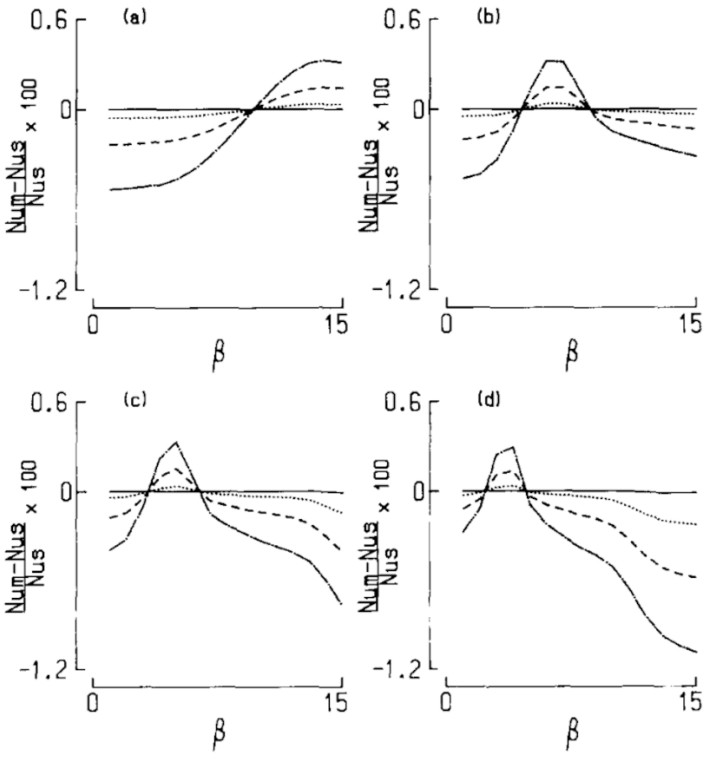

Figure 4-8: Plots of enhancement factor vs. β (= Womersley number) for dimensionless axial locations (a)$x = 01$; (b)$x = 0.05$; (c)$x = 0.10$ and (d)$x = 0.20$, at flow rate amplitudes of $A_0 = 0.01$,0.1,0.2 and 0.3. From Cho and Hyun [75].

Oscillatory temperatures showed a maximum value at a moderate pulsation frequency corresponding to $Wo = 1.2$ for a flow rate amplitude of $A_0 = 0.1$. The contrasting trend between the skin friction coefficient and heat transfer was first predicted by Cho and Hyun [75] where it was shown that for moderate and higher frequencies, the wall friction coefficient increased in magnitude while the heat transfer enhancement was reduced. This nature was also predicted by Cho and Hyun [76] in their extended study for a pulsating flow over a flat plate. However, lower

frequencies presented typical periodic variation of the wall friction coefficient and the oscillating velocity components were in phase with each other. Whereas at high pulsation frequencies, the axial evolution of friction coefficient was more pronounced with an existence of a phase lag in the pipe entrance regions. It was also observed that the quasi-steady Reynolds analogy was satisfied for very small pulsation frequencies while for greater values it lost its validity.

Using a perturbation approach for a uniform-heat flux boundary condition, expressions for time-dependent velocity and temperature were formulated for flow through parallel-plate channels and circular tubes under a pulsating forced convection flow in a study by Nield and Kuznetsov [77]. The axial conduction effects were neglected as the Péclet number was assumed to be sufficiently large. For the parallel-plates channel with a small Prandtl number of $Pr = 0.1$, a peak in the dimensionless transverse wall temperature was observed near the wall regions where the magnitude of the peak was directly proportional to the frequency in the range $0.1 \leq Wo \leq 10$. With variation of Prandtl number to up to $Pr = 10$, secondary peaks were observed along with a greater phase difference with the pressure gradient. A peak in the ratio of oscillating to steady Nusselt number was obtained for a pulsation frequency of $Wo = 5$. Similar behaviour at intermediate ranges of Wo was observed in the past literatures (e.g., Refs. [70] and [75]), while a decrease in the ratio was predicted as the fluid Pr increased. The results obtained for the circular tube showed higher magnitudes of oscillating to the steady Nusselt number ratio by a factor of about 2.5, thus predicting higher heat transfer enhancement in comparison with the parallel plate channel case. It was understood that due to the interaction with the boundary layer, the bulk fluid motion produces large enhancements of thermal and mass diffusions in contrast to steady flows.

Gedeon [78] studied the influence of section-averaged velocity and temperature (also known as mean parameters) using a one-dimensional approach to develop modified solutions for the energy and momentum equations. For model simplifications, a laminar fluid flow through a parallel plate channel was considered assuming negligible entrance effects. A linear time-averaged longitudinal temperature distribution was developed similar to the description from Kurzweg [68] which included time-independent and time-varying terms as a function of the transverse distance between the channel walls. For a fixed axial location, a uniform temperature gradient was obtained in the direction of fluid displacement at equal time period intervals in a cycle. Although in the transverse direction, the temperature gradient varied with time and position. This is attributed to the interaction of heat conduction from the heated wall with the bulk fluid to produce a net advection of energy over a cycle. The effect of increasing pulsation frequencies resulted in greater magnitudes of the ratio of advection to conduction, signifying convection dominated heat transfer with narrowing thermal boundary layer. Thus, it was shown that the section averaged equations

could be treated as exact solutions for the Navier-Stokes equations if the enhanced conductivity was defined considering the discrepancy in advected energies.

Based on the analytical solutions developed for parallel plate channels by Kurzweg [68] for low Reynolds number flows, a study performed by Liao *et al.* [79] dealt with an oscillating pressure gradient imposed for flow through a parallel plate channel with a heated bottom wall and an insulated top wall. A low oscillating frequency range corresponding to $0.1 \leq Wo \leq 2$ was investigated for two working fluids: air ($Pr = 0.6$) and water ($Pr = 6$). With the focus upon the application of the technique to electronics cooling, wall-fluid dependent thermal conductivity ratios, thermal diffusivity ratios, and geometric heights were defined. With increasing oscillating frequency ($Wo \geq 0.4$ for air and $Wo \geq 0.9$ for water), the heat transfer was found to greater than the steady flow case. The maximum value of time averaged Nu occurred with $Wo = 2$ for air. For over the range of oscillation frequencies, it was observed that at low frequencies the Nu deviation was significant with higher Nu for air in comparison to water as shown in Figure 4-9. This was since the water thermal conductivity being slightly lower than that of the wall material and hence the increased thermal resistance in the bottom wall thickness presented a major impact on the heat transfer and the transverse wall temperature profiles. Examining the time-dependent transverse wall temperature profiles for one oscillating cycle enabled the deviation to be understood. Figure 4-10 plots such profiles for water with $Wo = 2$. A maximum heat transfer enhancement factor of the order of 200% for oscillatory flows over steady flow was reported for $Wo = 2$. For air, since the thermal conductivity is much smaller than the wall material (considered in the study as $k = 0.0016\ W/mK$), temperature variations in the two wall regions are 0 and do not influence the temperature field in the fluid. With the water media, an interesting nature was observed since the difference in thermal conductivities of the wall material (considered in the study as $k = 0.05\ W/mK$) and water was comparatively small. Hence, the bottom wall conduction effects showed a pronounced effect in the heat transfer and time-dependent temperature profiles. Also, the top wall insulation thickness forced the bulk fluid temperature to be of the same magnitude as the top wall surface temperature, which reduced heat transfer between the two. It was identified that the added thermal resistance in the bottom wall thickness, reduced the wall surface temperatures for water media and correspondingly decreased the heat transfer.

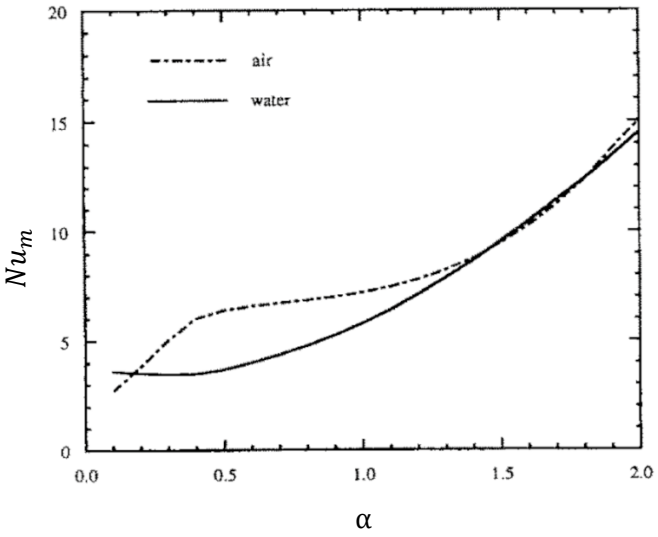

Figure 4-9: Average Nusselt number (Nu_m) variation vs. Womersley number (α) for air and water media, shown by Liao *et al.* [79]

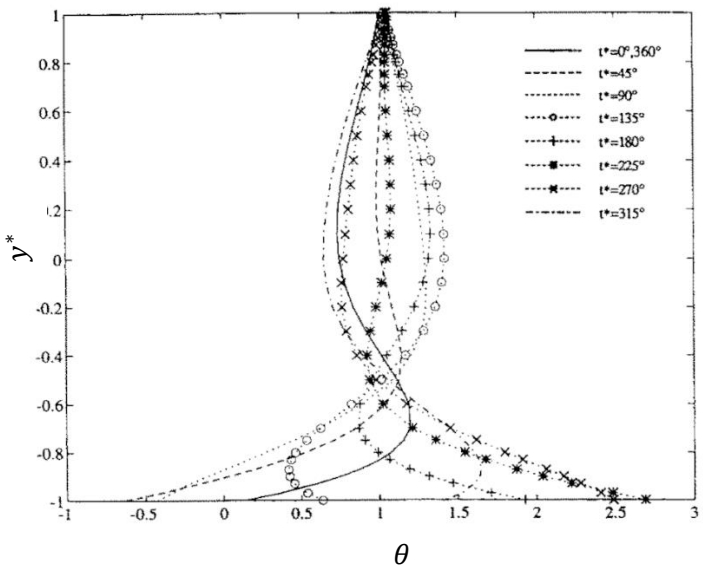

Figure 4-10: Time-dependent temperature (θ) profiles for one cycle with water as fluid at $Wo = 2$, shown by Liao *et al.* [79]

The effect of a constant wall heat flux was experimentally studied by Mosyak *et al.* [80]. The wall temperature fluctuations were examined for open flume and rectangular channel geometries. In the two cases, a constant axial heat flux boundary condition was considered; along with quasi-isothermal (no change in wall temperature along streamwise distance) in the periphery - identified as H1 (defined in Section 2.2.1) and quasi-iso flux (wall temperature fluctuations are non-zero) along the periphery - identified as H2 (defined in Section 2.2.1). Copper and stainless-steel heating elements were prepared for the experiments to maintain the desired boundary conditions. The

macro-scale thermal structures were observed on the wall in a turbulent flow for $8000 \leq Re_S \leq 10000$ for the flume and $10000 \leq Re_S \leq 20000$ for the channel geometry. The temperature distribution on the heated wall was visualised with infra-red or liquid crystal sheet techniques and the thermal distributions were found to be consistent with the previously established results. In the fully developed flow regime for the H1 case, the wall temperature fluctuations were seen to be a consequence of turbulent velocity fluctuations, depending on the Prandtl number and distance from the wall. Consequently, the wall temperature fluctuations were found to be independent of the thermal entrance length, while for the H2 case, the wall temperature fluctuations were found to lessen along the streamwise (axial) direction in the thermal entrance length. This suggested that the effect of imposed thermal boundary conditions on the wall temperature fluctuations was prominent. Additionally, the RMS value of the transverse (spanwise) wall temperature fluctuations for the H2 case were found to be about an order of magnitude higher than the H1 case.

Craciunescu and Clegg [81] numerically predicted the temperature distribution resulting from unsteady periodic flow for vessel geometries in the human body, *i.e.*, aorta, large arteries, terminal arterial branches, and arterioles. In their study blood was considered as a Newtonian fluid and the vessels as rigid bodies. Vessels with large diameter showed flow reversal while the narrow arteries showed parabolic velocity profiles for a range of frequencies between $0.017 \leq Wo \leq 10.25$. The thermal interaction between vessel and tissue was considered with convective heat transfer included for steady and pulsatile heat flux variations. In the case of the aorta and large vessels it was shown that greater frequencies resulted in smaller temperature amplitudes. For the same vessel size, flow reversal effects were noticed for large Reynolds numbers. A switch in velocity direction produced a sharp change in temperature (only near walls) leading to a deviation of the profile from a sinusoidal shape due to increased energy flux from the vessel wall to the fluid. A small difference in fluid temperature amplitudes was observed between forward and reverse flow. For terminal arteries and arterioles, no influence of frequency was seen on temperature distribution as blood flowing close to the wall was at the same temperature. Additionally, temperature profiles were no longer flatter and thus central laminae were seen to be involved in the heat transfer.

Heat transfer enhancements in rectangular minichannels using thermally developing and fully developed pulsating single-phase flows were estimated in an experimental study by Persoons *et al.* [82]. Results were compared with previous studies for a range of pulsating Reynolds number amplitude ratio $0.002 \leq Re_p/Re_s \leq 3$ and Womersley numbers in the range $6 \leq Wo \leq 17$. A novel pulsator device with membrane pump and pumping chambers was developed which was driven by a piezoelectric disk actuator. The flow in the test section was considered as thermally and hydrodynamically developing flow because the heat sink, described as a single rectangular channel

milled in an aluminium base plate, was shorter than the thermal entrance length. Nu correlations were compared with similar studies using parallel plates. For steady flow over a range of Re, heat transfer was observed to be higher than the parallel plate cases. The authors claimed this to be due to the influence of entrance flow effects in the heat sink which strongly affected the average Nu. For pulsating flows, a ratio of averaged heat transfer coefficient in pulsating flow to steady flow at the same steady value of *Re* was introduced. Results as reported in Figure 4-11 showed up to 40% enhancement for higher pulsation amplitudes, while no consistent dependence on pulsation frequency was reported. A reduction in cooling performance was noticed for a low pulsation amplitude ratio of $Re_p/Re_s < 0.05$. As the ratio exceeded a critical value of 0.23, *i.e.*, with higher pulsation amplitudes, a positive heat transfer enhancement was observed and was said to increase with further increases in Re_p/Re_s. A close agreement was found with the results of aforementioned numerical study of blood flow by Craciunescu and Clegg [81]. Theoretical expressions were obtained for the heat transfer enhancement factor based on Reynolds analogy, interlinking the characteristics of momentum and heat transfer.

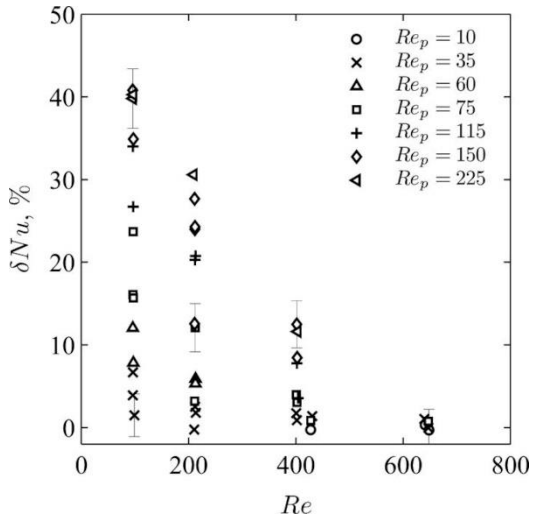

Figure 4-11: Percentage heat transfer enhancement (δNu) for pulsating flow through the heat sink as a function of the steady flow Reynolds number (Re) for different pulsating Reynolds numbers (Re_p). From Persoons *et al*. [83].

4.3 Transverse (Spanwise) Temperature Profiles

Sert and Beskok [84] numerically analysed reciprocating (or oscillating) forced convection in rectangular ducts. The walls are maintained with periodic repeating boundary conditions of top wall surface with regions specified as uniform heat flux and constant temperature, while the bottom wall was kept insulated. The results indicated that the thermal boundary layer thickness was

determined by Pr and the oscillating frequency of the fluid in the range of $1 \leq Wo \leq 10$. For certain cases of low fluid displacement amplitude ($F_0 = 5$) and low frequency, axial conduction effects dominated over convection. At maximum oscillation frequency and amplitude $F_0 = 10$, temperature contours were concentrated near the top wall due to the small boundary layer thickness and enhanced forced convection and the bulk fluid temperatures decreased due to even axial heat spread. Thus, by increasing the fluid displacement an increase in heat transfer was shown. For variations in fluid Prandtl number from $Pr = 1$ to 10, higher fluctuation of wall and bulk temperatures were observed in the transverse (radial) direction and a subsequent decrease in axial surface temperature and bulk temperature, thus signifying enhanced forced convection cooling. Variation of the oscillation frequency showed different heat transfer enhancement behaviour, symbolising that the velocity profiles significantly influence the heat transfer. The maximum time-averaged Nu occurred at the middle of the channel for $Wo = 1$, whereas for $Wo = 10$ the maximum time-averaged Nu was at the side walls. The heat transfer rate increased with fluid displacement amplitude, Prandtl number and frequency. Richardson's [38] annular effects were observed by the authors suggesting that high near wall velocity gradients led to increased removal of heat from the top surface.

Moschandreou and Zamir [85] performed an analytical study of pulsating flow in a tube with a constant wall heat flux and a fluid at a uniform inlet temperature. Heat transfer was affected through variation of the pulsation frequency and fluid Pr. As concluded from previous studies, the effect of pulsation was greatest for a range of moderate frequencies where the fluid bulk temperatures and Nu increased. The non-homogeneous Bessel equations for axial and radial fluctuating temperature were solved using Green's function to get an expression for the time-dependent oscillating temperature field. It was pointed out that the prime constituent in the calculation of relative heat transfer between steady and pulsating flows is the oscillatory bulk temperature. For the imposed boundary conditions, the effect of pulsation on heat transfer from the tube was consistent with the physics of pulsating heat transfer theory, wherein for a varying fluid bulk temperature relative to the wall temperature within the tube. For varying flow rate amplitudes ($A_0 = 0.1, 0.5, 1$) and a range of $Pr = 0.5, 1, 2.5,$ and 5.0 it was shown that the bulk temperature and heat transfer enhancement peaked at $Pr = 0.5$ for $Wo = 15$. This was attributed to a greater heat diffusivity which dominated the smaller momentum diffusivity. For the range of dimensionless pulsation frequencies studied ($1 \leq Wo \leq 40$), the heat transfer showed a maximum enhancement for $A_0 = 1$ at a frequency of $Wo = 15$, as is seen in Figure 4-12 and is in line with the predictions by Richardson [38]. This effect was reversed, however, for $Wo = 5$ and $Wo = 25$.

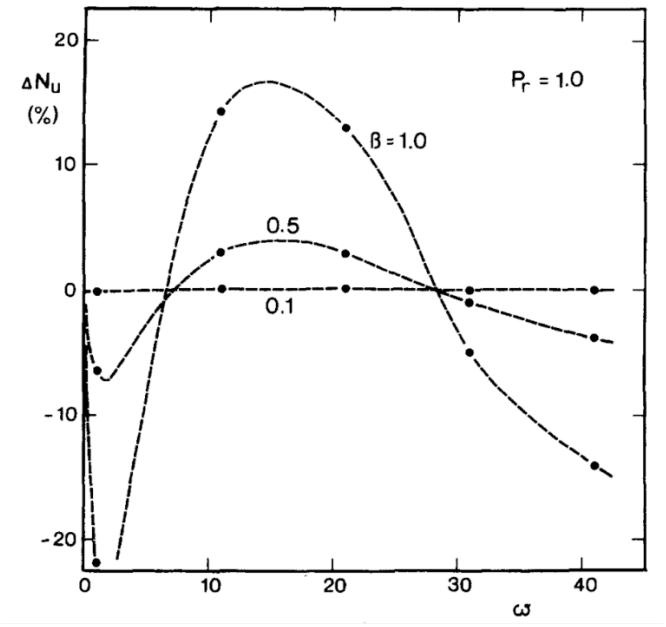

Figure 4-12: Percentage change in local Nusselt number (ΔN_u) relative to steady flow vs. Womersley number ($\omega = Wo$) for different pulsating flowrate amplitude ($\beta = A_0$) at $Pr = 1$, from Moschandreou and Zamir [85].

The heat transfer characteristics in a pipe with an oscillating flow of air was studied numerically by Zhao and Cheng [86], who used a constant wall temperature condition and a range of kinetic Reynolds number ($10 < Re_\omega < 400$), fluid displacement amplitude ratio ($5 \leq F_0 \leq 35$), length-to-diameter ratios and Pr. The bulk and wall temperature distributions in response to Re_ω, F_0 and along varying radial distances was studied. At $Re_\omega = 64$, a $52°$ phase difference between the axial velocity and temperature was observed since the fluid temperature dropped at the entrance during the first half of the cycle $0 \leq \theta \leq \pi$, while by the end of second half of the cycle $\pi \leq \theta \leq 2\pi$ the fluid temperature near the pipe entrance rose due to warmer fluid exiting the pipe. The phase difference was $86°$ for $Re_\omega = 250$. The phase difference near the pipe wall region was found to decrease with an increase in Re_ω while the opposite behaviour was observed in the core region. At higher Re_ω it was found that the heat transfer rate was greater near the wall, where fluid temperatures reacted faster to the velocity variations, due to the decreasing phase difference between the two. The annular effects as predicted by Richardson and Tyler [39] for velocity profiles were initially observed in the behaviour of the transient transverse temperature profiles, and the effect was more pronounced as the Re_ω is increased, particularly near the pipe entrance. At the centre of the pipe, flatter temperature profiles were observed as forced convection effects were less significant for low *Re*, with the opposite effect at high *Re*.

By analysing local instantaneous Nu at different axial locations from Figure 4-13, it was seen that the phase difference between the axial velocity and temperature variations between the entrance

and exit of the pipe was $180°$. At the pipe entrance, Nu increased and reached a maximum due to cold fluid attaining maximum velocity at a phase angle of $90°$. Beyond this point the heat transfer rate decreased as the fluid velocity decreased. Heat transfer rates were found to increase with increases in *Re* since the thermal boundary layer thickness diminished. At the pipe centre, the heat transfer rate was very low as most of the fluid from the middle region never exited the pipe in the oscillatory flow. For the space-averaged Nu, the heat transfer rate increased with an increase in both A_0 and Re_ω, as seen from Figure 4-14. With the variation of L/D it was found that the time-averaged Nu remained similar in the entrance region of the pipe. Although, in the middle region it increased with a decrease in L/D for a fixed $A_0 = 25$, as the ratio of fluid displacement to pipe length became larger, the heat carried from the pipe to the reservoirs was larger.

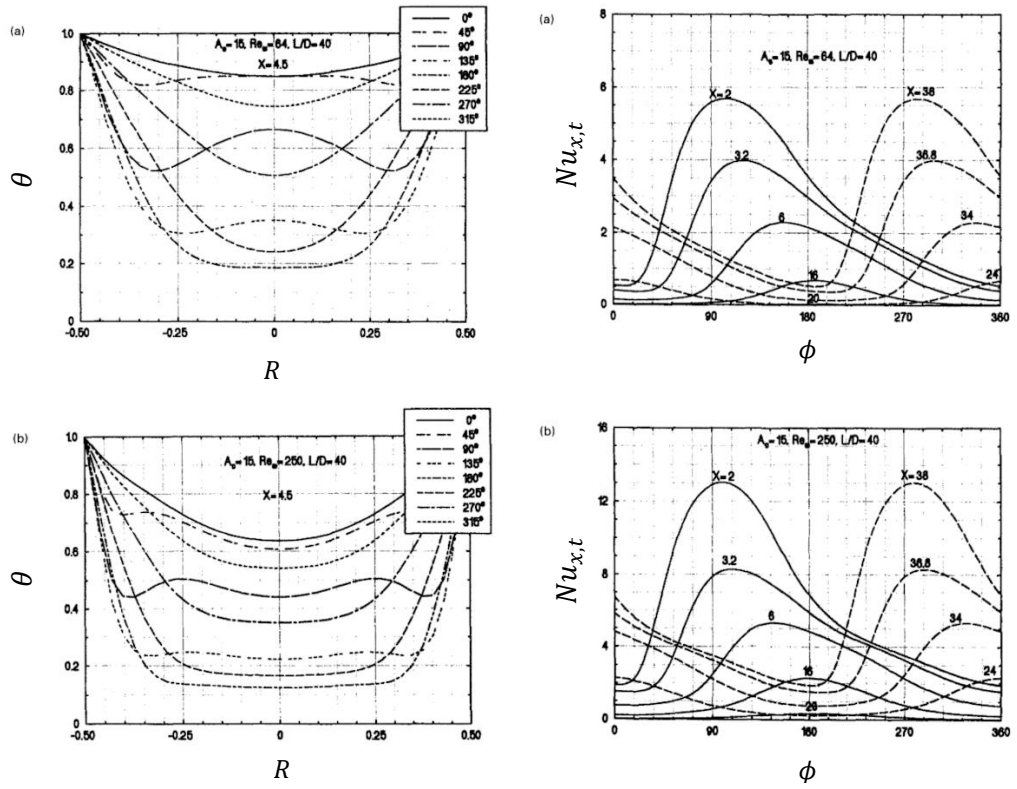

Figure 4-13: (LEFT) Phase-dependent dimensionless temperature (θ) profiles versus dimensionless radial location (R) at the axial location $X = 4.5$ for $L/D = 40$ and $A_0 = 15$. (a) $Re_\omega = 64$, (b) $Re_\omega = 250$. (RIGHT) Local instantaneous Nusselt number variations at different dimensionless axial positions (X) for $L/D = 40$ and $A_0 = 15$. (a) $Re_\omega = 64$, (b) $Re_\omega = 250$. From Zhao and Cheng [86].

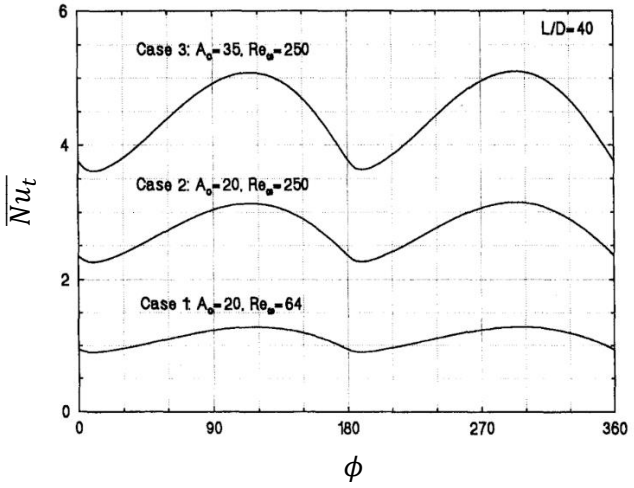

Figure 4-14: Effect of dimensionless flow rate amplitude F_0 and Re_ω on the space averaged instantaneous Nusselt number at $L/D = 40$, by Zhao and Cheng [86].

In their continued study, Zhao and Cheng [87] showed satisfactory agreement between experimental measurements and their numerical analysis [56]. Their test setup consisted of two coolers, two mixing chambers, and a heated thin-walled copper tube. The mixing chambers were located at either side of the long-heated tube. The oscillating flow motion was driven by a double-acting piston pump with a sinusoidal motion generator. The flow parameters were varied in the range $23 \leq Re_\omega \leq 464$ with a dimensionless displacement amplitude range of $8.5 \leq F_0 \leq 34.9$ to analyse the temperature profiles and corresponding heat transfer. For high oscillation amplitudes, the cross-sectional mean velocity reached a maximum and forced convection was dominant. As a result of which, the fluid temperature in the right mixing chamber rose sharply in the first half of the cycle $0 \leq \theta \leq \pi$, further following the flow reversal effect as hot fluid entered the left chamber over $\pi \leq \theta \leq 2\pi$, a sharp fall in the right mixing chamber fluid temperature is observed. While for lower oscillation amplitudes, the fluid velocity amplitudes were comparatively smaller and axial heat conduction effects presided at the first half of the cycle $0 \leq \theta \leq \pi$. Subsequently, the fluid temperature in right mixing chamber showed a slower response time compared to the velocity variations. Overall, the cycle-averaged wall temperature decreased with increases in oscillation amplitude and for an increase in Re_ω. since at higher amplitudes, large amounts of cold fluid entered the heated test section. Additionally, with an increase of Re_ω, the thermal boundary layer thickness reduced. Thus, the wall temperatures were reduced in both the cases.

The heat transfer between an oscillatory gas flow and an arrangement of hot and cold plates forming a parallel-plate channel in a thermoacoustic system was studied by Yu *et al.* [88] experimentally, using Planar Laser Induced Fluorescence (PLIF), and numerically, for a range of oscillation frequencies ($9.2 \leq Wo \leq 26.3$), fluid displacement amplitudes ($4.5 \leq F_0 \leq 50$), and

kinetics Reynolds numbers ($85 \leq Re_{\omega} \leq 690$). Time-dependent temperature fields are shown in Figure 4-15 for 20 phases. The images show two layers of higher temperature gas flowing from left to right along the channel for the phase angles $18°$ to $90°$, gradually penetrating the cold section. This feature was introduced as "temperature overshoot", illustrated in Figure 4-16. It was shown to be very apparent near the joint between cold and hot channels. At a phase angle of $90°$ it was observed to have reached an equilibrium state where the velocity had reached a maximum. The overshoot effect was very strong at phase angles of 90°, 108°, 126° but weakened beyond this point, subsequently disappearing at a phase angle of 180° (gas reached farthest to the right). In the reverse cycle, *i.e.*, as the gas moved from right-to-left along the channel, for phases 198°, 216° and 234°, a "temperature undershoot" effect was observed where the minimum gas temperature appeared in a region neither adjacent to the wall nor in the channel centre as in shown in Figure 4-16. As the layer of gas moves with a relatively high displacement it also affects the thermal diffusion from the wall. Hence the fluid is heated during phase angles of 0° to 180° and subsequently cooled during phase angles 180° to 360°. Overall, this effect was correlated to the annular effects pointed out by previous studies (see Zhao and Cheng [86]), suggesting that the steeper the temperature gradient, the stronger the effect.

For higher operating frequencies of 25 *Hz* to 50 *Hz*, the magnitude of the temperature overshoot reduced since it was controlled by the displacement of the gas within the cycle which was smaller and thus the temperature change was smaller. The phase lag between different layers of gas adjacent to the wall lead to large transverse temperature gradients.

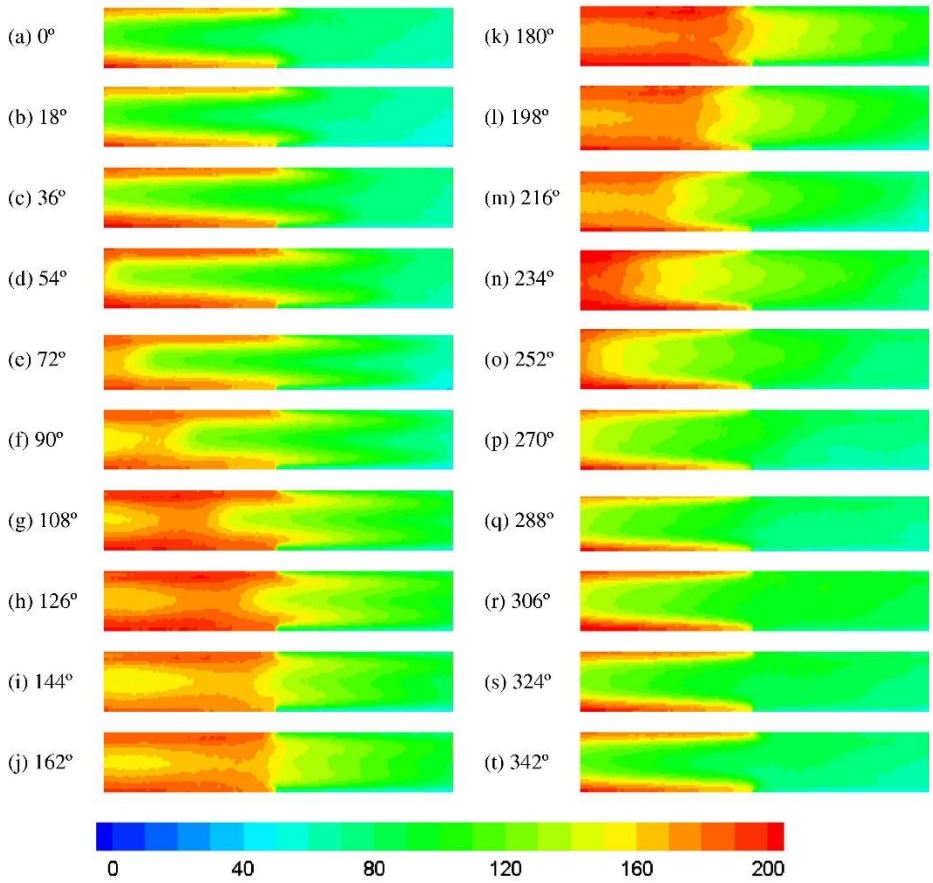

Figure 4-15: Oscillatory temperature fields (°C) in a parallel plate channel (lower legend levels depict the cold side and the hotter legend levels show the hot side) for $Wo = 11.3$, $F_0 = 3.7$, by Yu *et al*. [88].

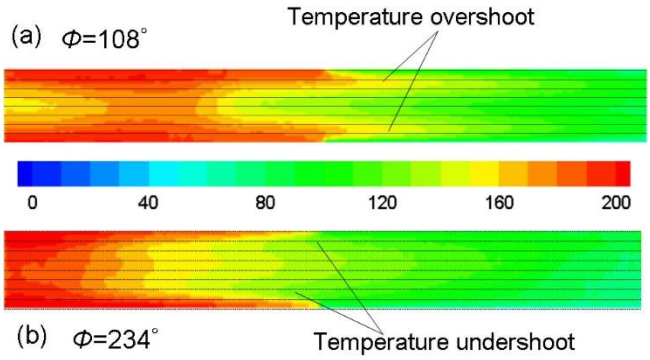

Figure 4-16: Zoomed in temperature fields (°C) for different phase angles, (a) $108°$ (b) $234°$, from Yu *et al*. [88].

Blythman *et al.* [89] used an analytical approach to obtain the a 2-D temperature profiles for a rectangular minichannel with two constant heat flux long walls (described earlier in Section 2.2.1 under the influence of pulsating flows for frequencies in the range $1.4 \leq Wo \leq 22.1$ and displacement amplitude $0.0035 \leq F_0 \leq 8.77$. It was observed that for high frequency pulsations, the transverse temperature profiles resembled closely the displacement profiles but were phase-

lagging the velocity profiles by 90° ($= \pi$). The larger wall temperature gradient led to larger temperature variations with subsequent increase in the fluid displacement, wherein the time dependent fluid temperature was increased, as the fluid displaced due to reversal effects is carried against the positive axial temperature gradient. Additionally, since the oscillations were very fast at high frequencies, no notable transverse diffusion occurred as the temperature profiles were plug-like in the fluid core regions. Near wall temperatures oscillations lead in phase compared to those in the bulk core regions, with higher displacement amplitudes. For low frequencies, since the thermal diffusion time scale was shorter compared to the excitation period, the temperature and displacement profiles could be significantly differentiated. Diffusion of heat was from the core region to the wall, and an appearance of phase lag between the displacement and wall temperatures was observed near the corners as an effect of longer thermal diffusion from the wall to core bulk fluid. Importantly, the temperature and displacement profiles were seen to be out of phase and independent of the pulsation frequency. Overall, with time-dependent bulk fluid temperature variation, the heat transfer was reduced in the first half-cycle and enhanced in the second half-cycle.

4.4 Effect of channel profile modifications

Ghaedamini *et al.* [90] performed numerical simulations on wavy walled microchannels under steady and pulsatile flow regimes to investigate heat transfer by chaotic advection. Significant heat transfer enhancement was noted in the steady flow case due to a large pressure drop in the presence of a chaotic advection regime. Additionally, increasing the wall waviness was considered to be a prime influence in the resulting heat transfer which is inferred from Figure 4-17. Flow separation from the walls caused chaotic advection with counter rotating vortices observed in the region, as seen in Figure 4-18. Poincaré maps for wall waviness factors were developed to aid the understanding of chaotic advection at various locations along the channel length. For a fixed channel aspect ratio of 0.8 and wall waviness = 0.15, a jump in heat transfer. Flows of $Re_s = 400$ were considered for the steady case and it is claimed that higher Re flows had greater impact with wavy walled channels.

For pulsating flows, the geometry was constant and considerable heat transfer increments were obtained, whilst maintaining a relatively small pressure drop. The pulsation Reynolds number amplitude ratio was between $0.13 \leq Re_p/Re_s \leq 0.70$ and a range of pulsation frequencies (f) from 10 *Hz* to 65 *Hz* were examined. Comparisons were obtained between *Nu* and friction factor

for the specified frequencies, and it was found that the thermally optimum frequency range was at smaller frequencies for larger pulsation amplitudes. A phenomenon of chaotic advection was established, showing that the maximum heat transfer occurred around a certain frequency range within the resonance region of the system as shown in Figure 4-17. The authors showed that the presence of chaotic advection reduced the thermal resistance and lead to a significant increase in heat transfer.

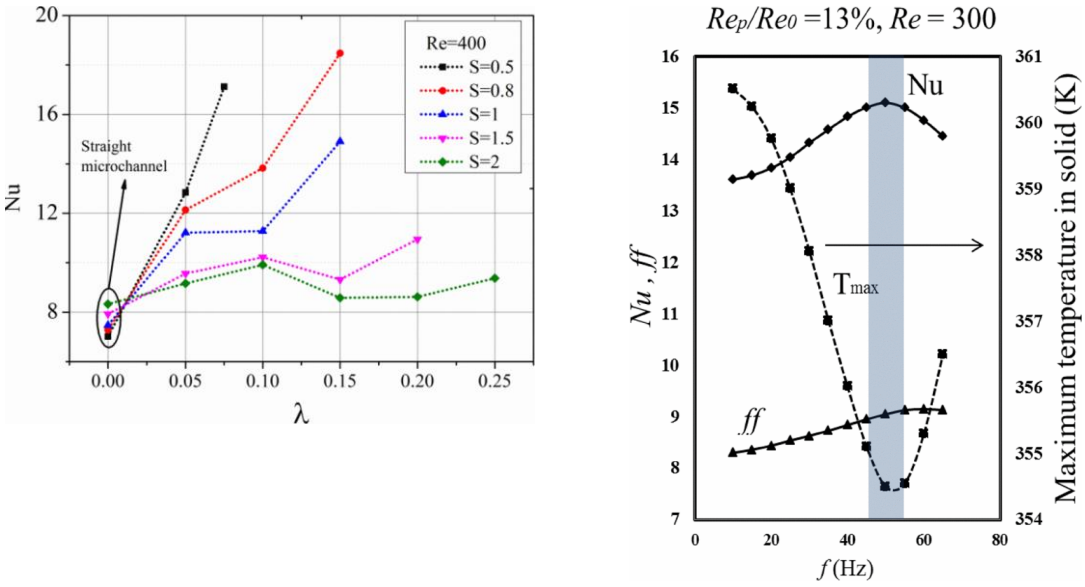

Figure 4-17: (LEFT) Nusselt number (Nu) as a function of wall waviness (λ) and channel aspect ratio (S) for $Re_s = 400$. (RIGHT) Time averaged Nusselt number (Nu), friction factor (ff) and maximum temperature in the solid as a function of pulsation frequency (f) for $Re_p/Re_s = 0.13$ and $Re_s = 300$ for wavy channel flows, by Ghaedamini *et al.* [90].

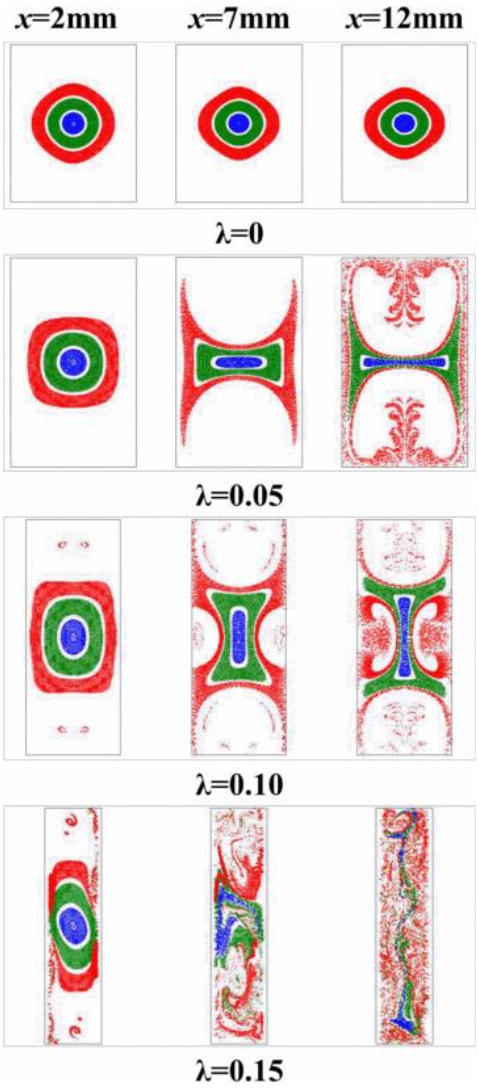

Figure 4-18: Poincaré sections for a fixed channel aspect ratio $S = 0.8$ and four levels of waviness (λ) extending from straight channels ($\lambda = 0$) to a highly modulated converging-diverging channel ($\lambda = 0.15$), by Ghaedamini *et al.* [90].

The effects of varying the rib angles upon the steady and pulsating flow and heat transfer in gas turbine ribbed channels were explored in a recent study by Yang *et al.* [91]. Flows with a steady flow Reynolds number range of $10000 \leq Re_s \leq 60000$ were simulated using an SST $k-\omega$ turbulence model. Selected results are presented in Figure 4-19. The flow created over the leading edge of the ribs was termed 'longitudinal secondary flow' for the angles 30°, 45°, 60°, while flow over the ribs at 90° was named 'transverse secondary flow'. The flow across the entire length of the channel close to the smooth wall was 'main secondary flow', effects shown in Figure 4-19.

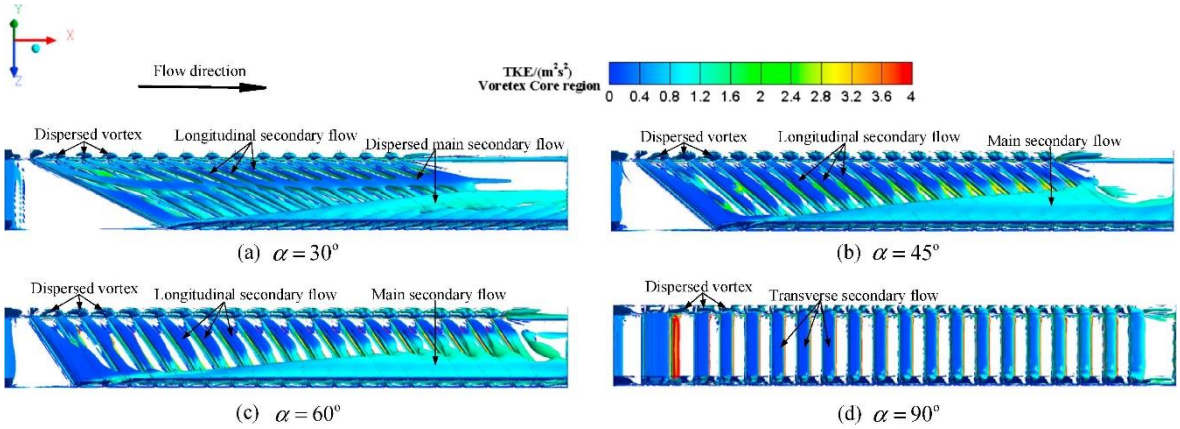

Figure 4-19: Secondary flow distribution for steady flow in the four channels at different rib angles (α) ($Re_s = 40{,}000$), Yang *et al.* [91].

For steady flow, the Nusselt number on the left wall was determined to be less than the right wall due to the longitudinal vortex formation moving downstream along the inclined ribs and eventually settling at the right-side surface. For the pulsating flow case at $Re = 40{,}000$, 150 *Hz*, and $A_0 = 0.2$, a higher Nu was recorded for the ribbed wall in comparison to steady flows, with a time-averaged value 16% higher. The increase was reported to be due to a corresponding increase in turbulence kinetic energy (TKE) for the pulsating case. At a rib angle of 90°, the severe deformation of secondary flows and consequent increase in TKE led to intense fluid mixing, with average Nu of 302 on ribbed surfaces, which was 68% higher than those obtained for steady flow and corresponding rib angles. The large pulsation amplitude of $A_0 = 0.7$ was shown to strengthen the mainstream fluctuation leading to an improvement of TKE (Figure 4-19). The peak Nu was recorded at a frequency of 150 *Hz* and turbulent bursts were found to occur in the near-wall boundary layer at a frequency known as the turbulent burst frequency. This led to resonance and violent mixing of fluid which enhanced the heat transfer. In general, an increase in heat transfer was obtained with increasing *Re*, as shown by Figure 4-20 and Figure 4-21.

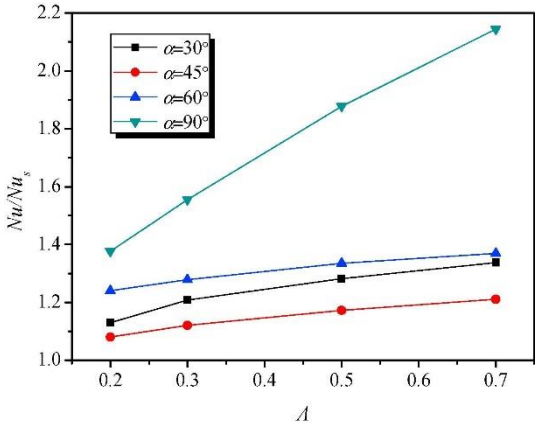

Figure 4-20: Heat transfer enhancement ratio (Nu/Nu_s) of four rib angle (α) channels at different flow rate amplitudes (A) at a frequency of 100 *Hz* and $Re_s = 40{,}000$, from Yang *et al.* [91].

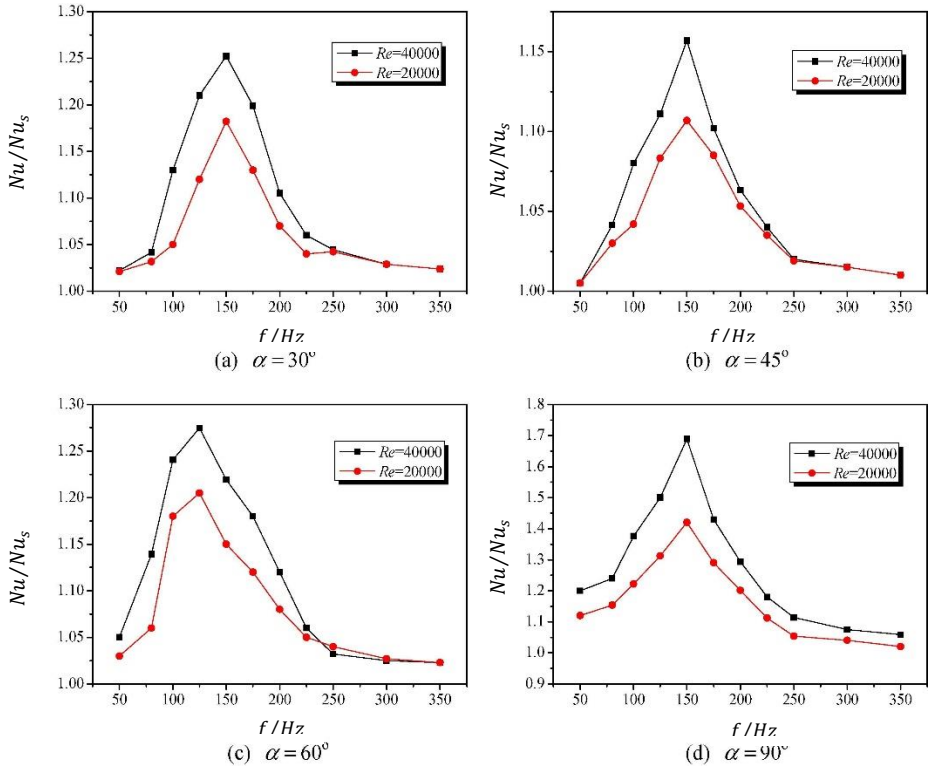

Figure 4-21: Heat transfer enhancement ratio for four channels vs. frequency (f) for different rib angles (α) and values of the steady flow Reynolds number (Re_s) for $A = 0.2$, from Yang *et al*. [91].

In a more recent study, Zhang *et al.* [92] studied the flow characteristics and heat transfer enhancement in grooved channels under pulsating flow using experimental and numerical techniques. The amplitude of flow pulsations and the flow patterns for $0 \leq Re_p \leq 1500$, and flow rate amplitudes in the range $1 \leq A_o \leq 2.5$ were examined for a range of pulsation frequencies of $0.0346 \leq f(Hz) \leq 1.6229$. The channel test section consisted of 30 rectangular stepped slots maintained with a constant wall temperature. For the numerical simulations, a RANS-based

turbulence model was used. Flow visualisations at $Re_s = 500$, $A_0 = 1$, and $0.0865 \leq f(\text{Hz}) \leq 0.5409$, were examined for two flow patterns in one period, *i.e.*, stable and unstable, as seen in Figure 4-22.

For steady flow there was no observed exchange between fluid in the mainstream region and the recirculation vortex. For unsteady cases, the mainstream fluid and recirculation vortex were fully mixed, leading to heat transfer enhancement. It was found that with an increase in frequency the onset of unstable flow was postponed, thus the size of recirculation vortexes was a frequency-dependent parameter. The local Nu distribution and pattern along a single groove (No. 27) was analysed over one periodic cycle. It was noted that due to differing velocity distribution inside the groove region, the right wall of the groove exhibited higher heat transfer compared to the left wall signifying non-linear variation of local Nu inside the groove. In the case of an inverse amplitude ratio ($P_t = 1/A_0$) the heat transfer coefficient decreased with an increase in the flow rate amplitude. Heat transfer was predicted to be higher at moderate Re and high pulsating frequency due to intense fluid mixing, shown in the Figure 4-23.

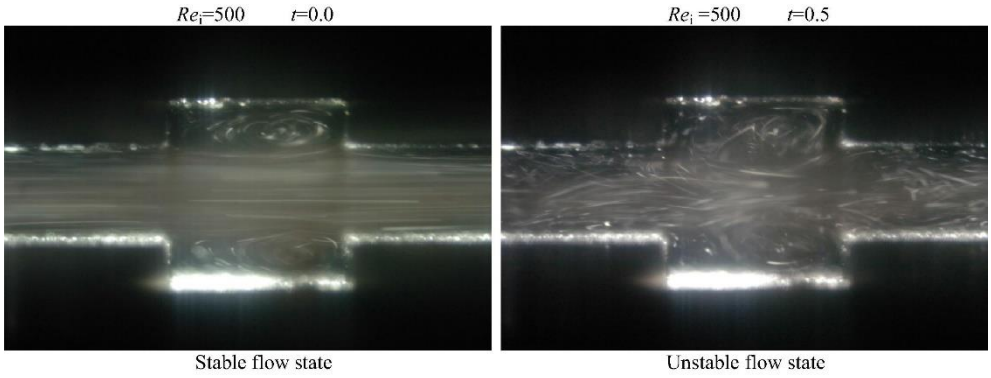

Figure 4-22: Pulsating flow patterns for $Re_p = 500$, $P_t = 1$, $f = 0.5409$, from Zhang *et al.* [92].

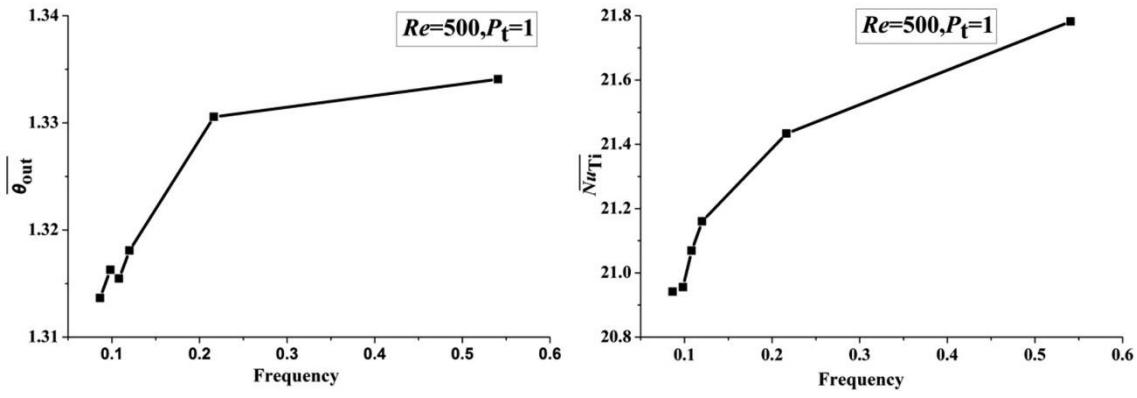

Figure 4-23: Dimensionless time-averaged outlet temperature $\overline{T_{out}}*$ and time-averaged wall Nusselt number ($\overline{Nu}$) for $Re_p = 500$, $P_t = 1$, from Zhang *et al*. [92].

Laminar pulsating flows exhibited significant heat transfer enhancement at low Re as the fluctuating velocity components disrupted the laminar boundary layer. The thermal performance was investigated in an experimental study by Khosravi-Bizhaem *et al.* [93] involving four uniformly heated helical coils over frequencies $16 \leq Wo \leq 40$ and $2000 \leq Re \leq 9500$. Optimal thermal performance at $Wo = 24$ was observed which led to an overall heat transfer enhancement of 19% compared to the steady flows.

Hydrodynamics and heat transfer characteristics associated with turbulent sinusoidal pulsating flows were examined experimentally for a sinusoidal minichannel with a uniform wall heat flux boundary condition by varying $4 \times 10^3 \leq Re \leq 7 \times 10^3$ and the nondimensional frequency in terms of Strouhal number $0.11 \leq St \leq 2.07$ in a study by Kurtulmus and Sahin [94] using PIV, shown in Figure 4-24. A comprehensive understanding of flow phenomena was developed in terms of separation of recirculation regions and thermal boundary layer disruption, and improvements of heat transfer over steady flow were observed. The wake flow or regions of negative velocity occupied the upper and lower spaces of the converging-diverging channel. The wakes were seen to shrink whilst the frequency of pulsation (St) increased and were dissipated into the core flow regions. In diverging-converging near wall regions, the flow recirculation's were seen to detach and interact with the bulk core flow for higher frequency flows. This phenomenon of high rate of fluid interaction indicated an enhancement in the average heat transfer rate with the pulsation frequency, attaining a maximum efficiency at $St = 1.03$.

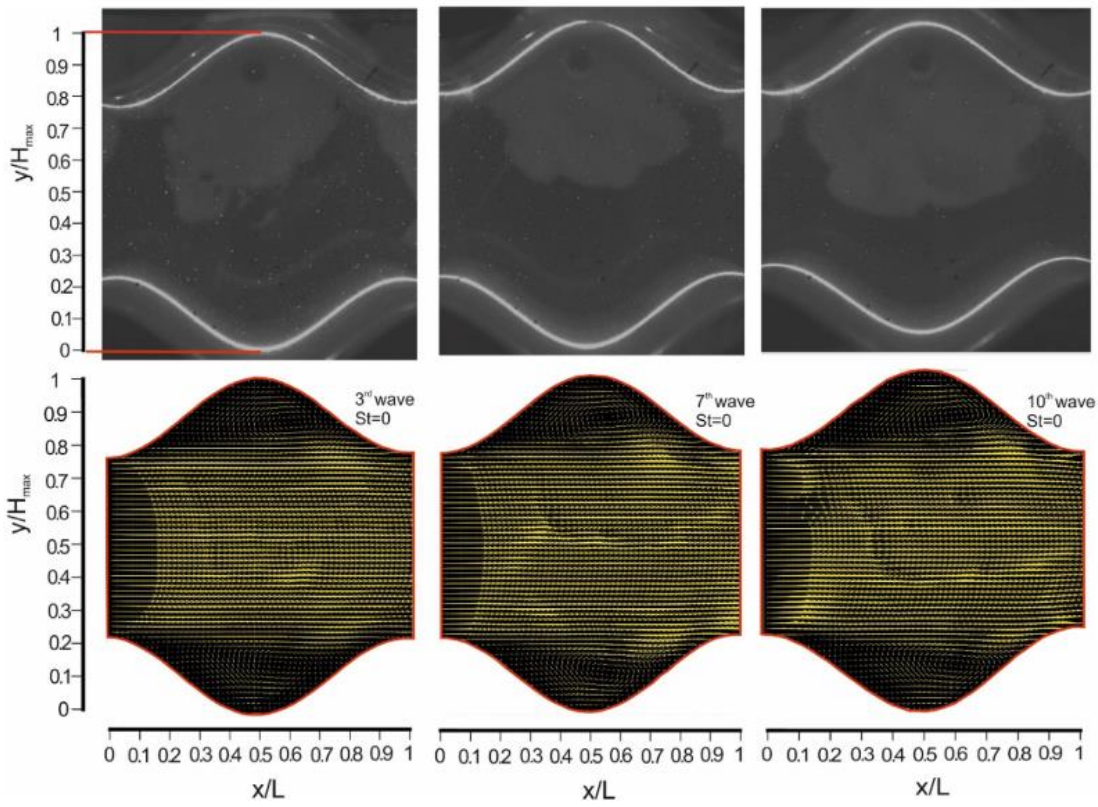

Figure 4-24: Raw images from the PIV (top row), time-averaged velocity vectors (bottom row) in a sinusoidal minichannel, by Kurtulmus and Sahin [94].

In a study by Hoang *et al.* [95], involving computational LES (Large Eddy Simulation) analysis of corrugated minichannel sinusoidal pulsating flows, heat transfer performance was evaluated by maintaining a uniformly heated wall. The parameters of interest were varying laminar to turbulent Reynolds number in the range $2371 \leq Re \leq 5379$, pulsation frequencies $0.16 \leq St \leq 0.79$ and flow rate amplitudes $0.2 \leq A_0 \leq 1$. Enhancements of heat transfer were observed with increasing Re without having a significant effect on the friction factor. The pulsating inlet flow characteristics exhibited turbulence, which led to the disruption of thermal boundary layers promoting heat transfer.

The steady flow presented significant changes in the flow development in the streamwise direction as seen from Figure 4-25. Turbulent flow vortices lead to sharp variations in the temperature contours. Similarly with a pulsation induced flow, the acceleration and deceleration in the velocity led to the development of vortices along the streamwise (axial) direction. Thus, significant effect on the wall temperature profiles is noted, indicating reduced magnitudes compared to steady flow.

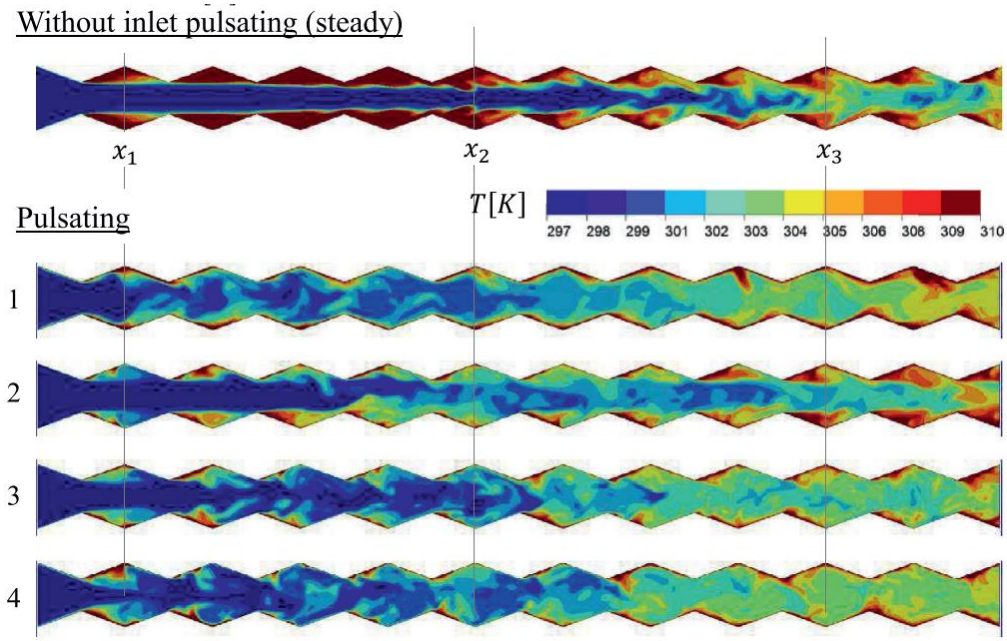

Figure 4-25: Instantaneous fluid temperature profiles along the axial direction for steady flow at 4 distinct time instances for pulsating flow at $A_0 = 0.8$, $St = 0.32$ and $Re = 2371$, by Hoang *et al.* [95].

Corrugated channels have generated recent interest and subsequent industrial applications owing to a substantial improvement in the thermal efficiency. These geometries are subjected to an increase in the surface area and stimulate flow oscillations leading to intense fluid mixing. A recent numerical study by Akcay [96] evaluated the thermal performance of corrugated channels with an addition of a discrete winglet mid channel for a sinusoidal pulsating flow. Comparisons were drawn for geometric variations in the winglet configurations for parallel surfaces under isothermal heating conditions for the parameter range $0.5 \leq A_0 \leq 1.5$, $2 \leq St \leq 8$ and $200 \leq Re \leq 1000$. The winglets were observed to have developed secondary flow loops by disrupting the flow structures for cases of pulsating and steady flow and the effect increased with A_0. Perforated winglets benefitted in reducing the friction factor compared to the solid designs. Due to the occurrence of homogenous mixing, recirculation zones were formed which led to an improvement in the heat transfer. The thermal performance factor presented a direct relation with the pulsation parameters Re, St and A_0. From Figure 4-26 the pulsation Nu showed increased amplitudes for higher pulsation amplitudes, while smaller fluctuations were noted for lower amplitudes. Similar effects were seen with the increase in Re as shown in the Figure 4-26, thus Re was considered as an important parameter in influencing the heat transfer performance. Maximum heat transfer enhancements occurred for the perforated case of winglet at $Re = 1000$, $A_0 = 1.5$ and $St = 8$.

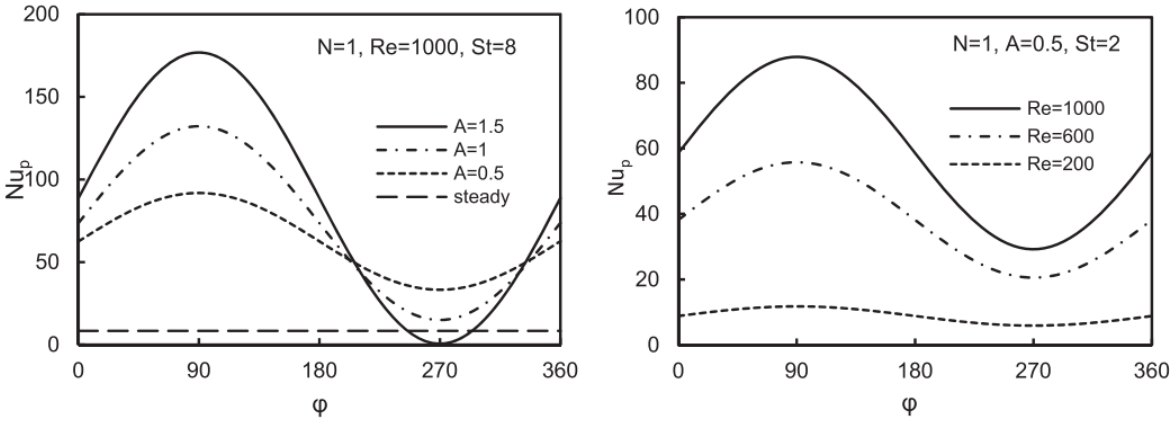

Figure 4-26: Temporal variation of solid winglet *Nu* for varying flow rate amplitudes (LEFT) and Reynolds numbers (RIGHT), by Akcay [96].

In a separate numerical and experimental investigation by Li *et al.* [97], a spherical version of corrugation was employed on a helical tube maintained with an isothermal condition for a square pulsating waveform. Pulsation parameters were varied between $25 \leq Wo \leq 71$ and $0.25 \leq A_0 \leq 0.75$. The flow disturbance due to pulsation was seen to improve the local flow field (in terms of transient pulsation characteristics) inside the spherical corrugation thereby promoting fluid mixing of the bulk core and near-wall regions. The occurrence of secondary flow field led by a pair of counter-rotating vortices and flow separation was amplified. This was a result of a combined action involving the turbulent intensity, imposed pulsation format and the corrugated wall structures promoted the convective heat transfer enhancement. For more than 60% of the pulsation time period, average circumferential Nu indicated significant enhancements compared to the steady flow. The thermal performance and friction factor decreased respectively with the increase of A_0, while for an optimum frequency of $Wo = 35$, the thermal performance peaked.

Singh *et al.* [98] conducted a computational study of pulsed flow in a uniformly heated minichannel with varying $300 \leq D_h(\mu m) \leq 700$ subjected to square wave pulsations, to explore the effect of surface roughness on heat transfer. The surface roughness was modelling as structured triangles. Geometric parameters were considered such as the peak to surface height and channel hydraulic diameter. As the hydraulic diameter of the ducts decreased, the time averaged Nusselt number increased significantly with a corresponding increase in peak-trough surface roughness heights, owing to increased fluid mixing led by vortices. Peak heat transfer enhancement of 32.7% was noted for pulsating flows at an optimum frequency $f = 5\ Hz$. The occurrence of vortices due to flow pulsations led to significant heat transfer enhancement over the conventional steady flows.

Recent works have explored the heat transfer performance of pulsating flows either by using viscoelastic fluids or nanofluids in addition to channel geometry modifications to examine the effect

on the heat transfer. Xu *et al.* [99] conducted an experimental study incorporating a pin-fin microchannel using nanofluids doped with graphene-oxide particles. Variations in mass concentrations of nanofluids for the ranges $1 \leq f(Hz) \leq 5$ and $272 \leq Re \leq 544$ were explored using a square pulsation waveform and the IR thermography technique. Heat transfer enhancements were observed by increasing the mass concentrations of the nanofluids and a corresponding increase in the average Re of pulsating flows. However, the low frequency $f < 2\ Hz$ pulsating flows exhibited insignificant heat transfer compared to the steady flow. A pulsation frequency of $f = 4\ Hz$ was determined to achieve the highest thermal performance.

Zhan *et al.* [100] performed geometric modifications of a rectangular microchannel by adopting a leaf-type design. The thermal performance and flow characteristics of viscoelastic fluids were evaluated for a laminar regime undergoing sinusoidal flow pulsations for a frequency range of $0.35 \leq Wo \leq 0.86$. The influence of flow reversal effects and efficient secondary effects of heat exchange between the bulk and the wall regions led to approximately 200% heat transfer enhancement. An optimal thermal performance occurred at $Wo = 0.61$ for the viscoelastic flow pulsations and the thermal performance decreased with higher Re.

4.5 Effect of pulsation profiles

The oscillatory motion of fluid produces a non-linear thermal boundary layer, which in very thin aspect ratio ducts can result in augmentation of the heat transfer coefficient. The heat transfer is therefore viewed as being dependent on the oscillatory motion, which includes the type of pulsation waveform format driving the flow, *e.g.*, sine, square, triangular. Yin and Ma [101] studied the effect of triangular waveforms in an oscillating, laminar, fully developed flow in a capillary tube with constant heat flux boundary condition. Analytical estimations of heat transfer enhancements were obtained for a wide range of parameters: $0.1 \leq Wo \leq 10$, $0.0001 \leq P_0 \leq 0.1$ and $0.1 \leq Pr \leq 1$. Results were compared with previous studies that used sinusoidal waveforms.

For $Pr = 0.1$, $A_0 = 0.01$ and $Wo = 0.1$, a peak transient $Nu = 18.08$ was achieved, while for the sinusoidal waveform it only reached 5.14, indicating that at optimum parameters a triangular waveform could increase the heat transfer coefficient significantly. When Wo was increased from 0.1 to 1.0 for an oscillating pressure amplitude (P_0) for a triangular waveform, the peak Nu was found to decrease significantly to 6.46, while for a sinusoidal waveform it was 4.803. Increasing the oscillating frequency beyond $Wo = 10$ resulted in the peak and average Nu approaching steady flow values. Variation of the oscillating pressure amplitude from 0.0001 to 0.1 for the triangular pressure waveform led to an increase in the peak Nu from 4.3 to 17.53, as viewed from Figure 4-27.

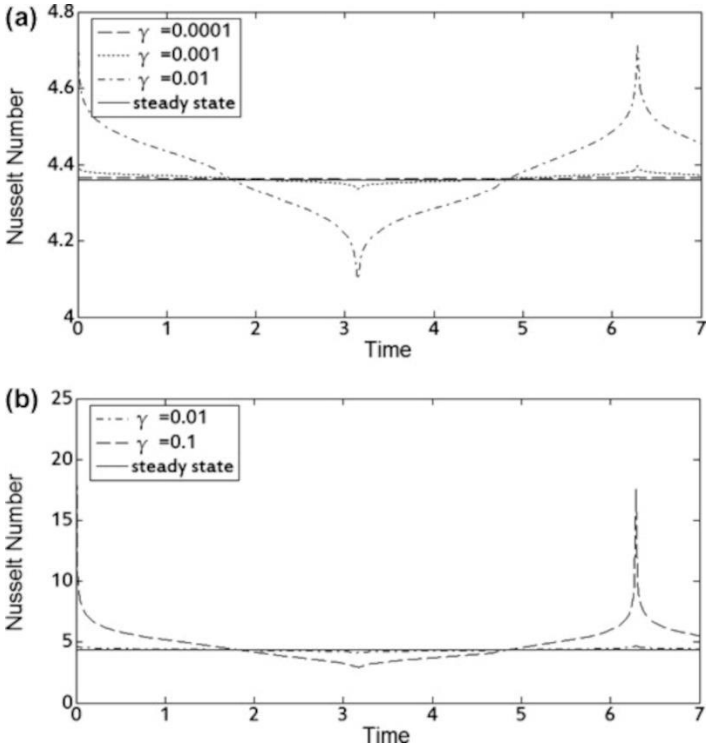

Figure 4-27*:* Effect of oscillation pressure amplitude on the Nusselt number for a triangular waveform at $Pr = 0.5$ and $Wo = 1.0$, (a) $\gamma\ (= P_0) = 0.0001\ to\ 0.01$ and (b) $\gamma\ (= P_0) = 0.01\ to\ 0.1$, by Yin and Ma [101].

Roslan *et al.* [102] extended the study of Yin and Ma [101] to include analytical expressions for sawtooth and square waveforms which were applied to laminar pipe flow and heat transfer at a fixed $Wo = 1$ and varying $0.01 \leq P_0 \leq 0.1$ and $0.1 \leq Pr \leq 1$. For a variation in axial position (z) and radial position (r) the peak temperature values for the three waveforms were shown to be significantly different (see Figure 4-28).

The general characteristics inferred were that varying amplitude of the pressure fluctuations, axial position and pipe radius led to differing heat transfer performance across the three waveforms, with a peak of dimensionless total temperature value (combination of steady and transient) of 0.80 obtained for the triangular waveform in comparison to sawtooth and square which were 0.7.

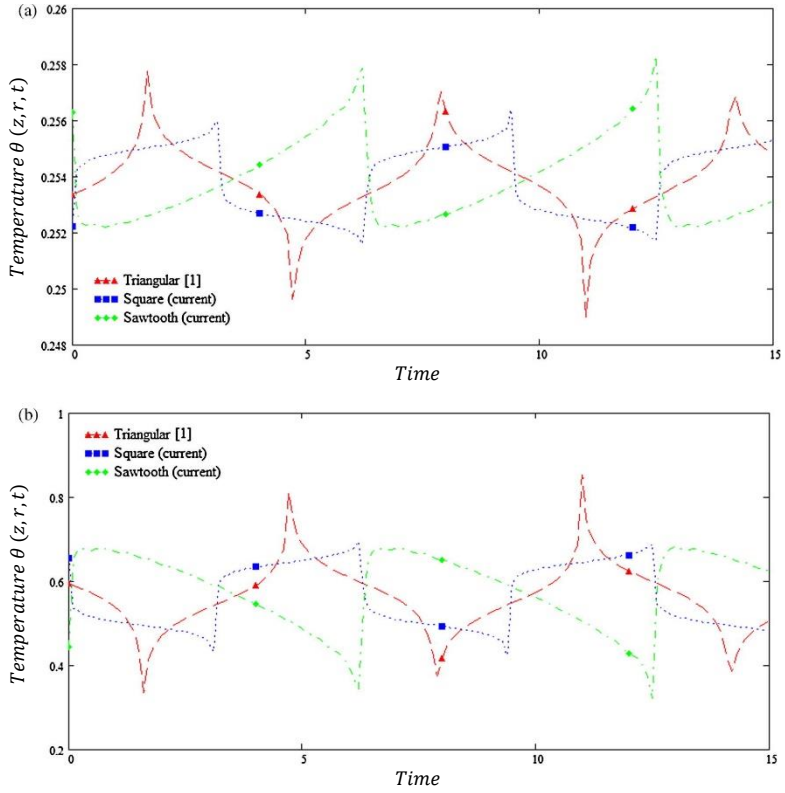

Figure 4-28: Waveform effects on temperature profiles at $P_0 = 0.01$, $Pr = 1$ and $Wo = 1$ (a) $z = r = 0.5$, (b) $z = r = 0.8$, by Roslan *et al*. [102].

Mehta and Khandekar [103] conducted an experimental study of thermally developing pulsating laminar flow in a square minichannel, where the flow was driven by a square waveform. The test setup consisted of an unheated length for hydrodynamic flow development followed by a heated length maintained with a 70 *mm* stainless steel foil which acted as a constant heat flux boundary. IR thermography was used to record temperature measurements from the foil. A fixed flow rate amplitude was used in the study with varying frequencies of $0.8 \leq Wo \leq 5.9$ to investigate the heat transfer by axial convection and transverse diffusion. Annular effects were observed for $Wo > 1$ while a conventional parabolic profile was observed for $\mathrm{Wo} < 1$.

The square waveform consisted of a half-on, half-off cycle with flow progressing through the channel for first half of cycle, and no flow for the second half. At low pulsation frequencies, longer convection times and longer diffusion times were observed with low thermal inertia, and higher values of oscillatory fluid and wall temperatures were noticed. For high pulsation frequencies, convection was still dominant, but the diffusion time scale was comparatively smaller, leading to smaller oscillatory fluid and wall temperature amplitudes. The prime reason for such effect at high frequencies could be due to the idea that disturbances created by imposed pulsations are weakened by the fluid viscous forces during motion. At low pulsation frequencies, the time

averaged Nu was found to be lower than the steady case, because the convection heat transfer was insignificant. For high pulsation frequencies, heat transfer enhancement was marginally better than for steady flow.

Zhang *et al.* [104] performed a numerical study of pulsating flow in a 33-slot manifold microchannel heat sink. The heat transfer performance was studied under multiple flow-driving waveforms such as sine, square, and semi-sinusoidal. Two non-Newtonian, shear thinning fluids were considered: CMC (Carboxyl Methyl Cellulose) and PEO (Polyethylene Oxide). With the case of square-wave pulsations, the time averaged $\overline{Nu}$ showed insignificant effect with varying pulsating frequencies $8 \leq Wo \leq 25$. However, for an optimal pulsation amplitude $A = 0.05\ m/s$, defined from a wave amplitude (*A* in *m/s*) a peak in pulsating heat transfer performance was noted which was up to 14.6% greater than the corresponding steady flow case as is noted from Figure 4-29. The authors inferred that the best thermal performance at a given amplitude typically occurred for $A = 0.08\ m/s$. Further a drop in thermal performance was seen with increase in velocity amplitude due to low drag induced by small amplitudes.

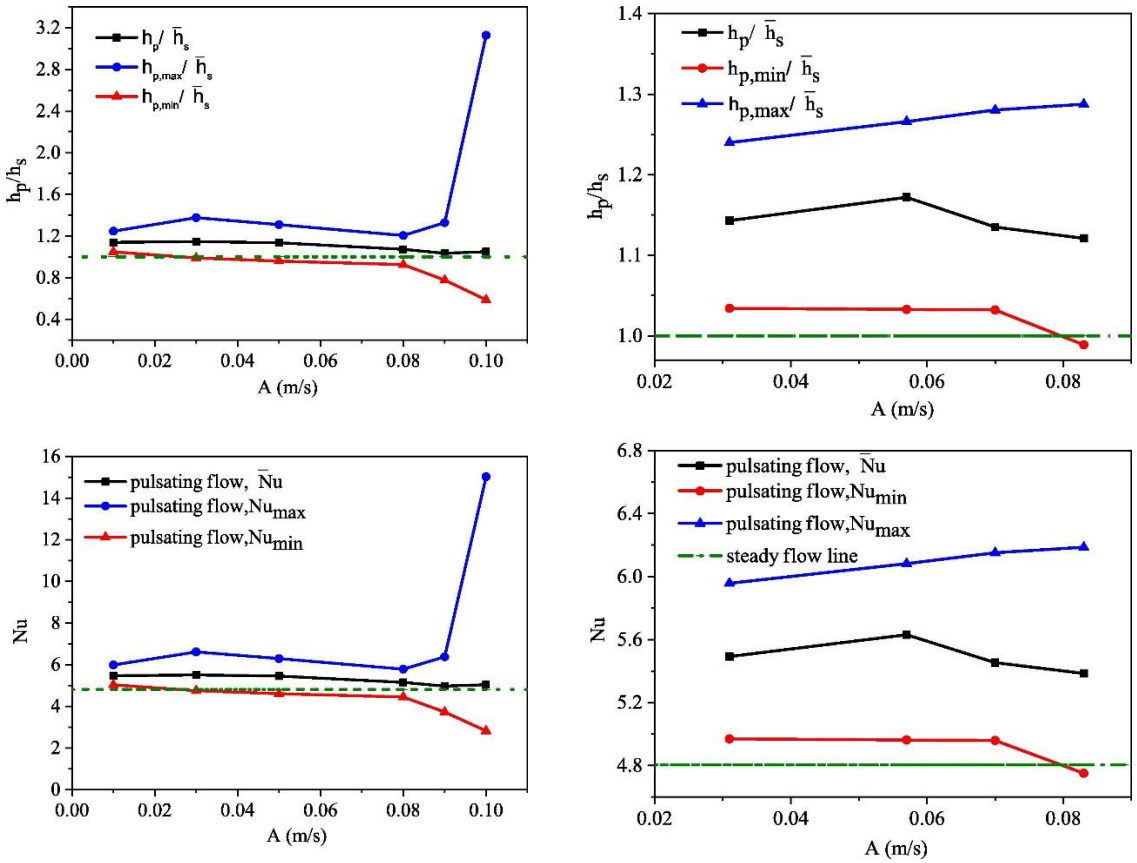

Figure 4-29: Influence of the wave amplitude (A) on the heat transfer performance of a pulsating flow for a square-wave (left) and sine wave (right). The upper row shows the heat transfer coefficient ratio of pulsating flow to steady flow (h_p/h_s) and the lower row shows Nu at $f = 25\ Hz$. From Zhang *et al.* [104].

From the streamlines and flow contours it was shown that secondary and inverse flow mixing occurred between the hot and cold fluids at intermediate regions between the two manifold branches, as shown in Figure 4-30. This enabled higher heat removal from the wall for a high pulsation frequency of $f = 25\ Hz$. In the case of sinusoidal pulsations, similar effects of pulsation amplitude and frequency were observed for a velocity amplitude range of $0 \leq A \leq 0.083\ m/s$. At an optimal amplitude of 0.057 *m/s* the overall maximum heat transfer enhancement was observed which reached up to 17.2%. It was also inferred that the sinusoidal-wave pulsating flow showed greater thermal performance compared to steady and square-wave flows. On the effect of pulsation frequency, it was noticed that for a pulsation frequency of 10 *Hz*, a maximum heat transfer enhancement (in terms of heat transfer coefficient) of up to 23% was achieved. For a semi-sinusoidal pulsation waveform, the heat transfer performance was found to worse than the steady case, as shown in Figure 4-30. The sinusoidal waveform resulted in better overall and local heat transfer performance.

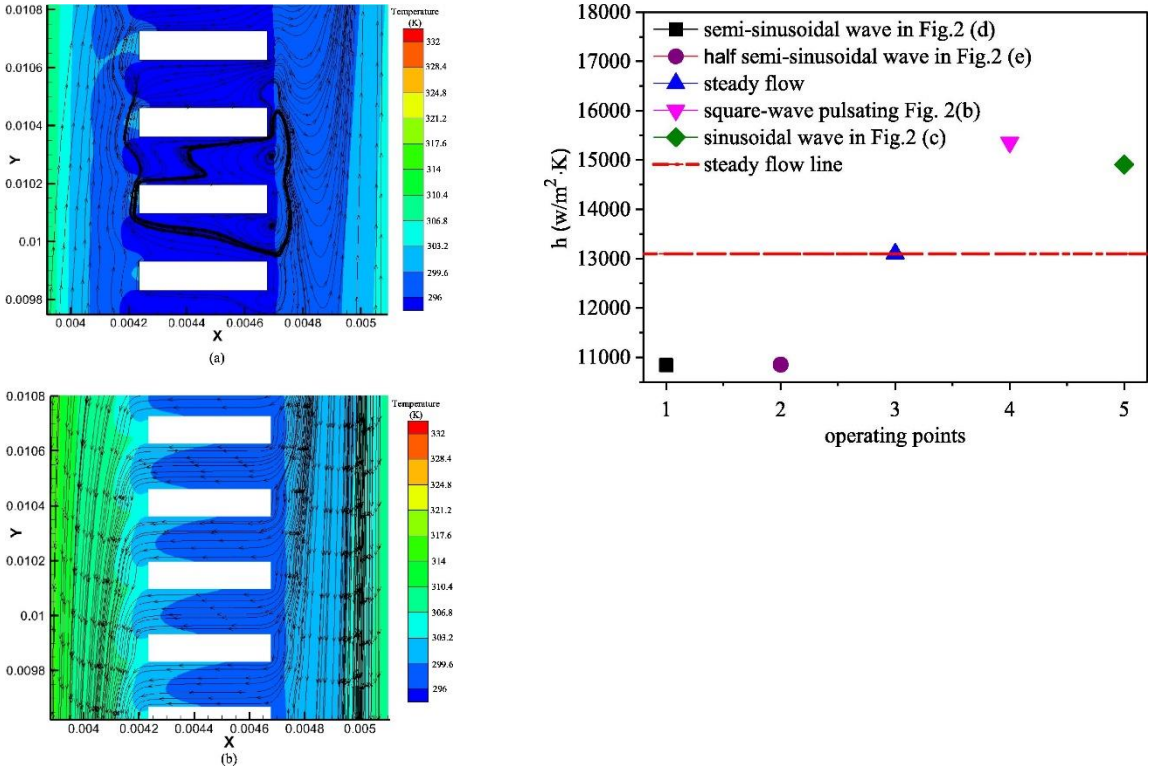

Figure 4-30: (LEFT) Flow fields and temperature contours in the centre region of manifold for the square-wave pulsating flow with $A = 0.08\ m/s$ and $f = 25\ Hz$ at different times. (a) $V = 0.18\ m/s$; (b) $V = 0.02\ m/s$. (RIGHT) Comparison of heat transfer coefficient at different pulsation formats. From Zhang *et al.* [104].

Leading and lagging asymmetric sinusoidal flows in a microchannel were experimentally investigated using the PIV technique by McEvoy *et al*. [105] for a range of $1 \leq Wo \leq 5$ and $A_0 = 0.0542$. Water was used as the working fluid and a 10 *W* uniformly heated copper block maintained

the thermal boundary condition. Low velocity, low frequency pulsations exhibited significant transverse (spanwise) variation in the fluctuating velocity components compared to the conventional pulsation formats such as symmetric sinusoidal and triangular. Consequently, as shown in Figure 4-31 for high frequency flows, the rapid flow acceleration and deceleration due to the asymmetric profiles lead to a sharp shift in the flow velocity, resulting in a lowering of the mean channel temperature. A promising heat transfer enhancement of up to 28% over the steady flow was determined for the lagging asymmetric profile at high frequency ($Wo = 5$).

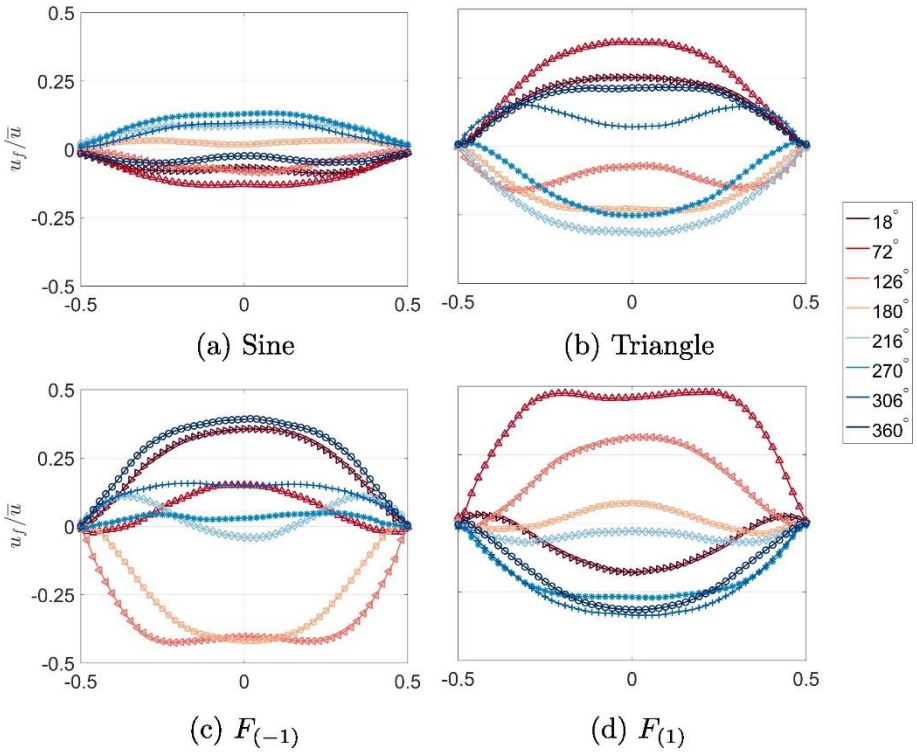

Figure 4-31: Phase averaged oscillating velocity profiles ($u_f/\bar{u} = U_{osc}/U_s$) at 25 *Hz* ($Wo = 5$) in a microchannel PIV study by McEvoy *et al.* [105].

The effect of flow rate modulations of square, triangular, sawtooth, and sinusoidal waveforms was experimentally investigated by Xu *et al.* [106] in a uniformly heated microchannel for the range $1 \leq f(Hz) \leq 4.5$ using IR thermography. The working fluid was a nanofluid, water doped with graphene-oxide-platelets, and comparisons were drawn against pure water. The convective heat transfer exhibited a distinct periodic nature wherein the heat transfer was intensified when the pulsating flow rate was at a peak i.e., in the first half of cycle and it turned weak in the second half of the cycle. The maximum temperature in the channel was noted to be oscillating around a median value and the peaks increased with higher flowrate amplitudes. The thermal resistance deceased with a decrease in frequency and flow rate amplitudes. At an optimal frequency of 3.5 *Hz* the minimum thermal resistance was noted for all four waveforms. For the square format, greater average Nu was seen compared to steady flow and enhancements increased across all the

frequencies and flow rate amplitudes, reaching a maximum of 16.5%. Conversely, triangular and sawtooth pulsation formats exhibited a deterioration in heat transfer. Minor enhancements were seen for sinusoidal flow rates in a small frequency window of $3 - 4.5\ Hz$. Nanofluid based flow pulsations showed substantial enhancements in heat transfer compared to pure water with the increase in average Nusselt number between $9.8\% - 16.5\%$.

4.6 Summary of heat transfer studies of pulsating flows

A literature review summary table is provided in Table 4-1. The major findings from the literature review are:

- Fundamental studies implied the typical understanding that a large oscillating temperature gradient existed when the fluid oscillates under a thermal gradient. There is an increase in heat transfer with thinner boundary layers and an increase in pulsation frequency (up to a certain extent).
- Solution concentration studies highlighted that the axial (streamwise) spread of concentration inside a channel/pipe was dependent on the axial convection and radial molecular diffusion. With a corresponding increase in oscillatory frequency, a rapid fall in the rate of axial dispersion was noted.
- The thermal boundary layer is deemed to be formed as a result of velocity profiles and thus the thickness of the thermal boundary layer coincided with the velocity boundary layer under pulsating flows. Heat transfer was shown to be dominated by transverse (spanwise) heat diffusion mechanism.
- A dependence of heat transfer enhancement on flow parameters highlights that for low Re flows at large flow rate amplitudes, the heat transfer effect was significant.
    - For low to moderate pulsating frequencies, the heat transfer was more pronounced at downstream axial locations.
    - For high frequency flows, minor changes were visible near the channel entrance regions. Hence the axial advective term of the energy equation is the main driving factor for heat transport in pulsating flows.
    - Maintaining $Pr < 1$ was determined to show a prominent effect on heat transfer as greater heat diffusivity dominated the smaller momentum diffusivity.

- With Newtonian fluids, vessels with large diameter showed flow reversal effects for large Re and enhanced the heat transfer due to a sharp change in the temperature profiles. While in small diameter vessels, the obtained parabolic velocity profile corresponded to weak heat transfer.
- For parallel plate studies, heat transfer enhancement up to 40% was noted for higher pulsation amplitudes.

- The time-averaged Nu decreased from a high value near the entrance region to a low value at far downstream locations for a study involving pipes.
- Annular effects as introduced previously for velocity profiles, were also observed in transverse temperature profiles, particularly at high oscillation frequencies. Large flow rate amplitudes led to steeper velocity gradients from the near wall to bulk fluid regions and consequently increased heat transfer enhancement.
- Low to high values of the kinetic Reynolds number (Re_ω) oscillations showed an increasing phase difference between the temporal variation of axial velocity and wall temperature profiles. Higher Re_ω also showed prominent annular effects near the pipe entrance regions and an increase in heat transfer enhancement.
- Modifications to the channel geometry such as wall waviness, ribbed channels, rectangular slots, can promote intense fluid mixing along the walls, thereby playing a significant role in heat transfer in both laminar and turbulent flows.
- Amongst various waveform profiles such as sinusoidal, square, sawtooth and triangular; based on an optimum band of pulsation frequencies and flow rate amplitudes, a significant heat transfer enhancement was analytically predicted.

Table 4-1: Summary of selective studies of pulsating or oscillating flow that focus on heat transfer understanding

Reference	Year	Flow/Type	Geometry	Analysis Technique	Fluid	Variables	Wo or f (Hz)	*Re*	A_0 or F_0
Siegal R [107]	1960	Forced convection/Heat	Circular; Parallel plate	Analytical	Water*	*T, v, q*			
Sparrow & De Farias [24]	1968	Oscillating/Heat	Rectangular	Analytical	Air	*T, ΔT, Nu*	1-100	-	-
Patel *et al.* [108]	1975	Pulsating/Mass	Circular	Diffusion controlled electrode	Electrolyte	*q*	1.86-8.57	330-1000	-
Ozawa & Kawamoto [70]	1991	Oscillating/Heat	Rectangular & circular	Analytical & Liquid-crystal tracer visualization	Water	*V, T*	7.1-23	0.1-50	-
Seo *et al.* [73]	1993	Pulsating/Heat	Parallel plate channel	Analytical		*V, space-time Nu*	1-10	50	0-0.75
Liao *et al.* [79]	1994	Oscillating/Heat	Rectangular	Analytical	Air, water	*T, space-time Nu*	0.1-2	10-1000	
Zhao & Cheng [86]	1995	Oscillating/Heat	Circular	Numerical	Air	Space-time *Nu*	-	10-400	5-35
Mosyak *et al.* [80]	2001	Oscillating/Heat	Flume & Rectangular	PLIF & Thermal Imaging Radiometer	Water	Tw	-	8000-20000	-
Craciunescu & Clegg [109]	2001	Pulsating/Heat	Circular	Numerical	Newtonian fluid	*Tb*	0.017-10.25	-	-
Bereton & Jiang [110]	2006	Pulsating/Heat	Rectangular & Circular	Analytical	Variable Pr	*q*, Space-time *Nu*	0-60	-	0.5-2.5
Walchli *et al.* [111]	2010	Oscillating/Heat	Rectangular	Experimental, TC	Water	Tw	0.8-3	-	-
Ray *et al.* [112]	2012	Pulsating/Mass	Circular	Numerical & Analytical	Non-Newtonian	*L/D*	0.1-20	100-2000	0.2-0.8
Persoons *et al.* [82]	2013	Pulsating/Heat	Rectangular	Thermocouple	Water	Space-time Nu	6-17	100-650	-
Zhuang *et al.* [21]	2014	Pulsating/Mass	Rectangular	Differential pressure & Analytical	Water	*Fr*	-	-	-
Yuan *et al.* [113]	2014	Pulsating/Heat	Rectangular	Analytical	Variable Pr	*ΔNu*	-	-	-
Ghaedamini *et al.* [90]	2014	Pulsating/Heat	Rectangular	Numerical	Water	*Nu*	-	-	0.13-0.4
Yin & Ma [101]	2014	Oscillating/Heat	Circular	Analytical	Variable Pr	*Nu*	0.1-10	-	-
Mehta & Khandekar [103]	2015	Pulsating/Heat	Rectangular	IR thermography	Water	Space-time *Nu*	0.8-5.9	-	-
Li *et al.* [114]	2016	Pulsating/Heat	Circular	Numerical	Air	*Nu, Rth*	15-30	-	-
Yang *et al.* [91]	2018	Pulsating/ Heat	Rectangular	Numerical	Air	*Nu*	50-350	$2x10^4$-$4x10^4$	-
Blythman *et al.* [115]	2018	Pulsating/ Heat	Rectangular	Analytical, Numerical & IR	Water	*Nu*	1.4 – 22.1	-	0.0035 – 8.77
Zhang *et al.* [92]	2019	Pulsating/Heat	Grooved	Flow visualization & Numerical	Water	Space-time *Nu*	0.0346-1.6229	0-1500	0.4-1
McEvoy *et al.* [105]	2019	Pulsating/Mass/Heat	Rectangular	PIV	Water	V, space-time Nu	1-5	-	0.0542
Xu *et al.* [106]	2020	Pulsating/Heat	Pin fin rectangular	IR	Nanofluid	Thermal resistance	1-4.5	272-544	-
Kurtulmus & Sahin [94]	2020	Pulsating/Mass/Heat	Sinusoidal	PIV	Water	V, space-time Nu	0.11-2.07	$4x10^3$-$7x10^3$	
Akcay [96]	2022	Pulsating/Heat	Corrugated	Numerical	Water	Time space Nu	2-8	200-1000	0.5-1.5
Li *et al.* [116]	2022	Pulsating/Mass/Heat	Spherical corrugated	TC, numerical	Water	V, space-time Nu	25-71	9940-19880	0.25-0.75

5) Experimental Methods

This chapter describes the design, assembly, and operation of the experimental rig, including the data acquisition methods. Experimental setup facilitates measurements of local time-dependent wall temperatures from a uniformly heated surface. Flow rate pulsations of varying characteristics such as modulating waveform, frequency and flow rate amplitudes are configured using a flow control system. Planar measurement technique in form of a high-resolution, high speed infrared camera is positioned in the downstream region ensuring that the flow is hydrodynamically and thermally fully developed. A comprehensive quantification of thermal losses and the uncertainties is discussed. A three-dimensional render of the rig is provided in Figure 5-1.

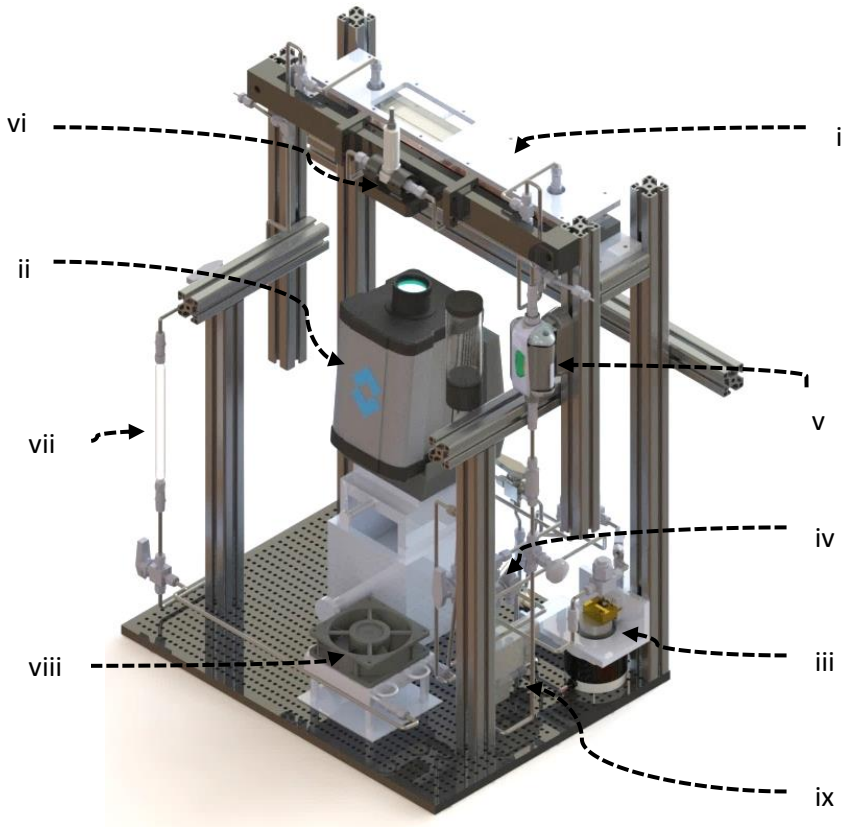

Figure 5-1: Three-dimensional render of the experimental rig with labels showing: i) minichannel plate assembly, ii) IR camera, iii) stepper motor system, iv) steady pump, v) flowmeter vi) pressure sensor, vii) membrane contactor, viii) fan driven heat exchanger and ix) solenoid valve.

5.1 Apparatus Details

5.1.1 Overview of test section

The experimental test section consists of a series of plates. An Ertacetal C heater support plate and acrylic channel profile plate are secured between two aluminium support plates, as shown in Figure 5-2. The support plates are required to distribute the clamping stresses to prevent the channel profile from cracking. The acrylic channel profile is ensured to be leak proof by machining a small 0.7 *mm* groove along its periphery, into which a 1 *mm* diameter nitrile rubber O-Ring is fixed. Threaded holes of 12.7 *mm* (1/2”) diameter are located in the upper aluminium support plate to deliver the working fluid to the minichannel.

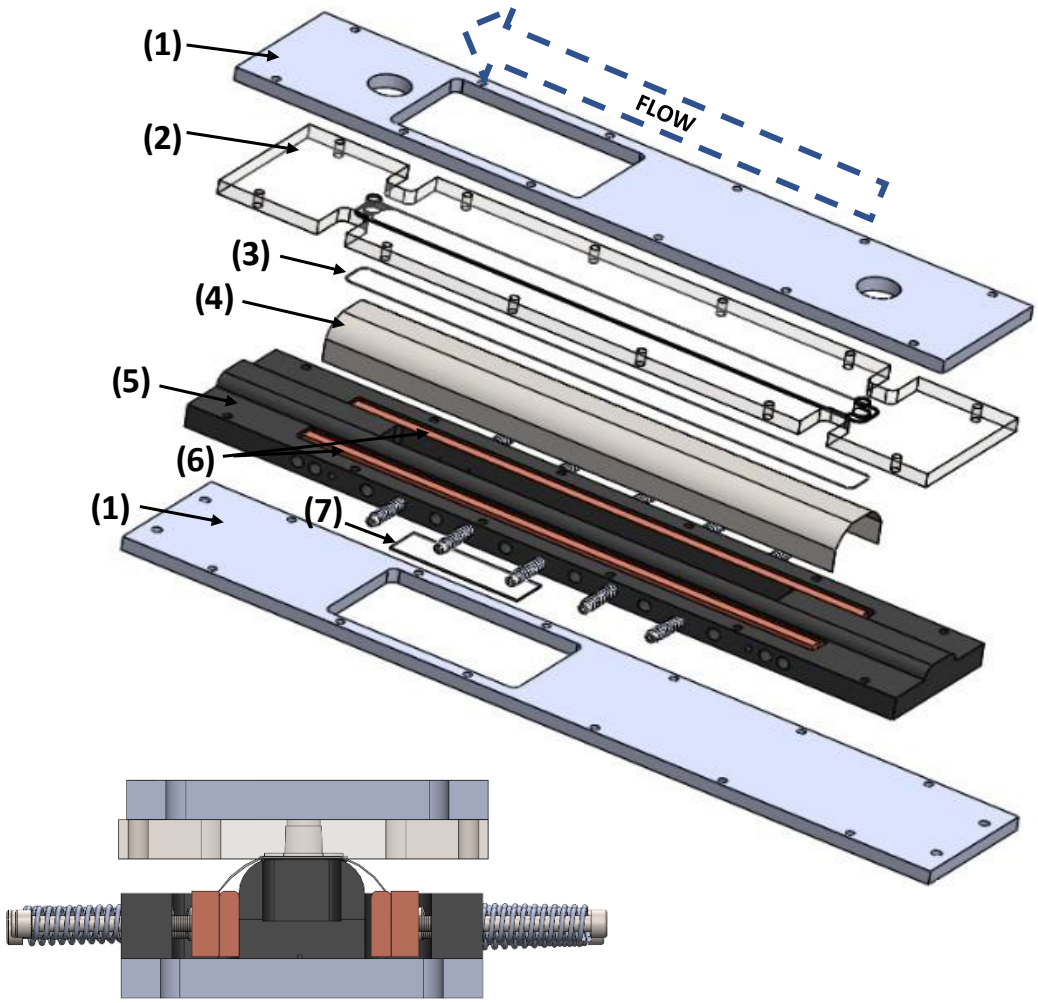

Figure 5-2: Exploded assembly view of test setup, showing (1) aluminium support plates, (2) channel profile plate, (3) O-Ring, (4) foil, (5) heater support plate, (6) copper busbars, (7) IR glass

5.1.2 Minichannel design

The working fluid (deionised water) is transported through the test section using a channel profile plate. The rectangular duct is milled from an acrylic base material. The bottom part of this profile forms the top wall of the minichannel, further discussed in detail below. The O-ring used for sealing has a negligible effect on the overall clamped channel height. The O-ring groove is machined outside the channel profile to the maintain a consistent hydraulic diameter (D_h) along the channel length. The channel dimensions are presented in Table 5-1.

Table 5-1: Experiment minichannel dimensions

Parameter	Unit	Symbol	Value
Channel length	*mm*	l	360
Channel height	*mm*	a	1.4
Channel width	*mm*	$2b$	20
Channel hydraulic diameter	*mm*	D_h	2.6

5.1.3 Foil tensioning mechanism

Tensioning of the foil is required to provide the flat surface that forms the bottom surface of the minichannel. To achieve this the foil is placed over a knife edge design, shown by a cross-sectional view in Figure 5-3 of the heater support plate. The foil is laterally tensioned using spring-loaded bolts. An inner array of bolts along the foil length maintains the essential electric contact between the foil and pairs of copper busbars. A layer of silver conductive grease is used to reduce electrical contact resistance. The knife edges form a wall between the busbars and the under-foil air gap to minimize the heat leakage. Each pair of busbars has two screw connections at the ends to enable the power supply via copper cables. The power supply is a Lambda GENESYS GEN6-200 DC source capable of delivering 6 *V* and 200 *A*. To maintain all materials within recommended operating temperature limits, a constant current mode of 41.9 *A* ensures steady heating of the foil and is invariant to any change in foil or power cable resistance due to heating [117].

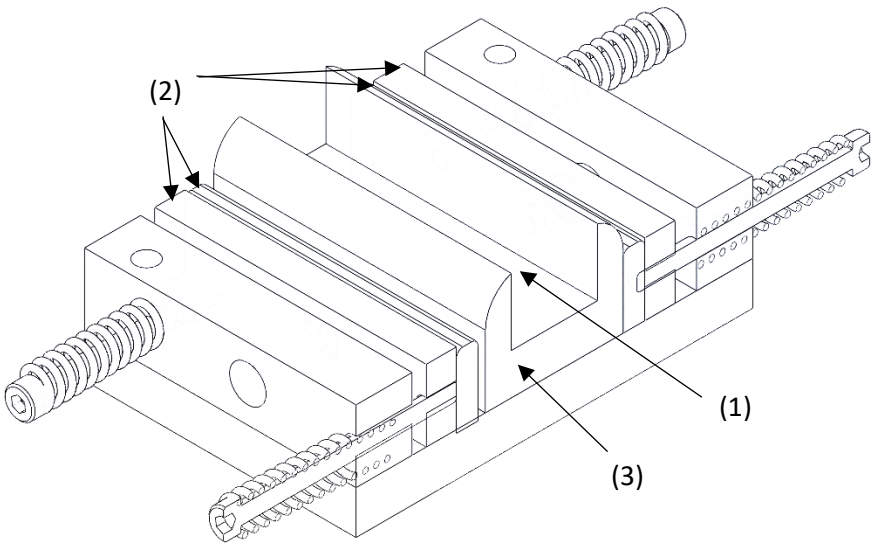

Figure 5-3: Cross-sectional view of knife-edge design of heater support assembly showing: (1) air gap, (2) busbars, (3) heater support plate.

5.1.4 Foil selection and preparation

Inconel 600 annealed foil (Ni72/Cr16/Fe8) of 12.5 μm thickness, supplied by Goodfellows, is chosen to form the bottom surface of the minichannel. Inconel was preferred over the various other foil materials under consideration (see Figure 5-4) for its favoured properties of high electrical resistivity and low thermal conductivity (to lessen the lateral conduction effects within foil). The underside of the foil is painted black [118] to provide a high emissivity surface for infrared thermography. Additionally, it reduces the Narcissus effect from foil reflections. The thin foil is cut precisely to $360\ mm \times 95\ mm$ (length x width) and cleaned using acetone prior to painting. Sections of the foil are masked using masking tape to confine the black paint within the central width of the foil to avoid end effects from the clamping regions. A spray paint gun is used with high temperature Electrolube matte black paint as the feeder. Paint is sprayed onto the foil at a nozzle inclination angle of approximately $15°$. The paint thickness of $20.4\ \mu m$ with a standard uncertainty of $\pm 0.89\ \mu m$ was evaluated using White Light Interferometry (WLI). Table 5-2 describes the foil and paint properties.

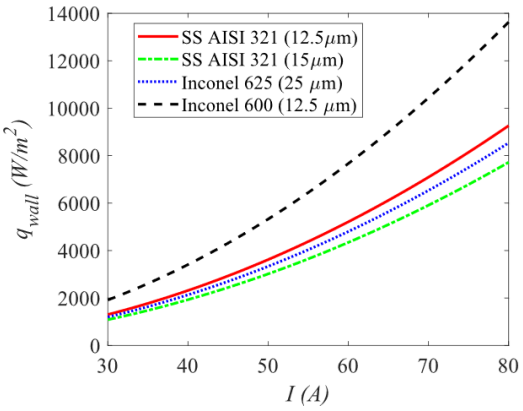

Figure 5-4: Comparison of various foil heat flux rates.

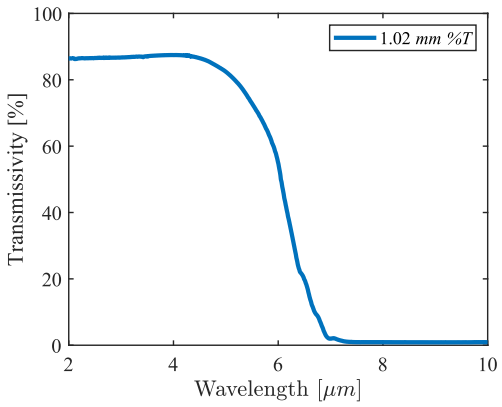

Figure 5-5: Sapphire (Al_2O_3) glass transmissivity with the wavelength range.

Table 5-2: Selected foil and paint properties *[108, 109]*

Parameter	Unit	Symbol	Foil ($_f$)	Paint ($_p$)
Thickness	μm	w	12.5	20.4
Electrical resistivity	$\mu\Omega{\cdot}cm$	σ	103	-
Density	kg/m^3	ρ	8420	1162
Thermal Conductivity	$W/m{\cdot}K$	k	14.8	0.095
Specific heat	$J/kg{\cdot}K$	C_p	444	2835
Emissivity	-	ε	0.13	0.95

5.1.5 Infrared thermography system

The thermal measurements are recorded using an infrared thermography (IRT) system. An infrared camera is focussed on the underside of the heated foil. The focal path between the camera lens and the painted foil surface includes a thin transparent IR glass window. The purpose of the window is to reduce convective losses from the underside of the foil whilst maintaining visual and IR access. To maintain a stagnant air gap (to provide insulation) of dimensions $75 \times 20 \times 12$ (length X width X height in *mm*), a sapphire glass (Al_2O_3) of thickness 1 *mm* is used, which is held close to the foil wall using a custom fabricated bracket. Sapphire glass has high percentage of transmissivity in the $2.5 - 5.1$ μm range of the infrared camera, as plotted in Figure 5-5. A 1 *mm* thick window of face area 95 *mm* × 75 *mm* facilitates thermal measurements with the IR camera. A sketch of the cross-section with spatial dimensions shown in Figure 5-6.

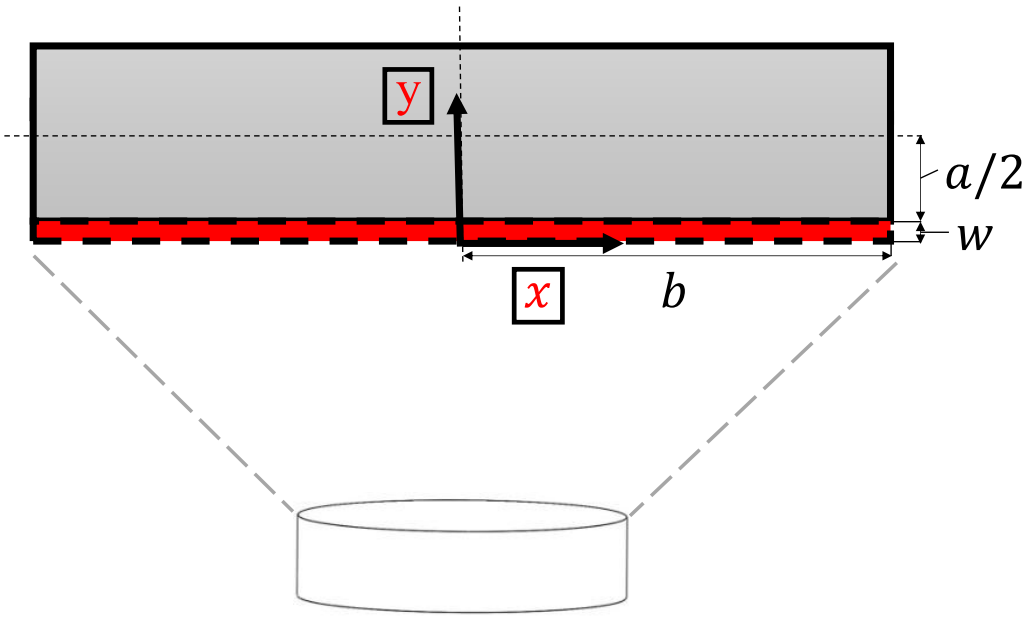

Figure 5-6: Cross-sectional view of the channel (grey) and foil (red) with custom coordinate system.

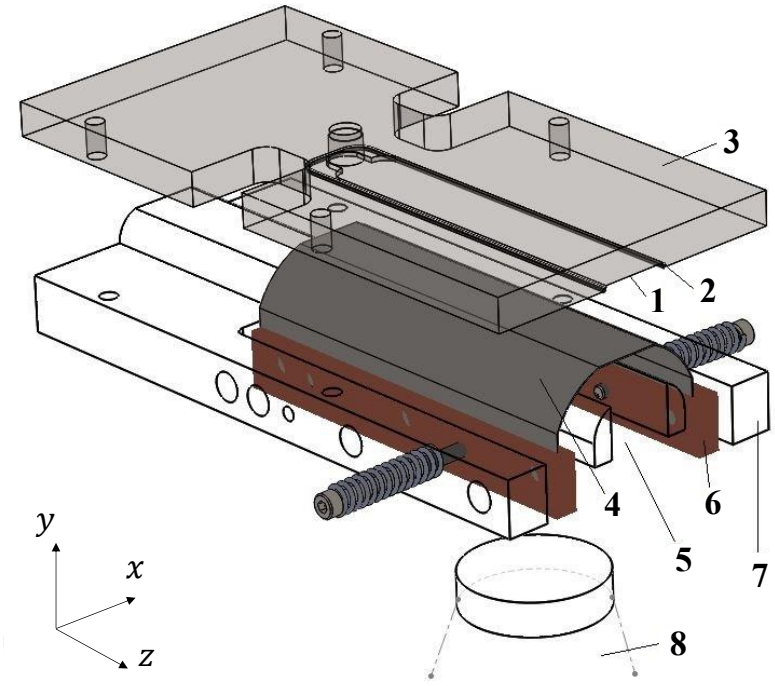

Figure 5-7: Test section assembly view showing the essential components: 1) minichannel profile, 2) O-Ring, 3) acrylic plate, 4) foil, 5) air gap, 6) busbars, 7) heater support plate, 8) IR lens (with custom coordinate system).

The heated foil surface, mounted as shown in Figure 5-7, is imaged non-intrusively using a high-speed, high-resolution FLIR SC6000 Infra-Red camera. The camera consists of a focal plane array (FPA) of indium antimonide (InSb) detectors, sensitive in the mid-wavelength infrared (MWIR) spectral range. The detectors within the camera are cooled to 78 *K* using a Sterling engine to avoid the infrared transmission being flooded from its own surroundings. The camera has 14-bit signal discretisation where each pixel reading is interpreted in the 0 to 16383 counts range (min-max). An integration time of 1.3 *ms* is set during calibration to maximize the exposure time in the above range. Further detail is provided in Section 5.2.1.

The mounting of the camera is achieved using a 3-axes translational optical stage with a motion range of $100\,mm \times 100\,mm \times 50\,mm$ (length X width X height). A custom fabricated base profile is used to provide the necessary rigid vertical clamping for the camera, shown previously in Figure 5-1. As recommended by the manufacturer, the camera is inclined at a 5° angle to minimise the reflections from the IR transparent glass window. For achieving high spatial resolution of the heated surface, a MW G0.5 F/3.0 close-up lens with a focal length of 225 ± 0.5 *mm* and maximum field of view 19.2×15.36 mm^2 is used for an image region of 320×256 pixels (x offset = 160, y offset = 76). The lens has $> 93\%$ transmission. The channel width measure 120 pixels providing a spatial resolution of 172.4 *µm/pixel*. The camera acquisition, as explained in the section below, is controlled using the FLIR ExaminIR integrated software (version 1.30.0) package. The video recordings are further post-processed using Matlab.

Table 5-3: Selected infrared camera specifications

Parameter	Unit	Value
Maximum Resolution	*pixels*	12.5
Wavelength Range	μm	$3-5$
Maximum frame rate	*Hz*	32000
Thermal Sensitivity	*mK*	< 20

5.1.6 Flow control system

The flow control system is associated with operating and directing steady and pulsating flows. The system consists of a micropump and stepper motor connected in line with a flowmeter. The flow line includes non-return valves to enable flow mode and flow direction control, allowing the operator to switch between steady, oscillating, or pulsating flow modes. The steady flow is generated using a centrifugal miniature pump (TCS M400) capable of attaining pulseless maximum flow rates of up to 2 *L/min*. The pulsating/oscillating flow is produced using a FESTO piston pump (ADNGF-25-20P-A, see Appendix 0 for specifications) with a high-performance McLennan 34HSX-108 stepper motor controlled by a ST5-Q-NN applied motion drive, which provides precise control over the pulse generation resolution with a range of 1-25000 steps per revolution and high

frequency up to 25 *kHz*. Further details on the control of pulsating flow formats are described in Section 5.1.7. Since precise instantaneous measurement of the flow rate is essential, a non-invasive Atrato 710 series ultrasonic flowmeter, operable within a volumetric flow range of 2-500 *mL/min*, is located in the flow loop close to the inlet. A high accuracy calibrated differential pressure transducer measures pressure differences up to 17.24 *kPa* (OMEGA PX 409 series) and its connections are located between the inlet and outlet sections of the minichannel.

The working fluid is de-ionised and de-gassed prior to testing. To achieve degassing, a membrane contactor is fitted near the outlet of the minichannel to filter out the gas bubbles and other impurities from the liquid. The side ports of the degasser are connected to a vacuum pump to eliminate the dissolved gases and air bubbles trapped between the filter membranes.

5.1.7 Pulsation drive mechanism

A scotch-yoke arrangement of the stepper motor and piston pump is programmed to develop the desired waveform formats for oscillating/pulsating flow. The stepper motor drive motion is part of an intricate and synchronous pulse-frequency modulation (PFM) control system used to generate the desired characteristic oscillation waveform. Examples of normalised pulsating flow (oscillating + steady)/(steady) waveforms are shown in Figure 5-8 for a flow rate amplitude of $A_0 = 1$. The waveform generation is controlled via LabVIEW.

5.1.7.1 Sinusoidal waveform format

The symmetric sinusoidal profile shown in Figure 5-8 is defined using the Express VI LabVIEW function. The waveform control parameters are the frequency and amplitude.

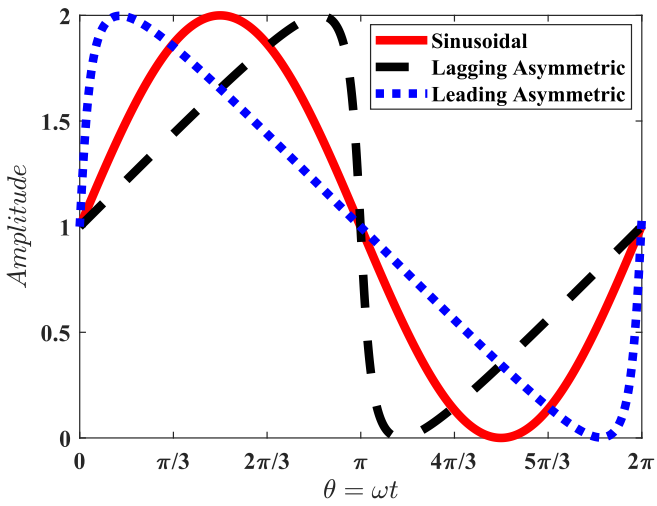

Figure 5-8: Example of normalised pulsating flowrate profiles (Q_p/Q_s) for symmetric sinusoidal and asymmetric sinusoidal waveforms for a flow rate amplitude of $A_0 = 1$.

5.1.7.2 Asymmetric sinusoidal waveform format

A customized trigonometric version of the Clausen Integral [121] shown in Equation (5-1), generates the asymmetric sinusoidal waveform via LabVIEW and must be multiplied by the flow rate amplitude to obtain the desired oscillating flow rate. The variable (j) is defined to generate the +ive or leading, and –ive or lagging, asymmetric sine functions, as indicated in Figure 5-8.

$$y(t) = \left(\frac{1}{j}\right) tan^{-1}\left(\frac{j \cdot sin(2\pi ft)}{(1 - j \cdot cos(2\pi ft))}\right); -1 \leq j \leq +1 \quad (5\text{-}1)$$

5.1.7.3 Half rectified sinusoidal waveform format

Additionally, two semi sinusoidal waveforms *i.e.*, the positive and negative halves of a sinusoidal waveform, are investigated. Example profiles are shown in Figure 5-9. The oscillating component of these waveforms does not result in a cycle averaged zero mass flow, and therefore they differ significantly from other pulsating flows investigated in this study. However, their characteristics show some interesting behaviour. These waveforms are produced by including a three-way SMC VX3130-02N-5DZ1-B solenoid valve in the flow loop. This valve does not necessitate any difference in pressure between the inlet and outlet ports to operate, allowing the valve to also function responsively in negative pressure circuits. The valve is placed close to the exit of the stepper control system and is externally powered by a 24 VDC supply. For responsive switching of the magnetised coil, a MOSFET transistor operating between 0-5 VDC is connected to the valve. The switching timing control is programmed in LabVIEW which executes a synchronous, sequenced, directional opening and closing of the valve as per the user configured pulsation frequency.

To generate a positive half rectified oscillating flow component, a bypass loop is developed to re-route the flow to the reservoir during the phases $\pi \leq \theta \leq 2\pi$. During the phases $0 \leq \theta \leq \pi$, the flow entry into the minichannel is initiated from the scotch-yoke mechanism, as before. To generate a negative half rectified oscillating flow component, the flow paths are manually interchanged on the ports of the three – way solenoid valve. This leads to supplying the flow during phases $0 \leq \theta \leq \pi$ to the inlet of the minichannel. For phases $\pi \leq \theta \leq 2\pi$, flow is bypassed into the reservoir, using a feedback loop mechanism.

The block diagram shown in Figure 5-10 describes the generic process, beginning with a user-defined waveform function controlled by amplitude and frequency. This signal is fed to a multiplier mechanism where the conversion to the steps to revolution (stepper performs up to 25000

steps/rev) and is regulated as per the instantaneous excitation waveform. A square wave signal (modulating waveform) is generated using the Express VI LabVIEW function. Its maximum frequency is registered, and a corresponding amplitude of the output is fixed at 5 *V*. Certain waveforms for flow pulsation require an additional direction control mechanism (wiper mechanism) to achieve precise control of signal generation, established with the motor speeds. The working principle is based on detecting the zero crossing of the amplitude of a signal and correspondingly, the scotch direction is reversed the instant it is toggled. Finally, the signal of the modulating square wave is transmitted at a high sampling rate of up to 50 *kHz* to a National instruments NI-9269 data acquisition module. The data acquisition system transfers the periodic waveform datapoints to the motion control driver, which is powered externally, and the signal culminates at the stepper motor which performs the desired oscillatory motion.

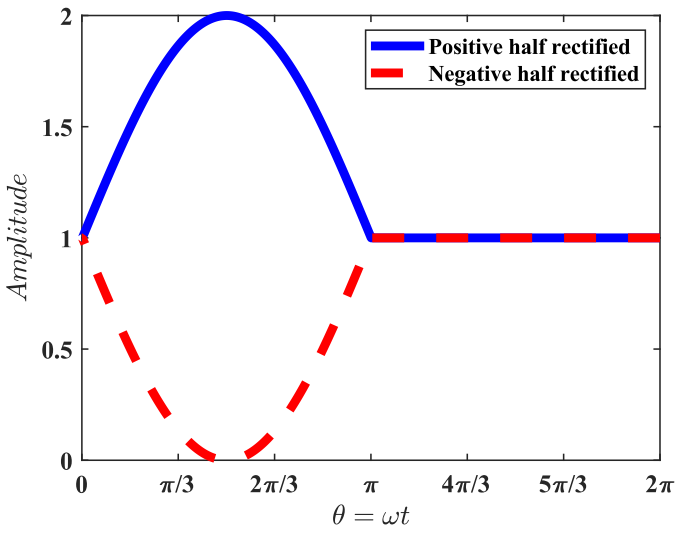

Figure 5-9: Example of normalised pulsating flowrate profiles (Q_p/Q_s) for half rectified sinusoidal waveforms for a flow rate amplitude of $A_0 = 1$. Here, for the negative half rectified waveform, the flow rate amplitude is defined as $-Q_{osc.min}/Q_s$.

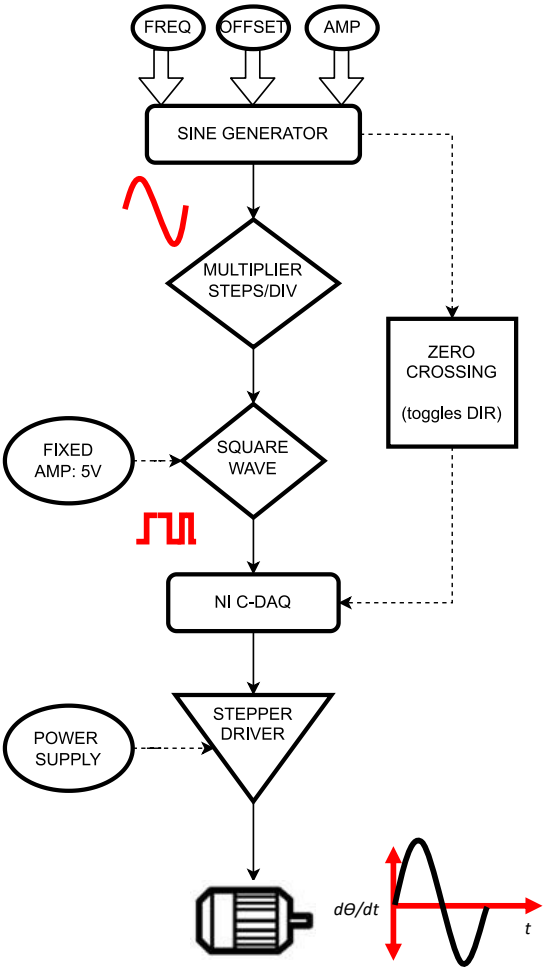

Figure 5-10: Pulse-frequency modulation (PFM) flowchart for stepper motor control system. Example shown here is for a symmetric sinusoidal flowrate profile.

5.1.8 Temperature sensors

Four calibrated type-T thermocouples are included to record and monitor the temperature fluctuations in the test section. Since the temperature range of operation is $< 200\ ℃$, a type-T thermocouple probe of 1 *mm* (diameter) and fabricated of copper-constantan alloy is a desirable selection for the experimental study, offering stability, repeatability, and fast response times. Two are placed at the inlet and outlet of the minichannel and the other two are used to measure the airgap temperatures in the cavity between the underside of the foil and the transparent IR glass window. The thermocouples enable estimation of the heat supplied to the water and help to identify a steady state temperature distribution across the minichannel before the commencement of pulsating flow testing sequence.

5.2 System Calibration

5.2.1 Thermal Camera

The infrared camera lens system is exposed to ambient noise as the sensor records varying amounts of incoming radiation energy. Such inhomogeneities in the field of view lead to distortion of measured counts. To mitigate this effect, a two-point non-uniformity correction (NUC) is employed prior to the temperature-to-counts calibration. The methodology involves observing a constant room temperature to set the desired integration time and window size. Another calibration plate is used which is heated to a temperature close to the maximum temperature expected in the experiments. Following this, the thermal camera is calibrated using a black body generator with a temperature probe and controller, manufactured by Santa Barbara Infrared. The black body surface is of an industry standard high emissivity of 0.95. The measurement stability is found to be accurate to < 1 *mK*. To follow a temperature calibration, the black body is heated between the range of 20 *°C* to 65 *°C* corresponding to the expected ambient temperature and maximum temperature value observed in the test, respectively.

In addition to the standard calibration procedure followed above, an in-situ measurement technique is carried out with the camera facing the test section, viewing through the IR glass window to capture calibration constants [115]. A matte black enclosure was placed surrounding the camera to prevent unwanted reflections. Additionally, to reduce the Narcissus effect the external camera elements are covered using black felt material. For in-situ calibration, water at intervals of $5\,℃$ is circulated through the test section from a Julabo F25 chiller, wherein the foil remains unheated. For every instance of measurement, thermal equilibrium is ensured by monitoring the thermocouples at the minichannel inlet and outlet, and air gap locations. Although the air gap temperatures take longer to stabilise, steady state is achieved in about 2 hours. The counts for the calibration are obtained by averaging a small spatial area in the viewing window, while the fluid temperature is obtained from the average of the inlet and outlet temperatures. A polynomial fit of the temperature calibration, as depicted in Figure 5-11 is obtained using MATLAB functions of *poly-val* and *poly-fit*.

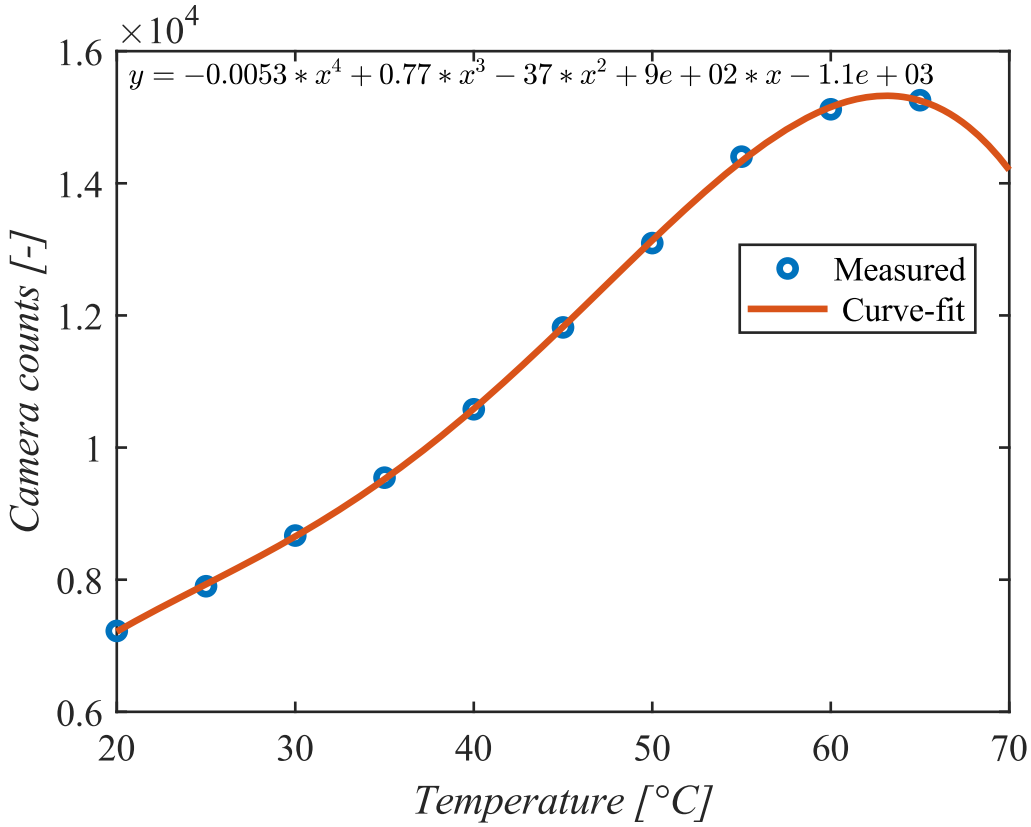

Figure 5-11: Calibration curve for the IR camera.

5.2.2 Thermocouple calibration

Four type-T thermocouples are calibrated and are positioned at the minichannel inlet, minichannel outlet, and two air gap locations separated by a distance of $50\ mm$. Calibrations of the four probes is carried out using a Julabo F25 constant-temperature water bath with a manufacturer-specified precision and accuracy of 0.5 $°C$. A Stanford Research Systems calibrated thermistor probe and programmable temperature controller are used to maintain the temperature setpoints for the thermocouples. Each of the probes was wrapped under insulation with the thermistor probe and immersed into the water bath to register the recordings using a National Instrument 9213 thermocouple module, connected to LabVIEW. The linear fit calibration of the thermocouples is shown in Figure 5-12.

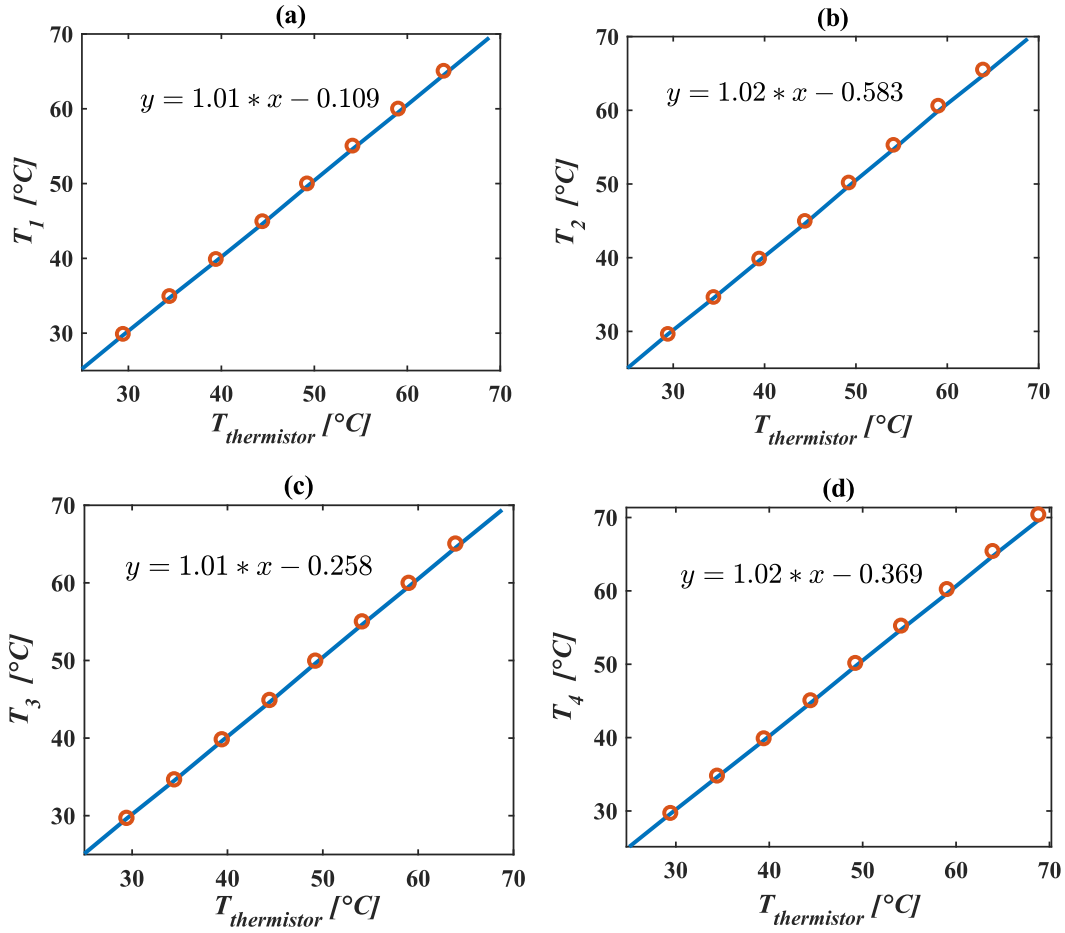

Figure 5-12: Calibration graphs for the type-T (T_1 – T_4) thermocouples

5.3 Experimental Procedure

Prior to testing, deionised water is circulated from the reservoir through the flow loop for about an hour to ensure there are no air bubbles in the test section. A vacuum jacket is connected to the degasser to maintain the system free of gas impurities.

A steady flow with a Reynolds number between $24 \leq Re_s \leq 100$ is supplied from the micropump to ensure there are no turbulent effects in the flow. The foil is heated until the minichannel inlet, outlet, and air gap temperatures stabilise. Thermal equilibrium is attained after approximately 2 hours. The heated working fluid that has passed through the minichannel is cooled to ambient by a fan-driven plate-fin heat exchanger attached in the loop. The instantaneous flowrate and differential pressure measurements are recorded at 10 *Hz.* The IR camera acquisition records the *.SFMOV* video files, which are exported to post-process the time-averaged wall temperature measurements.

For pulsating flow, the flow control system comprising of the piston-pump assembly is activated to generate an oscillating flow component in addition to the underlying steady component. A pulsation waveform of interest (*e.g.*, sinusoidal symmetric, sinusoidal asymmetric, half rectified) is configured via the data acquisition system with a set pulsation frequency and flow rate amplitude (as elucidated in the section 5.1.6). Frequencies of *f* = 0.02 *Hz*, 0.5 *Hz* and 2 *Hz* equivalent to $Wo = 0.51, 2.5$ and 5.1 are driven with the stepper motor. Experimental data does not exist for the highest frequency $f = 25\ Hz \approx Wo = 18.3$, since the rapid pulsation is physically limited due to a sharp rise in the pressure gradients with likelihood of causing determinantal effects. Pulsatile flow of $Re_p = Re_{osc,max} + Re_s = 250$ is circulated in the system. Thermal measurements are recorded in a phase-lock arrangement whereby the IR acquisitions are initiated by reading an externally triggered TTL pulse signal from the flow control system. A proximity sensor attached to the end of the piston pump synchronises with this signal by returning the detected position, such that the oscillatory motion for each cycle is accurately timed. Thus, for example, a camera fps is set at 2 *Hz* to extract 100 datapoints for 20 phases in each cycle, which depends on the pulsating frequency. 2000 thermal images from the FLIR ExaminIR software are recorded. The video files (format **.sfmov*) are exported to MATLAB for analysis, and the time-dependent fluctuating components of transverse wall temperature profiles are inspected using MATLAB's inbuilt *polyval* and *polyfit* functions.

5.4 Experimental Operating Conditions

Experiments are performed for a range of frequencies, flow rate amplitudes, and waveforms. Table 5-4 describes the investigated parameters.

Table 5-4: Experimental parameters investigated.

Waveform	***f***	***Wo***	Re_s	$Re_{osc.max}$	A_0
	[*Hz*]	**[-]**	**[-]**	**[-]**	**[-]**
Symmetric sinusoidal	**0.02, 0.5, 2**	**0.5, 2.5, 5.1**	$\mathbf{24-100}$	$\mathbf{40-150}$	**0.5, 1.0, 3.0**
Asymmetric sinusoidal	**0.02, 0.5, 2**	**0.5, 2.5, 5.1**	$\mathbf{24-100}$	$\mathbf{40-150}$	**0.5, 1.0, 3.0**
Half rectified sinusoidal	**0.02, 0.5, 2**	**0.5, 2.5, 5.1**	$\mathbf{24-100}$	$\mathbf{40-150}$	**0.5, 1.0, 3.0**

5.5 Experimental Data Analysis

5.5.1 Hydrodynamic parameters

The rectangular minichannel has the following dimensions: length (L) = 360 *mm*, height (a) = 1.4 *mm* and width (b) = 20 *mm*. The hydraulic diameter (D_h) of the minichannel is defined as:

$$D_h = \frac{2ab}{a+b} = 2.6 \times 10^{-3}\ (m) \tag{5-2}$$

The hydrodynamic entrance length (**≈** 29 *mm*) is calculated using Equation (5-3) at $Re_{max} = 250$ according to Refs. [48,49] and verified by assessing the relevant profiles. The maximum entrance length is upstream of the viewing window, so the flow is considered to be hydrodynamically fully developed. The entry length for pulsating pipe flow has been shown numerically to vary sinusoidally with an amplitude less than or equal to the steady flow value as studied by Durst *et al.* [18].

$$\frac{L_e}{D_h} = [(0.631)^{1.6} + (0.0442\ Re_{max})^{1.6}]^{1/1.6} \tag{5-3}$$

An instantaneous time-dependent analysis of steady/pulsating flowrate and differential pressure drop is performed in MATLAB. The **.lvm* files generated from LabVIEW are post-processed for each dataset.

5.5.2 Heat transfer parameters

The thermal entrance length (**≈** 204 *mm*) is calculated using Equation (5-4) is sufficiently smaller than the 220 *mm* heated length upstream of the viewing window so the flow is considered to be thermally fully developed.

$$L_{th} = Pr\ \times L_e \tag{5-4}$$

To evaluate the thermal performance of heated minichannels under pulsating inlet conditions, convective heat transfer parameters are introduced. For the equations presented below, time averaging is performed over one pulsation cycle (λ) once the periodic behaviour is established. Spatial averaging of IR data is performed on the underside of the heated foil over the range $0\ mm \leq y \leq 20\ mm$. All measurements are recorded at $z \geq 210$ *mm*, *i.e.*, where the flow is expected to be fully developed hydrodynamically and thermally. $\overline{T_w}$, as defined by Equation

(5-5), is the time-averaged heated wall temperature. $|T_w|$ is the instantaneous spatially averaged temperature at the heated wall (IR viewing area). $\overline{T_b}$ is the time-averaged bulk fluid temperature as given by Equation (5-6). T_{in} and T_{out} are instantaneous fluid temperatures determined from the inlet and outlet thermocouples. The time averaged Nusselt Number ($\overline{Nu}$) as given by Equation (5-7)

defines the relationship between the fluid thermal conductivity and surface convection. The time-averaged foil heat flux is defined as ($\bar{q}_w$). The normalised enhancement of heat transfer (dNu) compared to steady flow only is described by Equation (5-8) where Nu_s represents the steady flow Nusselt number.

$$\overline{T}_w = \frac{1}{\lambda} \int_0^{\lambda} |T_w| dt \tag{5-5}$$

$$\overline{T_b} = \frac{1}{\lambda} \int_0^{\lambda} \frac{(T_{in} + T_{out})}{2} dt \tag{5-6}$$

$$\overline{Nu} = \frac{\bar{q}_w \cdot D_h}{(\overline{T_w} - \overline{T_b}) \cdot k_l} \tag{5-7}$$

$$dNu = \frac{\overline{Nu} - Nu_s}{Nu_s} \tag{5-8}$$

The effect of heat transfer by natural convection is estimated. Natural convection involves motion and mixing of fluid resulting from the density variation within the fluid. The density of fluid near the heated surface is less than that of the colder fluid away from the heated surface, and gravity creates a buoyant force which raises the less dense, warmer fluid. Since density is a function of temperature, the variation of density of fluid with temperature at constant pressure is expressed in terms of volume expansion coefficient: $\beta_l = 1/T_l$, where T_l is the absolute temperature of fluid. The Grashof number (Gr) is a dimensionless quantity which represents the ratio of buoyancy forces to the viscous forces acting on the fluid:

$$Gr = \frac{g\beta_l(T_w - T_l)D_h^3}{\nu^2} \tag{5-9}$$

Here g is the gravitational acceleration. $Gr/Re_s^2 \ll 1$ predicts that forced convection is predominant and the effects of buoyancy are negligible [22]. Under the experimental operating conditions, the maximum $Gr = 13826$, using averaged bulk and mean wall temperatures. For the current study the maximum value of $Gr/Re_s^2 \approx 0.33$, which indicates insignificant natural convection, and the forced convection effect is dominant.

The Fourier number characterises transient heat conduction. It represents the transport rate of conduction relative to the rate of storage in the solid. The Fourier number calculated is $Fo = 4.03 \times 10^3$ signifies transient heat conduction rate through the solid.

$$Fo = \frac{\alpha_f}{(\omega \cdot w_f)} \tag{5-10}$$

Where, α_f is the thermal diffusivity of the foil and w_f is the foil thickness. The Biot number represents the ratio of temperature gradient in the solid, *i.e.*, conduction to the temperature difference induced between the wall and fluid, *i.e.*, convection.

$$Bi = \frac{h \cdot w_f}{k_f} \tag{5-11}$$

Where, k_f is the thermal conductivity of the solid and h is the heat transfer coefficient. If $Bi \ll 0.1$, the lumped system is applicable and, in this case, $Bi = 0.0042$ which predicts that the resistance to heat flow within the solid is small relative to the resistance presented by the convection process at the surface [22, 111]. This infers that the internal temperature (spatial) distribution in the solid is relatively uniform at any instant of a time dependent process.

5.5.3 Foil energy balance

To estimate the convection to the fluid, one must account for other heat transfer processes taking place, such as lateral conduction in the foil and paint, radiation from the foil and paint surfaces, and conduction to the stagnant air gap between the foil and IR glass. An energy balance is applied to each pixel in the captured IR image. A differential control volume for the foil and paint layers with dimensions $dx \times dz \times (w_f + w_p)$ is shown in Figure 5-13, where the subscripts *f* and *p* represent the foil and paint respectively [115, 119, 120, 122].

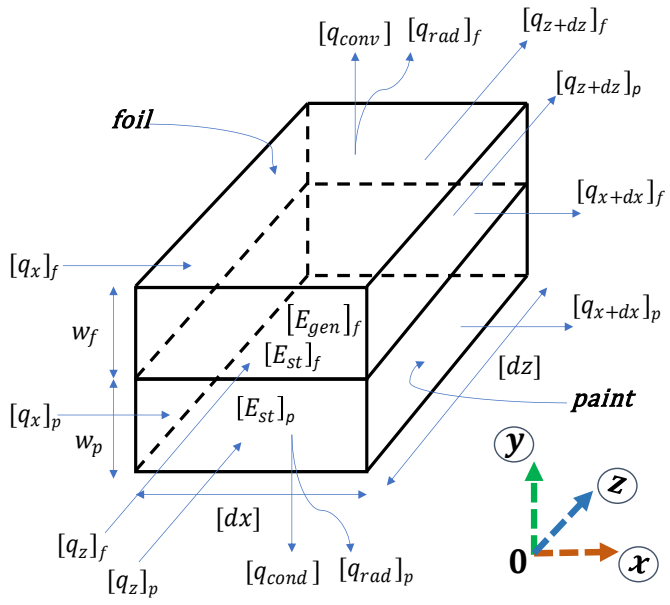

Figure 5-13: Control volume thermal energy balance for foil and paint thicknesses w_f and w_p respectively.

Heat generated in the foil is transferred between neighbouring foil and paint elements by lateral conduction, to the fluid by forced convection and radiation, and to the stagnant air gap by 1-D

conduction and radiation. The energy may also be used to increase the temperature of the foil. The material thicknesses are assumed constant, with negligible contact resistance between the foil and paint layers. The conservation of energy method as given in [22] is described as:

$$\dot{E}_{in} + \dot{E}_{gen} - \dot{E}_{out} = \Delta\dot{E}_{st} \tag{5-12}$$

wherein $\dot{E}_{in}$ and $\dot{E}_{out}$ represent the rate of energy transport in and out of the control volume, and $\dot{E}_{gen}$ and $\dot{E}_{st}$ are the rates of generated and stored thermal energy in the control volume respectively. The expanded energy balance applied to a control volume can be expressed as:

$$\begin{aligned} &[q_x]_{,f} + [q_z]_{,f} + [q_x]_{,p} + [q_z]_{,p} + \dot{q}_{gen} dxdz \cdot w_f \\ &- [q_{x+dx}]_{,f} - [q_{z+dz}]_{,f} - [q_{x+dx}]_{,p} - [q_{z+dz}]_{,p} - \\ &q_{conv} dxdz - q_{cond} dxdz - q_{rad} dxdz - q_{cap} dxdz = 0 \end{aligned} \tag{5-13}$$

$\dot{q}_{gen}$ is the heat generated per unit volume, q_{conv} is the convective heat flux to the fluid, q_{cond} is the conductive heat flux loss to the air gap, q_{rad} is the radiative heat flux to the surroundings from the foil and paint, and q_{cap} is the storage heat flux. The heat rate terms in square brackets have units of Watts. The conduction heat transfer rate through the control volume for the foil and paint layers can be estimated using Fourier's Law:

$$q_x = -k \cdot w \cdot dz \left(\frac{\partial T}{\partial x}\right) \tag{5-14}$$

$$q_z = -k \cdot w \cdot dx \left(\frac{\partial T}{\partial \mathrm{z}}\right) \tag{5-15}$$

Similarly, the conduction heat flow on the opposite side of the control volume can be determined as:

$$q_{x+dx} = q_x + \frac{\partial q_x}{\partial x} dx \tag{5-16}$$

$$q_{z+dz} = q_z + \frac{\partial q_z}{\partial z} dz \tag{5-17}$$

Substituting Equations (5-14), (5-15), (5-16), (5-17) into (5-13) and rearranging gives:

$$q_{gen} = q_{conv} + q_{cap} + q_{cond} + q_{rad} - \left(k_f w_f + k_p w_p\right)\left(\frac{\partial^2 T}{\partial x^2} + \frac{\partial^2 T}{\partial z^2}\right) \tag{5-18}$$

The Equation (5-18) describes the pulsating heat flux (consists of time-average and time-dependent components). The time-averaged components can be expressed by Equation (5-19) where the time-average of capacitive term is zero.

$$q_{gen,s} = q_{conv,s} + q_{cond,s} + q_{rad,s} + q_{lc,s} \quad (5\text{-}19)$$

The time-dependent relation is given by Equation (5-20) where the heat generation is assumed uniform in time, and the oscillating components are calculated by subtracting the mean components from the pulsating components.

$$0 = q_{conv,osc} + q_{cap,osc} + q_{cond,osc} + q_{rad,osc} + q_{lc,osc} \quad (5\text{-}20)$$

The convention used dictates heat flow out of an element has a positive sign. Hence, the generated heat in the foil is removed by forced convection of the flow, but heat transfer by lateral conduction, heat storage, conduction in the air gap and radiation must be accounted for [109, 111].

5.5.3.1 Energy Balance Terms:

The electrical resistance (R) of the foil is determined by Equation (5-21) where ρ_f is the electrical resistivity of the foil. As illustrated from Figure 5-7, $a_f = 95\ mm$ is the heated transverse length between the foil contact on inner copper electrodes and the outermost clamping points on the electrodes, L_f is the length of the foil in the axial direction, and w_f is the foil thickness.

$$R = \frac{\rho_f a_f}{L_f w_f} \quad (5\text{-}21)$$

The small thickness of the foil approximates an iso-flux wall boundary condition with one heated long wall and approximates the experimental configuration known in the literature as H2-1L (See Section 2.2.1) as performed by Blythman *et al.* [88, 111]. The uniform electrical heat generation in the foil given by Joule heating in each element is calculated by Equation (5-22), where *I* and *R* are the current through and resistance across the foil and *a* is the minichannel width. The resultant heat flux generation is 5.3 kW/m^2 and is verified with the voltage drop measured across the heated ends of foil in transverse direction.

$$q_{gen} = \frac{I^2 R}{L_f a} \quad (5\text{-}22)$$

Lateral conduction

The fluid transport phenomenon can be expressed in terms of Péclet number which is defines the ratio between the rate of advection to rate of diffusion. For steady flows, $Pe = Pr \times Re_s = 170$, since $Pe > 100$, the axial conduction in the wall and fluid can be neglected, i.e., $\partial^2 T / \partial z^2$ [123]. Experimental thermal data presents that the $\partial^2 T / \partial z^2$ component is less than 7% of the lateral component $\partial^2 T / \partial x^2$ and is neglected. The heat flux by lateral conduction in foil and paint layers, q_{lc}, is obtained from the spatial derivative terms of the energy balance, given by:

$$q_{lc} = \left(k_f w_f + k_p w_p\right)\frac{\partial^2 T}{\partial x^2} \tag{5-23}$$

The second partial derivative is also known as the Laplacian operator (∇^2). The second derivative is calculated using MATLAB's *gradient* function twice. To attenuate the noise developed as a result of differentiation, a median filter *medfilt2* function (typically a nonlinear operation that performs median filtering of an image in two dimensions) is used before each numerical differentiation. The space-averaged amplitude of the oscillating component of the lateral conduction term is 8.1 *W/m²*. The lateral conduction in the paint layer constitutes to only 0.2% of the total. The high magnitudes of lateral conduction effects, observed typically for low flow rate amplitude cases as reported in Table 5-5 for leading asymmetric pulsation waveform. These peaks are observed to occur in the vicinity close to the corners of heated walls which accounts for the heat leakage from the copper busbars. The space-averaged value of lateral conduction in a steady case is -78.3 *W/m²*, representing about 1.5% of the generated heat flux.

Table 5-5: Oscillating component of the lateral conduction heat flux for leading asymmetric case with varying *Wo* and A_0

Wo	0.51			2.51			5.1		
A_0	0.5	1	3	0.5	1	3	0.5	1	3
q_{lc} (cycle max.) [*W/m²*]	80	28	13	63	19	6	89	31	16
q_{lc} (cycle min.) [*W/m²*]	-51	-26	-7	-28	-8	-3	-47	-21	-12

Heat storage

As the flow exhibits an unsteady and periodic motion, the $\partial\, T/\, \partial t$ is non-zero and the heat storage must be accounted for:

$$q_{cap} = -\left(\rho_f c_{p,s} w_f + \rho_p c_{p,p} w_p\right) \cdot \frac{\partial T}{\partial t} \tag{5-24}$$

The space-averaged amplitude of the capacitance term is 40.7 *W/m²,* consisting of about 0.7% of generated heat flux. Heat storage in the paint layers consists of up to 34.2% of the total. Peak capacitance values occur at low flow rate amplitude cases for the given case of leading asymmetric pulsation, as shown in the Table 5-6.

Table 5-6: Oscillating component of the capacitance heat flux for Leading Asymmetric case with varying *Wo* and A_0

Wo	0.51			2.51			5.1		
A_0	0.5	1	3	0.5	1	3	0.5	1	3
q_{cap} (cycle max.) [W/m^2]	35	29	23	37	31	18	36	32	27
q_{cap} (cycle min.) [W/m^2]	-33	-34	-20	-28	-27	-15	-33	-28	-24

Heat losses to air gap

The air gap depth of 12 mm enclosed by the sapphire glass window creates an insulative barrier to heat loss from the underside of the foil. Since no circulation occurs in the air cavity, 1-D heat conduction is established [124]. The temperature varies linearly in the vertical y direction in accordance with the foil temperature distribution in x and z. Fourier's law in y leads to:

$$q_{cond} = -k_a \frac{dT}{dy} \tag{5-25}$$

Where k_a is the thermal conductivity of air and dT/dy is the linear temperature gradient normal to the foil. The air gap temperature is measured in two locations by thermocouples located at 11 mm from the foil and in the 12 mm high air gap. The space-averaged oscillating and steady components of this conductive heat loss are 2.4 W/m^2 and -20.8 W/m^2 respectively, representing 0.3% of the generated heat flux. The negative q_{cond} values indicate a flow of heat from air gap to the foil, caused by heat leakage from the busbars at $T_{busbar} \approx 90$℃. To verify the mode of heat transfer, the local Rayleigh number is estimated, which measures the ratio of conductive and convective heat transfer for natural convection flows:

$$Ra = \frac{g\beta_a(T_w - T_a)L_c^3}{\upsilon_a \alpha_a} = 2049 \tag{5-26}$$

Here $\beta_a, \upsilon_a, \alpha_a,$ are the thermal expansion coefficient, kinematic viscosity, thermal diffusivity of air respectively, and L_c *i*s the characteristic length. T_{ag} is the average air gap temperature and $T_{w,x}$ is the local foil temperature. Considering symmetry at the mid-plane, half of the minichannel width is used as characteristic length and the temperature difference accounts for the busbars and air gap temperatures, the Rayleigh number is calculated as $Ra = 2049$ which indicates the relevance of conduction in the (stagnant) air gap. However, the changes reflected in the mode of heat transfer led by 2-D effects contribute negligibly to the generated heat flux.

Table 5-7: Oscillating component of the conduction heat flux for leading asymmetric case with varying *Wo* and A_0

Wo	0.51			2.51			5.1		
A_0	0.5	1	3	0.5	1	3	0.5	1	3
q_{cond} (cycle max.) [*W/m²*]	1.9	1.5	1.2	1.3	0.8	0.5	0.9	0.7	0.6
q_{cond} (cycle min.) [*W/m²*]	-1.7	-1.5	-1	-1	-0.7	-0.3	-0.7	-0.6	-0.6

Radiation losses

Planck's law states the spectral distribution of radiation intensity emitted from a black body E_b. The radiation emitted from the foil surface in the $3-5\ \mu m$ wavelength range is measured by the thermal camera, although radiation across the entire wavelength spectrum is emitted. The radiation losses at longer wavelengths are estimated by the q_{rad}. Inconel 600 has a low emissivity (about 15%, lower than the paint). The radiation from water side is therefore assumed negligible.

$$q_{rad} = \varepsilon_p \sigma (T_w^4 - T_\infty^4) \tag{5-27}$$

Where ε_p is the emissivity of the paint, σ is the Stefan-Boltzman constant, T_w is the foil and paint temperature and T_∞ is the underside average airgap temperature, assumed to be the cavity's ambient air temperature. The oscillating component of the radiation term presents a spatially averaged amplitude of 3.1 *W/m²*, while the steady component is 65.5 *W/m²* which forms 1.2% of the generated heat flux for the sinusoidal waveform at $Wo = 2.5, A_0 = 1$.

Table 5-8: Oscillating component of the radiation heat flux for leading asymmetric case with varying *Wo* and A_0

Wo	0.51			2.51			5.1		
A_0	0.5	1	3	0.5	1	3	0.5	1	3
q_{rad} (cycle max.) [*W/m²*]	3.7	3.2	2.7	3.5	3	2.8	3.7	3.3	2.9
q_{rad} (cycle min.) [*W/m²*]	-2.6	-2.5	-2.3	-2.9	-2.4	-2.1	-2.5	-3.0	-2.6

Table 5-9: Summary of energy balance components

[W/m²]	***Oscillating component***	***Steady component***
$\boldsymbol{q_{gen}}$	**0**	**5302**
$\boldsymbol{q_{cond}}$	**2.4**	**-20.8**
$\boldsymbol{q_{cap}}$	**40.7**	**0**
$\boldsymbol{q_{lc}}$	**8.1**	**-78.3**
$\boldsymbol{q_{rad}}$	**3.1**	**65.5**

5.6 Experimental Uncertainty

The following section introduces the mathematical formulation used to determine the uncertainty associated with experimental measurements. The goal of measurement is to establish a numerical value for the measurand and is associated with three components. These are the measurand, the measuring instrument, and the environment. An error is inherent within a measurement and is defined as the difference between the measured value and the true value of the measurand. The errors can further be distinguished into two categories: random error and systematic error [125].

5.6.1 Random Error

Randoms errors are errors encountered when there exists a variation in measurement despite a consistent, tightly controlled experimental environment. The perfect repeatability characteristic of a measurement is linked to either the instrument in operation, the measurand, or a combination of two. Random errors can be reduced by performing multiple measurements under the same experimental conditions and averaging the dataset. Thus, it yields a net error close to zero and precision of the results can be established. The best estimate of a true value is generally obtained by calculating the mean ($\bar{x}$) of *n* (sample) values, given by:

$$\bar{x} = \frac{\sum_{i=1}^{n} x_i}{n} \tag{5-28}$$

Where x_i is the *i* th value obtained through the measurement. The standard deviation, (*s*) for a set of multiple measurements is given by:

$$s = \sqrt{\frac{\sum_{i=1}^{n}(x_i - \bar{x})^2}{n-1}} \tag{5-29}$$

The standard uncertainty, $u(\bar{x})$, of the mean considering uncorrelated measurements is given by:

$$u(\bar{x}) = \frac{s}{\sqrt{n}} \tag{5-30}$$

The degree of freedom for uncorrelated measurements is:

$$v = n - 1 \tag{5-31}$$

5.6.2 Systematic Errors

During measurements, there are errors that remain constant when the experiment is repeated under identical environmental conditions, *e.g.*, a constant offset in the measuring instrument. These are systematic errors and are inherently multiplicative and are unlikely to be reduced through multiple measurements or by performing averaging methods. The systematic errors can be identified by two standardised approaches, first by reviewing specific information for the measurement instrument from the calibration report supplied by the manufacturer, and second by changing the experimental setup to measure the quantity by different means or a known quantity by same means. A single measurement can be quantified as:

$$M = x + Z \tag{5-32}$$

Where M is the true value of the quantity, x is the recorded measurement and Z is the best estimate of the correction incorporating the systematic errors. The best estimate of the offset is dependent on calibration error and resolution error. Thus, the standard uncertainty in the offset $u(Z)$ due to resolution error is given as:

$$u(Z) = \frac{e}{\sqrt{3}} \tag{5-33}$$

The proportional uncertainty, $pu(Z)$ is defined as the ratio of resolution error compared to the actual measurement, given by:

$$pu(Z) = \frac{e}{x} \times 100 \tag{5-34}$$

The degree of freedom, v associated with a single measurement is stated as:

$$v = \frac{0.5}{\sqrt{pu(Z)}} \tag{5-35}$$

5.6.3 Categories of Uncertainty

The ISO Guide 98 outlines two specific types of uncertainty analysis: (i) a Type A analysis of uncertainty is based on the application of statistical methods on the obtained measurements, effectively estimating the random error sources, and (ii) a Type B analysis determines specific information about a measurand from a calibration or a data book, to be evaluated using non-statistical methods. The calibration report includes the estimated uncertainty in the value of the

measurand and accessing this information is the primary purpose of a device calibration. Type B uncertainties constitute the systematic error analysis.

5.6.4 Correlation and Covariance

Correlations demonstrate the interdependency associated between the data points x and y. The linear correlation coefficient r_{cor} is expressed as:

$$r_{cor} = \frac{covariance(x,y)}{s(x) \times s(y)} \tag{5-36}$$

Where in the covariance (x,y) is given as:

$$covariance(x,y) = \frac{\sum_{i=1}^{n}(x_i - \overline{x})(y_i - \bar{y})}{n-1} \tag{5-37}$$

Generally, the uncorrelated dataset indicates $r_{cor} = 0$ and yet be mutually dependent and perfectly correlated dataset presents $r_{cor} = 1$. The autocorrelation technique is typically considered for time varying data points and cross correlation is used to capture data points simultaneously. For thermal data processing, autocorrelation was applied to determine the time dependency of uncertainty associated with the storage term (q_{cap}) of the heat balance equation. Additionally, cross correlation was used for determining the uncertainty linked to the lateral conduction term (q_{lc}) of the energy balance equation.

5.6.5 Expanded Combined Uncertainty

The combined standard uncertainty, $u(y)$, whether Type A or Type B, can be written in the form of 'root sum squares' of the experimental measurements and its individual standard uncertainty is given by:

$$\begin{aligned} u(y) = \Bigg(\left(\frac{\partial y}{\partial x_1}\right)^2 u^2(x_1) + \left(\frac{\partial y}{\partial x_2}\right)^2 u^2(x_2) + \cdots + \left(\frac{\partial y}{\partial x_n}\right)^2 u^2(x_n) \\ + 2r_{cor}(x_1,x_2)\frac{\partial y}{\partial x_1}\frac{\partial y}{\partial x_2}u(x_1)(x_2) + 2r_{cor}(x_1,x_3)\frac{\partial y}{\partial x_1}\frac{\partial y}{\partial x_3}u(x_1)(x_3) \\ + \cdots 2r_{cor}(x_i,x_j)\frac{\partial y}{\partial x_i}\frac{\partial y}{\partial x_j}u(x_i)(x_j) + \cdots \Bigg)^{\frac{1}{2}} \end{aligned} \tag{5-38}$$

Here *y* is the measurand formed by individual input measurements and attached standard uncertainty. The partial derivatives, $\left(\frac{\partial y}{\partial x_i}\right)$, also called as sensitivity coefficients, are incorporated to signify the propagation of uncertainties of each individual measurement with the combined

measurement and its uncertainty. The effective degrees of freedom (v_{eff}) accounts for the standard combined measurand and is given by:

$$v_{eff} = \frac{u^4(y)}{\sum_{i=1}^{n} \frac{\left(\frac{\partial y}{\partial x_i}\right)^4 u^4(x_i)}{v_i}} \tag{5-39}$$

A coverage factor, *k*, is defined as the interval within a probability distribution function where a true value of measurand lies. It is determined based on the experimental uncertainty of 95% as a function of the number of degrees of freedom:

$$U(y) = ku(y) \tag{5-40}$$

The expanded uncertainty, $U(y)$ estimates the result for an experimental measurement exists within a 95% level of confidence. The resulting measurement value and its associated expanded uncertainty can be expressed as:

$$y \pm U(y) \tag{5-41}$$

5.6.6 Uncertainty Interpretations

5.6.6.1 Uncertainty in velocity

The functional dependencies of hydrodynamic parameters can be expressed in the form of:

$$u_s = f(Q, \omega, \nabla P, a, b, \rho_l, \nu) \tag{5-42}$$

The volumetric flow rate (Q) and axial pressure gradient ∇P are measured from instruments and the variation in ρ_l and ν can be assumed negligible. The propagation of individual uncertainties (x_i) is expressed in a combined format to estimate the relative uncertainty in u_s. The expanded uncertainty is determined using the Taylor Series Method (TSM) [125] for the experimental parameter space:

$$u_s = \pm\left[\left(\frac{\partial u_s}{\partial Q}\right)^2 u_Q^2 + \left(\frac{\partial u_s}{\partial \omega}\right)^2 u_\omega^2 + \left(\frac{\partial u_s}{\partial \nabla P}\right)^2 u_{\nabla P}^2 + \left(\frac{\partial u_s}{\partial a}\right)^2 u_a^2 + \left(\frac{\partial u_s}{\partial b}\right)^2 u_b^2 + \left(\frac{\partial u_s}{\partial \rho_l}\right)^2 u_{\rho_l}^2 + \left(\frac{\partial u_s}{\partial \nu}\right)^2 u_\nu^2\right]^{1/2} \tag{5-43}$$

The derivatives are computed using finite-difference schemes, as shown by:

$$\frac{\partial u_s}{\partial Q} \approx \frac{\Delta u_s}{\Delta Q} \approx \frac{u_{Q+\Delta Q} - u_Q}{\Delta Q} \tag{5-44}$$

The expanded uncertainties of individual measurement and percentage uncertainty is given in Table 5-10. All listed values are accounted to a 95% confidence interval and is determined using student's t-distribution for N-2 degrees of freedom using default MATLAB function *tinv*. For controlling the pulsations, the stepper motor offers high precision motion at $1.8°$ step angle. The ultrasonic flowmeter and the differential pressure sensor are calibrated for steady flows, offering an accuracy of $\pm 1\%$. The uncertainty in the channel height is slightly higher which accounts for the gaskets.

$$\frac{U_{Re}}{Re} = \pm \sqrt{\left(\frac{U_Q}{Q}\right)^2 + \left(-\frac{U_{D_h}}{D_h}\right)^2} \tag{5-45}$$

The expanded uncertainty in Re incorporates the relative uncertainties in the volumetric flow rate and minichannel hydraulic diameter. The relative uncertainties in the fluid parameters (density and viscosity) is $\pm 1\%$.

5.6.6.2 Uncertainty in temperature

The functional dependence of thermal parameters can be expressed in the form of:

$$T_s = f(Q, \omega, a, b, q, Pr, k_s) \tag{5-46}$$

Where Pr and k_s are the associated fluid Prandtl number and thermal conductivity of foil respectively. The expanded uncertainty in the curve fit of counts and temperature is approximately constant over the temperature range $20 - 55$ ℃ with $U_T = \pm 0.08\, K$. The uncertainty in the thermal parameters is noted to be generally higher. The expanded uncertainty in the generated heat flux given by Equation (5-47) is 6.1% due to the accumulation of individual uncertainties.

$$\frac{U_{g_{gen}}}{q_{gen}} = \pm \sqrt{\left(\frac{U_I}{I}\right)^2 + \left(\frac{U_R}{R}\right)^2 + \left(-\frac{U_{L_s}}{L_s}\right)^2 + \left(-\frac{U_{a_s}}{a_s}\right)^2} \tag{5-47}$$

The expanded uncertainty associated with the time average Nusselt Number $(\overline{Nu})$ is given by the expression Equation (5-48) and is calculated as 9.1%.

$$\frac{U_{\overline{Nu}}}{\overline{Nu}} = \pm \sqrt{\left(\frac{U_{q_{gen}}}{q_{gen}}\right)^2 + \left(\frac{U_{D_h}}{D_h}\right)^2 + \left(-\frac{U_{T_w - T_b}}{T_w - T_b}\right)^2} \tag{5-48}$$

Where,

$$\frac{U_{T_w-T_b}}{T_w-T_b} = \pm\sqrt{\left(\frac{U_{T_w}}{(T_w-T_b)}\right)^2+\left(\frac{U_{T_b}}{(T_w-T_b)}\right)^2} \tag{5-49}$$

5.6.6.3 Uncertainty in heat flux

The expanded uncertainty in the convective heat flux is given by Equation (5-50). The propagation of individual uncertainties in the heat flux components from the heat balance equation is incorporated using a similar form of TSM as shown in Equation (5-43) on a pixel-pixel basis [115, 122].

$$\frac{U_{q_{conv}}}{q_{conv}} = \sqrt{\left(\frac{U_{q_{gen}}}{q_{gen}}\right)^2+\left(\frac{U_{q_{lc}}}{q_{lc}}\right)^2+\left(\frac{U_{q_{cond}}}{q_{cond}}\right)^2+\left(\frac{U_{q_{rad}}}{q_{rad}}\right)^2} \tag{5-50}$$

Since the lateral conduction term involves double differentiation, a central difference scheme is used in MATLAB by implementing the *gradient* function twice, indicated with a shortened version in Equation (5-51). Although the errors are accumulated subsequently with the determination of lateral conduction term, cross-correlation techniques are employed as explained in Section 5.5.3. A median filter *medfilt2* is applied before each numerical differentiation [109, 111], substantially reduces the noise amplifications from the second derivatives.

$$q_{lc,f,i} \approx -\left(k_f w_f\right)\cdot\left(\frac{T_{i+2}-2T_i+T_{i-2}}{4\Delta_y^2}\right) \tag{5-51}$$

The expanded uncertainties in the heat flux components of the energy balance are expressed in the Table 5-10.

Table 5-10: Summary of experimental uncertainties.

Parameter		Expanded Uncertainty	Unit		Percentage Uncertainty [%]
a	$\pm$	0.006	*mm*	$\pm$	0.03
b	$\pm$	0.08	*mm*	$\pm$	5
L	$\pm$	0.005	*mm*	$\pm$	0.001
D_h	$\pm$	0.06	*mm*	$\pm$	2.3
Q	$\pm$	0.046	*L/min*	$\pm$	1.4
∇P	$\pm$	0.02	*Pa/m*	$\pm$	2.1
Re	$\pm$	0.03	-	$\pm$	0.1
T_s	$\pm$	0.54	*K*	$\pm$	0.1
T_∞	$\pm$	0.56	*K*	$\pm$	0.2
$T_{in,out}$	$\pm$	0.52	*K*	$\pm$	0.2
T_{airgap}	$\pm$	0.57	*K*	$\pm$	0.1
q_{gen}	$\pm$	84.63	W/m^2	$\pm$	1.6
q_{lc}	$\pm$	38.22	W/m^2	$\pm$	48.8
q_{cap}	$\pm$	2.14	W/m^2	$\pm$	5.2
q_{cond}	$\pm$	0.47	W/m^2	$\pm$	2.2
q_{rad}	$\pm$	0.38	W/m^2	$\pm$	0.5
q_{conv}	$\pm$	92.86	W/m^2	$\pm$	3.7

6) Computational Methods

A numerical model was developed to approximate the experimental conditions with the aim of simultaneously corroborating the experimental results and validating the numerical approach. A conjugate heat transfer model is required to properly represent the fluid flow and the heated foil section. The commercial software package ANSYS CFX is favoured to perform the computational analysis. CFX provides flexibility in setting up customizable and user defined solver parameters, offering powerful pre- and post-processing capabilities. It eliminates the need for an external compiler for defining customised mathematical expressions since an inbuilt programming language called CCL (CFX Command Language) is directly made applicable. Multi body, three-dimensional geometries are easily adaptable and configurable in CFX, providing versatility in modelling and simulating Conjugate Heat Transfer (CHT) problems.

6.1 Computational domain

Domains are regions of space in which the governing equations of fluid mechanics and/or heat transfer are solved. A domain can further be classified by assigning the boundaries with specific fluid and/or thermal properties. Domains can be generated from a list of assemblies and/or three-dimensional primitive regions that are associated with a volume of an imported mesh. Internal three-dimensional regions can be assigned to create sub-domains which permit the creation of volumetric sources of mass, momentum, and energy. For this study, the domain is of dimensions $360\ mm \times 10\ mm \times 1.40125\ mm$ (length x width x height) is illustrated in Figure 6-1. The height here is inclusive of a solid domain (*i.e.*, the foil) and a fluid domain (the minichannel internal height), as shown in Figure 6-2. A symmetry condition, to be discussed further in Section 6.5.5, is applied to reduce the computational effort and retain a sufficient mesh resolution.

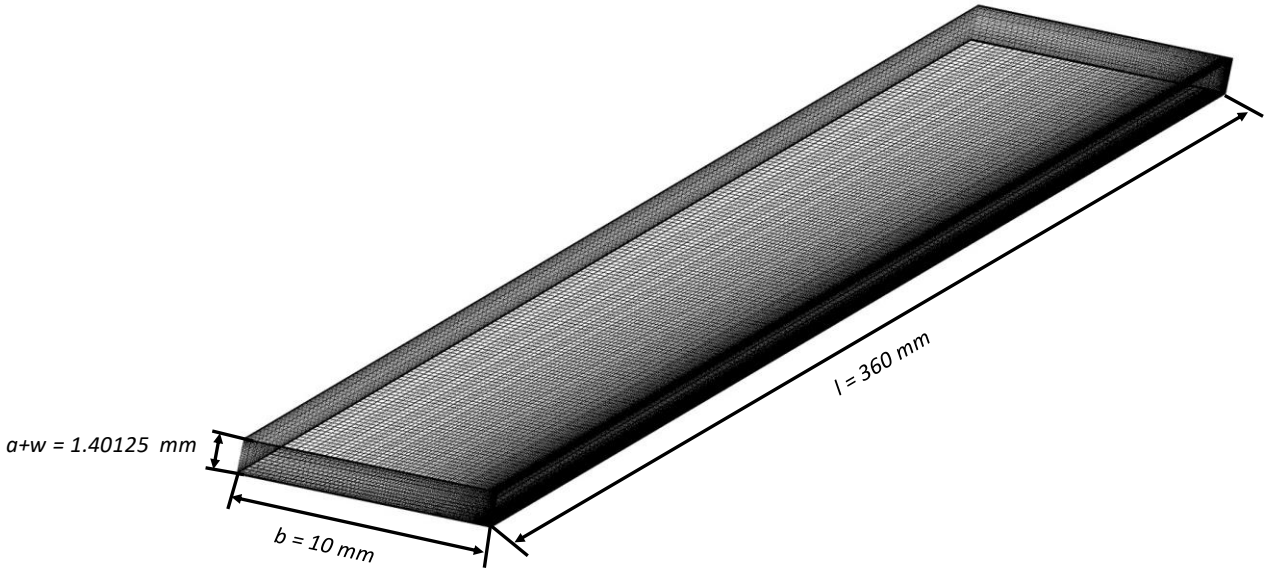

Figure 6-1: Full-scale numerical model with outer dimensions.

The solid domain is specified as a conducting solid. To replicate heating of the Inconel foil used in the experiment, a volumetric heat source is defined by creating a subdomain. A subdomain is a three-dimensional region within a predefined domain that can be used to specify values for volumetric sources. A volumetric heat generation of $3 \times 10^8\, W/m^3$ is applied for all simulations. The fluid domain is specified with various physical models applicable for an Eulerian fluid flow. The Eulerian representation defines a control volume within which the fluid flow properties are expressed as fields. Each property such as velocity, temperature, and pressure is described as a function of time and space.

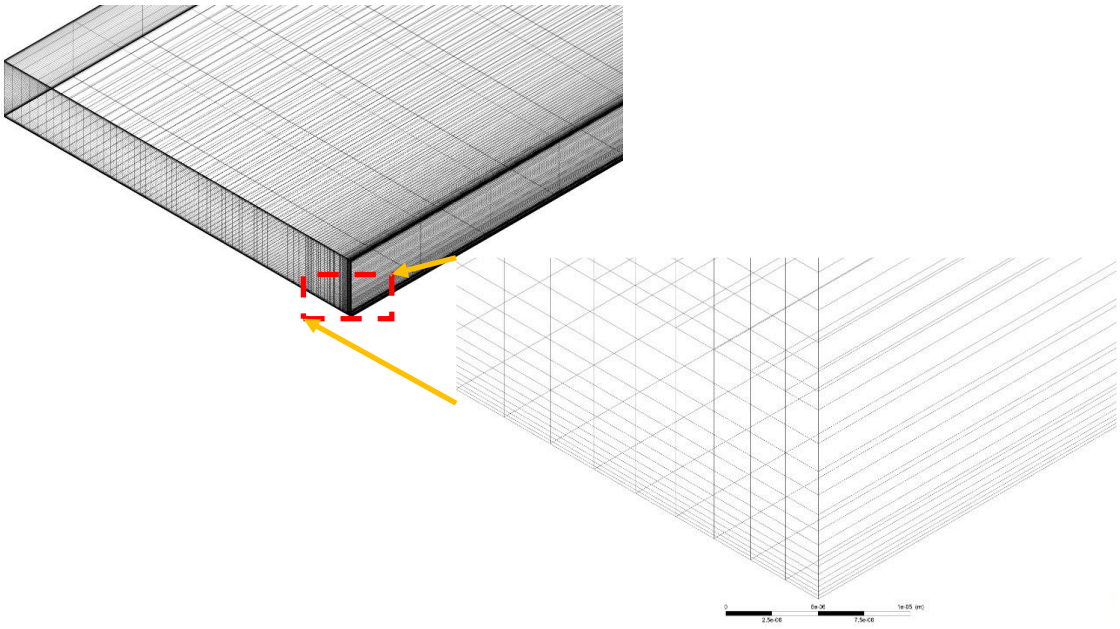

Figure 6-2: A two-stage zoomed three-dimensional isometric view of the three-dimensional mesh inclusive of the solid and fluid domains.

6.2 Working fluid and solid material properties

The fluid domain is defined with water as the working fluid. The thermo-physical properties of both the fluid and solid are provided in Table 6-1 and these properties are considered as being invariable with temperature.

Table 6-1: Thermo-physical properties of fluid and solid applicable to computational modelling [22, 119].

Material	Properties			
	Density	Specific heat	Thermal conductivity	Dynamic viscosity
	(kg/m^3)	$(J/kg \cdot K)$	$(W/m \cdot K)$	$(Pa \cdot s)$
Solid (Inconel)	8420	444	14.80	n/a
Fluid (Water)	997	4184	0.598	0.001

6.3 Viscous model

A laminar viscous model is adopted for the steady and transient computations. The governing equations are solved using a finite volume technique. No viscous dissipation (heating) effects are included.

6.4 Grid/mesh generation

The computational domains are discretised by the generation of a grid, also known as meshing. A mesh or grid consists of volumes, cells, or elements that represent the physical shape. In three-dimensions, this process results in a large number of control volumes that together should represent as closely as possible the shape of the geometry under investigation. The location of each cell centre and its vertices or nodes is known for the chosen coordinate system, and each cell is bounded by neighbouring cells or the boundaries of the domain.

Grids are typically classified as structured, unstructured, or hybrid, as shown in Figure 6-3. For this study, the straight rectangular minichannel allows for the use of a highly structured grid comprising 3-D hexahedral elements (see Figure 6-4). Structured grids are sometimes favoured for the ease of their design, controllability of the various grid parameters, and they can require less computer memory. Mesh density is considered to be a crucial parameter which controls the solution accuracy. While using a high quality and fine resolution meshes, although the computational effort and solution time are extended, the consistency of numerical solution and accuracy is successively achieved. Furthermore, structured grids allow for a detailed, methodical investigation of spatial convergence (see Section6.8). For straight duct flows, proper alignment of structured cells in the flow direction typically results in accurate representation of characteristics of fully developed flow whilst using fewer cells.

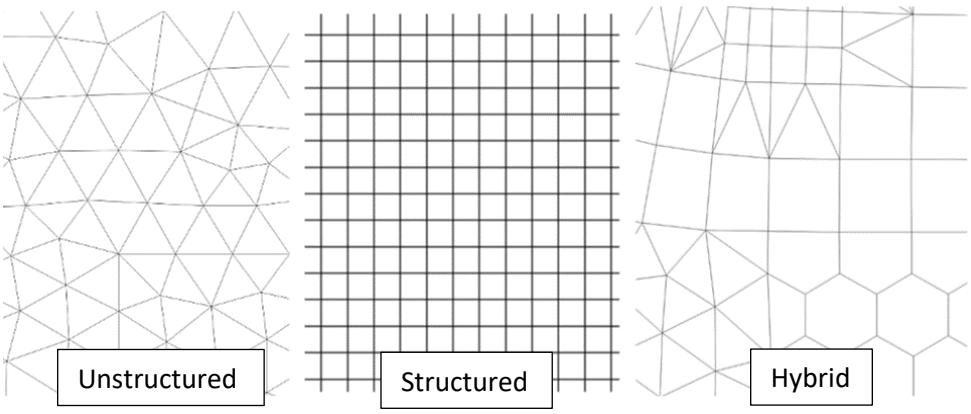

Figure 6-3: Types of meshes: Unstructured, Structured and Hybrid [126].

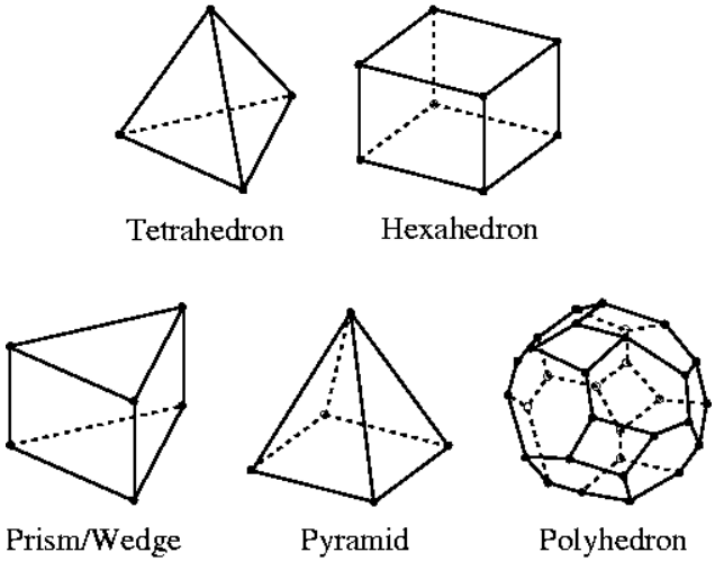

Figure 6-4: Types of three-dimensional mesh elements [126].

In this study, a finely resolved structured grid, shown in Figure 6-5 for both fluid and solid domains, is used which includes inflation layers at the minichannel boundaries to capture the steep velocity and temperature gradients near the walls. Several mesh metrics such as aspect ratio, skewness, and orthogonal quality are analysed to determine overall mesh quality. The aspect ratio (b/a) of a mesh element is defined as the ratio of the shortest length to the longest length of the element. $b/a = 1$ refers to a symmetric hexahedral element as shown in Figure 6-6 (a), which for this study represents $\sim 70\%$ of the total cells. Skewness determines the relation between angular measure of element quality and the angles of an ideal element type. The acceptable range for the skewness metric is within (best) $0 - 0.5$ (worst). From Figure 6-6 (b) the cell skewness is 0.05 for $\sim 99\%$ of the total cells and the remaining elements exhibit a skewness value of up to 0.2. Mesh orthogonal quality refers to the relation between adjacent element face angles and optimal cell angle. Orthogonal quality range is (worst) $0 - 1$ (best). Figure 6-6 (c) shows 99% of mesh orthogonal quality is equal to 1. A minimum element size of 1.99×10^{-3} *mm* is chosen, resulting in a total number of cells ≈ 1.71 million. A near perfect area-averaged orthogonal quality of 0.999 is obtained, with an average skewness ratio of 2.81×10^{-3}.

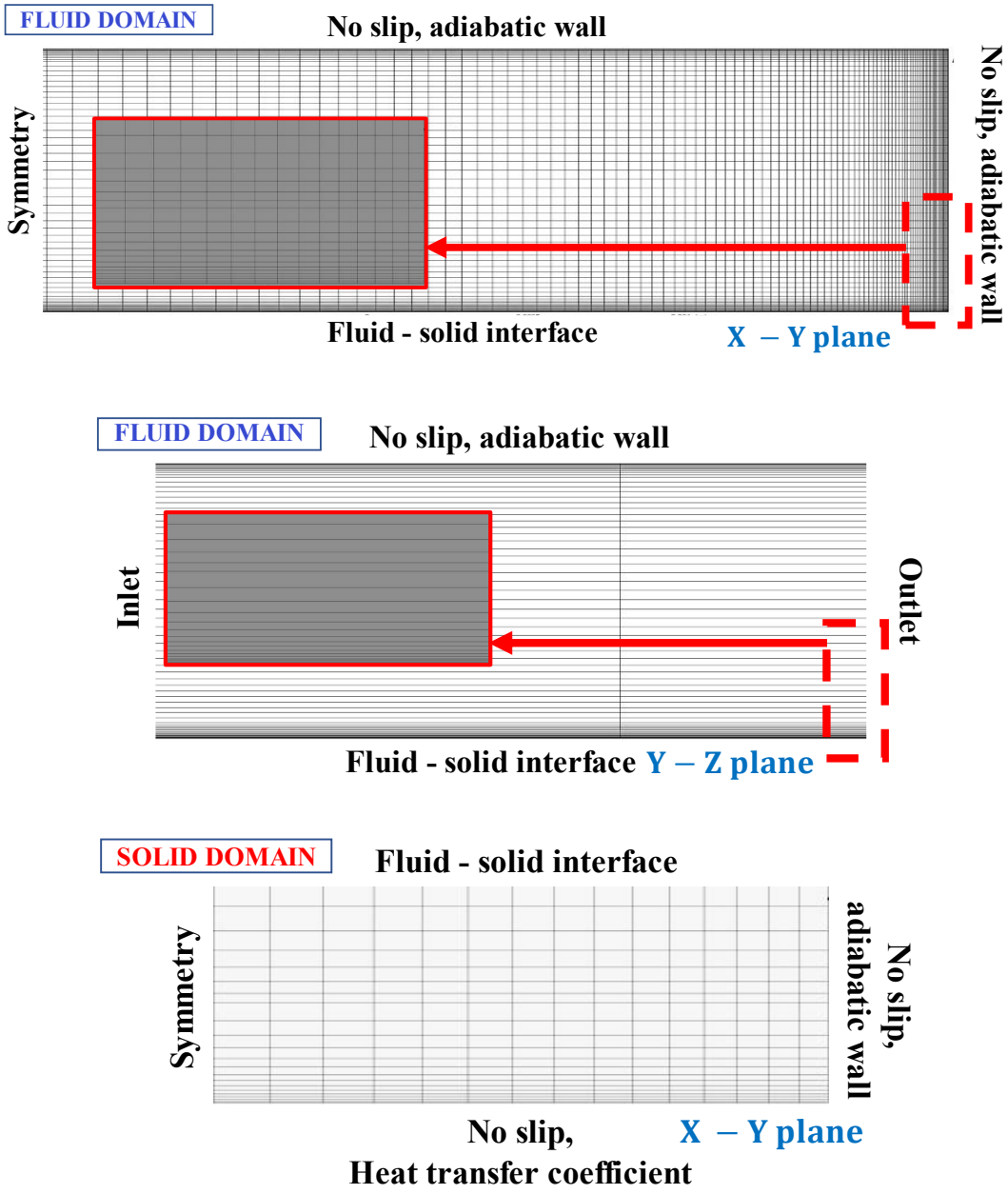

Figure 6-5: Cross-sectional view of structured grid of fluid and solid domains.

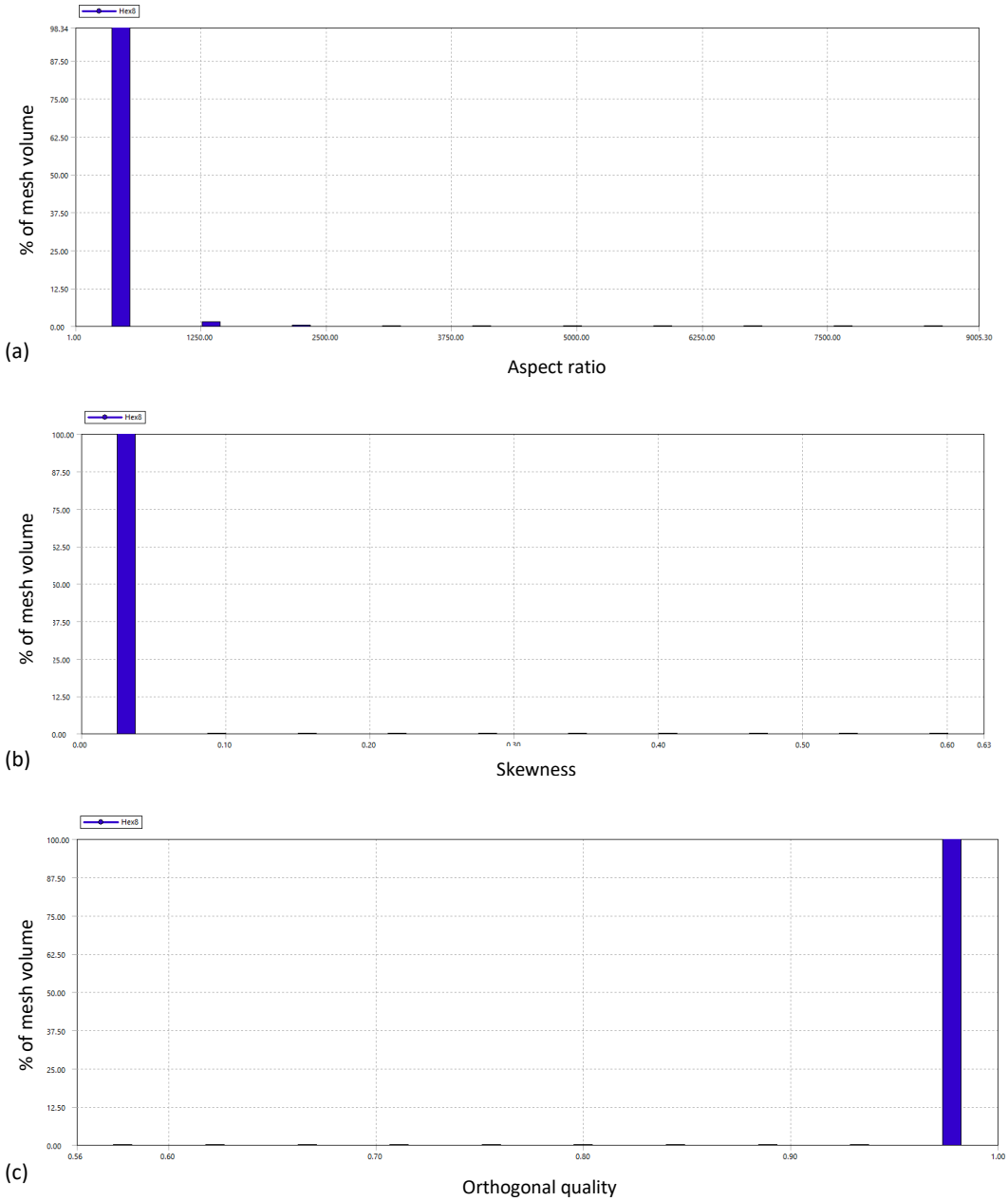

Figure 6-6: Mesh quality information with parameters such as: (a) Aspect ratio, (b) skewness and (c) orthogonal quality.

6.5 Boundary Conditions

CFX simplifies the complexity of conjugate heat transfer, wherein the many numbers of walls involved is managed with independent domain controls. Each domain creates an interface layer to ensure the connectivity between the two and the correct implementation of heat transfer. The domain interface allows for an exchange of thermal energy with the fluid domain. All boundary conditions are specified in Table 6-2 and Figure 6-7 illustrates a general overview of the imposed boundary conditions.

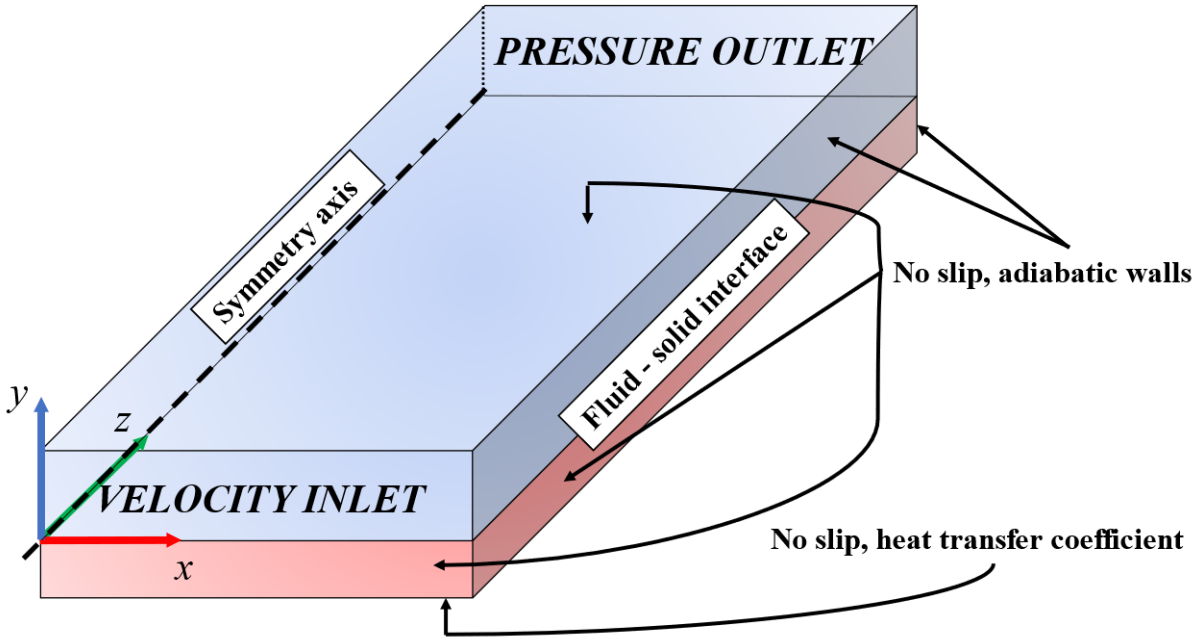

Figure 6-7: Three-dimensional computational domain and boundary conditions. Blue and red regions are fluid and solid domains respectively.

6.5.1 Inlet

For steady flow simulations, constant and uniform velocity (U_s) in the range $0.012 \leq U_s \leq 0.67$ m/s corresponding to $24 \leq Re_s \leq 100$ and constant and uniform temperature ($T_{in} = 295$ K) are specified at the minichannel inlet. An exception is where Re_s extends to 2205 for model validation study, see Section 6.9. For pulsating flow, the same temperature condition is used, but the inlet velocity is defined with a User Defined Function (UDF) and is initialised in the fluid domain using Cartesian velocity components.

For symmetric sinusoidal pulsations, the following equation specifies the inlet velocity:

$$U_z = U_s + U^*_{max} sin(2\pi f t) \tag{6-1}$$

For asymmetric sinusoidal pulsating flow:

$$U_z = U_s + \left(\frac{U^*_{max}}{j}\right) * tan^{-1} \frac{j * sin(2 * \pi * f * t)}{1 \pm j * cos(2 * \pi * f * t)} \tag{6-2}$$

For half rectified sinusoidal pulsating flow:

$$U_z = U_s \pm U^*_{max} \left(((sin(2 * f * t)) - |(sin(2 * f * t))|\right) \tag{6-3}$$

In the above set of Equations (6-1), (6-2), and (6-3), U_z is the inlet velocity along the axial (z) direction and f is the pulsating frequency. The flow rate amplitude expressed by the parameter $Q_{osc,max}/Q_s$ is equal to $U_{osc,max}/U_s$, as the cross-sectional area of the minichannel is constant.

The asymmetric parameter *j* refers to the deviation of the waveform profile from the sinusoidal pulsation format. To generate extremities of asymmetric, *j* is set at 0.9 as shown in the Figure 6-8.

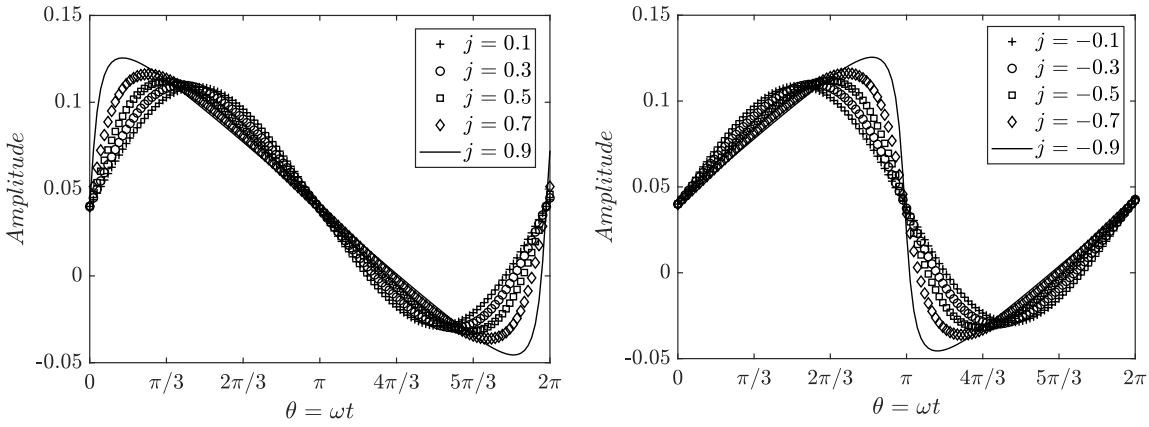

Figure 6-8: Leading (left) and lagging (right) asymmetric variants.

6.5.2 Outlet

According to the Neumann boundary conditions, a static pressure outlet corresponding to the gauge pressure is specified (i.e., an operating pressure of 101325 Pa) and a zero gradient of velocity boundary condition is imposed at exit of the minichannel.

$$P_{static} = P_{gauge}, \frac{dU}{dz} = 0 \tag{6-4}$$

6.5.3 Top and side walls

The no-slip condition is applied to the top and side walls of the fluid domain. These walls are approximated as adiabatic. The bottom and side walls of the solid domain are maintained as adiabatic as shown in Figure 6-7.

$$U_{wall} = V_{wall} = 0 \tag{6-5}$$

$$q_{wall} = -k\frac{dT}{dy} = 0 \tag{6-6}$$

6.5.4 Bottom wall

The bottom wall of the solid domain is maintained with the no-slip condition. A heat transfer coefficient is defined on this surface which accounts for the approximated experimental heat loss from the underside of the heated foil, calculated from the energy balance in Section 5.5.3.

$$h_{wall} = \frac{q_{wall}}{\left(T_{wall} - T_{airgap}\right)} \tag{6-7}$$

6.5.5 Symmetry plane

A symmetry condition is imposed on one face of the minichannel and foil geometries to reduce the computational requirements. This assumes that the flow and heat transfer are symmetric about the minichannel mid-plane of the transverse direction (x). More specifically a symmetry boundary assumes zero flux of all quantities across it. Since there is no transfer of convective flux across the symmetry plane, the normal velocity component is zero. Similarly, there is no diffusion flux transfer across the plane, thus the normal gradients of all flow variables are zero.

6.5.6 Fluid-solid Interface

A domain interface is a powerful resource which can be adopted in several specific requirements such as:

- Domains with different physical types can be connected. For example, energy may flow through a fluid-solid interface.
- A domain may contain multiple mesh blocks. Non-matching interfaces can be linked together using a domain interface.
- Domain interfaces reduce mesh generation effort, wherein a single mesh for the entire domain space can be simplified by generating a series of meshes which can be connected.
- Domains are required to connect multiple unmatched meshes within a domain (for example, when there is a hexahedral mesh volume and a tetrahedral mesh volume within a single domain) and to connect separate domains.

For this study, a fluid-solid interface type is the preferred interface. A general-connection interface model is used to connect the mesh regions together. The preferred model adapts to the connection between non-matching grids and in cases of change of frame of reference across the interfaces. The mesh connection across the domain interface is controlled by the General Grid Interface (GGI) connection. This is the preferred method for applicable cases of a direct correspondence in the nodes on either side of the interface. The GGI technique permits non-matching of node locations, element type, surface shape, and the flow physics across the connection are adaptable. For simulations involving conjugate heat transfer the GGI connection is widely preferred since the discretization of heat flow through a solid-fluid domain is treated symmetrically.

Table 6-2: Listings of boundary conditions used for computational model

Domains	***Boundary***	***Conditions Imposed***
Fluid Domain (WATER)	Top wall	Adiabatic, no slip
	Inlet	Velocity, Temperature
	Outlet	Pressure outlet
	Side long wall (external)	Adiabatic, no slip
	Side long wall (internal)	Symmetry
	Interface – Contacts	No slip, Conservative Interface flux for heat transfer
Solid Domain (FOIL)	Bottom Wall	Heat transfer coefficient
	Side short walls	Adiabatic
	Side long wall (external)	Adiabatic
	Side long wall (internal	Symmetry

6.6 Governing equations & assumptions

Simulations are performed by discretizing and linearising the mass, momentum, and energy conservation equations using ANSYS CFX 2020 R2 which is based on the finite volume method. CFX follows a vertex-centred approach, thus the solution variables are stored in the mesh vertices (nodes). The model includes the following assumptions:

i. The working fluid (water) is incompressible.
ii. The flow is laminar with no viscous dissipation (heating) effects.
iii. Uniform conditions exist at the inlet and a zero gradient boundary condition is applied at the outlet.
iv. The influence of body forces (*i.e.*, gravity) is negligible.
v. The thermo-physical properties of both the fluid and solid are invariable with temperature.
vi. Radiation heat losses are negligible.
vii. The flow and heat transfer are symmetric about the minichannel mid-plane of the transverse direction (x).

The governing equations of mass, momentum, and energy for a laminar, incompressible flow of a Newtonian fluid are given as follows:

$$\frac{\partial u}{\partial x}+\frac{\partial v}{\partial y}+\frac{\partial w}{\partial z}\ =\ 0 \tag{6-8}$$

$$\frac{\partial u}{\partial t}+\left(u\frac{\partial u}{\partial x}\right)+\left(v\frac{\partial u}{\partial y}\right)+\left(w\frac{\partial u}{\partial z}\right)=-\frac{1}{\rho}\frac{\partial P}{\partial x}+\nu\left(\frac{\partial^2 u}{\partial x^2}+\frac{\partial^2 u}{\partial y^2}+\frac{\partial^2 u}{\partial z^2}\right)+g_x \tag{6-9}$$

$$\frac{\partial v}{\partial t}+\left(u\frac{\partial v}{\partial x}\right)+\left(v\frac{\partial v}{\partial y}\right)+\left(w\frac{\partial v}{\partial z}\right)=-\frac{1}{\rho}\frac{\partial P}{\partial y}+\nu\left(\frac{\partial^2 v}{\partial x^2}+\frac{\partial^2 v}{\partial y^2}+\frac{\partial^2 v}{\partial z^2}\right)+g_y \tag{6-10}$$

$$\frac{\partial w}{\partial t}+\left(u\frac{\partial w}{\partial x}\right)+\left(v\frac{\partial w}{\partial y}\right)+\left(w\frac{\partial w}{\partial z}\right)=-\frac{1}{\rho}\frac{\partial P}{\partial z}+\nu\left(\frac{\partial^2 w}{\partial x^2}+\frac{\partial^2 w}{\partial y^2}+\frac{\partial^2 w}{\partial z^2}\right)+g_z \tag{6-11}$$

$$\rho c_p\left(\frac{\partial T}{\partial t}+\left(u\ \frac{\partial T}{\partial x}+v\ \frac{\partial T}{\partial y}+w\ \frac{\partial T}{\partial z}\right)\right)=\dot{q}_{gen}+k\left(\frac{\partial^2 T}{\partial x^2}+\frac{\partial^2 T}{\partial y^2}+\frac{\partial^2 T}{\partial z^2}\right)+S \tag{6-12}$$

Where *u*, *T* represent the velocity and temperature fields, and ρ, ν, *k*, c_p are the density, kinematic viscosity, thermal conductivity, and specific heat of the fluid, respectively. *g* represents gravitational acceleration and *P* represents the fluid pressure. *x, y, z* are the three dimensional coordinates and its corresponding velocity components are *u, v, w* respectively. *S* represents the volumetric heat generation. Equation (6-12) is easily manipulated for application to the solid phase.

Regarding assumption (ii), the Womersley number range is $0.5 \leq Wo \leq 18.33$ and the steady and maximum pulsating Reynolds numbers are $24 \leq Re_s = (U_m D_h)/\nu \leq 100$ and $Re_{p,max} = U_{z,max} D_h/\upsilon$ = 250 respectively, thus a laminar flow approximation. A thermal energy model is used which enables the transport of enthalpy through the fluid and is suitable for modeling heat transfer in low-speed flows.

Although assumption (iii) is not physically realistic, a sufficiently long channel is modelled to allow for the hydrodynamic ($\sim 39\ mm$) and thermal ($\sim 203\ mm$) entrance lengths which are calculated using Equations (5.3) and (5.4) according to Refs. [18, 115] and verified by assessing the relevant profiles resulting from the simulations. Regarding assumption (iv), gravity acts perpendicular to the flow and the maximum Archimedes number $Ar = Gr/Re_s^2$ is $0.3 \ll 1$, thus natural convection heat transfer will be dominated by forced convection. Simulations were performed with gravitational forces and buoyancy included via the Boussinesq approximation [127] but no significant change in results was determined. The temperature range in this investigation is 295 *K* to 313 *K*, such that assumptions (v) and (vi) are deemed reasonable. Regarding assumption (vii), several previous studies of low Reynolds number pulsating flows have predicted or shown symmetry in the velocity, pressure, and temperature distributions, such as studies by [35, 45, 117] and [71, 88]. The

application of the symmetry condition significantly reduces computational effort and enables the necessary mesh refinement and was hence deemed appropriate for the current study.

6.7 Solution Methods

CFX is primarily a pressure-based coupled solver which employs an algorithm where the governing equations are solved simultaneously and in a coupled manner [118, 119]. Since the governing equations are non-linear and coupled, the solution is looped iteratively such that the convergence rate of the numerical solution is greatly enhanced compared to sequential solvers. Pressure-based solves are widely adopted for incompressible flows with Mach number $M \ll 1$, *i.e.*, subsonic. Coupled solvers such as CFX incorporate all three momentum equations (see Section 6.6) and the pressure correlation equation obtained from Rhie Chow interpolation (see Section 6.7.3.3) in a common matrix and are solved simultaneously. The pressure-velocity coupling is inherent in the solution procedure such that the co-located (non-staggered) grid mechanism adopted by CFX is preferential as the control volumes are identical for all transport equations. For comparison, uncoupled or segregated solvers such as those used in ANSYS FLUENT compute the three momentum equations sequentially. Subsequently, using the calculated velocity field, the pressure-correction equation is computed by employing algorithms such as SIMPLE, SIMPLEC and PISO for continuity until convergence is reached. However, coupled solvers utilize higher computational time per iteration and are memory intensive. The data matrixes are larger, and convergence is reached faster as non-linear terms are solved exclusively. Whereas, for segregated solvers the objective of convergence is dependent on both the non-linear terms and pressure-velocity coupling.

Steady flows are carried out at a set value of 2000 maximum iterations with additional control on the fluid time scales which govern the internally calculated physical time scale on the boundary conditions, flow condition, domain physics and geometry parameters. To achieve faster and a robust convergence by managing the solver determined physical time scale, length scale option is set to aggressive. The residuals are a measure of local imbalances of each control volume conservation equation. Residuals plays a key factor in accessing convergence. A residual convergence target of 1×10^{-6} is used which signifies a tight convergence. CFX defaults to using normalized residuals and when the residual target is met the solver concludes its run.

A residual convergence target of 1×10^{-5} is used for transient simulations (see reasoning in Section 6.8.2). The unsteady simulations are considered periodic when the RMS deviations of the time-averaged velocity and temperature values between two successive cycles do not exceed

0.1%. This occurs after about 10 full cycles of flow pulsation subject to the associated pulsation flowrate format, frequency, and flow rate amplitude.

6.7.1 Time step selection

Transient pulsating flows are simulated with adaptive time stepping, wherein the adaption is in accordance with the limits set based on the number of iterations. The adaptive time stepping is based on an automatic determination of time step size operating between the extents of 2×10^{-10} (as minimum timestep) and 2×10^{10} (as maximum timestep) that involves an estimation of global and local truncation error associated with the time integration scheme. Thus, if the truncation error is smaller than the specified tolerance, the time step size is increased, and vice versa. Subsequently, the upper and lower limits for the number of iterations associated with a time step are set. The resulting time step size varies between 10^{-3} and 10^{-4} and is dependent on the simulation case.

For unsteady, time-dependent simulations, the maximum allowable time step is based on two important factors, *i.e.*, solver stability and solution accuracy which can be dynamically controlled by the time step size. The accuracy of the solution is highly dependent on the right estimation of time step size which is obtained by employing adaptive time stepping.

6.7.2 CFL number

The Courant Friedrichs–Lewy number, also known more simply as the Courant number or CFL number, is of fundamental importance for transient flows. For a one-dimensional mesh cell, it is defined by Equation (6-13) where u is flow velocity, Δt is the timestep, and Δx is indicative of the mesh cell size.

$$CFL = \frac{u\Delta t}{\Delta x} \tag{6-13}$$

The Courant number calculation in ANSYS CFX is a multidimensional generalization of this expression where the velocity and length scales are based on the mass flow into the control volume and the dimension of the control volume. Since the CFX solver is based on an implicit formulation (explained in Section 6.7), ANSYS CFX does not unequivocally require the Courant number to be small for stability, unlike other explicit solvers. Additionally, the role of adaptive time-stepping in transient simulations ensures $CFL_{max} < 1$, effectively meaning that the fluid particles through each timestep of the unsteady simulation are not propagating through more than one mesh cell, leading to solution stability and robustness in achieving convergence.

6.7.3 Discretisation and interpolation schemes

ANSYS CFX uses an element-based finite volume method, which first involves discretizing the spatial domain applicable on a mesh. The mesh forms a fundamental constituent to construct finite volumes (described in Figure 6-9), which are designated to conserve the relevant quantities such as mass, momentum, and energy. The non-linearity of governing equations is to be solved using iterative techniques. Iterations are typically used to advance a solution through a sequence of steps from an initial state to a final, converged state. For a steady state case, the implicit scheme predominantly adopted by CFX is favourable since implicit solvers are notably stable in accelerating the convergence.

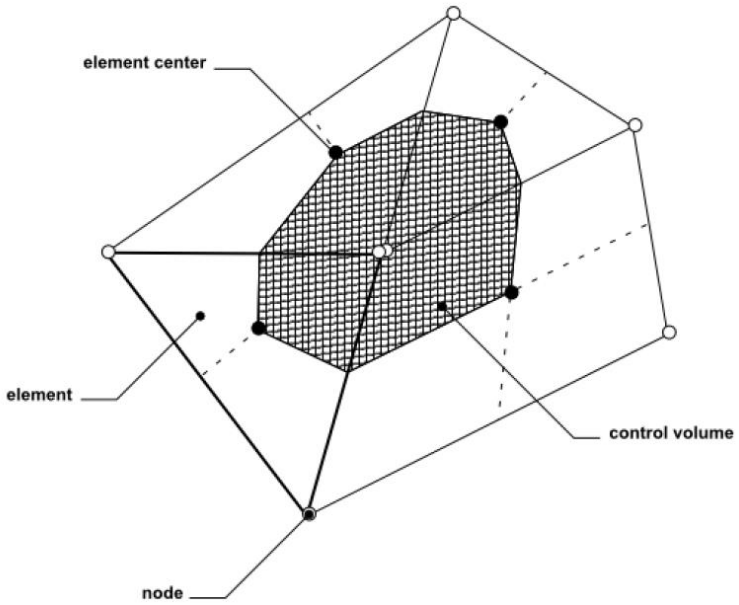

Figure 6-9: Schematic defining a control volume [126].

6.7.3.1 Advection Schemes

Advection refers to the transport of a fluid property through the solution domain. A high-resolution advection scheme is preferred as it optimises between the first and second order differencing to maintain solution boundedness. Additionally, it operates with far less numerical diffusion (truncation error propagation is reduced). This results in slower but higher accuracy of convergence.

6.7.3.2 Transient Schemes

To account for transient effects, the governing equations are discretised in time. The temporal discretisation involves integration of every term in the differential equation, *i.e.*, diffusion, convection, and source term over the time step Δt. A second order backward Euler scheme is preferred since it is second order accurate and is the recommended scheme for transient computations involving adaptive time stepping.

6.7.3.3 Interpolation Schemes

Interpolation schemes are used in CFX to transform cell-centre quantities to face-centre values to compute gradients, assess divergence, *etc*. The default recommended trilinear type interpolation for pressure and velocity is considered. The pressure interpolation method involves interpolation of nodal pressures to integration points for the pressure gradient term of the momentum equation. However, typical co-located methods lead to decoupled pressure field. Rhie and Chow [118–120] introduced an alternative discretization for the mass flows to avoid the decoupling. The discretization involved applying momentum equations to each integration point (located at the centre of each surface segment within an element, shown in the Figure 6-10), wherein the averaging of adjacent vertex velocities is augmented by high-order pressure variation and is scaled by the grid spacing. A fourth order level of accuracy pressure-redistribution term is generated using face and cell values that is significantly smaller than the average of vertex velocities as the grid is refined to reasonable levels. Thus, in effect, the large pressure gradients are effectively captured. Velocity interpolation method refers to interpolating nodal velocities to integration points to account for the velocity divergence term of continuity equation.

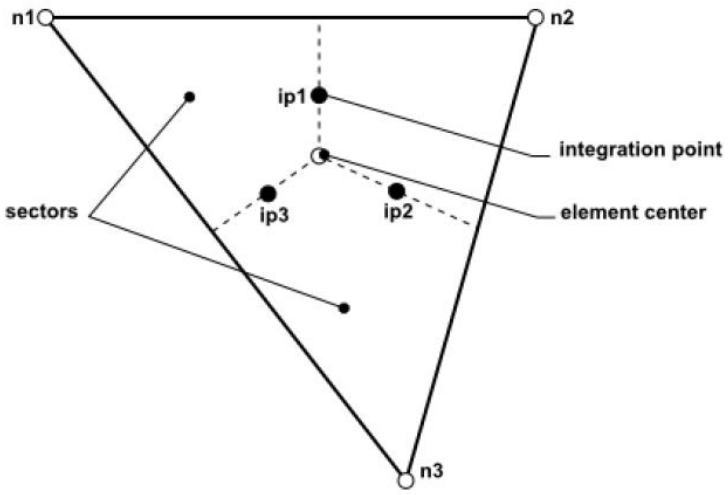

Figure 6-10: Schematic defining a mesh element,[126].

6.8 Spatial/grid verification

Solution errors in the form of numerical diffusion or truncation are associated with the chosen grid discretization schemes. A discrepancy in the numerical results between the asymptotic value and true physical solution prevails. Thus, a threshold is to be established below which the solution is recognised to be independent of the mesh resolution [129]. A verification study is performed to evaluate the level of mesh (in)dependence and the consistency of results, and this process requires quantification of discretization and truncation errors [121, 122]. A method of analysing grid convergence is suggested by Celik *et al.* [133], as recommended by the ASME Journal of Fluids Engineering. The advantage of this technique is that successively doubling the grid resolution to obtain a finely resolved grid is unnecessary.

The Grid Convergence Index (GCI) is a measure of percentage error which provides a confidence bound around the estimated error signifying the estimation of numerical model uncertainty. Characteristically, three different sets of grids are used for this technique. Three grids were created using ANSYS meshing; Grid 1 (1718669 cells) is the fine grid, Grid 2 (622504 cells) is the medium grid and Grid 3 (206005 cells) is the coarse grid. The results based on the three grids and derived parameters such as axial pressure gradient, wall shear stress, time averaged Nusselt number and time averaged friction factors are presented in Table 6-3. Sample plots from this analysis are provided in Figure 6-11 and Figure 6-12. The difference in solution parameter values between the medium and coarse grids and the reference fine grid is low. For example, time averaged Nusselt numbers are almost identical and the trend in transient wall shear stress indicates oscillatory convergence behaviour. The maximum numerical uncertainty for the three grids shown in Table 6-3 indicate that the solutions are within the asymptotic range of convergence. The global order of accuracy for fine grid size is 1.15 as oscillatory convergence occurs at 75% of the grid points shown in Figure 6-11 and Figure 6-12. Thus, the fine grid with an acceptable GCI factor is the preferred mesh for the study, which yields an acceptable level of accuracy and the best performance with respect to computational time. Due to the low discrepancy between the results for the meshes presented, oscillatory convergence is considered acceptable. Further mesh refinement showed no significant benefit. Indeed, it is improbable that the asymptotic range for all parameters that could be investigated in this grid convergence study is likely to be reached, since the results are spatially and time averaged for certain parameters which also introduces errors. Note that discretization error bars for the fine grid solution aren't shown in the figures for clarity.

Table 6-3: Selected results from mesh independence study for $Wo = 11.5$, $A_0 = 1$.

	Coarse	Medium	Fine
Refinement factor	1	3	2.83
Cell count	2×10^5	6×10^5	1.7×10^6
$\nabla P_{min}[Pa/m]$	-6588.9	-6620.7	-6711.1
$(\%\ deviation)$	(1.82)	(1.35)	$(-)$
$\tau_{max}[Pa/m]$	0.4568	0.4548	0.4645
$(\%\ deviation)$	(1.66)	(2.10)	$(-)$
$\overline{Nu}$	5.083	5.082	5.081
$(\%\ deviation)$	(0.045)	(0.029)	$(-)$
$\overline{\sigma_p}$	0.813	0.815	0.818
$(\%\ deviation)$	(0.61)	(0.36)	$(-)$
$GCI_{max}(\%)$	$(-)$	$(-)$	1.3

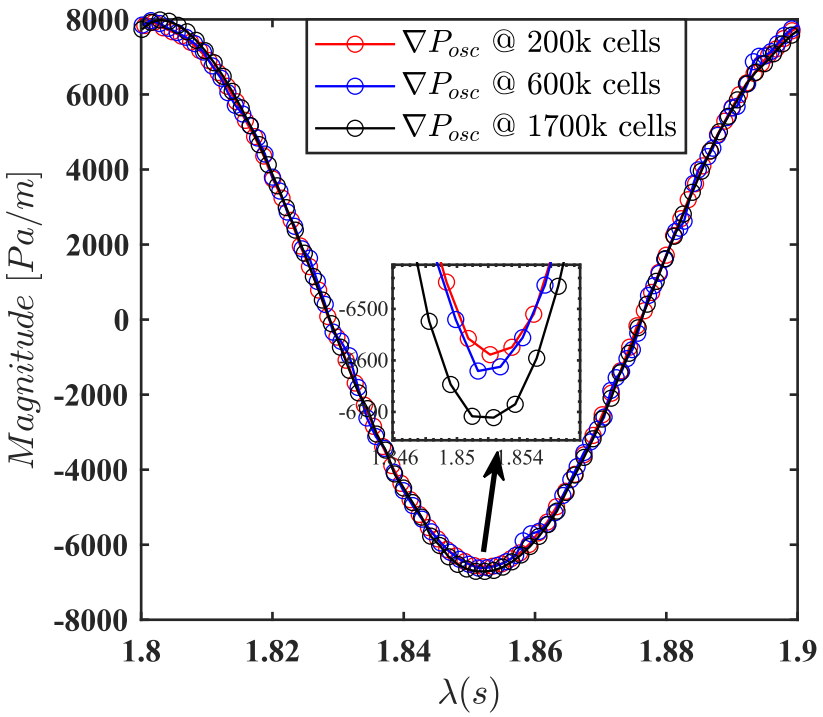

Figure 6-11: Oscillating axial pressure gradient for one pulsation cycle for different mesh densities at a frequency of 10 *Hz* ($Wo = 11.5$) and $A_0 = 1$. Fine grid numerical uncertainty is about 1.3%.

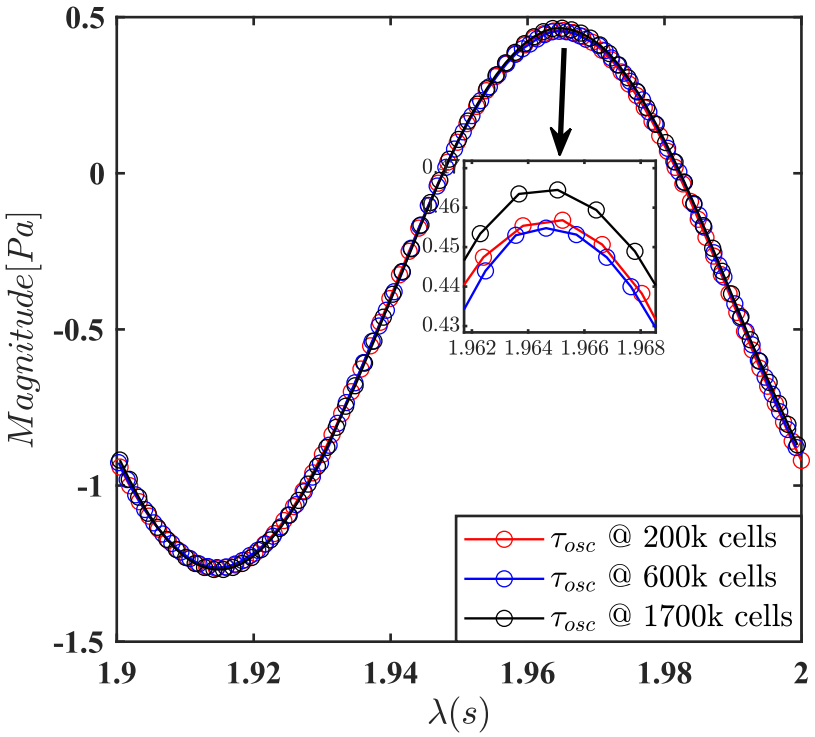

Figure 6-12: Oscillating bottom wall shear stress for one pulsation cycle for different mesh densities at a frequency of 10 *Hz* ($Wo = 11.5$) and $A_0 = 1$.

6.8.1 Residuals convergence limit sensitivity analysis

A sensitivity analysis of the residual convergence limit is performed on the fine mesh for a transient case of 0.5 *Hz* ($Wo = 2.5$). Axial pressure gradient is the parameter considered under a range of root mean square (RMS) residual targets of 1E-3, 1E-4, 1E-5, 1E-6. To capture the transient effects of a pulsating flow accurately, the residual convergence limits 1E-3 and 1E-4 are considered loose and consequently such limits generate higher numerical uncertainty as can be inferred from Figure 6-13. Additionally, significant deviations are observed in regions nearing the maximum and minimum magnitudes as compared to the residual convergence limits of 1E-5 and 1E-6. An acceptable level of agreement is obtained for the axial pressure gradient for the residual convergence limits of 1E-5 and 1E-6, although the latter involves a substantially higher computational cost and time to attain the residual target. Transient simulations are therefore performed with the residual limit of 1E-5 to balance the numerical accuracy and use of computational resources.

6.8.2 Judging convergence of periodic behaviour

The unsteady simulations are considered periodic when the RMS deviations of the time-averaged wall temperature values between two successive cycles do not exceed 0.1%. This occurs after about $10 - 25$ full cycles of flow pulsation, although it is subjected to the flow format of pulsation, frequency, and flow rate amplitude. Figure 6-14 indicates the temporal evolution of bottom wall (solid domain) temperature convergence for a sample case of sinusoidal pulsation at frequency of 2 *Hz* ($Wo = 5.1$) and $A_0 = 1$. The wall temperature parameter indicates convergence after about 15 pulsation flow cycles and is subjected to increase for higher frequency flows.

The velocity and pressure values typically converge after 2 cycles. The convergence history of mass flow rate profiles at the inlet and outlet are shown in Figure 6-15 for a sinusoidal pulsation at 25 *Hz* ($Wo = 18.3$) and $A_0 = 1$ for 30 periodic cycles. The inlet and outlet mass flow rate magnitudes tend to cancel out each other, thus the global net mass transport of the domain is recognised to be conserved.

6.9 Validation of the computational model

Validation of the computational model is carried out by comparing the results with established analytical and/or experimental results.

6.9.1 Hydrodynamic parameters

Derived parameters such as the Darcy friction factor (σ_s) and Nusselt number (Nu) are used for the comparative analysis as described below. Figure 6-16 indicates a validation of the computational model for steady flow based on the variation of σ_s vs. Re_s for a steady flow ($Wo = 0$). 6 distinct cases of laminar steady flow Reynolds number were simulated, and the friction factors were compared with the analytical predictions for flow through a rectangular duct of Shah and London [19, 124] and the experimental work of Zhuang *et al.* [15, 21]. The current study shows an excellent agreement with the literature [19] wherein the fully developed flow Darcy friction factor $\sigma_s \times Re_s$ follows a consistent value of 87.5. For rectangular ducts with aspect ratio (AR) in the range $0.066 \leq b/a \leq 0.083$, $21.58 \leq \sigma_f \times Re_s \leq 22.01$, equivalent to $86.32 \leq \sigma_s \times Re_s \leq 88.04$ [19].

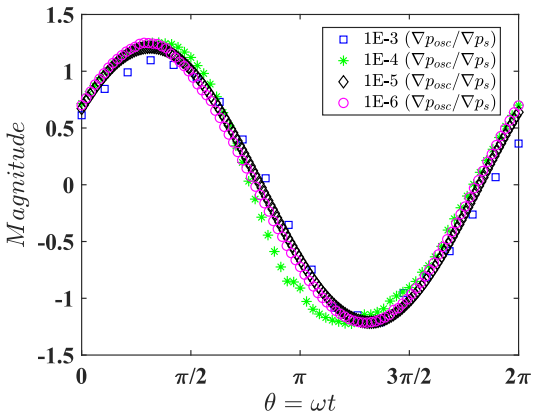

Figure 6-13: Convergence criteria sensitivity test on axial pressure gradient for 0.5 *Hz* ($Wo = 2.5$) and $A_0 = 1$ sinusoidal pulsating flow.

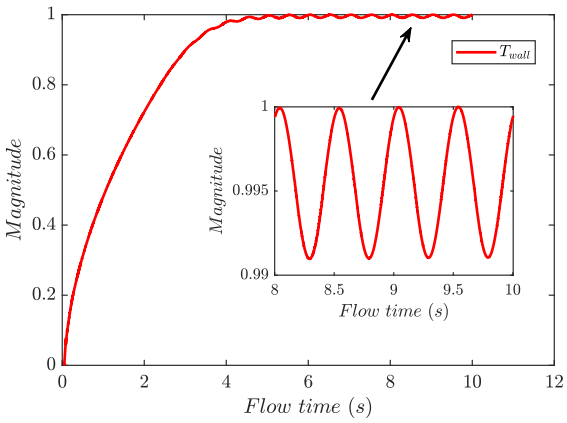

Figure 6-14: Temporal convergence history of the normalized bottom (solid domain) wall temperature for 2 *Hz* ($Wo = 5.1$) and $A_0 = 1$ when undergoing sinusoidal pulsating flow over 20 cycles.

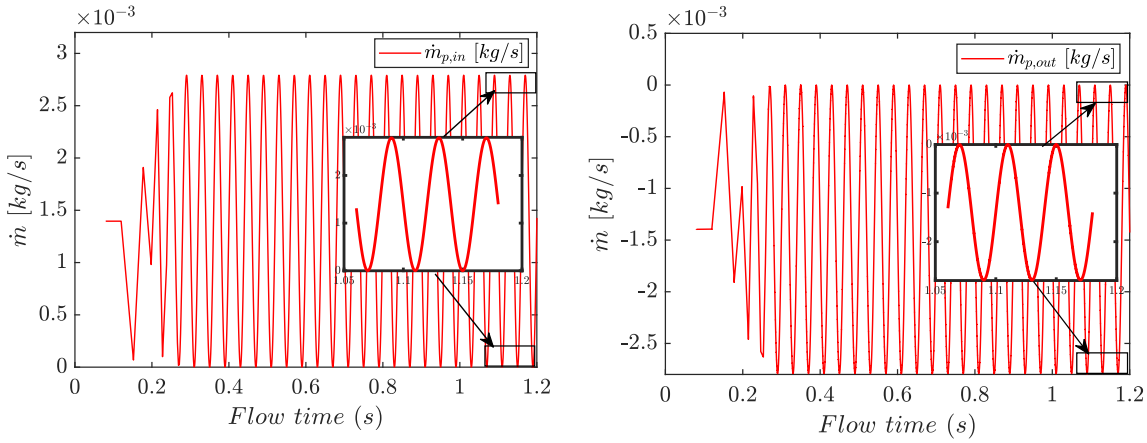

Figure 6-15: Temporal convergence history of mass flowrate at inlet (left) and outlet (right) for a sinusoidal pulsation flow with $f = 25$ *Hz* ($Wo = 18.3$), and $A_0 = 1$ over 30 pulsation cycles.

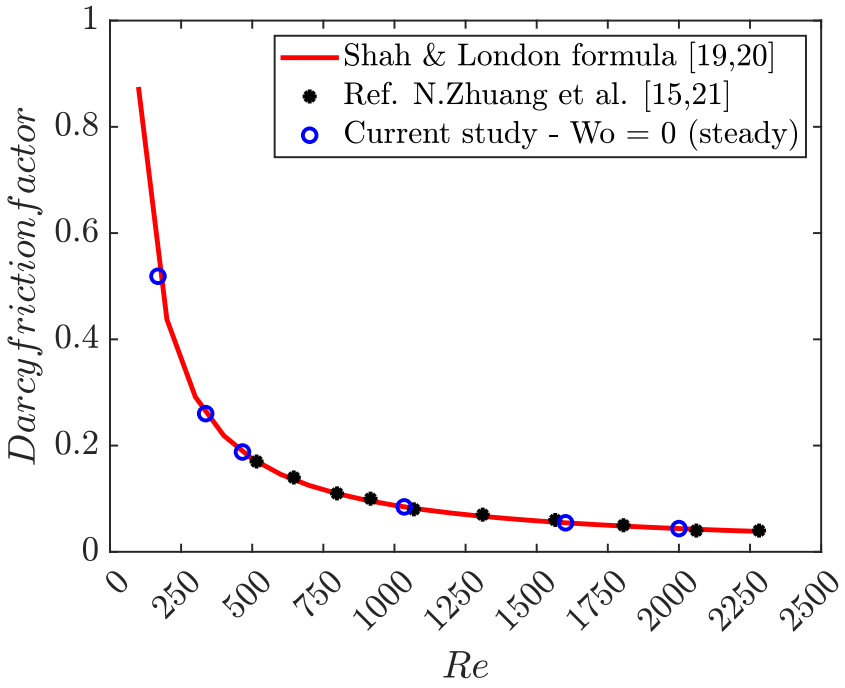

Figure 6-16: Comparison of Darcy friction factor (σ_s) with Re_s for a laminar hydrodynamically fully developed flow in a rectangular duct.

6.9.2 Thermal parameters

A volumetric heat source is used for the current conjugate heat transfer study, the rectangular duct with a heated bottom wall is similar to a H2 (1L) thermal boundary condition described by Refs. [27, 136, 137], *i.e.*, constant wall axial and peripheral heat flux, where (1L) represents one heated long side and three insulated or adiabatic sides (See Section 2.2.1). For the current study, the rectangular duct has a height of 1.4 *mm* and a width of 20 *mm* and, therefore, an aspect ratio: $a/2b = 0.07$.

Table 6-4, row 2 presents Nusselt number (Nu) data for steady ($Wo = 0$) and time averaged Nusselt number data ($\overline{Nu}$) for pulsating ($Wo > 0$) flow cases. The current study predicts a steady flow Nusselt number of 5.083 which shows reasonable agreement with the published literature for laminar duct flows with H2 (1L) condition. Analytical solutions developed by Spiga & Morini [28] indicates that Nu must be greater than 4.558 which was calculated based on a duct aspect ratio of 0.1. Using the correlation described by Spiga & Morini [28] $Nu = 4.667$ is estimated, which is presented here in Table 6-4 Row 3. Their analysis assumed fully developed flow of a Newtonian fluid with constant fluid properties, no axial thermal conduction, no natural convection, zero viscous dissipation, and with rigid and non-porous duct walls. For context, for a steady laminar fully developed slug flow with an aspect ratio ($2b/a$) range of $0.625 \leq 2b/a \leq 0.1$, Table XII in Morini [26] suggests $5.457 \leq Nu \leq 5.647$ for the H2 (1L) thermal condition.

Table 6-4, row 4 presents the percentage difference in Nusselt numbers (dNu [%]), described by Equation (6-20), for the pulsating ($Wo > 0$) flow cases investigated in the current study. The table shows a small negative effect of pulsation on the overall heat transfer. Comparisons are made with the results presented in Yuan *et al.* [113] for a parallel plate pulsatile flow with constant wall heat flux, and with Hemida *et al.* [136] for a pulsating flow in pipe with constant wall heat flux. The current study shows similar trends to that reported by Yuan *et al.* [113] and Hemida *et al*. [136]. As shown in Table 6-4 the Nu for laminar steady flow is 5.083 which is approximately equal to the time-averaged Nusselt number obtained for a quasi-steady pulsating flow at $Wo \geq 18.3$.

Solutions to a generalized H2 thermal boundary condition for rectangular ducts are described analytically by Shah and Shah & London in Refs. [19, 25, 137]. For an aspect ratio $2b/a = 0.125$, $Nu = 2.904$ was determined from the literature. However, the stated value is obtained for the condition where all four walls are transferring heat, which differs from the imposed thermal condition investigated in the current study.

Table 6-4: Nusselt number data and comparisons with published literature for steady flow and pulsating flow cases.

$Wo \rightarrow$	**0**	**0.5**	**2.5**	**5.1**	**8.1**	**11.5**	**18.3**	**25.9**
Nu *or* $\overline{Nu}$ (current study)	5.083	5.062	5.070	5.086	5.081	5.081	5.083	5.083
Nu (Spiga & Morini [28])	$\approx$ **4.667**							
dNu (Eq. 14, current study)	0	-0.413 %	-0.245 %	-0.063 %	-0.032 %	-0.028 %	-0.0001 %	-0.0001 %
dNu (Fig. 5, Yuan *et al.* 2014 [113], parallel plates)	-	-0.985 %	-0.293 %	-	-	-	-	-
dNu (Fig. 2, Hemida *et al.* 2002 [136], circular pipe)	-	-	-0.118 %	-0.004 %	-	-	-	-

6.9.3 Sinusoidal pulsating flow

Validation of the computational model is carried out by comparing results against established studies of sinusoidal pulsating flow in channels from Haddad *et al.* [51] and Majdalani [138], as shown in Figure 6-17 and Figure 6-18. Mass flow rate-imposed pulsations in the fully developed region was studied analytically by Haddad *et al.* [51] using a Fourier series method. The deviation of results at higher frequencies (maximum deviation of 5%) observed in Figure 6-17 is reasonable

considering the disparity in the modelling characteristics adopted, *i.e.*, two-dimensional analytical predictions versus a three-dimensional finite volume method conjugate heat transfer model. Pressure gradient-imposed flow pulsations were investigated by Majdalani [138] using a Fourier series approximation. The results presented in Figure 6-18 for wall shear amplitudes and phase angles relative to the axial pressure gradient indicate a good agreement (maximum deviation of 3%) with each other.

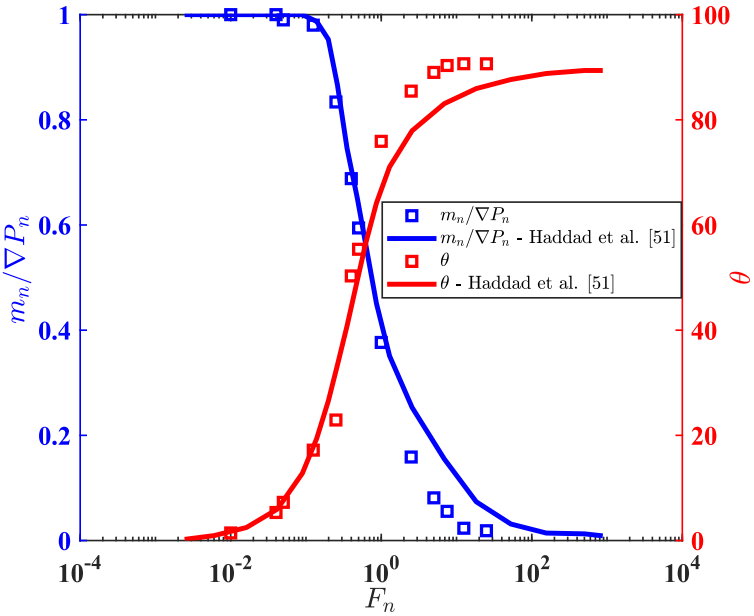

Figure 6-17: Variation of normalized mass flow rate amplitudes with respect to the normalized axial pressure gradient and the associated phase differences as a function of dimensionless frequency $\left(F_n = f * (a^2/\nu)\right)$. Symbols represent the current study, while lines represent analytical solutions from Haddad *et al.* [51].

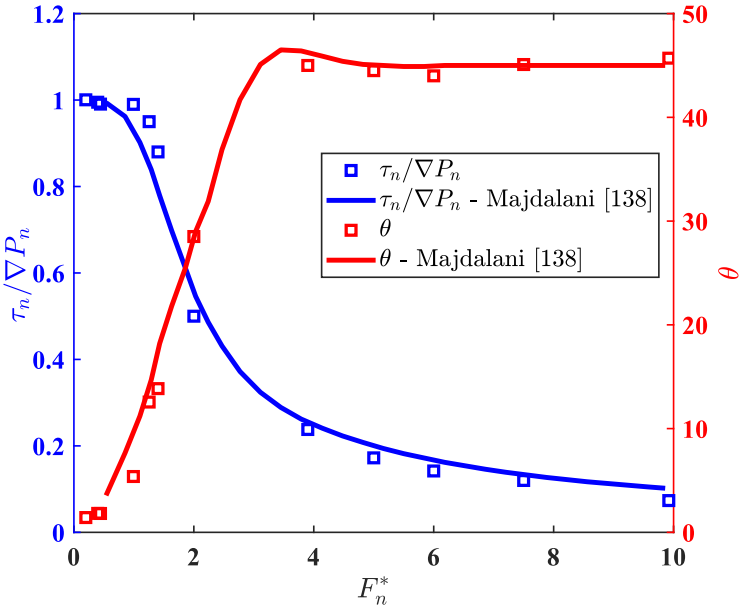

Figure 6-18: Variation of normalized wall shearing stress with respect to normalized axial pressure gradient and the phase differences as a function of dimensionless frequency $\left(F_n^* = \sqrt{Re_k}\right)$. Symbols represent current numerical study, while lines represent analytical solution for a channel flow from Majdalani [138].

6.10 Post-Processing

Comprehensive temporal and spatial analyses are performed on the generated pulsating flow hydrodynamic and thermal data. The spatial and temporal data is recorded at a user selectable frequency for the various parameters of interest until a converged solution is attained.

6.10.1 Temporal analysis

Several hydrodynamic parameters such as the volumetric flow, axial pressure gradient, and wall shear stress are recorded from the hydrodynamically and thermally fully developed region of the minichannel after the solution is fully converged for one full pulsation cycle extending from $0 - 2\pi$ (as shown in the schematic, Section 6.1). The volumetric flow rate (Q) is measured at the inlet to the minichannel. The axial pressure gradient (∇P) is calculated as the per unit length difference between the inlet (gauge) pressure and the local pressure at the location $y = 0.0007\ m, z = 0.3\ m$ presented in the Figure 6-19. The wall shear stress is determined from the interface location between fluid and solid domains at $y = 0\ m$ and $z = 0.3\ m$.

Similarly, thermal parameters such as the oscillating wall temperature (the difference between time dependent and time averaged component), and bulk temperature are reported. The instantaneous spatially averaged wall temperature is sampled along the bottom wall ($y = 0\ m$) over the range

$0 \leq x \leq 0.01\ m$ in the thermally fully developed region at $z = 0.3\ m$. The instantaneous spatially averaged bulk temperature is calculated by averaging the recorded minichannel inlet temperature at $z = 0\ m$ and outlet temperature at $z = 0.345\ m$. Further post-processing is carried out in MATLAB which involves normalization of parameters with respect to the time-averaged (*i.e.*, the steady) component for symmetric and asymmetric sinusoidal waveforms.

6.10.2 Spatial analysis

The spatial dependent fluid parameters such as axial velocities and wall shear stresses and thermal parameters such as wall temperatures and wall heat flux profiles are evaluated in the fully developed regions and post-processed in multiple stages.

Axial velocities are exported as a **.csv* file using a customised .c session script file functioning in a loop inside CFD post which outputs planar data (along x and y) for every mesh nodal value of velocity and the respective time steps for a full pulsation cycle with (x, y, z) coordinates $(0, 0.0007, 0.3)\ m$ and $(0.01, 0.0007, 0.3)\ m$. Similarly, the wall shear stresses, and wall temperatures are recorded as a **.csv* file along a transverse sampling line with coordinates $(0,0,0.3)\ m$ and $(0.01,0,0.3)\ m$ as depicted in Figure 6-19.

Subsequently, the n number of **.csv* files are imported into MATLAB, where n refers to each timestep and are sorted in accordance with every spatial (x coordinate) datapoint to generate a 3-D matrix. The matrix comprises of geometric coordinates x, y and the parameter of interest over a number of timesteps. A single flow pulsation is divided into 10 equal phase intervals. Further, to obtain the oscillatory component, the time averaged component is subtracted from its corresponding time dependent value in the matrix. Thus, the resulting outcome is the instantaneous oscillating data along the transverse direction.

The transient nature of fully developed velocity profile is analysed by generating a discrete sampling line extending vertically across the fluid domain. The time dependent axial velocity component is sampled from the location: $y = 0\ m$ to $y = 0.0014\ m$ along the symmetry plane at ($z = 0.3\ m$) location. The computed axial velocity is exported and post-processed for a full periodic pulsation cycle using a user defined .c session script file.

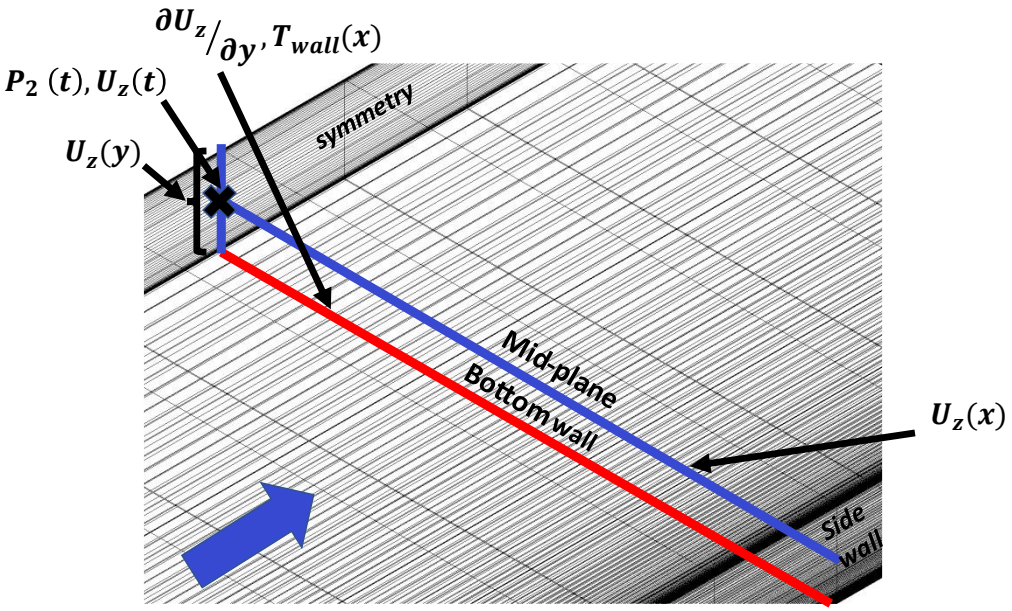

Figure 6-19: Illustration example showing a few sampling locations in the fully developed region.

6.10.3 Derived parameters

User defined expressions are scripted in CFD-post to compute the following derived hydrodynamic and thermal parameters: wall shear stress, heat transfer coefficient, Nusselt number, and the Darcy friction factor.

The wall shear stress as defined by Equation (6-14) is obtained from the velocity gradient computed along the interface $y = 0\ m$ between the fluid and solid domain in the fully developed region $z = 0.3\ m$ along the extents of $x = 0\ m$ and $x = 0.01\ m$ sampling location. The time averaged friction factor for pulsating flow $(\overline{\sigma_p})$ is obtained from Darcy-Weisbach Equation [139], described in Equation (6-15) where (ΔP) is the pressure drop. (σ_s) is the corresponding friction factor value for steady flow at the same Reynolds number (Re).

$(\overline{T_w})$ is the time-averaged heated wall temperature in the fully developed region given by Equation (6-16). $(\overline{T_b})$ is the time-averaged bulk fluid temperature as given by Equation (6-17) [104]. $(|T_w|)$, $(|T_{in}|)$ and $(|T_{out}|)$ are instantaneous spatial-averaged temperature at the wall, channel inlet $(z = 0\ m)$ and outlet $(z = 0.345\ m)$, respectively. To determine and evaluate the thermal performance of heated minichannels under pulsating inlet conditions, convective heat transfer parameters are introduced. The time averaged Nusselt Number $(\overline{Nu})$ as given by Equation (6-19) defines the relationship between fluid thermal conductivity and surface convective heat transfer rate, averaged over one pulsation cycle (λ), and requires estimation of the time-space averaged heat transfer coefficient $(|\bar{h}|)$ as given by Equation (6-18), wherein $(|\overline{q_w}|)$, is the time-space

averaged bottom wall heat flux. The normalised enhancement of heat transfer compared to steady flow only is described by Equation (6-20), where (Nu_s) represents the steady flow Nusselt number.

To characterize the performance of flow pulsations in a minichannel simultaneously in terms of heat transfer and pressure drop, a thermal performance parameter (η) is defined in the Equation (6-21).

$$\tau_w = \mu \left(\frac{\partial U_z}{\partial y}\right)_{y=0} \tag{6-14}$$

$$\overline{\sigma_p} = \frac{1}{\lambda}\int_0^{\lambda} \frac{2(\Delta P/L)D_h}{\rho U_s^2}\, dt \tag{6-15}$$

$$\overline{T_w}(or\ \overline{q_w}) = \frac{1}{\lambda}\int_0^{\lambda} |T_w(or\ q_w)|dt \tag{6-16}$$

$$\overline{T_b} = \frac{1}{\lambda}\int_0^{\lambda} \frac{(|T_{in}| + |T_{out}|)}{2}\, dt \tag{6-17}$$

$$\left|\bar{h}\right| = \frac{|\overline{q_w}|}{\overline{T_w} - \overline{T_b}} \tag{6-18}$$

$$\overline{Nu} = \frac{\bar{h}D_h}{k} \tag{6-19}$$

$$dNu = \frac{\overline{Nu} - Nu_s}{Nu_s} \tag{6-20}$$

$$\eta = \left(\frac{\overline{Nu}}{Nu_s}\right).\left(\frac{\overline{\sigma_p}}{\sigma_s}\right)^{-1/3} \tag{6-21}$$

6.11 Computational Matrix

The numerical data matrix as shown in Table 6-5 below consists of different pulsation flow formats such as symmetrical sinusoidal, leading and lagging asymmetric sinusoidal and positive and negative half rectified sinusoidal. Simulations are performed over a wide range of frequencies between $0.02 \leq f(Hz) \leq 25$ corresponding to $0.5 \leq Wo \leq 18.3$ for three distinct flow rate amplitudes $A_0 = 0.5$, $A_0 = 1$ and $A_0 = 3$ as were investigated in the experimental study, see Section 5.4.

Table 6-5: Computational parameter space involving different pulsation flow formats, frequencies and flow rate amplitudes.

SYMMETRIC SINUSOIDAL FLOWS				
f [Hz]	0.02	0.5	2	25
Wo	0.5	2.5	5.1	18.3
A_0	*0.5* *1* *3*			
LEADING AND LAGGING ASYMMETRIC SINUSOIDAL FLOWS				
f [Hz]	0.02	0.5	2	25
Wo	0.5	2.5	5.1	18.3
A_0	*0.5* *1* *3*			
POSITIVE AND NEGATIVE HALF RECTIFIED SINUSOIDAL FLOWS				
f [Hz]	0.02	0.5	2	25
Wo	0.5	2.5	5.1	18.3
A_0	*0.5* *1* *3*			

7) Results and Discussion

In this chapter the results from both the experiments and computational simulations are presented, in some cases together. For the CFD investigation a minimum of 4 frequencies ($Wo = 0.5, 2.5, 5.1, 18.3$) and 3 flow rate amplitudes ($A_0 = 0.5, 1, 3.0$) were investigated for 5 different pulsation waveforms (symmetrical sinusoidal, asymmetric leading sinusoidal, asymmetric lagging sinusoidal, half rectified positive and half rectified negative). A similar parameter range was investigated experimentally, apart from the highest frequency which was not tested due to the limitations of the equipment used.

Analysis of the hydrodynamics and associated heat transfer has resulted in the generation of many graphs and CFD images. Where possible, multiple parameters are graphed together to reduce the number of figures. To make the analysis and discussion more coherent, and to avoid the reader having to scroll back and forth between figures and text descriptions, plots are grouped together for each waveform.

This chapter describes first the hydrodynamic aspects of the flows. Section 7.1 describes the temporal evolution of some key parameters, namely the normalised oscillating volumetric flow rate ($Q_{osc.}/Q_s$), normalised oscillating pressure gradient ($\nabla p_{osc.}/\nabla p_s$), and normalised oscillating bottom wall shear stress ($\tau_{osc.}/\tau_s$). Comparison between CFD and experimental data is provided where possible. Section 7.2 presents spatial information derived from the CFD simulations and provides a clear understanding of the variation of various flow parameters across the channel height and width. Section 7.3 shows a comparative study based on the friction factor ratio which compares the pulsating with steady components. Section 7.4 presents the temporal evolution of oscillating bulk $T_{osc,bulk}$ and wall $T_{wall,osc}$ temperature profiles. Section 7.5 describes spatial information of oscillating bulk temperature profiles produced from the CFD simulations across channel height and the oscillating wall temperature profiles which are generated from both CFD simulations and IR measurements across channel width. Section 7.6 shows Nusselt number distributions in the form of instantaneous space-averaged comparisons between the waveforms for varying A_0 and fixed frequencies of $Wo = 2.5$ and $Wo = 5.1$. Comparative analysis is drawn for

evolution of space-averaged instantaneous Nu at fixed $A_0 = 3$ with varying Wo. Overall enhancements and reductions in heat transfer rate are discussed for both variations in Wo and A_0. A thorough understanding between the interlinked efficiencies of hydrodynamics and heat transfer is developed by quantifying a thermal performance parameter is presented in Section 7.7.

7.1 Temporal variation of hydrodynamic parameters

This section describes the time dependent behaviour of key flow parameters for each pulsation waveform. Each column within each figure in this section shows the effect of increasing flow rate amplitude (A_0). Each row indicates the effects of increasing Womersley number (Wo). Both CFD and experimental data is presented. CFD results represent instantaneous data from a single pulsation once periodic flow has been established and convergence has been achieved, whereas experimental data is phase-averaged over 10 periodic cycles. There is no experimental data for wall shear stress, nor is there any experimental data available at the highest frequency of pulsation $Wo = 18.3$ ($f = 25\ Hz$) as the objectives of this study does not account for flow visualization techniques and the physical restrictions due to substantially high-pressure gradients which can lead to detrimental effects for a very sensitive and thin bottom boundary of the test setup. Generally, there is good agreement between the CFD and experimental datasets. The agreement is better at low frequencies and low flow rate amplitudes. The experimental data presents increased deviation from the CFD results at higher frequencies due to limitations in the experimental setup.

7.1.1 Symmetric sinusoidal pulsation

The figures highlight the complex interdependence of the flow parameters. For a sinusoidal waveform (Figure 7-1), an increase in A_0 results in an increased flow rate and corresponding increases in the pressure gradient and wall shear stress. This is true for all frequencies, but at the lowest frequency *i.e.*, viscous dominated flows, the shear stress and pressure gradient are in phase with the flow rate since fluid displacement time scales are longer. The ratio between the mass flowrate and pressure gradient is unity and thus the phase shift is non-existent as is inferred from Figure 6-17. The flow behaves in a quasi-steady manner. Whereas with increasing frequency a successive phase lag is developed and reaches a maximum.

Increasing Wo at the same A_0, the time scale of pulsation is shorter and is in synchronous with the fluid displacement time scales. Thus, viscous diffusion of momentum is the primary driving force for the flow and subsequently higher-pressure amplitudes are required with the increasing frequency of pulsation. This results in a very evident phase lag between the flow rate and pressure gradient. A large increase in pressure gradient with a maximum phase shift of $\pi/2$ is observed from

Figure 6-17 for the highest frequency *i.e.*, inertia dominated flows, which is due to the rapid fluctuations (or the shuttling effect) in the fluid displacement time scales. This phenomenon was established by Womersley [42] for a constant axial pressure gradient with a varying oscillating flow rate in a cylinder. A phase lag exists between the mass flowrate and pressure gradient profiles which is primarily due to the delay in the evolution of the pressure gradient along the streamwise direction as the faster moving oscillating mass flow responds quicker along the streamwise direction in the channel.

However little effect of Wo on the shear stress is observed. At $Wo = 2.5$ and $A_0 = 0.5$ the pressure gradient and shear stress appear to be in phase, with a phase lag of $12°$ to the flow rate, but as A_0 is increased the behaviour changes, and the flow rate and shear stress appear to be almost in phase. This is as a result of greater fluid momentum in the spanwise direction led by the increased flow rate amplitudes. With a subsequent increase in the pulsation frequency $Wo = 5.1, 18.3$ and flowrate amplitude A_0, the wall shear stress magnitudes attain a maximum phase shift of $\pi/4$ with the axial pressure gradient due to increased viscous forces in the near-wall regions of the channel due to the presence of maximum fluid velocity and thus high velocity gradients are present. This relationship between wall shear stress and pressure gradient as a function of pulsation frequency is in agreement with the widely established analytical study by Uchida [33] and experimental studies by Ojha *et al.* [48], Hughes and How [55] and Ünsal *et al.* [49] An extensive understanding on the distinct traits associated with the spatial distribution of velocity and shear stress gradients for pulsation waveforms are discussed in the following Section 7.2.

There exists a good general agreement associated between the experimental and the CFD results for the normalized volumetric flow rate. Although there is some deviation between the two datasets for the pressure gradient, in particular for the high frequency and respective high flow rate amplitudes due to the oscillations induced by the thin foil boundary to accommodate for such large pressure gradients developed by the high frequency symmetric sinusoidal waveform.

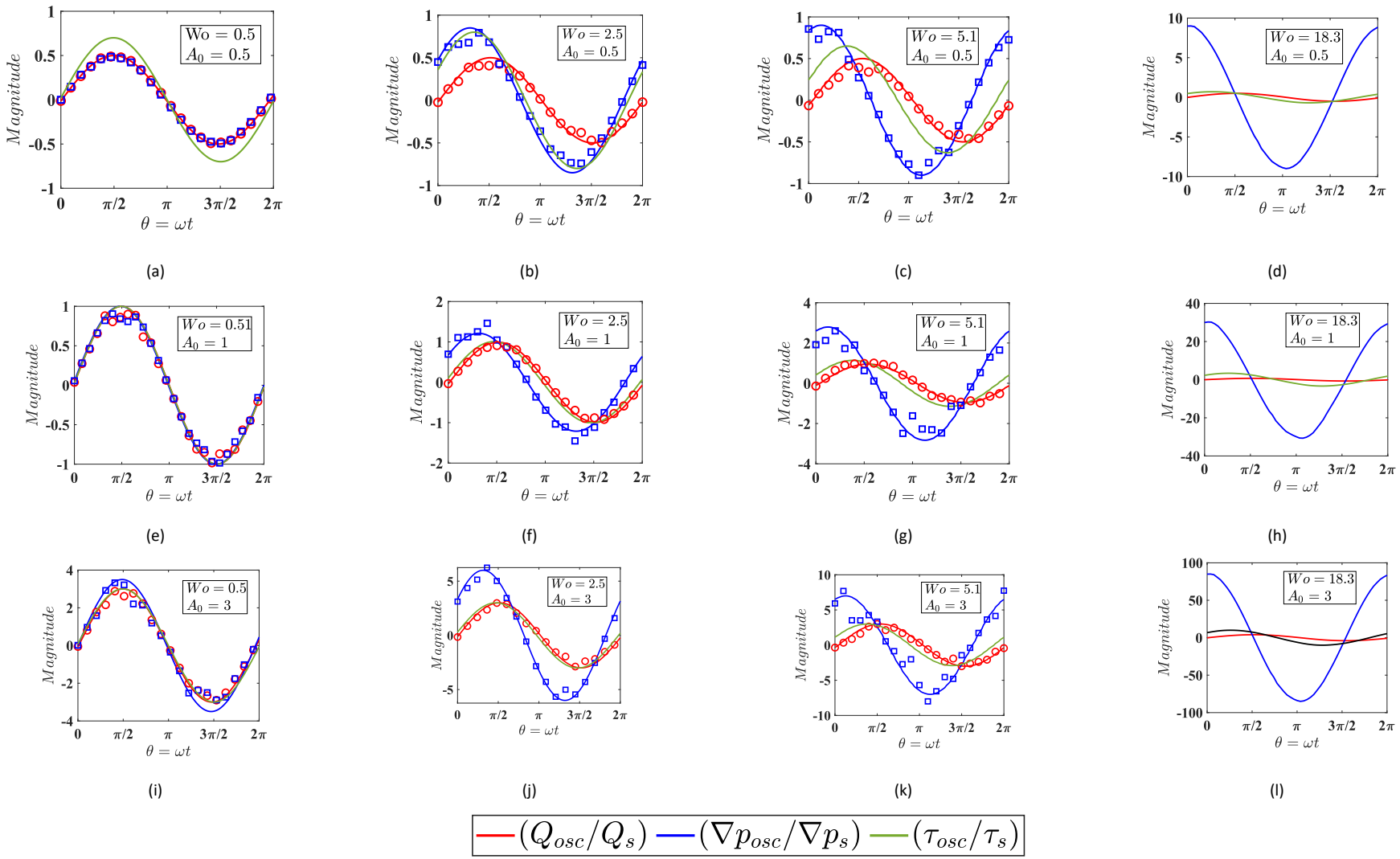

Figure 7-1: (a-l) Temporal variation of normalized flowrate, axial pressure gradient, and bottom wall shear stress and for a **symmetric sinusoidal pulsation waveform**. Moving across each row shows the effects of increasing Wo for the same A_0. Moving down a column shows the effects of increasing A_0 for a fixed Wo. Solid lines present the CFD results, and markers show the experimental results. Note that no experimental data exists for the wall shear stress, nor for the higher frequency $Wo = 18.3$ cases.

7.1.1 Asymmetric sinusoidal pulsations

7.1.1.1 Leading Asymmetric

Figure 7-2 presents the temporal variation of the normalised oscillating volumetric flow rate, pressure gradient, and wall shear stress in response to a leading asymmetric pulsation waveform. This waveform is characterised by an initial period of rapid acceleration followed by a more gradual deceleration before another rapid acceleration phase as the cycle restarts. The fluctuations induced due to the asymmetric flow rates result in a substantial increase in pressure gradient as both Wo and A_0 are increased, though the effect is much more pronounced for higher Wo. Compared to the symmetric sinusoidal waveforms in as seen from Figure 7-1, the rapid accelerating and decelerating flows at higher frequencies, *e.g.*, $Wo = 5.1$ and $Wo = 18.3$, generate a sharp impulse of flow momentum in the inertia dominated regime, leading to significant pressure fluctuations and an overall increased pressure drop in the channel. This effect aligns with the experimental observations made by McEvoy *et al.* [105] who used PIV techniques for flow pulsations through a microchannel.

For all flow rate amplitudes at the lowest frequency of $Wo = 0.5$, the pressure gradient and wall shear stress profiles follow the shape of the flow rate profile. As the frequency is increased to $Wo = 2.5$ a phase lag appears to develop between the pressure gradient and the other profiles. Furthermore, the pressure gradient profile has also changed and no longer mimics that of the flow rate (see Figure 7-2 (f) especially). This deviation between the profiles continues for $Wo = 5.1$ and above, with the pressure gradient profile assuming a u-shaped form with very high magnitudes during the acceleration phases at the beginning and end of the pulsation. Increasing the flow rate amplitude at a given Wo has the effect of increasing the pressure gradient, and this is consistent for all frequencies except for $Wo = 18.3$ which shows a dramatic increase in pressure gradient for the highest $A_0 = 3$. A distortion in the waveform exists and the inherent asymmetric characteristics show a deformation at the highest frequency, as is also described by [105] in their experimental study involving high frequency pulsations in a microchannel.

Contrastingly, increasing Wo appears to have a minimal effect on the magnitude of the normalised oscillating bottom wall shear stress. At low values of Wo, the wall shear stress appears to remain in phase with the flow rate, whereas for higher Wo a small phase lag develops. Increasing the flow rate amplitude results in an increase in shear stress for all Wo since the maximum fluid velocity, and associated velocity gradients, increase. This behaviour is like that observed for the symmetric sinusoidal waveforms in Figure 7-1. In terms of magnitude, the leading asymmetric pulsation waveform appears to result in a distinct increase of bottom wall shear stress when compared to

the symmetric sinusoidal pulsation waveform. However, at the highest frequency $Wo = 18.3$, higher magnitudes of shear stress exits while due to the magnified effects of the pressure gradients, the normalized values of shear stress are not evidently clear.

The agreement between the experimental and CFD results for the normalised volumetric flow rate is generally good for the cases of low-moderate frequencies. Regarding the normalised pressure gradient, the trends and magnitudes are in close agreement for low to moderate frequencies ($Wo \leq 2.5$). However, the agreement worsens at higher frequencies, especially for higher flow rate amplitudes. This is in part due to the oscillations induced by the thin foil boundary to accommodate for such large pressure gradients developed by the high frequency asymmetry waveform.

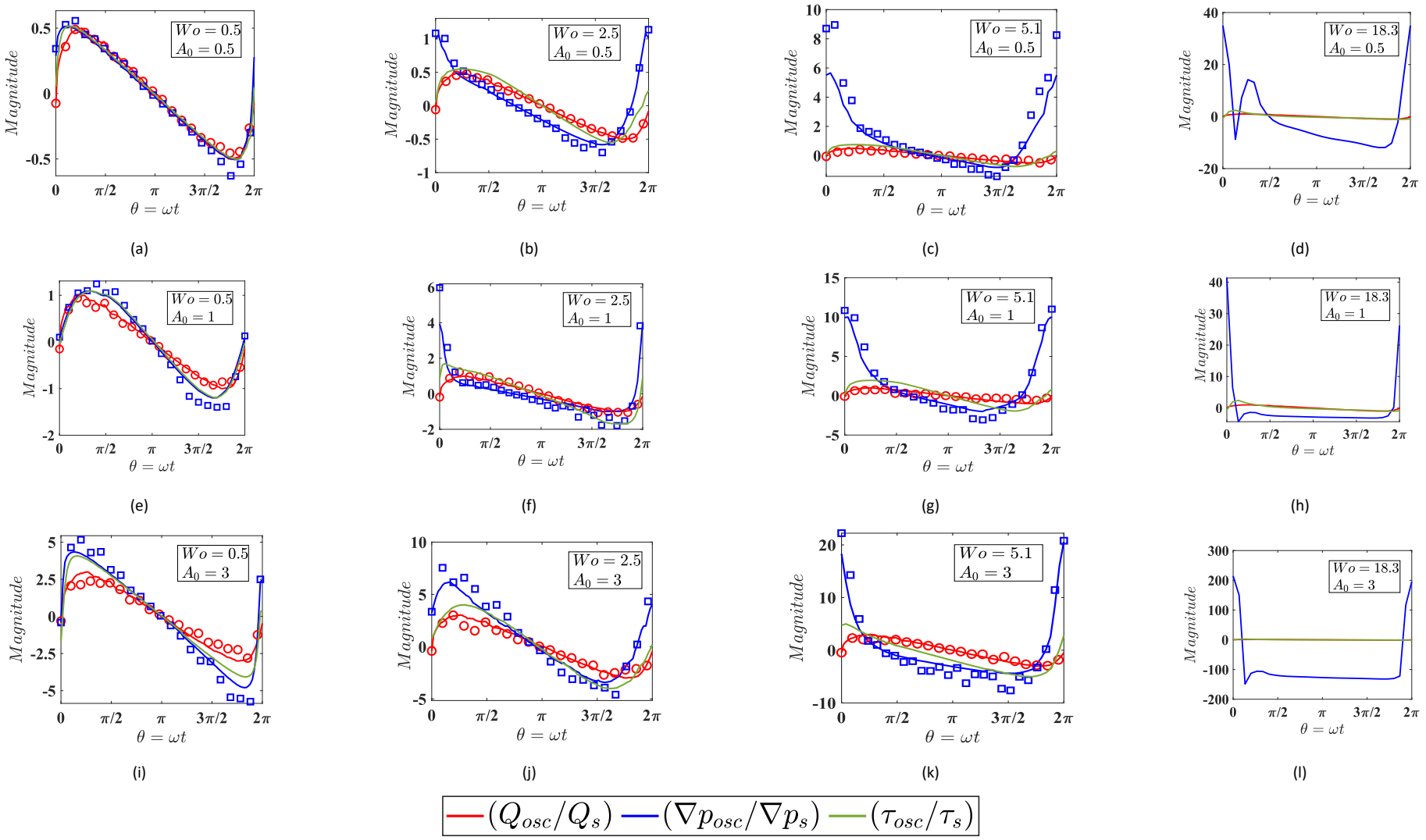

Figure 7-2: (a-l) Temporal variation of normalized flowrate, axial pressure gradient, and bottom wall shear stress for a **leading asymmetric sinusoidal waveform**, across the rows is an increase in Wo and down the column is increasing A_0. Solid lines present the CFD results, and markers show the experimental results. Note that no experimental data exists for the wall shear stress and for the higher frequency $Wo = 18.3$ cases.

7.1.1.2 Lagging Asymmetric

Figure 7-3 presents the temporal variation of normalised oscillating volumetric flow rate, pressure gradient and wall shear stress in response to a lagging asymmetric pulsation waveform. This waveform features an initial period of gradual acceleration followed by a shortened acute shift in the deceleration stage before another gradual acceleration stage as the cycle restarts. As a result of the rapidly altering flow rate over a short interval, a sharp impulse in the pressure gradient is observed evidently from the moderate pulsation frequencies onwards to further increasing Wo and A_0. Although as noted for the leading asymmetric pulsation, the fluctuations induced by the asymmetry are more pronounced for the higher Wo even in the case of lagging asymmetry. Whereas, compared to the symmetric sinusoidal waveforms in Figure 7-1, the faster and stronger decelerating asymmetry characteristic of higher frequencies, $Wo = 5.1$ and $Wo = 18.3$ shows distinct increase in the pressure gradient.

With a similarity to the leading asymmetry, the lagging asymmetry at the lowest frequency $Wo = 0.5$ over all flow rate amplitudes exhibit in phase characteristics, thus the pressure gradient and shear stress profiles follow the shape of the flow rate profile. As the frequency is increased to $Wo = 2.5$ a phase lag develops between the pressure gradient and flow rate profiles. Equivalently, the pressure gradient profile presents a sharp impulse with high magnitudes as a result of the rapidly fluctuating fluid momentum during the deceleration stage, which is strikingly evident from Figure 7-1b, Figure 7-1f, Figure 7-1j in particular at phase π. Increasing the flow rate amplitude at a given Wo results in a further increase of pressure gradient and is even more pronounced at very high A_0. In particular, the pressure gradient magnitudes are sharply increased for the highest frequency $Wo = 18.3$ and $A_0 = 3$. This understanding aligns with the leading asymmetry discussions.

The normalized oscillating bottom wall shear stress presents in-phase characteristics with the flow rate at low values of Wo in an agreement to the discussions on the leading asymmetry waveform. Increasing the Wo, a minimal effect is noticed on the wall shear stress magnitudes, however a phase lag develops and is less prominent compared to the pressure gradient profiles. With an increase in the flow rate amplitude, the resulting shear stress increases over the range of Wo which is typically as a result of the enhanced bulk flow fluctuations. At the highest frequency $Wo = 18.3$, due to increased magnitudes of pressure gradients, the high shear stress magnitudes are not distinctly evident. This nature follows in agreement with the leading asymmetry and the symmetric sinusoidal pulsation waveform.

Generally, there exists a good agreement between the experimental and CFD results for the normalized volumetric flow rate profiles for the cases of low-moderate frequencies. The agreement

worsens at high frequencies for pressure gradient magnitudes and some deviation between the two datasets is noticed over the variations of A_0. This deviation can be attributed to the increased amplitude of oscillations induced in the experimental measurements by the thin foil boundary to accommodate for such large pressure gradients developed by the high frequency asymmetry waveform.

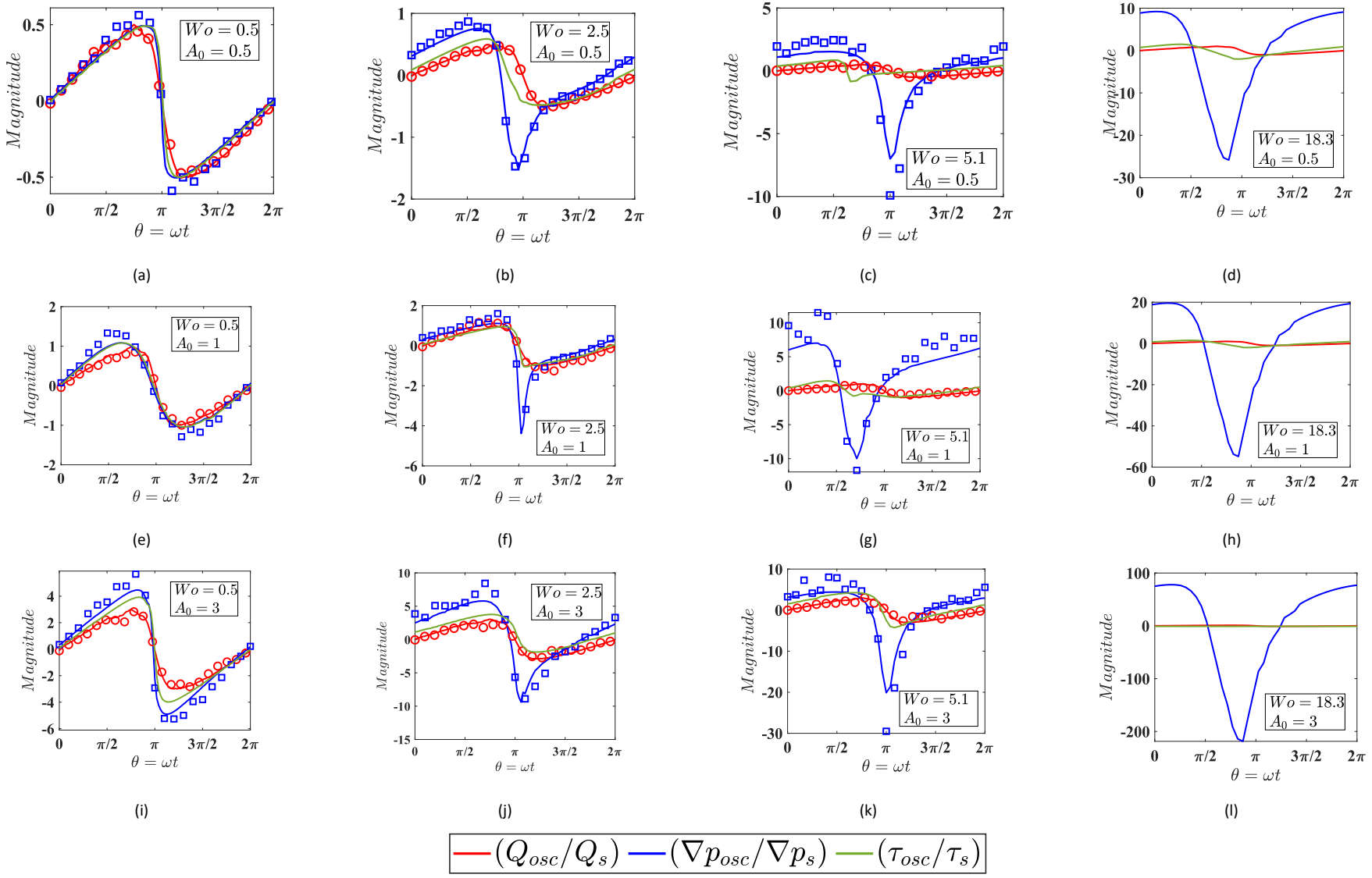

Figure 7-3: (a-l) Temporal variation of normalized flowrate, axial pressure gradient, and bottom wall shear stress for a **lagging asymmetric sinusoidal waveform**, across the rows is an increase in Wo and down the column is increasing A_0. Solid lines present the CFD results, and markers show the experimental results. Note that no experimental data exists for the wall shear stress and for the higher frequency $Wo = 18.3$ cases.

7.1.2 Half rectified sinusoidal pulsations

7.1.2.1 Positive half rectified profile

Figure 7-4 presents the temporal variation of the normalized oscillating volumetric flow rate, pressure gradient, and shear stress in response to a positive half rectified pulsation waveform. This waveform features an equal interval combination of a steady component and a (net forward directed) sinusoidal component co-existing in one cycle of pulsation. The effect of sinusoidal impulse is widely evident with the resulting pressure gradient amplification observed with the simultaneous increase in Wo and A_0. Although a substantial rise in pressure gradient is evident for higher Wo as has been seen for the two cases of asymmetry pulsation waveform. Compared to the symmetric sinusoidal waveforms from Figure 7-1 for higher frequencies $Wo = 5.1$ and $Wo = 18.3$, the characteristic traits of co-existence of pulsation presents a sharp impulse momentarily in the pressure gradient magnitudes as the flow rate tends to readjust and respond to the fast-oscillating, inertial dominant, forward directed sinusoidal component within the half-interval. An extensive hydrodynamics study offered by the positive half rectified waveforms lacks in the literature and previously has only been investigated for potentials of heat transfer enhancement by [110] and [104].

Typically, as inferred from the characteristics of symmetric sinusoidal and asymmetric sinusoidal for the lowest frequency of $Wo = 0.5$ across the range of A_0, the pressure gradient and the shear stress follow the shape of the flow rate profile. As the frequency is increased to $Wo = 2.5$ a developing phase lag is evident between the pressure gradient and the flow rate profiles. Additionally, there appears a distinct impulse (spike) in the pressure gradient profiles and the nature of profile differs during the commencement of sinusoidal flow rate component of half rectified waveform following to which the effect evens out to follow the sinusoidal flow pattern. Increased magnitudes of pressure gradient momentarily existing at phase π is observed across increasing Wo and is consistent with the increasing flow rate amplitude. Although there exists a considerable increase in the pressure gradient for the highest frequency $Wo = 18.3$ and highest flow rate amplitude $A_0 = 3$ compared to the symmetric sinusoidal pulsation waveforms.

Contrastingly, increasing Wo presents to have a minimal effect on the magnitude of the normalized oscillating bottom wall shear stress. At low values of Wo the shear stress remains in phase with the flow rate, while for higher Wo a phase lag develops and crucially is less compared to the pressure gradient. Increasing the flow rate amplitude results in an increase in the shear stress across the range of Wo as the corresponding fluid velocity and velocity gradients increase. This behaviour is typically also seen for the cases of asymmetric and symmetric sinusoidal pulsations.

There exists a good general agreement associated between the experimental and the CFD results for the normalized volumetric flow rate at the cases of low-moderate frequencies. The agreement worsens at high frequencies and corresponding A_0 for pressure gradient magnitudes with some deviation, existing due to the inflection points at the commencement of the sinusoidal component of the flow rate. This deviation is attributed to the amplified impulse produced from the solenoid control mechanism in experiments which governs the half rectified waveform.

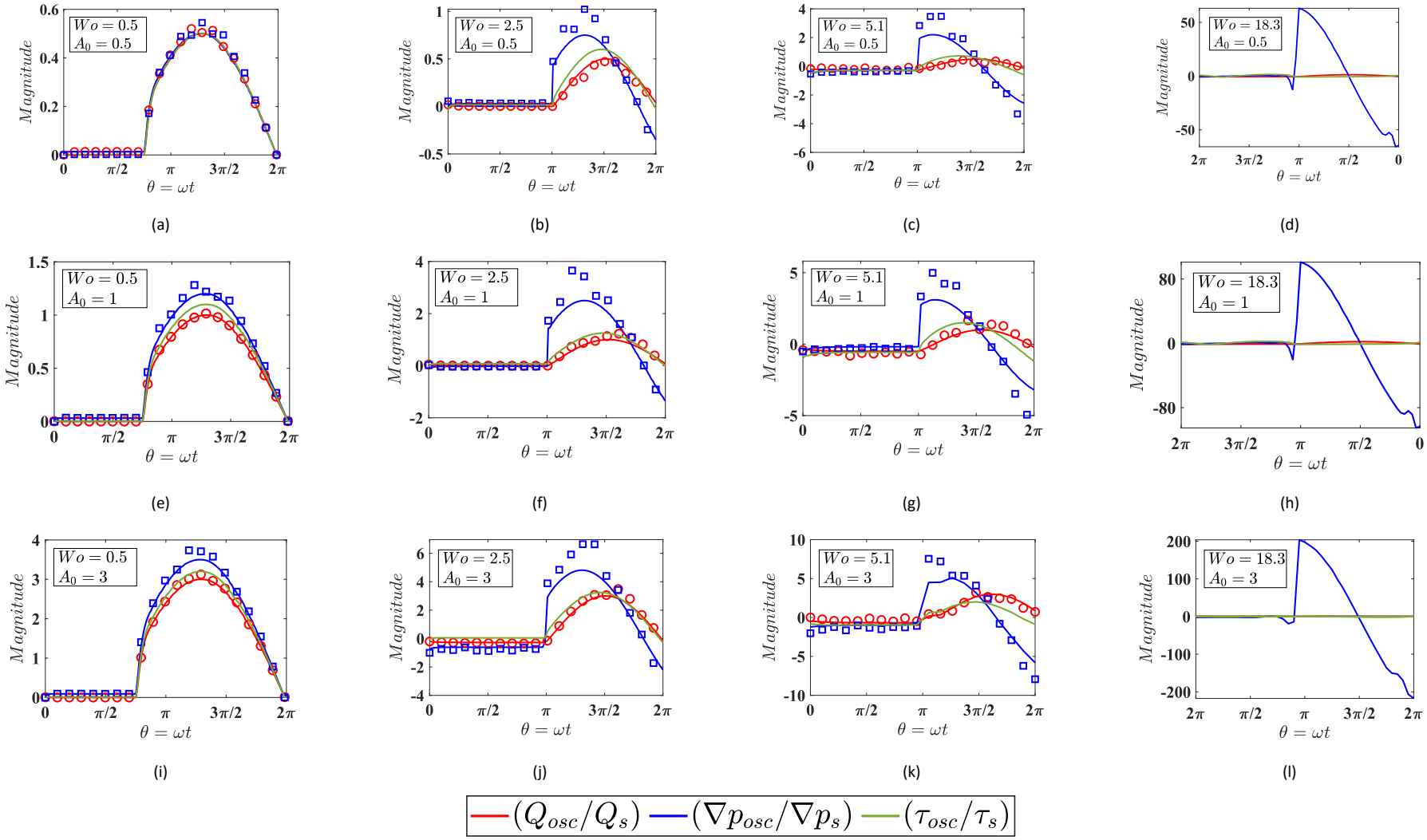

Figure 7-4: (a-l) Temporal variation of normalized flowrate, axial pressure gradient, and wall shear stress for a **positive half rectified waveform**, across the rows is an increase in Wo and down the column is increasing A_0. Solid lines present the CFD results, and markers show the experimental results. Note that no experimental data exists for the wall shear stress and for the higher frequency $Wo = 18.3$ cases.

7.1.2.2 Negative half rectified profile

Figure 7-5 presents the temporal variation of the normalized oscillating volumetric flow rate, pressure gradient, and shear stress in response to a negative half rectified pulsation waveform. This waveform features an equal interval combination of a steady component and a (net backward directed) sinusoidal component co-existing in one cycle of pulsation. The effect of sinusoidal impulse causing a withdrawal of flow rate is widely evident with the resulting pressure gradient amplification observed with the simultaneous increase in Wo and A_0. Although a substantial rise in pressure gradient is evident for higher Wo as has been seen for the two cases of asymmetry pulsation waveform. Compared to the symmetric sinusoidal waveforms from Figure 7-1 for higher frequencies $Wo = 5.1$ and $Wo = 18.3$, the characteristic traits of co-existence of pulsation presents a sharp impulse in the pressure gradient magnitudes as the flow rate tends to readjust and respond to the fast oscillating fast-oscillating, inertial dominant, backward directed sinusoidal component within the half-interval leading to a stronger withdrawal of the fluid. An extensive hydrodynamics study offered by the negative half rectified waveforms lacks in the literature and previously has only been investigated for potentials of heat transfer enhancement by [110] and [104].

A broadly similar inference can be drawn to the characteristics of symmetric sinusoidal and asymmetric sinusoidal for the lowest frequency of $Wo = 0.5$ across the range of A_0, the pressure gradient and the shear stress follow the shape of the flow rate profile. As the frequency is increased to $Wo = 2.5$ a developing phase lag is evident between the pressure gradient and the flow rate profiles. Additionally, there appears a distinct impulse (spike) in the pressure gradient profiles and the nature of profile differs during the commencement of sinusoidal flow rate component of half rectified waveform, as was also evident for the positive half rectified format. Increased magnitudes of pressure gradient at phase π is observed across increasing Wo and is consistent with the increasing flow rate amplitude. Although there exists a considerable increase in the pressure gradient for the highest frequency $Wo = 18.3$ and highest flow rate amplitude $A_0 = 3$ compared to the symmetric sinusoidal pulsation waveforms. Thus, a similar understanding is drawn in line with the positive half rectified waveform.

Contrastingly and in similar understanding to the positive half rectified waveform, increasing Wo presents to have a minimal effect on the magnitude of the normalized oscillating bottom wall shear stress. At low values of Wo the shear stress remains in phase with the flow rate, while for higher Wo a phase lag develops and crucially is less compared to the pressure gradient. Increasing the flow rate amplitude results in an increase in the shear stress across the range of Wo as the

corresponding fluid velocity and velocity gradients increase. This behaviour is typically also seen for the cases of asymmetric and symmetric sinusoidal pulsations.

There exists a good general agreement associated between the experimental and the CFD results for the normalized volumetric flow rate at the cases of low-moderate frequencies. The agreement worsens at high frequencies and corresponding A_0 for pressure gradient magnitudes with some deviation, existing due to the inflection points at the commencement of the sinusoidal component of the flow rate. This deviation is attributed to the amplified impulse produced from the solenoid control mechanism in experiments which governs the half rectified waveform.

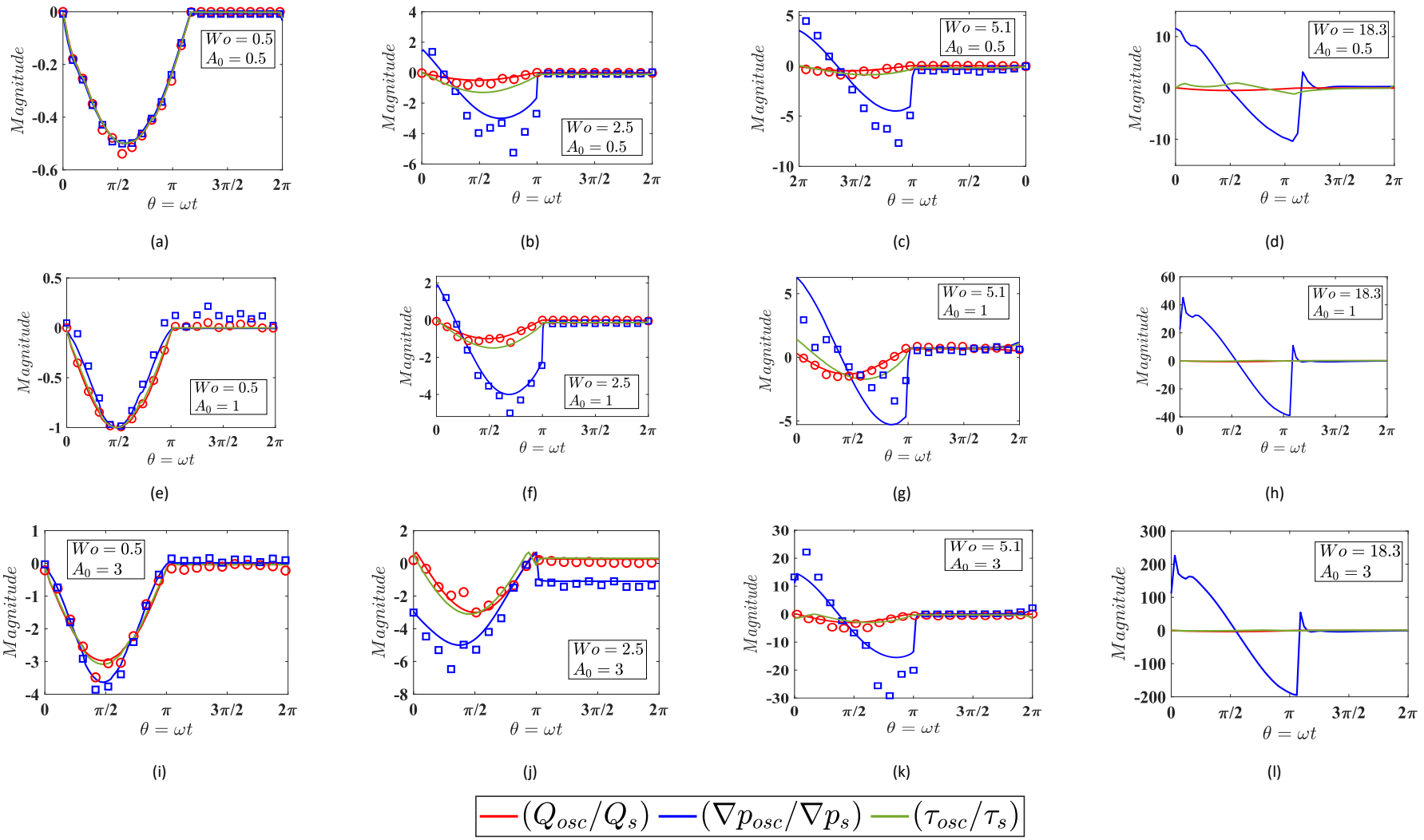

Figure 7-5: (a-l) Temporal variation of normalized flowrate, axial pressure gradient, and wall shear stress for a negative half rectified waveform, across the rows is an increase in Wo and down the column is increasing A_0. Solid lines present the CFD results, and markers show the experimental results. Note that no experimental data exists for the wall shear stress and for the higher frequency $Wo = 18.3$ cases.

7.2 Spatial variation of hydrodynamic parameters

Figure 7-6 presents a comparison of near side-wall effects at mid-plane $Y = y/a = 0.5$, along the transverse dimension $X = x/b$ observed for low to moderate frequency $Wo = 0.5, 2.5$ (top) higher frequencies $Wo = 5.1, 18.3$ (bottom) for a sinusoidal flowrate waveform at $A_0 = 0.5$. Low to moderate frequency oscillations exhibit parabolic profiles typical of laminar flow since viscous forces are dominant. However, as the frequency is increased, flattening of velocity profiles is observed in the bulk core regions, whereas the peak velocities (directionally independent) are attained in the vicinity of the near-wall regions $0.9 \leq x/b \leq 1$ as is seen for $Wo = 5.1$ at phase 2π and for $Wo = 18.3$ at phases $0\pi, 1.2\pi$. At higher frequencies, inertial forces are dominant in the core bulk region although viscous forces exist in the near-wall regions and are amplified. Since flow in the core regions cannot respond to the changing mass flow as fast as near the wall regions. These characteristics, termed as “annular effects”, were established by Richardson [38] and Richardson and Tyler [39] in their experimental study visualizing oscillatory flow through circular, square and ovular duct geometries. Subsequently several analytical and experimental studies by [83, 85], [124, 125] have reported these novel features offered by oscillatory flows. The oscillations are known to demonstrate a redistribution of bulk flow momentum in the transverse direction as the frequency is increased.

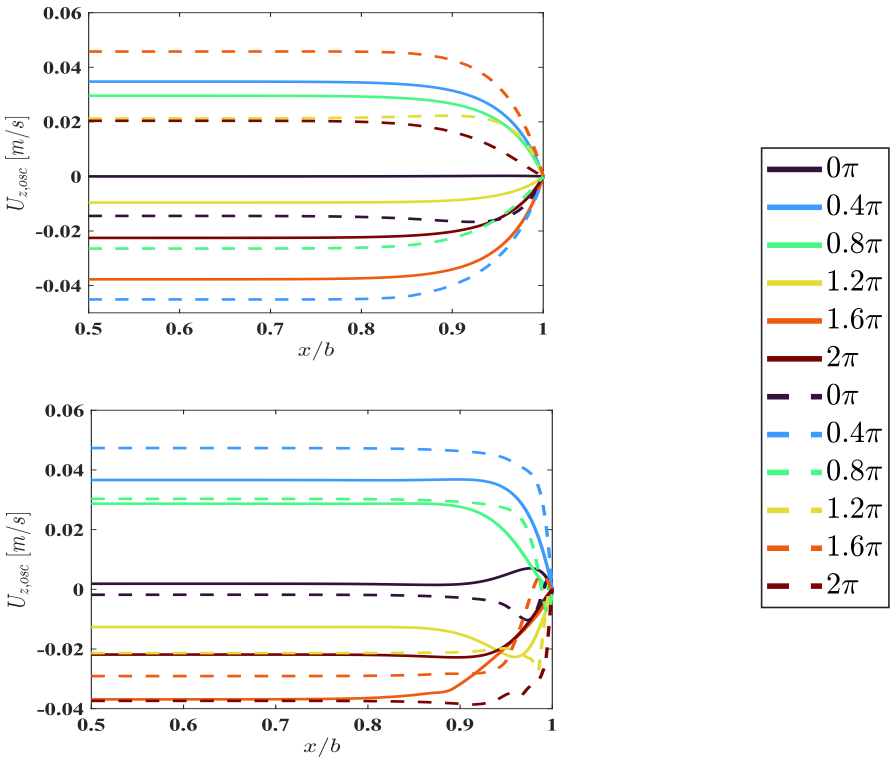

Figure 7-6: Near side-wall effects upon the oscillating axial velocity $U_{z,osc}$ for a sinusoidal pulsation waveform and flow rate amplitude $A_0 = 0.5$ at mid-plane $Y = y/a = 0.5$. The top image is for and $Wo = 0.5$ (solid lines) or $Wo = 2.5$ (dash lines). The bottom image is for $Wo = 5.1$ (solid lines) or $Wo = 18.3$ (dash lines)

Figure 7-7 presents the effect of ratio of mass flow rate to the velocity for the channel core at $y/a = 0$ and near-wall at $y/a = 0.95$ with varying pulsation frequencies for a symmetric sinusoidal waveform. Three distinct frequency regimes I, II and III are classified based on the characterisitics of the flow field and the evolution of velocity profiles. For a low-frequency regime (I), as a result of a quasi-steady behaviour exhibited by the typical parabolic velocity profiles, the ampltiude ratio is equal to unity. In the moderate-high frequency regime (II), with a corresponding increase in the frequency the ampliutde ratio begins to deviate from the quasi-steady value. It is worth noting that the change in the mass flowrate-velocity amplitude ratio is non-uniform throughout the cross-section of the duct. In the core regions $y/a = 0$, the magnitude of velocity decreases (as shown by the "annular effects" above) and in the near-wall vicinity at $y/a = 0.95$ the velocity magnitudes increase with a subsequent increase in Wo. In the case of high-highest frequency regime (III), it is observed that beyond a certain frequency, the velocity magnitudes in the near-wall region do not deviate further and are asymptotically constant. Thus the changes in the amplitude ratio of this regime becomes insignificant as the variation of velocity profile is very small.

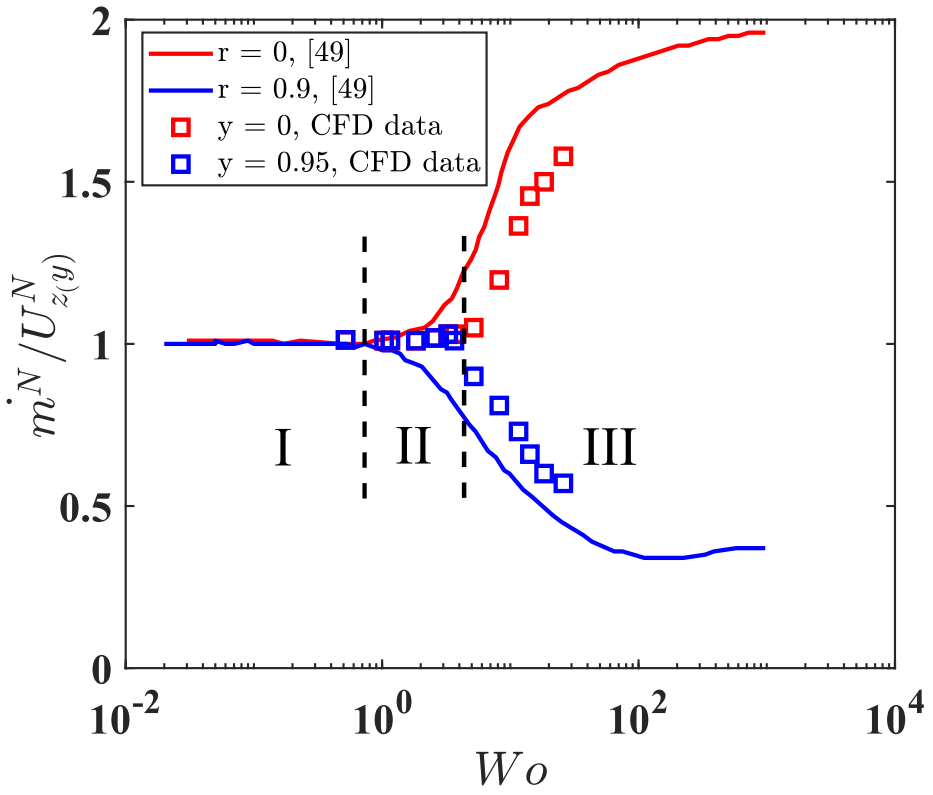

Figure 7-7: Variation of normalized mass flow rate amplitudes with respect to the normalized axial velocity at channel core $y/a = 0$ and near side-wall $y/a = 0.95$ as a function of the pulsation frequency Wo for symmetric sinusoidal at $A_0 = 1$. Symbols represent the CFD data while lines represent analytical solutions from Ünsal *et al.* [49].

Flow reversal phenomenon is widely experineced in applications involving metering of flow rate, mixing and entrainment [51] Separately, in medical applications the measurement of flow reversal is crucial in the celebrospinal fluid motion in the human brain and the blood flow through uterine during uterine contraction stages [51]. Flow reversal can be described as the coexistence of positive and negative magnitudes of velocities at a given time instant. Flow reversal typically exists in the near-wall vicinites for high frequency flows and simultaneously propogates away from wall at certain instances. Occurrence of flow reversal is dependent on the associated pulsation frequency Wo and the flowrate amplitude A_0. At high frequency cases, as the shear stress magnitude diminishes in the direction of flow, a flow reversal commences in the near side-wall vicinity, termed as “near-wall reversal” with a maximum amplitude of reversal. As the flowrate amplitude is increased, the maximum flow reversal amplitude is shifted away from the near-wall vicinity and thus is termed as “off-wall reversal”. Flow reversal is found to enhance the spanwise (transverse) momemtum transport of the flow. These have been previously observed in experimental studies by Ünsal *et al.* [49], Aygun and Aydin [53], Haddad *et al.* [51] for high frequency pulsations through channels and pipes.

In the current study, flow reversal is identified across all the waveforms studied. The phenomenon exists for various combinations of Wo and A_0 and can be visualised in the CFD results by examining the pulsation axial velocity ($U_{z,p}$) profiles along the duct height (y/a) at $x/b = 0$. A few cases of interest are highlighted in Figure 7-8 where the occurence of near-wall and off-wall flow reversal is clearly distinguished for the highest frequnecy of $Wo = 18.3$. For example, in the case of a lagging asymmetric waveform at a low flowrate amplitude $A_0 = 0.5$ a small near-wall flow reversal is evident for the phase 1.2π. For the half rectified waveforms at high flowrate amplitude $A_0 = 3$, the distinction between two flow reversal phenomenon is evident wherein near side-wall flow reversal occurs at $0.4\pi, 0.8\pi$ and $0\pi, 1.8\pi$ for the two cases of negative and positive half rectification respectively and an off-wall flow reversal occurs for phases $0.4\pi, 0.8\pi$ of positive half recitifed profile.

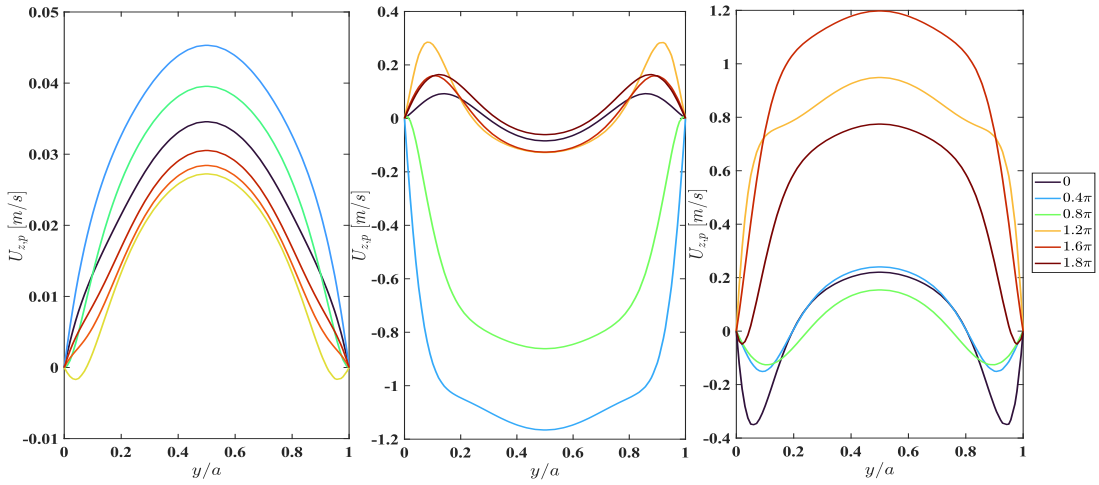

Figure 7-8: Pulsation velocity ($U_{z,p}$) profiles at $x/b = 0$ and along the duct height y/a for (a) Lagging asymmetric waveform at $Wo = 18.3, A_0 = 0.5$, (b) Negative half rectified waveform at $Wo = 18.3, A_0 = 3$ and (c) Positive half rectified waveform at $Wo = 18.3, A_0 = 3$. Data is presented for 6 equidistant time intervals of a cycle.

7.2.1 Velocity and shear stress distributions

In this section the spatial and temporal variation of the oscillating axial velocity profile ($U_{z,osc}$) is described in the fully developed region of the channel at $z = 0.3\ m$. The corresponding oscillating fluid shear stress (τ_{osc}) profiles are also provided. Line plots are shown as a function of the non-dimensional minichannel height ($Y = y/a$) for near-sidewall ($x/b = 0.95$) and core ($x/b = 0$) regions of the minichannel. Additionally, for each set of images, slice plane contour and vector plots

of the pulsating axial velocity ($U_{z,p}$) and pulsating fluid shear stress (τ_p) are shown for 5 phases of the pulsation in phase steps of $\pi/2$. The vectors for the velocity plots capture the directional variation and magnitudes induced by the effect of flow pulsation. The same velocity plot scale is used for all planes, whereas the shear stress plots are qualitative only, showing only the shear stress distribution in the cross-section. The pulsating data helps to better understand the annular and flow reversal effects described previously, as this information cannot be clearly understood from the oscillating data alone. Data for this section is obtained solely from the CFD model.

7.2.1.1 Symmetric sinusoidal pulsation waveform

Figure 7-9, Figure 7-10, Figure 7-11 respectively represent flow fields resulting from sinusoidal waveforms at a frequency of 0.02 *Hz* ($Wo = 0.5$) and flow rate amplitudes of $A_0 = 0.5, 1, 3$. These flows exhibit quasi-steady behaviour due to the prominence of viscous effects and the resulting oscillating velocity profiles resemble the parabolic profiles of a conventional laminar duct flow. As a result, the phase shift between the velocities in the channel core and near-wall is non-existent [35, 41]. The maximum magnitude of the oscillatory velocity occurs at the centre of the minichannel ($x/b = 0,\ y/a = 0.5$) and a minimum exists in the near-wall regions. Correspondingly the shear stress profiles react in a similar manner to the slow momentum transport of the pulsation. The presence of viscous forces in the near-wall regions lead to an increased velocity gradient and is distinctly noted from the profiles at $x/b = 0.95$ which indicates a local peak at $y/a = 0.5$, whereas in the channel core regions $x/b = 0$, the profiles converge to zero as the velocity reaches a maximum. The velocity contours and vectors, Figure 7-9 (e-i) show an acceleration portion of the flow pulsation between phases $0 - \pi$ with a maximum velocity magnitude at $\pi/2$. The deceleration portion of the cycle is followed between the phases $\pi - 2\pi$ with the cycle minimum occurring at $3\pi/2$. However, the withdrawal of flow is ineffective due for the weak flow rate amplitude of $A_0 = 0.5$. The shear stress contours show the conventional effect with the existence of high gradients of velocity in the near-wall regions and a local minimum in the central regions. Thus, the features exhibited due to a pulsation are not distinctly evident due to slow pulsation timescales across the intervals in a cycle. For $A_0 = 1$ and $A_0 = 3$, the effect of oscillation is further pronounced wherein the velocity profiles respond swiftly at $A_0 = 1$ during both acceleration and deceleration stages. The deceleration cycle cancels out the underlying steady flow as is seen from the velocity contours and vectors, Figure 7-10 (e-i) for phase $3\pi/2$. At the highest flowrate amplitude of $A_0 = 3$, Figure 7-11, the pulsation velocity contours and vectors show a distinct effect of the increased strength of the oscillation component over the steady flow across all time intervals. Correspondingly there is an increase in the shear stress magnitudes as noted from the contours (j-n) and further increased velocity gradients exist in the near-wall regions which is evident from the shear stress profiles.

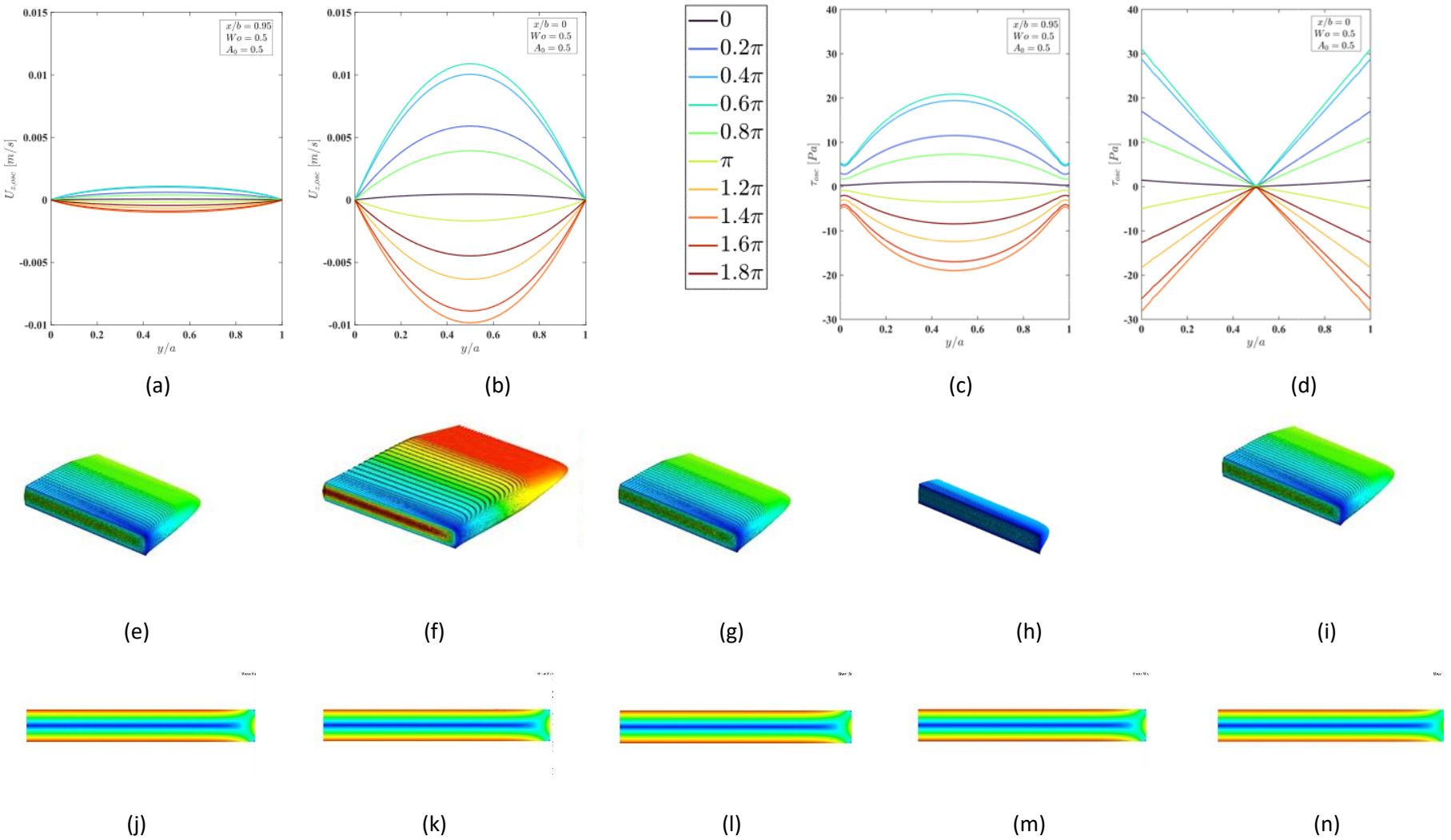

Figure 7-9: Sinusoidal waveform with flow rate amplitude $A_0 = 0.5$ and frequency 0.02 Hz ($Wo = 0.5$). (a-d) oscillating axial velocity ($U_{z,osc}$) and fluid shear stress (τ_{osc}) profiles along the duct height (y/a) for near-side-wall ($x/b = 0.95$) and central ($x/b = 0$) regions. (e-i) pulsating velocity contour plots at z = 300mm for 5 phases of a pulsation, and (j-n) corresponding fluid shear stress contours.

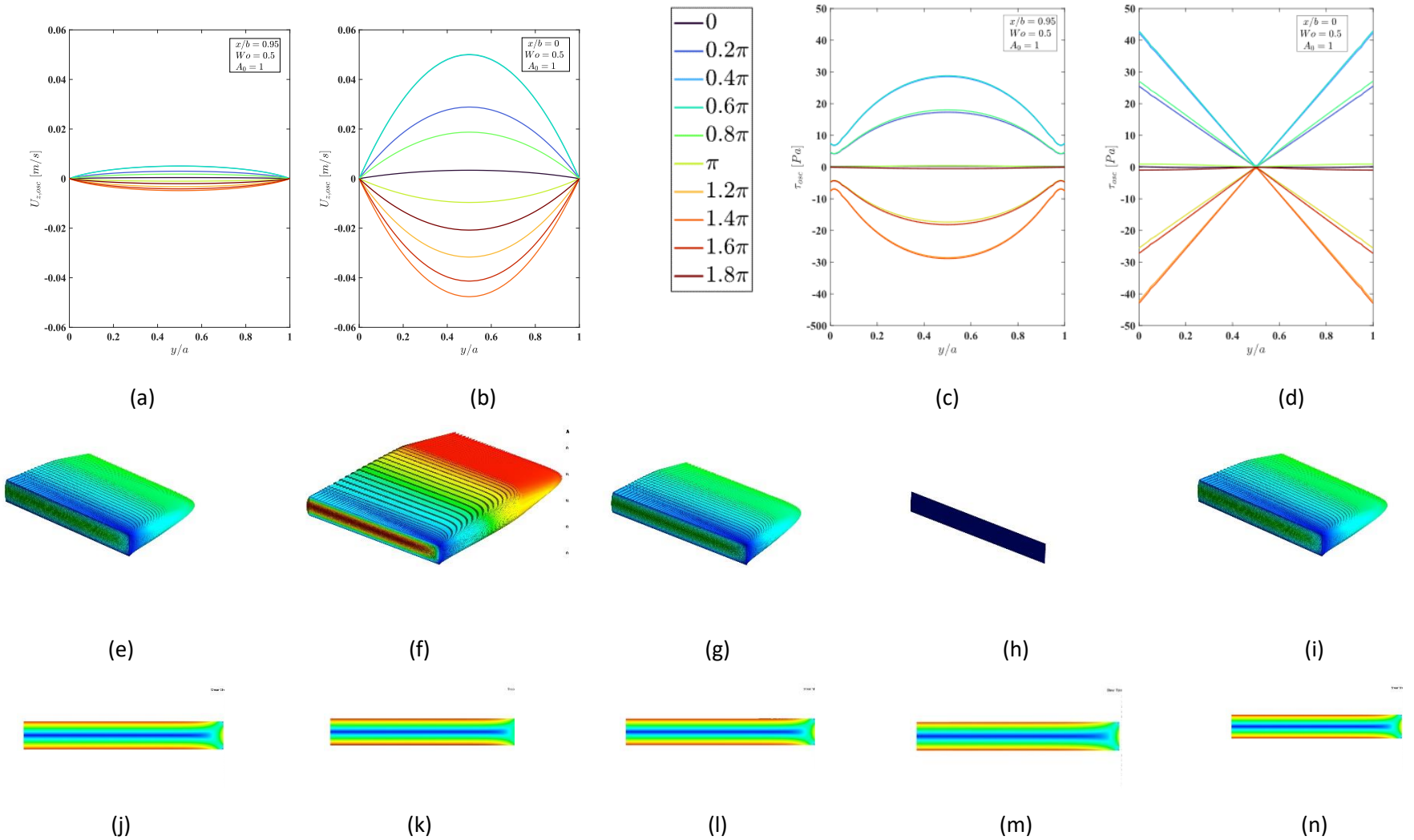

Figure 7-10: Sinusoidal waveform with flow rate amplitude $A_0 = 1$ and frequency 0.02 Hz ($Wo = 0.5$). (a-d) oscillating axial velocity ($U_{z,osc}$) and fluid shear stress (τ_{osc}) profiles along the duct height (y/a) for near-side-wall ($x/b = 0.95$) and central ($x/b = 0$) regions. (e-i) pulsating velocity contour plots at z = 300mm for 5 phases of a pulsation, and (j-n) corresponding fluid shear stress contours.

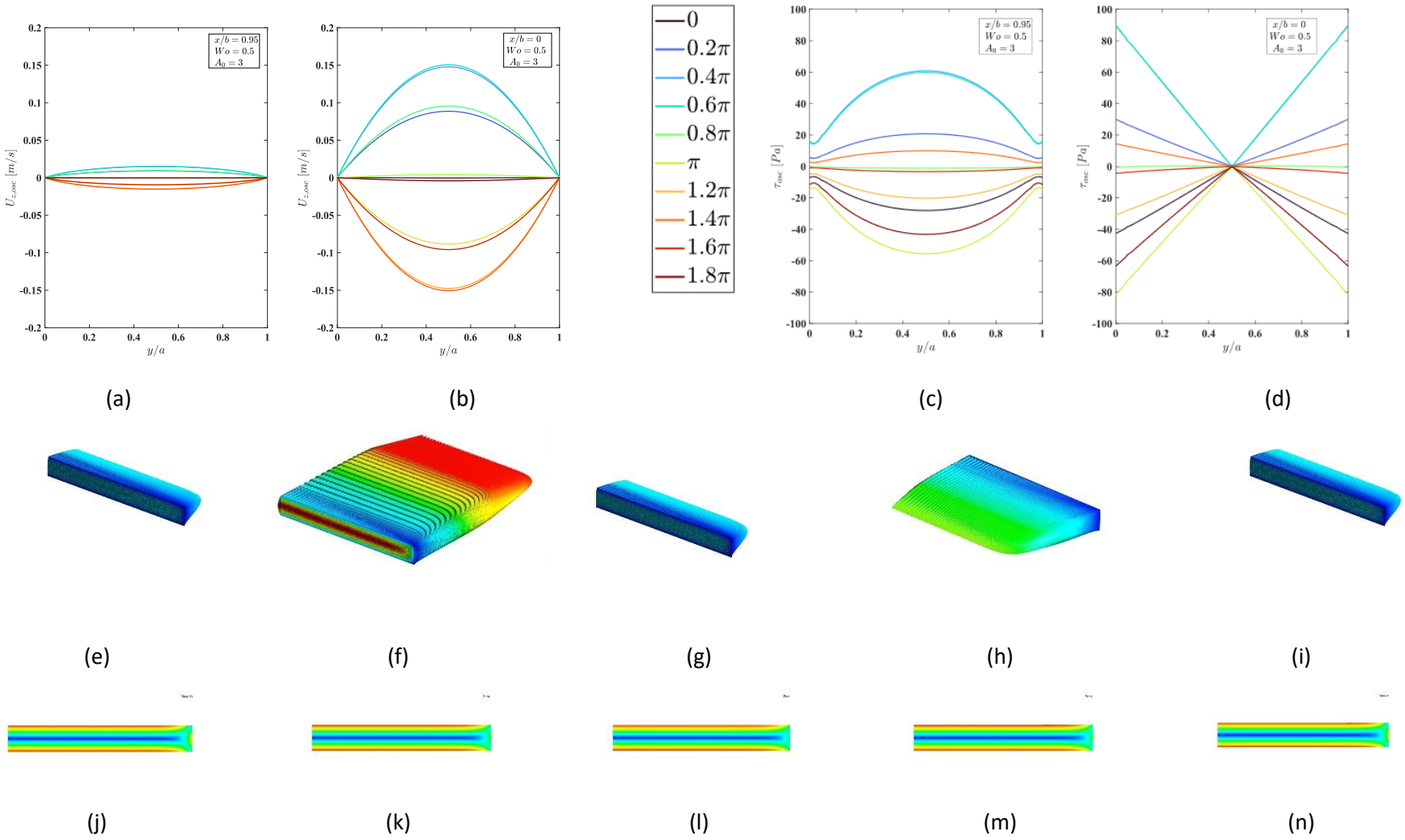

Figure 7-11: Sinusoidal waveform with flow rate amplitude $A_0 = 3$ and frequency 0.02 Hz ($Wo = 0.5$). (a-d) oscillating axial velocity ($U_{z,osc}$) and fluid shear stress (τ_{osc}) profiles along the duct height (y/a) for near-side-wall ($x/b = 0.95$) and central ($x/b = 0$) regions. (e-i) pulsating velocity contour plots at z = 300mm for 5 phases of a pulsation, and (j-n) corresponding fluid shear stress contours.

Figure 7-12, Figure 7-13, Figure 7-14, respectively represent flow fields resulting from sinusoidal waveforms at a frequency of 0.5 Hz ($Wo = 2.5$) and flow rate amplitudes of $A_0 = 0.5,1,3$.

Low flow rate amplitude $A_0 = 0.5, 1$ flows highlight the influence of a build-up of inertial forces in the bulk core regions of the channel as the oscillating axial velocity profiles reflect a directional change for certain intervals of the cycle due to the faster fluid momentum, as the time scale of pulsation are short. Sinusoidal flows at $Wo = 2.5$ and $A_0 = 0.5$ indicate a minor effect of pulsation on the oscillating axial velocity profiles as the oscillating amplitude of flow is weaker compared to the stronger underlying steady flow, which can also be interpreted from the velocity contours and vectors across the cycle. However, the early signs of a phase shift between the channel core velocity profiles and near-wall velocity profiles for majority of the phases between $0 - 1.8\pi$ are observed since the presence of near-wall viscous forces tends to influence the effect of pulsation [51, 57]. The shear stress magnitudes also indicate a slight increase compared to the low frequency case of $Wo = 0.5$. Further at $A_0 = 1$, the oscillating component shows an existence of steeper velocity gradients between the wall and core regions at $x/b = 0$ which results from an increased velocity of pulsation. Similarly, the velocity contours and vectors Figure 7-13 (e-i) demonstrate the pronounced effect of pulsation, and the decelerating stage of motion between phases $\pi - 2\pi$ is distinguishable from the contours Figure 7-13 (j-n) of the shear stress magnitude.

High flowrate amplitude $A_0 = 3$ case shows a sharp increase in the oscillating velocity magnitudes in the channel core at $x/b = 0$, since the effect of oscillating is far stronger compared to the underlying steady component. However due to the inherent traits of a slow symmetric sinusoidal pulsation, near wall $x/b = 0.95$ velocity magnitudes continue to be maintained to a minimum and only a minor phase lag exists between the two regions as noted from the oscillating velocity profiles. The velocity contours and vectors reflect a substantial increase in the magnitudes of pulsation velocities during the peaks of acceleration stage $\pi/2$ and deceleration stage $3\pi/2$ compared to the low flowrate amplitudes. Overall, there exist high magnitudes of oscillating shear stress during both accelerating and decelerating stages in the near-wall and core channel regions, which also is a result of the phase lag between the flowrate and pressure gradient as noted from Figure 7-1 (j) and increased magnitudes of velocity at $A_0 = 3$. This effect can also be identified from the pulsating shear stress contour plots Figure 7-14 (j-n) for the cases of $\pi/2$ and $3\pi/2$ which presents a sharp reaction to higher amplitude of pulsation.

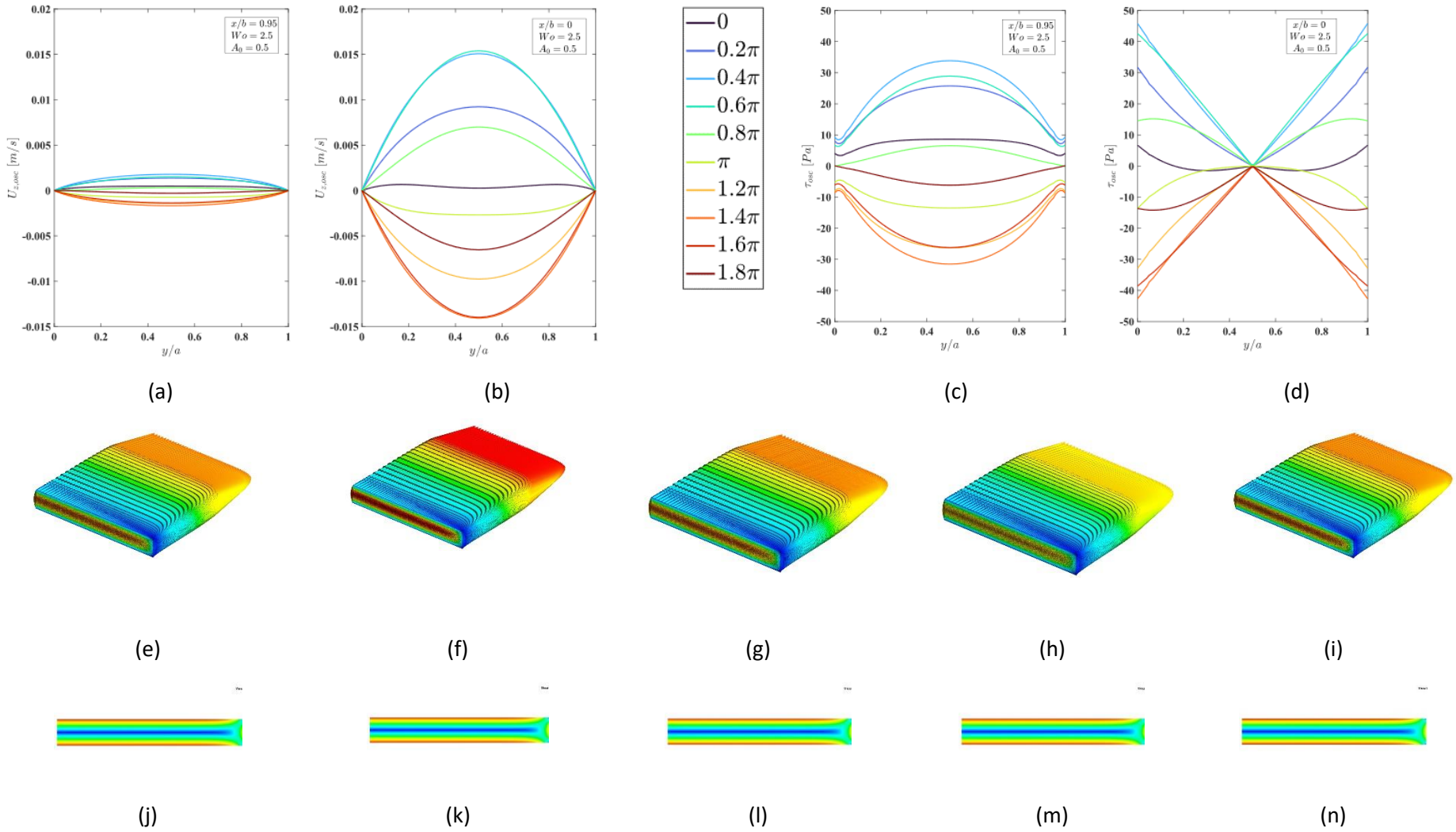

Figure 7-12: Sinusoidal waveform with flow rate amplitude $A_0 = 0.5$ and frequency 0.5 Hz ($Wo = 2.5$). (a-d) oscillating axial velocity ($U_{z,osc}$) and fluid shear stress (τ_{osc}) profiles along the duct height (y/a) for near-side-wall ($x/b = 0.95$) and central ($x/b = 0$) regions. (e-i) pulsating velocity contour plots at z = 300mm for 5 phases of a pulsation, and (j-n) corresponding fluid shear stress contours.

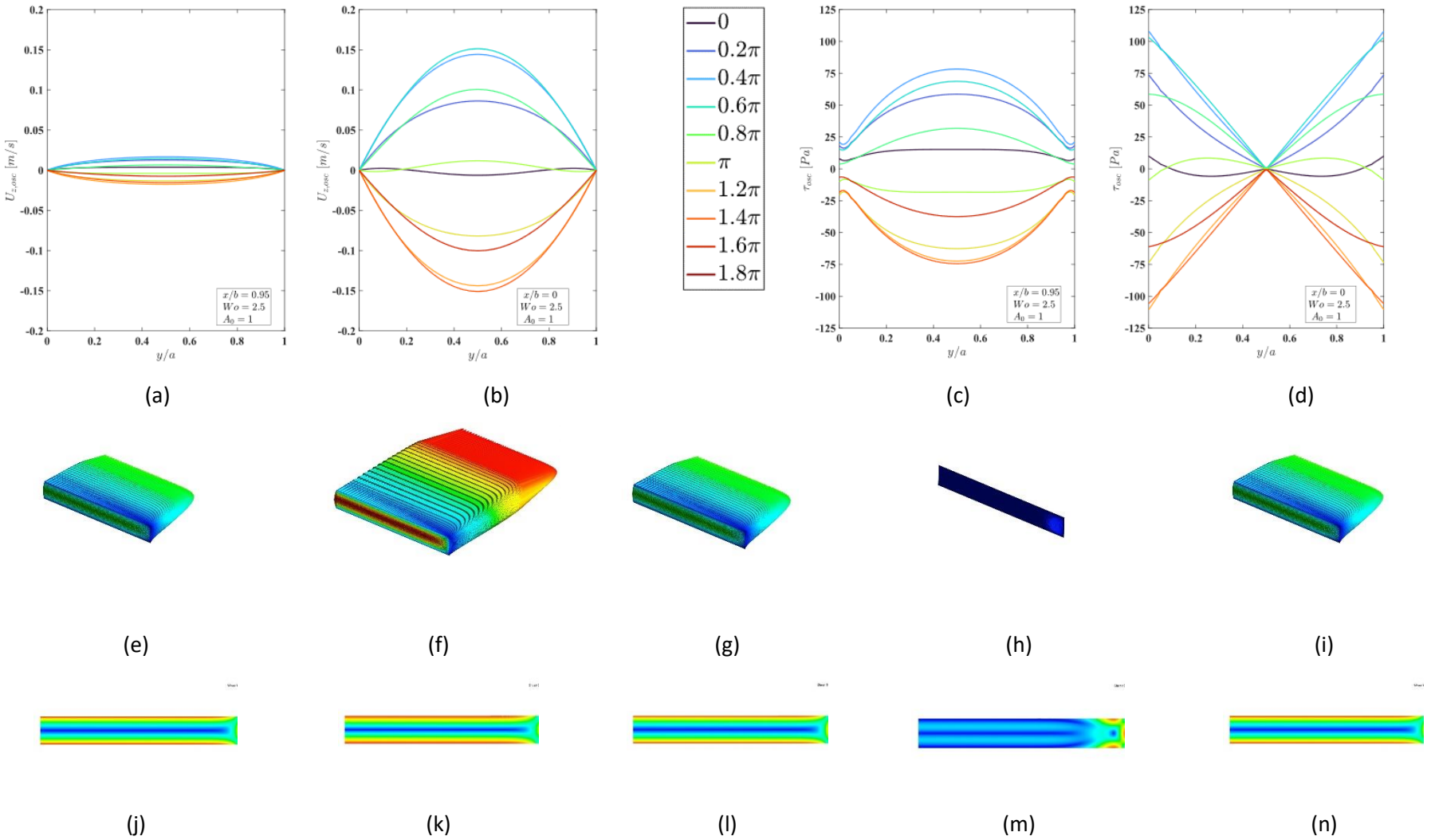

Figure 7-13: Sinusoidal waveform with flow rate amplitude $A_0 = 1$ and frequency 0.5 Hz ($Wo = 2.5$). (a-d) oscillating axial velocity ($U_{z,osc}$) and fluid shear stress (τ_{osc}) profiles along the duct height (y/a) for near-side-wall ($x/b = 0.95$) and central ($x/b = 0$) regions. (e-i) pulsating velocity contour plots at z = 300mm for 5 phases of a pulsation, and (j-n) corresponding fluid shear stress contours.

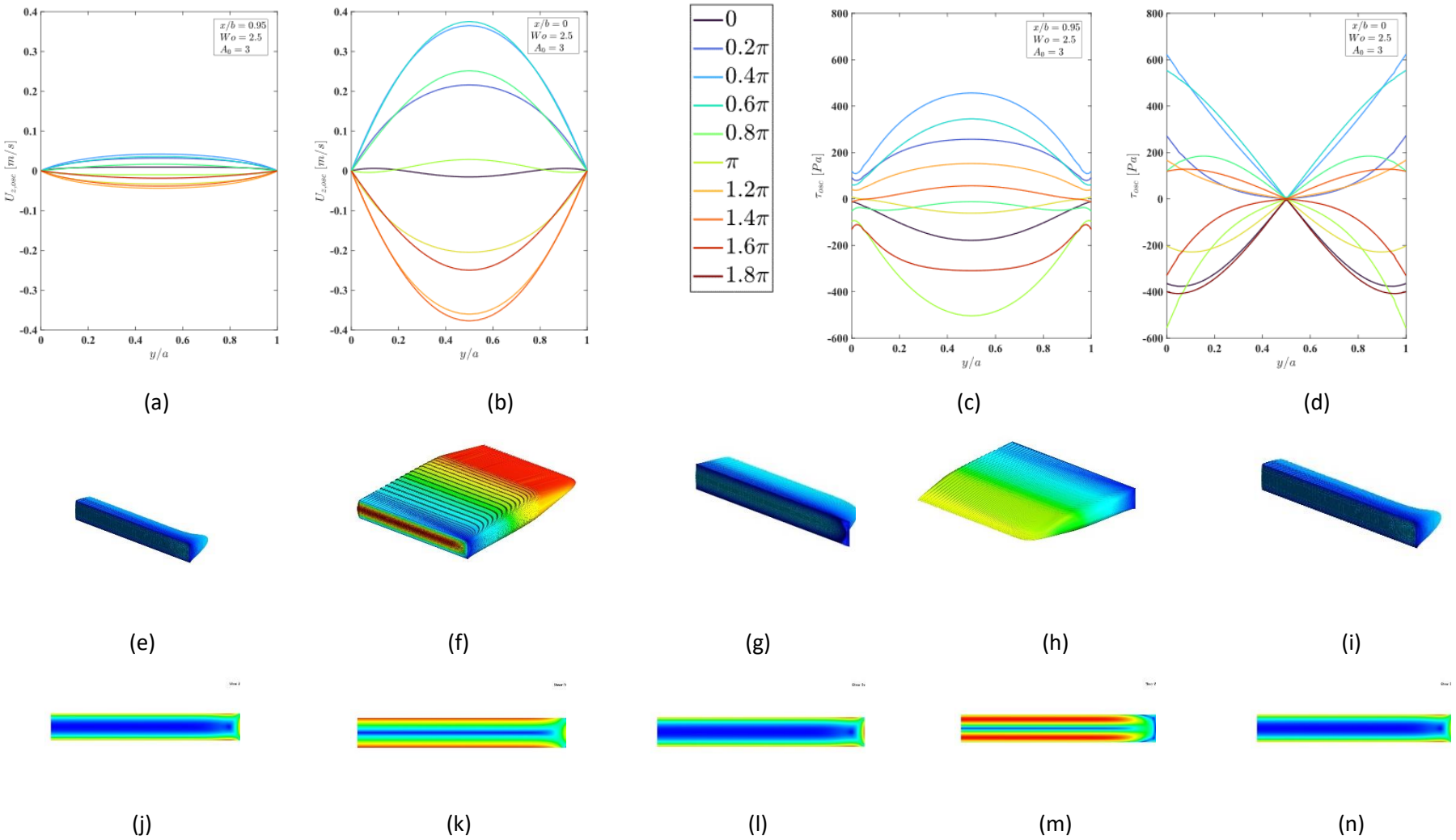

Figure 7-14: Sinusoidal waveform with flow rate amplitude $A_0 = 3$ and frequency 0.5 Hz ($Wo = 2.5$). (a-d) oscillating axial velocity ($U_{z,osc}$) and fluid shear stress (τ_{osc}) profiles along the duct height (y/a) for near-side-wall ($x/b = 0.95$) and central ($x/b = 0$) regions. (e-i) pulsating velocity contour plots at z = 300mm for 5 phases of a pulsation, and (j-n) corresponding fluid shear stress contours.

Figure 7-15, Figure 7-16, Figure 7-17 respectively represent flow fields resulting from sinusoidal waveforms at a frequency of 2 Hz ($Wo = 5.1$) and flow rate amplitudes of $A_0 = 0.5,1,3$.

Low flowrate amplitude $A_0 = 0.5$ presents an amplified effect of pulsation for the symmetric sinusoidal despite maintaining the less effective flow rate amplitude compared to be previous low-moderate frequency cases. A phase lag between the channel core $x/b = 0$ oscillating velocity magnitudes and the near-wall $x/b = 0.95$ exists for of phases $0, 0.6\pi, \pi, 1.6\pi, 1.8\pi$. The velocity profiles at the centre of the minichannel no longer follow a parabolic profile at all phases of the pulsation. Peak velocities are observed near the top and bottom walls for phases 0π and 1.8π. This is attributed to the strengthening of inertial forces in the core regions and the presence of high wall viscous effects as the fluid displacement time scales are shorter. Similarly, the peak magnitudes of velocity in the near wall and core channel region at $y/a = 0.5$ are higher compared to the low frequency cases. The contour charts for velocity and shear stress Figure 7-15 (e-i), (j-n) do not show any distinctive features of pulsation due to the weaker flow rate amplitude of oscillation, while a typical maximum and minimum velocity magnitude exists for phases $\pi/2$ and $3\pi/2$ respectively.

Similarities exist in the inherent nature of velocity profiles at $A_0 = 1$, as the stronger oscillating component results in a more varied spanwise effect of the oscillating velocity. The velocity contours and vector plots present a maximum magnitude of acceleration cycle at phase $\pi/2$. A weaker deceleration cycle with high local near wall velocity exists for phase $3\pi/2$. Analogous to the velocity profiles, a spanwise amplification in the velocity gradients is observed from the shear stress profiles in the near-wall and core regions.

At the highest flowrate amplitude ($A_0 = 3$) for this frequency, the fast oscillations result in a phase shift between the channel core $x/b = 0$ and near-wall $x/b = 0.95$ regions for the velocity profiles. In addition to the increased mass flowrate the time scale of pulsation is reduced to the fluid viscous time scales in comparison to the lower frequency case, significant effects in the spanwise direction of the velocity contours and vectors are observed. The peak cycle pulsation is attained during the acceleration stage at phase $\pi/2$ from Figure 7-17, while pronounced near wall velocity is evident throughout the other intervals of the pulsation cycle and is particularly amplified for the deceleration stage at phase $3\pi/2$, Figure 7-17 (h). As a result of increased near-wall velocities [48, 49, 57] explained using the phenomenon of Richardson's annular effects demonstrated by Figure 7-6, the resulting high oscillating velocity gradients (shear stress magnitudes) as seen from Figure 7-17 (j-n), reflect the influence of high near-wall velocity magnitudes leading to the onset of flow reversal for both the near-wall and core regions. The phenomenon of flow reversal as explained in Figure 7-8 shows a co-existence of simultaneous positive and negative magnitudes of velocity at given instant phase π is seen in Figure 7-17 (g).

Furthermore, as an effect of an increased phase lag between the flowrate and pressure gradient from the Figure 7-1 (k), an occurrence of a phase shift for the oscillating shear stress profiles during both stages of acceleration and deceleration is evident.

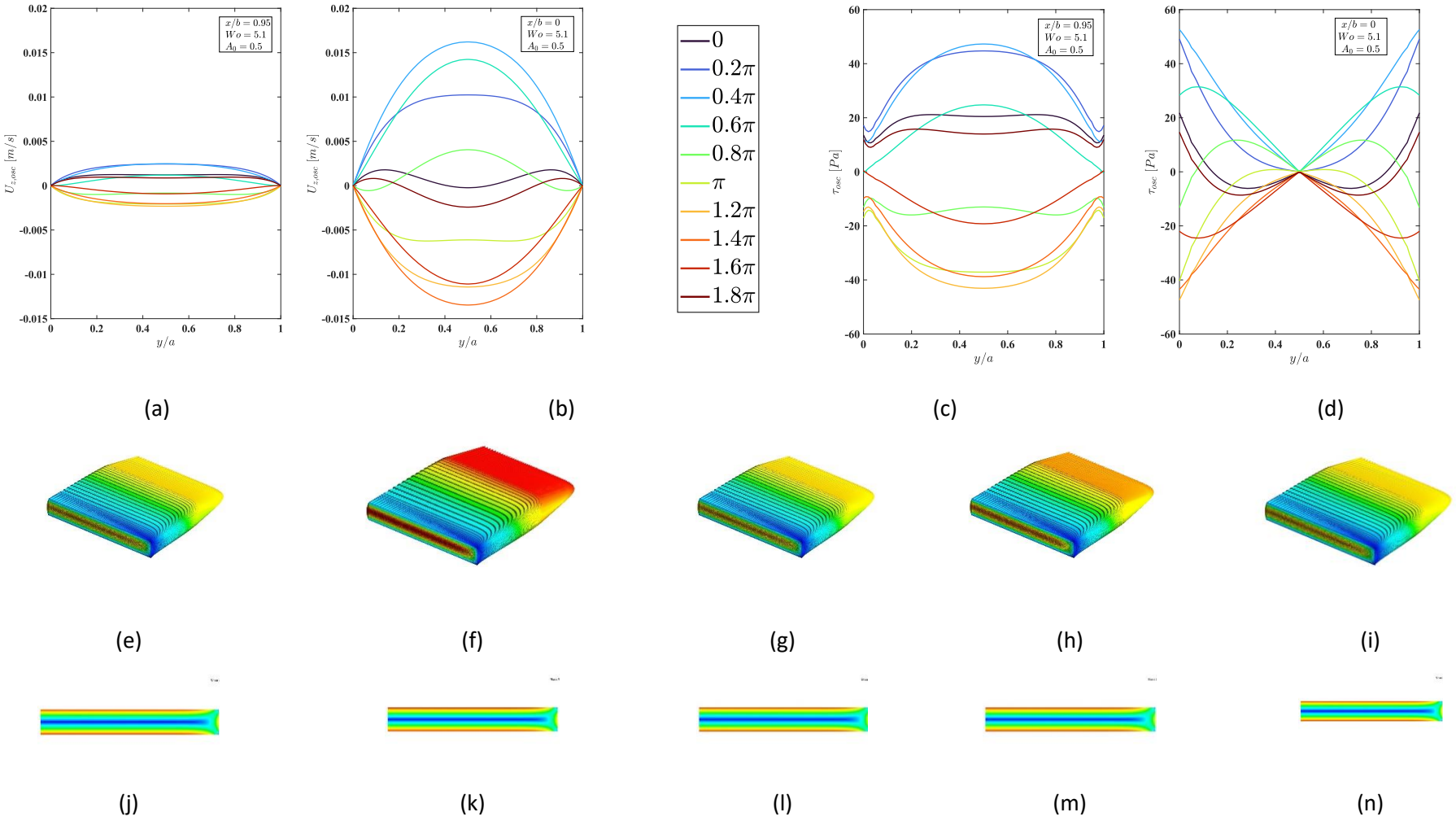

Figure 7-15: Sinusoidal waveform with flow rate amplitude $A_0 = 0.5$ and frequency 2 Hz ($Wo = 5.1$). (a-d) oscillating axial velocity ($U_{z,osc}$) and fluid shear stress (τ_{osc}) profiles along the duct height (y/a) for near-side-wall ($x/b = 0.95$) and central ($x/b = 0$) regions. (e-i) pulsating velocity contour plots at z = 300mm for 5 phases of a pulsation, and (j-n) corresponding fluid shear stress contours.

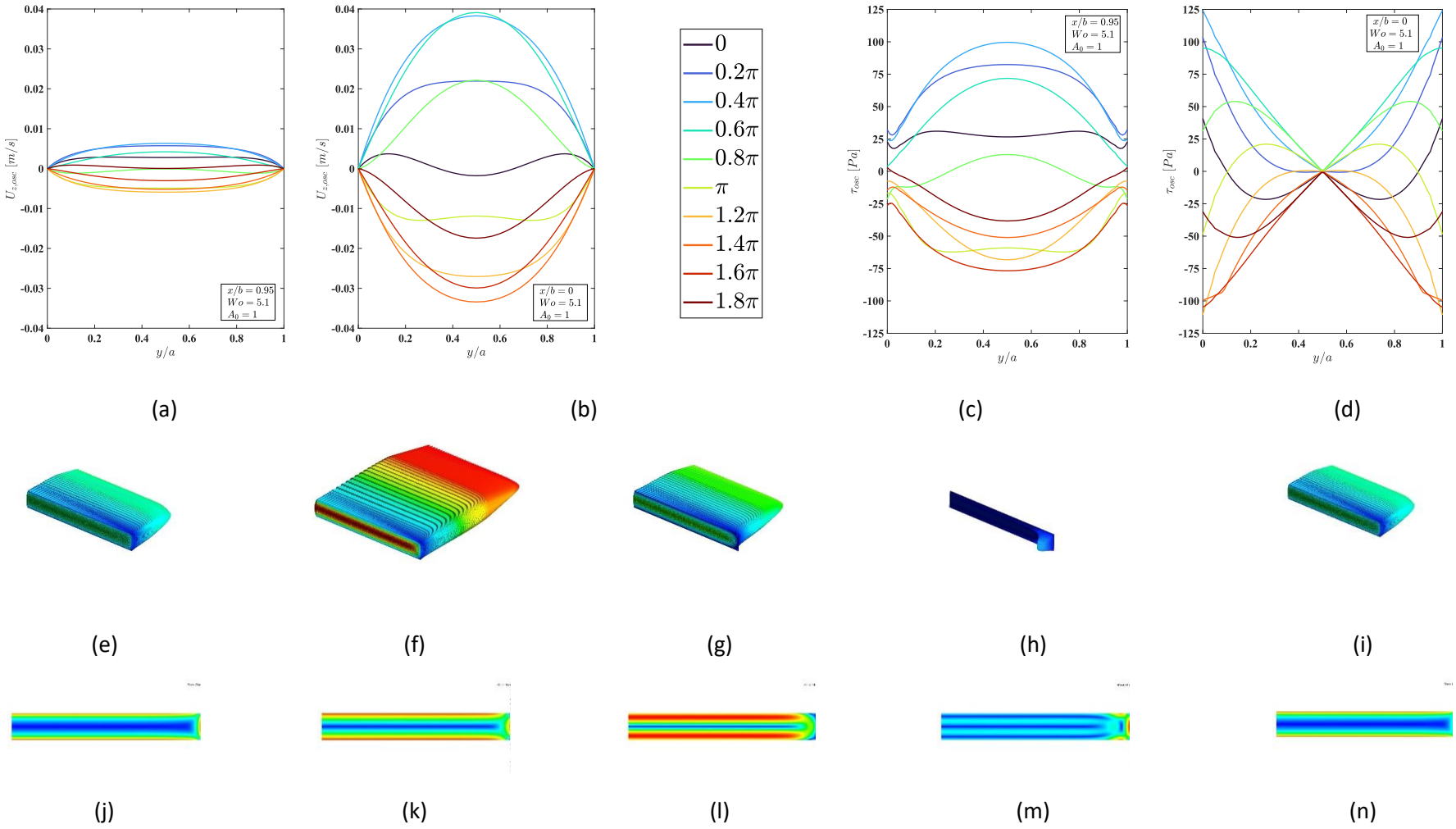

Figure 7-16: Sinusoidal waveform with flow rate amplitude $A_0 = 1$ and frequency 2 Hz ($Wo = 5.1$). (a-d) oscillating axial velocity ($U_{z,osc}$) and fluid shear stress (τ_{osc}) profiles along the duct height (y/a) for near-side-wall ($x/b = 0.95$) and central ($x/b = 0$) regions. (e-i) pulsating velocity contour plots at z = 300mm for 5 phases of a pulsation, and (j-n) corresponding fluid shear stress contours.

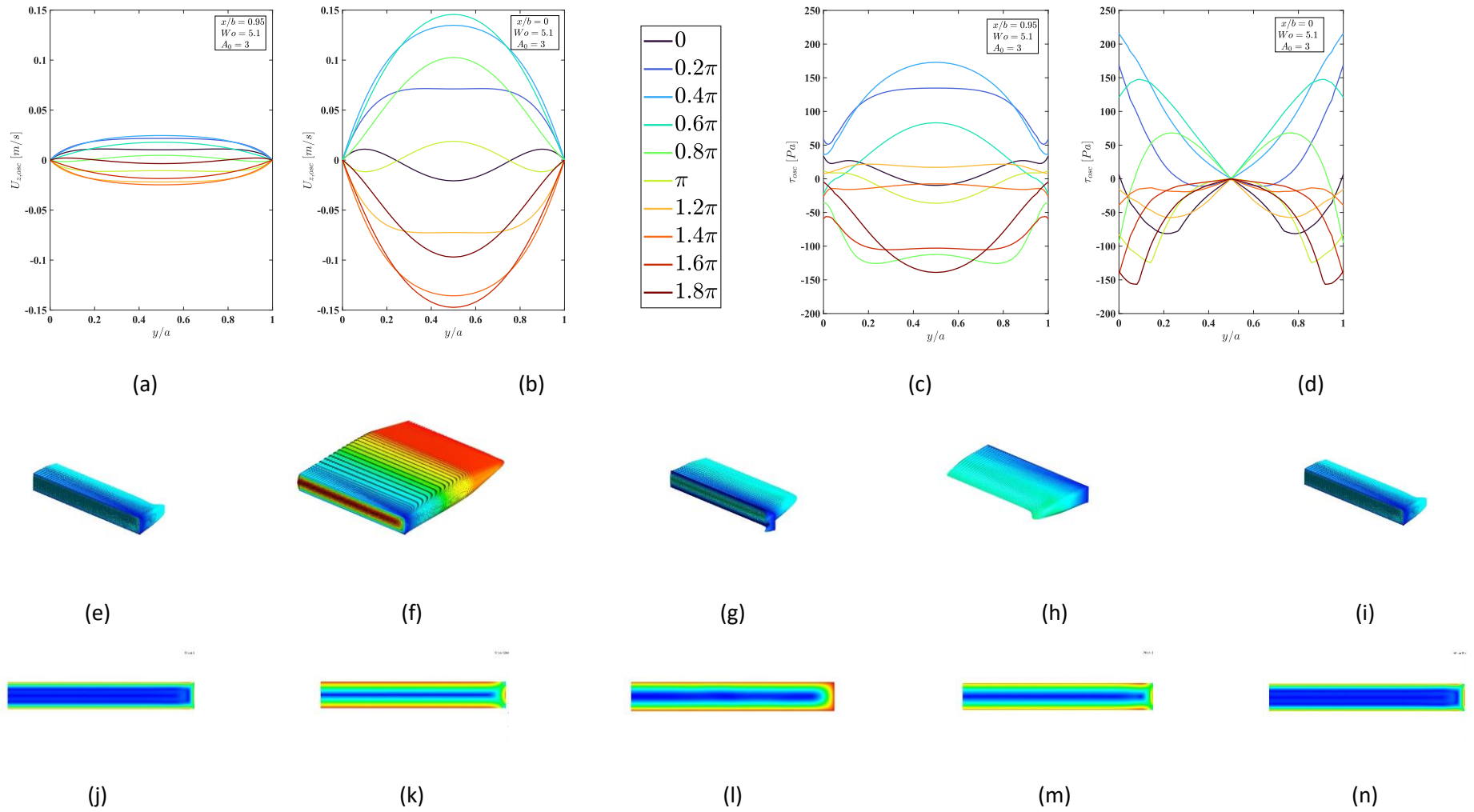

Figure 7-17: Sinusoidal waveform with flow rate amplitude $A_0 = 3$ and frequency 2 Hz ($Wo = 5.1$). (a-d) oscillating axial velocity ($U_{z,osc}$) and fluid shear stress (τ_{osc}) profiles along the duct height (y/a) for near-side-wall ($x/b = 0.95$) and central ($x/b = 0$) regions. (e-i) pulsating velocity contour plots at z = 300mm for 5 phases of a pulsation, and (j-n) corresponding fluid shear stress contours.

Figure 7-18, Figure 7-19, Figure 7-20 respectively represent flow fields resulting from sinusoidal waveforms at a frequency of 25 Hz ($Wo = 18.3$) and flow rate amplitudes of $A_0 = 0.5,1,3$. The lower flowrate amplitude $A_0 = 0.5$ and 1 demonstrate interesting effects of oscillation upon the velocity profiles. Since the variations in flow field does not show any significant change to the increased oscillation frequency, the core bulk flow presents flattening of velocity profile with peak values obtained in the near-wall regions. This behaviour exists across all the phases of acceleration and deceleration cycle of oscillation. Further, there also exists a distinct phase lag between the core $x/b = 0$ and the near wall $x/b = 0.95$ regions. Due to the faster oscillations, a strong influence of near side-wall viscous effects is evident for the majority of the pulsation period from the corresponding velocity contours vectors and the equivalent shear stress contours, Figure 7-18, Figure 7-19 (e-i), (j-n). Of particular interest are the deceleration stages shown by phases $\pi - 2\,\pi$, wherein despite the low flowrate amplitude of oscillation, strong effects of local near-wall flow-reversal are observed [51]. This leads to substantially high values of velocity gradients which widely exists across the spanwise locations.

Similarities in the observations are made for $A_0 = 1$. This results in a significant increase in the velocity gradients in both the near side-wall $x/b = 0.95$ and channel core $x/b = 0$ regions. Also, to note the evidence of a phase lag exists between the near-wall and core shear stress magnitude profiles. Due to a strong influence of the inertial forces in the central region for $x/b = 0$ at $y/a = 0.5$, the shear profiles decay to zero across a wider spanwise locations. This can be attributed to the fact that the flow in the core regions does not respond any further to the rapidly fluctuating mass flow rate as fast as the flow reacts in the near-wall regions. Thus, this effect results in significantly high magnitudes of oscillating shear stress, as is seen for $A_0 = 1$ compared to all the previous cases of low - high frequencies.

High flowrate amplitude $A_0 = 3$ highlights a prominent influence on the characteristics of oscillation and reversal effects [49] across the various cases of waveform. A significant variation of the oscillating velocity component across the cross-section is distinct viewed for all waveforms which reveals that the pulsations cause a redistribution of momentum in the spanwise (transverse) direction. The oscillating velocity profiles in the acceleration $0 - \pi$ and deceleration stages $\pi - 1.8\pi$ present the evidence of annular effects across the entire time intervals of oscillation. Flatter profiles of oscillating velocity are observed from Figure 7-20 across the spanwise direction which is due to the effect of increased oscillation flowrate amplitude, leading to a rapid increase of bulk inertial forces. The shorter timescale of fluid displacement affects the bulk core which shows weak reaction to the spanwise variations of flow field. There exists a phase lag of oscillating velocity profiles between the core and near-wall regions due to the stronger influence of wall viscous effects on the oscillation cycle. The near-wall velocity profiles present high magnitudes in comparison to

the previous frequencies. The pulsation velocity contours and vectors highlight interesting features of the stronger amplitude of oscillation on the higher frequency, Figure 7-20 (e-i). As seen previously, the maximum magnitudes are reached for the acceleration stage at $\pi/2$ and the corresponding deceleration stage at $3\pi/2$ shows a strengthening impact of flow withdrawal. A substantial development of near-wall flow reversal is seen for phase interval at π as the bulk flow momentum performs a directional shift to accommodate for the fast-moving oscillation. A significant rise in the shear stress magnitudes is noticed for the both near-wall and core regions and a phase lag develops, which suggests that the wall viscous effects for the highest frequency oscillation are strengthened substantially. As a result of the high frequency a greater phase lag attaining a maximum of $\pi/2$ as seen from Section 6.9.3 Figure 6-17 between the pressure gradient and the mass flow rate exists and the magnitudes of pressure gradients is increased significantly. Similarly, the phase lag between the wall shear stress and the pressure gradient increases to a maximum of $\pi/4$, as is evident from Section 6.9.3, Figure 6-18.

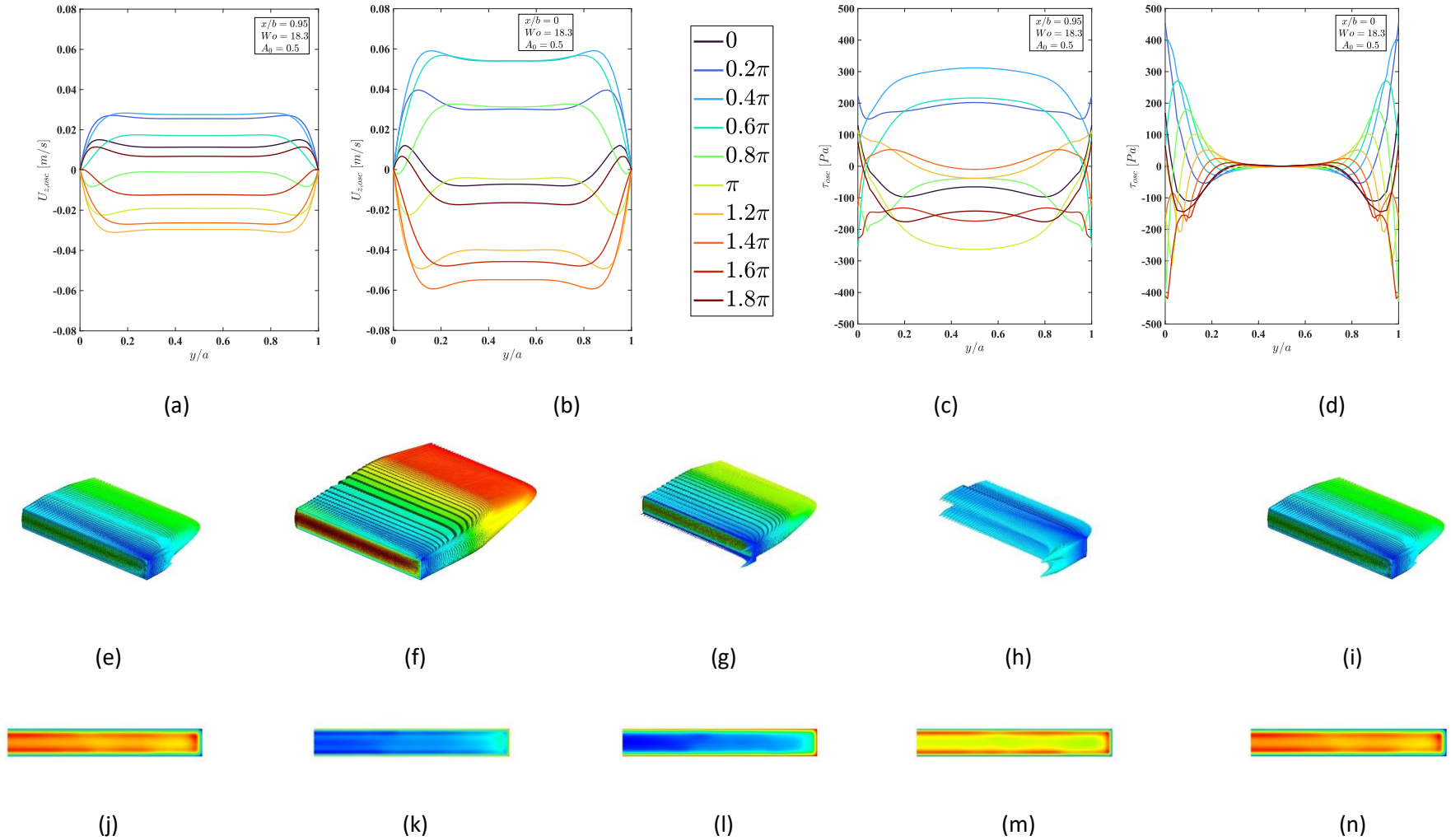

Figure 7-18: Sinusoidal waveform with flow rate amplitude $A_0 = 0.5$ and frequency 25 Hz ($Wo = 18.3$). (a-d) oscillating axial velocity ($U_{z,osc}$) and fluid shear stress (τ_{osc}) profiles along the duct height (y/a) for near-side-wall ($x/b = 0.95$) and central ($x/b = 0$) regions. (e-i) pulsating velocity contour plots at z = 300mm for 5 phases of a pulsation, and (j-n) corresponding fluid shear stress contours.

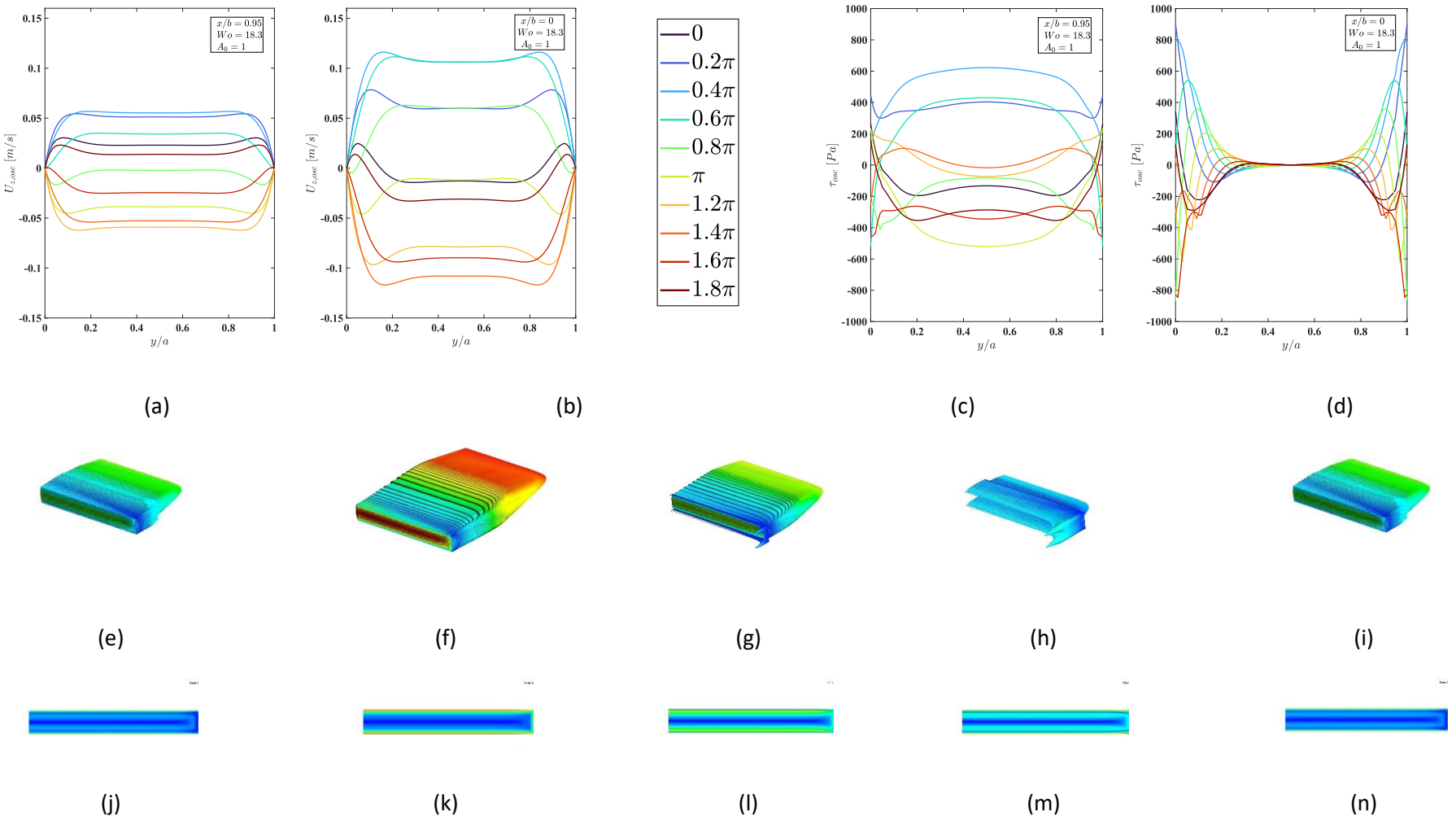

Figure 7-19: Sinusoidal waveform with flow rate amplitude $A_0 = 1$ and frequency 25 Hz ($Wo = 18.3$). (a-d) oscillating axial velocity ($U_{z,osc}$) and fluid shear stress (τ_{osc}) profiles along the duct height (y/a) for near-side-wall ($x/b = 0.95$) and central ($x/b = 0$) regions. (e-i) pulsating velocity contour plots at z = 300mm for 5 phases of a pulsation, and (j-n) corresponding fluid shear stress contours.

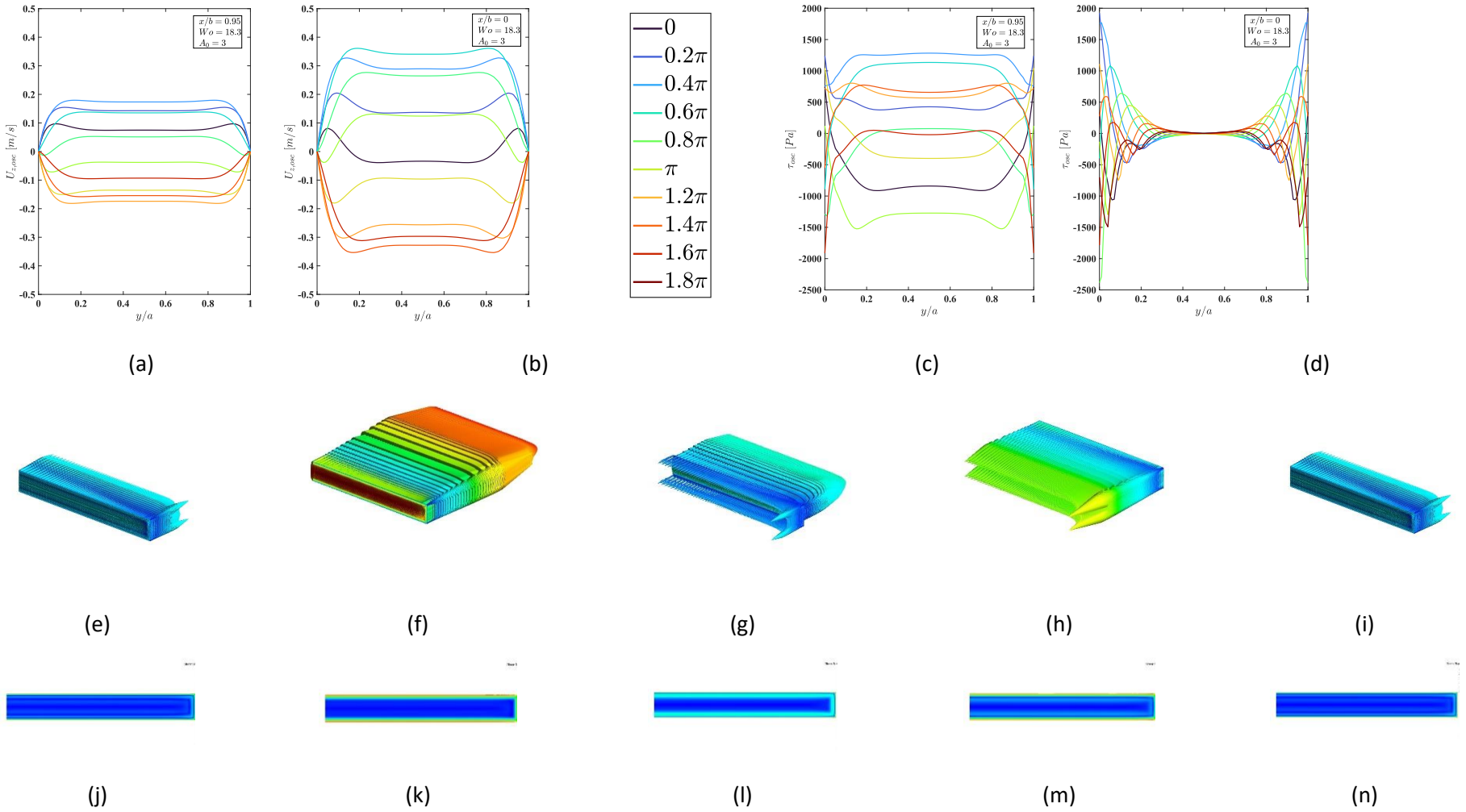

Figure 7-20: Sinusoidal waveform with flow rate amplitude $A_0 = 3$ and frequency 25 Hz ($Wo = 18.3$). (a-d) oscillating axial velocity ($U_{z,osc}$) and fluid shear stress (τ_{osc}) profiles along the duct height (y/a) for near-side-wall ($x/b = 0.95$) and central ($x/b = 0$) regions. (e-i) pulsating velocity contour plots at z = 300mm for 5 phases of a pulsation, and (j-n) corresponding fluid shear stress contours.

7.2.1.2 Asymmetric sinusoidal pulsation waveform

Following the analysis in the previous section, a similar parametric study of the effects of flow rate amplitude and Womersley number on the spatial and temporal oscillating and pulsating velocity and shear stress profiles was conducted for both leading and lagging asymmetric sinusoidal pulsation waveforms. For many of the cases studied (*i.e.*, $Wo = 0.5$ for $A_0 = 0.5, 3$ and $Wo = 2.5$ for $A_0 = 0.5, 3$), no significant differences between the leading/lagging asymmetric and symmetric waveforms was observed. Therefore, those plots have been included in the Appendix (see Figures: Figure 0-1, Figure 0-2, Figure 0-3, Figure 0-4, Figure 0-5, Figure 0-6) as a reference should the reader find them relevant. The more interesting cases are presented henceforth.

Figure 7-21 and Figure 7-22 respectively represent the flow fields resulting from leading asymmetric sinusoidal waveforms at a frequency of 0.5 Hz ($Wo = 2.5$) and flow rate amplitudes of $A_0 = 0.5, 3$. At $A_0 = 0.5$ no significant effect of pulsation is observed, and similarities are established with the corresponding case of the symmetric sinusoidal pulsed flow. Minor differences compared to the low frequency cases are seen for oscillating velocity profiles in the core region for e.g., at phases 0 and 1.8π. At $A_0 = 3$, the oscillating velocity profiles in the channel core region shows an increase and decrease of the peak velocity in both acceleration and deceleration stages in the respective intervals. Phases 0 and 0.2π illustrate minor deviations from the conventional parabolic velocity profiles as observed for symmetric sinusoidal at $Wo = 2.5$. The effect of asymmetry remains similar to the previously described velocity profile case for low flowrate amplitude of $A_0 = 0.5$ with a minor phase shift between the near-wall and core. The velocity contours and vectors indicate the influence of the high flowrate amplitude with a maximum velocity during the acceleration stage at phase $\pi/2$, Figure 7-22 (f) and the other time intervals present a less effective steady underflow. The shear stress magnitudes however are sharply increased compared to the case of low flowrate amplitude in both near-wall and core regions. Peak gradients of velocity are evident for phases $0.4\pi - 0.6\pi$, Figure 7-22 (c,d) which indicates the strong accelerating component of the oscillation. Whereas the deceleration stage shows a comparatively lower velocity gradient as seen for phases $1.2\pi - 1.8\pi$.

Figure 7-23 and Figure 7-24 respectively represent flow fields resulting from leading asymmetric sinusoidal waveforms at a frequency of 2 *Hz* ($Wo = 5.1$) and flow rate amplitudes of $A_0 = 0.5, 3$. At $Wo = 5.1$ and $A_0 = 0.5$ a stronger influence of the asymmetry of pulsation is evident from oscillating velocity profiles when compared to the lower frequencies. The centreline core region $x/b = 0$ shows a peak velocity magnitude, Figure 7-23 (b) during the deceleration cycle for phase 1.6π. Effects of the imposed asymmetry profile can be clearly noted from the oscillating velocity profiles for the majority phases of the cycle compared to the analogous case of symmetric

sinusoidal case. A clear phase shift is also observed from Figure 7-23 (a,b) between the near-wall and central core velocity profiles for the phases $0 - 1.4\pi$. Since the oscillating velocity is more prominent in the deceleration stages of the cycle, a steeper velocity gradient is evident from the core region and near-wall shear stress profiles since the near-wall viscous forces are stronger due to higher steady flowrate. Whereas for $A_0 = 3$, the annular effect is noticeable for the oscillating velocity profiles in both the acceleration stage during the phases $0 - 0.4\pi$ and in the deceleration stage during the phases $\pi - 1.6\pi$ in the channel core region $x/b = 0$, Figure 7-24 (b). The bulk flow is driven by the fast inertial leading to a rapid shift in the fluid momentum. The near-wall and core velocity profiles indicate a phase lag, prominently seen for the acceleration stage in phases $0 - \pi$ Figure 7-24 (a,b). High local near-wall oscillating velocities exist for the majority of the phases of the pulsation. The shear stress magnitudes are sharply increased in contrast to the case of low A_0. High near-wall velocity gradients are determined from the shear stress magnitude profiles at $x/b = 0$, Figure 7-24 (d) and maximum values are reached in the near-wall vicinity for most phases as noted from $x/b = 0.95$, Figure 7-24 (c). The phase lag between the pressure gradient and the flowrate is further amplified for the fast-moving high frequency and can be implied from Figure 7-2.

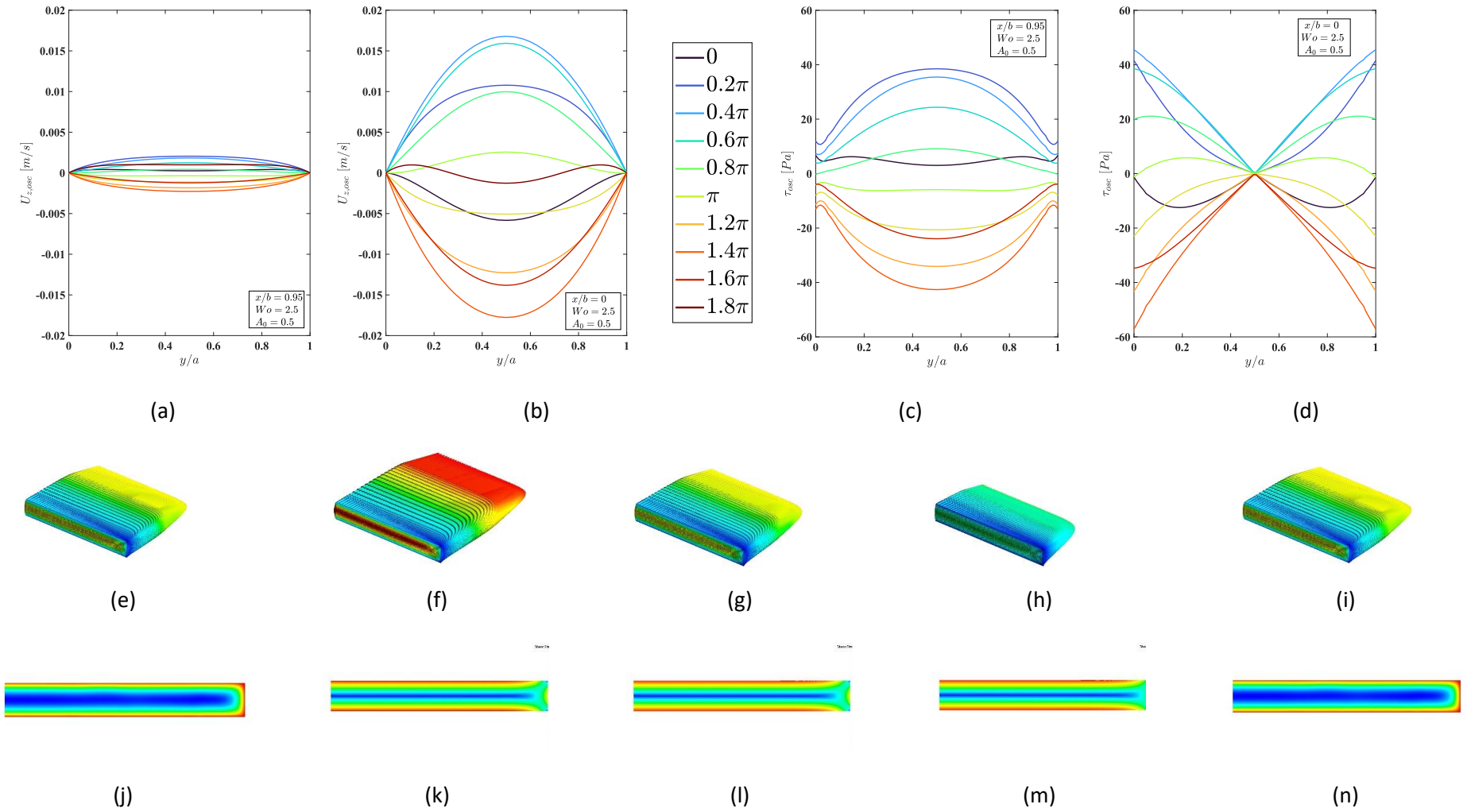

Figure 7-21: Leading Asymmetric sinusoidal waveform with flow rate amplitude $A_0 = 0.5$ and frequency 0.5 Hz ($Wo = 2.5$). (a-d) oscillating axial velocity ($U_{z,osc}$) and fluid shear stress (τ_{osc}) profiles along the duct height (y/a) for near-side-wall ($x/b = 0.95$) and central ($x/b = 0$) regions. (e-i) pulsating velocity contour plots at z = 300mm for 5 phases of a pulsation, and (j-n) corresponding fluid shear stress contours.

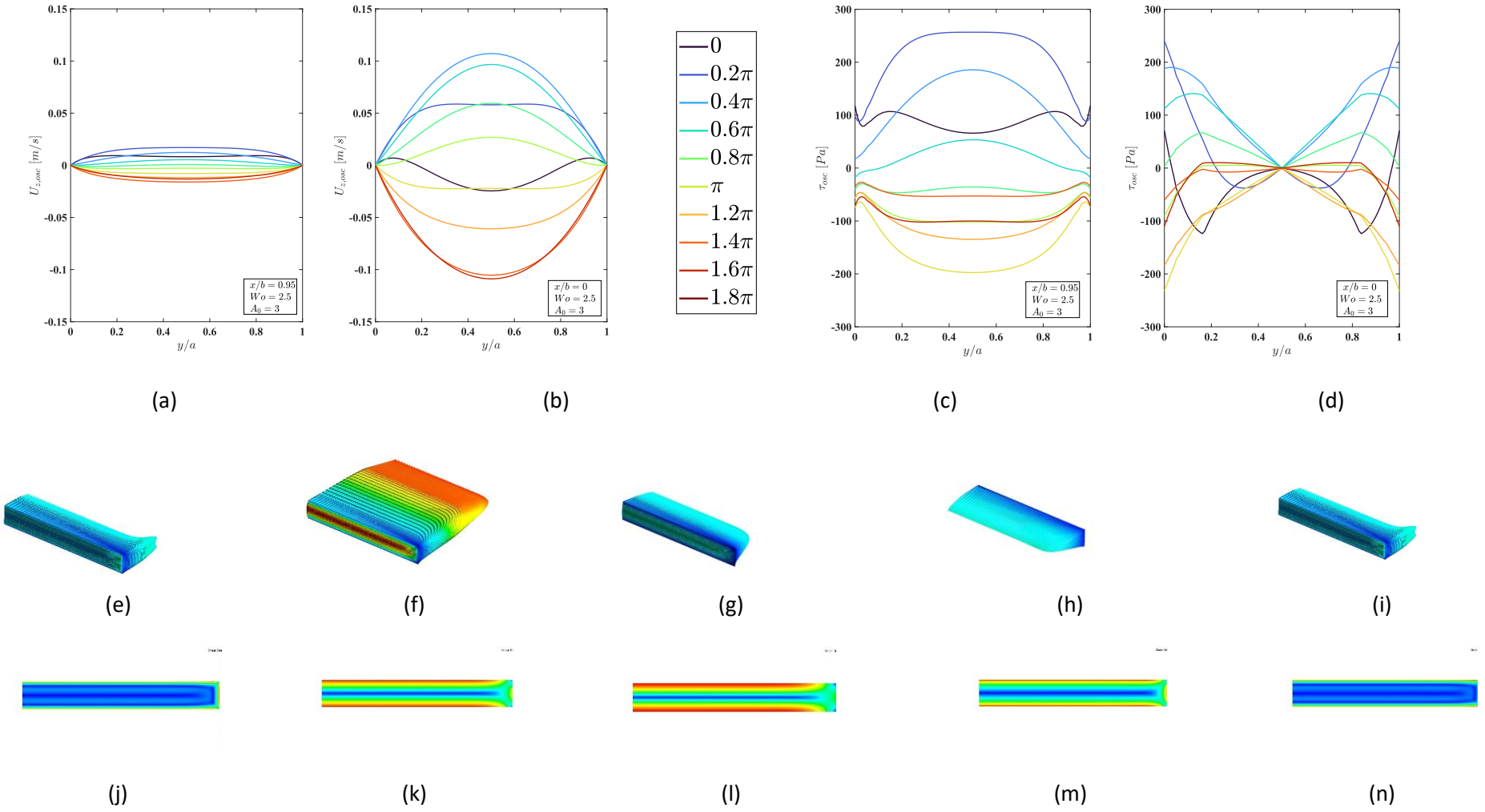

Figure 7-22: Leading Asymmetric sinusoidal waveform with flow rate amplitude $A_0 = 3$ and frequency 0.5 Hz ($Wo = 2.5$). (a-d) oscillating axial velocity ($U_{z,osc}$) and fluid shear stress (τ_{osc}) profiles along the duct height (y/a) for near-side-wall ($x/b = 0.95$) and central ($x/b = 0$) regions. (e-i) pulsating velocity contour plots at z = 300mm for 5 phases of a pulsation, and (j-n) corresponding fluid shear stress contours.

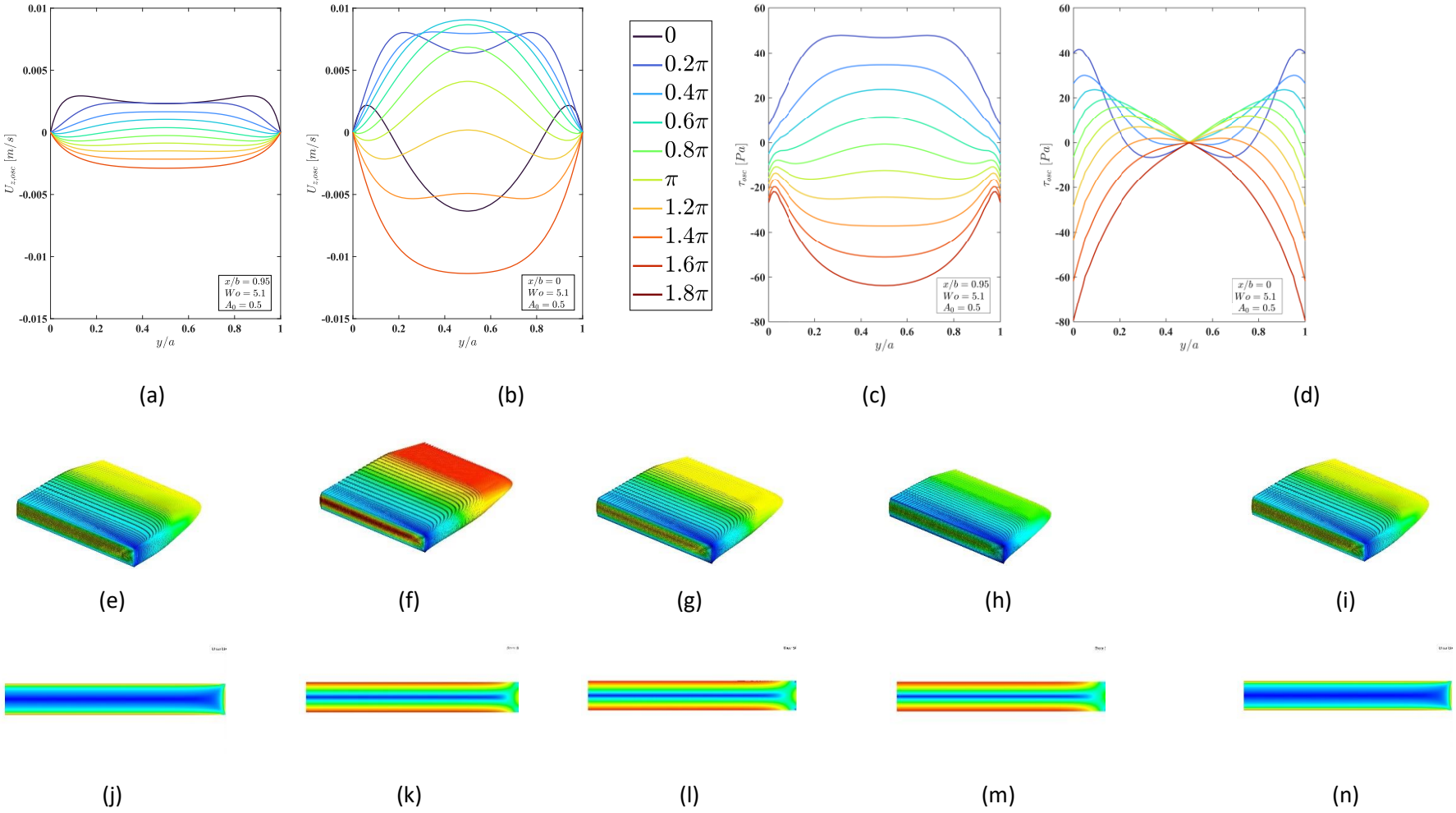

Figure 7-23: Leading Asymmetric sinusoidal waveform with flow rate amplitude $A_0 = 0.5$ and frequency 2 Hz ($Wo = 5.1$). (a-d) oscillating axial velocity ($U_{z,osc}$) and fluid shear stress (τ_{osc}) profiles along the duct height (y/a) for near-side-wall ($x/b = 0.95$) and central ($x/b = 0$) regions. (e-i) pulsating velocity contour plots at z = 300mm for 5 phases of a pulsation, and (j-n) corresponding fluid shear stress contours.

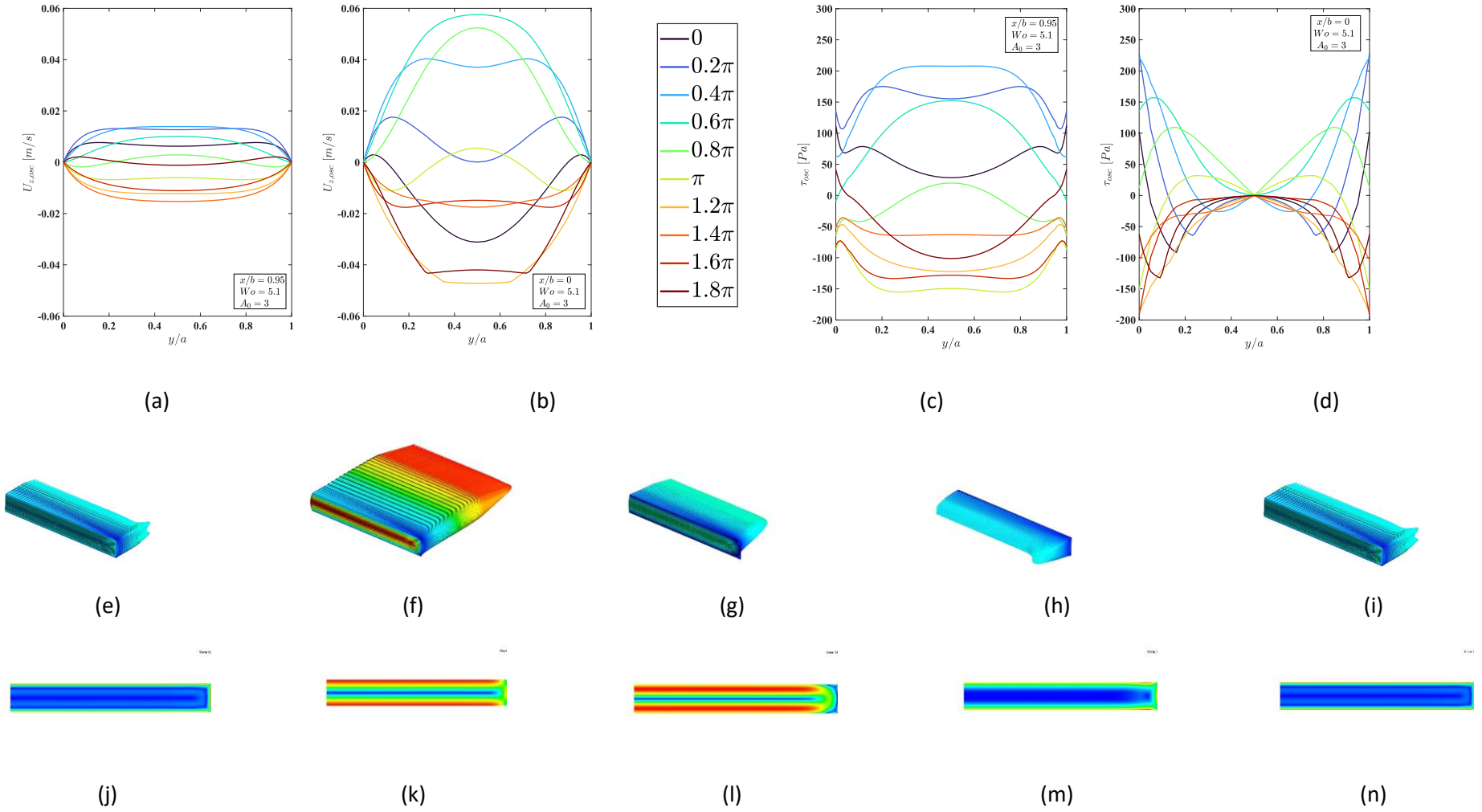

Figure 7-24: Leading Asymmetric sinusoidal waveform with flow rate amplitude $A_0 = 3$ and frequency 2 Hz ($Wo = 5.1$). (a-d) oscillating axial velocity ($U_{z,osc}$) and fluid shear stress (τ_{osc}) profiles along the duct height (y/a) for near-side-wall ($x/b = 0.95$) and central ($x/b = 0$) regions. (e-i) pulsating velocity contour plots at z = 300mm for 5 phases of a pulsation, and (j-n) corresponding fluid shear stress contours.

Figure 7-25 and Figure 7-26 respectively represent flow fields resulting from leading asymmetric sinusoidal waveforms at a frequency of 25 Hz ($Wo = 18.3$) and flow rate amplitudes of $A_0 = 0.5, 3$. The oscillating velocity magnitudes present a clear effect of the asymmetry. The acceleration phases $0 - \pi$ attain higher magnitudes of oscillating velocity compared to the deceleration stages $\pi - 1.8\,\pi$ for a full cycle. Due to the weaker oscillation component compared to the stronger underlying steady flow, the deceleration stages show a prominent reaction to the annular effects, whereas a reduction in near-wall velocity magnitudes was seen for the case of sinusoidal flows at $Wo = 18.3$ and $A_0 = 0.5$, Figure 7-18. However, the acceleration stage demonstrates a pronounced effect for velocities profiles in the core region and near-wall with a phase lag existing between the two. The velocity contours and vectors, Figure 7-25 (e-i) do not however indicate any significant spanwise variation resulting from the imposed pulsation waveform which can be attributed to the fact that the bulk flow in the core shows weak reaction to the rapidly changing mass flow offered by the asymmetry. The shear stress contours reflect the occurrence of a high near-wall velocity gradient, and a narrow region of low velocity gradients appear in the vicinity of corner regions during the deceleration stages seen from Figure 7-25 (m,n). Owing to a significant rise of the pressure gradient with a peak phase lag of $\pi/2$ between pressure gradient and mass flow rate as seen from Figure 7-2 (d), the oscillating shear stress profiles show large deviations in the core and near-wall regions. The near side-wall oscillating bottom wall shear stress profiles indicate a reduced influence of viscous effects, whereas the core region show occurrence of steep gradients.

At $A_0 = 3$ (Figure 7-26), the oscillating velocity profiles do not show distinct characteristics of the asymmetry profile as was observed for the other frequencies. As a result of which peak magnitudes are obtained equivalently during both acceleration and deceleration stages of the oscillation. There exists a phase lag between the near-wall and core regions and high near side-wall velocities exist in contrast to the other frequencies. A possible reason for this occurrence is a gradual decline in fluid momentum which leads to an even distribution of the flow in the core region which is observed through phases $\pi/2$ and $3\pi/2$, *i.e.*, between the peaks of the acceleration and deceleration stages. The asymmetric features of the pulsation are suppressed by the high flow rate amplitude. The velocity contours and vectors, Figure 7-26 (e-i) present broadly comparable behaviour to the sinusoidal profile at $Wo = 18.3$. The asymmetric case leads to a significant impact on the flow-reversal. Overall, the near-wall viscous effects sharply exist in the wall vicinity as is determined from the shear stress contours except for the case where the flow reversal shows presence of gradients in off-wall location as seen from Figure 7-26 (i-n). On comparing the near-wall and core profiles for the oscillating shear stress profiles, a clear phase lag exists, whereas the magnitudes are not significantly high as was observed for the sinusoidal waveform at $Wo = 18.3$ and $A_0 = 3$.

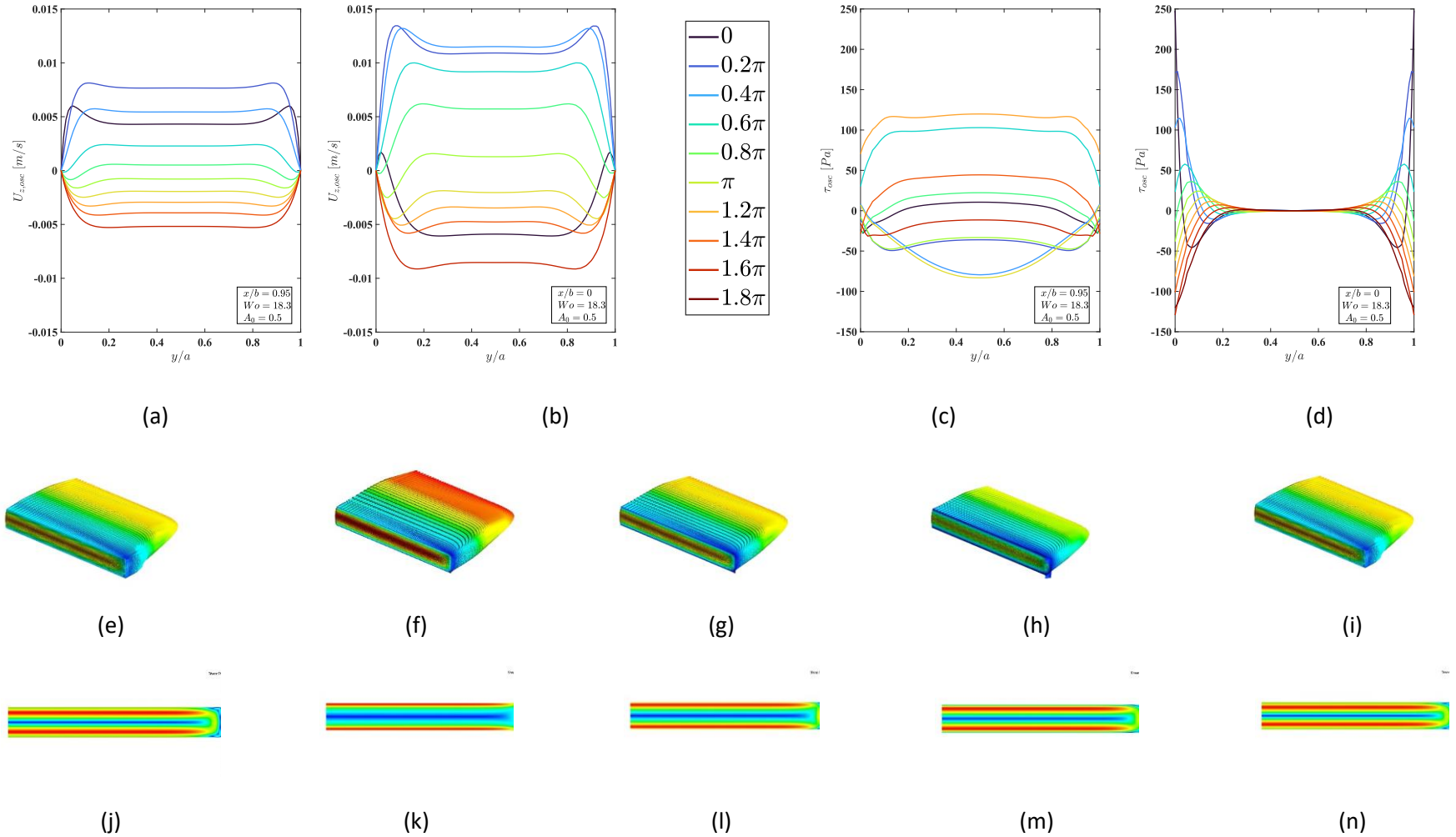

Figure 7-25: Leading Asymmetric sinusoidal waveform with flow rate amplitude $A_0 = 0.5$ and frequency 25 Hz ($Wo = 18.3$). (a-d) oscillating axial velocity ($U_{z,osc}$) and fluid shear stress (τ_{osc}) profiles along the duct height (y/a) for near-side-wall ($x/b = 0.95$) and central ($x/b = 0$) regions. (e-i) pulsating velocity contour plots at z = 300mm for 5 phases of a pulsation, and (j-n) corresponding fluid shear stress contours.

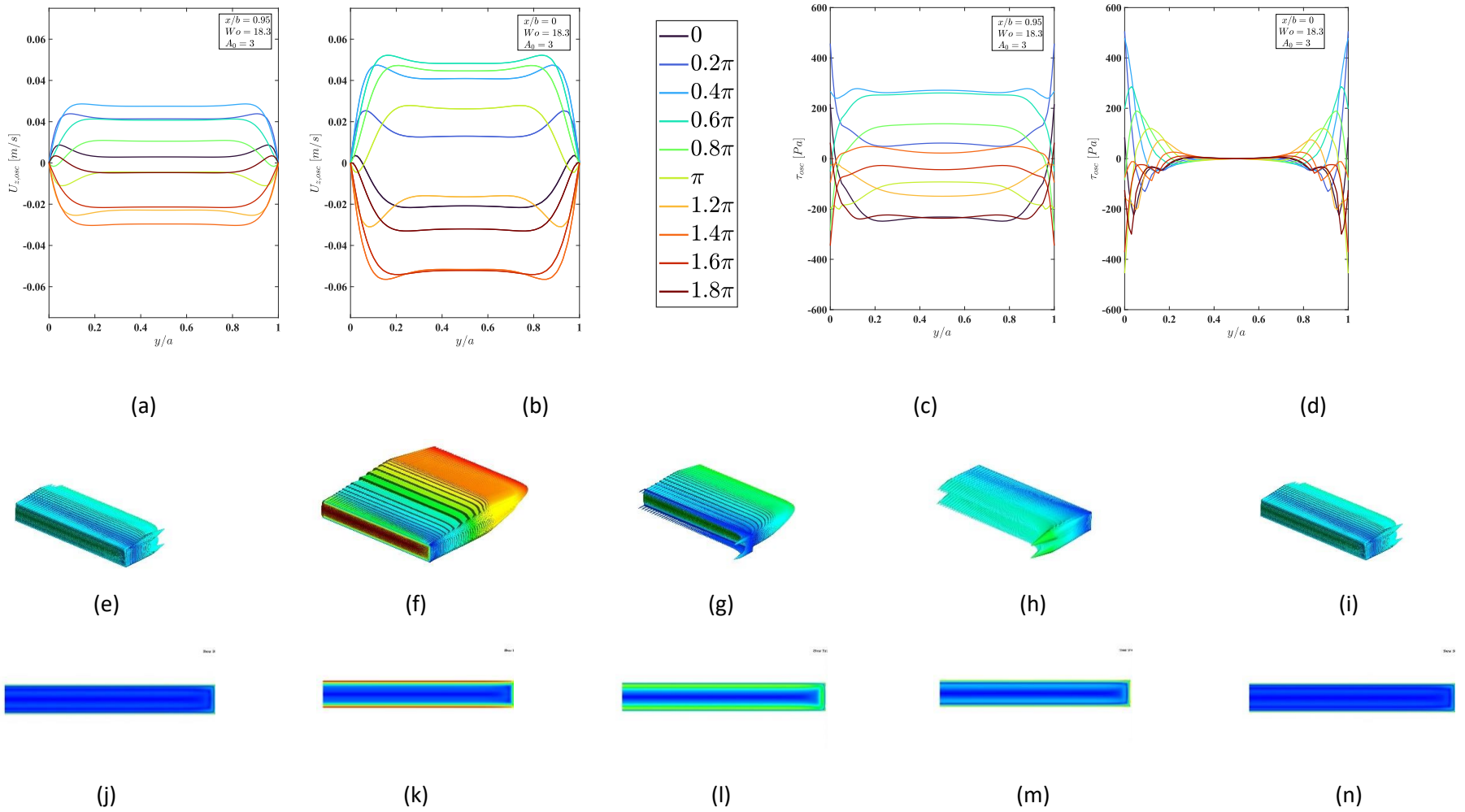

Figure 7-26: Leading Asymmetric sinusoidal waveform with flow rate amplitude $A_0 = 3$ and frequency 25 Hz ($Wo = 18.3$). (a-d) oscillating axial velocity ($U_{z,osc}$) and fluid shear stress (τ_{osc}) profiles along the duct height (y/a) for near-side-wall ($x/b = 0.95$) and central ($x/b = 0$) regions. (e-i) pulsating velocity contour plots at z = 300mm for 5 phases of a pulsation, and (j-n) corresponding fluid shear stress contours.

Figure 7-27, Figure 7-28 respectively represent flow fields resulting from lagging asymmetric sinusoidal waveforms at a frequency of 2 Hz ($Wo = 5.1$) and flow rate amplitudes of $A_0 = 0.5, 3$. For $Wo = 5.1$ and $A_0 = 0.5$, the influence of the waveform compared to the sinusoidal and leading asymmetric pulsations is evident from the velocity profiles in the core ($x/b = 0$). A peak in the oscillating velocity magnitude is observed during the acceleration stage of the cycle as seen from Figure 7-27 (b). However due to the higher underlying steady flowrate, the deceleration stage of the cycle presents weaker velocity magnitudes. A phase lag exists between the near-wall and core channel regions, prominently for the deceleration phases $\pi - 1.8\,\pi$. Due to the weaker oscillating component during deceleration, the velocity gradients are lower, and the shear stress profiles are less steep for phases $1.2\pi - 1.8\pi$ compared to the faster moving accelerating phases $0.2\pi - 0.8\,\pi$. The pulsating velocity and shear stress magnitudes contours, however, follow the similar pattern as was noticed for the leading asymmetric case and do not show a clear indication of the asymmetry due to weaker oscillating component compared to the steady flow as seen from Figure 7-27 (e-i), (j-n).

For $A_0 = 3$, a more pronounced effect of the asymmetry characteristics can be attributed in comparison to the leading waveform. During the acceleration stage of cycle at phases $0 - 0.8\,\pi$ a sharp increase in the oscillating velocity magnitude is seen from Figure 7-28 (b). However, from the phase π to the end of deceleration stage, strong spanwise variations in the oscillating velocity magnitude profiles are noted. A clear indication of a phase lag is noted between the near-wall and core velocities profiles with the deceleration cycle $\pi - 2\pi$. Interestingly, the velocity contours and vectors reflect on the effects of an existence of a weak flow reversal for phase π. There is a consequent and a substantial increase of velocity gradients in the core and near-wall regions with a distinct phase lag based on the rapid fluctuations induced due to the asymmetry. Due to the presence of high near-corner viscous effect, the oscillating shear stress magnitudes show local occurrence of peaks for $x/b = 0.95$, Figure 7-28 (b).

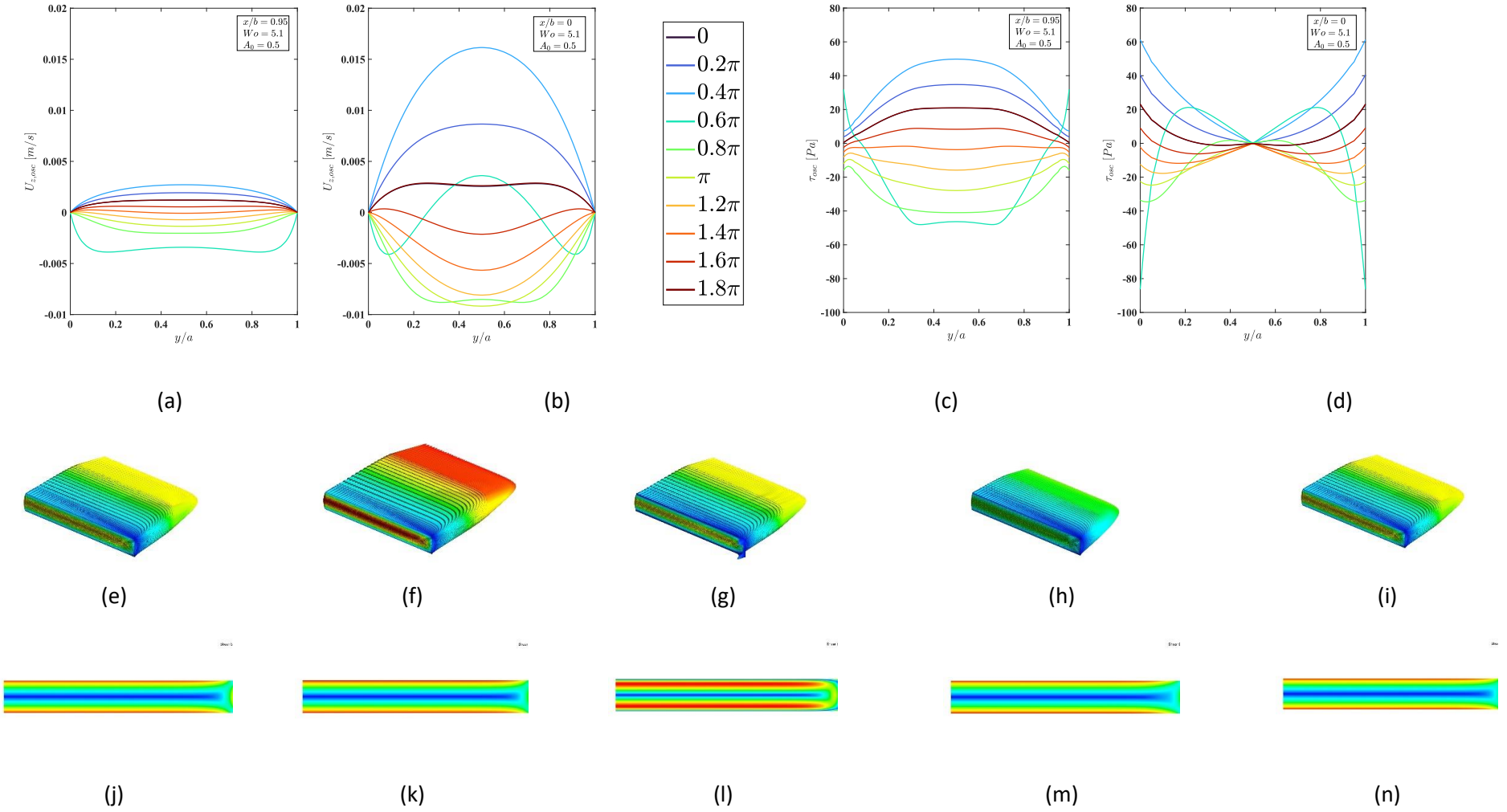

Figure 7-27: Lagging Asymmetric sinusoidal waveform with flow rate amplitude $A_0 = 0.5$ and frequency 2 Hz ($Wo = 5.1$). (a-d) oscillating axial velocity ($U_{z,osc}$) and fluid shear stress (τ_{osc}) profiles along the duct height (y/a) for near-side-wall ($x/b = 0.95$) and central ($x/b = 0$) regions. (e-i) pulsating velocity contour plots at z = 300mm for 5 phases of a pulsation, and (j-n) corresponding fluid shear stress contours.

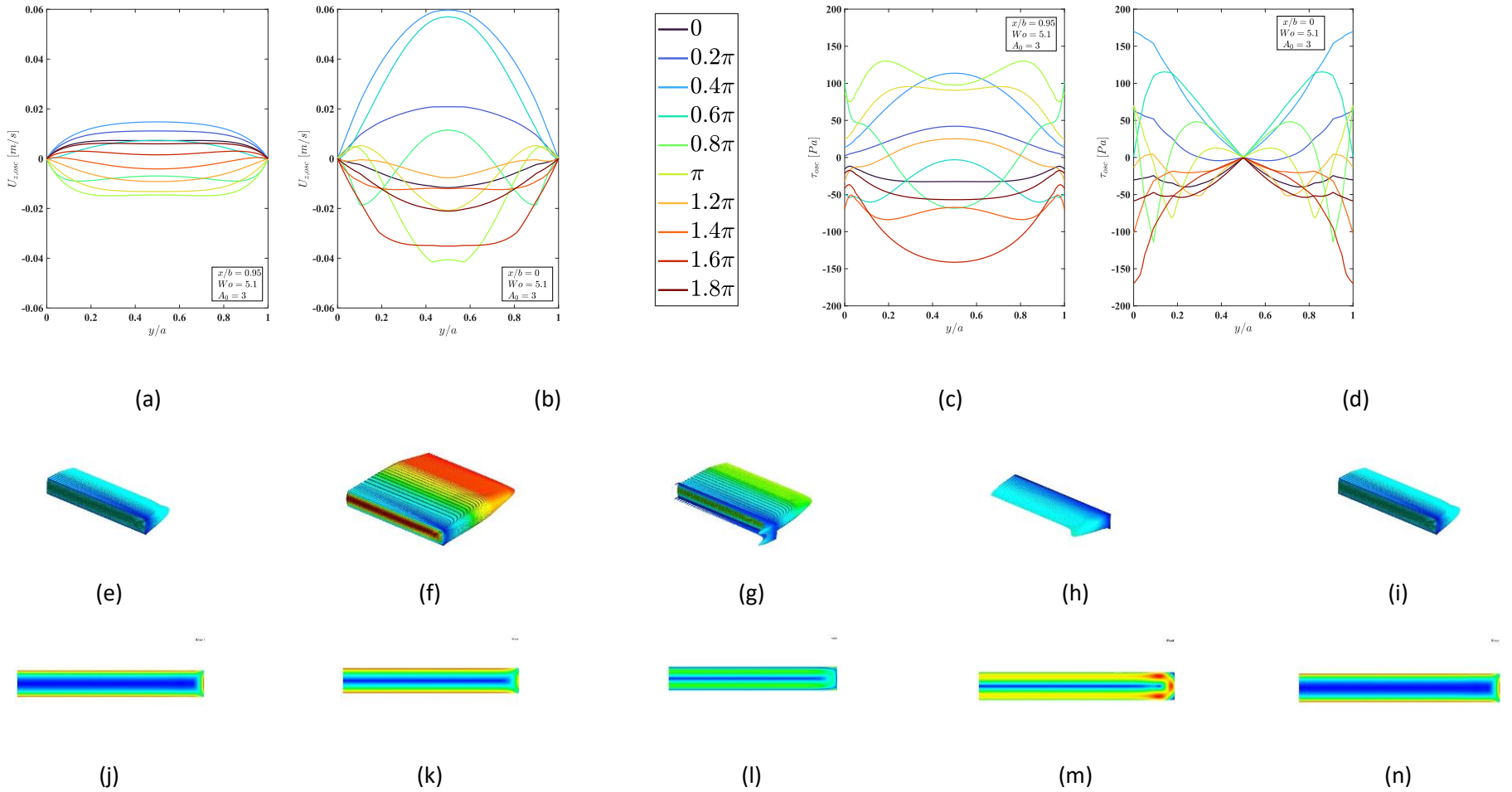

Figure 7-28: Lagging Asymmetric sinusoidal waveform with flow rate amplitude $A_0 = 3$ and frequency 2 Hz ($Wo = 5.1$). (a-d) oscillating axial velocity ($U_{z,osc}$) and fluid shear stress (τ_{osc}) profiles along the duct height (y/a) for near-side-wall ($x/b = 0.95$) and central ($x/b = 0$) regions. (e-i) pulsating velocity contour plots at z = 300mm for 5 phases of a pulsation, and (j-n) corresponding fluid shear stress contours.

Figure 7-29 and Figure 7-30, respectively represent flow fields resulting from lagging asymmetric sinusoidal waveforms at a frequency of 25 Hz ($Wo = 18.3$) and flow rate amplitudes of $A_0 = 0.5, 3$. For lower flowrate amplitude $A_0 = 0.5$ case, the fast-moving oscillating flow shows the influence of asymmetry despite the weaker oscillation amplitude. The acceleration stage presents a peak in velocity magnitudes for the phases $0 - \pi$ and a peak with reduced magnitude is observed for the corresponding deceleration stage for phases $\pi - 1.8\pi$. The annular effects are further pronounced for the oscillating velocity profiles in both the core and near-wall regions with an existence of a phase lag between the two compared to the previous Wo. The pulsating velocity and contour and vectors do not highlight the features of the asymmetry due to the lower amplitude of oscillation compared to the dominant steady underflow. The shear stress contours suggest the characteristics of the leading asymmetry which is governed by the changing direction of the impulse stroke for the phases π and $3\pi/2$ as is seen from Figure 7-29 (l,m). Similarly, the shear stress profiles show reduced magnitudes in the near-wall regions whereas spanwise variation exists in particular for the deceleration stages of the cycle due to a shift in the fluid momentum. Whereas a significant phase lag between the near-wall and core profile exists and stepper profiles of velocity gradients are seen in the core regions due to the sharp shift in the phase lag with the pressure gradient as also seen in Figure 7-3 (d).

At $A_0 = 3$, a pronounced effect of the asymmetry is distinctly observed from the oscillating velocity profiles at the core $x/b = 0$ and near-wall $x/b = 0$. This is attributed to the sharp acting impulse stroke of the lagging asymmetry at phase π from Figure 7-3 (l), which drives the rapid bulk flow momentum of the fast-moving oscillation across the spanwise locations. As expected, the acceleration stage $0 - \pi$ reaches a peak value of oscillating velocity profile compared to the deceleration stage. There exists a phase lag between the near-wall and core regions of oscillating velocity with the near-wall magnitudes attaining subsequent high values in contrast to the other frequencies. The velocity contours and vectors, Figure 7-30 (e-i) indicate interesting features of the lagging asymmetry, wherein stronger flow reversals are seen for phases π and $3\pi/2$ compared to the leading asymmetry. The corresponding shear stress contours, Figure 7-30 (j-n) show the presence of near-wall viscous effects which are amplified due to the flow reversal. Local high values of shear stress magnitudes are observed for the lagging case in both near sidewall and core regions. However, the peaks are far lower compared to the equivalent sinusoidal waveform at $Wo = 18.3$ and $A_0 = 3$. A phase lag exists between the profiles and the peak magnitudes in the core region are concentrated to near-wall only due to the influence of a strong bulk inertial motion. A substantially high-pressure gradient exists, although is lower compared to the leading asymmetry and lags the flowrate by $\pi/2$ Figure 7-3 (l).

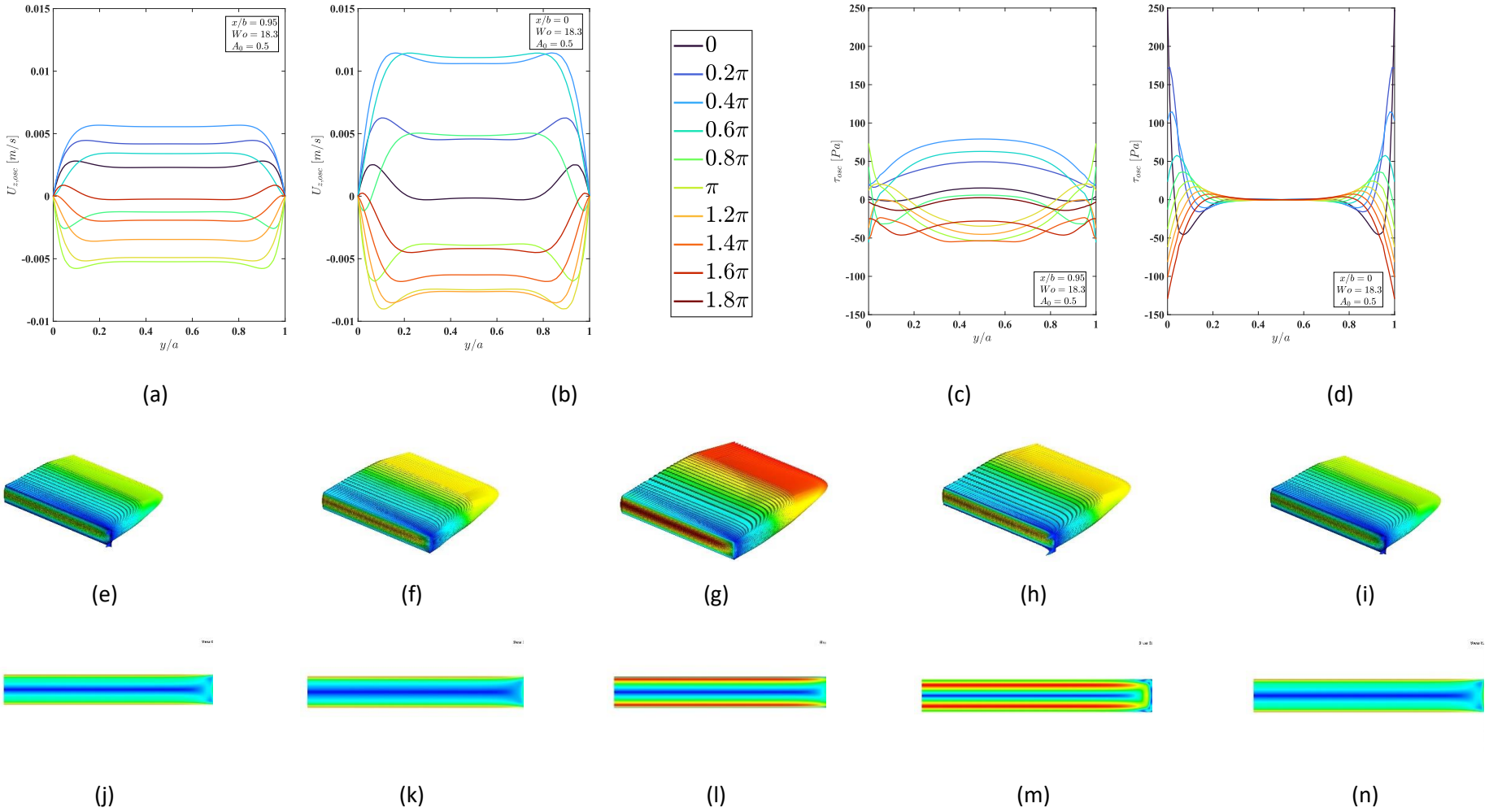

Figure 7-29: Lagging Asymmetric sinusoidal waveform with flow rate amplitude $A_0 = 0.5$ and frequency 25 Hz ($Wo = 18.3$). (a-d) oscillating axial velocity ($U_{z,osc}$) and fluid shear stress (τ_{osc}) profiles along the duct height (y/a) for near-side-wall ($x/b = 0.95$) and central ($x/b = 0$) regions. (e-i) pulsating velocity contour plots at z = 300mm for 5 phases of a pulsation, and (j-n) corresponding fluid shear stress contours.

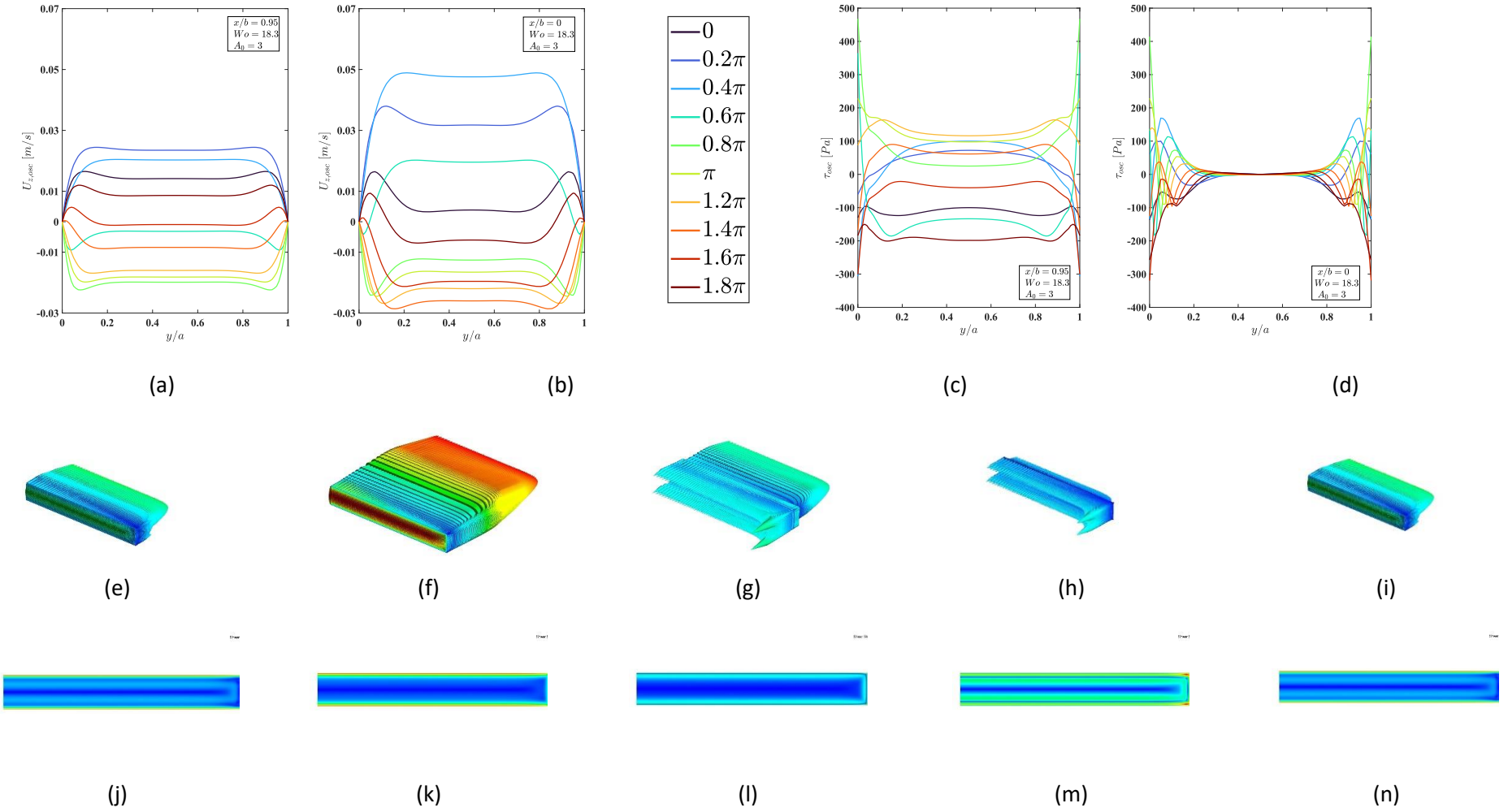

Figure 7-30: Lagging Asymmetric sinusoidal waveform with flow rate amplitude $A_0 = 3$ and frequency 25 Hz ($Wo = 18.3$). (a-d) oscillating axial velocity ($U_{z,osc}$) and fluid shear stress (τ_{osc}) profiles along the duct height (y/a) for near-side-wall ($x/b = 0.95$) and central ($x/b = 0$) regions. (e-i) pulsating velocity contour plots at z = 300mm for 5 phases of a pulsation, and (j-n) corresponding fluid shear stress contours.

7.2.1.3 Half rectified pulsation waveform

Figure 7-31 and Figure 7-32 respectively represent flow fields resulting from positive half rectified waveforms at a frequency of 0.5 Hz ($Wo = 2.5$) and flow rate amplitudes of $A_0 = 0.5, 3$. Figure 7-31 at $Wo = 2.5$ and $A_0 = 0.5$ shows distinct features of pulsation as a maximum velocity magnitude is obtained at $y/a = 0.5$ for the acceleration cycle between phases $\pi - 2\pi$ in channel core region $x/b = 0$ and from the velocity contours and vectors at phase $3\pi/2$, whereas the rest of the cycle follows the steady flow pattern. A phase lag exists between the velocity profiles at near-wall ($x/b = 0.95$) and in core channel ($x/b = 0$) regions. A significant rise in velocity gradients is seen compared to similar cases (Figure 7-11) for the symmetric sinusoidal and asymmetric profiles which can be attributed to the sharp impulse of flow from the sinusoidal component of the half rectified profile, which exists only for one half of a full pulsation cycle. The highest shear stress magnitudes are attained by positive half rectified waveform compared to the subsequent waveforms for the case of $Wo = 2.5$ and $A_0 = 0.5$.

For $A_0 = 3$, Figure 7-32 shows an occurrence of maximum oscillating velocity magnitude during the acceleration cycle from phases $\pi - 2\pi$. Only a slight variation in velocity profiles is observed compared to the low flowrate amplitude, however the phase lag between the channel core and near-wall regions is more pronounced at high flowrate amplitudes. The influence of pulsation is evident from the contours and vectors of velocity as the steady flowrate is insignificant in contrast to the high velocity magnitudes reached during the pulsation. The near-wall and core shear stress profiles reflect a simultaneous increase in the velocity gradients as an effect of the high flowrate amplitude; however, the profiles resemble the observations of the low flowrate amplitude ($A_0 = 0.5$) case (Figure 7-31). The underlying steady at the end of the pulsation cycle (phase -2π) shows a small withdrawing effect as is noticeable from the velocity contours and vectors at phase 2π. Observations from the shear stress contours imply an existence of a weak near-wall velocity gradient and a distinct appearance of high gradients in the off-wall regions.

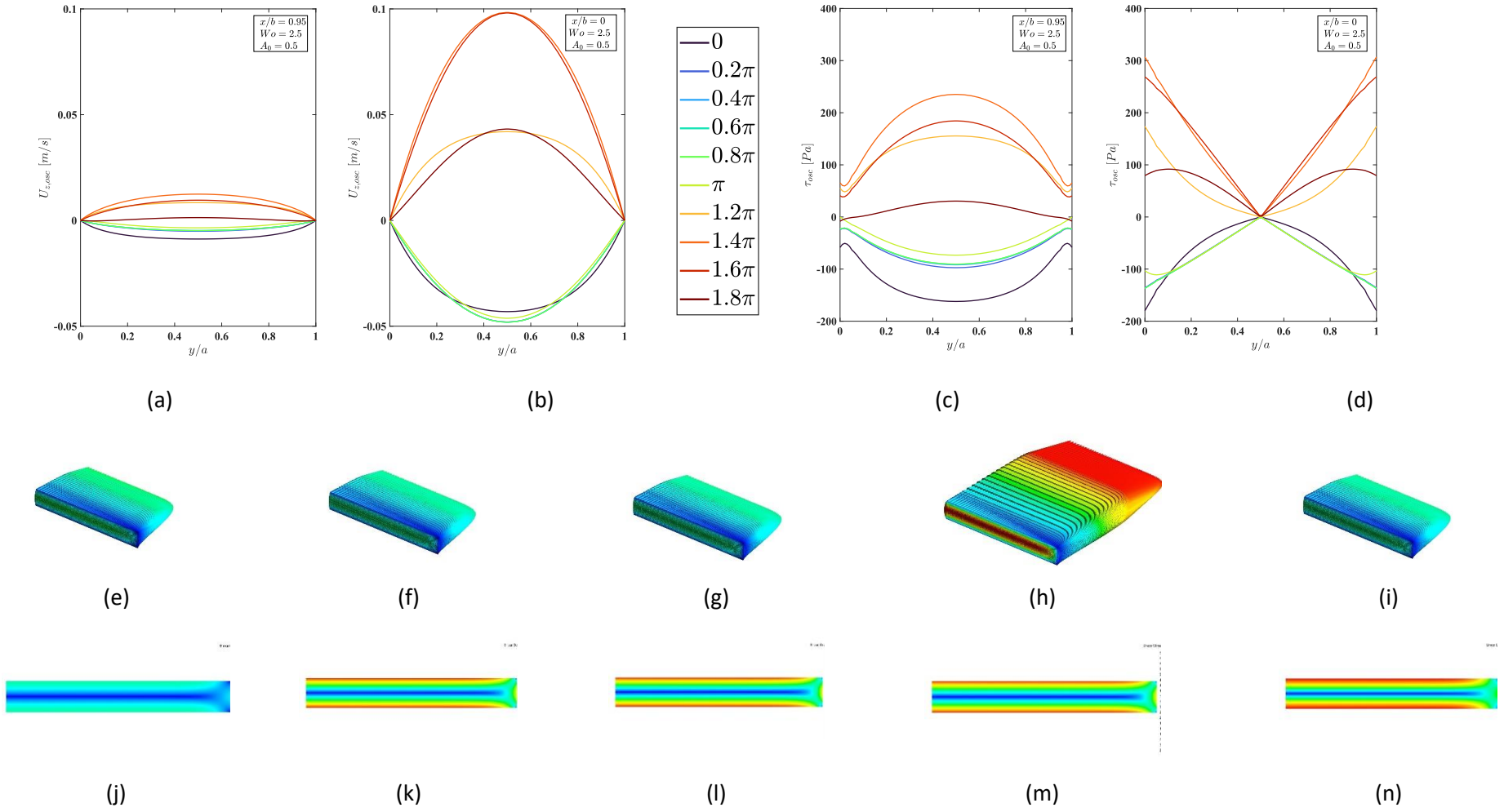

Figure 7-31: Positive half rectified sinusoidal waveform with flow rate amplitude $A_0 = 0.5$ and frequency 0.5 Hz ($Wo = 2.5$). (a-d) oscillating axial velocity ($U_{z,osc}$) and fluid shear stress (τ_{osc}) profiles along the duct height (y/a) for near-side-wall ($x/b = 0.95$) and central ($x/b = 0$) regions. (e-i) pulsating velocity contour plots at z = 300mm for 5 phases of a pulsation, and (j-n) corresponding fluid shear stress contours.

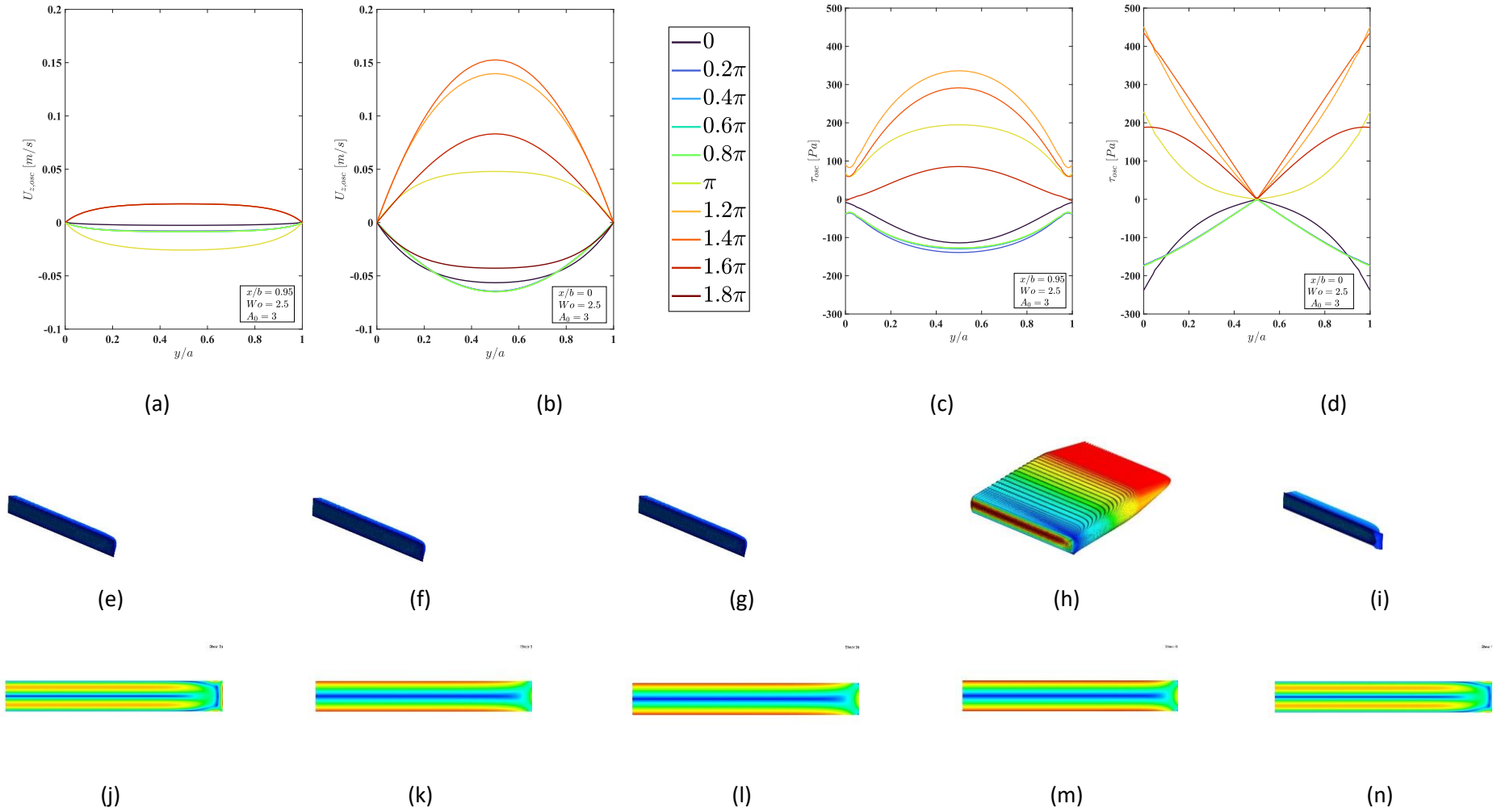

Figure 7-32: Positive half rectified sinusoidal waveform with flow rate amplitude $A_0 = 3$ and frequency 0.5 Hz ($Wo = 2.5$). (a-d) oscillating axial velocity ($U_{z,osc}$) and fluid shear stress (τ_{osc}) profiles along the duct height (y/a) for near-side-wall ($x/b = 0.95$) and central ($x/b = 0$) regions. (e-i) pulsating velocity contour plots at z = 300mm for 5 phases of a pulsation, and (j-n) corresponding fluid shear stress contours.

Figure 7-33 and Figure 7-34 respectively represent flow fields resulting from positive half rectified waveforms at a frequency of 2 Hz ($Wo = 5.1$) and flow rate amplitudes of $A_0 = 0.5, 3$. Figure 7-33 presents clear evidence of a phase shift between the near-wall and core oscillating velocity magnitudes for a majority of the acceleration stage, *i.e.*, during phases $1.2\,\pi - 1.8\,\pi$. This occurs as a result of the existence of predominant bulk inertial forces which is a characteristic trait of high frequency flows. A peak in oscillating velocity magnitude is determined in the acceleration stage which is also represented in the velocity contours and vectors for the $3\pi/2$ interval. The remaining phases show the steady flow behaviour. A steep increase in the shear stress magnitudes is noticed overall for $Wo = 5.1$, from Figure 7-33 (c,d) which is because of the amplified near-wall velocity gradients. There is a phase lag of $\pi/2$ with the pressure gradient, as noticed from the temporal profiles Figure 7-4 (c). Higher magnitudes of shear stress exist in both regions of near-wall and core during the acceleration stage of the cycle.

For $A_0 = 3$ (Figure 7-34) case, a significant spanwise distribution of velocity occurs compared to the case of low flowrate amplitude $A_0 = 0.5$. Pronounced features of a high frequency oscillation is evident from the core channel velocity magnitudes as the acceleration stage $\pi - 1.8\pi$ shows a progressive development of annular effects. Consequently, a phase lag is observed between the near-wall and core oscillating velocity profiles due to the fast-moving oscillation, Figure 7-34 (a,b). The distinct features of half rectified flowrate can be identified from the velocity contours and vectors, wherein strong reversal effects exists in the near-wall vicinity during the steady flow instances. Since the underlying steady component is much lower compared to the stronger oscillation component at $A_0 = 3$, a local peak in the acceleration cycle at phase $3\pi/2$, Figure 7-34(h) appears and the bulk steady flow features are supressed from the other instances of cycle. The shear stress contours present the existence of a strong velocity gradient due to the existence of high viscous effects occurring in the near-wall and corner regions of the duct for all the time intervals. Similarly, a significant amplification of oscillating shear stress magnitudes generally exists for the entire pulsation cycle compared to the low flowrate amplitude (Figure 7-33). A distinct phase lag is noticeable between the near-wall and core regions of shear stress profiles which is as a result of the sharp increase in the pressure gradient during the acceleration stage of oscillation which can be identified from Figure 7-4 (k).

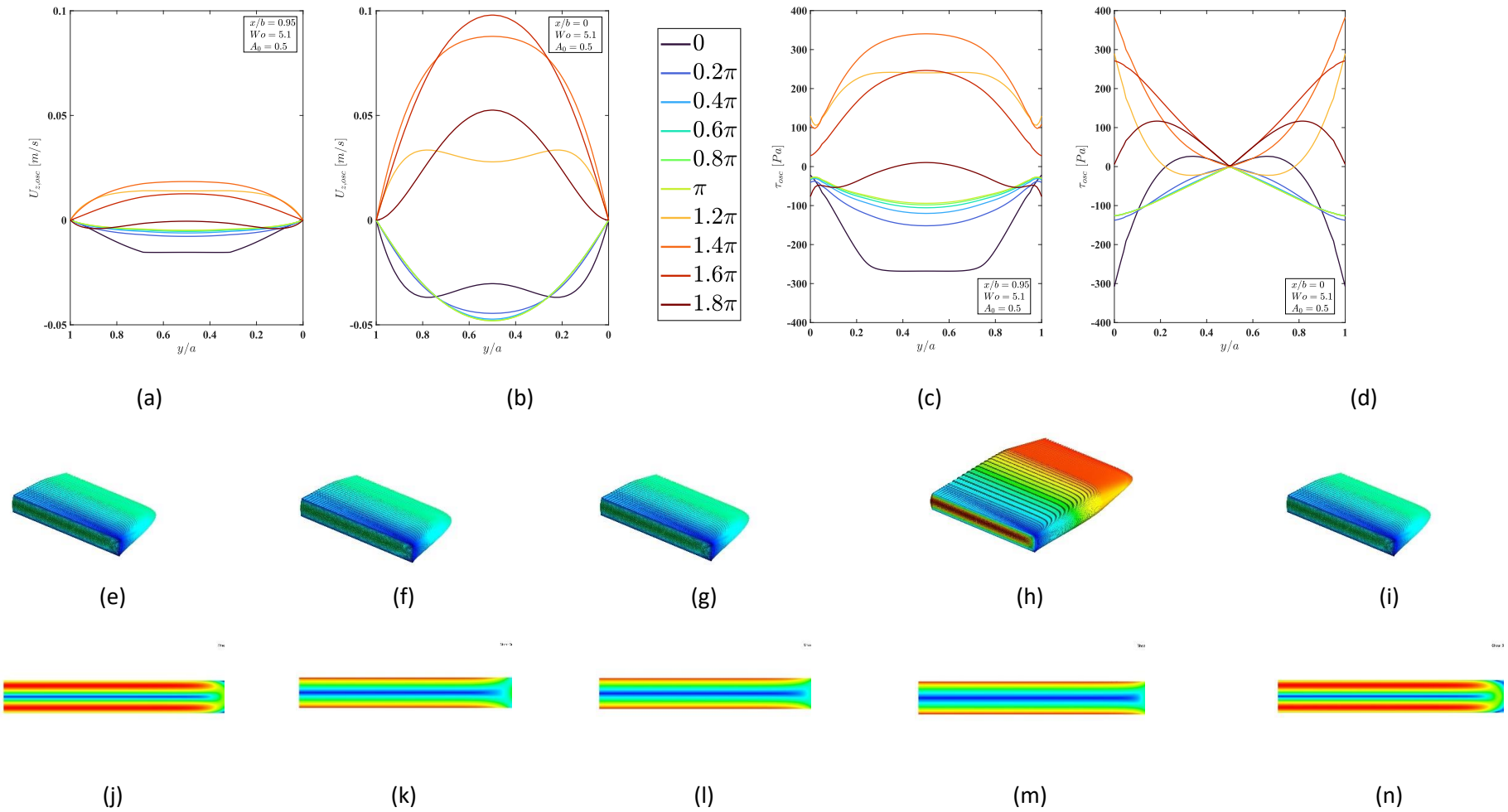

Figure 7-33: Positive half rectified sinusoidal waveform with flow rate amplitude $A_0 = 0.5$ and frequency 2 Hz ($Wo = 5.1$). (a-d) oscillating axial velocity ($U_{z,osc}$) and fluid shear stress (τ_{osc}) profiles along the duct height (y/a) for near-side-wall ($x/b = 0.95$) and central ($x/b = 0$) regions. (e-i) pulsating velocity contour plots at z = 300mm for 5 phases of a pulsation, and (j-n) corresponding fluid shear stress contours.

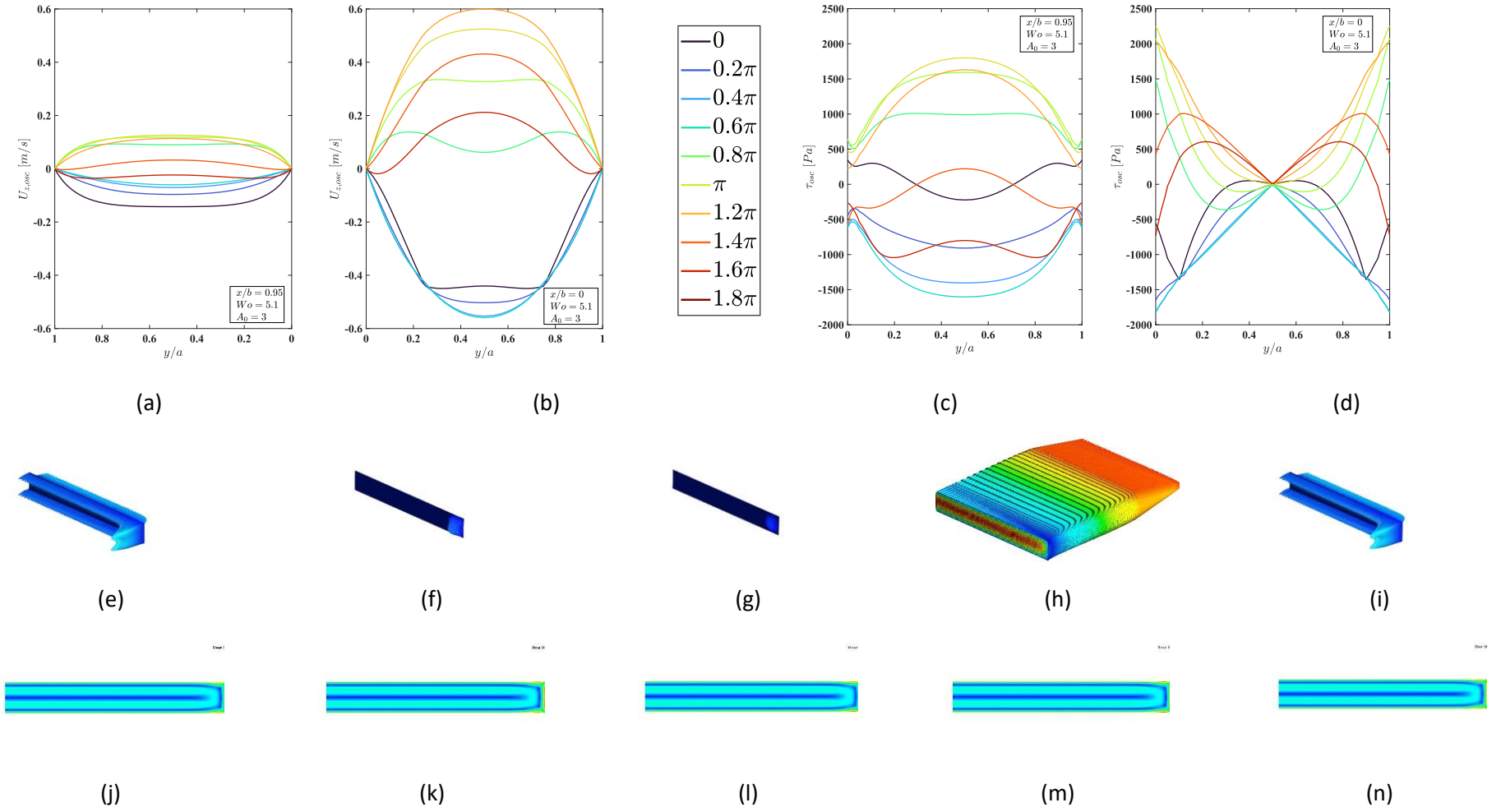

Figure 7-34: Positive half rectified sinusoidal waveform with flow rate amplitude $A_0 = 3$ and frequency 2 Hz ($Wo = 5.1$). (a-d) oscillating axial velocity ($U_{z,osc}$) and fluid shear stress (τ_{osc}) profiles along the duct height (y/a) for near-side-wall ($x/b = 0.95$) and central ($x/b = 0$) regions. (e-i) pulsating velocity contour plots at z = 300mm for 5 phases of a pulsation, and (j-n) corresponding fluid shear stress contours.

Figure 7-35 and Figure 7-36 respectively represent flow fields resulting from positive half rectified waveforms at a frequency of 25 Hz ($Wo = 18.3$) and flow rate amplitudes of $A_0 = 0.5, 3$. For $A_0 = 0.5$, Figure 7-35 shows a distinct forward directed flow (as is expected) from the velocity profiles in the core region during the acceleration stage $\pi - 1.8\,\pi$. With the influence of a higher frequency oscillation, the annular effects are observed in both core and near-wall regions. Due to the shorter axial displacement time scales, the semi-sinusoidal component of the waveform is quick to react with a forward impulse generated from the bulk inertial momentum of flow. This phenomenon is evident from the velocity contours and vectors where the local increase in the magnitude exists at phase $3\pi/2$, Figure 7-35 (h). Additionally, the phase lag between the near-wall $x/b = 0.95$ and core $x/b = 0$ reaches a maximum in comparison to the other frequencies. As a result of the forward directed velocity magnitude, the shear stress contours reflect peak velocity gradients correspondingly for the phase $3\pi/2$, Figure 7-35 (m). Similarly, the shear stress profiles indicate a substantially steep gradient of velocity which occurs primarily in the acceleration stage for phases $\pi - 1.8\,\pi$. Due to a sharp amplification in the pressure gradient for $Wo = 18.3$ as seen Figure 7-4 (d), higher magnitudes of shear stress are observed in both the core and near-wall regions for the positively directed oscillation component.

Figure 7-36 presents the effects of a stronger oscillation flow rate amplitude ($A_0 = 3$) on the velocity profiles. A distinct forward directed velocity magnitude is observed in the core regions $x/b = 0$ during the acceleration stage $\pi - 1.8\pi$. The remaining phases of the cycle represent the weaker underlying steady component. Annular effects exist across all intervals of the oscillations in the core region. A phase lag occurs between the core and near-wall velocity profiles and is prominent for the forward directed acceleration stage, Figure 7-36 (a,b). A significant spanwise effect of the flow reversal is observed from the velocity contours and vectors across all time intervals of pulsation except the acceleration stage at $3\pi/2$. Due to the shorter time scale of the pulsation at $Wo = 18.3$, the bulk core flow tends to readily adjust for the interval between the steady component and the sinusoidal component of the half rectified cycle. As the flow experiences a sudden shift in the (near-wall) viscous momentum to a much stronger (bulk core) inertial momentum within a single pulsation cycle. The shear stress contours, Figure 7-36 (j-n) present the occurrence of high velocity gradients in the near wall regions, however due to the effect of flow reversal, significant gradients exist in locations away from wall as seen for phases $\pi/2$ and π. Similarly, the oscillating shear stress profile highlights substantially high gradients of velocity in existence from wall to core regions, due the amplified wall viscous effects. The highest values of oscillating shear stress magnitude are observed for $Wo = 18.3, A_0 = 3$ compared to the entire range of symmetric and asymmetric sinusoidal waveforms of varying frequency and flowrate amplitudes.

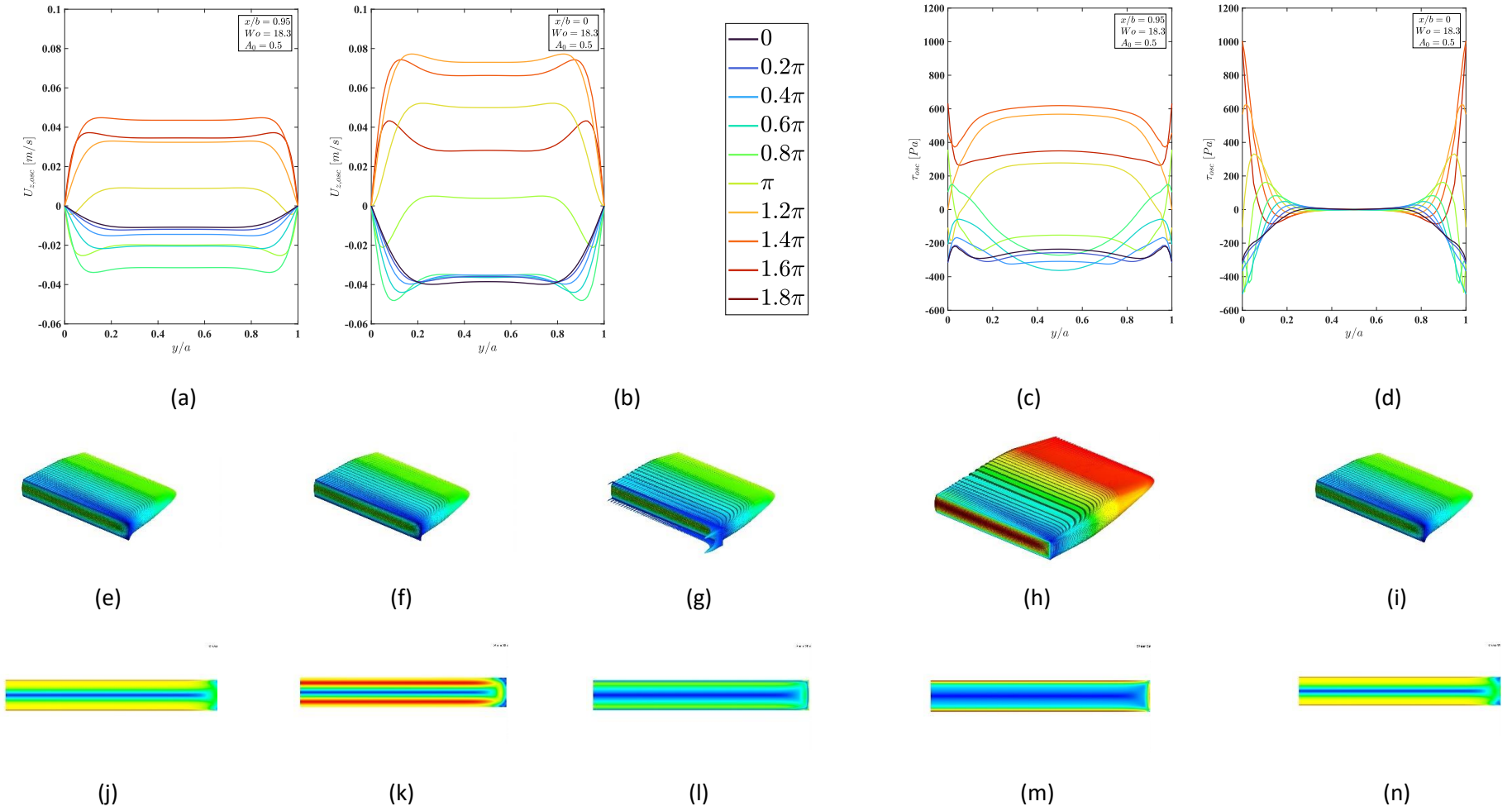

Figure 7-35: Positive half rectified sinusoidal waveform with flow rate amplitude $A_0 = 0.5$ and frequency 25 Hz ($Wo = 18.3$). (a-d) oscillating axial velocity ($U_{z,osc}$) and fluid shear stress (τ_{osc}) profiles along the duct height (y/a) for near-side-wall ($x/b = 0.95$) and central ($x/b = 0$) regions. (e-i) pulsating velocity contour plots at z = 300mm for 5 phases of a pulsation, and (j-n) corresponding fluid shear stress contours.

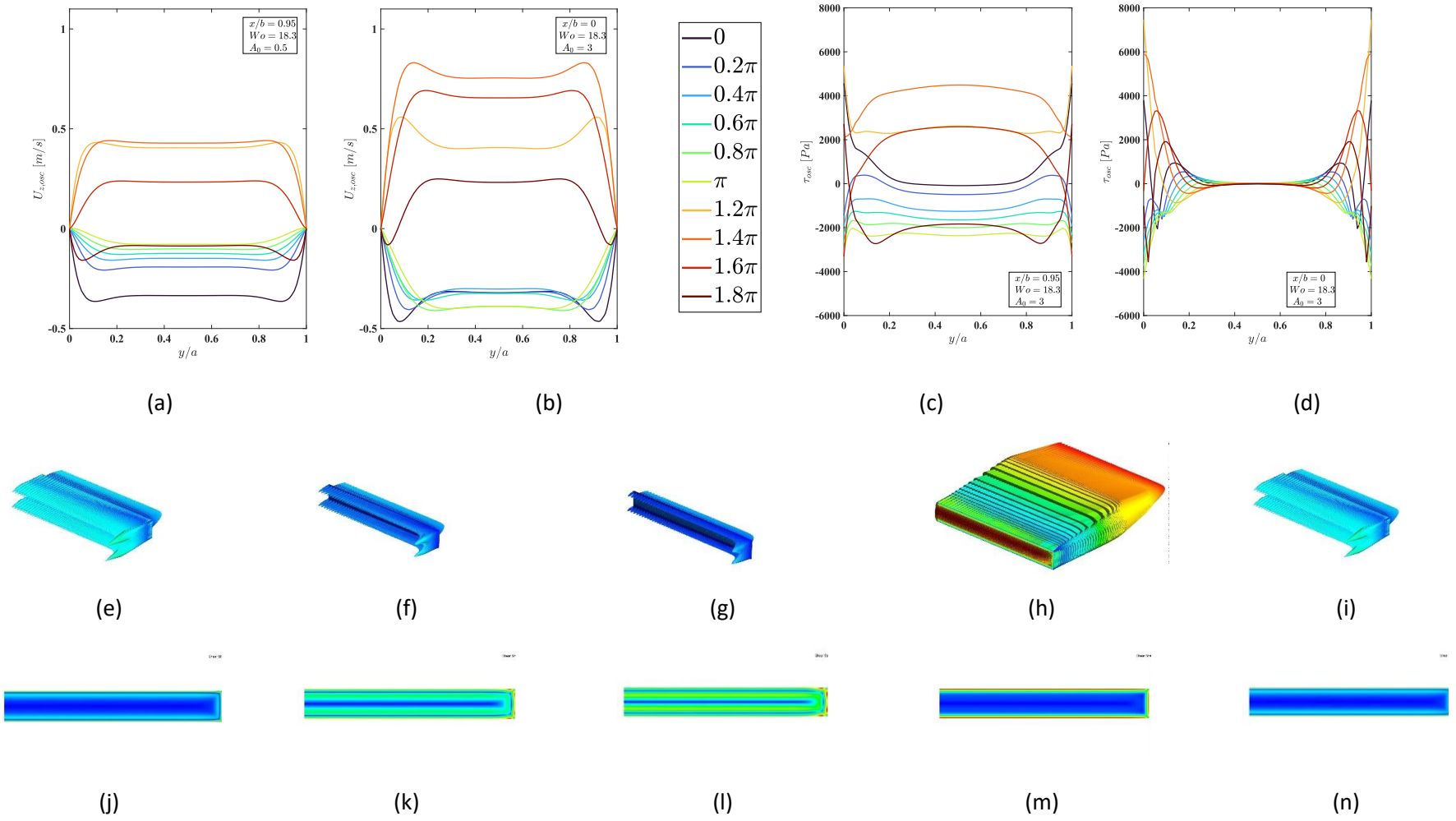

Figure 7-36: Positive half rectified sinusoidal waveform with flow rate amplitude $A_0 = 3$ and frequency 25 Hz ($Wo = 18.3$). (a-d) oscillating axial velocity ($U_{z,osc}$) and fluid shear stress (τ_{osc}) profiles along the duct height (y/a) for near-side-wall ($x/b = 0.95$) and central ($x/b = 0$) regions. (e-i) pulsating velocity contour plots at z = 300mm for 5 phases of a pulsation, and (j-n) corresponding fluid shear stress contours.

Figure 7-37 and Figure 7-38, respectively represent flow fields resulting from negative half rectified waveforms at a frequency of 0.5 Hz ($Wo = 2.5$) and flow rate amplitudes of $A_0 = 0.5, 3$. At $Wo = 2.5$ and $A_0 = 0.5$ there exists a distinct low velocity magnitude in the deceleration cycle between phases $\pi - 2\pi$ as seen in the velocity profiles at $x/b = 0$ and from the velocity contours and vectors at phase $3\pi/2$, Figure 7-37 (h). This occurs because of the weaker effect of oscillation created as a result of a dominant steady underflow which is prominent during the remaining phases of the pulsation. A similar pattern of high velocity gradients exists in the near wall and channel core regions for the negative half rectified waveforms as discussed for the positive half rectified profile. For $A_0 = 3$, Figure 7-38 (b) presents a sharp distinct increase of oscillating velocity magnitude during the peak deceleration cycle for phases $\pi - 2\pi$. A phase shift between the near-wall and core regions is not particularly evident due to the moderate frequency of pulsation however, typically the velocity profiles are suppressed in the near-wall regions due to presence of high near wall viscous forces leading to high velocity gradients. The evidence of a high flowrate amplitude is clearer from the velocity vectors and contours during the peak deceleration stage at phase $3\pi/2$, Figure 7-38 (h) of the pulsation cycle. The corresponding shear stress contour, Figure 7-38 (j-n) shows a weakened near-wall velocity gradient. Since the steady component is insignificant compared to the stronger influence of oscillation, the remaining time intervals of the velocity contour present minimum cycle values Figure 7-38 (e,f,g,i). As a result of the high flowrate amplitude, the peak velocity gradients are nearly doubled compared to the low flowrate amplitude case.

Figure 7-39 and Figure 7-40, respectively represent flow fields resulting from negative half rectified waveforms at a frequency of 2 Hz ($Wo = 5.1$) and flow rate amplitudes of $A_0 = 0.5, 3$.

For $A_0 = 0.5$ and $Wo = 5.1$ in Figure 7-39, peak magnitudes of oscillating velocity exist in the channel core region $x/b = 0$ during phases $1.2\pi - 1.8\,\pi$. A phase lag is evident between the near-wall and core oscillating velocity profiles and is similar to the observations made from the positive half rectified case at $Wo = 5.1$ (Figure 7-33). Peak magnitudes in the pulsating velocity contour and vector plots are seen for phases $\pi/2\,, \pi$, Figure 7-39 (f,g) representing a stronger influence of the underlying steady component, whereas the weaker effect of oscillation during the deceleration motion led by the negative half rectification is distinctly seen for phase $3\pi/2$, Figure 7-39 (h). A larger near-wall velocity gradient is identified in the deceleration stage and consequent shear stress profiles show higher gradients of velocity for phases $1.2\pi - 1.8\pi$ compared to other instances of the cycle. For $A_0 = 3$, Figure 7-40 presents similarities with the oscillating velocity profiles in the core regions observed for $A_0 = 0.5$ for most of the cycle. However, the effect of the stronger flow rate amplitude is evident. Further, the influence of higher oscillation velocity component can be deduced from the velocity contours and vectors, Figure 7-40 (e-i) with an emphasis on the near-

wall regions. A positive impulse of the steady velocity component occurs consistently for all intervals of the pulsation. A strong backward directed velocity magnitude is noticeable during the deceleration cycle at phase $3\pi/2$. The shear stress contours show varied features compared to the case of low flowrate amplitude and thus the influence of high near-wall velocity magnitude is noticeable, resulting in high velocity gradients, Figure 7-40 (j-n). At the start (0) and end (2π) of the pulsation cycle, these large gradients primarily occur in the corner regions with lower values observed in the off-wall regions. Whereas a sharp gradient exists for the remaining intervals of cycle in the surrounding near-wall regions. The oscillating shear stress profiles, Figure 7-40 (c,d) present a differing nature compared to the low flowrate amplitude case which reflect the reaction of a stronger acting oscillation component. This is due to the presence of substantially high near-wall viscous effects. Similarly, a consistent phase lag is evident between the near-wall and core regions of the oscillating shear stress profiles.

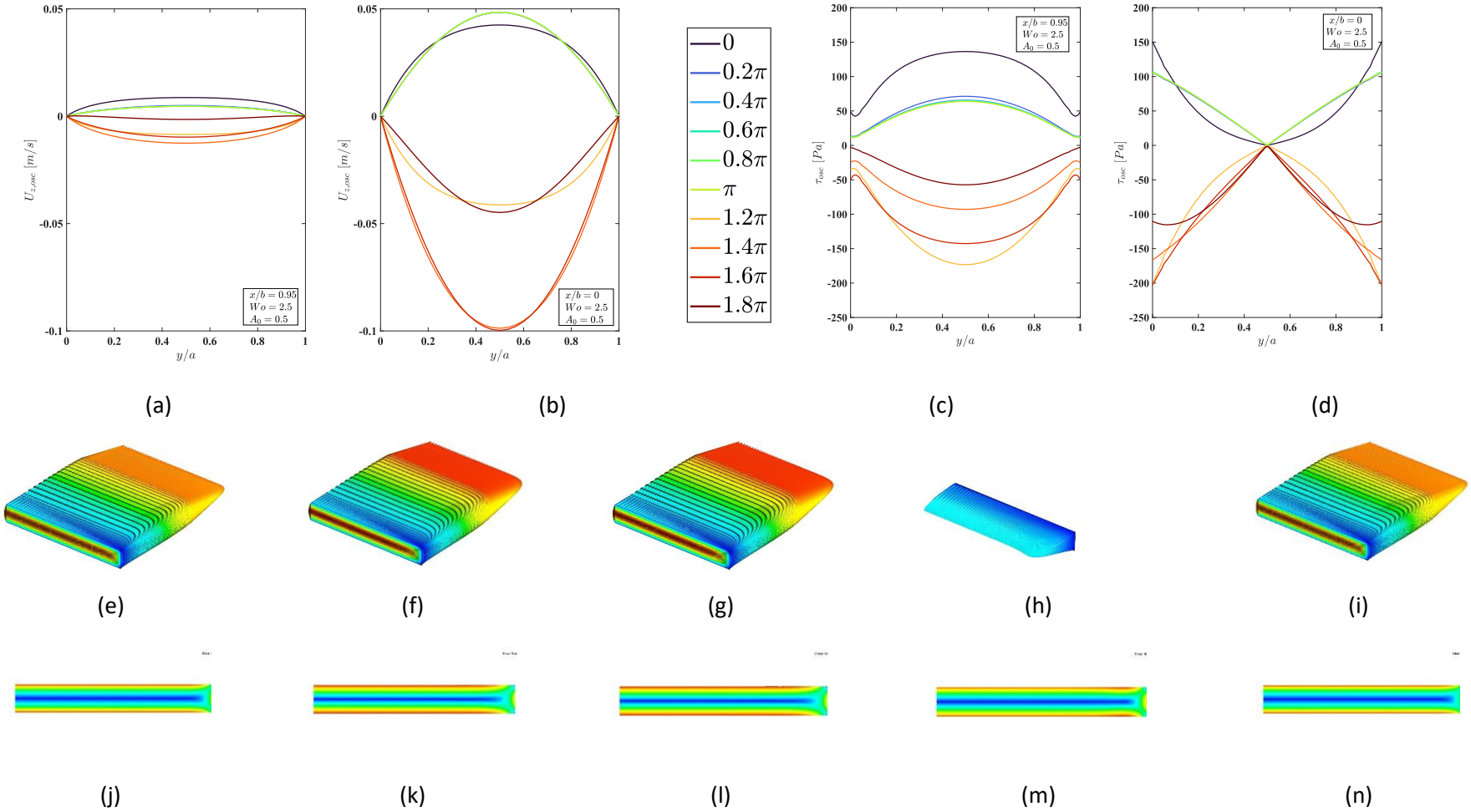

Figure 7-37: Negative half rectified sinusoidal waveform with flow rate amplitude $A_0 = 0.5$ and frequency 0.5 Hz ($Wo = 0.5$). (a-d) oscillating axial velocity ($U_{z,osc}$) and fluid shear stress (τ_{osc}) profiles along the duct height (y/a) for near-side-wall ($x/b = 0.95$) and central ($x/b = 0$) regions. (e-i) pulsating velocity contour plots at z = 300mm for 5 phases of a pulsation, and (j-n) corresponding fluid shear stress contours.

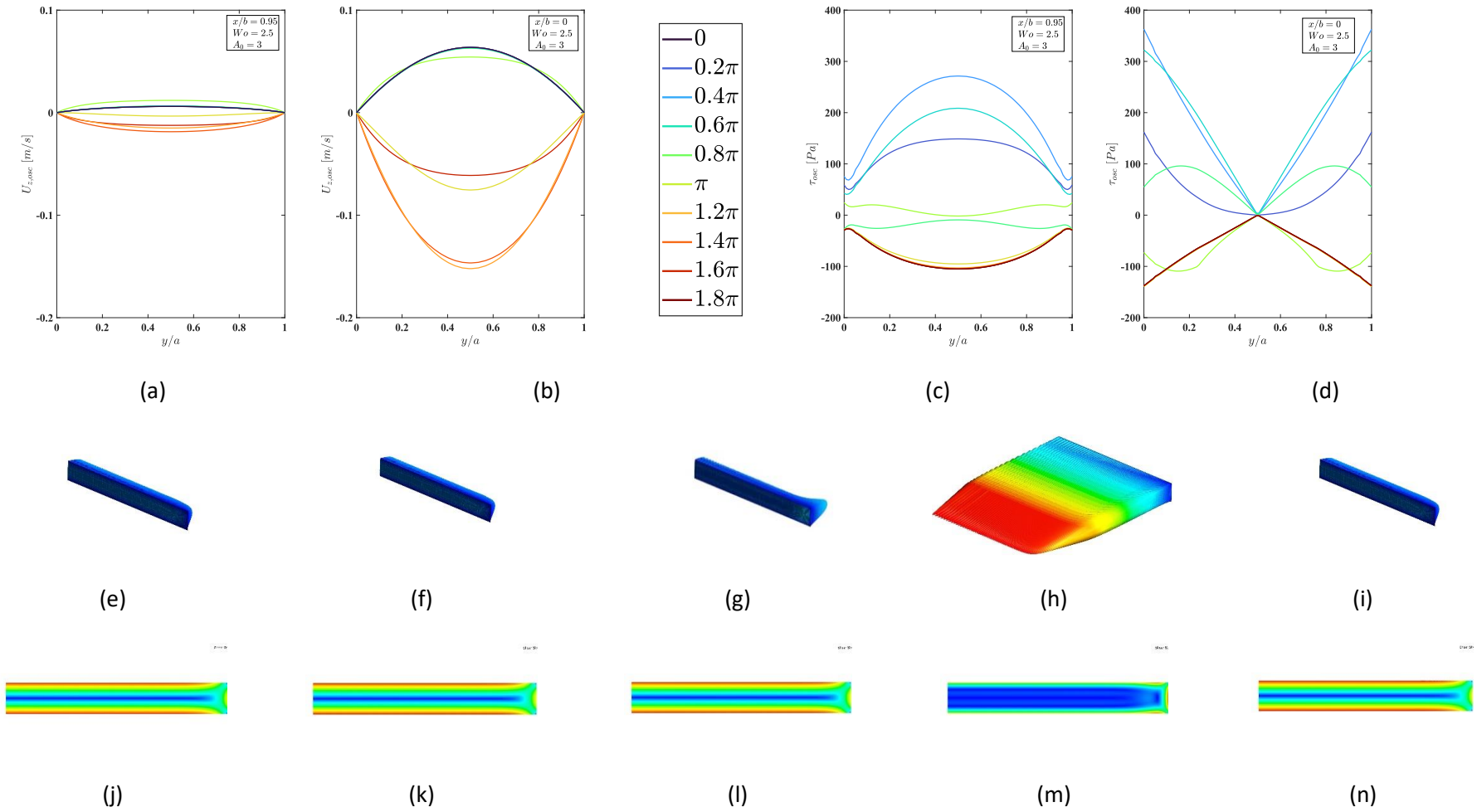

Figure 7-38: Negative half rectified sinusoidal waveform with flow rate amplitude $A_0 = 3$ and frequency 0.5 Hz ($Wo = 2.5$). (a-d) oscillating axial velocity ($U_{z,osc}$) and fluid shear stress (τ_{osc}) profiles along the duct height (y/a) for near-side-wall ($x/b = 0.95$) and central ($x/b = 0$) regions. (e-i) pulsating velocity contour plots at z = 300mm for 5 phases of a pulsation, and (j-n) corresponding fluid shear stress contours.

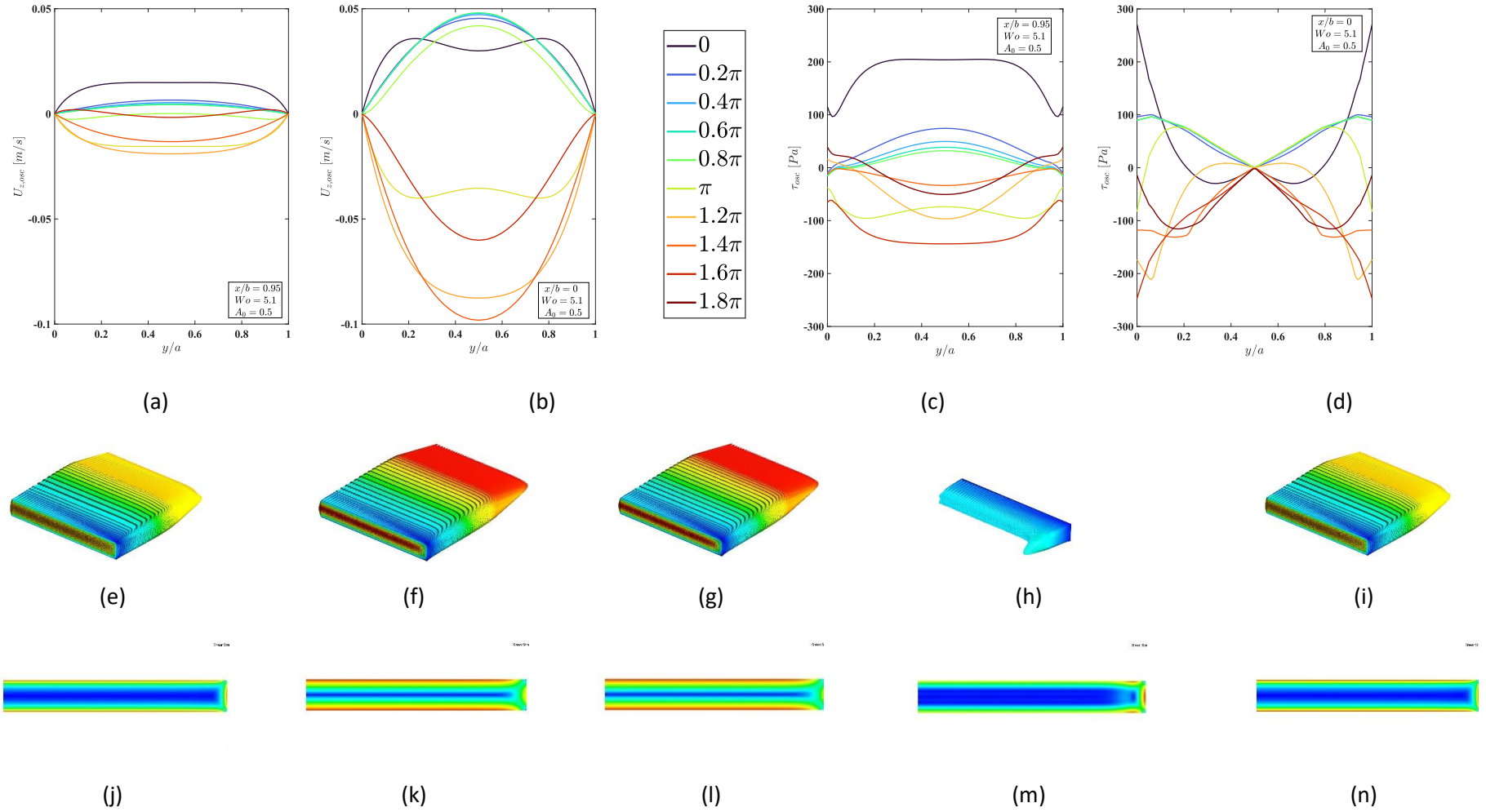

Figure 7-39: Negative half rectified sinusoidal waveform with flow rate amplitude $A_0 = 0.5$ and frequency 2 Hz ($Wo = 5.1$). (a-d) oscillating axial velocity ($U_{z,osc}$) and fluid shear stress (τ_{osc}) profiles along the duct height (y/a) for near-side-wall ($x/b = 0.95$) and central ($x/b = 0$) regions. (e-i) pulsating velocity contour plots at z = 300mm for 5 phases of a pulsation, and (j-n) corresponding fluid shear stress contours.

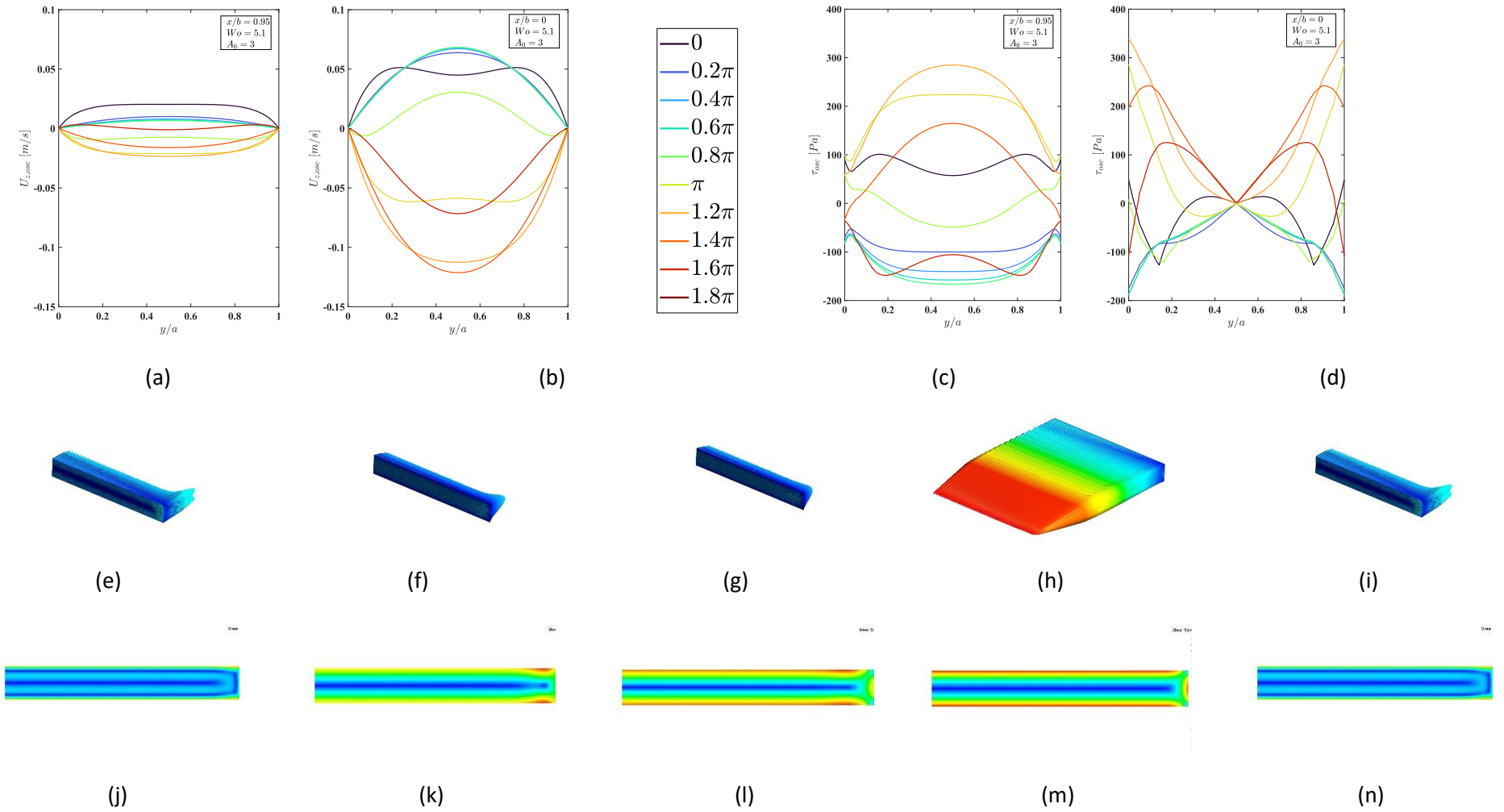

Figure 7-40: Negative half rectified sinusoidal waveform with flow rate amplitude $A_0 = 3$ and frequency 2 Hz ($Wo = 5.1$). (a-d) oscillating axial velocity ($U_{z,osc}$) and fluid shear stress (τ_{osc}) profiles along the duct height (y/a) for near-side-wall ($x/b = 0.95$) and central ($x/b = 0$) regions. (e-i) pulsating velocity contour plots at z = 300mm for 5 phases of a pulsation, and (j-n) corresponding fluid shear stress contours.

Figure 7-41 and Figure 7-42, respectively represent flow fields resulting from negative half rectified waveforms at a frequency of 25 Hz ($Wo = 18.3$) and flow rate amplitudes of $A_0 = 0.5, 3$. For $A_0 = 0.5$, Figure 7-41 shows amplified effect of the backward directed flow for phases $\pi\ to\ 2\pi$. Annular effects which are a characteristic trait of such high frequencies are observed for the velocity profiles in the core region. There exists a phase lag between the velocity profiles at near-wall and core regions, Figure 7-41 (a,b). As a result of stronger steady component of the flow, the backward component of oscillation is dampened out as is evident from the velocity contour and vectors. Across all intervals of the cycle, the influence of underlying steady component is seen, while for the deceleration stage at phase $3\pi/2$, a weaker influence of oscillation amplitude is visible, with the presence of a near side-wall flow reversal seen in Figure 7-41 (h). Although the backward directed flow as was seen for the other frequencies is not evident, this can be attributed to the shorter time scales of fluid displacement at higher frequency which creates to a diminishing impact on the rectified flowrate profile. The magnitudes of the gradients of velocity are substantially lower for both near-wall and core regions compared to the other frequencies. The presence of high near wall viscous effects is seen from the oscillating shear stress profiles, Figure 7-41 (c,d). There exists a sharp increase in the pressure gradient amplitude and a phase lag of $\pi/2$ can be seen from the Figure 7-5 (d).

For $A_0 = 3$, Figure 7-42 presents a relatively greater backward directed flow in the core regions $x/b = 0$ during the deceleration stage $\pi - 1.8\pi$ as a result of the stronger oscillation component. The underlying steady component is strengthened for the remaining phases of the cycle. A phase lag is seen between the near-wall and core velocity profiles and the substantially high velocity magnitudes exist as a result of the annular effects. A strong flow reversal is noticed for the successive durations of the cycle from the velocity contours and vectors, Figure 7-42 (e-i). This effect is attributed to the rapidly shifting fluid momentum in the shorter displacement timescale due the existence of both stronger viscous and inertial effects. As a result of the half rectified profile, the flow field reacts slowly to accommodate the high frequency impulse driven by the oscillation. Correspondingly the shear stress contours, Figure 7-42 (j-n) present the evidence of the significantly high near-wall viscous forces, and the near-wall influence of flow reversal shows a sharp change in gradients of velocities as seen for phases 0, 2π. The shear stress profiles in the core and near-wall region, Figure 7-42 (c,d) show a significant impact of the high amplitude and shorter timescale oscillation component. Greater magnitudes of velocity gradient are seen in the core region due to presence of high viscous forces as a result of the significant effects of flow-reversal and flatter profiles are evident in the vicinity of $y/a = 0.5$ due to the strong inertial impulse. Thus, the magnitudes of shear stress and the pressure gradient obtained are by far the highest compared across the entire range of pulsation waveforms, Wo and A_0.

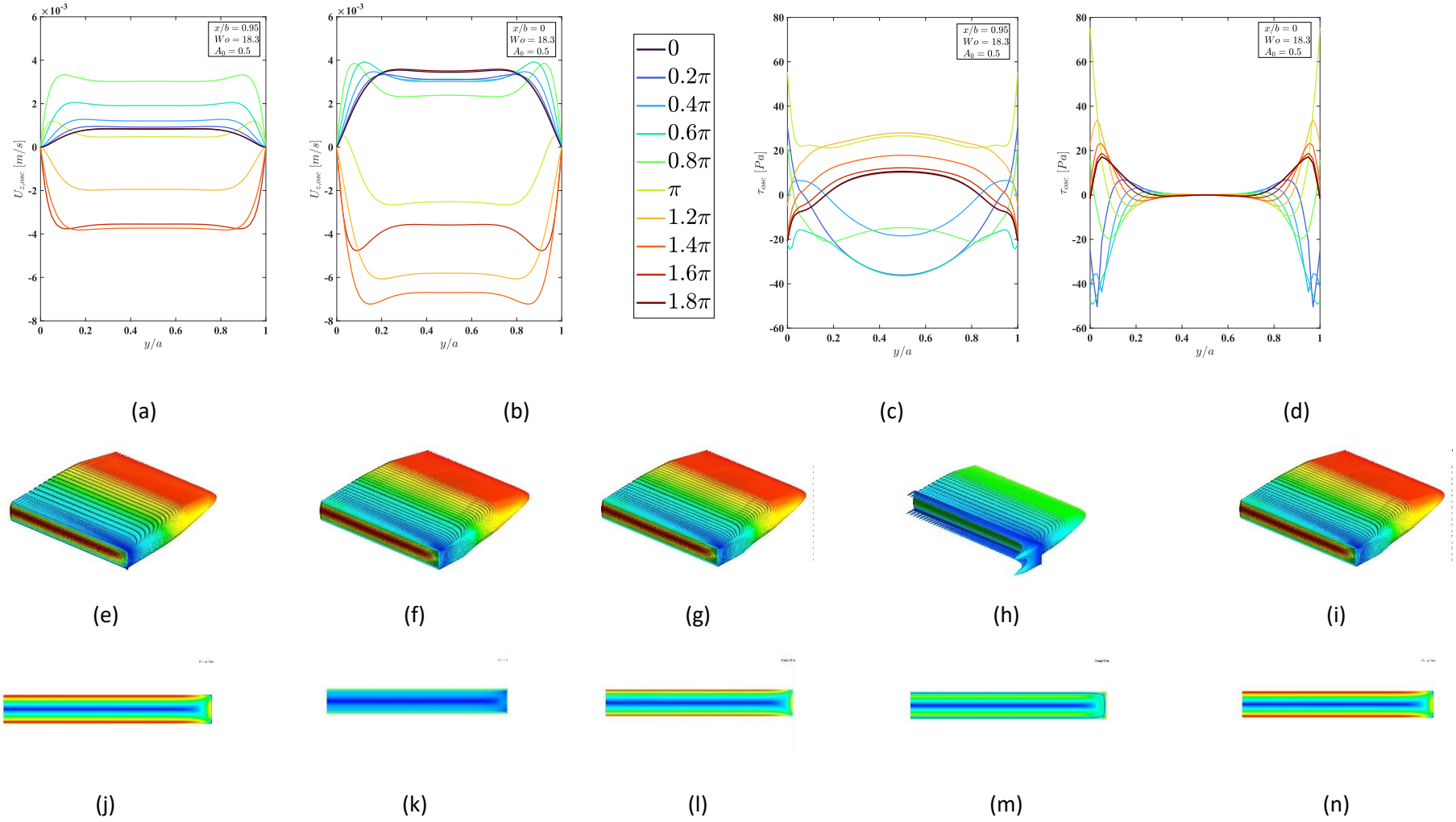

Figure 7-41: Negative half rectified sinusoidal waveform with flow rate amplitude $A_0 = 0.5$ and frequency 25 Hz ($Wo = 18.3$). (a-d) oscillating axial velocity ($U_{z,osc}$) and fluid shear stress (τ_{osc}) profiles along the duct height (y/a) for near-side-wall ($x/b = 0.95$) and central ($x/b = 0$) regions. (e-i) pulsating velocity contour plots at z = 300mm for 5 phases of a pulsation, and (j-n) corresponding fluid shear stress contours.

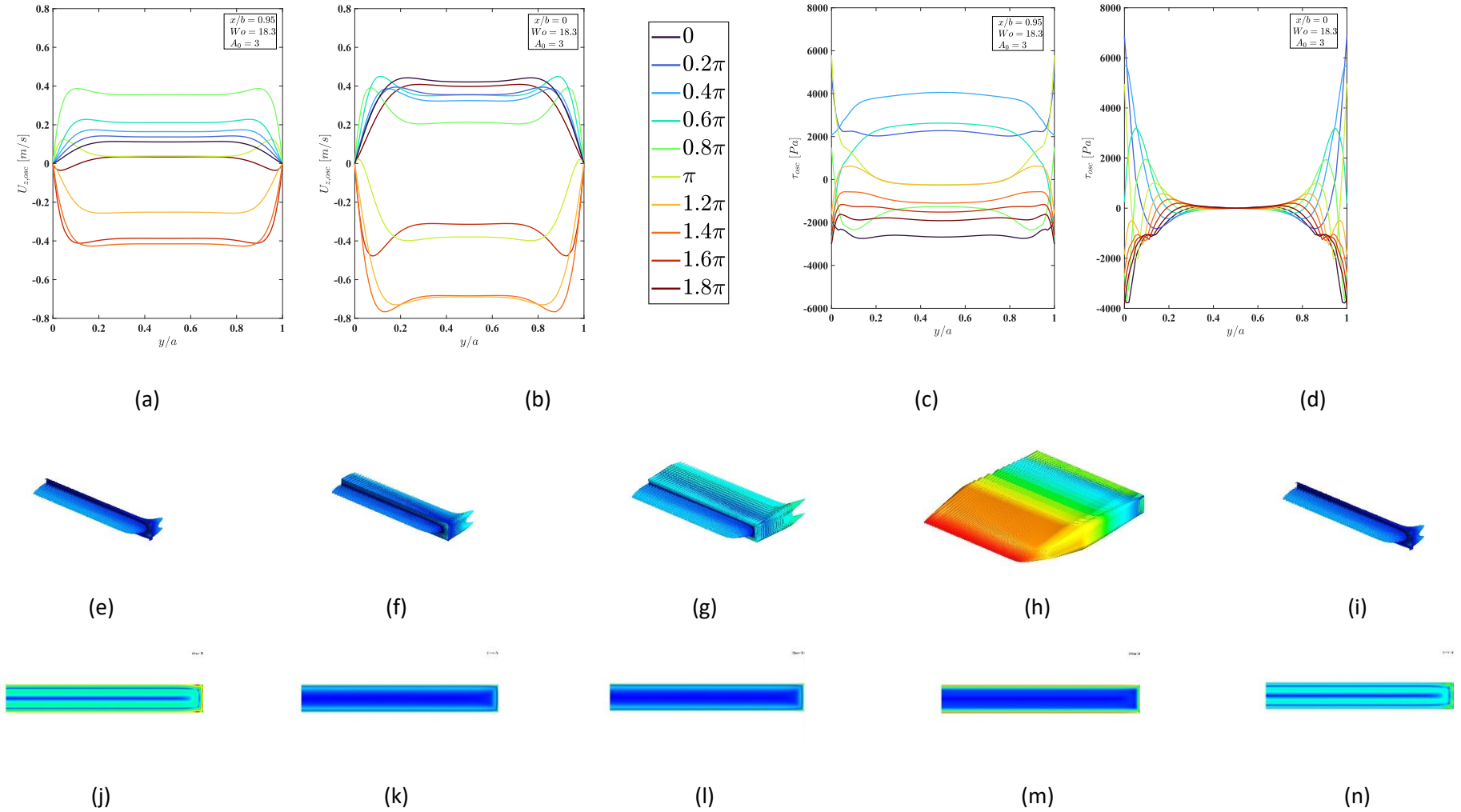

Figure 7-42: Negative half rectified sinusoidal waveform with flow rate amplitude $A_0 = 3$ and frequency 25 Hz ($Wo = 18.3$). (a-d) oscillating axial velocity ($U_{z,osc}$) and fluid shear stress (τ_{osc}) profiles along the duct height (y/a) for near-side-wall ($x/b = 0.95$) and central ($x/b = 0$) regions. (e-i) pulsating velocity contour plots at z = 300mm for 5 phases of a pulsation, and (j-n) corresponding fluid shear stress contours.

7.3 Friction Factor

Figure 7-43 plots the variation of the friction factor ratio ($\bar{\sigma}_p/\sigma_s$) versus Womersley number (Wo) for varying flow rate amplitude (A_0) for multiple pulsation waveforms. $\bar{\sigma}_p/\sigma_s$ is a ratio of the time-averaged pulsating flow friction factor to the steady flow friction factor, parameters are defined in section 6.10.3. For symmetric sinusoidal pulsations at low frequencies and low-to-moderate A_0, the ratio is approximately equal to 1 [56, 126]. This indicates little effect of pulsation on the friction factor as the shear stress magnitudes are lower compared to the cases at higher flowrate amplitude. However, the influence of higher flow rate amplitudes on the friction factor ratio is distinctly evident, reflecting a strengthening of the wall shear stresses as is understood with an increase in velocity [15, 21]. For higher frequencies $Wo \geq 5$, the increased wall shear stress results in a magnification of the friction factor ratio and the effects are further pronounced for $A_0 = 3$.

A similar understanding is determined from the cases of asymmetric sinusoidal (leading and lagging) waveform profiles, Figure 7-43(b). Due to the features exhibited by asymmetric flowrate such as rapid fluctuations in the acceleration and deceleration stages of pulsation, the friction factor is further increased compared to the symmetric sinusoidal cases. This is reflected by a substantial build-up of wall shear stresses for $Wo \geq 5$ with a maximum value of $\bar{\sigma}_p/\sigma_s$ at $Wo = 18.3$ and $A_0 = 3$.

The positive and negative half rectified waveforms, Figure 7-43 (c) present overall increased values of friction factor ratio compared to the symmetric sinusoidal profiles. This can be attributed to the co-existence of steady and sinusoidal components of the flowrate. In order to accommodate this transition within a pulsation cycle, there is an increase in shear stress magnitudes which leads to substantially high time-averaged friction factors. The maximum value of the friction factor is reached at $Wo = 18.3$ and $A_0 = 3$ for the negative half rectified profile.

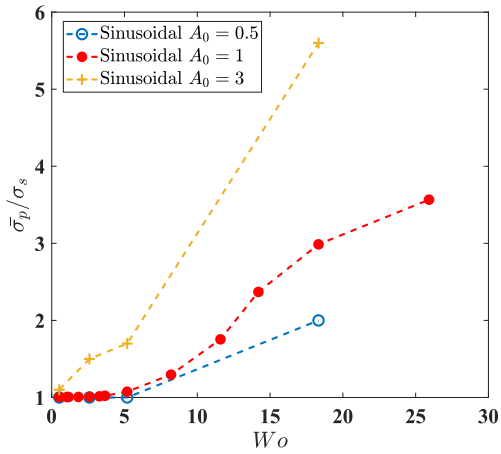

(a)

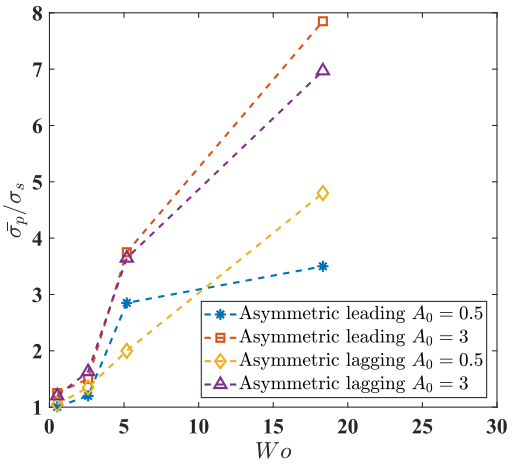

(b)

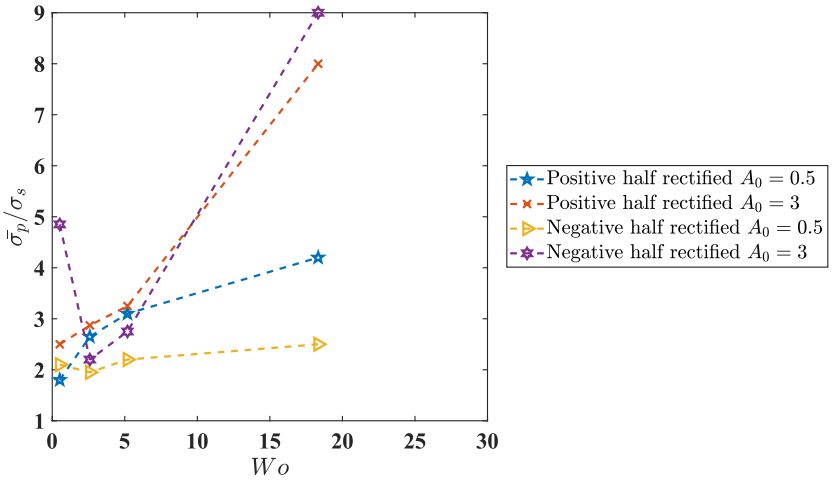

(c)

Figure 7-43: Variation of friction factor ratio with Wo and A_0 for (a): Symmetric sinusoidal waveform, (b): Leading and lagging asymmetric waveform and (c): Positive and negative half rectified waveform.

7.4 Temporal variation of thermal parameters

This section describes the time dependent behaviour of key thermal parameters for each pulsation waveform. Each column within each figure in this section shows the effect of increasing flow rate amplitude (A_0). Each row indicates the effects of increasing Womersley number (Wo). Both CFD and experimental data is presented. CFD results represent instantaneous data from a single pulsation once periodic flow has been established and convergence has been achieved, whereas experimental data is phase-averaged over 10 periodic cycles. There is no experimental data for the highest frequency of pulsation $Wo = 18.3$ $(f = 25\ Hz)$ as a result of the physical restrictions of a very sensitive and thin bottom boundary of the test setup. Additionally, the temperature differences obtained are acutely small scale [115] and thus the spectral resolution of the data obtained from infrared thermography is reduced significantly and falls within the measurement error band. Generally, there exists appreciable agreement between the CFD and experimental datasets. The agreement is better at low frequencies and low flow rate amplitudes. The experimental data presents increased deviation from the CFD results at higher frequencies and higher flow rate amplitudes due to the limitations in the experimental setup.

Typically for a flow pulsation maintained under a thermal gradient, the heat transfer characteristics are governed by the time scales of axial convection and transverse diffusion [102, 127]. The determination of heat transfer enhancement is dependent purely on the coupled influence of imposed flow frequency and flow rate amplitude. It is understood (for conventional waveform formats: symmetric sinusoidal and asymmetric sinusoidal that during the acceleration stages of the pulsation cycle) i.e., $0 \leq \theta \leq \pi$, the bulk core fluid drives the heat flow within the fluid boundary layers. While during the deceleration stage of the pulsation $\pi \leq \theta \leq 2\pi$, the transverse diffusion of heat develops from the heated walls to the fluid core regions as a result of high near-wall viscous effects.

7.4.1 Symmetric sinusoidal pulsation

Figure 7-44 plots the oscillating wall and oscillating bulk fluid temperature profiles as well as the difference between the two for a symmetric sinusoidal waveform format. The figures indicate an interlinked nature of the wall and bulk temperatures associated with the effect of pulsation. A close understanding is established between the features of flowrate profile and its corresponding temperature profile. During the acceleration stage of pulsation $0 \leq \theta \leq \pi$, the temperature profiles react with a decrease in magnitudes, attaining a lowest at interval π. While in the deceleration pulsation stage $\pi \leq \theta \leq 2\pi$, as the core fluid retards, an increase in the temperature magnitude is observed towards the end of the cycle. Since the bottom heated wall has high thermal

conductivity and low thermal mass, the wall temperature varies in both space and time. For a sinusoidal waveform (Figure 7-44), an increase in A_0 results in a reduction in the temperature difference between the wall and bulk. This is valid for all frequencies since increased amplitudes of flow oscillations, lead to a rapid withdrawal of heat from the wall to the core fluid regions due to an increase in *Re* and an enhanced effect of convection [84, 87]. The cases result in significantly lower bulk temperatures compared to the wall temperatures observed at lower A_0, thus further promoting heat transfer.

Increasing Wo, the magnitudes of wall temperatures decrease since the thickness of thermal boundary layer decreases (or the thermal boundary layer becomes thinner) due to the existence of high near-wall viscous forces (See Section 7.1.1, Figure 7-1) at high frequencies. The viscous dominant low frequency flow exhibits in phase characteristics of wall and bulk temperatures. This is as a result of longer displacement timescales leading to higher temperature gradients from the heated wall to bulk core regions. With the case of inertial high frequency flow, an evolution of phase lag for $Wo = 2.5$ is evident between the wall and bulk temperatures which is as a result of shorter fluid displacement timescales. The phase lag subsequently increases to a maximum of angle $18°$ for $Wo = 5.1$ and 18.3. This leads to smaller magnitudes of temperature profiles, as seen for e.g., Figure 7-44 (c), (d), (h), (l). It is evident at the highest frequency $Wo = 18.3$, the fast-moving oscillation produces insignificant effect on the bulk and wall temperatures, thus the magnitudes are far lower compared to the corresponding cases of Wo.

There exists a reasonable agreement associated between the experimental and the CFD results for the oscillating wall and bulk temperature profiles at low-moderate frequencies. Although the agreement worsens and there is some deviation between the two datasets particularly for the high frequency and respective high flow rate amplitudes due to the oscillations and non-linearities induced by the thin foil boundary to accommodate for such large pressure gradients developed by the high frequency symmetric sinusoidal waveform.

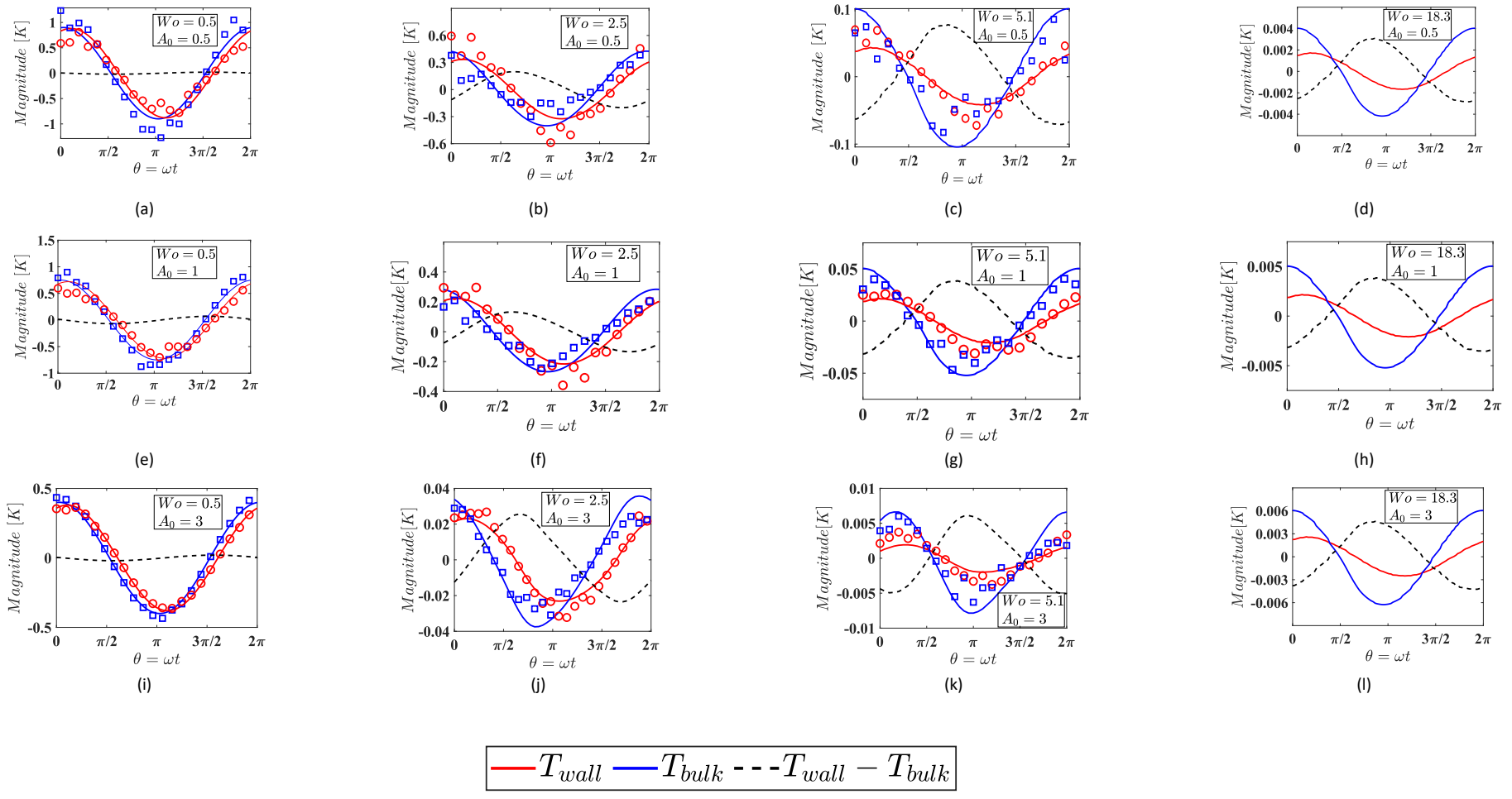

Figure 7-44 (a-l): Temporal variation of wall, bulk temperature and the driving temperature difference for a **symmetric sinusoidal pulsation waveform**. Moving across each row shows the effects of increasing Wo for the same A_0. Moving down a column shows the effects of increasing A_0 for a fixed Wo. Solid lines present the CFD results, and markers show the experimental results. Note that no experimental data exists for the higher frequency $Wo = 18.3$ cases.

7.4.2 Asymmetric sinusoidal pulsation waveform

7.1.1.1 Leading Asymmetric

Figure 7-45 plots the oscillating wall and oscillating bulk fluid temperature profiles as well as the difference between the two for a leading asymmetric waveform format. The figures present a clear influence of the imposed asymmetric profile on the temporal evolution of wall and bulk temperature profiles. As understood from 7.1.1.1, the flowrate profile features a brief interval of rapid acceleration at the start of the cycle, the moderate-highest frequency cases at $Wo = 2.5, 5.1$ and 18.3 from

Figure 7-45 (b-d, f-h, j-l) capture this effect by indicating a simultaneous decrease in the wall and bulk temperatures at the commencement of the oscillating cycle. Further, as a result of a gradual deceleration stage, a steady increase in the magnitudes of temperature profiles is observed throughout the phases $\pi \leq \theta \leq 3\pi/2$. However towards the end of deceleration cycle, which comprises of a brief accelerating flow, the wall and bulk oscillating temperature profiles do not evidently adjust to this directional change of flowrate and thus, settle with a steady increase of magnitudes. However, the oscillating wall and bulk temperatures at low frequency case, $Wo = 0.5$ responds gradually to the longer time period-imposed oscillation. Thus, despite the asymmetric characteristics as described above, there is an increase in the consequent wall and bulk temperatures for the longer deceleration period for interval $\pi/2 \leq \theta \leq 3\pi/2$, eventually followed by a decrease in magnitudes to reflect the concluding acceleration stage of asymmetry. With an increase in A_0, the bulk temperature shows pronounced effect with stepper magnitudes suggesting enhanced removal of heat. This is induced by the rapidly changing characteristics of leading asymmetric flowrate, see Figure 7-2. However, the wall temperature shows a delayed (weak) reaction to the fast-moving pulsation. The driving temperature difference shows a higher magnitude during the first half of the acceleration stage suggesting effective heat withdrawal while the magnitudes settle towards the latter half as the deceleration cycle is weaker in comparison.

Increasing Wo shows a decreasing trend of wall and bulk temperature magnitudes across the range of frequencies and follows the similar inference drawn from the symmetric sinusoidal waveform. It is noticeable that the low-moderate frequencies respond and react quicker to the onset of the acceleration cycle of the leading asymmetric flowrate. However, the high-highest frequencies show a delayed response of temperature profile due to the shorter displacement timescale of the flowrate. The driving temperature difference reaches a maximum towards the latter half of the deceleration stage for $Wo = 5.1, 18.3$, whereas for the low-moderate frequency cases it is the

contrary. The characteristics offered by an asymmetric flowrate profile on the distinct evolution of oscillating temperature profiles are evident in comparison to the cases of symmetric sinusoidal.

There exists a reasonable agreement associated between the experimental and the CFD results for the oscillating wall and bulk temperature profiles at low-moderate frequencies. Although the agreement worsens and there is some deviation between the two datasets particularly for the high frequency and respective high flow rate amplitudes due to the oscillations and non-linearities induced by the thin foil boundary to accommodate for such large pressure gradients developed by the high frequency asymmetric sinusoidal waveform.

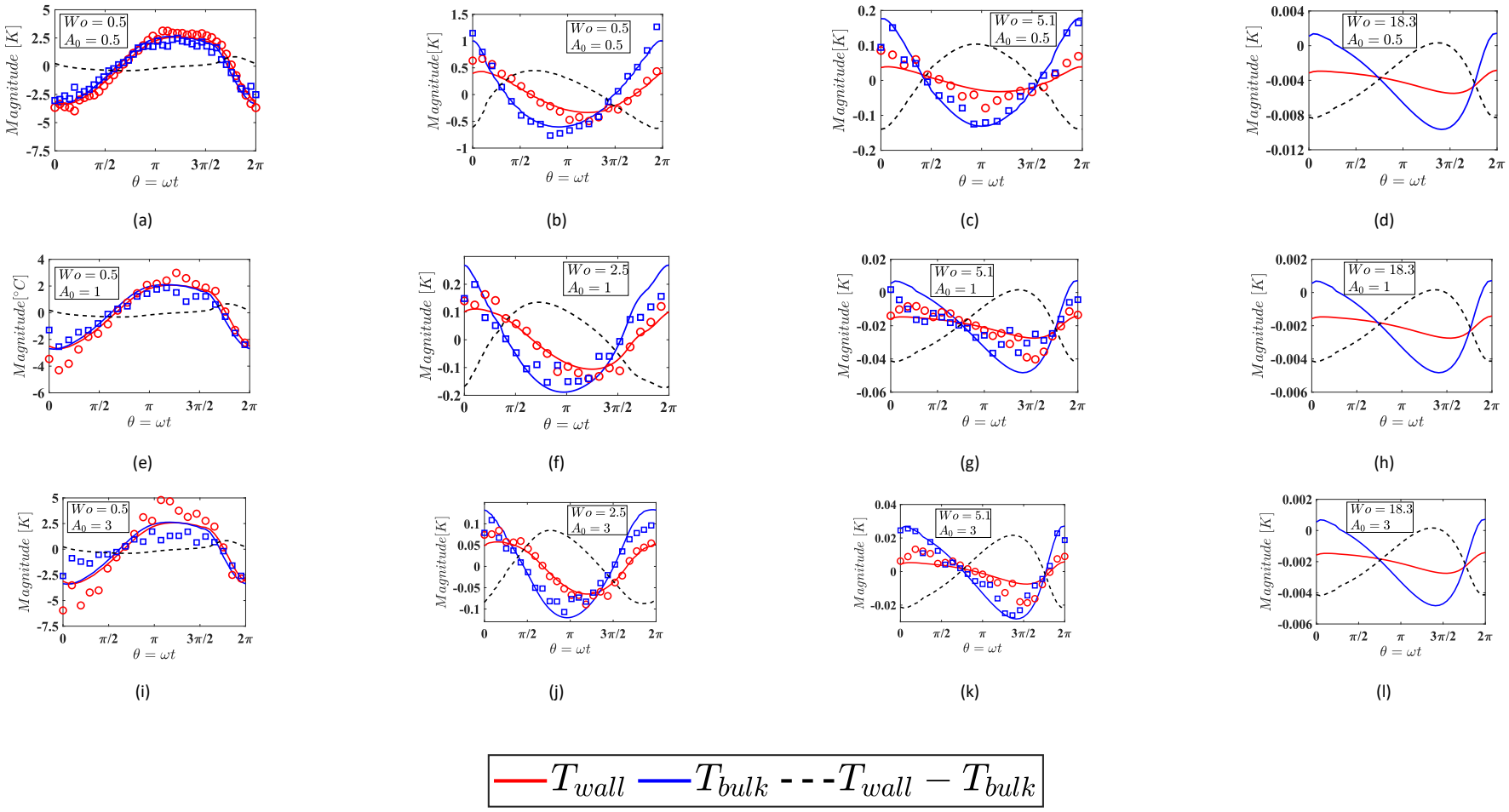

Figure 7-45 (a-l): Temporal variation of wall, bulk temperature and the driving temperature difference for a **leading asymmetric sinusoidal waveform**. Moving across each row shows the effects of increasing Wo for the same A_0. Moving down a column shows the effects of increasing A_0 for a fixed Wo. Solid lines present the CFD results, and markers show the experimental results. Note that no experimental data exists for the higher frequency $Wo = 18.3$ cases.

7.1.1.2 Lagging Asymmetric

Figure 7-46 plots the oscillating wall and oscillating bulk fluid temperature profiles as well as the difference between the two for a lagging asymmetric waveform format. The figures present a clear influence of the imposed asymmetric profile on the temporal evolution of wall and bulk temperature profiles. As understood from Section 7.1.1.2, the flowrate profile features gradual acceleration at the start of the cycle, the moderate-highest frequency cases at $Wo = 2.5, 5.1$ and 18.3 from Figure 7-46 (b-d, f-h, j-l) capture this effect by indicating a simultaneous decrease in the wall and bulk temperatures at the commencement of the oscillating cycle. Further, as a result of an acute directional shift in the flowrate before the deceleration stage, peak lower temperatures are reached, as noticed at about phase π. The wall and bulk temperatures thereafter increase gradually to a maximum magnitude towards the gradual deceleration stage at end of the cycle. However, the oscillating wall and bulk temperatures at low frequency case, $Wo = 0.5$ presents a significant delay in response to the longer time period-imposed oscillation. Thus, despite the asymmetric characteristics as described above, there is an increase in the consequent wall and bulk temperatures for the gradual acceleration stage for interval $0 \leq \theta \leq \pi/2$, and gets further extended till up to the phase $3\pi/2$, followed by a decrease in magnitudes to reflect the concluding stage of asymmetry. With an increase in A_0, the bulk temperature shows pronounced effect with stepper magnitudes suggesting enhanced removal of heat. This is induced by the rapidly changing characteristics of leading asymmetric flowrate. However, the wall temperature shows a delayed (weak) reaction to the fast-moving pulsation. The driving temperature difference shows a higher magnitude during the first half of the acceleration stage suggesting effective heat withdrawal while the magnitudes settle towards the latter half as the deceleration cycle is weaker in comparison.

Increasing Wo shows a decreasing trend of wall and bulk temperature magnitudes across the range of frequencies and follows the similar inference drawn from the symmetric sinusoidal waveform. It is noticeable that the low-moderate frequencies respond and react quicker to the onset of the acceleration cycle of the lagging asymmetric flowrate compared to the leading asymmetric profiles. Additionally, the high-highest frequencies demonstrate a swifter response of temperature profile particularly in the acceleration stage $0 \leq \theta \leq \pi/2$ due to the shorter displacement timescale of the flowrate. The driving temperature difference reaches a maximum towards the end of acceleration at $\pi/2$ in advance of the sharp directional flowrate shift for $Wo = 5.1, 18.3$ cases, whereas for the low-moderate frequency cases it is slight delayed and further slowed for the former. The characteristics offered by an asymmetric flowrate profile on the distinct evolution of oscillating temperature profiles are evident in comparison to the cases of symmetric sinusoidal.

There exists a reasonable agreement associated between the experimental and the CFD results for the oscillating wall and bulk temperature profiles at low-moderate frequencies. Although the agreement worsens and there is some deviation between the two datasets particularly for the high frequency and respective high flow rate amplitudes due to the oscillations and non-linearities induced by the thin foil boundary to accommodate for such large pressure gradients developed by the high frequency asymmetric sinusoidal waveform.

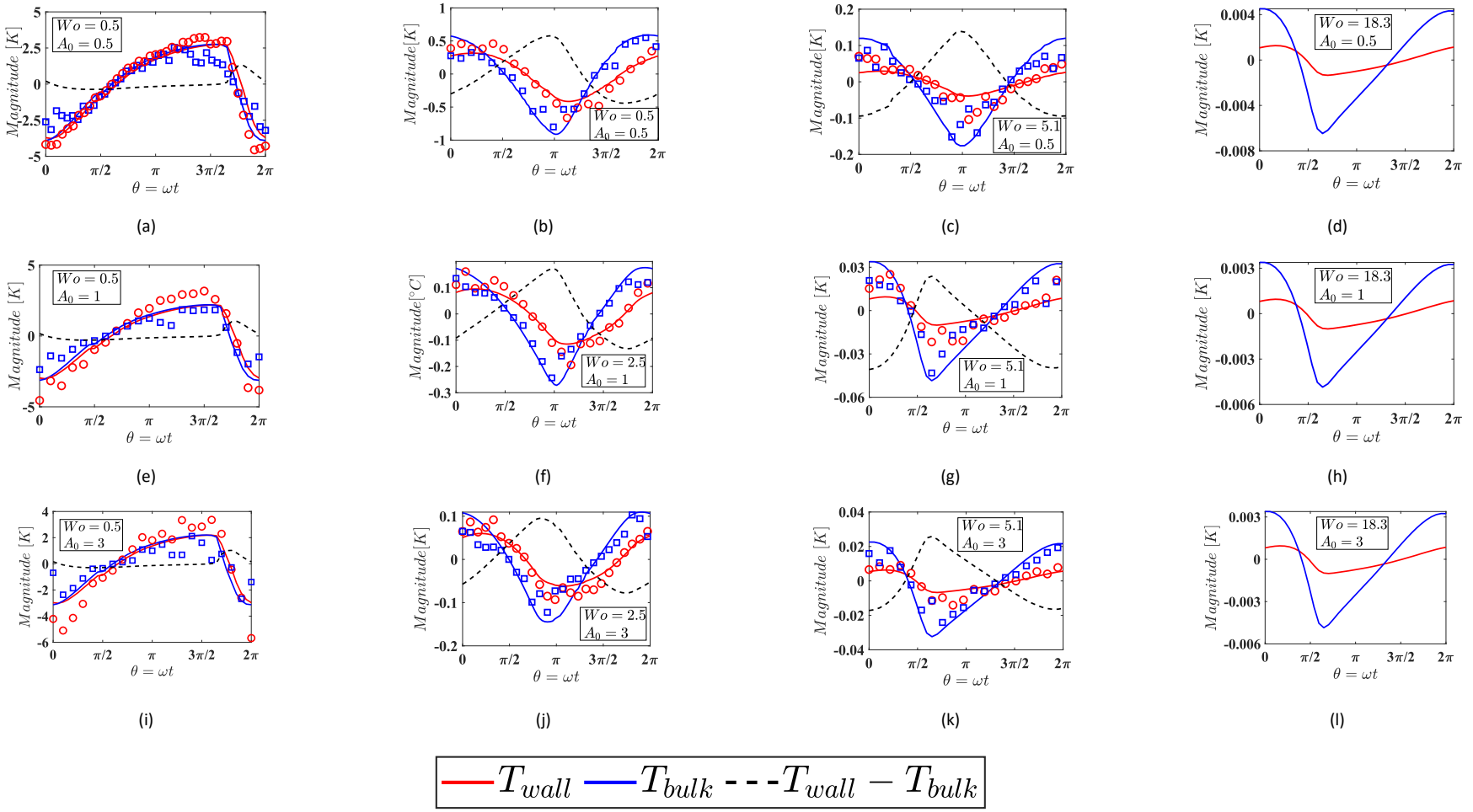

Figure 7-46 (a-l): Temporal variation of wall, bulk temperature and the driving temperature difference for a **lagging asymmetric sinusoidal waveform**. Moving across each row shows the effects of increasing Wo for the same A_0. Moving down a column shows the effects of increasing A_0 for a fixed Wo. Solid lines present the CFD results, and markers show the experimental results. Note that no experimental data exists for the higher frequency $Wo = 18.3$ cases.

7.4.3 Half rectified sinusoidal pulsation waveform

7.1.1.3 Positive half rectified profile

Figure 7-47 plots the oscillating wall and oscillating bulk fluid temperature profiles as well as the difference between the two for a positive half rectified waveform format. The figures present a clear influence of the imposed rectified profile on the temporal evolution of wall and bulk temperature profiles. As understood from 7.1.2.1 the flowrate profile features a half interval of steady component at the start of the cycle, the wall and bulk temperatures indicate a small increase followed by stabilisation of temperature throughout the steady interval, identified from the low frequency case at $Wo = 0.5$, (a, e, i). Further with the onset of acceleration stage (i.e., forward directed impulse) the temperature profile decreases momentarily till up to phase $3\pi/2$ with a proportional increase in temperature towards the end of the deceleration stage of half rectified profile.

However, for the moderate-highest frequency cases at $Wo = 2.5, 5.1$ and 18.3 from (b-d, f-h, j-l) the wall and bulk temperature profiles respond with a delay to the shorter timescale of oscillation. Further, as a result of a co-existence of steady and a semi-sinusoidal component in equal time intervals within a cycle, the temperature profiles present a steady increase in magnitudes between phases $0 \leq \theta \leq \pi$, followed a sharp decline between the semi-sinusoidal stages of the cycle before a small rise towards the end of the cycle. It can be inferred that the temperature profile does not cope to the fast impulse reactions resulted from the half rectified waveform that features a consequent rapid change in the bulk flow direction. With an increase in A_0, the bulk temperature shows pronounced effect with stepper magnitudes, suggesting enhanced removal of heat. This is induced by the rapidly changing characteristics of the increased flowrate half rectified format of oscillation. However, the wall temperature shows a delayed (weak) reaction to the fast-moving pulsation. The driving temperature difference shows a higher magnitude during the first half of the acceleration stage suggesting effective heat withdrawal while the magnitudes settle towards the latter half as the deceleration cycle is weaker in comparison.

Increasing Wo shows a decreasing trend of wall and bulk temperature magnitudes across the range of frequencies and follows the similar inference drawn from the symmetric sinusoidal waveform. It is noticeable that the low frequency flow responds and reacts slowly to the onset of semi-sinusoidal flowrate profile thus resembling the format. Whereas the high-highest frequencies demonstrate a swifter response of temperature profile particularly in the semi-sinusoidal component stage at phases $\pi/2 \leq \theta \leq 3\pi/2$ due to the shorter displacement timescale of the flowrate. The driving temperature difference reaches a high peak towards the end of the semi-sinusoidal component

with a low peak at the onset of the semi-sinusoidal stage at phase $\pi/2$ for $Wo = 5.1, 18.3$ cases. Whereas for the low-moderate frequency cases it is slightly advanced towards the onset of the semi-sinusoidal component and further gets slowed for the former. The characteristics offered by a half rectified flowrate profile on the distinct evolution of oscillating temperature profiles are evident in comparison to the cases of symmetric sinusoidal.

There exists a reasonable agreement associated between the experimental and the CFD results for the oscillating wall and bulk temperature profiles at low-moderate frequencies. Although the agreement worsens and there is some deviation between the two datasets particularly for the high frequency and respective high flow rate amplitudes due to the oscillations and non-linearities induced by the thin foil boundary to accommodate for such large pressure gradients developed by the high frequency half rectified waveform.

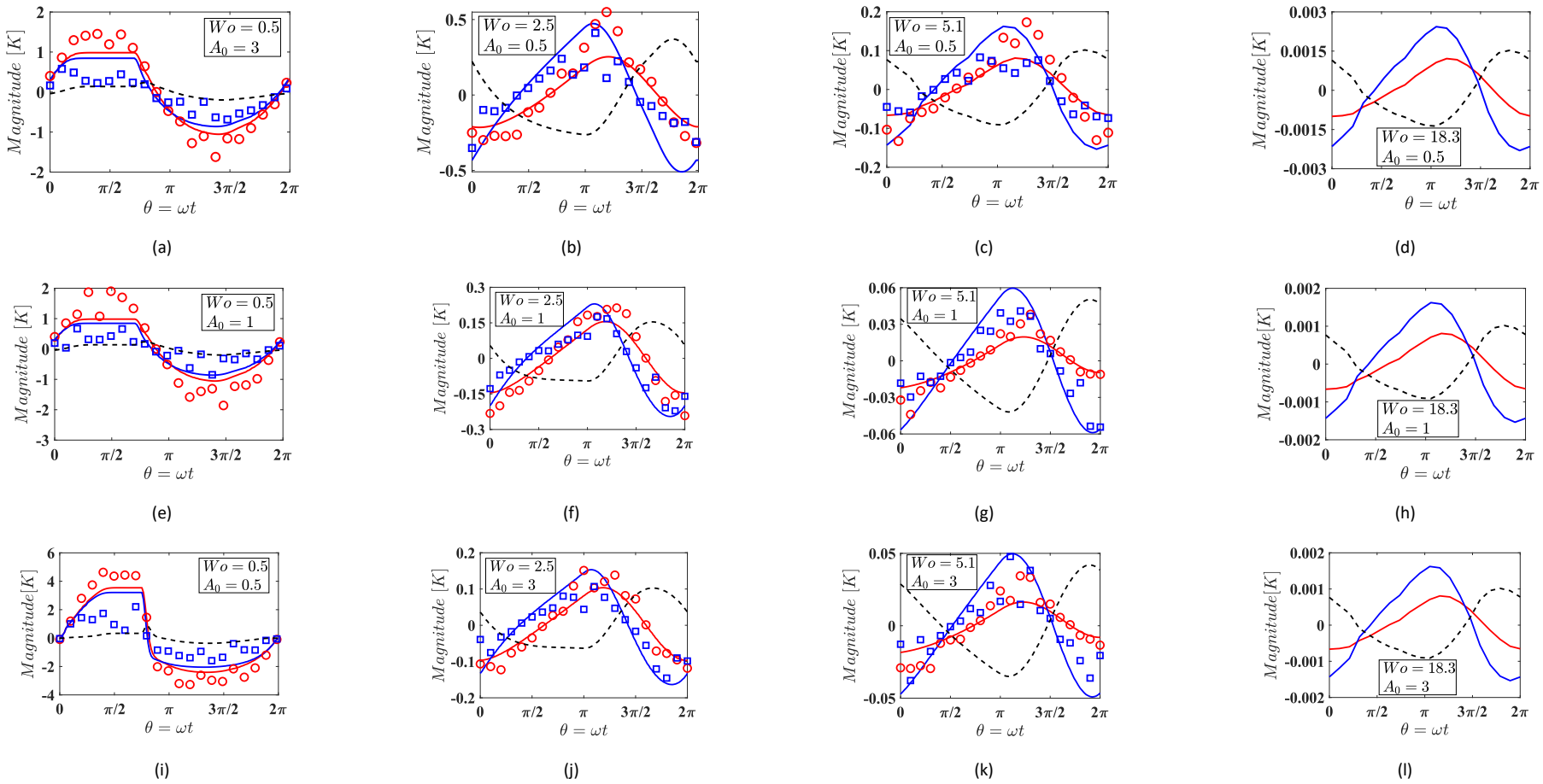

Figure 7-47 (a-l): Temporal variation of wall, bulk temperature and the driving temperature difference for a **positive half rectified waveform**. Moving across each row shows the effects of increasing Wo for the same A_0. Moving down a column shows the effects of increasing A_0 for a fixed Wo. Solid lines present the CFD results, and markers show the experimental results. Note that no experimental data exists for the higher frequency $Wo = 18.3$ cases.

7.1.1.4 Negative half rectified profile

Figure 7-49 plots the oscillating wall and oscillating bulk fluid temperature profiles as well as the difference between the two for a negative half rectified waveform format. The figures present a clear influence of the imposed rectified profile on the temporal evolution of wall and bulk temperature profiles. As understood from Section 7.1.2.2, the flowrate profile features a half interval of steady component at the start of the cycle, the wall and bulk temperatures indicate a small increase followed by stabilisation of temperature throughout the steady interval, identified from the low frequency case at $Wo = 0.5$, Figure 7-49 (a, e, i).

Further with the onset of acceleration stage (i.e., backward directed impulse) the temperature profile increases momentarily till up to phase $3\pi/2$ due to the influx of warmer fluid, followed by a proportional decrease in temperature magnitude towards the end of the deceleration stage of half rectified profile.

However, for the moderate-highest frequency cases at $Wo = 2.5, 5.1$ and 18.3 from Figure 7-49 (b-d, f-h, j-l) the wall and bulk temperature profiles respond with a delay to the shorter timescale of oscillation. Further, as a result of a co-existence of steady and a semi-sinusoidal component in equal time intervals within a cycle, the temperature profiles present a steady decrease in magnitudes between phases $0 \leq \theta \leq \pi$, followed a sharp rise between the semi-sinusoidal stages of the cycle before a small drop towards the end of the cycle. It can be inferred that the temperature profile does not cope to the fast impulse reactions resulted from the half rectified waveform that features a consequent rapid change in the bulk flow direction. With an increase in A_0, the bulk temperature shows pronounced effect with stepper magnitudes, suggesting enhanced removal of heat. This is induced by the rapidly changing characteristics of the increased flowrate half rectified format of oscillation. However, the wall temperature shows a delayed (weak) reaction to the fast-moving pulsation. The driving temperature difference shows a higher magnitude during the first half of the acceleration stage suggesting effective heat withdrawal, while the magnitudes settle towards the latter half as the deceleration cycle is weaker in comparison.

Increasing Wo shows a decreasing trend of wall and bulk temperature magnitudes across the range of frequencies and follows the similar inference drawn from the symmetric sinusoidal waveform. It is noticeable that the low frequency flow responds and reacts slowly to the onset of semi-sinusoidal flowrate profile thus resembling the format. Whereas the high-highest frequencies demonstrate a swifter response of temperature profile particularly in the semi-sinusoidal component stage at phases $\pi/2 \leq \theta \leq 3\pi/2$ due to the shorter displacement timescale of the flowrate. The driving temperature difference reaches a high peak towards the end of the semi-sinusoidal component

with a low peak at the onset of the semi-sinusoidal stage at phase $\pi/2$ for $Wo = 5.1, 18.3$ cases. Whereas for the low-moderate frequency cases it is slightly advanced towards the onset of the semi-sinusoidal component and further gets slowed for the former. The characteristics offered by a half rectified flowrate profile on the distinct evolution of oscillating temperature profiles are evident in comparison to the cases of symmetric sinusoidal.

There exists a reasonable agreement associated between the experimental and the CFD results for the oscillating wall and bulk temperature profiles at low-moderate frequencies. Although the agreement worsens and there is some deviation between the two datasets particularly for the high frequency and respective high flow rate amplitudes due to the oscillations and non-linearities induced by the thin foil boundary to accommodate for such large pressure gradients developed by the high frequency half rectified waveform.

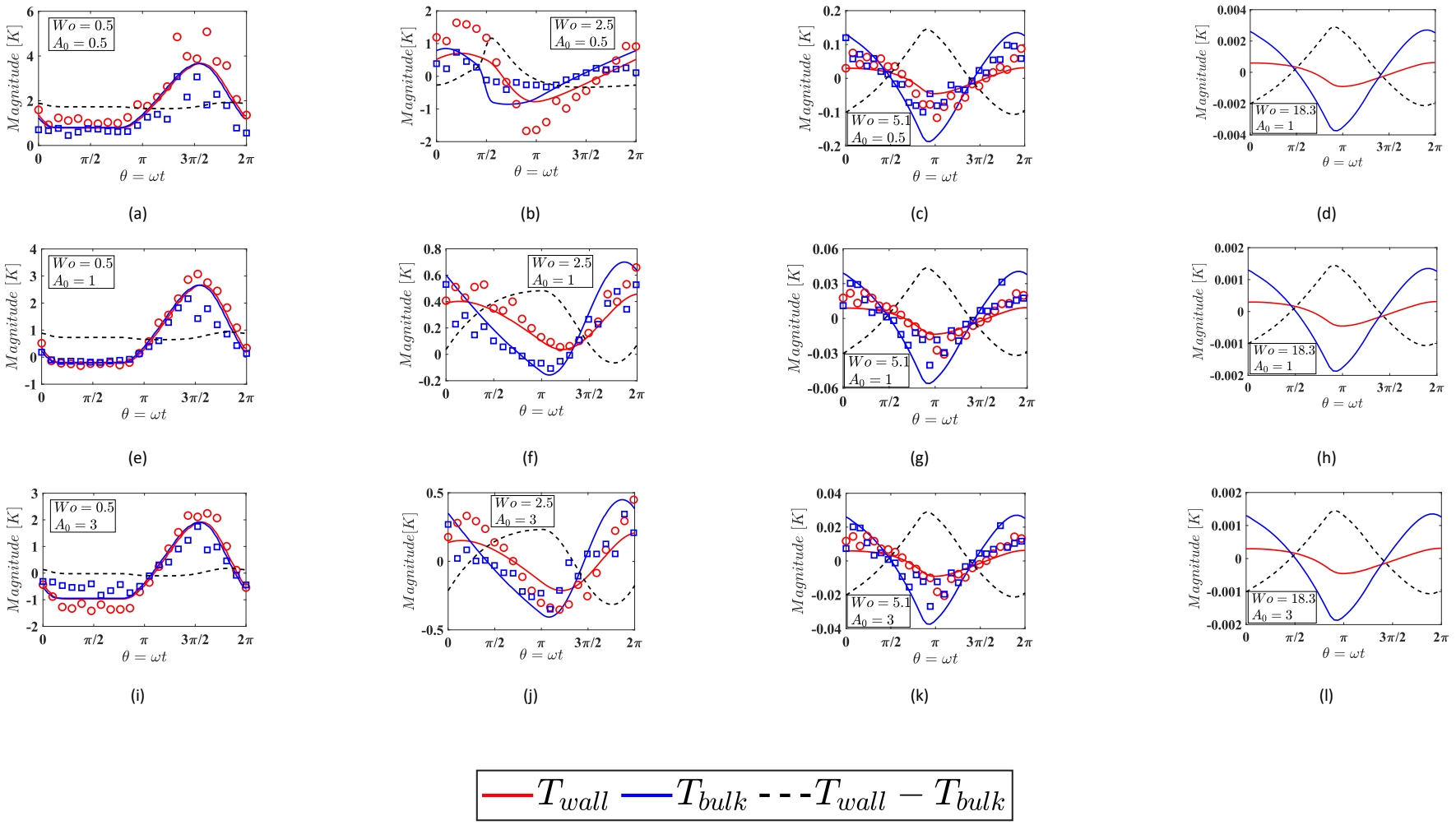

Figure 7-48 (a-l): Temporal variation of wall, bulk temperature and the driving temperature difference for a **negative half rectified waveform**. Moving across each row shows the effects of increasing Wo for the same A_0. Moving down a column shows the effects of increasing A_0 for a fixed Wo. Solid lines present the CFD results, and markers show the experimental results. Note that no experimental data exists for the higher frequency $Wo = 18.3$ cases.

7.5 Spatial variation of thermal parameters

7.5.1 Bulk and Wall Temperature distributions

In this section the spatial variation of the oscillating bulk temperatures ($T_{b,osc}$) and the spanwise variation of oscillating wall temperatures ($T_{w,osc}$) is described in the fully developed region of the channel at $z = 0.3\,m$. Line plots for bulk temperature are shown as a function of the non-dimensional minichannel height ($Y = y/a$) in the core ($x/b = 0$) region of the minichannel. The line and marker plots for the wall temperature are CFD and experimental data respectively shown as a function of non-dimensional minichannel width (x/b) along the bottom heated wall at ($y/a = 0$).

7.1.1.5 Symmetric sinusoidal pulsation

Figure 7-49 (a-f) represents the spatial and spanwise variation of temperature profiles resulting from sinusoidal waveforms at a frequency of 0.02 *Hz* ($Wo = 0.5$) and flow rate amplitudes of $A_0 = 0.5,1,3$. For a viscous dominated low frequency flow, similar features exist between the oscillating velocity profiles as seen from (Section 7.2.1.1, Figure 7-9, Figure 7-10 Figure 7-11) and the wall temperature profiles [111, 127, 128]. Low frequency flows are typically exhibit significant amount of heat diffusion from the bottom wall to the core bulk fluid. Additionally, the thermal diffusion time scales are shorter compared to the longer pulsation periods and due to a low wall thermal inertia. This phenomenon leads to a substantial increase in the bulk fluid temperature as is evident from Figure 7-49 (b). During the acceleration stage between phases $0 \leq \theta \leq \pi$, the bulk temperature of fluid decreases as is evident from phases 0.2π and $0.4\,\pi$ due to colder fluid entering the heated section as an effect to the stronger influence of underlying steady flow at low frequency pulsation. However, towards the end of the acceleration stage and an onset of deceleration stage $\pi \leq \theta \leq 2\pi$, the fluid temperature rises further as seen for phases $1.2\,\pi$ and $1.4\,\pi$ as the warmer bulk flow exits the channel.

On increasing the A_0, the wall temperature magnitudes decrease. The effect of oscillation is further amplified due to the influx of higher flowrate of the colder fluid in the heated channel. Similarly, the oscillating bulk temperatures reflect a drop in the magnitudes as enhanced forced convection cooling is evident. There exists a generally good agreement of the CFD and the experimental data. Minor deviations exist between the wall temperature profiles and are as a result of the assumptions undertaken in the energy equation of the three-dimensional numerical modelling which does not account for the heat losses.

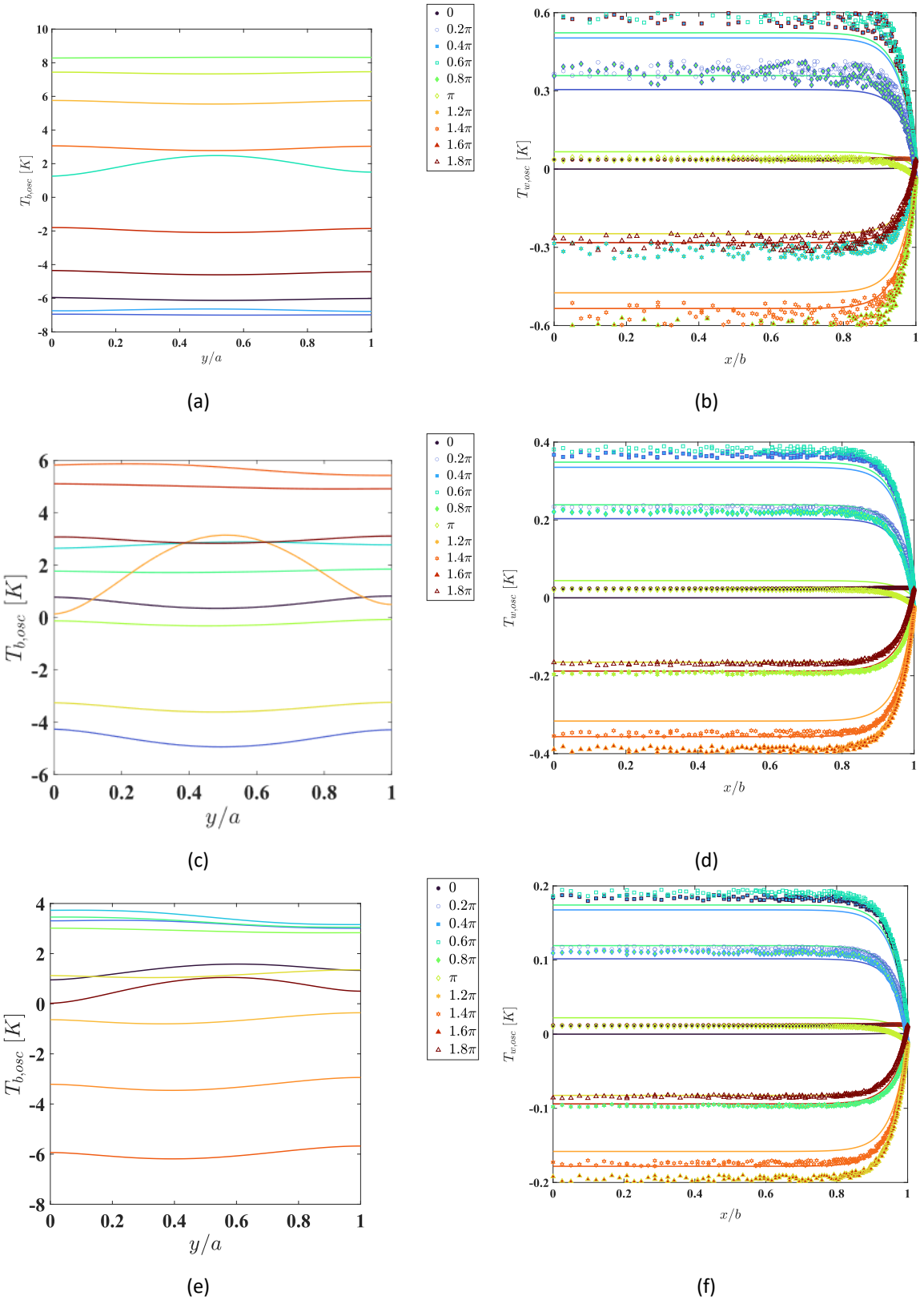

Figure 7-49: Symmetric sinusoidal waveform with flowrate amplitude $A_0 = 0.5, 1, 3$ (a-f) and frequency 0.02 Hz ($Wo = 0.5$). All lines represent CFD data. Markers represent experimental data. (LEFT) Oscillating bulk temperature profile vs. normalised minichannel height (y/a) at $x/b = 0$. (RIGHT) Oscillating temperature profiles at the heated wall ($y/a = 0$) along the normalised spanwise direction (x/b).

Figure 7-50 (a-f) represents the spatial and spanwise variation of temperature profiles resulting from sinusoidal waveforms at a frequency of 0.5 Hz ($Wo = 2.5$) and flow rate amplitudes of $A_0 = 0.5,1,3$. The flow at moderate frequency presents a gradual build-up of bulk core inertial forces, although the viscous forces continue to prevail as is evident from the Figure 7-12, Figure 7-13, Figure 7-14. The influence of transverse diffusion is seen to decrease, wherein a decrease in the magnitudes of bulk temperature is observed compared to the $Wo = 0.5$ case. The bulk oscillating temperature profiles react in a different manner compared to the low frequency case $Wo = 0.5$ and the influence of oscillation shown by steeper gradients is noticeable for both stages of acceleration and deceleration. As a result of a minor deviation from the parabolic velocity profiles seen in the case of moderate frequency oscillation, an increase in the near-wall viscous forces is understood. This feature of $Wo = 2.5$ case can be identified from the wall temperature profiles and are no longer parabolic and the maximum magnitudes of temperatures are shifted to the near side-wall regions $0.4 \leq x/b \leq 0.5$. The resulting temperature profiles reflect a decrease in the magnitudes compared to the low frequency $Wo = 0.5$ cases as the thickness of the thermal boundary layer decreases [74, 88, 127].

On increasing A_0, similar observations are drawn as with the low frequency case and the forced convection effect leads to a drop in the magnitudes of both wall and bulk temperatures.

There exists a generally good agreement of the CFD and the experimental data for the oscillating wall temperature profiles of moderate frequency case. Minor deviations exist between the wall temperature profiles in the near-wall vicinity and are as a result of the assumptions undertaken in the energy equation of the three-dimensional numerical modelling which does not account for the heat losses.

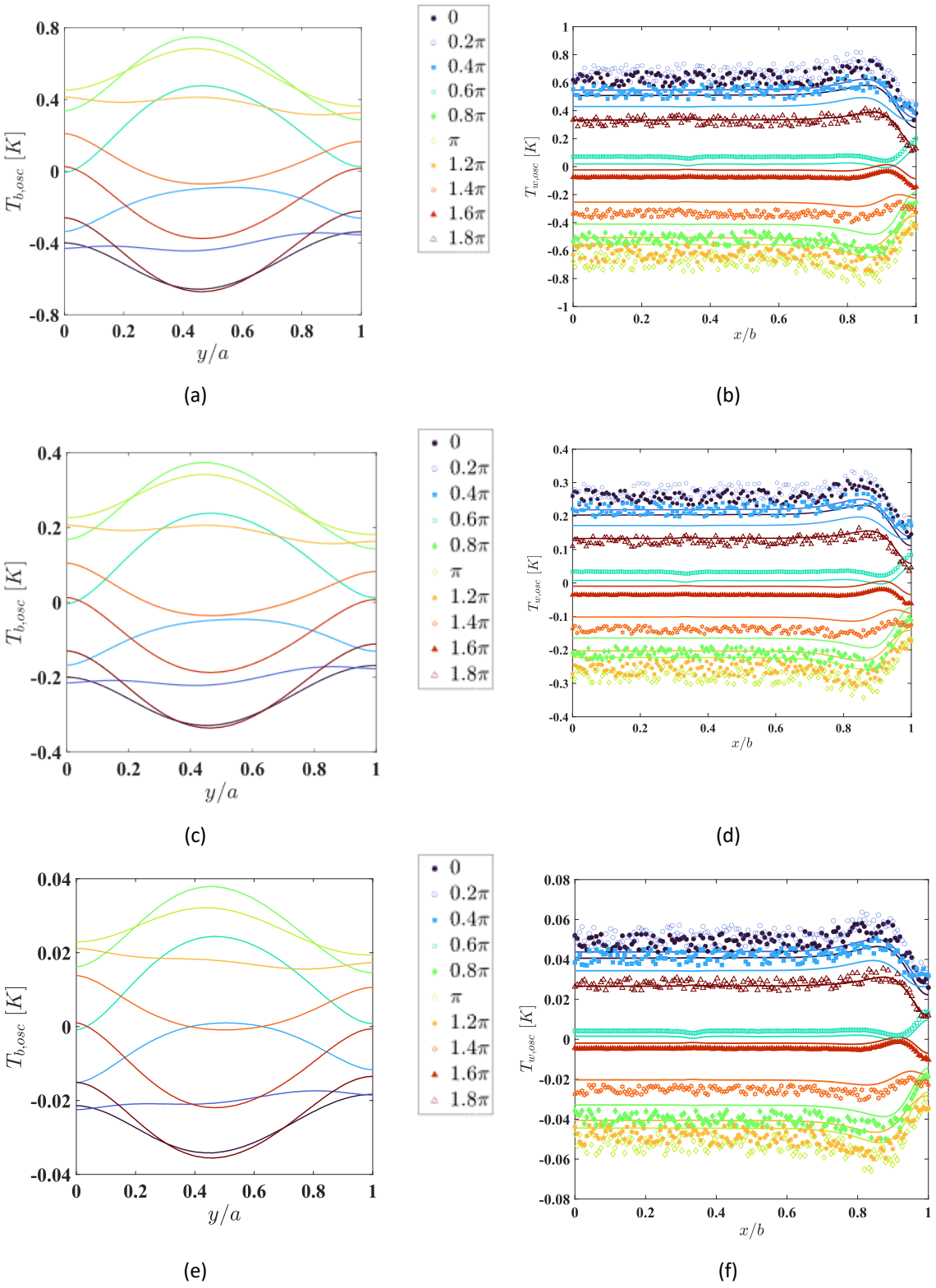

Figure 7-50: Symmetric sinusoidal waveform with flowrate amplitude $A_0 = 0.5, 1, 3$ (a-f) and frequency 0.5 Hz ($Wo = 2.5$). All lines represent CFD data. Markers represent experimental data. (LEFT) Oscillating bulk temperature profile vs. normalised minichannel height (y/a) at $x/b = 0$. (RIGHT) Oscillating temperature profiles at the heated wall ($y/a = 0$) along the normalised spanwise direction (x/b).

Figure 7-51 (a-f) represents the spatial and spanwise variation of temperature profiles resulting from sinusoidal waveforms at a frequency of 2 Hz ($Wo = 5.1$) and flow rate amplitudes of $A_0 = 0.5, 1, 3$. Flows at high frequency typically exhibit the strengthening of bulk core inertial forces while the viscous effects continue to be dominant in the near side-wall vicinity, this can be deduced from the Figure 7-15, Figure 7-16 and Figure 7-17. Since the pulsation periods are shorter, convection heat transfer is dominant throughout and as a result the transverse thermal diffusion is viewed to be ineffective. The oscillating bulk temperature profile reflects this phenomenon with a further reduction in magnitudes compared to the low to moderate frequency cases. The acceleration and deceleration stage of oscillation at $0.2\pi, 0.4\pi$ and $1.2\pi, 1.4\pi$ respectively shows a weakening effect of the shorter axial displacement high frequency oscillation. Further, the oscillating wall temperature profile indicates a steep thermal gradient in the near side-wall regions $0.4 \leq x/b \leq 0.5$ due to a pronounced influence of higher fluid viscous effects. Similar to the observations from $Wo = 2.5$ albeit with a reduction in the temperature values, the existence of maximum magnitudes of wall temperatures are shifted to the near side-wall vicinity. The peak magnitude of temperature in the near side-wall region decreases since the shear stress magnitudes are strengthened for high frequency flows and the thickness of thermal boundary layer further decreases. The phenomenon of annular effects is established with the oscillating wall temperature profiles for high frequency flows as has been widely observed for the corresponding cases of velocity and shear stress profiles [74, 88, 127, 129, 130], described from Figure 7-15, Figure 7-16 and Figure 7-17. Inertial forces are evidently stronger in the core region, leading to flatter oscillating wall temperatures in the core region. Increasing A_0 leads to a strengthening of near side-wall viscous forces as is also noticeable from Figure 7-17, thus there is a steeper gradient in the near side-wall temperatures. As a result of enhanced convection effect, a subsequent decrease in the bulk fluid and wall temperature magnitudes is generally observed [75, 83, 85].

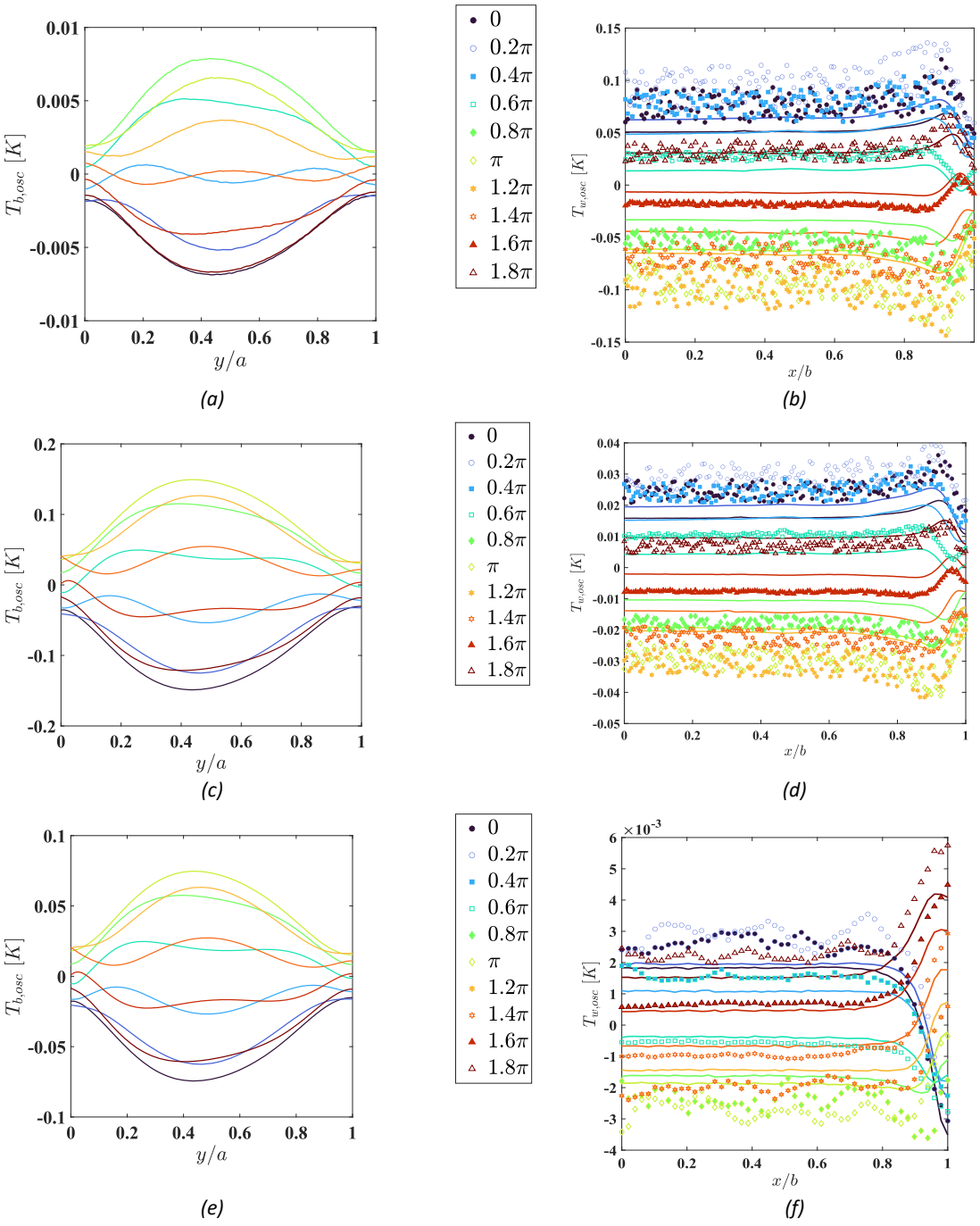

Figure 7-51: Symmetric sinusoidal waveform with flowrate amplitude $A_0 = 0.5, 1, 3$ (a-f) and frequency 2 Hz ($Wo = 5.1$). All lines represent CFD data. Markers represent experimental data. (LEFT) Oscillating bulk temperature profile vs. normalised minichannel height (y/a) at $x/b = 0$. (RIGHT) Oscillating temperature profiles at the heated wall ($y/a = 0$) along the normalised spanwise direction (x/b).

For the highest frequency of 25 Hz ($Wo = 18.3$) in Figure 7-52, a stronger influence of the near-wall viscous forces with the co-existence of bulk inertial forces can be observed. The oscillating wall temperatures show similarity with the previous cases of high frequency ($Wo = 5.1$), and the peak magnitudes are obtained in the near side-wall vicinity $0.4 \leq x/b \leq 0.5$. However, the maximum magnitudes and the thermal gradients are substantially reduced. Pronounced annular effects, previously observed from the oscillating velocity and shear stress profiles for highest frequency, are also reflected from the oscillating wall temperature profiles. The transverse diffusion of heat flow is weakened, and flatter oscillating wall temperatures profiles are seen in a wide spanwise region between $0 \leq x/b \leq 0.4$. Correspondingly, the oscillating bulk temperature profiles reflect an insignificant effect introduced by the short axial displacement oscillation in both the acceleration and deceleration stages. The temperature gradients are further reduced in comparison to the previous lower frequency cases. This feature of the highest frequency can be attributed to the increased influence of the flow reversal effect. Increasing A_0, the wall and bulk temperature profiles present reduced magnitudes due to the amplified effect of shear stress magnitudes and the influence of stronger oscillation amplitude is not pertinently evident from the slow reacting thermal profiles. The highest frequency flow is therefore classified as pseudo-steady [127, 128].

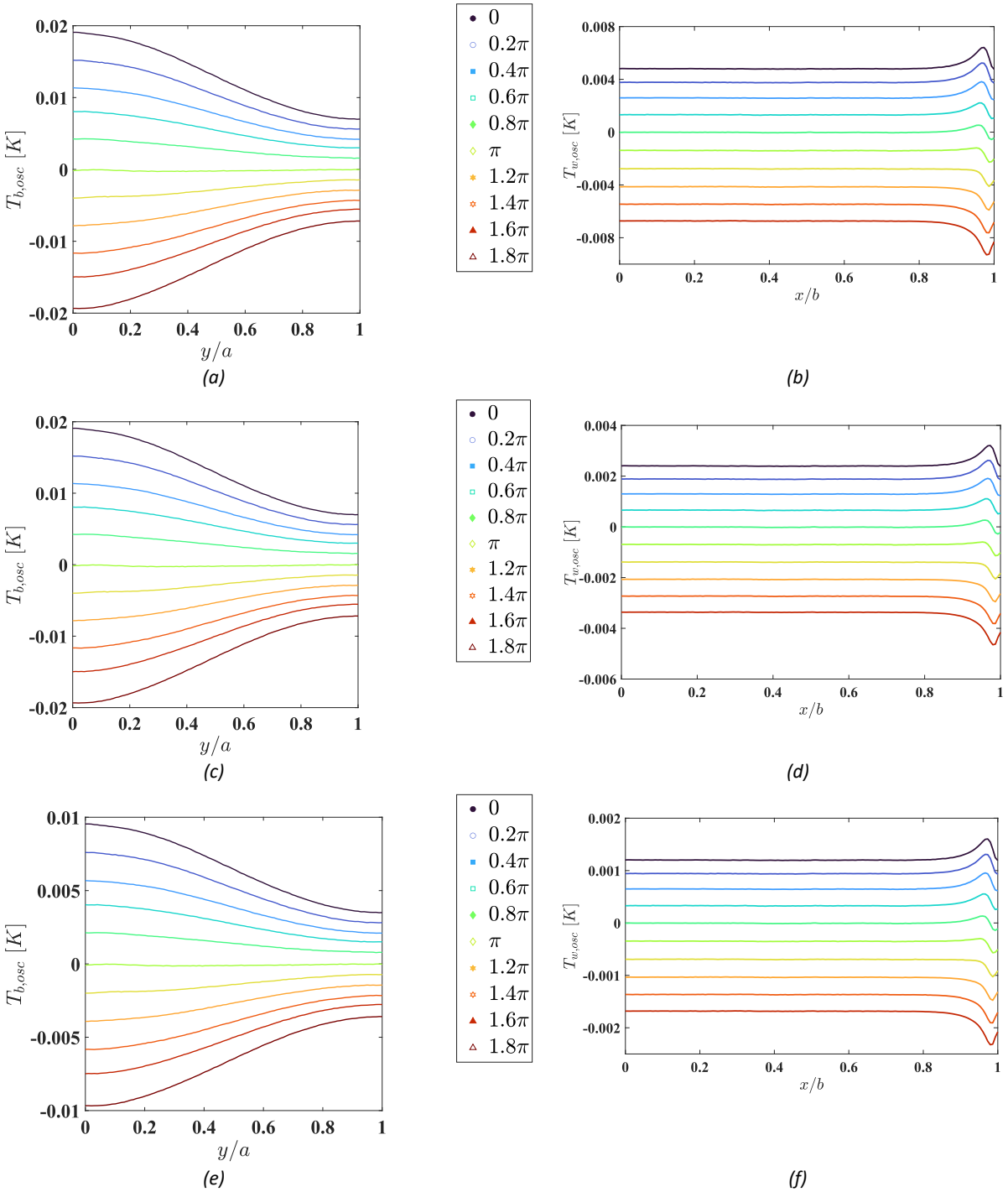

Figure 7-52: Symmetric sinusoidal waveform with flowrate amplitude $A_0 = 0.5, 1, 3$ (a-f) and frequency 25 Hz ($Wo = 18.3$). All lines represent CFD data. Markers represent experimental data. (LEFT) Oscillating bulk temperature profile vs. normalised minichannel height (y/a) at $x/b = 0$. (RIGHT) Oscillating temperature profiles at the heated wall ($y/a = 0$) along the normalised spanwise direction (x/b).

7.1.1.6 Asymmetric sinusoidal pulsation

Figure 7-53 respectively represent the spatial and spanwise variation of temperature profiles resulting from leading asymmetric sinusoidal waveforms at a frequency of 0.02 *Hz* ($Wo = 0.5$) and flow rate amplitudes of $A_0 = 0.5{,}3$. For a viscous dominated low frequency flow, similarities in the feature exists between the oscillating velocity profiles as seen from (Figure 0-1 and Figure 0-2) and the wall temperature profiles. Low frequency flows are typically exhibit significant amount of heat diffusion from the bottom wall to the core bulk fluid. Additionally, the thermal diffusion time scales are shorter compared to the longer pulsation periods and due to a low wall thermal inertia. This phenomenon leads to a substantial increase in the bulk fluid temperature as is evident from Figure 7-50 (a) similar in agreement with the symmetric sinusoidal cases. During the acceleration stage between phases $0 \leq \theta \leq \pi$, the bulk temperature of fluid decreases as is evident from phases 0.2π and $0.4\ \pi$ due to colder fluid entering the heated section as an effect to the stronger influence of underlying steady flow at low frequency pulsation. However, towards the end of the acceleration stage and an onset of deceleration stage $\pi \leq \theta \leq 2\pi$, the fluid temperature rises further as seen for phases $1.2\ \pi$ and $1.4\ \pi$ as the warmer bulk flow exits the channel.

On increasing the A_0, the wall temperature magnitudes decrease. The effect of oscillation is further amplified due to the influx of higher flowrate of the colder fluid in the heated channel. Similarly, the oscillating bulk temperatures reflect a drop in the magnitudes as enhanced forced convection cooling is evident.

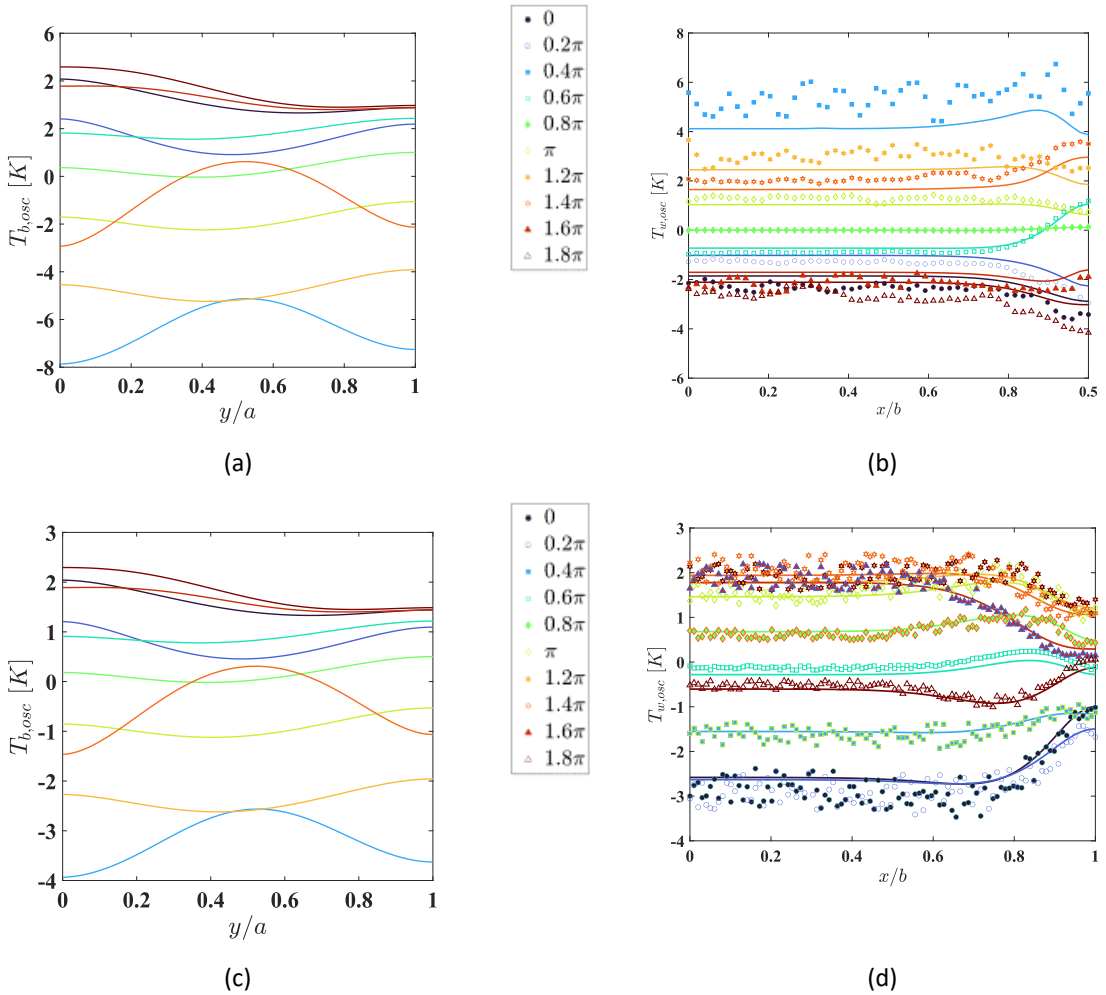

Figure 7-53: Leading asymmetric sinusoidal waveform with flowrate amplitude $A_0 = 0.5,\ 3$ (a-f) and frequency 0.02 Hz ($Wo = 0.5$). All lines represent CFD data. Markers represent experimental data. (LEFT) Oscillating bulk temperature profile vs. normalised minichannel height (y/a) at $x/b = 0$. (RIGHT) Oscillating temperature profiles at the heated wall ($y/a = 0$) along the normalised spanwise direction (x/b).

Figure 7-54 respectively represent the spatial and spanwise variation of temperature profiles resulting from leading asymmetric sinusoidal waveforms at a frequency of 0.5 *Hz* ($Wo = 2.5$) and flow rate amplitudes of $A_0 = 0.5,3$. The flow at moderate frequency presents a gradual build-up of bulk core inertial forces, although the viscous forces continue to prevail as is evident from the Figure 7-21, Figure 7-22. The influence of transverse diffusion is seen to decrease, wherein a decrease in the magnitudes of bulk temperature is observed compared to the $Wo = 0.5$ case. The bulk oscillating temperature profiles react in a different manner compared to the low frequency case $Wo = 0.5$ and the influence of oscillation observed with steeper temperature gradients is noticeable for both stages of acceleration and deceleration. As a result of minor deviation from the parabolic velocity profiles seen in the case of moderate frequency oscillation, an increase in the near-wall viscous forces is understood. This feature of $Wo = 2.5$ case can be identified from the wall temperature profiles and are no longer parabolic and the maximum magnitudes of

temperatures are shifted to the near side-wall regions $0.4 \leq x/b \leq 0.5$. The resulting temperature profiles reflect a decrease in the magnitudes compared to the low frequency $Wo = 0.5$ cases as the thickness of the thermal boundary layer decreases.

On increasing A_0, stepper thermal gradients are obtained in the near side-wall vicinity $0.4 \leq x/b \leq 0.5$ for both oscillating wall and bulk temperature profiles as the effect of a more pronounced acceleration stages during phases $0 \leq \theta \leq \pi/2$ and $3\pi/2 \leq \theta \leq 2\pi$ from

Figure 7-45 (f,j) of leading asymmetry. The magnitudes reflect a similar observation as with the low frequency case and the forced convection effect leads to a drop in the magnitudes of both wall and bulk temperatures.

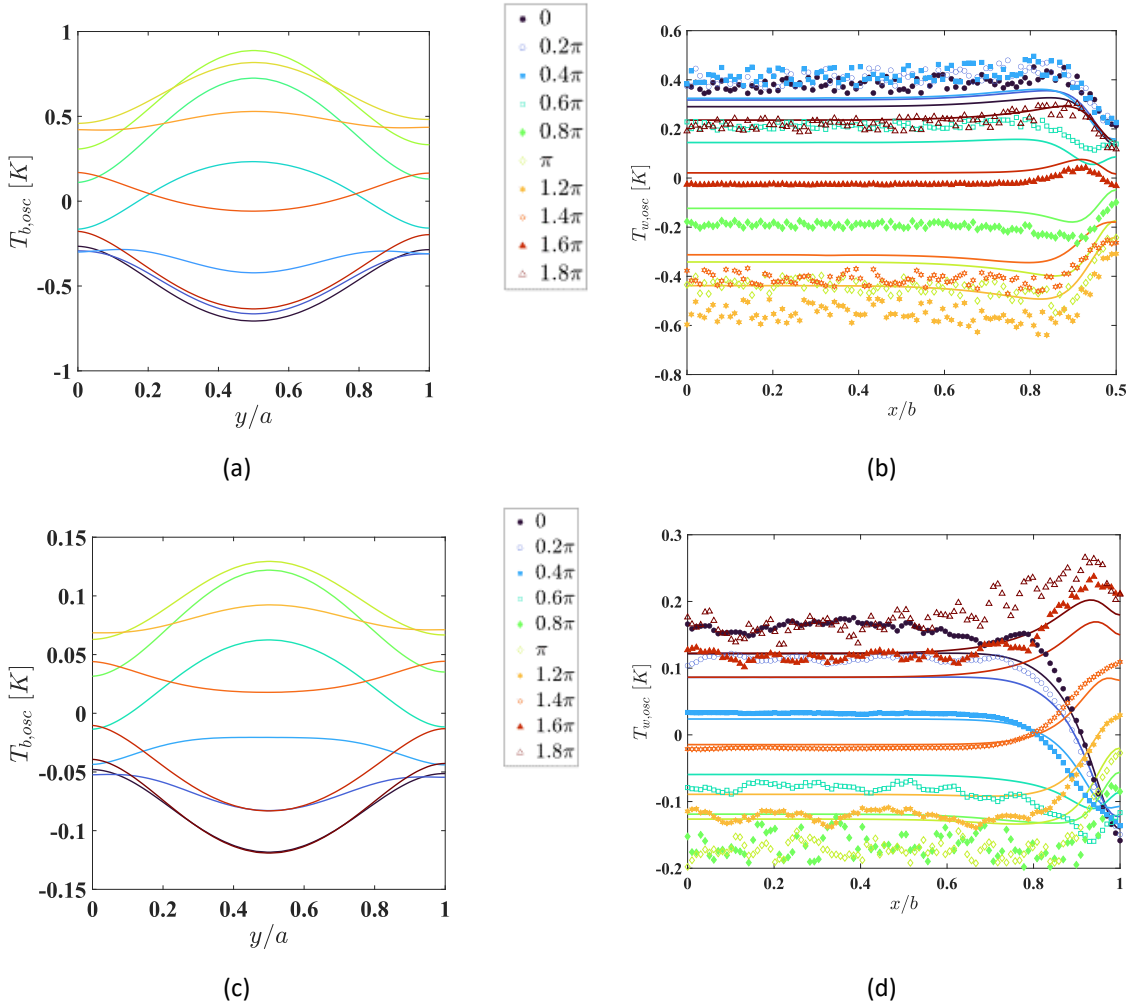

Figure 7-54: Leading asymmetric sinusoidal waveform with flowrate amplitude $A_0 = 0.5, 3$ (a-f) and frequency 0.5 Hz ($Wo = 2.5$). All lines represent CFD data. Markers represent experimental data. (LEFT) Oscillating bulk temperature profile vs. normalised minichannel height (y/a) at $x/b = 0$. (RIGHT) Oscillating temperature profiles at the heated wall ($y/a = 0$) along the normalised spanwise direction (x/b).

Figure 7-55 (a-d) represent the spatial and spanwise variation of temperature profiles resulting from leading asymmetric sinusoidal waveforms at a frequency of 2 *Hz* ($Wo = 5.1$) and flow rate amplitudes of $A_0 = 0.5,3$. Flows at high frequency typically exhibits the strengthening of bulk core inertial forces while the viscous effects continue to be dominant in the near side-wall vicinity, this can be deduced from the Figure 7-23 and Figure 7-24. Since the pulsation periods are shorter, convection heat transfer is dominant throughout and as a result the transverse thermal diffusion is viewed to be ineffective. The oscillating bulk temperature profile reflects this phenomenon with a further reduction in magnitudes compared to the low-moderate frequency cases. The lengthened gradual deceleration stage of oscillation at $0.8\pi, \pi$ and $1.2\pi, 1.4\pi$ respectively leads to a noticeable asymmetry of bulk temperatures in comparison to the symmetric sinusoidal of similar shorter axial displacement high frequency oscillation. Further, the oscillating wall temperature profile indicates a steep thermal gradient in the near side-wall regions $0.4 \leq x/b \leq 0.5$ evidently towards the end of the cycle for phases $1.6\pi, 1.8\pi$ due to the pronounced influence of higher fluid viscous effects. The features of temperature profile differ from the observations at $Wo = 2.5$ and the influence of an asymmetric flowrate are quite evident for cases of $Wo = 5.1$. Varied effects in wall temperature profiles are observed with the presence of thermal gradients extending to off-wall locations in addition to the presence of maximum magnitudes of wall temperatures shifted to the near side-wall vicinity. The peak magnitude of temperature in the near side-wall region decreases at high frequency since the shear stress magnitudes are strengthened for high frequency flows and the thickness of thermal boundary layer further decreases. The phenomenon of annular effects is established with the oscillating wall temperature profiles for high frequency flows as has been widely observed for the corresponding cases of velocity and shear stress profiles, described from Figure 7-23 and Figure 7-24.

Increasing A_0 leads to a further strengthening of near wall viscous forces as is noticeable from Figure 7-24, thus there is a simultaneous decrease in the bulk core fluid and wall temperature magnitudes. As a result of increased flow rate amplitude i.e., enhanced convection, the steep thermal gradients are concentrated in the near-side wall vicinity unlike the delayed dissipation observed from $A_0 = 0.5$ case. The traits of an asymmetric flowrate profile can be identified from the spatial spread of the oscillating bulk temperature profile in particular for phases $\pi - 1.6\pi$ and phases $1.6\pi - 1.8\pi$ from the wall temperature profile.

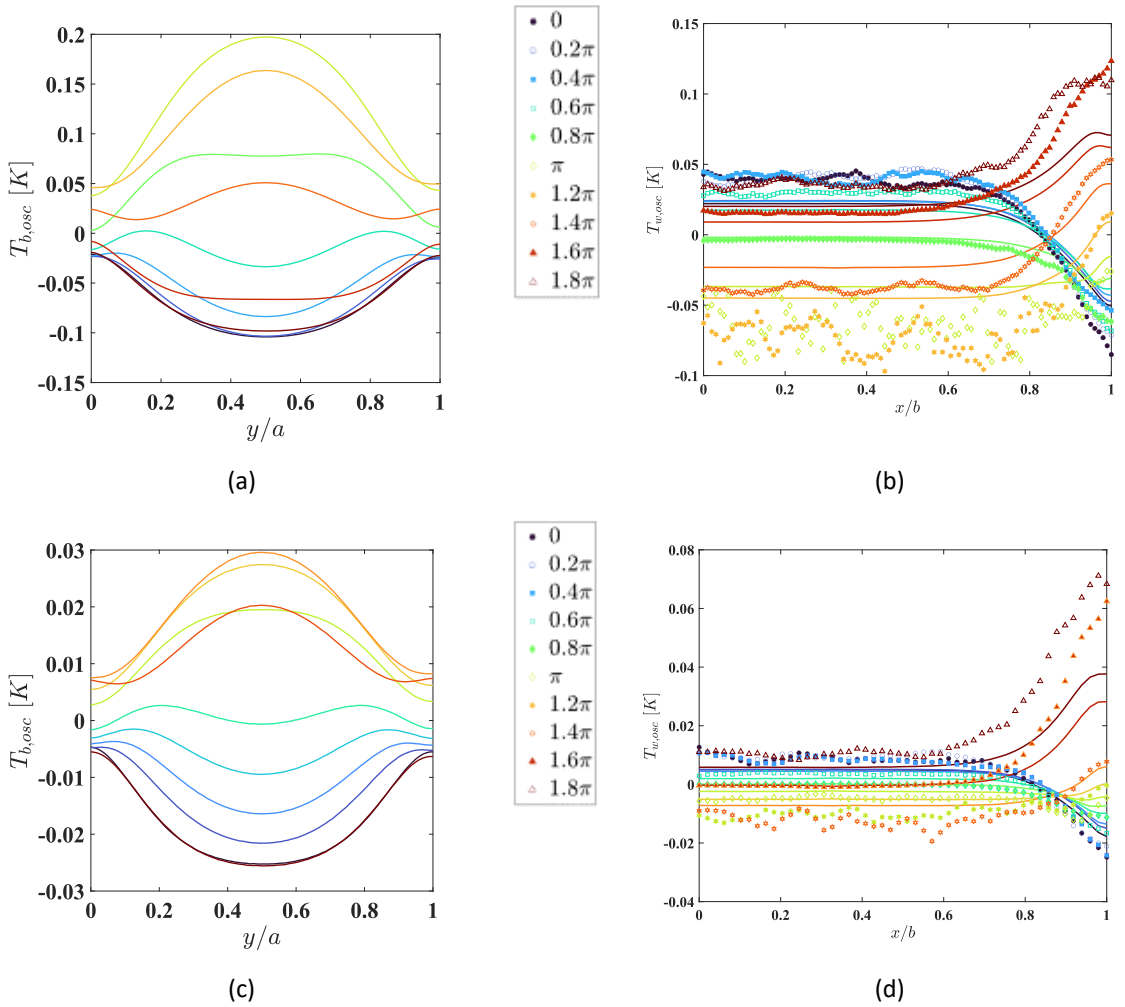

Figure 7-55: Leading asymmetric sinusoidal waveform with flowrate amplitude $A_0 = 0.5, 3$ (a-f) and frequency 2 Hz ($Wo = 5.1$). All lines represent CFD data. Markers represent experimental data. (LEFT) Oscillating bulk temperature profile vs. normalised minichannel height (y/a) at $x/b = 0$. (RIGHT) Oscillating temperature profiles at the heated wall ($y/a = 0$) along the normalised spanwise direction (x/b).

Figure 7-56 (a-d) respectively represent the spatial and spanwise variation of temperature profiles resulting from lagging asymmetric sinusoidal waveforms at a frequency of 0.02 *Hz* ($Wo = 0.5$) and flow rate amplitudes of $A_0 = 0.5,3$. For a viscous dominated low frequency flow, similarities in the feature exists between the oscillating velocity profiles as seen from (Figure 0-3 and Figure 0-4) and the wall temperature profiles. Low frequency flows are typically exhibit significant amount of heat diffusion from the bottom wall to the core bulk fluid. Additionally, the thermal diffusion time scales are shorter compared to the longer pulsation periods and due to a low wall thermal inertia. This phenomenon leads to a substantial increase in the bulk fluid temperature as is evident from Figure 7-56 (b) similar in agreement with the symmetric sinusoidal cases. During the acceleration stage between phases $0 \leq \theta \leq \pi$, the bulk temperature of fluid decreases as is evident from phases 0.2π and $0.4\ \pi$ due to colder fluid entering the heated section as an effect to the stronger influence of

underlying steady flow at low frequency pulsation. However, towards the end of the acceleration stage and an onset of deceleration stage $\pi \leq \theta \leq 2\pi$, the fluid temperature rises further as seen for phases $1.2\ \pi$ and $1.4\ \pi$ as the warmer bulk flow exits the channel.

On increasing the A_0, the wall temperature magnitudes decrease. The effect of oscillation is further amplified due to the influx of higher flowrate of the colder fluid in the heated channel. Similarly, the oscillating bulk temperatures reflect a drop in the magnitudes as enhanced forced convection cooling is evident.

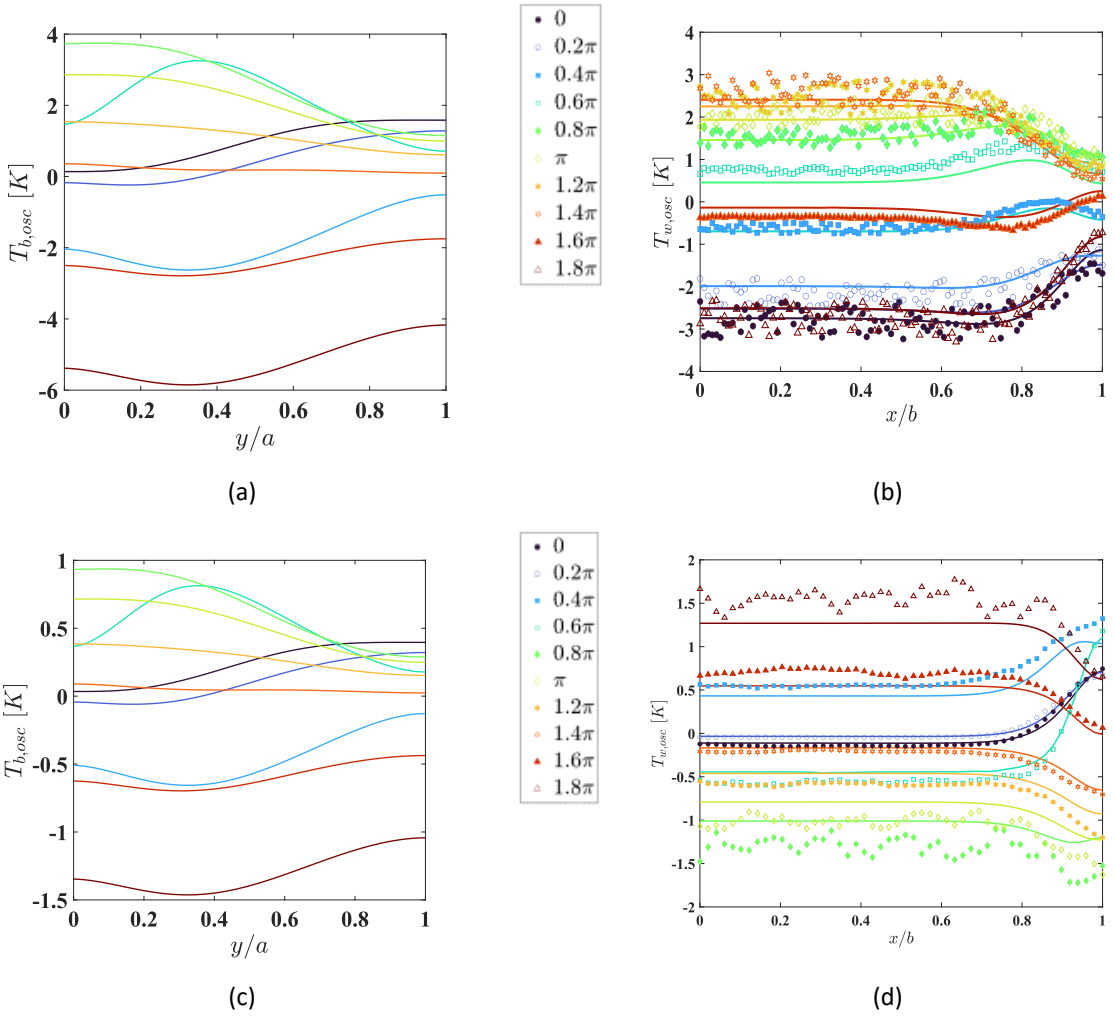

Figure 7-56: Lagging asymmetric sinusoidal waveform with flowrate amplitude $A_0 = 0.5, 3$ (a-f) and frequency 0.02 Hz ($Wo = 0.5$). All lines represent CFD data. Markers represent experimental data. (LEFT) Oscillating bulk temperature profile vs. normalised minichannel height (y/a) at $x/b = 0$. (RIGHT) Oscillating temperature profiles at the heated wall ($y/a = 0$) along the normalised spanwise direction (x/b).

Figure 7-57 respectively represent the spatial and spanwise variation of temperature profiles resulting from lagging asymmetric sinusoidal waveforms at a frequency of 0.5 *Hz* ($Wo = 2.5$) and flow rate amplitudes of $A_0 = 0.5$,3. The flow at moderate frequency presents a gradual build-up of bulk core inertial forces, although the viscous forces continue to prevail as is evident from the Figure

0-5 and Figure 0-6. The influence of transverse diffusion is seen to decrease, wherein a decrease in the magnitudes of bulk temperature is observed compared to the $Wo = 0.5$ case. The bulk oscillating temperature profiles react in a different manner compared to the low frequency case $Wo = 0.5$ and the influence of oscillation observed with steeper temperature gradients is noticeable for both stages of acceleration and deceleration. As a result of minor deviation from the parabolic velocity profiles seen in the case of moderate frequency oscillation, an increase in the near-wall viscous forces is understood. This feature of $Wo = 2.5$ case can be identified from the wall temperature profiles and are no longer parabolic and the maximum magnitudes of temperatures are shifted to the near side-wall regions $0.4 \leq x/b \leq 0.5$. The resulting temperature profiles reflect a decrease in the magnitudes compared to the low frequency $Wo = 0.5$ cases as the thickness of the thermal boundary layer decreases.

On increasing A_0, stepper thermal gradients are obtained in the near side-wall vicinity $0.4 \leq x/b \leq 0.5$ for both oscillating wall and bulk temperature profiles as the effect of a more pronounced acceleration stages during phases $0 \leq \theta \leq \pi/2$ and $3\pi/2 \leq \theta \leq 2\pi$ from lagging asymmetry Figure 7-3. The magnitudes reflect a similar observation as with the low frequency case and the forced convection effect leads to a drop in the magnitudes of both wall and bulk temperatures.

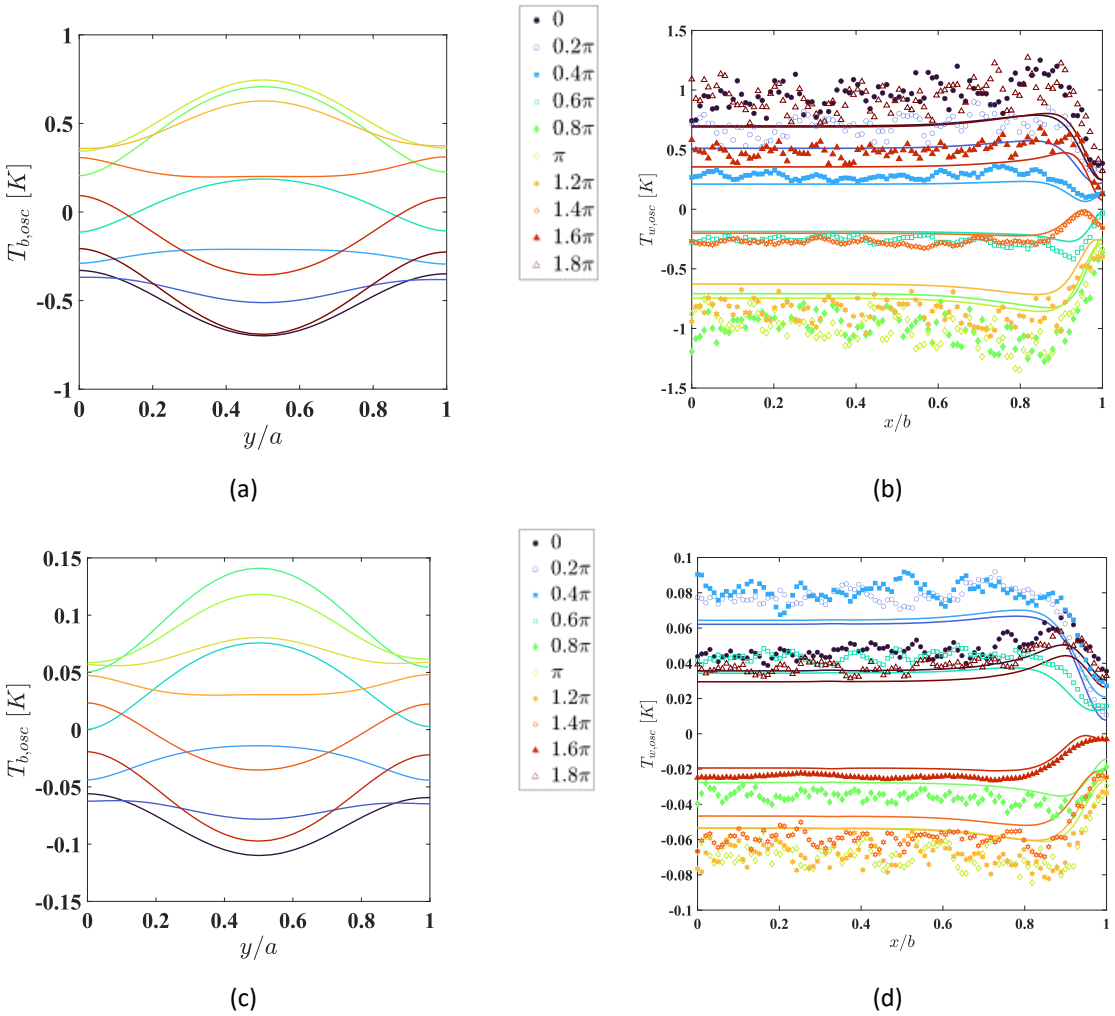

Figure 7-57: Lagging asymmetric sinusoidal waveform with flowrate amplitude $A_0 = 0.5, 3$ (a-f) and frequency 0.5 Hz ($Wo = 2.5$). All lines represent CFD data. Markers represent experimental data. (LEFT) Oscillating bulk temperature profile vs. normalised minichannel height (y/a) at $x/b = 0$. (RIGHT) Oscillating temperature profiles at the heated wall ($y/a = 0$) along the normalised spanwise direction (x/b).

Figure 7-58 respectively represent the spatial and spanwise variation of temperature profiles resulting from lagging asymmetric sinusoidal waveforms at a frequency of 2 *Hz* ($Wo = 5.1$) and flow rate amplitudes of $A_0 = 0.5,3$. Flows at high frequency typically exhibits the strengthening of bulk core inertial forces while the viscous effects continue to be dominant in the near side-wall vicinity, this can be deduced from the Figure 7-27 and Figure 7-28 . Since the pulsation periods are shorter, convection heat transfer is dominant throughout and as a result the transverse thermal diffusion is viewed to be ineffective. The oscillating bulk temperature profile reflects this phenomenon with a further reduction in magnitudes compared to the low-moderate frequency cases. The acute directional shift observed on the onset of the deceleration stage of oscillation at phases $1.4\pi, 1.6\pi$ and 1.8π respectively leads to a noticeable asymmetry of bulk temperatures in comparison to the symmetric sinusoidal of similar shorter axial displacement high frequency oscillation. Further, the oscillating wall temperature profile indicates a steep thermal gradient in

the near side-wall regions $0.4 \leq x/b \leq 0.5$ evidently towards the end of the cycle for phases $1.6\pi, 1.8\pi$ due to the pronounced influence of higher fluid viscous effects. The features of temperature profile differ from the observations at $Wo = 2.5$ and the influence of an asymmetric flowrate are quite evident for cases of $Wo = 5.1$. Varied effects in wall temperature profiles are observed with the presence of thermal gradients extending to off-wall locations in addition to the presence of maximum magnitudes of wall temperatures shifted to the near side-wall vicinity. The peak magnitude of temperature in the near side-wall region decreases at high frequency since the shear stress magnitudes are strengthened for high frequency flows and the thickness of thermal boundary layer further decreases. The phenomenon of annular effects is established with the oscillating wall temperature profiles for high frequency flows as has been widely observed for the corresponding cases of velocity and shear stress profiles, described from Figure 7-27 and Figure 7-28.

Increasing A_0 leads to a further strengthening of near wall viscous forces as is noticeable from Figure 7-28, thus there is a simultaneous decrease in the bulk core fluid and wall temperature magnitudes. As a result of increased flow rate amplitude i.e., enhanced convection, the steep thermal gradients are concentrated in the near-side wall vicinity during the deceleration stage unlike the delayed dissipation observed from $A_0 = 0.5$ case. The traits of an asymmetric flowrate profile can be identified from the spatial spread of the oscillating bulk temperature profile in particular for phases $\pi - 1.6\pi$ and phases $1.6\pi - 1.8\pi$ from the wall temperature profile.

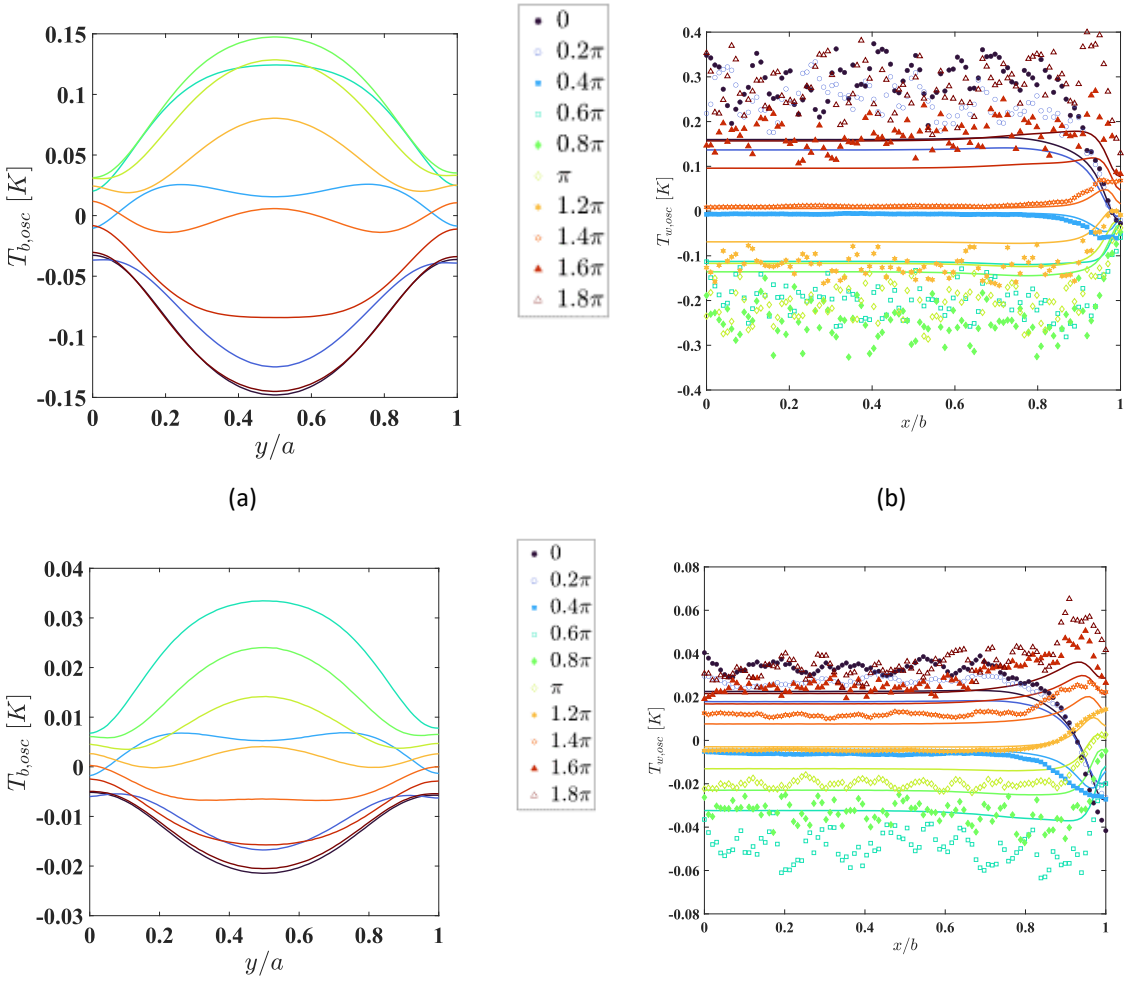

Figure 7-58: Lagging asymmetric sinusoidal waveform with flowrate amplitude $A_0 = 0.5, 3$ (a-f) and frequency 2 Hz ($Wo = 5.1$). All lines represent CFD data. Markers represent experimental data. (LEFT) Oscillating bulk temperature profile vs. normalised minichannel height (y/a) at $x/b = 0$. (RIGHT) Oscillating temperature profiles at the heated wall ($y/a = 0$) along the normalised spanwise direction (x/b).

7.1.1.7 Half rectified pulsation sinusoidal profile

Figure 7-59 respectively represent the spatial and spanwise variation of temperature profiles resulting from positive half rectified waveform at a frequency of 0.02 *Hz* ($Wo = 0.5$) and flow rate amplitudes of $A_0 = 0.5{,}3$. For a viscous dominated low frequency flow, similarities in the feature exists between the oscillating velocity profiles as seen from (Figure 0-7 and Figure 0-8) and the wall temperature profiles. Low frequency flows are typically exhibit significant amount of heat diffusion from the bottom wall to the core bulk fluid. Additionally, the thermal diffusion time scales are shorter compared to the longer pulsation periods and due to a low wall thermal inertia. This phenomenon leads to a substantial increase in the bulk fluid temperature as is evident from Figure 7-50 (a) similar in agreement with the symmetric sinusoidal cases. During the onset of the semi-sinusoidal acceleration-deceleration stage for phases $\pi \leq \theta \leq 2\pi$, the bulk temperature of fluid shows a minimal change as the oscillation amplitude is weaker compared to the steady due to colder fluid entering the heated section as an effect to the low frequency pulsation. The bulk temperature is higher at the bottom of the channel $y/a = 0$ due to the increased diffusion of heat laterally and attains a minimum at the top region of channel $y/a = 1$. The oscillating wall temperatures reflect a gradual change in the spanwise direction and thus the effects of an oscillating component are not significantly evident.

On increasing the A_0, the wall temperature magnitudes decrease. The effect of oscillation is further amplified due to the influx of higher flowrate of the colder fluid in the heated channel. Similarly, the oscillating bulk temperatures reflect a drop in the magnitudes as enhanced forced convection cooling is evident.

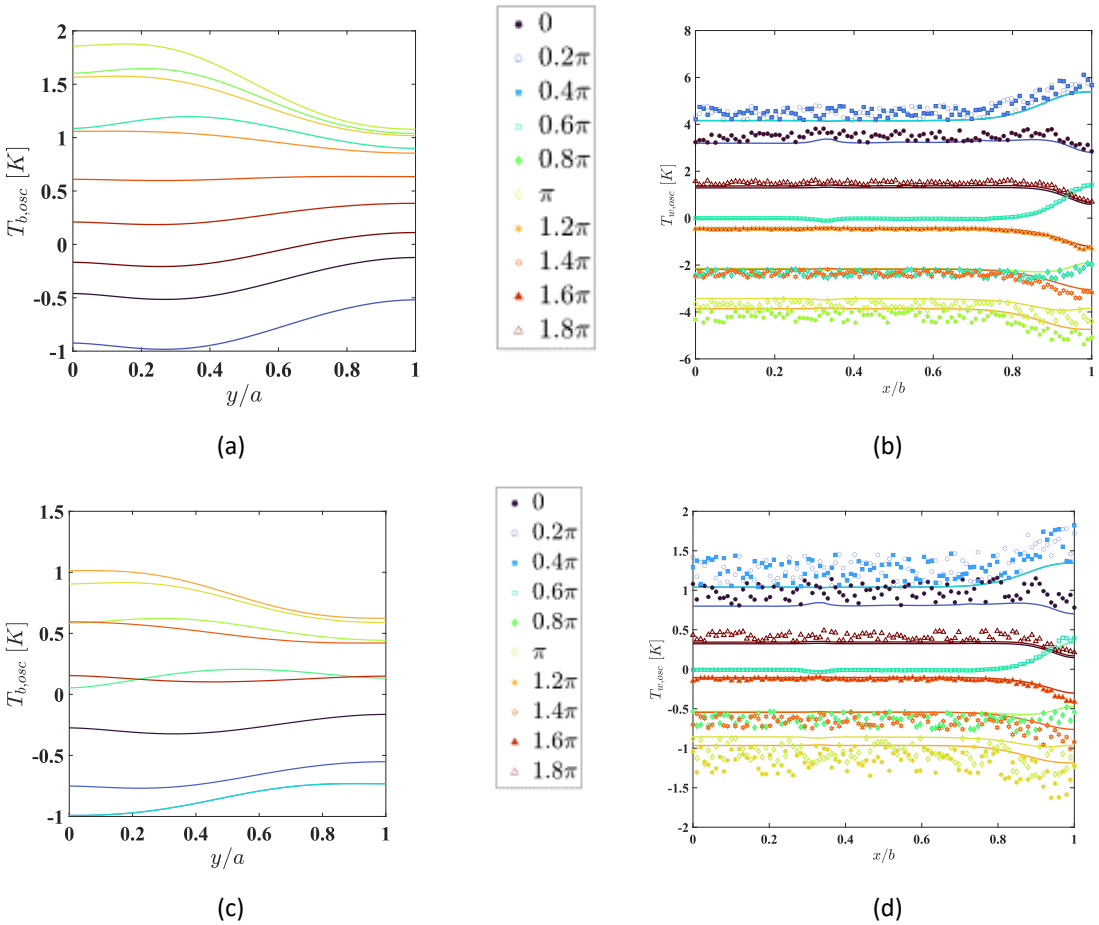

Figure 7-59: Positive half rectified waveform with flowrate amplitude $A_0 = 0.5, 3$ (a-f) and frequency 0.02 Hz ($Wo = 0.5$). All lines represent CFD data. Markers represent experimental data. (LEFT) Oscillating bulk temperature profile vs. normalised minichannel height (y/a) at $x/b = 0$. (RIGHT) Oscillating temperature profiles at the heated wall ($y/a = 0$) along the normalised spanwise direction (x/b).

Figure 7-60 respectively represent the spatial and spanwise variation of temperature profiles resulting from positive half rectified waveforms at a frequency of 0.5 *Hz* ($Wo = 2.5$) and flow rate amplitudes of $A_0 = 0.5$,3. The flow at moderate frequency presents a gradual build-up of bulk core inertial forces, although the viscous forces continue to prevail as is evident from the Figure 7-31 and Figure 7-32. The influence of transverse diffusion is seen to decrease, wherein a decrease in the magnitudes of bulk temperature is observed compared to the $Wo = 0.5$ case. The bulk oscillating temperature profiles react in a different manner compared to the low frequency case $Wo = 0.5$ and the influence of oscillation shown by steeper gradients is noticeable for both stages of acceleration and deceleration. As a result of a minor deviation from the parabolic velocity profiles seen in the case of moderate frequency oscillation, an increase in the near-wall viscous forces is understood. This feature of $Wo = 2.5$ case can be identified from the wall temperature profiles and are no longer parabolic and the maximum magnitudes of temperatures are shifted to the near side-wall regions $0.4 \leq x/b \leq 0.5$. The resulting temperature profiles reflect a decrease in the

magnitudes compared to the low frequency $Wo = 0.5$ cases as the thickness of the thermal boundary layer decreases.

On increasing A_0, similar observations are drawn as with the low frequency case and the forced convection effect leads to a drop in the magnitudes of both wall and bulk temperatures.

There exists a generally good agreement of the CFD and the experimental data for the oscillating wall temperature profiles of moderate frequency case. Minor deviations exist between the wall temperature profiles in the near-wall vicinity and are as a result of the assumptions undertaken in the energy equation of the three-dimensional numerical modelling which does not account for the heat losses.

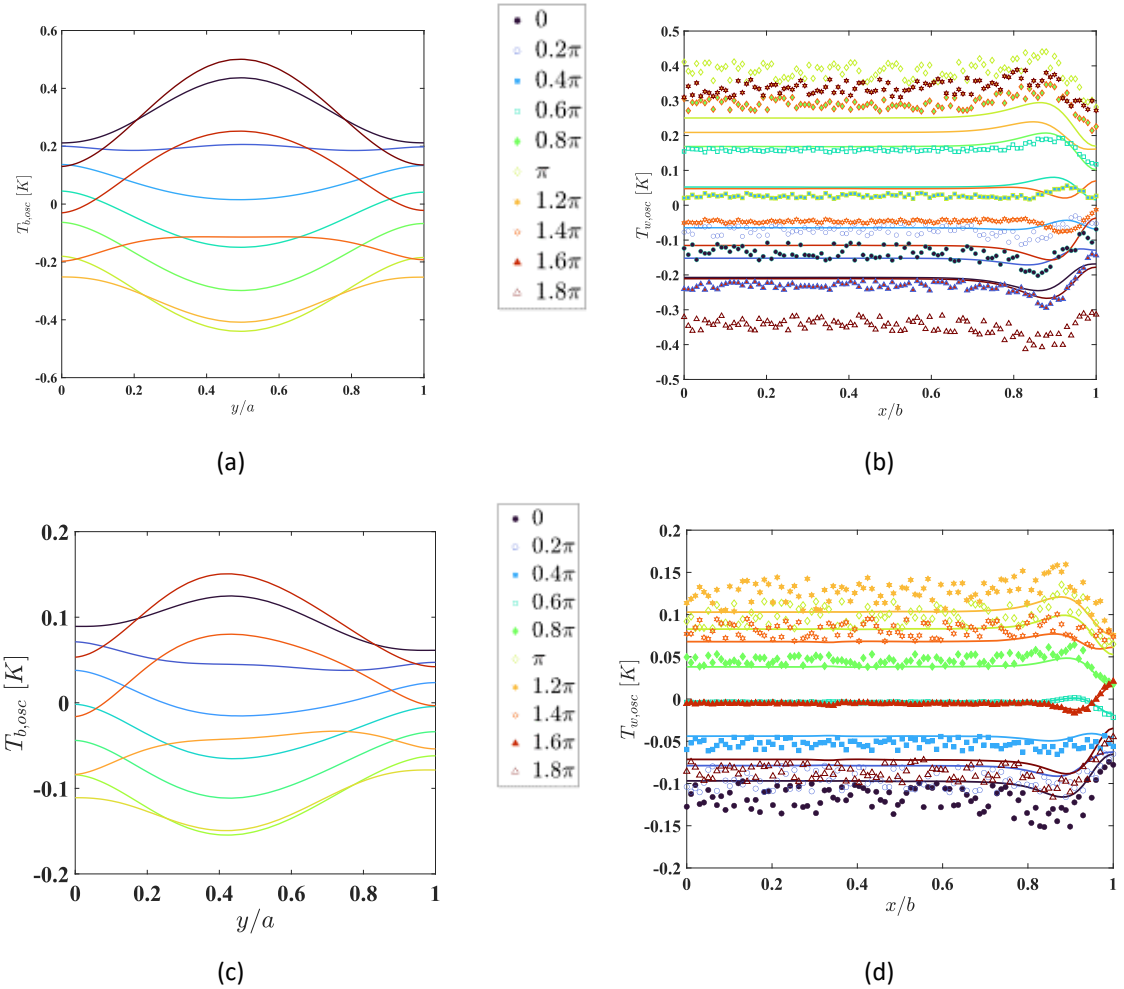

Figure 7-60: Positive half rectified waveform with flowrate amplitude $A_0 = 0.5, 3$ (a-f) and frequency 0.5 Hz ($Wo = 2.5$). All lines represent CFD data. Markers represent experimental data. (LEFT) Oscillating bulk temperature profile vs. normalised minichannel height (y/a) at $x/b = 0$. (RIGHT) Oscillating temperature profiles at the heated wall ($y/a = 0$) along the normalised spanwise direction (x/b).

Figure 7-61 respectively represent the spatial and spanwise variation of temperature profiles resulting from positive half rectified waveforms at a frequency of 2 *Hz* ($Wo = 5.1$) and flow rate amplitudes of $A_0 = 0.5,3$. Flows at high frequency typically exhibits the strengthening of bulk core inertial forces while the viscous effects continue to be dominant in the near side-wall vicinity, this can be deduced from Figure 7-33 and Figure 7-34. Since the pulsation periods are shorter, convection heat transfer is dominant throughout and as a result the transverse thermal diffusion is viewed to be ineffective. The oscillating bulk temperature profile reflects this phenomenon with a further reduction in magnitudes compared to the low-moderate frequency cases. As an effect of the semi-sinusoidal component of half rectified waveform, the oscillating wall temperature profile resembles closely to the case of symmetric sinusoidal at $Wo = 5.1, A_0 = 0.5$ (Figure 7-51 (b)). However, due to the influence of a stronger steady component, the oscillating bulk temperatures show significant lateral diffusion of heat from the bottom heated regions $0 \leq y/a \leq 0.3$ during the start and end of cycle. The peak magnitude of temperature in the near side-wall region decreases at high frequency since the shear stress magnitudes are strengthened for high frequency flows and the thickness of thermal boundary layer further decreases. The phenomenon of annular effects is established with the oscillating wall temperature profiles for high frequency flows as has been widely observed for the corresponding cases of velocity and shear stress profiles, described from Figure 7-15. Due to the flatter oscillating wall temperatures in the core bulk region.

Increasing A_0 leads to a further strengthening of near wall viscous forces as is noticeable from Figure 7-17, thus there is a simultaneous decrease in the bulk core fluid and wall temperature magnitudes. As a result of increased flow rate amplitude i.e., enhanced convection, steeper thermal gradients are concentrated for the oscillating wall temperature profile in the near-side wall vicinity for all the time intervals of cycle. The bulk temperatures reflect a pronounced effect in the bulk core regions of the channel at $y/a = 0.5$ which correlates to the strengthening of core inertial forces in order to accommodate for co-existence features established by the half rectified profile.

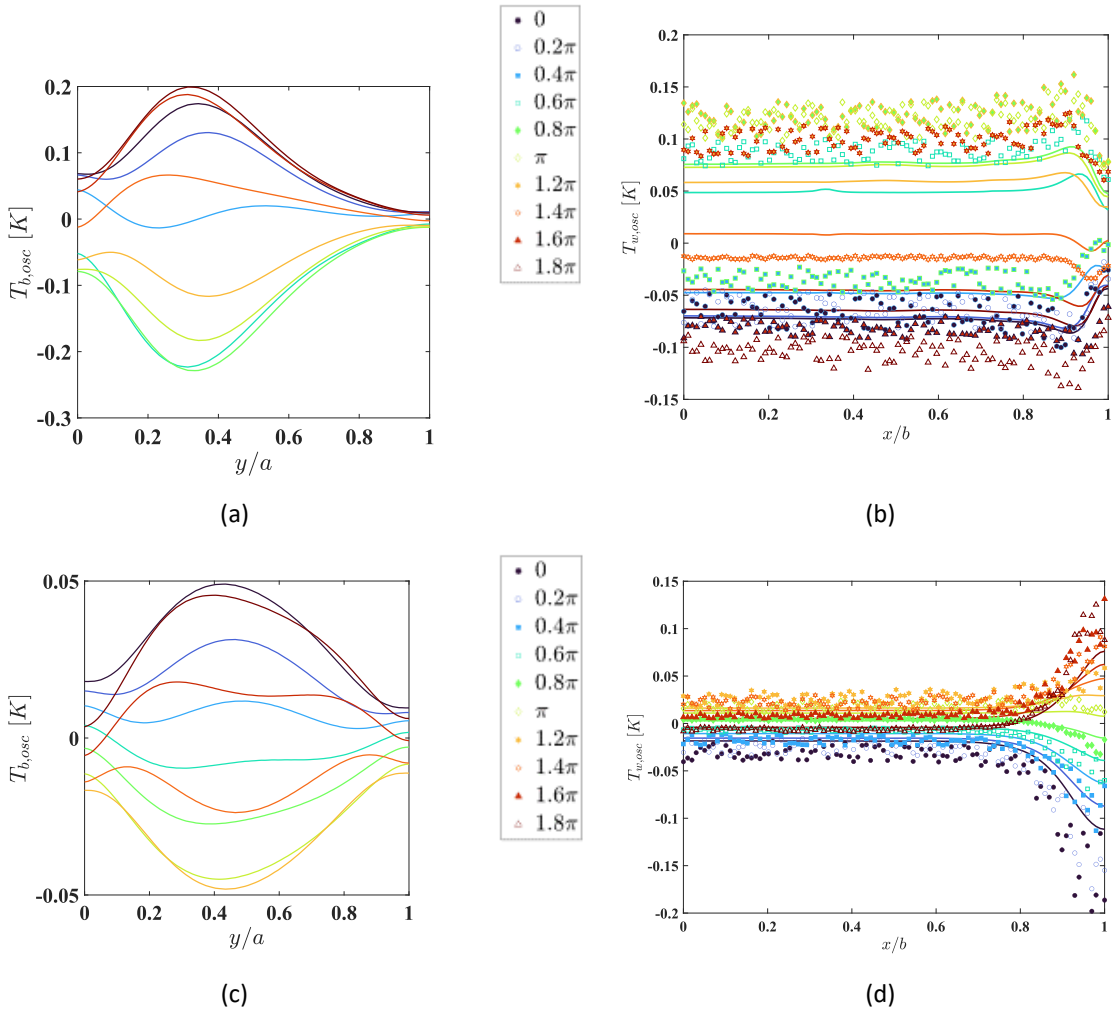

Figure 7-61: Positive half rectified waveform with flowrate amplitude $A_0 = 0.5, 3$ (a-f) and frequency 2 Hz ($Wo = 5.1$). All lines represent CFD data. Markers represent experimental data. (LEFT) Oscillating bulk temperature profile vs. normalised minichannel height (y/a) at $x/b = 0$. (RIGHT) Oscillating temperature profiles at the heated wall ($y/a = 0$) along the normalised spanwise direction (x/b).

Figure 7-62 (a-d) respectively represent the spatial and spanwise variation of temperature profiles resulting from negative half rectified waveforms at a frequency of 0.5 *Hz* ($Wo = 2.5$) and flow rate amplitudes of $A_0 = 0.5,3$. The flow at moderate frequency presents a gradual build-up of bulk core inertial forces, although the viscous forces continue to prevail as is evident from the Figure 7-37 and Figure 7-38. The influence of transverse diffusion is seen to decrease, wherein a decrease in the magnitudes of bulk temperature is observed compared to the $Wo = 0.5$ case. The bulk oscillating temperature profiles react in a different manner compared to the low frequency case $Wo = 0.5$ and the influence of oscillation shown by steeper gradients is noticeable for both stages of acceleration and deceleration. As a result of a minor deviation from the parabolic velocity profiles seen in the case of moderate frequency oscillation, an increase in the near-wall viscous forces is understood. This feature of $Wo = 2.5$ case can be identified from the wall temperature profiles and are no longer parabolic and the maximum magnitudes of temperatures are shifted to the near side-wall regions $0.4 \leq x/b \leq 0.5$. The resulting temperature profiles reflect a decrease in the

magnitudes compared to the low frequency $Wo = 0.5$ cases as the thickness of the thermal boundary layer decreases.

On increasing A_0, the oscillating bulk temperatures present the increased influence of a stronger oscillation component. Withdrawal of heat during the semi-sinusoidal interval of acceleration-deceleration stage is evident for phases $1.4\pi - 1.8\pi$. As a result of developing inertial forces wide thermal gradients are seen at all intervals of the cycle. Additionally, the oscillating wall temperature presents a stepper gradient of temperature in the near-wall and off-wall vicinity between $0.3 \leq x/b \leq 0.5$ with the latter phases of the cycle showing a decreasing magnitude of temperature.

There exists a generally good agreement of the CFD and the experimental data for the oscillating wall temperature profiles of moderate frequency case. Minor deviations exist between the wall temperature profiles in the near-wall vicinity and are due to the assumptions undertaken in the energy equation of three-dimensional numerical modelling which does not account for heat losses.

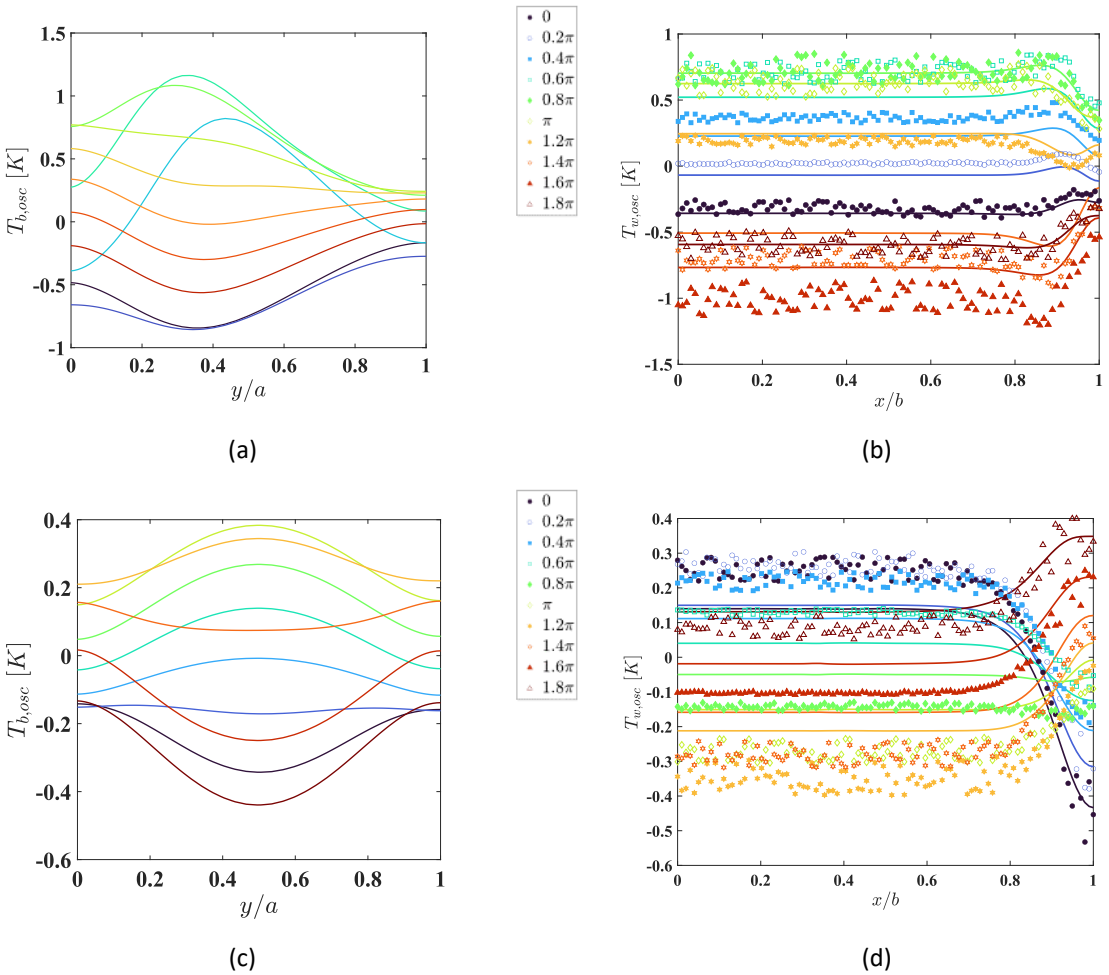

Figure 7-62: Negative half rectified waveform with flowrate amplitude $A_0 = 0.5, 3$ (a-f) and frequency 0.5 Hz ($Wo = 2.5$). All lines represent CFD data. Markers represent experimental data. (LEFT) Oscillating bulk temperature profile vs. normalised minichannel height (y/a) at $x/b = 0$. (RIGHT) Oscillating temperature profiles at the heated wall ($y/a = 0$) along the normalised spanwise direction (x/b).

Figure 7-63 (a-d) respectively represent the spatial and spanwise variation of temperature profiles resulting from negative half rectified waveforms at a frequency of 2 *Hz* ($Wo = 5.1$) and flow rate amplitudes of $A_0 = 0.5,3$. Flows at high frequency typically exhibits the strengthening of bulk core inertial forces while the viscous effects continue to be dominant in the near side-wall vicinity, this can be deduced from the Figure 7-39 and Figure 7-40. Since the pulsation periods are shorter, convection heat transfer is dominant throughout and as a result the transverse thermal diffusion is viewed to be ineffective. The oscillating bulk temperature profile reflects this phenomenon with a further reduction in magnitudes compared to the low-moderate frequency cases. As an effect of the semi-sinusoidal component of half rectified waveform, the oscillating wall temperature profile resembles closely to the case of symmetric sinusoidal at $Wo = 5.1, A_0 = 0.5$ (Figure 7-51 (b)). However, due to the influence of a stronger steady component, the oscillating bulk temperatures show significant lateral diffusion of heat from the bottom heated regions $0 \leq y/a \leq 0.3$ during the start and end of cycle. The peak magnitude of temperature in the near side-wall region decreases at high frequency since the shear stress magnitudes are strengthened for high frequency flows and the thickness of thermal boundary layer further decreases. The phenomenon of annular effects is established with the oscillating wall temperature profiles for high frequency flows as has been widely observed for the corresponding cases of velocity and shear stress profiles, described from Figure 7-39 and Figure 7-40.

Increasing A_0 leads to a further strengthening of near wall viscous forces as is noticeable from Figure 7-40, thus there is a simultaneous decrease in the bulk core fluid and wall temperature magnitudes. As a result of increased flow rate amplitude i.e., enhanced convection, steeper thermal gradients are concentrated for the oscillating wall temperature profile in the near-side wall vicinity for all the time intervals of cycle. The bulk temperatures reflect a pronounced effect in the bulk core regions of the channel at $y/a = 0.5$ which correlates to the strengthening of core inertial forces in order to accommodate for co-existence features established by the half rectified profile.

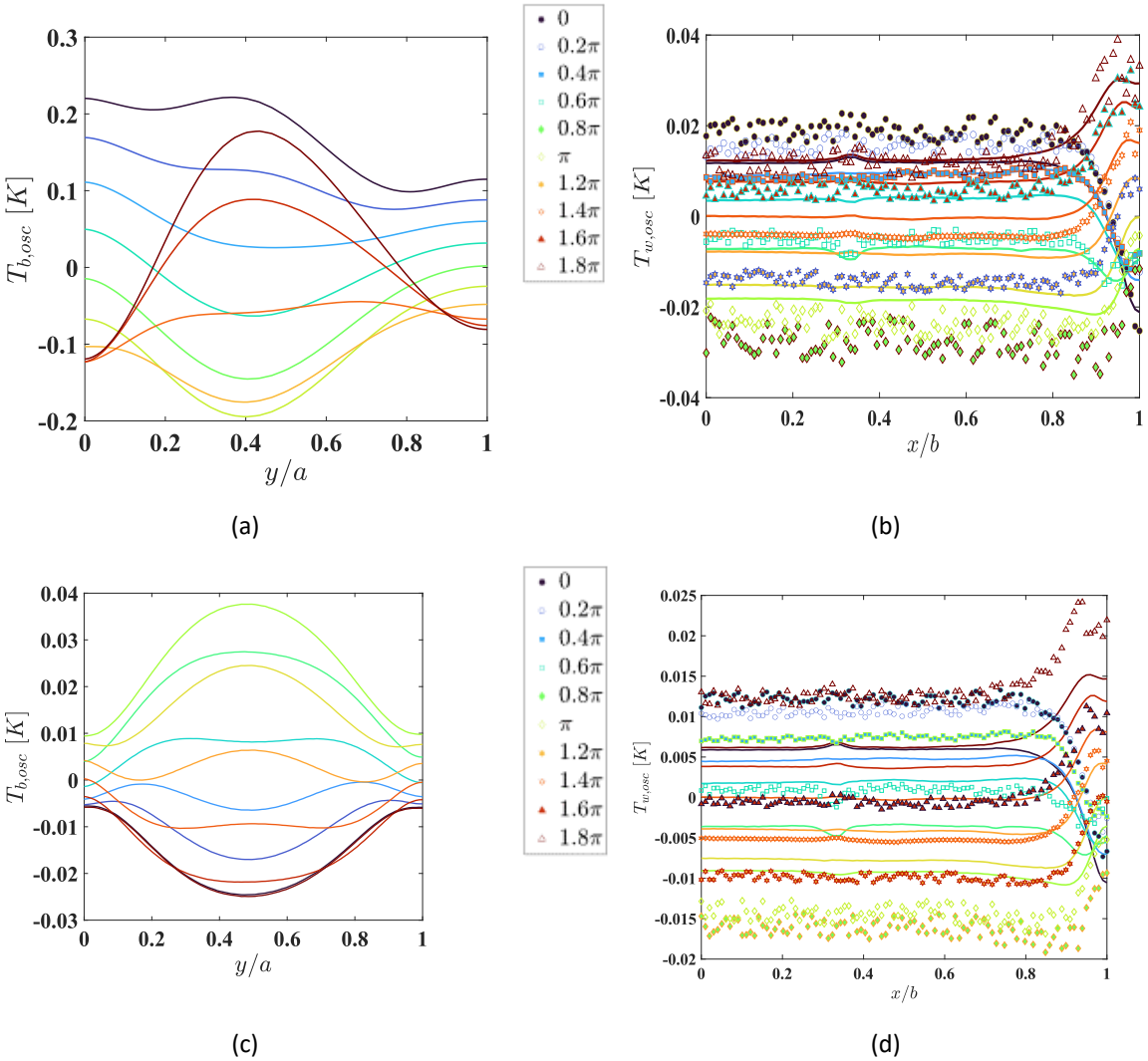

Figure 7-63: Negative half rectified waveform with flowrate amplitude $A_0 = 0.5, 3$ (a-f) and frequency 2 Hz ($Wo = 5.1$). All lines represent CFD data. Markers represent experimental data. (LEFT) Oscillating bulk temperature profile vs. normalised minichannel height (y/a) at $x/b = 0$. (RIGHT) Oscillating temperature profiles at the heated wall ($y/a = 0$) along the normalised spanwise direction (x/b).

Figure 7-64 (a-d) illustrate the temporal variations of temperature and axial velocity in the fully developed region for a symmetric sinusoidal waveform of pulsation frequency 0.5 *Hz* ($Wo = 2.5$) and 2 *Hz* ($Wo = 5.1$) at $A_0 = 1$. For moderate frequency oscillation at $Wo = 2.5$, the bulk and wall temperature Figure 7-64 (a), (b) react relatively quickly compared to the high frequency oscillation at $Wo = 5.1$ Figure 7-64 (c), (d). During the onset of acceleration stage $0 \leq \theta \leq \pi$ (from velocity profile), a sharp drop in the bulk temperature is observed as the convection heat transfer mechanism is enhanced, whereas the wall temperature responds with a gradual drop in its magnitude. The bulk temperature is raised towards the end of acceleration and the onset of deceleration stage $\pi \leq \theta \leq 2\pi$ (velocity profile) as the higher temperature core fluid exits the channel. Similar features are noticed for the high frequency case $Wo = 5.1$, with a gradual phase

shift between the temperature and velocity profiles. The phase difference between the axial velocity and bulk temperature profile for $Wo = 2.5$ is about 48°, while for the $Wo = 5.1$ case it is about 56°. In the near wall regions as shown at $x/b = 0.95$, the phase difference between the velocity and temperature is more pronounced. It can be inferred that the phase difference between the velocity and temperature profile in the core bulk region increases with the pulsation frequency. However, the phase difference in the near-wall vicinity decreases with the consequent increase in the Wo [86]. This phenomenon can be attributed to a faster heat transfer rate in the near wall and the temperature near the wall reacts promptly at high Wo due to the presence of annular effects in the velocity profiles as discussed in Section 7.5.

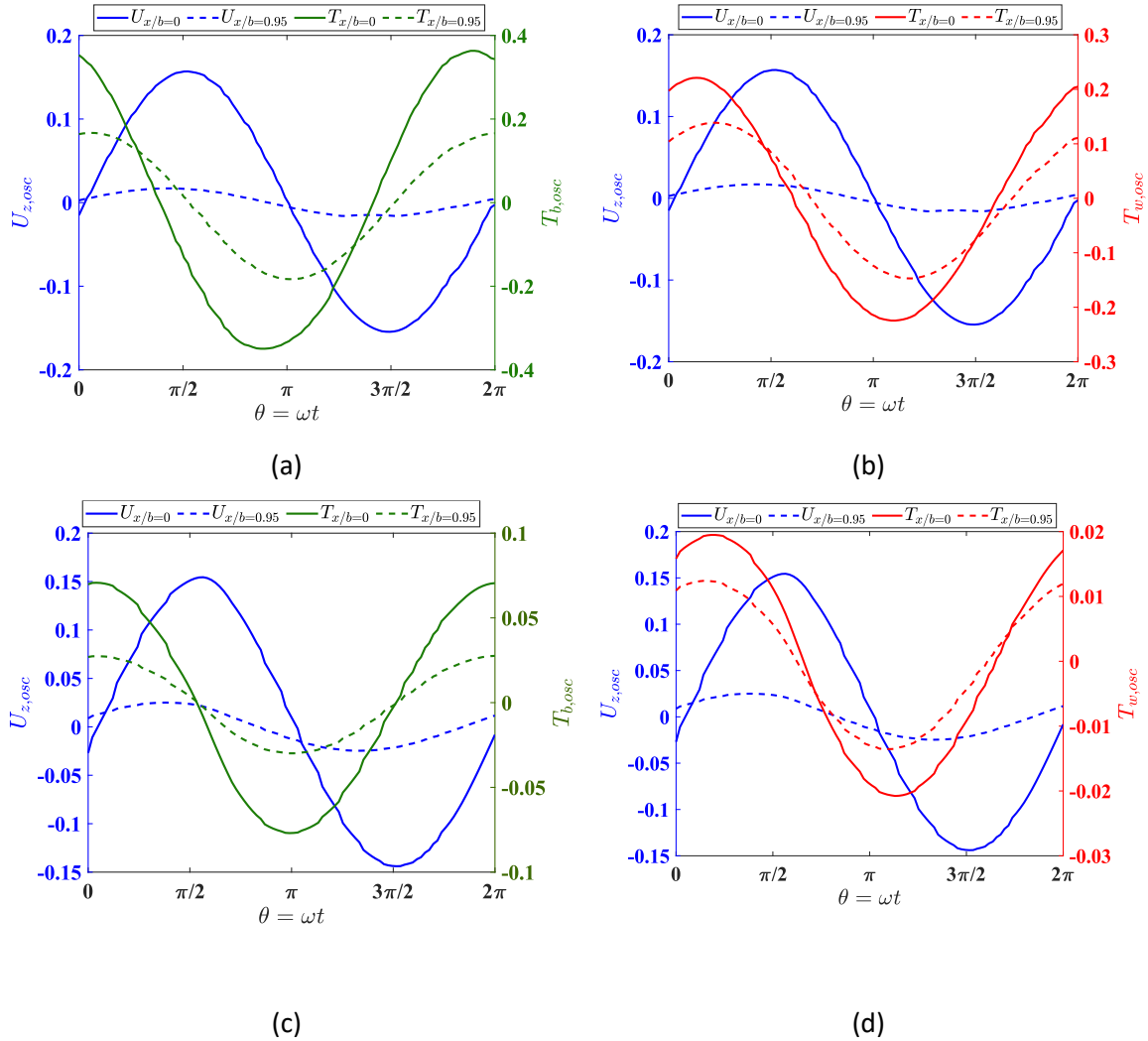

Figure 7-64: Temporal variation of oscillating temperature versus oscillating axial velocity at channel core $x/b = 0$ and near side-wall $x/b = 0.95$ for symmetric sinusoidal waveform at $A_0 = 1$ from CFD data. (LEFT) plots the bulk temperature for (a) $Wo = 2.5$ (c) $Wo = 5.1$. (RIGHT) plots the bottom wall temperature for (a) $Wo = 2.5$ (d) $Wo = 5.1$.

7.6 Nusselt number distributions

7.6.1 Space averaged instantaneous Nusselt number

Figure 7-65 plots the variation of the space-averaged instantaneous Nusselt number $|Nu|$ for a single pulsation for varying flow rate amplitude A_0. Each row represents data from a different pulsation waveform. The figures in the left column represent a frequency of $Wo = 2.5$ whereas figures in the right column represent $Wo = 5.1$. Data is shown selectively for these frequencies as both $Wo = 2.5$ and $Wo = 5.1$ show distinct features of pulsation, thus leading to higher heat transfer rates compared to the lowest frequency of $Wo = 0.5$ and the highest frequency $Wo = 18.3$ (discussed and compared in more detail in the subsequent Section 7.6.2).

It is clearly evident across all pulsation waveform formats that the highest flowrate amplitude $A_0 = 3$ produces a maximum effect on the $|Nu|$ profile. This can be attributed towards an increased influx of colder fluid as a result of a stronger oscillating flow component over the underlying steady flow component, thus promoting an increased heat transfer rate. This phenomenon is linked to the energy Equation [86], wherein for a fixed value of the kinetic Reynolds number (Re_ω, which correlates to Wo) and fluid Prandtl number (Pr), the convection term becomes pronounced with an increasing magnitude of A_0.

$|Nu|$ for the symmetric sinusoidal case (Figure 7-65 a, b) increases with the onset of pulsation and reaches a maximum value at phase π, before deceasing towards the end of the cycle. Due to increased effect of transverse diffusion at $Wo = 2.5$ with the consequent influence of convection at $A_0 = 3$, $|Nu|$ is higher compared to the high frequency flow $Wo = 5.1$. However due to weaker effect of oscillation for $A_0 = 0.5$ and $A_0 = 1$, $|Nu|$ is lower and is reduced [111, 127] compared to the steady flow $Nu_s = 5.08$ of Table 6-4.

The asymmetric flowrate profiles result in a unique shape of the space-averaged temporal Nu. As discussed in Section 7.1.1.1, the leading asymmetric waveform (Figure 7-65 c, d) features a rapid acceleration component followed by a gradual deceleration stage before another rapid acceleration as the cycle restarts. The corresponding $|Nu|$ profiles react gradually to accommodate for the above effect and the peak magnitude is shifted away from phase π compared with the symmetric sinusoidal case. Interestingly, at the higher frequency, the $|Nu|$ profile reflects a delayed response with a gradual increment to reach a peak magnitude followed by a sharp decline with an appearance of a reduction in magnitude towards the deceleration stage of pulsation. As a result of a longer deceleration stage of leading pulsation format, the $|Nu|$ magnitudes are marginally higher compared to the symmetric sinusoidal case for $W_0 = 2.5$. Although for the shorter axial displacement timescale high frequency flow $Wo = 5.1$, the $|Nu|$ value is relatively higher

compared to the higher flowrate amplitude $A_0 = 3$ of symmetric sinusoidal waveform and can be linked to the vigorous effects shown by the oscillating velocity profiles from Figure 7-24.

For the lagging asymmetric $|Nu|$ profiles (Figure 7-65 e, f), the acute shift in the deceleration stage is reflected by the evolution of the shape. A peak in $|Nu|$ occurs just before phase π which is evident from the moderate frequency flow $Wo = 2.5$, and is more pronounced for the high frequency flow. As a result of amplified bulk flow effects in the spanwise velocity profiles which lead to an increased transverse diffusion of heat, higher magnitudes of $|Nu|$ are reached for the highest flow rate amplitude $A_0 = 3$. Due to the presence of flow reversal effects at $Wo = 5.1$ and $A_0 = 3$, the $|Nu|$ shows a high value compared to similar high frequency leading asymmetric sinusoidal and symmetric sinusoidal pulsation formats, this phenomenon is in agreement with [74, 83, 85].

The positive and negative half rectified profiles show varied effects of the pulsation waveforms on $|Nu|$. For the case of positive half rectified pulsations at $Wo = 2.5$ and $Wo = 5.1$ (Figure 7-65 g, h), there appears a peak $|Nu|$ towards the beginning/end of the pulsation cycle. A minimum value of $|Nu|$ is observed close to phase π which indicates an insignificant effect of the steady component of the cycle and the onset of the semi-sinusoidal forward directed component. The influence of semi-sinusoidal half of the cycle leads to an increase in $|Nu|$ between the deceleration stages $\pi \leq \theta \leq 2$, whereas the steady component of the half rectified shows a marginal reduction in the $|Nu|$ compared to the steady flow.

The negative half rectified waveform (Figure 7-65 i, j) results in an increase in the magnitude of $|Nu|$ with the onset of the backward directed sinusoidal part for phases $\pi \leq \theta \leq 3\pi/2$ for the moderate frequency at $Wo = 2.5$. However, for the faster moving high frequency flow, a gradual increase in Nu magnitude is seen as the transients of temperature profiles are slow to react and respond to the co-existing semis-sinusoidal and steady flow components of the waveform. The magnitudes are evidently higher for both cases of $Wo = 2.5$ and $Wo = 5.1$ at $A_0 = 3$.

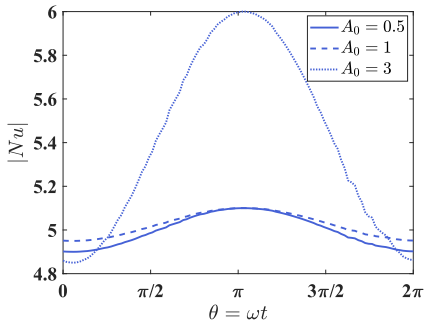

(a) Symmetric sinusoidal waveform, $Wo = 2.5$

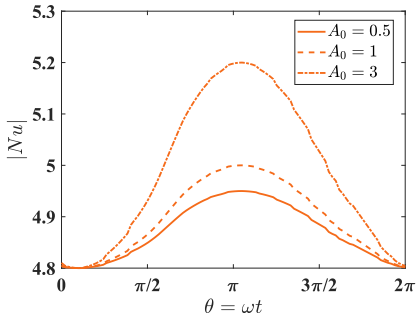

(b) Symmetric sinusoidal waveform, $Wo = 5.1$

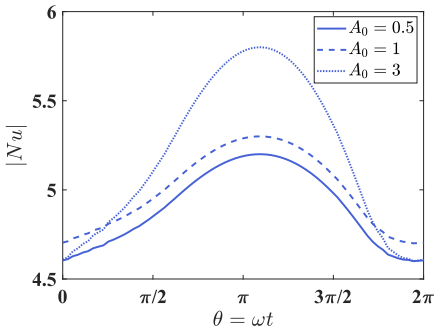

(c) Leading asymmetric sinusoidal waveform, $Wo = 2.5$

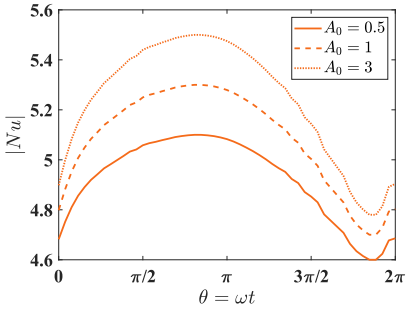

(d) Leading asymmetric sinusoidal waveform, $Wo = 5.1$

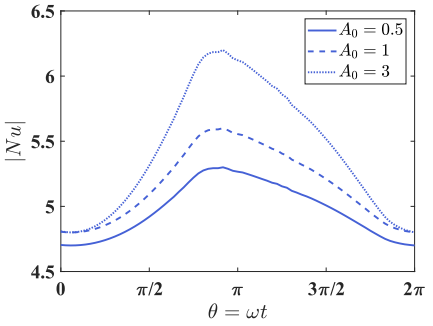

(e) Lagging asymmetric sinusoidal waveform, $Wo = 2.5$

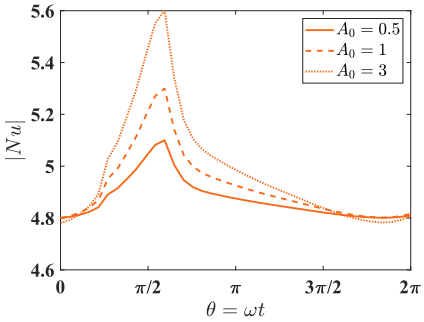

(f) Lagging asymmetric sinusoidal waveform, $Wo = 5.1$

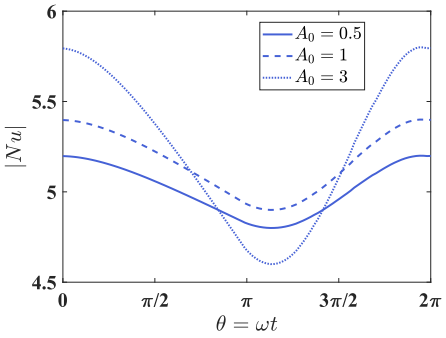

(g) Positive half rectified waveform, $Wo = 2.5$

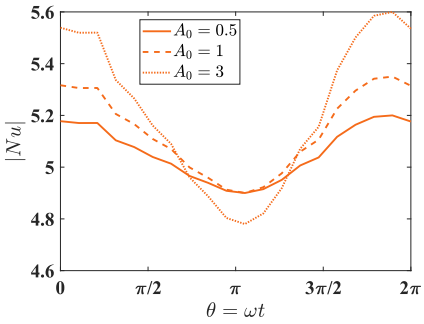

(h) Positive half rectified waveform, $Wo = 5.1$

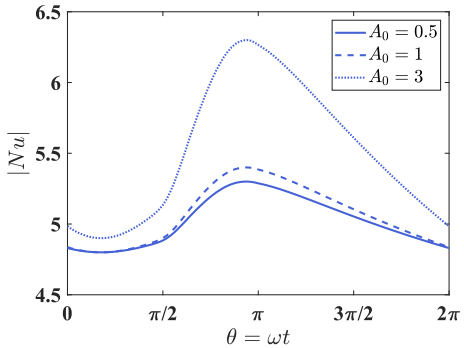

(i) Negative half rectified waveform, $Wo = 2.5$

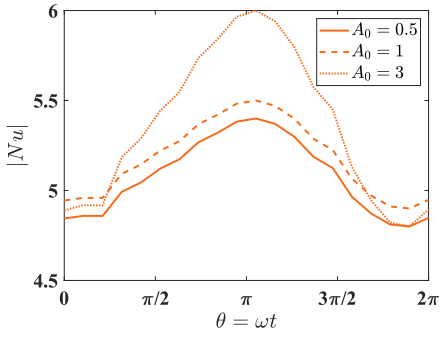

(j) Negative half rectified waveform, $Wo = 5.1$

Figure 7-65: Temporal variation of space-averaged instantaneous Nusselt number for each waveform at $Wo = 2.5$ and $Wo = 5.1$ at $A_0 = 0.5,1,3$.

The following Figure 7-66 present the temporal instantaneous space-averaged Nu profiles for varying Wo between $0.5 \leq Wo \leq 18.3$ at a fixed $A_0 = 3$. The high flowrate amplitude is particularly preferred to highlight the prominence of heat transfer augmentation across the varied waveform formats. For all cases of pulsation waveforms, the instantaneous space-averaged Nu increases with increase in Wo up to a certain optimal value of pulsation frequency. It implies that the heat transfer rate increases with a corresponding increase in the pulsation frequency. This phenomenon is linked with the thickness of the thermal boundary, which decreases (becomes thinner) with an increase in Wo [74, 85]. The thermal boundary layer thickness (δ_{th}) for an oscillatory flow can be described as:

$$\delta_{th} \propto \left(\frac{1}{Re_{\omega}}\right)^{1/2} \tag{7-1}$$

Wherein the Re_{ω}, (corresponds to Wo) in the heat transfer associated for oscillatory flows, Ref [86] controls the thickness of the boundary layer, and has a similar significance to the Reynolds number for an unidirectional steady flow. There evidently exists a range of intermediate frequencies resulting in $|Nu|$ being greater than Nu_s. These trends are further amplified with the increase in A_0. It is inferred that the heat transfer rate either increases or decreases from the corresponding steady value for certain range of phase intervals subjected to a range of pulsation frequency. However, the cycle averaged $|Nu|$ is increased compared to the analogous steady flow $|Nu|$, as elaborated further in Section 7.6.2.

An optimum pulsation frequency falls within a narrow band denoted by $f_l \leq f \leq f_h$ (*Hz*), where f_l and f_h denote the lower and upper limit of the frequency respectively. For the current study, the optimum pulsation frequency range is determined to exist between $0.5 \leq f \leq 2$. For the cases of extreme low and high pulsation frequencies i.e., $f = 0.02\ Hz$ and $f = 25\ Hz$ a deterioration (or reduction) in heat transfer compared to the steady flow is observed across all pulsation waveform formats despite the varied influence of stronger flow rate amplitude A_0. Similar understanding was established by previous studies [74, 75, 85, 86, 102, 127] for an analytical heat transfer study maintained with isothermal wall of a pipe undergoing sinusoidal pulsations with $0.1 \leq A_0 \leq 0.30$ and $1 \leq Wo \leq 15$.

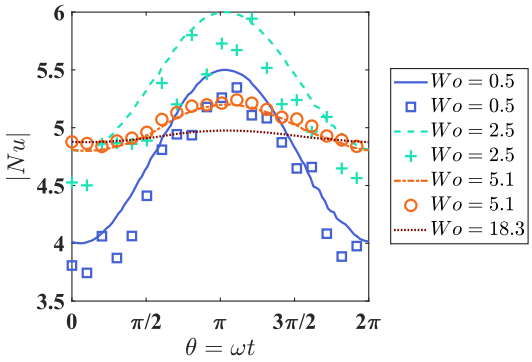

(a) Symmetric sinusoidal waveform, $A_0 = 3$

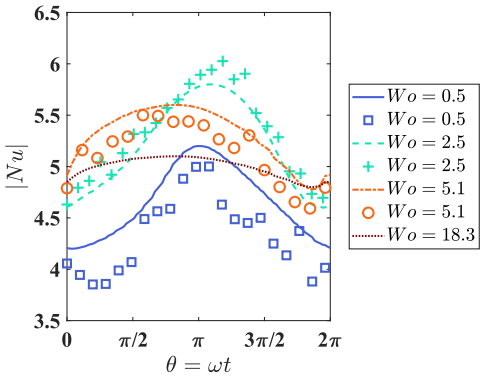

(b) Leading asymmetric sinusoidal waveform, $A_0 = 3$

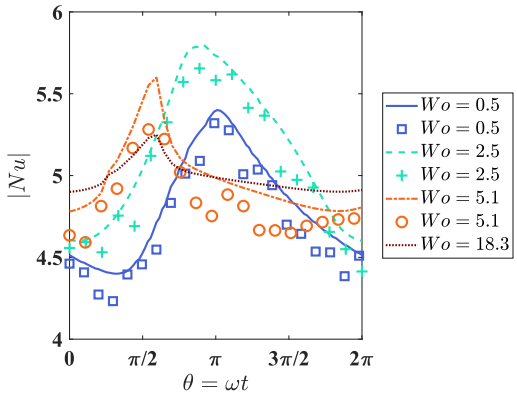

(c) Lagging asymmetric sinusoidal waveform, $A_0 = 3$

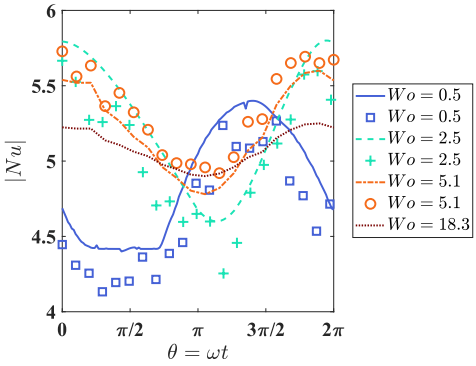

(d) Positive half rectified waveform, $A_0 = 3$

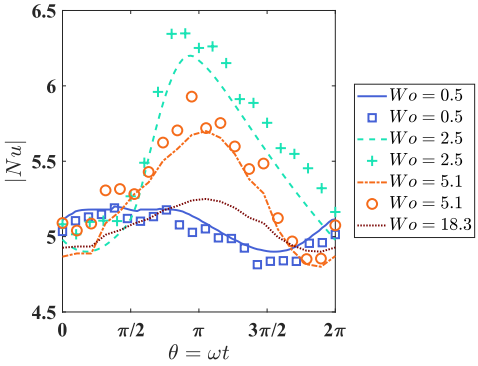

(e) Negative half rectified waveform, $A_0 = 3$

Figure 7-66: Temporal variation of space-averaged instantaneous Nusselt number for all waveforms with varying $Wo = 0.5, 2.5, 5.1$ and 18.3 at a fixed $A_0 = 3$. Line plots present CFD results and markers present experimental results.

7.6.2 Space and time averaged Nusselt number

Figure 7-67 (a-c) indicates a difference in Nusselt number (calculated by Equation (6-20) with a variation in A_0 and Wo for the studied pulsation waveform formats. Generally, with the effects of increasing flow rate amplitude and pulsation frequency, the time-space averaged Nu increases with both quantities up to a certain extent [86]. For a sinusoidal waveform, the difference in Nusselt

number shows an increasing trend with an increase in frequency in particular for $A_0 = 0.5$ and $A_0 = 1$. It is described that the fluid pulsation parameters demonstrate an interdependence on the heat transfer due to a time-varying velocity profile, temperature profile and wall thermal inertial effects [113]. Results presented are compared with analytical trends established for a sinusoidal pulsatile flow in a channel by Yuan *et al.* [113] and for a pipe flow by Hemida *et al.* [136]. Mehta and Khandekar [103] presented similar characteristics in an experimental study involving a square waveform in a heated channel. For $A_0 = 0.5$ and 3, the difference in the Nusselt number was noted to be always negative overall. The difference reaches zero at higher pulsation frequencies since the flow exhibits a quasi-steady behaviour. However, under a stronger effect of convection developed at $A_0 = 3$, there exists a heat transfer enhancement of 6.7% evidently for $Wo = 2.5$ compared to the steady flow.

Similarly, the cases of leading and lagging asymmetric profile follow the trends of sinusoidal profiles at lower flow rate amplitudes $A_0 = 0.5$. However, pronounced effects of heat transfer are determined from the stronger oscillatory influence at higher flow rate amplitudes. The leading asymmetry presents a moderate heat transfer enhancement of about 4.2% which is weaker than the sinusoidal flowrate at $Wo = 0.5, A_0 = 3$. Although the influence of asymmetric flow rate characteristics reflects with an enhancement of about 2.1% at high frequency $Wo = 5.1$. Further, the lagging asymmetric flowrate generates a greater enhancement of about 11.1% at $Wo = 2.5$ and $A_0 = 3$ with a subsequent 4% enhancement at high frequency $Wo = 5.1$. The lowest and the highest frequencies $Wo = 0.5$ and $Wo = 18.3$ show a significant reduction in heat transfer compared to the steady flow Nu.

The positive and negative half rectified present differing effects on heat transfer between the two cases over the same parameter space. The positive half rectified waveform shows an inconclusive heat transfer (deterioration) compared to the steady flow for lower flow rate amplitude of $A_0 = 0.5$. However, the backward driven negative half rectified waveform, produces a marginal heat transfer enhancement of about 0.3% for $Wo = 2.5$ and 0.4% for $Wo = 5.1$ at $A_0 = 0.5$. The heat transfer enhancement is further pronounced at higher flow rate amplitudes at $Wo = 2.5$, with an increase of 9% and a simultaneous increase of 6% at $Wo = 5.1$. The positive half rectified in comparison to the other studied waveforms generates a weaker heat transfer enhancement at $A_0 = 3$.

It is inferred that the enhancement and deterioration of mean Nusselt number is conditional and is subjected to the excitation waveform and the flow parameters.

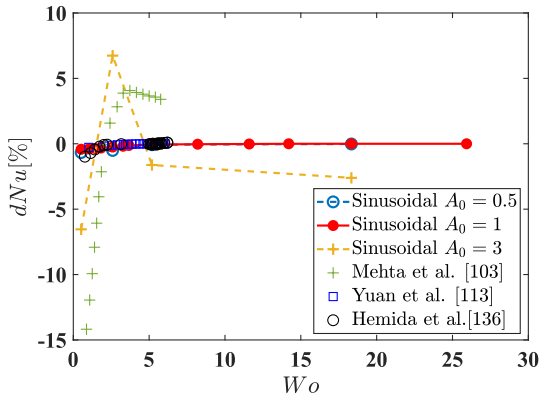

(a)

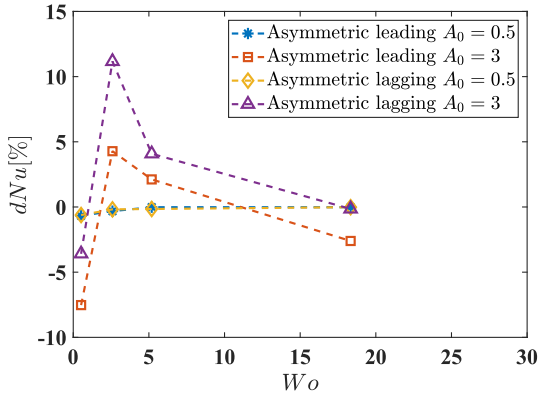

(b)

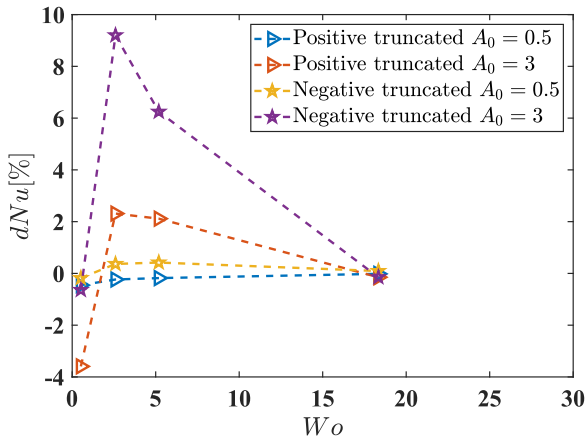

(c)

Figure 7-67: Variation of % difference in space and time averaged Nusselt number with respect to steady Nusselt number with Wo and A_0 (a) Symmetric sinusoidal waveform, (b) Asymmetric leading and lagging waveforms, (c) Positive and negative half rectified waveforms. Markers only mark the literature data for [103, 113 and 136].

7.7 Thermal performance

Figure 7-68 presents the overall thermal performance (as defined by Equation (6-21)) as a factor of varying Wo, A_0 and the associated pulsation waveform format. For the case of symmetric sinusoidal waveform, evidently for low-moderate flow rate amplitude the thermal performance is $\eta \leq 1$. This is primarily due to the symmetric characteristics offered by a sinusoidal profile which tends to attain a quasi-equilibrium with the cyclic process of heat removal and retention in the channel. However, with the strengthening of oscillation component at $A_0 = 3$, the thermal performance reaches its peak with $\eta \approx 2$ and can be quantitively associated with the enhancement of heat transfer with a subsequent lower friction factor.

Similar nature of η profiles are followed for the asymmetric sinusoidal waveforms for varying Wo and A_0. The low flow rate amplitude $A_0 = 0.5$ flows result in inconclusive heat transfer and thus the thermal performance is worst. However, as a result of an appreciable enhancement for the higher flow rate amplitudes $A_0 = 3$, a peak value of performance is achieved $\eta = 2.5$ for $Wo = 2.5$ despite the existence of relatively high magnitudes of shear stress for the lagging asymmetric waveform. The leading shows a reduced effect on thermal performance due to a combination of low heat transfer enhancement and higher shear stress at $A_0 = 3$.

The half rectified waveforms present relatively high thermal performance and is evidently seen for the negative half rectified waveform at $A_0 = 0.5$ and $A_0 = 3$. Although due to the underlying influence of greater shear stress magnitudes, the peak value of η is lower compared to the lagging asymmetric case for both frequencies $Wo = 2.5$ and $Wo = 5.1$. The positive-half rectified waveform presents a marginal increase in its thermal performance and the primary effect is linked to the existence of higher wall shear stress.

Overall, the peak optimum thermal performance exists between the moderate-high frequency band i.e., $2.5 \leq Wo \leq 5.1$ for most waveforms.

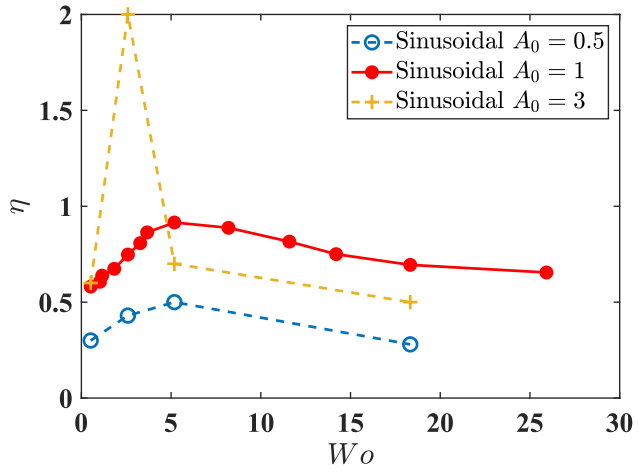

(a)

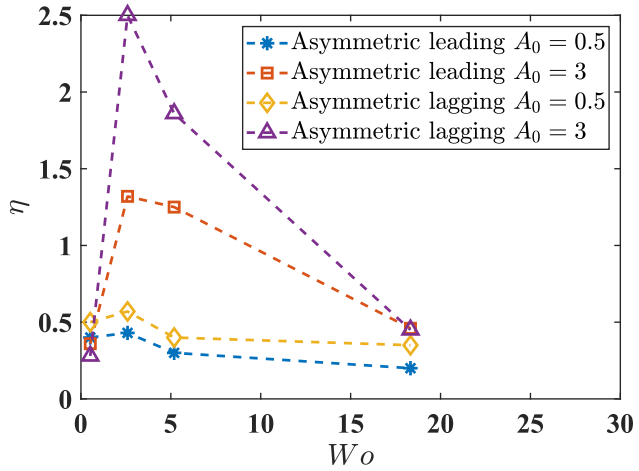

(b)

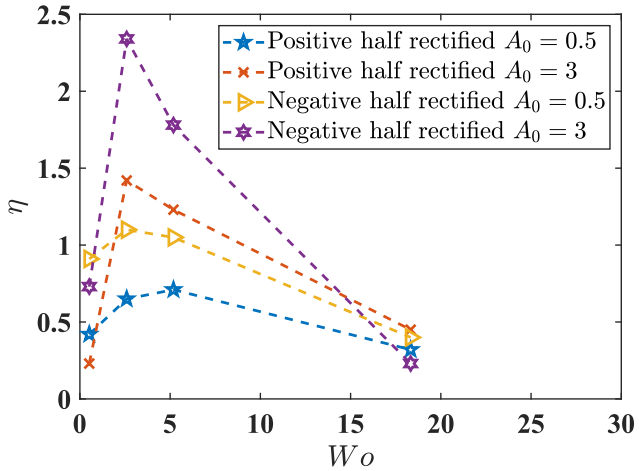

(c)

Figure 7-68: Variation of thermal performance with Wo and A_0 for (a) Symmetric sinusoidal waveform, (b) Asymmetric leading and lagging waveforms, (c) Positive and negative half rectified waveforms.

8) Summary and Conclusions

8.1 Summary

The study provides a comprehensive understanding of the complex and interlinked flow field and heat transfer characteristics associated with pulsating laminar flow in a rectangular minichannel with a heated bottom wall. A combination of experimental and computational methodologies is employed. Temporal and spatial distributions of hydrodynamic and thermal parameters are discussed based on results analysed from the hydrodynamically and thermally fully developed region of the minichannel. Results are obtained for 3 flow rate amplitudes ($A_0 = Q_{osc.max}/Q_s = 0.5, 1, 3$), 4 pulsation frequencies ($f = 0.02Hz, 0.5Hz, 2Hz, 25Hz$, corresponding to Womersley numbers of $Wo = 0.5, 2.5, 5.1, 18.3$) and 5 pulsating waveform formats (symmetric sinusoidal, asymmetric leading sinusoidal, asymmetric lagging sinusoidal, positive half rectified sinusoidal, negative half rectified sinusoidal).

In the experiment, a uniformly heated thin foil approximates a constant heat flux bottom wall of the minichannel. A small viewing windows permits the imaging of heated surface using a non-intrusive high resolution, high-speed imaging Infra-red camera. The camera system is calibrated using a two-point standard calibration in addition to an in-situ calibration to reduce the radiation distortion of its sensor. Pulsations are driven using a scotch-yoke mechanism comprising a stepper motor in an arrangement with a constant flowrate micropump. A pulse-frequency modulation control system is developed to generate the desired oscillatory waveform profile. Precise instantaneous measurements of flowrates are carried out by a non-intrusive ultrasonic flowmeter. A high accuracy differential pressure transducer is connected in line between the inlet and outlet ports of the minichannel. The working fluid is de-ionised water and is de-gassed prior to testing using a membrane contactor connected to a vacuum pump which filters out the dissolved gases and impurities. Four calibrated thermocouples are included to record and monitor temperatures between the inlet, outlet of the minichannel and the airgap cavity of test section. Experiments are carried out in a closed loop mechanism and the heated working fluid exiting the test section runs

through a plate-fin heat exchanger to return the fluid at an ambient temperature. A phase-lock arrangement is setup to have precise synchronous recordings of IR thermal images in accordance with the frequency of the excitation waveform.

The conjugate heat transfer CFD model is developed using ANSYS CFX. The minichannel geometry from the experiment is replicated in the model. Mesh and time step sensitivities studies are performed. The model is validated against published data from the literature and against the experimental data from this study. The CFD model enables a deeper analysis of the flow and thermal fields experienced under a pulsation. A three-dimensional CFD model is developed which is classified into fluid and solid domains. A symmetry plane is imposed which simplifies the geometry and reduces the computational requirements. The fluid domain is defined with a constant temperature velocity inlet and pressure outlet. The fluid-solid interface acts to permit an energy flow and aids in mesh adaption between the two domain entities. The solid domain is specified with a volumetric uniform heat generation. All walls of the model are maintained under adiabatic conditions, except the bottom wall of the solid domain specified with heat transfer coefficient which replicates the heat loss estimated from the experiments into the airgap region. The pulsation parameters and waveforms characteristics of symmetric, asymmetric and half rectified profiles are defined using UDFs (user defined functions). A laminar transient model is adopted to effectively capture the instantaneous features exhibited by the pulsations. The pulsation parameters in the numerical model are defined in coherence with the experimental parameter space and the maximum pulsation frequency is extended to the highest $Wo = 18.3$. An adaptive time stepping technique is employed to estimate the appropriate timestep for solutions which favours both solution accuracy and stability. A comprehensive spatial verification study using GCI technique is performed and oscillatory convergence is obtained for the preferred fine mesh. Further a residual sensitivity analysis is performed, and a computationally optimum residual limit is obtained for the pulsation cases.

8.2 Conclusions

Typically, the symmetric sinusoidal flowrate involves a peak acceleration stage at phase $\pi/2$ and a consequent deceleration peak at phase $3\pi/2$. The leading asymmetric format is characterised by a rapid increase in the acceleration stage, followed by a long gradual deceleration before the onset of acceleration stage as the cycle restarts. The lagging asymmetric format presents a novel effect wherein there is an initial period of gradual acceleration followed by a short acute shift in the deceleration stage before another gradual acceleration as the cycle restarts. The positive and

negative half rectified waveforms feature an equal interval combination of a steady component and a net forward-backward directed sinusoidal component respectively.

Viscous dominant, low frequency flows are typically characterised by parabolic oscillating velocity profiles and the hydrodynamic parameters such as the axial pressure gradient and wall shear stress are in-phase. Further, increases in the flow rate amplitudes leads to an increase in the pressure gradient and a simultaneous increase in shear stress magnitudes since the mass flowrate of the oscillation component is strengthened. These observations existed for the entire set of waveforms. Inertia dominant high frequency flows typically demonstrate the presence of high near-wall oscillating velocity components, and the phenomenon is widely termed as annular effects. This is as a result of greater inertial influence in the bulk core with subsequently high near-wall viscous forces. As a direct effect of this phenomenon, the shear stress magnitudes are substantially increased with a maximum phase difference of $\pi/4$ between the wall shear stress and axial pressure gradient. Correspondingly, there appears a distinct phase difference between the flowrate, axial pressure gradient and the wall shear stress profiles, reaching a maximum of $\pi/2$. Amongst the waveforms, leading, lagging asymmetric and positive, negative half rectified formats demonstrate flow reversal in the near and off-wall vicinity which is further amplified at the highest frequency $Wo = 18.3$. The evidence of flow reversal leads to a further strengthening of near-wall viscous forces as the flow field tends to readjust and reorient itself under the influence of imposed oscillations. Amongst all waveforms studied, the rectified formats show peak values of axial pressure gradient and shear stress magnitudes. This is attributed to the co-existence of an interval of semi-sinusoidal and steady part within one pulsation cycle. The friction factor ratio is substantially increased for the cases of high frequency and high flowrate amplitude and the magnitudes of ratio are highest for the half rectified profiles.

Heat transfer characteristics of a flow induced with oscillations is typically governed by the time scales of axial convection and transverse diffusion. The estimation of heat transfer in enhancement or reduction terms is dependent on the coupled influence of imposed flow frequency and flow rate amplitude. An understanding is established between the imposed flowrate profile and the corresponding temperature profile. Due to existence of a heated boundary, the wall temperature varies in both spatially and temporally. In the case of low frequency flows, the spanwise oscillating wall temperature profile resembling the parabolic velocity profiles, while the bulk temperature shows greater differences in the magnitudes sine the pulsating time periods are longer. As a result of longer displacement timescales, higher temperature gradients are present. The instantaneous bulk and wall temperatures exhibit in phase characteristics. With an increase in frequency, annular effects are distinctly evident in the wall temperature profiles, resembling to the well-established phenomenon of spanwise oscillating velocity profiles and exits across all of the waveforms. The

maximum wall temperature magnitudes are shifted to the near wall regions where the near side-wall viscous effects are significant. Whereas the core bulk regions demonstrate flatter temperature profiles due to the influence of stronger inertial forces. As a result of shorter displacement time scales, there exists an incremental phase difference with a maximum 17˚ between the bulk and wall temperature profiles with a drop in magnitudes. The magnitudes of wall and bulk temperatures are reduced further for the highest frequency case since the thickness of thermal boundary layer deceases. Low flow rate amplitudes present increased diffusion of heat from the heated wall to the bulk core flow. While with a subsequent increase in the flow rate amplitudes, both the bulk and wall temperatures are reduced. This is due to the strengthening of mass flow rate which represents increased forced convection effects as the flow progresses in the streamwise direction. Thus, it leads to an enhancement in the heat transfer compared to $A_0 = 0.5$. At the highest flow rate amplitude, prominent effects in the space averaged instantaneous Nusselt number is seen over the lower amplitude ratios for all waveform profiles. With varying Wo, the space averaged instantaneous Nusselt number (heat transfer rate) increased with an increase in Wo up to a certain optimal frequency. It is inferred that the heat transfer rate either increases or decreases from the corresponding steady value for certain range of phase intervals subjected to the frequency of pulsation. The optimum pulsation frequency band lies between $0.5 \leq f \leq 2\ Hz$ which demonstrates enhancements in the heat transfer, whereas a deterioration is observed compared to the steady flow value for the cases outside the range. Symmetric sinusoidal flows present 6.7% heat transfer enhancement over the steady flow at $Wo = 2.5, A_0 = 3$ with a peak thermal performance factor. The leading and lagging cases of asymmetric sinusoidal present an enhancement of 4.2% and 11.1% respectively for $Wo = 2.5$ at $A_0 = 3$, with moderate enhancements at $Wo = 5.1$. Lagging asymmetry pulsations show improved heat transfer performance compared to the leading asymmetric waveforms. The half rectified waveforms present differing effects on the heat transfer between the two waveform cases over a similar parameter space. For the positive half rectified waveform, marginal enhancement in heat transfer of 2.2% for $Wo = 2.5, A_0 = 3$ was obtained, which leads to a marginal reduction in thermal performance due to the presence of high shear stresses. Whereas the negative half rectified case leads to a heat transfer enhancement of 9% and 6% for $Wo = 2.5$ and $Wo = 5.1$ respectively, with a substantially high thermal performance.

9) Future Work & Scope

The current research has concluded by exploring the potential of heat transfer enhancement with variations of associated pulsation characteristics for a case involving hydrodynamically and thermally fully developed laminar flow through a rectangular duct. A comprehensive understanding of the flow field is established, and particular emphasis is directed towards the flow reversal phenomenon and its effect on the heat transfer rate. The future works should be focussed primarily on extending this understanding to complex cases such as (elaborated further in Section 9.1) involving channel profile modifications which promote fluid mixing, determined the promotion of heat transfer rate by using nano-fluid concentrations and exploring the prospects of a two-phase pulsating flow through a channel.

9.1 Experimental studies

9.1.1 Channel profile modifications

Recent literatures have shown appreciable enhancement of heat transfer associated with flow rate pulsations through ducts with geometric modifications, sample illustrations shown in Figure 9-1 and Figure 9-2. Although the majority of studies are numerical analysis, there is a lack of local-time dependent analysis of the effects on flow field and the associated heat transfer potential. Presence of wavy wall geometry of channel profile has shown the influence of chaotic advection on the pulsation flow field, in a numerical study by [90]. At an optimum aspect ratio of the duct and wall waviness a significant effect on heat transfer enhancement is determined while maintaining reasonable pressure drop. Channel configuration involving backward facing, (Figure 9-3) or forward-facing step has been viewed to lead to flow separation which further promotes heat transfer as a result of recirculation zones and increased convection. In an another computational study by [98] the effect of duct wall surface roughness on the heat transfer was investigated for a with square waveform pulsating flow. Geometric parameters of the surface structures were varied

and a peak heat transfer enhancement of about 33% was determined compared to conventional steady flows, as a result of increased to fluid mixing led by vortices.

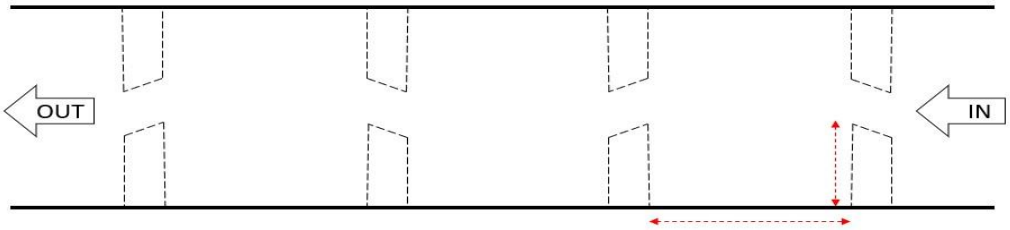

Figure 9-1: Sample channel geometry sketch showing baffles.

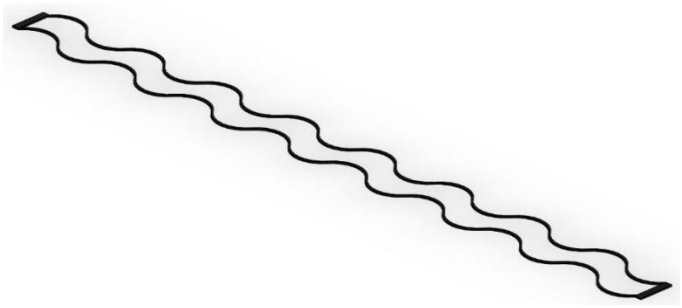

Figure 9-2: Sample channel geometry sketch showing wavy wall profiles.

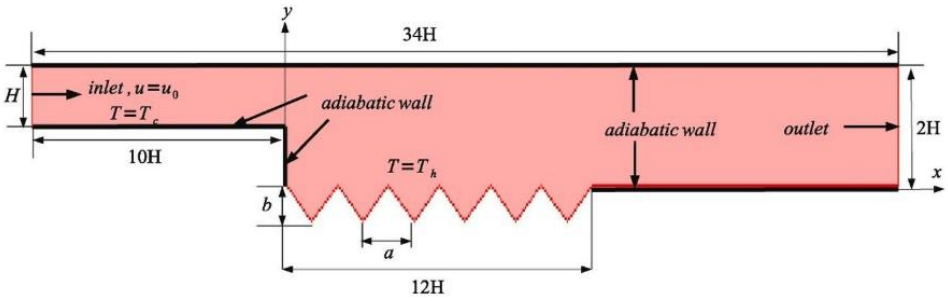

Figure 9-3: Computational domain of backward-facing step with corrugated bottom wall, by [147].

9.1.2 Influence of nano-fluids

Nanofluids are new generation fluids resulting from the dispersion of nanoparticles in the conventional fluids. Nanoparticles feature high thermal conductivity and thereby increase the fluid's thermal conductivity. Several studies explored the physical properties of nanofluids and achieved an improvement of thermal properties compared to base conventional fluids. Applications of nanofluids combined with pulsating flows to investigate the heat transfer enhancements is an area of large interest [148], as shown by a sample illustration in Figure 9-4. Numerical investigations using nanofluid pulsating flow through a duct showed a direct relationship between the increase in heat transfer enhancement and the increase of particle volume fraction and oscillation flow rate

amplitude. In another experimental study involving a turbulent pulsating flow within a spiral coil tube, an overall heat transfer enhancement of 23% was determined. Nanofluid mixture of Al_2O_3 and water at volume fractions of 0.5, 1 and 1.5% was studied [149]. A numerical study involving triangular wavy channel using $CuO - H_2O$ nanofluid pulsating flows demonstrated a significant improvement of thermal performance, with an increase in the flowrate amplitude and nano-particle concentrations, albeit with a slight increase in the pressure drop [148].

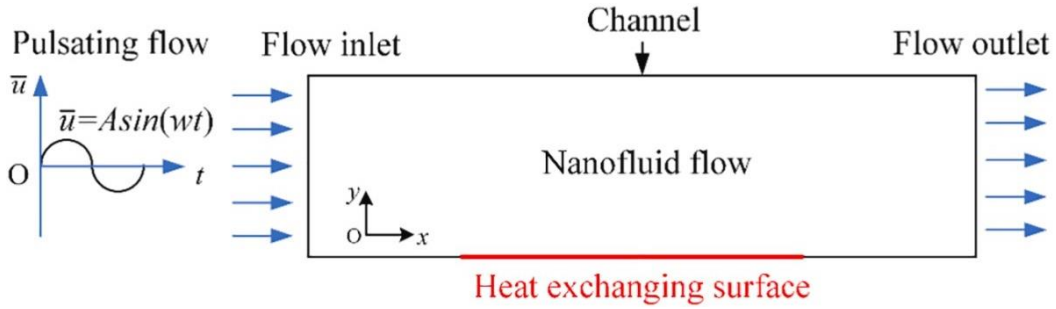

Figure 9-4: A sample illustration of pulsating channel domain under the influence of a nanofluid [150].

9.1.3 Two-phase pulsating flows

Regarding two-phase flows illustrated in Figure 9-5, one of the prominent areas of study governing the heat and mass transfer enhancement methodology is boiling under pulsating flow. As a result of phase change latent heat, boiling offers high heat transfer coefficients with low temperature differences. Experimental studies investigated the heat transfer coefficient under unsteady boiling pulsating flow which led to an enhancement of 26% compared to the steady flow for higher Reynolds number flows using a square waveform. In another study involving subcooled boiling under high frequency oscillating flow, a maximum critical heat flux increases up to 42.3% was obtained. However, for a pulsating flow, the CHF decreased overall irrespective of increase in the pulsation amplitude and frequency.

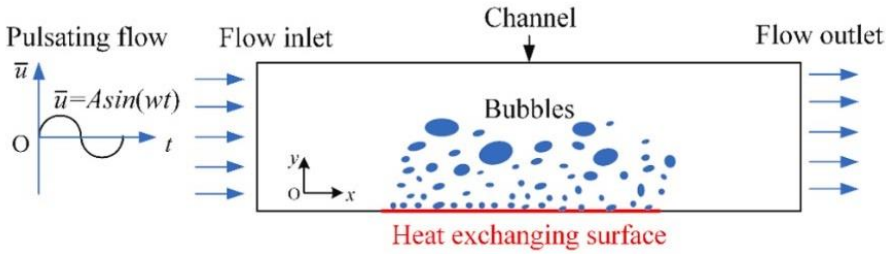

Figure 9-5: Illustration of 2-phase pulsating flow in a duct [150].

References

[1] X. H. Yang and J. Liu, “Liquid metal enabled combinatorial heat transfer science: toward unconventional extreme cooling,” *Front. Energy*, vol. 12, no. 2, pp. 259–275, 2018, doi: 10.1007/s11708-017-0521-3.

[2] M. Waldrop, “The chips are down for Moore’s law,” *Nat. News*, vol. 530, p. 144, 2016, doi: 10.1038/530144a.

[3] B. Agostini, M. Fabbri, J. E. Park, L. Wojtan, J. R. Thome, and B. Michel, “State of the art of high heat flux cooling technologies,” *Heat Transf. Eng.*, vol. 28, no. 4, pp. 258–281, 2007, doi: 10.1080/01457630601117799.

[4] J. B. Marcinichen, J. A. Olivier, and J. R. Thome, “On-chip two-phase cooling of datacenters: Cooling system and energy recovery evaluation,” *Appl. Therm. Eng.*, vol. 41, pp. 36–51, 2012, doi: 10.1016/j.applthermaleng.2011.12.008.

[5] C. Huber and R. Kuhn, “Thermal management of batteries for electric vehicles,” *Adv. Batter. Technol. Electr. Veh.*, pp. 327–358, 2015, doi: 10.1016/B978-1-78242-377-5.00013-3.

[6] Y. Zhang and N. Ansari, “Green data centers,” *Handb. Green Inf. Commun. Syst.*, vol. 331, 2012.

[7] M. Iyengar *et al.*, “Server liquid cooling with chiller-less data center design to enable significant energy savings,” in *2012 28th Annual IEEE Semiconductor Thermal Measurement and Management Symposium (SEMI-THERM)*, Mar. 2012, vol. 1, pp. 212–223, doi: 10.1109/STHERM.2012.6188851.

[8] H. Oprins, V. der V G., C. C. S. Nicole, C. J. M. Lasance, and M. Baelmans, “On-chip liquid cooling with integrated pump technology,” *IEEE Trans. Components Packag. Technol.*, vol. 30, no. 2, pp. 209–217, 2007, doi: 10.1109/TCAPT.2007.898301.

[9] G. Tang, Y. Han, B. L. Lau, X. Zhang, and D. M. Rhee, “An efficient single phase liquid cooling

system for microelectronic devices with high power chip," *Proc. Electron. Packag. Technol. Conf. EPTC*, vol. 2016-Febru, no. c, 2016, doi: 10.1109/EPTC.2015.7412300.

[10] S. V Garimella and V. Singhal, "Single-Phase flow and heat transport and pumping considerations in microchannel heat sinks," *Heat Transf. Eng.*, vol. 25, no. 1, pp. 15–25, 2004, doi: 10.1080/01457630490248241.

[11] V. Singhal, S. V Garimella, and A. Raman, "Microscale pumping technologies for microchannel cooling systems," *Appl. Mech. Rev.*, vol. 57, no. 1–6, pp. 191–221, 2004, doi: 10.1115/1.1695401.

[12] D. J. Laser and J. G. Santiago, "A review of micropumps," *J. Micromechanics Microengineering*, vol. 14, no. 6, 2004, doi: 10.1088/0960-1317/14/6/R01.

[13] R. Zengerle, J. Ulrich, S. Kluge, M. Richter, and A. Richter, "A bidirectional silicon micropump," *"Sensors and Actuators, A: Physical,"* vol. 50, no. 1–2. pp. 81–86, 1995, doi: 10.1016/0924-4247(96)80088-4.

[14] P. Woias, "Micropumps—past, progress and future prospects," *Sensors and Actuators*, vol. 105, pp. 28–38, 2004, doi: 10.1016/j.snb.2004.02.033.

[15] N. Zhuang, S. Tan, and H. Yuan, "The friction characteristics of low-frequency transitional pulsatile flows in narrow channel," *Exp. Therm. Fluid Sci.*, vol. 76, pp. 352–364, 2016, doi: 10.1016/j.expthermflusci.2016.03.030.

[16] Y. A. Cengel and J. M. Cimbala, *Fluid Mechanics - Fundamental and applications*, vol. 4, no. 1. 2006.

[17] J. G. Knudse and D. L. Katz, *Fluid Dynamics and Heat Transfer*. McGraw-Hill, 1958.

[18] F. Durst, S. Ray, B. Ünsal, and O. A. Bayoumi, "The Development Lengths of Laminar Pipe and Channel Flows," *J. Fluids Eng.*, vol. 127, no. 6, p. 1154, 2005, doi: 10.1115/1.2063088.

[19] R. K. Shah and A. L. London, *Laminar Flow Forced Convection in Ducts: A Source Book for Compact Heat Exchanger Analytical Data*, vol. Suppl. 1. Academic Press, 1978.

[20] R. K. Shah, "Laminar Flow Forced Convection Heat Transfer and Flow Friction in Straight and Curved Ducts - a summary of analytical solutions," Stanford University, Stanford, California, 1972.

[21] N. Zhuang, S. Tan, H. Yuan, and C. Zhang, "Flow resistance characteristics of pulsating laminar flow in rectangular channels," *Ann. Nucl. Energy*, vol. 73, pp. 398–407, 2014, doi: 10.1016/j.anucene.2014.06.057.

[22] F. P. Incropera, D. P. Dewitt, T. L. Bergman, and A. S. Lavine, *Fundamentals of Heat and Mass Transfer*. 2007.

[23] R. Siegel, “Heat transfer for laminar flow in ducts with arbitrary time variations in wall temperature,” *J. Appl. Mech. Trans. ASME*, vol. 27, no. 2, pp. 241–249, 1960, doi: 10.1115/1.3643945.

[24] E. M. Sparrow and F. N. De Farias, “Unsteady heat transfer in ducts with time-varying inlet temperature and participating walls,” *Int. J. Heat Mass Transf.*, vol. 11, no. 5, pp. 837–853, 1968, doi: 10.1016/0017-9310(68)90128-2.

[25] R. K. Shah and A. L. London, “Thermal Boundary Conditions and Some Solutions for Laminar Duct Flow Forced Convection,” *J. Heat Transfer*, vol. 96, no. 2, pp. 159–165, 1974.

[26] G. L. Morini, “Thermal characteristics of slug flow in rectangular ducts,” *Int. J. Therm. Sci.*, vol. 38, no. 2, pp. 148–159, 1999, doi: 10.1016/S1290-0729(99)80052-0.

[27] S. X. Gao and J. P. Hartnett, “Analytical Nusselt number predictions for slug flow in rectangular duct,” *Int. Commun. Heat Mass Transf.*, vol. 20, no. 5, 1993.

[28] M. Spiga and G. L. Morini, “Nusselt numbers in laminar flow for H2 boundary conditions,” *Int. J. Heat Mass Transf.*, vol. 39, no. 6, pp. 1165–1174, 1996, doi: 10.1016/0017-9310(95)00205-7.

[29] R. Siegel ; J. M. Savino, “An Analytical solution of the Effect of Peripheral Wall Conduction on Laminar Forced Convection in Rectangular Channels,” *J. Heat Transfer*, pp. 59–66, 1965.

[30] J. M. Savino and R. Siegel, “Laminar Forced Convection in rectangular channels with unequal heat addition on adjacent sides,” *Int. J. Heat Mass Transf.*, vol. 7, pp. 733–741, 1964.

[31] S. R, Siegel ; J, M, “An Analytical Solution of the Effect of Peripheral Wall Condution on Laminar Forced Convection in Rectangular Channels,” *J. Heat Transfer*, pp. 59–66, 1965.

[32] E. M. Sparrow and R. Siegel, “Application of variational methods to the thermal entrance region of ducts,” *Int. J. Heat Mass Transf.*, vol. 1, no. 2, pp. 161–172, 1960, doi: https://doi.org/10.1016/0017-9310(60)90020-X.

[33] S. Uchida, “The pulsating viscous flow superposed on the steady laminar motion of incompressible fluid in a circular pipe,” *Zeitschrift für Angew. Math. und Phys. ZAMP*, vol. 7, no. 5, pp. 403–422, 1956, doi: 10.1143/JPSJ.19.117.

[34] H. Ito, “Theory of laminar flow through a pipe with non-steady pressrue gradients,” *Proc. Inst. High Speed Mech.*, p. 163, 1953.

[35] C. Fan and B. T. Chao, “Unsteady, laminar, incompressible flow through rectangular ducts,” *Zeitschrift für Angew. Math. und Phys. ZAMP*, vol. 16, no. 3, pp. 351–360, 1965, doi: 10.1007/BF01591915.

[36] G. G. Stokes, “On the effect of the Internal Friction of Fluids on the Motion of Pendulums,” *Trans. Cambridge Philos. Soc.*, vol. 9, pp. 75–129, 1851, doi: 10.1017/cbo9780511702242.005.

[37] M. Quadrio and P. Ricco, “The laminar generalized Stokes layer and turbulent drag reduction,” *J. Fluid Mech.*, vol. 667, pp. 135–157, 2011, doi: 10.1017/S0022112010004398.

[38] E. G. Richardson, “The amplitude of sound waves in resonators,” *Proc. Phys. Soc.*, vol. 40, no. 1, pp. 206–220, 1927, doi: 10.1088/0959-5309/40/1/328.

[39] E. G. Richardson and E. Tyler, “The transverse velocity gradient near the mouths of pipes in which an alternating or continuous flow of air is established,” *Proc. Phys. Soc.*, vol. 42, no. 1, pp. 1–15, 1929, doi: 10.1088/0959-5309/42/1/302.

[40] D. B. Holmes and J. R. Vermeulen, “Velocity profiles in ducts with rectangular cross sections,” *Chem. Eng. Sci.*, vol. 23, no. 7, pp. 717–722, 1968, doi: 10.1016/0009-2509(68)85006-7.

[41] J. Harris, G. Peev, and W. L. Wilkinson, “Velocity profiles in laminar oscillatory flow in tubes,” *J. Phys. E.*, vol. 2, no. 11, pp. 913–916, 1969, doi: 10.1088/0022-3735/2/11/301.

[42] J. R. Womersley, “Method for the calculation of velocity, rate of flow and viscous drag in arteries when the pressure gradient is known,” *J. Physiol.*, vol. 127, no. 3, pp. 553–563, 1955, doi: 10.1113/jphysiol.1955.sp005276.

[43] T. Sexl, “Über den von E. G. Richardson entdeckten ‘Annulareffekt,’” *Zeitschrift für Phys.*, vol. 61, no. 5–6, pp. 349–362, 1930, doi: 10.1007/BF01340631.

[44] R. G. Lingford and N. W. Ryan, “Pulsatile flow in rigid tubes,” *J. Applie Physiol.*, vol. 20, no. 5, pp. 1078–1082, 1965, doi: 10.1152/jappl.1965.20.5.1078.

[45] E. B. Denison and W. H. Stevenson, “Oscillatory flow measurements with a directionally sensitive laser velocimeter,” *Rev. Sci. Instrum.*, vol. 41, no. 10, pp. 1475–1478, 1970, doi: 10.1063/1.1684313.

[46] T. Muto and K. Nakane, “Unsteady flow in circular tube: Velocity distribution of pulsating flow,” *Bull. JSME*, vol. 23, no. 186, pp. 1990–1996, 1980, [Online]. Available: http://www.mendeley.com/research/geology-volcanic-history-eruptive-style-yakedake-volcano-group-central-japan/.

[47] M. Clamen and P. Minton, “An experimental investigation of flow in an oscillating pipe,” *J. Fluid Mech.*, vol. 81, no. 3, pp. 421–431, 1977, doi: 10.1017/S0022112077002146.

[48] M. Ojha, R. L. Hummel, S. C. Cobbold, and K. W. Johnston, “Development and evaluation of a high resolution photochromic dye method for pulsatile flow studies,” *J. Phys. E.*, vol. 21, no. 10, pp. 998–1004, 1988, doi: 10.1088/0022-3735/21/10/018.

[49] B. Ünsal, S. Ray, F. Durst, and Ö. Ertunç, “Pulsating laminar pipe flows with sinusoidal mass flux variations,” *Fluid Dyn. Res.*, vol. 37, no. 5, pp. 317–333, 2005, doi: 10.1016/j.fluiddyn.2005.06.002.

[50] F. Durst, U. Heim, B. Ünsal, and G. Kullik, “Mass flow rate control system for time-dependent laminar and turbulent flow investigations,” *Meas. Sci. Technol.*, vol. 14, no. 7, pp. 893–902, 2003, doi: 10.1088/0957-0233/14/7/301.

[51] K. Haddad, Ö. Ertunç, M. Mishra, and A. Delgado, “Pulsating laminar fully developed channel and pipe flows,” *Phys. Rev. E - Stat. Nonlinear, Soft Matter Phys.*, vol. 81, no. 1, pp. 1–13, 2010, doi: 10.1103/PhysRevE.81.016303.

[52] C. Aygun and O. Aydin, “Hydrodynamics of piston-driven laminar pulsating flow: Part 1. Developing Flow,” *Nucl. Eng. Des.*, vol. 274, pp. 164–171, 2014, doi: 10.1016/j.nucengdes.2014.02.018.

[53] C. Aygun and O. Aydin, “Hydrodynamics of piston-driven laminar pulsating flow: Part 2. Fully developed flow,” *Nucl. Eng. Des.*, vol. 274, pp. 172–180, 2014, doi: 10.1016/j.nucengdes.2014.02.018.

[54] P. Qi, X. Li, F. Qiu, S. Qiao, S. Tan, and X. Wang, “Application of particle image velocimetry measurement technique to study pulsating flow in a rod bundle channel,” *Exp. Therm. Fluid Sci.*, vol. 113, no. January, p. 110047, 2020, doi: 10.1016/j.expthermflusci.2020.110047.

[55] P. E. Hughes and T. V. How, “Pulsatile Velocity Distribution and Wall Shear Rate Measurement Using Pulsed Doppler Ultrasound,” *J. Biomech.*, vol. 27, no. I, pp. 103–110, 1994.

[56] T. S. Zhao and P. Cheng, “The friction coefficient of a fully developed laminar reciprocating flow in a circular pipe,” *Int. J. Heat Fluid Flow*, vol. 17, no. 2, pp. 167–172, 1996, doi: 10.1016/0142-727X(96)00001-X.

[57] M. Omhi, M. Iguchi, and T. Usui, “Flow Pattern and Frictional Losses in Pulsating Pipe Flow: Part 5 Wall Shear and Flow Pattern in a Laminar Flow,” *Bull. JSME*, vol. 24, no. 187, pp. 75–

81, 1981, doi: https://doi.org/10.1299/jsme1958.24.75.

[58] Z. Mao and T. J. Hanratty, “Measurement of wall shear rate in large amplitude unsteady reversing flows,” *Exp. Fluids*, vol. 12, no. 4–5, pp. 342–350, 1992, doi: 10.1007/BF00187312.

[59] R. Blythman, T. Persoons, N. Jeffers, and D. B. Murray, “Effect of oscillation frequency on wall shear stress and pressure drop in a rectangular channel for heat transfer applications,” *J. Phys. Conf. Ser.*, vol. 745, no. 3, 2016, doi: 10.1088/1742-6596/745/3/032044.

[60] R. Blythman, T. Persoons, N. Jeffers, K. P. Nolan, and D. B. Murray, “Localised dynamics of laminar pulsatile flow in a rectangular channel,” *Int. J. Heat Fluid Flow*, vol. 66, pp. 8–17, 2017, doi: 10.1016/j.ijheatfluidflow.2017.05.006.

[61] M. Faghri, K. Javdani, and A. Faghri, “Heat transfer with laminar pulsating flow in a pipe,” *Lett. Heat Mass Transf.*, vol. 6, no. 4, pp. 259–270, 1979, doi: 10.1016/0094-4548(79)90013-4.

[62] G. Taylor, “Dispersion of soluble matter in solvent flowing slowly through a tube,” *Proc. R. Soc. London. Ser. A. Math. Phys. Sci.*, vol. 219, no. 1137, pp. 186–203, 1953, doi: 10.1098/rspa.1953.0139.

[63] P. C. Chatwin, “The approach to normality of the concentration distribution of a solute in a solvent flowing along a straight pipe,” *J. Fluid Mech.*, vol. 43, no. 2, pp. 321–352, 1970, doi: 10.1017/S0022112070002409.

[64] P. C. Chatwin, “On the longitudinal dispersion of passive contaminant in oscillatory flows in tubes,” *J. Fluid Mech.*, vol. 71, 1975.

[65] E. J. Watson, “Diffusion in oscillatory pipe flow,” *J. Fluid Mech.*, vol. 133, pp. 233–244, 1983, doi: 10.1017/S0022112083001883.

[66] R. Smith, “Contaminant dispersion in oscillatory flows,” *J. Fluid Mech.*, vol. 114, pp. 379–398, 1982, doi: 10.1017/S0022112082000214.

[67] C. H. Joshi, R. D. Kamm, J. M. Drazen, and A. S. Slutsky, “An experimental study of gas exchange in laminar oscillatory flow,” *J. Fluid Mech.*, vol. 133, no. HY8, pp. 245–254, 1983, doi: 10.1017/S0022112083001895.

[68] U. H. Kurzweg, “Enhanced heat conduction in oscillating viscous flows within parallel-plate channels,” *J. Fluid Mech.*, vol. 156, no. 1, p. 291, Jul. 1985, doi: 10.1017/S0022112085002105.

[69] J. . Zhang and U. H. Kurzweg, “Numerical Simulation of Time-dependent heat transfer in

oscillating pipe flow," *J. Thermophys. Heat Transf.*, vol. 5, no. 3, pp. 401–406, 1991.

[70] M. Ozawa and A. Kawamoto, "Lumped-parameter modeling of heat transfer enhanced by sinusoidal motion of fluid," *Int. J. Heat Mass Transf.*, vol. 34, no. 12, pp. 3083–3095, 1991, doi: 10.1016/0017-9310(91)90078-S.

[71] D.-Y. Lee, S.-J. Park, and S. Tack Ro, "Heat transfer in the thermally developing region of a laminar oscillating pipe flow," *Cryogenics (Guildf).*, 1998, doi: 10.1016/S0011-2275(98)00020-4.

[72] R. Siegal, "Influence of Oscillation-Induced Diffusion on Heat Transfer in a Uniformly Heated Channel," *J. Heat Transfer*, vol. 109, no. February, pp. 244–247, 1987.

[73] Y. K. Seo, H. K. Byung, and Jae M. H., "Heat transfer in the thermally developing region of a pulsating channel flow," *Int. J. Heat Mass Transf.*, vol. 36, no. 17, pp. 4257–4266, 1993, doi: 10.1016/0017-9310(93)90088-N.

[74] R. Siegel and M. Perlmutter, "Heat transfer for pulsating laminar duct flow," *J. Heat Transfer*, vol. 84, no. 2, pp. 111–122, 1962, doi: 10.1115/1.3684307.

[75] H. W. Cho and J. M. Hyun, "Numerical solutions of pulsating flow and heat transfer characteristics in a pipe," *Int. J. Heat Fluid Flow*, vol. 11, no. 4, pp. 321–330, 1990, doi: 10.1016/0142-727X(90)90056-H.

[76] H. W. Cho and J. M. Hyun, "Motion and heat transfer in the Blasius flow containing a pulsating component," *Int. J. Heat Fluid Flow*, vol. 10, no. 4, pp. 349–357, 1989, doi: 10.1016/0142-727X(89)90025-8.

[77] D. A. Nield and A. V. Kuznetsov, "Forced convection with laminar pulsating flow in a channel or tube," *Int. J. Therm. Sci.*, vol. 46, no. 6, pp. 551–560, 2007, doi: 10.1016/j.ijthermalsci.2006.07.011.

[78] D. Gedeon, "Mean-parameter modeling of oscillating flow," *J. Heat Transfer*, vol. 108, no. 3, pp. 513–518, 1986, doi: 10.1115/1.3246964.

[79] Q. D. Liao, K. T. Yang, and V. W. Nee, "An analysis of conjugate heat transfer from a heated wall in a channel with zero-mean oscillatory flow for small oscillatory flow Reynolds numbers," *Int. J. Heat Mass Transf.*, vol. 37, no. SUPPL. 1, pp. 415–423, 1994, doi: 10.1016/0017-9310(94)90041-8.

[80] A. Mosyak, E. Pogrebnyak, and G. Hetsroni, "Effect of constant heat flux boundary condition on wall temperature fluctuations," *J. Heat Transfer*, vol. 123, no. 2, pp. 213–218, 2001, doi:

10.1115/1.1345886.

[81] O. I. Craciunescu and S. T. Clegg, “Pulsatile Blood Flow Effects on Temperature Distribution and Heat Transfer in Rigid Vessels,” *J. Biomech. Eng.*, vol. 123, no. 5, p. 500, 2001, doi: 10.1115/1.1392318.

[82] T. Persoons, T. Saenen, T. Van Oevelen, and M. Baelmans, “Effect of Flow Pulsation on the Heat Transfer Performance of a Minichannel Heat Sink,” *J. Heat Transfer*, 2012, doi: 10.1115/1.4006485.

[83] T. Persoons, T. Saenen, T. Van Oevelen, and M. Baelmans, “Effect of Flow Pulsation on the Heat Transfer Performance of a Minichannel Heat Sink,” *J. Heat Transfer*, vol. 134, no. 9, p. 91702, 2012, doi: 10.1115/1.4006485.

[84] C. Sert and A. Beskok, “Numerical simulation of reciprocating flow forced convection in two-dimensional channels,” *J. Heat Transfer*, vol. 125, no. 3, pp. 403–412, 2003, doi: 10.1115/1.1565092.

[85] T. Moschandreou and M. Zamir, “Heat transfer in a tube with pulsating flow and constant heat flux,” *Int. J. Heat Mass Transf.*, vol. 40, no. 10, pp. 2461–2466, 1997, doi: 10.1016/S0017-9310(96)00266-9.

[86] T. Zhao and P. Cheng, “A numerical solution of laminar forced convection in a heated pipe subjected to a reciprocating flow,” *Int. J. Heat Mass Transf.*, vol. 38, no. 16, pp. 3011–3022, 1995, doi: 10.1016/0017-9310(95)00017-4.

[87] T. S. Zhao and P. Cheng, “Oscillatory heat transfer in a pipe subjected to a laminar reciprocating flow,” *J. Heat Transfer*, vol. 118, no. 3, pp. 592–597, 1996, doi: 10.1115/1.2822673.

[88] Z. Yu, X. Mao, and A. J. Jaworski, “Experimental study of heat transfer in oscillatory gas flow inside a parallel-plate channel with imposed axial temperature gradient,” *Int. J. Heat Mass Transf.*, vol. 77, pp. 1023–1032, 2014, doi: 10.1016/j.ijheatmasstransfer.2014.06.031.

[89] R. Blythman, T. Persoons, N. Jeffers, and D. B. Murray, “Heat transfer of laminar pulsating flow in a rectangular channel,” *Int. J. Heat Mass Transf.*, vol. 128, pp. 279–289, 2019, doi: 10.1016/j.ijheatmasstransfer.2018.08.109.

[90] H. Ghaedamini, P. S. Lee, and C. J. Teo, “Forced pulsatile flow to provoke chaotic advection in wavy walled microchannel heat sinks,” *Thermomechanical Phenom. Electron. Syst. - Proceedings Intersoc. Conf.*, pp. 680–687, 2014, doi: 10.1109/ITHERM.2014.6892347.

[91] B. Yang, T. Gao, J. Gong, and J. Li, “Numerical investigation on flow and heat transfer of pulsating flow in various ribbed channels,” *Appl. Therm. Eng.*, vol. 145, no. September, pp. 576–589, 2018, doi: 10.1016/j.applthermaleng.2018.09.041.

[92] F. Zhang, Y. Bian, Y. Liu, J. Pan, Y. Yang, and H. Arima, “Experimental and numerical analysis of heat transfer enhancement and flow characteristics in grooved channel for pulsatile flow,” *Int. J. Heat Mass Transf.*, vol. 141, pp. 1168–1180, Oct. 2019, doi: 10.1016/j.ijheatmasstransfer.2019.06.100.

[93] H. Khosravi-Bizhaem, A. Abbassi, and A. Zivari Ravan, “Heat transfer enhancement and pressure drop by pulsating flow through helically coiled tube: An experimental study,” *Appl. Therm. Eng.*, vol. 160, no. April, p. 114012, 2019, doi: 10.1016/j.applthermaleng.2019.114012.

[94] N. Kurtulmuş and B. Sahin, “Experimental investigation of pulsating flow structures and heat transfer characteristics in sinusoidal channels,” *Int. J. Mech. Sci.*, vol. 167, no. October 2019, 2020, doi: 10.1016/j.ijmecsci.2019.105268.

[95] V. Q. Hoang, T. T. Hoang, C. T. Dinh, and F. Plourde, “Large eddy simulation of the turbulence heat and mass transfer of pulsating flow in a V-sharp corrugated channel,” *Int. J. Heat Mass Transf.*, vol. 166, p. 120720, 2021, doi: 10.1016/j.ijheatmasstransfer.2020.120720.

[96] S. Akcay, “Numerical analysis of heat transfer improvement for pulsating flow in a periodic corrugated channel with discrete V-type winglets,” *Int. Commun. Heat Mass Transf.*, vol. 134, p. 105991, 2022, doi: 10.1016/j.icheatmasstransfer.2022.105991.

[97] G. Li, Y. Zheng, G. Hu, and Z. Zhang, “Experimental investigation on heat transfer enhancement from an inclined heated cylinder with constant heat input power in infrasonic pulsating flows,” *Exp. Therm. Fluid Sci.*, vol. 49, pp. 75–85, 2013, doi: 10.1016/j.expthermflusci.2013.04.003.

[98] S. Singh, S. K. Singh, H. S. Mali, and R. Dayal, “Numerical investigation of heat transfer in structured rough microchannels subjected to pulsed flow,” *Appl. Therm. Eng.*, vol. 197, no. July, p. 117361, 2021, doi: 10.1016/j.applthermaleng.2021.117361.

[99] C. Xu, S. Xu, S. Wei, and P. Chen, “Experimental investigation of heat transfer for pulsating flow of GOPs-water nanofluid in a microchannel,” *Int. Commun. Heat Mass Transf.*, vol. 110, no. November 2019, 2020, doi: 10.1016/j.icheatmasstransfer.2019.104403.

[100] Z. Zhan *et al.*, “Numerical study on heat transfer enhancement by viscoelastic fluid pulsating laminar flow in rectangular microchannel heat sinks,” *Appl. Therm. Eng.*, vol. 213, no.

December 2021, p. 118734, 2022, doi: 10.1016/j.applthermaleng.2022.118734.

[101] D. Yin and H. B. Ma, “Analytical solution of heat transfer of oscillating flow at a triangular pressure waveform,” *Int. J. Heat Mass Transf.*, vol. 70, pp. 46–53, 2014, doi: 10.1016/j.ijheatmasstransfer.2013.10.016.

[102] R. Roslan, M. Abdulhameed, I. Hashim, and A. J. Chamkha, “Non-sinusoidal waveform effects on heat transfer performance in pulsating pipe flow,” *Alexandria Eng. J.*, vol. 55, no. 4, pp. 3309–3319, 2016, doi: 10.1016/j.aej.2016.08.012.

[103] B. Mehta and S. Khandekar, “Local experimental heat transfer of single-phase pulsating laminar flow in a square mini-channel,” *Int. J. Therm. Sci.*, 2015, doi: 10.1016/j.ijthermalsci.2015.01.008.

[104] H. Zhang, S. Li, J. Cheng, Z. Zheng, X. Li, and F. Li, “Numerical study on the pulsating effect on heat transfer performance of pseudo-plastic fluid flow in a manifold microchannel heat sink,” *Appl. Therm. Eng.*, vol. 129, pp. 1092–1105, 2018, doi: 10.1016/j.applthermaleng.2017.10.124.

[105] J. McEvoy, S. Alimohammadi, and T. Persoons, “Experimental investigation of flow pulsation waveforms in rectangular mesochannels for high heat flux electronics cooling,” *Exp. Therm. Fluid Sci.*, vol. 109, no. August, p. 109885, 2019, doi: 10.1016/j.expthermflusci.2019.109885.

[106] C. Xu, S. Xu, Z. Wang, and D. Fenga, “Experimental investigation of flow and heat transfer characteristics of pulsating flows driven by wave signals in a microchannel heat sink,” *Int. Commun. Heat Mass Transf.*, vol. 125, p. 105343, 2021, doi: 10.1016/j.icheatmasstransfer.2021.105343.

[107] R. Siegel, “Heat transfer for laminar flow in ducts with arbitrary time variations in wall temperature,” *J. Appl. Mech. Trans. ASME*, vol. 27, no. 2, pp. 241–249, 1960, doi: 10.1115/1.3643945.

[108] R. D. Patel, J. J. McFeeley, and K. R. Jolls, “Wall mass transfer in laminar pulsatile flow in a tube,” *AIChE J.*, vol. 21, no. 2, pp. 259–267, 1975, doi: 10.1002/aic.690210206.

[109] O. I. Craciunescu and S. T. Clegg, “Pulsatile blood flow effects on temperature distribution and heat transfer in rigid vessels,” *J. Biomech. Eng.*, vol. 123, no. 5, pp. 500–505, 2001, doi: 10.1115/1.1392318.

[110] G. J. Brereton and Y. Jiang, “Convective heat transfer in unsteady laminar parallel flows,” *Phys. Fluids*, vol. 18, no. 10, 2006, doi: 10.1063/1.2359742.

[111] R. Wälchli, T. Brunschwiler, B. Michel, and D. Poulikakos, “Self-contained, oscillating flow liquid cooling system for thin form factor high performance electronics,” *J. Heat Transfer*, vol. 132, no. 5, pp. 1–9, 2010, doi: 10.1115/1.4000456.

[112] S. Ray, B. Ünsal, and F. Durst, “Development length of sinusoidally pulsating laminar pipe flows in moderate and high Reynolds number regimes,” *Int. J. Heat Fluid Flow*, 2012, doi: 10.1016/j.ijheatfluidflow.2012.06.001.

[113] H. Yuan, S. Tan, N. Zhuang, and L. Tang, “Theoretical analysis of wall thermal inertial effects on heat transfer of pulsating laminar flow in a channel,” *Int. Commun. Heat Mass Transf.*, vol. 53, pp. 14–17, 2014, doi: 10.1016/j.icheatmasstransfer.2014.02.003.

[114] G. Li, Y. Zheng, H. Yang, and Y. Xu, “Numerical investigation of heat transfer and fluid flow around the rectangular flat plane confined by a cylinder under pulsating flow,” *J. Appl. Fluid Mech.*, vol. 9, no. 4, pp. 1569–1577, 2016, doi: 10.18869/acadpub.jafm.68.235.24140.

[115] R. Blythman, *Laminar Pulsating Flow in a Rectangular Channel*, no. October. Ph. D. Thesis, 2018.

[116] Y. Li, Q. Yu, S. Yu, B. Gong, and J. Zhang, “Numerical investigation of pulsating flow structures and heat transfer enhancement performance in spherical corrugated helical tube,” *Appl. Therm. Eng.*, vol. 213, no. December 2021, p. 118647, 2022, doi: 10.1016/j.applthermaleng.2022.118647.

[117] R. Mathie, *Unsteady and Conjugate Heat Transfer in Convective-Conductive Systems*, no. August. Ph. D. Thesis, 2012.

[118] C. Meola and G. Carlomagno, “Recent advances in the use of infrared thermography,” *Meas. Sci. Technol.*, vol. 15, p. R27, 2004, doi: 10.1088/0957-0233/15/9/R01.

[119] D. B. Donoghue, *Bubble Impingement and the mechanisms of heat transfer enhancement*, no. April. Ph. D. Thesis, 2014.

[120] M. J. Gibbons, *Electrospray Cooling and Droplet Evaporation*, no. October. Ph. D. Thesis, 2016.

[121] M. Abramowitz and I. Stegun, *Handbook of Mathematical Functions with Formulas, Graphs, and Mathematical Tables*. 1972.

[122] R. O’Reilly Meehan, *Flow Structures and Heat Transfer Enhancement in the wakes of sliding bubbles*, no. March. Ph. D. Thesis, 2016.

[123] W. M. Kays, M. E. Crawford, and B. Weigand, *Convective Heat and Mass Transfer*. Tata

McGraw-Hill Education, 2012.

[124] A. Bejan, *Convection heat transfer*. John wiley & sons, 2013.

[125] HUGHW. COLEMAN and W. GLENN STEELE, *Uncertainty Analysis for Engineers Uncertainty Analysis for Engineers*. 1989.

[126] "ANSYS CFX-Solver Theory Guide," no. August, 2017.

[127] S. M. O'Shaughnessy and A. J. Robinson, "The Influence of the Magnitude of Gravitational Acceleration on Marangoni Convection About an Isolated Bubble under a Heated Wall," *Heat Transf. Eng.*, vol. 30, no. 13, pp. 1096–1107, Nov. 2009, doi: 10.1080/01457630902922251.

[128] E. B. Denison, W. H. Stevenson, and R. W. Fox, "Pulsating laminar flow measurements with a directionally sensitive laser velocimeter," *AIChE J.*, vol. 17, no. 4, pp. 781–787, 1971, doi: 10.1002/aic.690170405.

[129] Ansys, "ANSYS CFX-Solver Modeling Guide," no. August, 2017.

[130] S. Zhang, X. Zhao, and S. Bayyuk, "Generalized formulations for the Rhie–Chow interpolation," *J. Comput. Phys.*, vol. 258, pp. 880–914, 2014, doi: https://doi.org/10.1016/j.jcp.2013.11.006.

[131] S. Alimohammadi, D. B. Murray, and T. Persoons, "Experimental validation of a computational fluid dynamics methodology for transitional flow heat transfer characteristics of a steady impinging jet," *J. Heat Transfer*, vol. 136, no. 9, pp. 1–9, 2014, doi: 10.1115/1.4027840.

[132] S. Alimohammadi, D. B. Murray, and T. Persoons, "International Journal of Thermal Sciences On the numerical e experimental analysis and scaling of convective heat transfer to pulsating impinging jets," *Int. J. Therm. Sci.*, vol. 98, pp. 296–311, 2015, doi: 10.1016/j.ijthermalsci.2015.07.022.

[133] I. B. Celik, U. Ghia, P. J. Roache, C. J. Freitas, H. Coleman, and P. E. Raad, "Procedure for estimation and reporting of uncertainty due to discretization in CFD applications," *J. Fluids Eng. Trans. ASME*, vol. 130, no. 7, pp. 0780011–0780014, 2008, doi: 10.1115/1.2960953.

[134] R. K. Shah and A. L. London, "Thermal Boundary Conditions for Laminar Duct Flow Forced Convection Heat Transfer," *J. Heat Transfer*, vol. 96, no. 2, pp. 159–165, 1974.

[135] G. L. Morini, "Thermal characteristics of slug flow in rectangular ducts," *Int. J. Therm. Sci.*, vol. 38, no. 2, pp. 148–159, 1999, doi: 10.1016/S1290-0729(99)80052-0.

[136] H. N. Hemida, M. N. Sabry, A. Abdel-Rahim, and H. Mansour, “Theoretical analysis of heat transfer in laminar pulsating flow,” *Int. J. Heat Mass Transf.*, vol. 45, pp. 1767–1780, 2002, doi: 10.1016/S0017-9310(01)00274-5.

[137] R. K. Shah, “Laminar flow friction and forced convection heat transfer in ducts of arbitrary geometry,” *Int. J. Heat Mass Transf.*, vol. 18, no. 7–8, pp. 849–862, 1975, doi: 10.1016/0017-9310(75)90176-3.

[138] J. Majdalani, “Exact Navier-Stokes solution for pulsatory viscous channel flow with arbitrary pressure gradient,” *J. Propuls. Power*, vol. 24, no. 6, pp. 1412–1423, 2008, doi: 10.2514/1.37815.

[139] P. K. Kundu, I. M. Cohen, and D. R. Dowling, *Fluid mechanics*. Academic press, 2015.

[140] O. Mamoru and K. Akira, “Lumped-parameter modeling of heat transfer enhanced by sinusoidal motion of fluid,” *Int. J. Heat Mass Transf.*, vol. 34, no. 12, pp. 3083–3095, 1991, doi: 10.1016/0017-9310(91)90078-S.

[141] L. Shi, X. Mao, and A. J. Jaworski, “Application of planar laser-induced fluorescence measurement techniques to study the heat transfer characteristics of parallel-plate heat exchangers in thermoacoustic devices,” *Meas. Sci. Technol.*, vol. 21, no. 11, 2010, doi: 10.1088/0957-0233/21/11/115405.

[142] D. Hershey and G. Song, “Friction factors and pressure drop for sinusoidal laminar flow of water and blood in rigid tubes,” *AIChE J.*, vol. 13, no. 3, pp. 491–496, 1967, doi: 10.1002/aic.690130318.

[143] P. S. Kumavat, S. Alimohammadi, and S. M. O’Shaughnessy, “A computational conjugate heat transfer study of a rectangular minichannel undergoing sinusoidal flow pulsations,” *Int. J. Therm. Sci.*, vol. 182, p. 107790, 2022, doi: 10.1016/j.ijthermalsci.2022.107790.

[144] R. Blythman, S. Alimohammadi, N. Jeffers, D. B. Murray, and T. Persoons, “Heat Transfer Analysis of Laminar Pulsating Flow in a Rectangular Channel Using Infrared Thermography,” *J. Heat Transfer*, vol. 144, no. 1, pp. 1–9, 2022, doi: 10.1115/1.4052686.

[145] P. S. Kumavat, R. Blythman, D. B. Murray, and S. M. O’Shaughnessy, “Study of Heat Transfer Enhancement by Pulsating Flow in a Rectangular Mini Channel,” in *Advances in Heat Transfer and Thermal Engineering*, 2021, pp. 253–257.

[146] P. Kumavat and S. M. O’Shaughnessy, “Experimental Investigation of Heat Transfer Enhancement by Pulsating Flow in a Minichannel,” *J. Phys. Conf. Ser.*, vol. 2116, no. 1, p.

012031, Nov. 2021, doi: 10.1088/1742-6596/2116/1/012031.

[147] F. Selimefendigil and H. F. Öztop, “Forced convection and thermal predictions of pulsating nanofluid flow over a backward facing step with a corrugated bottom wall,” *Int. J. Heat Mass Transf.*, vol. 110, pp. 231–247, 2017, doi: https://doi.org/10.1016/j.ijheatmasstransfer.2017.03.010.

[148] M. Hemmat Esfe, M. Bahiraei, A. Torabi, and M. Valadkhani, “A critical review on pulsating flow in conventional fluids and nanofluids: Thermo-hydraulic characteristics,” *Int. Commun. Heat Mass Transf.*, vol. 120, no. December 2020, p. 104859, 2021, doi: 10.1016/j.icheatmasstransfer.2020.104859.

[149] F. I. Doshmanziari, A. E. Zohir, H. R. Kharvani, D. Jalali-Vahid, and M. R. Kadivar, “Characteristics of heat transfer and flow of Al2O3/water nanofluid in a spiral-coil tube for turbulent pulsating flow,” *Heat Mass Transf.*, vol. 52, no. 7, pp. 1305–1320, 2016, doi: 10.1007/s00231-015-1651-y.

[150] Q. Ye, Y. Zhang, and J. Wei, “A comprehensive review of pulsating flow on heat transfer enhancement,” *Appl. Therm. Eng.*, vol. 196, no. May, p. 117275, 2021, doi: 10.1016/j.applthermaleng.2021.117275.

Appendix A

A.1 Tensioning Mechanism Instructions:

The test setup preparation involves an ordered arrangement of the plate profiles. Foremost, the painted foil is placed and clamped between the bus bars and a layer of Silver conductive grease. This arrangement is then shifted onto the heater support plate where the foil gets tensioned thoroughly using the spring-loaded tensioning mechanism. The foil needs to be ensured that it is crease-free throughout its axial length. The base section of heater support plate and aluminium support profile is clamped together. The acrylic channel profile fitted with an O-ring, is placed on the top of the foil and the entire arrangement of plates is secured. On the exterior regions, a few gaskets and soft printed blocks are placed such that the exposed areas of the foil are covered from the ambient and a thermally stable system can be maintained.

A.2 Additional Results and Discussions:

Figure 0-1 and Figure 0-2 respectively represent flow fields resulting from the leading asymmetric sinusoidal waveforms at a frequency of 0.02 *Hz* ($Wo = 0.5$) and flow rate amplitudes of $A_0 = 0.5, 3$. These flows exhibit quasi-steady behaviour due to the prominence of viscous effects and the resulting oscillating velocity profiles resemble the parabolic profiles of a conventional laminar duct flow. For this pulsation waveform at $A_0 = 3$, the oscillating velocity profiles respond quicker to the stronger oscillation component as is evident from the core region $x/b = 0$. However, the effects of the asymmetric characteristics are inconclusive from the velocity contours and vectors, and they resemble closely the profiles resulting from the symmetric sinusoidal pulsation. This is due to a slow-moving pulsation as the time scale of pulsation is longer than viscous time scales. An increase in the near-wall velocity gradients as an effect of the stronger oscillation with presence of high near-wall velocities is seen from the shear stress magnitude contours and profiles.

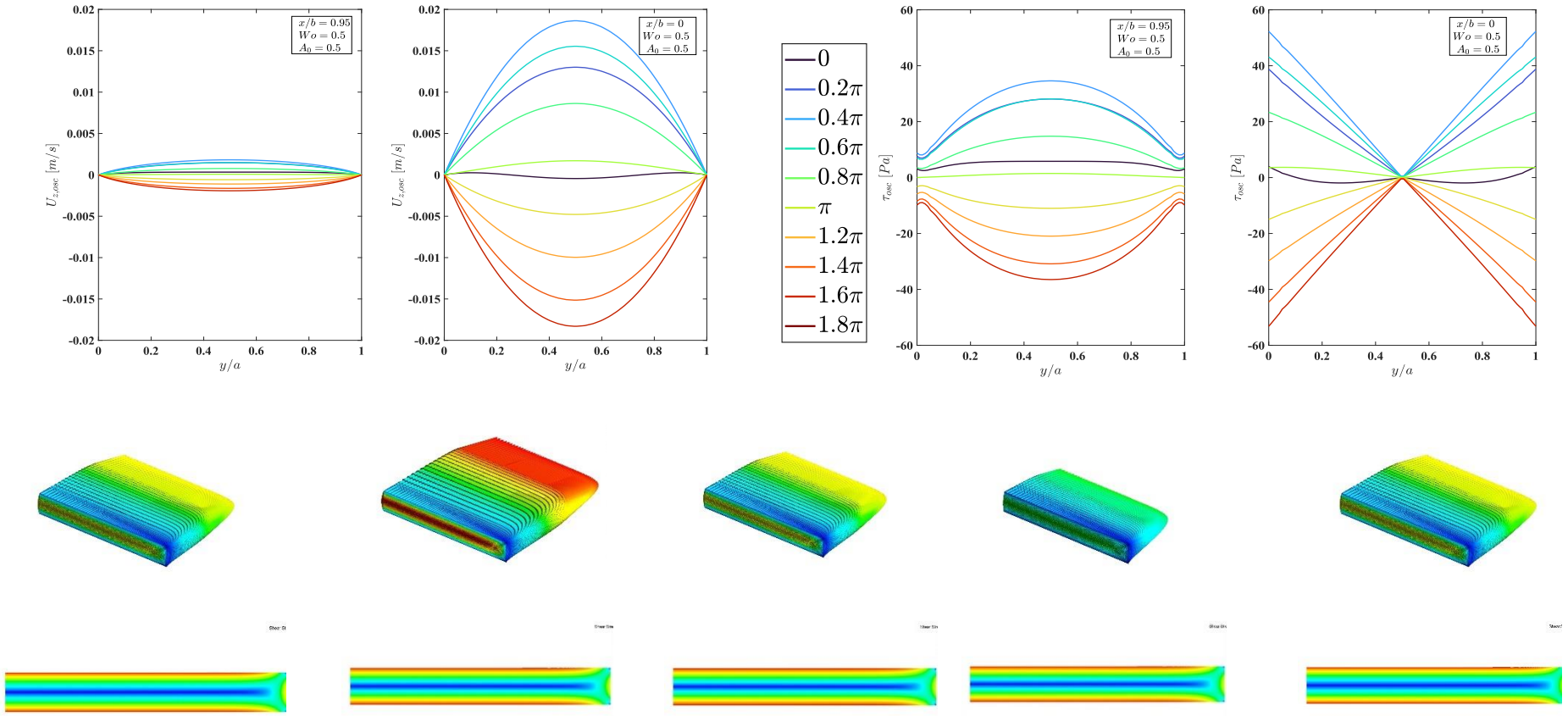

Figure 0-1: Leading Asymmetric sinusoidal waveform with flow rate amplitude $A_0 = 0.5$ and frequency 0.02 Hz ($Wo = 0.5$). (Top row) oscillating axial velocity ($U_{z,osc}$) and fluid shear stress (τ_{osc}) profiles along the duct height (y/a) for near-side-wall ($x/b = 0.95$) and central ($x/b = 0$) regions. (Middle row) pulsating velocity contour plots at z = 300mm for 5 phases of a pulsation, and (bottom row) corresponding fluid shear stress contours.

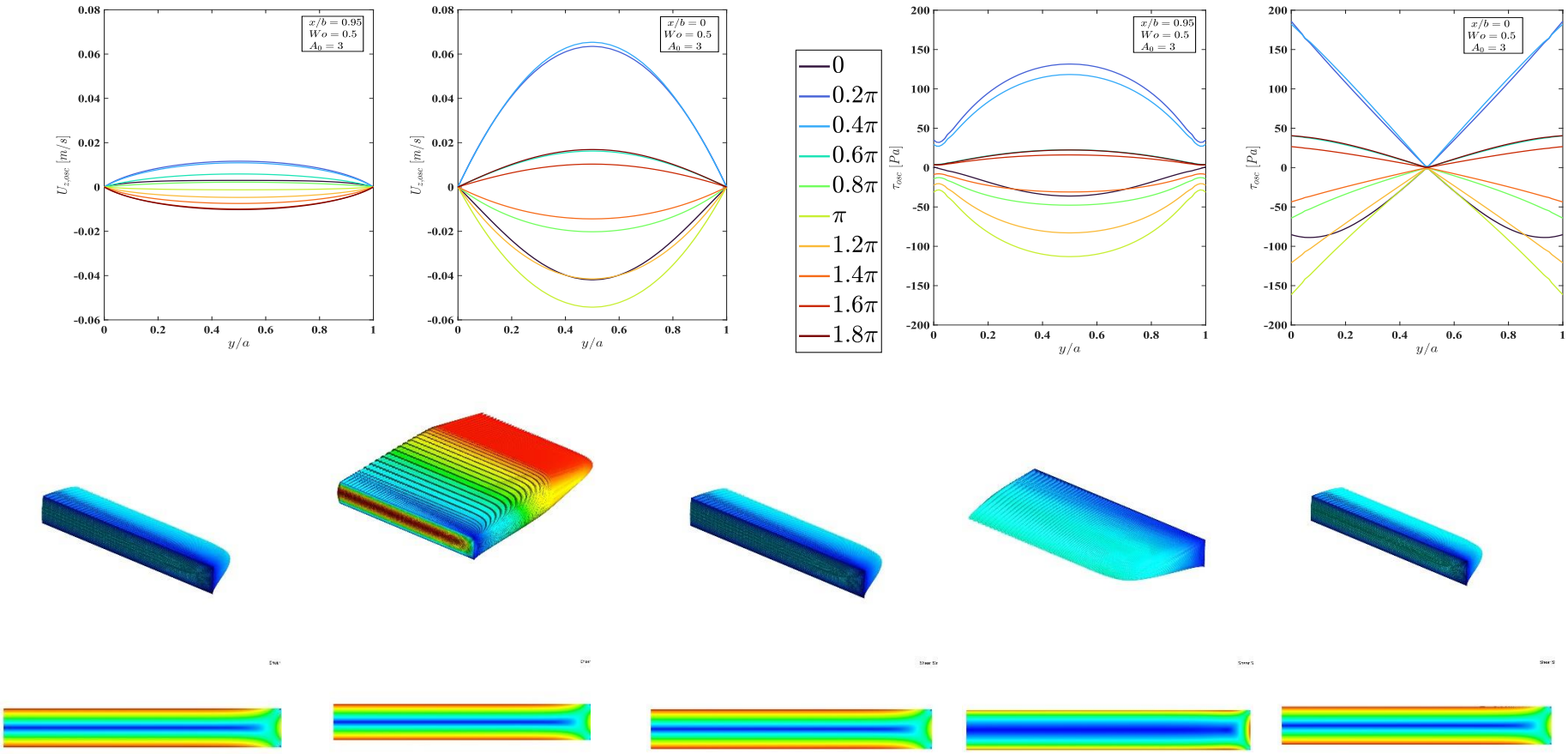

Figure 0-2: Leading Asymmetric sinusoidal waveform with flow rate amplitude $A_0 = 3$ and frequency 0.02 Hz ($Wo = 0.5$). (Top row) oscillating axial velocity ($U_{z,osc}$) and fluid shear stress (τ_{osc}) profiles along the duct height (y/a) for near-side-wall ($x/b = 0.95$) and central ($x/b = 0$) regions. (Middle row) pulsating velocity contour plots at z = 300mm for 5 phases of a pulsation, and (bottom row) corresponding fluid shear stress contours.

Figure 0-3 and Figure 0-4 respectively represent flow fields resulting from lagging asymmetric sinusoidal waveforms at a frequency of 0.02 *Hz* ($Wo = 0.5$) and flow rate amplitudes of $A_0 = 0.5, 3$. For lagging asymmetric profiles, the velocity profiles resemble those obtained for the symmetric sinusoidal waveform as the sharper impulse of oscillation occurring at interval π is less effective due to longer displacement time scales. Although the shear stress contours highlight the strong amplification of near wall velocity gradients at phase π. Figure 0-5 and Figure 0-6 respectively represent flow fields resulting from lagging asymmetric sinusoidal waveforms at a frequency of 0.5 *Hz* ($Wo = 2.5$) and flow rate amplitudes of $A_0 = 0.5, 3$. However, the lagging asymmetric case presents a sharp increase in the velocity magnitude during the acceleration stage of the cycle, *i.e.*, for phases $0 - \pi$ compared to the deceleration stage. The steep shift in fluid momentum is in agreement with the observed nature of the temporal profiles for $Wo = 2.5$. Correspondingly an increase in the velocity gradients is noticed for both near wall $x/b = 0.95$ and channel core $x/b = 0$ regions compared to the cases of symmetric sinusoidal and lagging asymmetric.

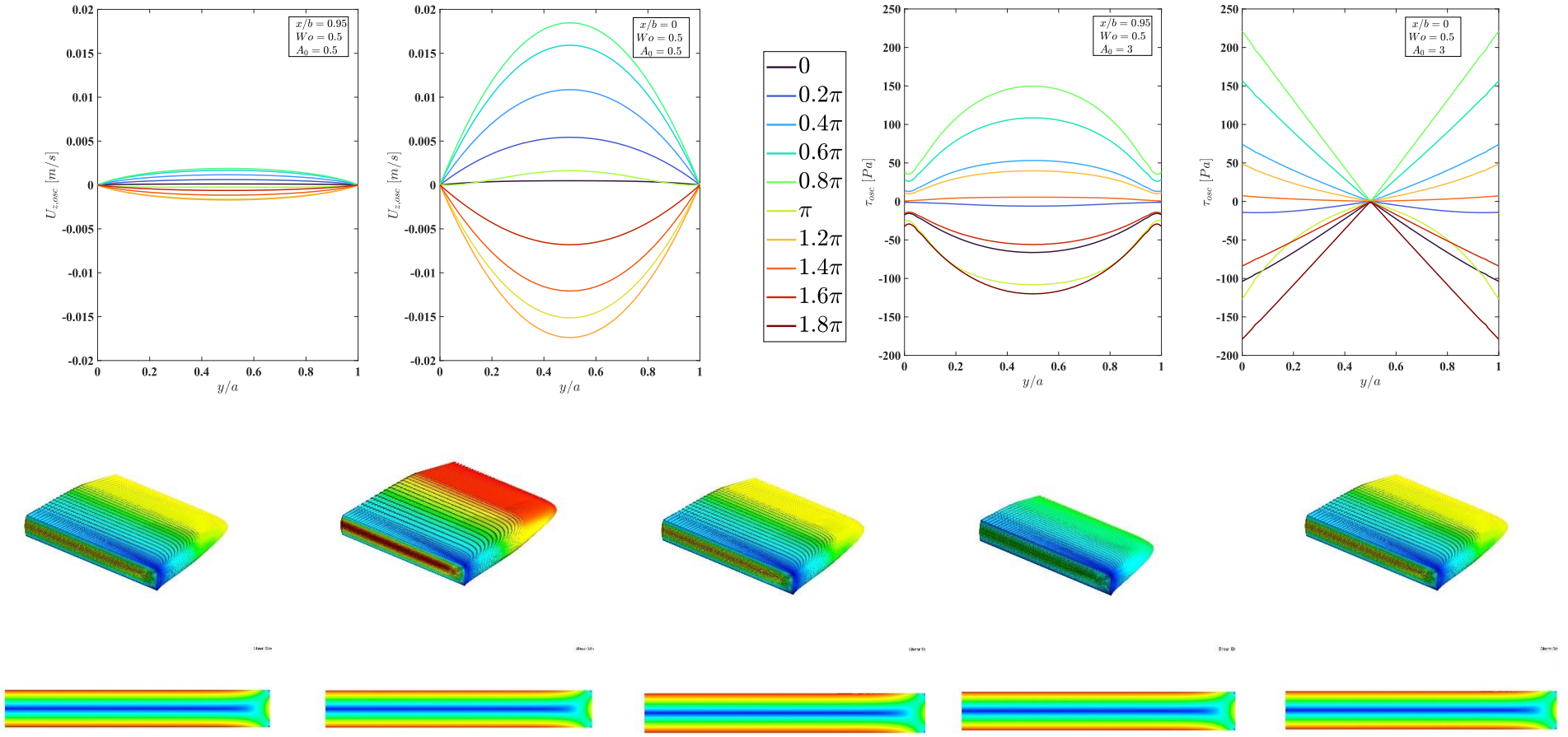

Figure 0-3: Lagging Asymmetric sinusoidal waveform with flow rate amplitude $A_0 = 0.5$ and frequency 0.02 Hz ($Wo = 0.5$). (Top row) oscillating axial velocity ($U_{z,osc}$) and fluid shear stress (τ_{osc}) profiles along the duct height (y/a) for near-side-wall ($x/b = 0.95$) and central ($x/b = 0$) regions. (Middle row) pulsating velocity contour plots at z = 300mm for 5 phases of a pulsation, and (bottom row) corresponding fluid shear stress contours.

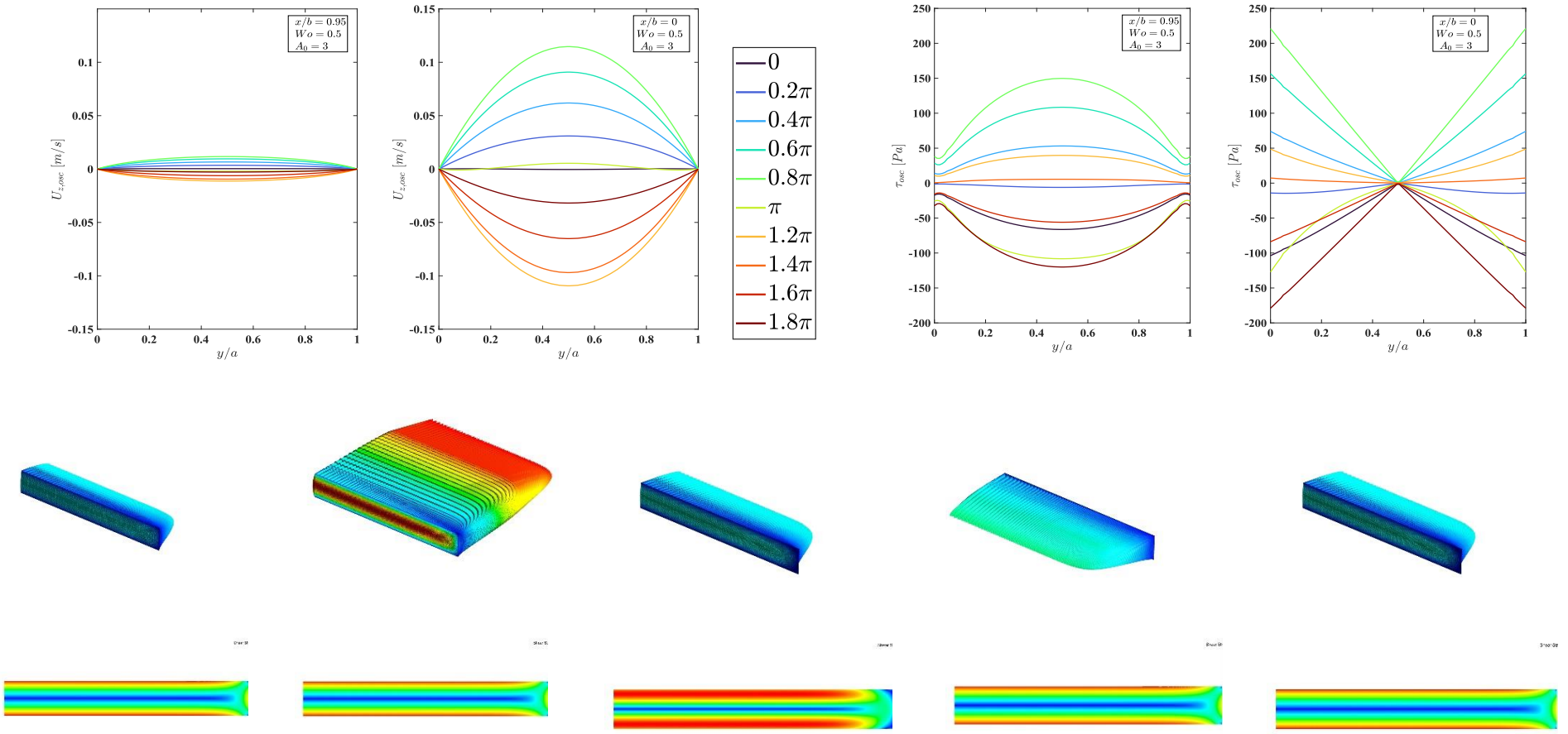

Figure 0-4: Lagging Asymmetric sinusoidal waveform with flow rate amplitude $A_0 = 0.5$ and frequency 0.02 Hz ($Wo = 0.5$). (Top row) oscillating axial velocity ($U_{z,osc}$) and fluid shear stress (τ_{osc}) profiles along the duct height (y/a) for near-side-wall ($x/b = 0.95$) and central ($x/b = 0$) regions. (Middle row) pulsating velocity contour plots at z = 300mm for 5 phases of a pulsation, and (bottom row) corresponding fluid shear stress contours.

Figure 0-5 and Figure 0-6 respectively represent flow fields resulting from lagging asymmetric sinusoidal waveforms at a frequency of 0.5 *Hz* ($Wo = 2.5$) and flow rate amplitudes of $A_0 = 0.5,3$.

However, the lagging asymmetric case presents a sharp increase in the velocity magnitude during the acceleration stage of the cycle i.e., for phases $0 - \pi$ compared to the deceleration stage. The steep shift in fluid momentum is in agreement with the observed nature of temporal profiles for $Wo = 2.5$. Correspondingly an increase in the velocity gradients is noticed for both near wall $x/b = 0.95$ and channel core $x/b = 0$ regions compared to the cases of symmetric sinusoidal and lagging asymmetric.

For the case of lagging asymmetric pulsation, the oscillating velocity profiles react in the similar manner to the low flowrate amplitude case i.e., with a minor phase shift between the near-wall and core regions. Although the features of the asymmetry are not widely evident either from the velocity profiles or from the contours and vectors. This can be attributed to the fact due to a rapid shift in the fluid momentum during both the acceleration and deceleration stage as a result of the high pulsation amplitude. The flow is unable to respond swiftly to the longer fluid displacement timescales of the moderate frequency and thus a pseudo-sinusoidal behaviour exists. However, the shear stress magnitudes reflect increased velocity gradients compared to the low flowrate amplitudes during both the accelerating and decelerating stages of oscillation. A higher velocity gradient exits for the core region at $x/b = 0$ and a resulting phase lag is observed with the pressure gradient as seen in Figure 7-2 (temporal plots), following the similar understanding of the leading asymmetry.

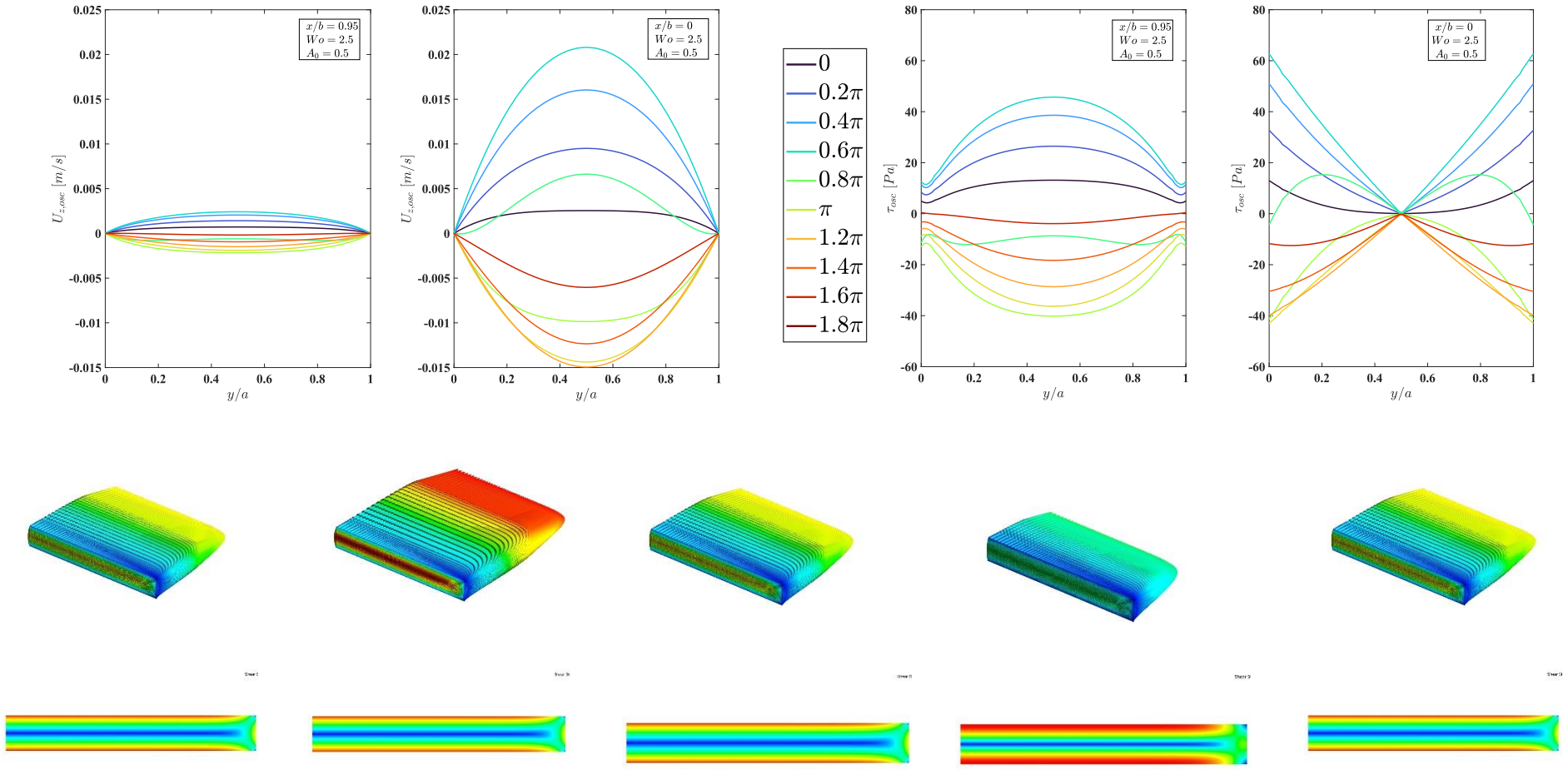

Figure 0-5: Lagging Asymmetric sinusoidal waveform with flow rate amplitude $A_0 = 0.5$ and frequency 0.5 Hz ($Wo = 2.5$). (Top row) oscillating axial velocity ($U_{z,osc}$) and fluid shear stress (τ_{osc}) profiles along the duct height (y/a) for near-side-wall ($x/b = 0.95$) and central ($x/b = 0$) regions. (Middle row) pulsating velocity contour plots at z = 300mm for 5 phases of a pulsation, and (bottom row) corresponding fluid shear stress contours.

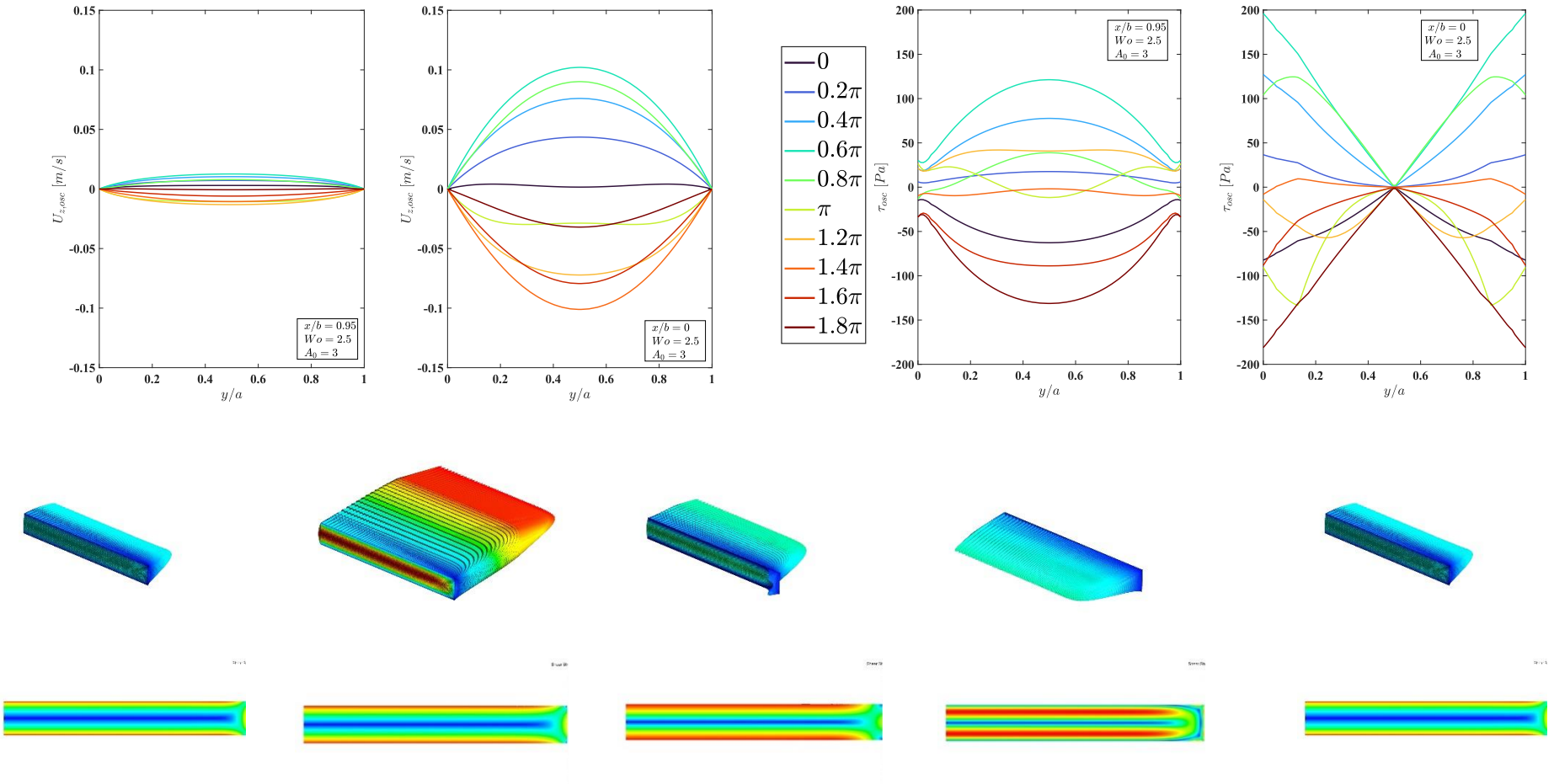

Figure 0-6: Lagging Asymmetric sinusoidal waveform with flow rate amplitude $A_0 = 3$ and frequency 0.5 Hz ($Wo = 2.5$). (Top row) oscillating axial velocity ($U_{z,osc}$) and fluid shear stress (τ_{osc}) profiles along the duct height (y/a) for near-side-wall ($x/b = 0.95$) and central ($x/b = 0$) regions. (Middle row) pulsating velocity contour plots at z = 300mm for 5 phases of a pulsation, and (bottom row) corresponding fluid shear stress contours.

Figure 0-7 and Figure 0-8 respectively represent flow fields resulting from positive half rectified waveforms at a frequency of 0.02 *Hz* ($Wo = 0.5$) and flow rate amplitudes of $A_0 = 0.5, 3$. For $A_0 = 0.5$, (see Figure 0-7) a parabolic oscillating velocity profile is obtained as was demonstrated by the other waveforms at $Wo = 0.5$. A peak in velocity magnitude is evident during the acceleration stage between $\pi - 1.8\pi$ which corresponds to the sinusoidal component of the profile. The near-wall velocities are in phase with the core regions and show substantially reduced magnitudes due to the presence of high near-wall viscous effects and. The pronounced effect of the steady component over the oscillation component is evident from the velocity contours for phases $0, \pi/2, \pi, 2\pi$ with an impulse acceleration of sinusoidal component at $3\pi/2$. Increased velocity gradients are observed in the near-wall regions compared to the other waveforms which is due to the characteristics associated with the combined effect of steady and sinusoidal components of the viscous dominated half rectification. The influence of a high oscillation amplitude at $A_0 = 3$ (see Figure 0-8) can be deduced clearly from the oscillating velocity profiles in the core region at $x/b = 0$, wherein the acceleration stage presents a sharp peak magnitude and similarly the velocity contours and vectors show a stronger effect of acceleration at phase $3\pi/2$, whereas the weaker response of the steady flow component is seen for the other phases.

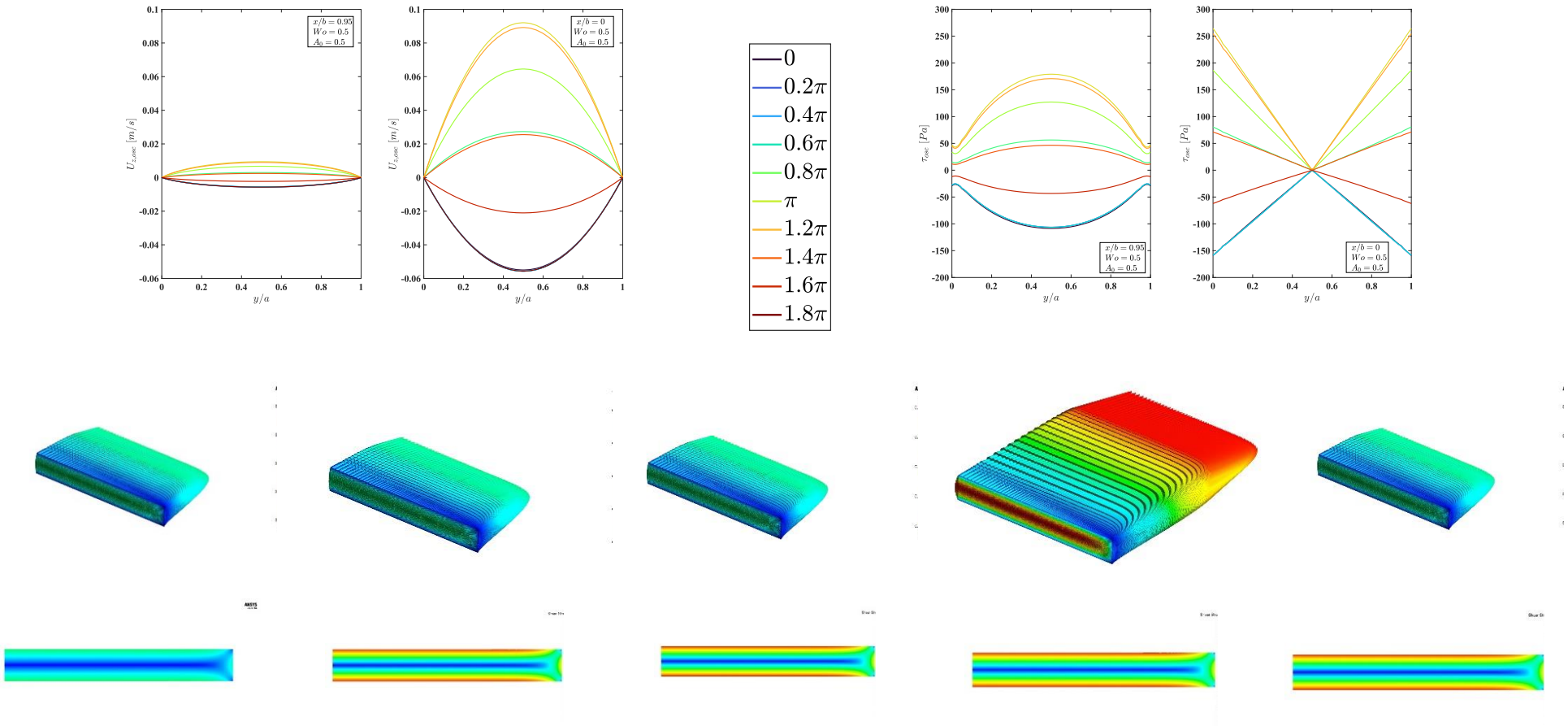

Figure 0-7: Positive half rectified sinusoidal waveform with flow rate amplitude $A_0 = 0.5$ and frequency 0.02 Hz ($Wo = 0.5$). (Top row) oscillating axial velocity ($U_{z,osc}$) and fluid shear stress (τ_{osc}) profiles along the duct height (y/a) for near-side-wall ($x/b = 0.95$) and central ($x/b = 0$) regions. (Middle row) pulsating velocity contour plots at z = 300mm for 5 phases of a pulsation, and (bottom row) corresponding fluid shear stress contours.

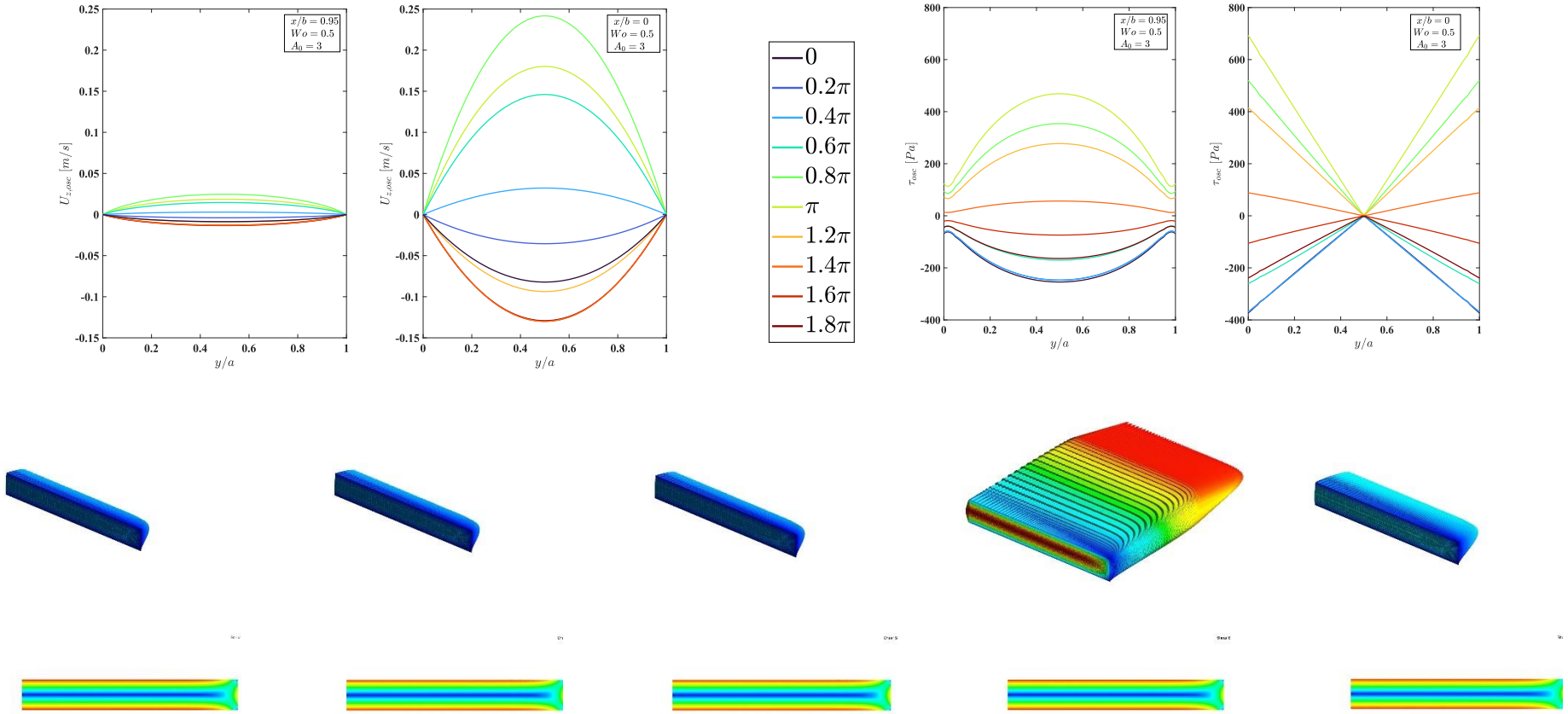

Figure 0-8: Positive half rectified sinusoidal waveform with flow rate amplitude $A_0 = 3$ and frequency 0.02 Hz ($Wo = 0.5$). (Top row) oscillating axial velocity ($U_{z,osc}$) and fluid shear stress (τ_{osc}) profiles along the duct height (y/a) for near-side-wall ($x/b = 0.95$) and central ($x/b = 0$) regions. (Middle row) pulsating velocity contour plots at z = 300mm for 5 phases of a pulsation, and (bottom row) corresponding fluid shear stress contours.

Figure 0-9, Figure 0-10 respectively represent flow fields resulting from negative half rectified waveforms at a frequency of 0.02 *Hz* ($Wo = 0.5$) and flow rate amplitudes of $A_0 = 0.5, 3$.Similarities of understanding from the cases of positive half rectified waveforms can be drawn for the negative half rectified waveform at $A_0 = 0.5$ (Figure 0-9) which presents a maximum velocity magnitude during the deceleration cycle $\pi - 1.8\pi$ due to an increase in the withdrawal effect as a part of the sinusoidal component of the profile. The stronger steady underflow of the pulsation is seen from the velocity contours and vectors for phases $0, \pi/2, \pi, 2\pi$. Only a minor effect of the weaker decelerating sinusoidal flow component is seen on the pulsation for phase $3\pi/2$. In line with the understanding from positive half rectification, high magnitudes of shear stress magnitudes are obtained for the half rectified waveform in contrast to the sinusoidal and asymmetric profiles. At a high flowrate amplitude of $A_0 = 3$ (Figure 0-10), the oscillation velocity profiles show an increase in the magnitudes during the deceleration stage. Similarly, the velocity contours and vectors present a stronger effect on the backward directed flow attaining a maximum at phase $3\pi/2$. A substantial increase in the magnitudes of shear stress contours and profiles is evident in the near-wall regions of the viscous dominated flow.

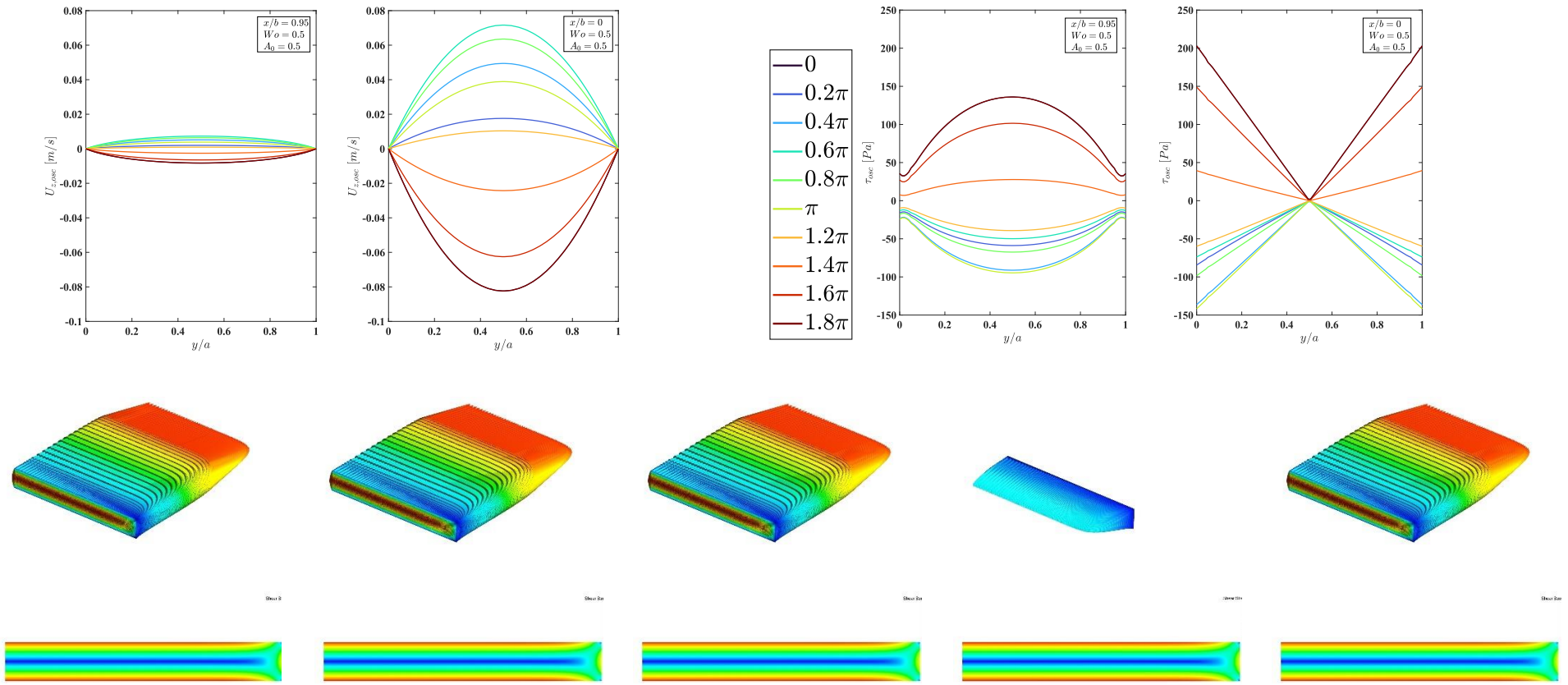

Figure 0-9: Negative half rectified sinusoidal waveform with flow rate amplitude $A_0 = 0.5$ and frequency 0.02 Hz ($Wo = 0.5$). (Top row) oscillating axial velocity ($U_{z,osc}$) and fluid shear stress (τ_{osc}) profiles along the duct height (y/a) for near-side-wall ($x/b = 0.95$) and central ($x/b = 0$) regions. (Middle row) pulsating velocity contour plots at z = 300mm for 5 phases of a pulsation, and (bottom row) corresponding fluid shear stress contours.

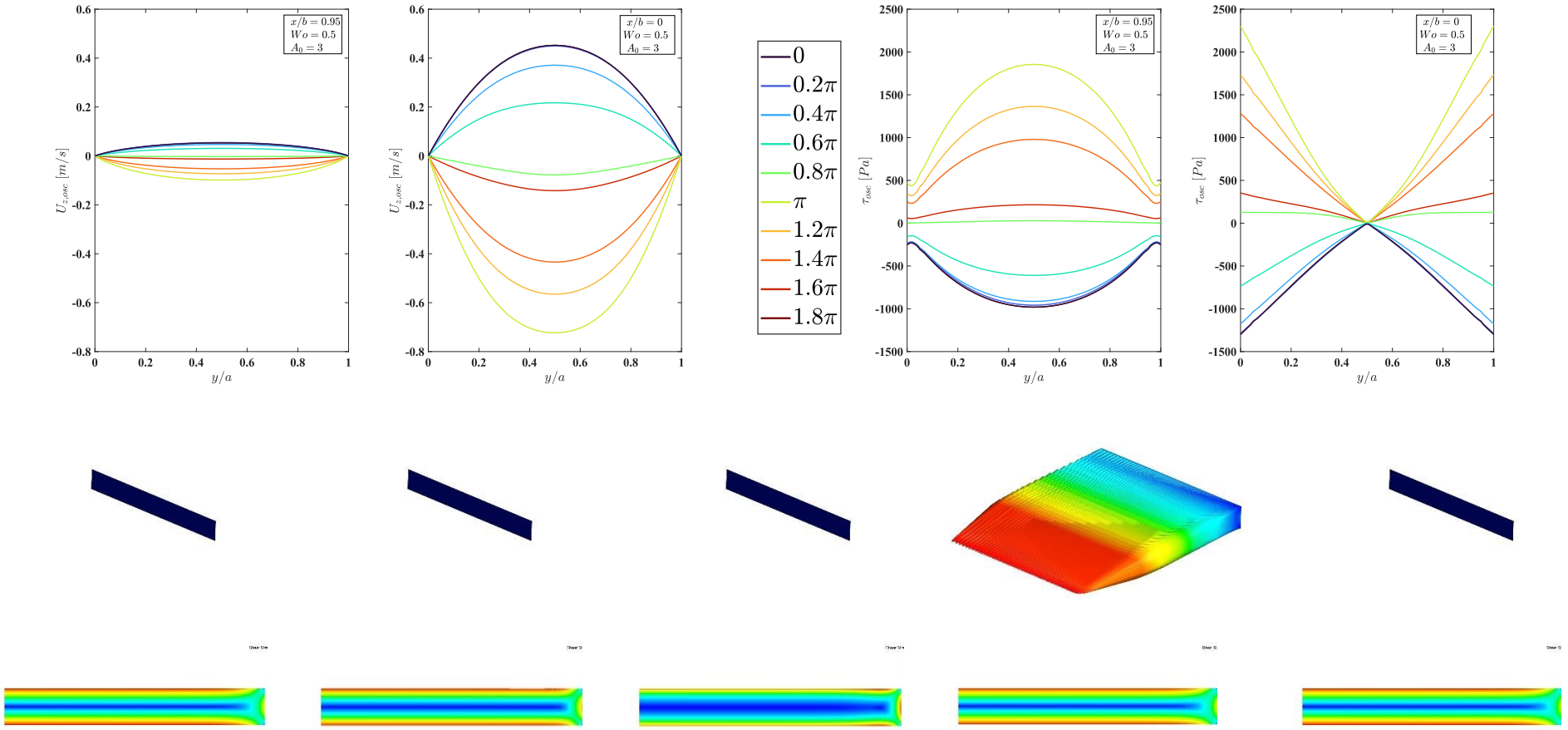

Figure 0-10: Negative half rectified sinusoidal waveform with flow rate amplitude $A_0 = 3$ and frequency 0.02 Hz ($Wo = 0.5$). (Top row) oscillating axial velocity ($U_{z,osc}$) and fluid shear stress (τ_{osc}) profiles along the duct height (y/a) for near-side-wall ($x/b = 0.95$) and central ($x/b = 0$) regions. (Middle row) pulsating velocity contour plots at z = 300mm for 5 phases of a pulsation, and (bottom row) corresponding fluid shear stress contours.

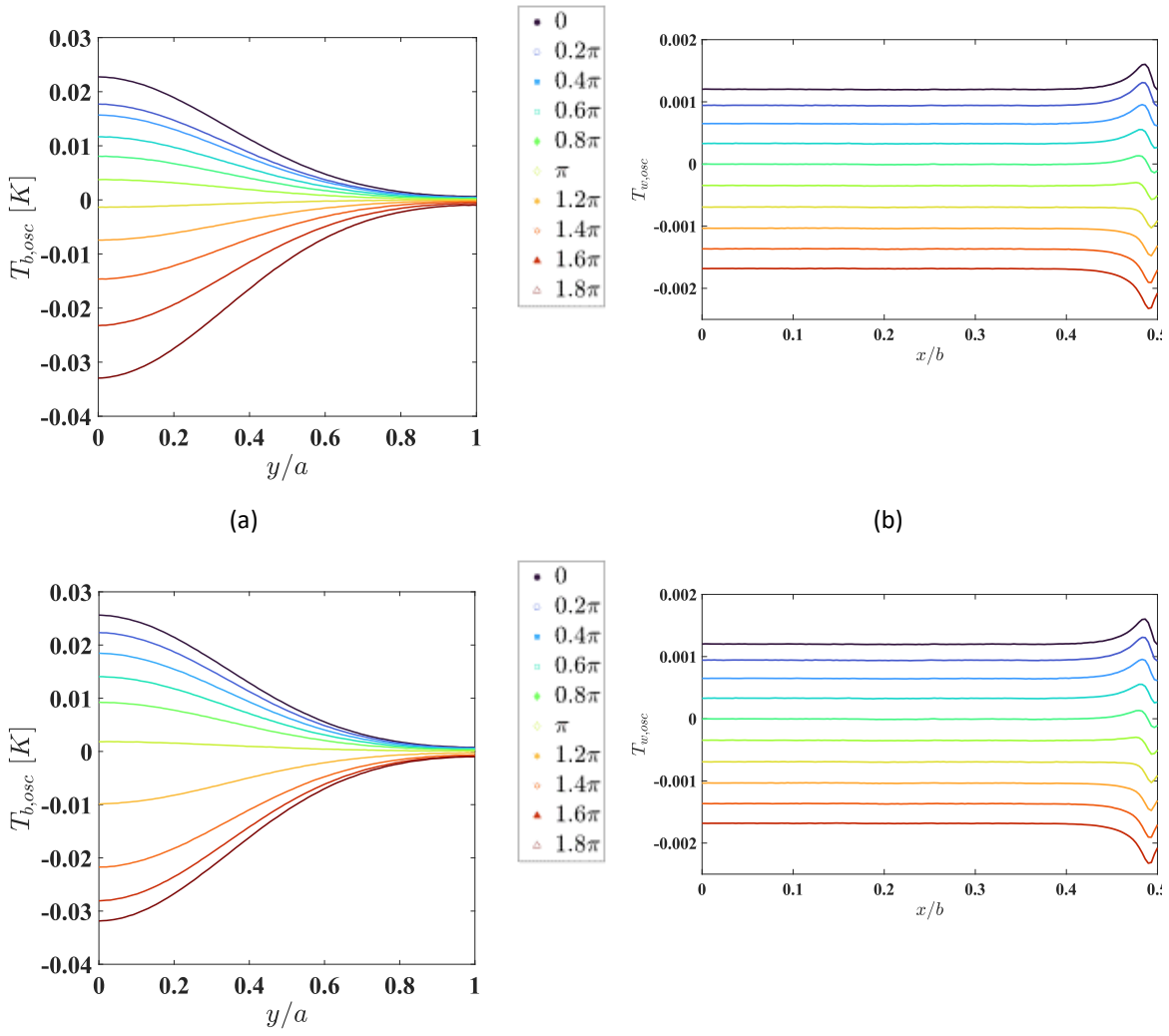

Figure 0-11: Leading asymmetric sinusoidal waveform with flowrate amplitude $A_0 = 0.5, 3$ (top, middle, bottom row respectively) and frequency 25 Hz ($Wo = 18.3$). All lines represent CFD data. Markers represent experimental data. (LEFT) Oscillating bulk temperature profile vs. normalised minichannel height (y/a) at $x/b = 0$. (RIGHT) Oscillating temperature profiles at the heated wall ($y/a = 0$) along the normalised spanwise direction (x/b).

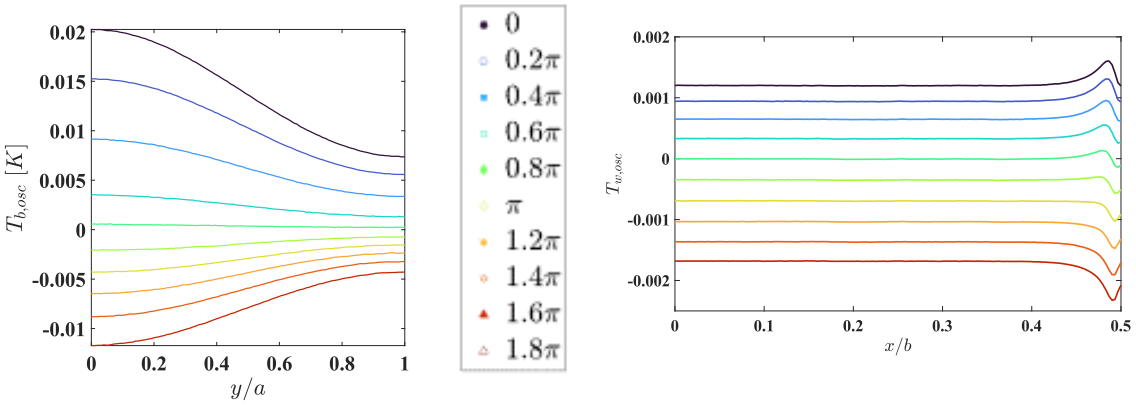

(a) (b)

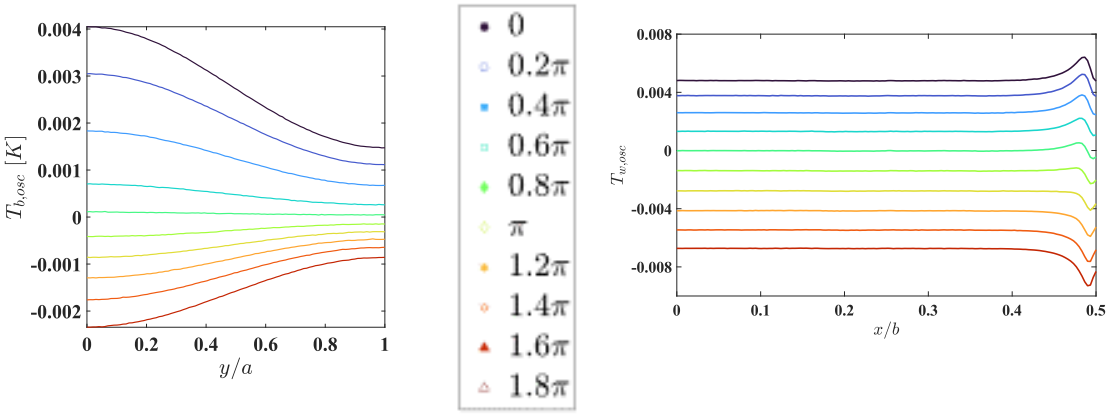

(c) (d)

Figure 0-12: Lagging asymmetric sinusoidal waveform with flowrate amplitude $A_0 = 0.5, 3$ (top, middle, bottom row respectively) and frequency 2 Hz ($Wo = 5.1$). All lines represent CFD data. Markers represent experimental data. (LEFT) Oscillating bulk temperature profile vs. normalised minichannel height (y/a) at $x/b = 0$. (RIGHT) Oscillating temperature profiles at the heated wall ($y/a = 0$) along the normalised spanwise direction (x/b).

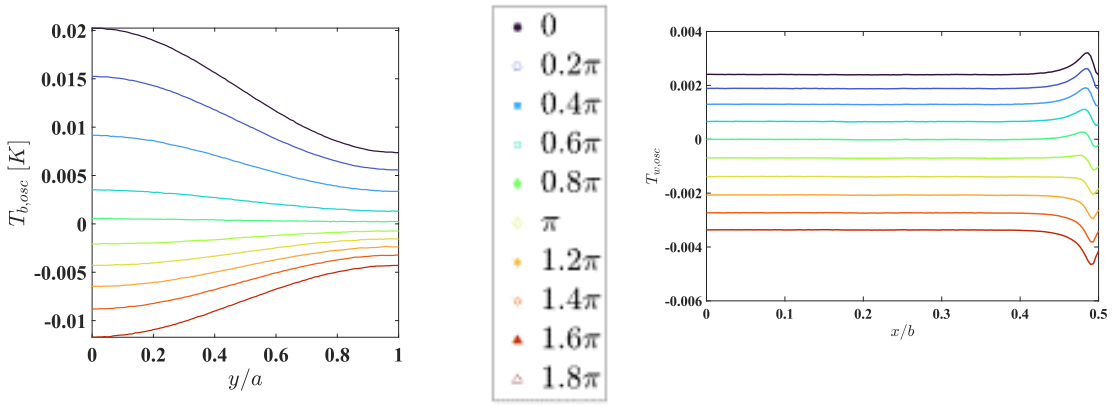

(a) (b)

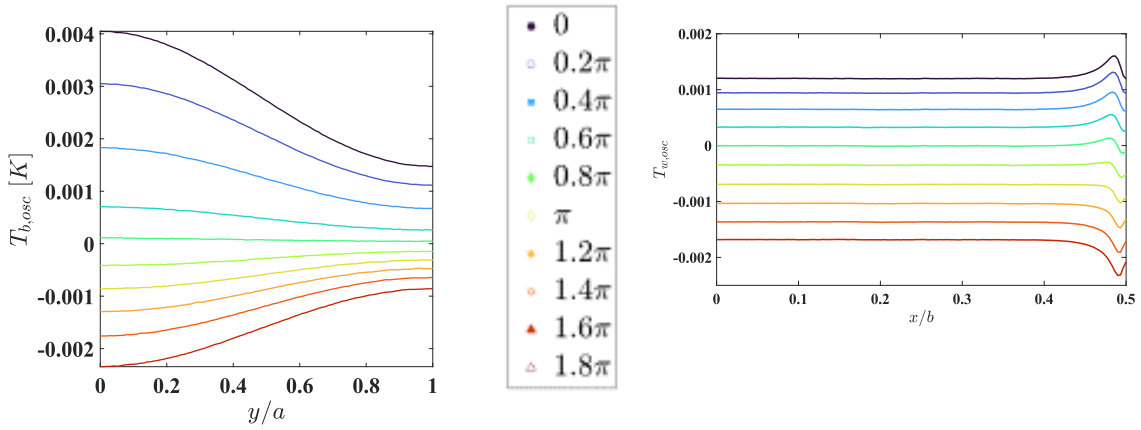

(c) (d)

Figure 0-13: Positive half rectified waveform with flowrate amplitude $A_0 = 0.5, 3$ (top, middle, bottom row respectively) and frequency 0.02 Hz ($Wo = 0.5$). All lines represent CFD data. Markers represent experimental data. (LEFT) Oscillating bulk temperature profile vs. normalised minichannel height (y/a) at $x/b = 0$. (RIGHT) Oscillating temperature profiles at the heated wall ($y/a = 0$) along the normalised spanwise direction (x/b).

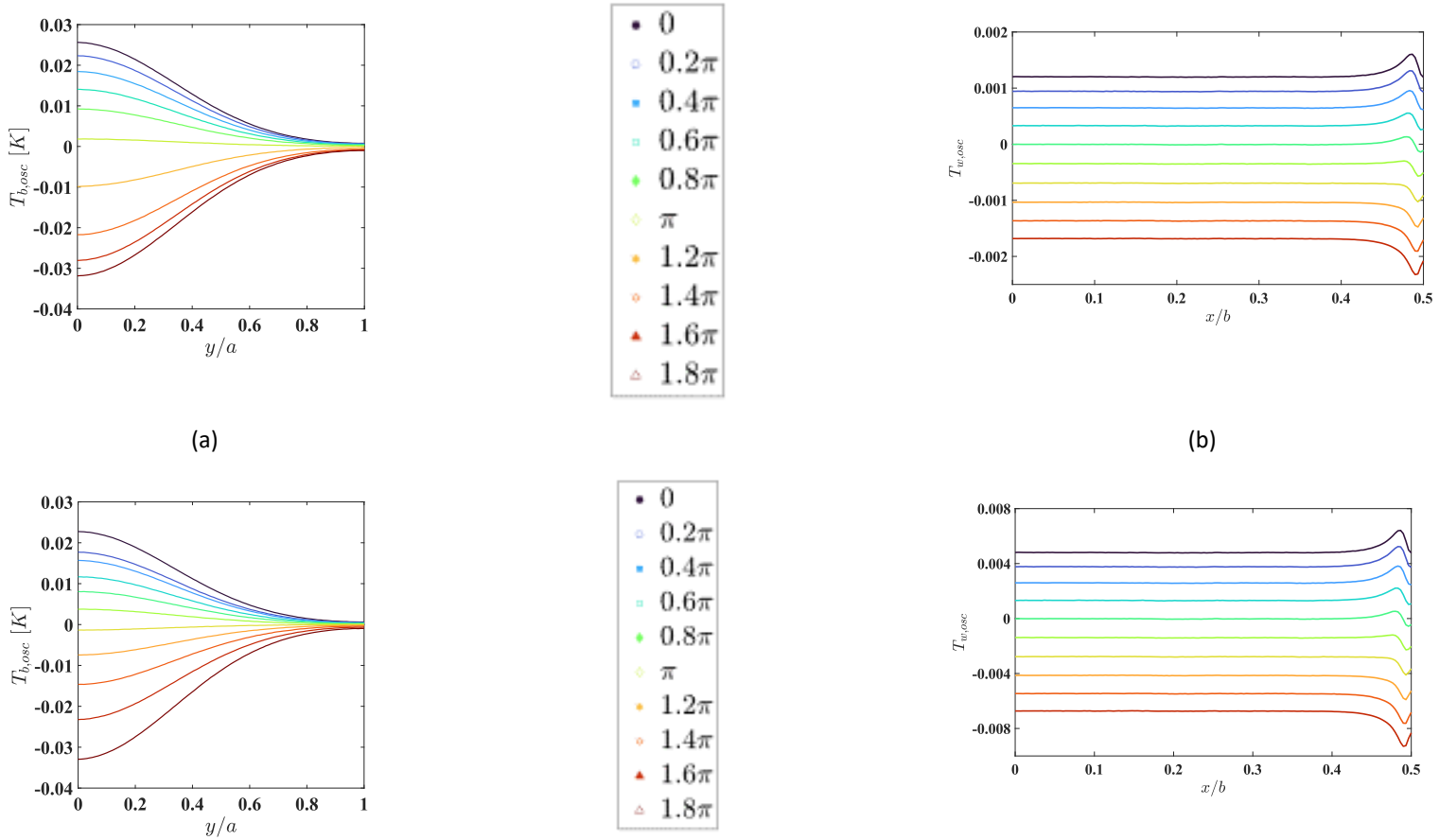

Figure 0-14: Negative half rectified waveform with flowrate amplitude $A_0 = 0.5, 3$ (top, middle, bottom row respectively) and frequency 25 Hz ($Wo = 18.3$). All lines represent CFD data. Markers represent experimental data. (LEFT) Oscillating bulk temperature profile vs. normalised minichannel height (y/a) at $x/b = 0$. (RIGHT) Oscillating temperature profiles at the heated wall ($y/a = 0$) along the normalised spanwise direction (x/b).

Figure 0-15 (a-d) (**appendix**) respectively represent the spatial and spanwise variation of temperature profiles resulting from negative half rectified waveform at a frequency of 0.02 *Hz* ($Wo = 0.5$) and flow rate amplitudes of $A_0 = 0.5{,}3$. For a viscous dominated low frequency flow, similarities in the feature exists between the oscillating velocity profiles as seen from (Figure 0-9 and Figure 0-10) and the wall temperature profiles. Low frequency flows are typically exhibit significant amount of heat diffusion from the bottom wall to the core bulk fluid. Additionally, the thermal diffusion time scales are shorter compared to the longer pulsation periods and due to a low wall thermal inertia. This phenomenon leads to a substantial increase in the bulk fluid temperature as is evident from Figure 7-50 (a) similar in agreement with the symmetric sinusoidal cases. During the onset of the semi-sinusoidal acceleration-deceleration stage for phases $\pi \leq \theta \leq 2\pi$, the bulk temperature of fluid shows a minimal change as the oscillation amplitude is weaker compared to the steady due to colder fluid entering the heated section as an effect to the low frequency pulsation. The bulk temperature settles with a uniform distribution along the spatial region due to the prevalence of increased diffusion of heat laterally. The oscillating wall temperatures reflect a gradual change in the spanwise direction and thus the effects of an oscillating component are not significantly evident.

On increasing the A_0, the wall temperature magnitudes decrease. The effect of oscillation is further amplified due to the influx of higher flowrate of the colder fluid in the heated channel. Similarly, the oscillating bulk temperatures reflect a drop in the magnitudes as enhanced forced convection cooling is evident.

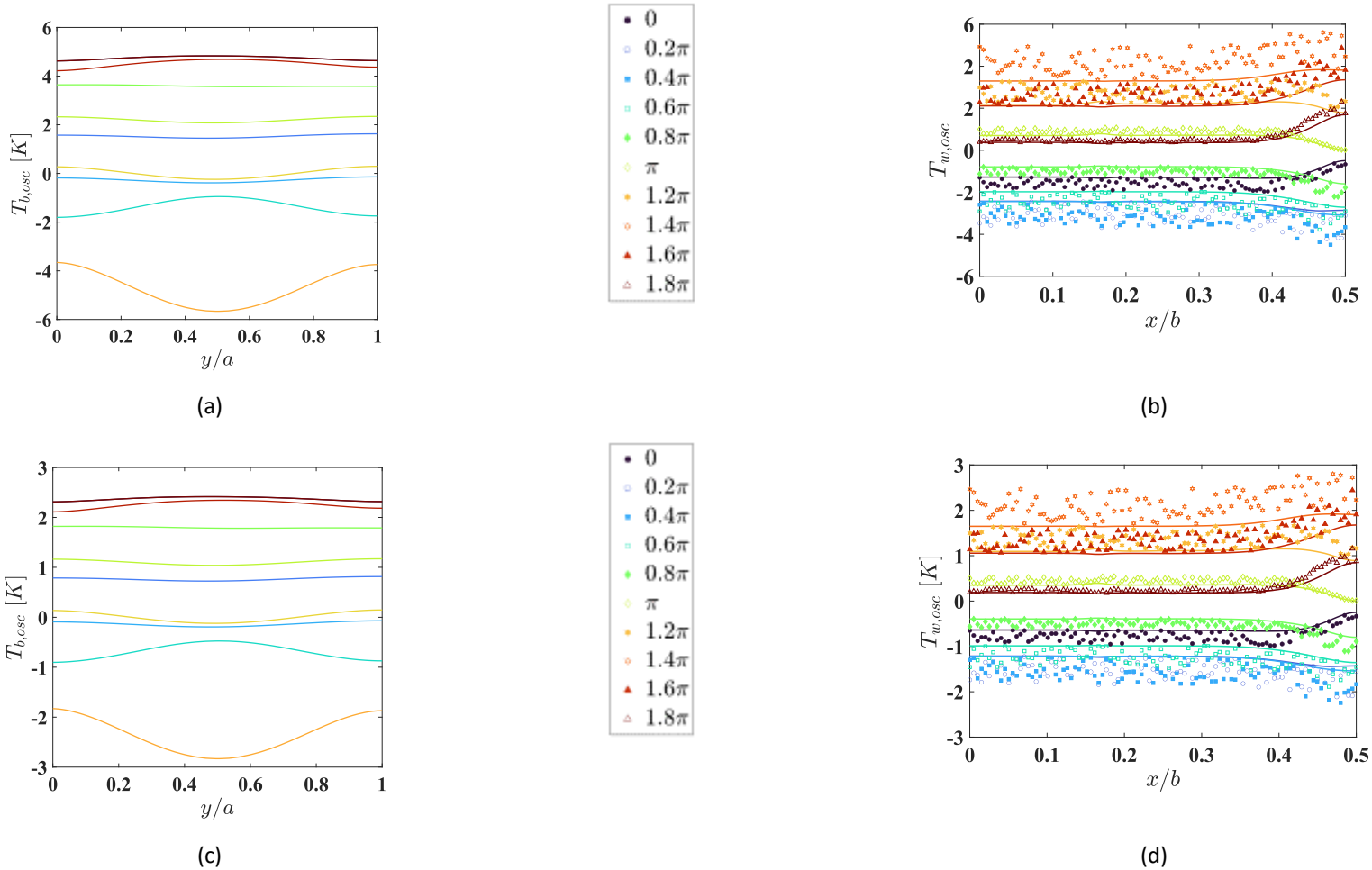

Figure 0-15: Negative half rectified waveform with flowrate amplitude $A_0 = 0.5, 3$ (top, middle, bottom row respectively) and frequency 0.02 Hz ($Wo = 0.5$). All lines represent CFD data. Markers represent experimental data. (LEFT) Oscillating bulk temperature profile vs. normalised minichannel height (y/a) at $x/b = 0$. (RIGHT) Oscillating temperature profiles at the heated wall ($y/a = 0$) along the normalised spanwise direction (x/b).